Jihočeská univerzita v Českých Budějovicích

Přírodovědecká fakulta

Mitochondrial adaptations throughout the *Trypanosoma brucei* life cycle

Habilitační práce

RNDr. Alena Panicucci Zíková, Ph.D

2022

Table of Contents

Acknowledgments

I would like to thank the current and former team members for their daily commitment, enthusiasm for science, stimulating discussions, and pleasant working environment. It has been a pleasure to be surrounded by them.

I would like to thank my collaborators and colleagues from different institutions across the continents for broadening my horizons, sharing their personal and scientific experiences, and shaping me as a scientist. Thanks to the fruitful collaborations across various fields of science, my work is incredibly colorful.

Last but not least, I would like to thank my husband Brian for always pushing me to take the next step and my whole family for their tireless support and love.

A summary of my research to date

I was introduced to the world of trypanosomatid parasites by Prof. Julius Lukeš when I was a master's student. As a young student, I was fascinated by the biology of parasites and intrigued by the new possibilities of molecular biology. RNAi interference had just been introduced in *Trypanosoma brucei*, making it feasible to decipher the functions of individual genes. Suddenly it was possible to find out what makes trypanosomes such successful parasites. My scientific path was sealed. After a fruitful postdoctoral stay in the USA, where I was involved in mapping the mitochondrial proteome of *T. brucei*, I decided to accept the offer to become a group leader and develop my independent research projects.

The early days of my independent carrier proved to be very challenging in terms of equipping the laboratory, hiring students, and obtaining grants. Nevertheless, in the first five years, I managed to procure several exceptional grants that enabled me to build a coherent and competent research team equipped with the necessary equipment. Gradually, the laboratory grew and gained recognition in the field of parasitology and mitochondrial bioenergetics, which helped to create a network of established scientists in the Czech Republic and abroad.

My lab utilizes *Trypanosoma brucei*, a powerful model organism that naturally progresses through distinct life cycle forms as it adapts to the various nutritional availabilities and temperature differences encountered in the bloodstream of their mammalian hosts and their insect vector, a tsetse fly. Importantly, it possesses just a single mitochondrion that undergoes striking changes in both its energy metabolism and mitochondrial ultrastructure throughout the parasite life cycle.

One of the main topics in the lab is to elucidate how the metabolic rewiring of *T. brucei* generates mitochondrial signals that are propagated throughout the cell to drive parasite differentiation. This retrograde signaling consists of bioenergetic and metabolic by-products (e.g. reactive oxygen species, tricarboxylic acid cycle intermediates) that are able to post-translationally modify proteins affecting their activity, localization, and stability. Our initial studies involving *T. brucei* rely on our implementation of the RBP6-based *in vitro* differentiation system, which demonstrated that levels of radical oxygen species (e.g. H_2O_2) rise during life cycle progression and impede differentiation when scavenged. The ability to manipulate the levels of ROS or TCA cycle intermediates within this system can be scrutinized by multi-omics analyses to explain how these signals drive differentiation. These studies can also be expanded to include *T. congolense* parasites, which are able to undergo *in vitro* differentiation spontaneously or upon a stress signal. This model system will be more suitable for Cas9-based subgenomic screens that can reveal molecular entities involved in mitochondrial signaling. These compelling tools will allow us to elucidate fundamental features of an intricate communication relay between mitochondria and the rest of the cell.

Another focus of the lab centers on the relationship between mitochondrial ultrastructure and the bioenergetics of the F_oF_1-ATP synthase dimers. Here again, *T. brucei* represents an excellent model to answer some long-standing seminal questions concerning the evolutionary advantage of mitochondrial F-ATP synthase dimers. The *T. brucei* mitochondrion is a highly branched organelle containing cristae during the insect stage but undergoes drastic remodeling as it transforms into a simpler tubular structure without clearly detectable cristae in the bloodstream form. It is now generally accepted that the shapes of dimeric F-ATP synthases and the lengths at which they form rows along the cristae ridges are instrumental in determining the various types of cristae structures found throughout the tree of life. We have solved the structure of the *T. brucei* F-ATP synthase dimer through cryo-EM studies and functionally determined that the loss of a single subunit destabilizes dimers but not the intact functional monomers. This ability to uncouple monomers from dimers is unique in *T. brucei* and it will allow us to address if the primary function of the dimers is to simply increase the enzymatic efficiency of the nanomotor. In addition, generating both bloodstream and insect forms of the parasite without this subunit will provide an alluring new tool to explore the role of F-ATP synthase dimers in discoidal cristae biogenesis.

In addition to my research, in 2012, my colleague Dr. Alena Krejčí and I created a new course on Molecular Biology that is mandatory for all BSc students. We developed these lectures from scratch using textbooks such as Molecular Biology of the Gene and Molecular Biology of the Cell. This course explains the central principles of DNA structure, replication and repair mechanisms, transcription, regulation of gene expression, translation and the determination of protein structures. To better reach the younger generation of students, we implemented new technologies such as online quizzes during class to keep the students engaged. These have become very popular as they allow us and the students to assess in real-time if the topic was clearly presented and understood. At the end of each weekly lecture, pre-selected teams of students present a seminar on Nobel prize winners related to the relevant topic of that lecture. This leads them to a better understanding of the classic molecular biology mechanisms while also encouraging them to understand how basic research unearthed these great discoveries.

I am also invited to give various university lectures and seminars around the Czech Republic, to participate in summer school programs for PhD students and present simplified presentations for high school teachers and their students. It is rewarding to spread my passion for molecular biology and parasitology and hopefully influence future generations of biologists while also enhancing the scientific literacy of the general public.

Abstract

The unicellular parasite *Trypanosoma brucei* has a digenetic life cycle that alternates between a mammalian host and an insect vector. During programmed development, this extracellular parasite encounters strikingly different environments that determine its energy metabolism. Functioning as a bioenergetic, biosynthetic, and signaling center, the single mitochondrion of *T. brucei* is drastically remodeled to support the dynamic cellular demands of the parasite. This thesis provides an up-to-date overview of how the distinct *T. brucei* developmental stages differ in their mitochondrial metabolic and bioenergetic pathways, with a focus on the electron transport chain, proline oxidation, TCA cycle, acetate production, and ATP generation. Although mitochondrial metabolic rewiring has always been simply viewed as a consequence of the differentiation process, the possibility that certain mitochondrial activities reinforce parasite differentiation will be explored.

This work was also submitted as an invited review to the Journal of Eukaryotic Microbiology for peer review. The manuscript was accepted for publication on March 18, 2022.

1. Introduction

African trypanosomes are extracellular parasites with a digenetic life cycle requiring the tsetse fly vector and a mammalian host. These single-cell parasites are causative agents of sleeping sickness in humans (*Trypanosoma brucei gambiense, T. b. rhodesiense*) and nagana in cattle (*T. b. brucei, T. congolense, T. vivax*). Both are debilitating diseases with devastating socio-economic consequences for Sub-Saharan Africa (Assefa and Shibeshi 2018). Over the last six decades of extensive investigations, *T. brucei brucei* (hereafter simply referred to as *T. brucei*) has become the model organism of African trypanosomes (Horn 2022). As such, it will be the focus of this review.

The complex life cycle of *T. brucei* is demarcated by several distinct developmental stages. Each of these occurs in a specific environmental niche and is characterized by a unique morphology and gene expression profile that underlies differences in cellular metabolism, surface protein coats and mitochondrial physiology and ultrastructure. Parasite differentiation is triggered by extracellular signals that induce signal transduction pathways that allow the parasite to colonize various tissues of its fly vector and a mammalian host (Walsh and Hill 2021). In response to differentiation cues

and/or new environments, the parasite´s single mitochondrion undergoes remarkable metabolic rewiring and ultrastructure remodeling to rapidly meet the ever-changing cellular needs.

A typical aerobic mitochondrion is most often associated with the chemiosmotic mechanism of energy conversion to ATP implemented by an electron transport chain working in conjunction with oxidative phosphorylation. While the organelle is a bioenergetic hub, it is also involved in a variety of biosynthetic and signaling pathways that include the following: i) biosynthesis of tricarboxylic acid (TCA) cycle intermediates; ii) ATP production by substrate-level phosphorylation; iii) biosynthesis of cardiolipin; iv) control of the mitochondrial NADH/NAD^+ ratio; and v) generation of reactive oxygen species (ROS) as signaling molecules.

Here, I will provide a comprehensive overview of the multifaceted mitochondrial contributions to *T. brucei* programmed development. In the past, mitochondrial metabolic remodeling was always considered a mere consequence of the differentiation process to meet energy requirements. However, I will also summarize recent data suggesting that certain mitochondrial activities are required to reinforce parasite differentiation.

With regards to the "house-keeping" functions of this semi-autonomous organelle (i.e. mitochondrial genome replication, mitochondrial gene expression, RNA editing, mitochondrial protein import, iron-sulfur cluster assembly, and translation), I refer the reader to comprehensive reviews on these topics (Schneider and Ochsenreiter 2018, Schneider 2020, Verner et al. 2015, Lukes and Basu 2015, Aphasizheva et al. 2020).

1.1. *T. brucei* journey through two different hosts

Before describing how *T. brucei* mitochondrial functions are linked with parasite differentiation, it is essential to understand the life cycle of the parasite and its distinct developmental stages. First, a tsetse fly bites an infected mammal (human, cow, wild animal) and ingests a bloodmeal containing the bloodstream form short stumpy parasites. Once these growth-arrested parasites enter the insect midgut, they are triggered primarily by environmental stimuli (drop in temperature, novel chemical cues, increase in pH) to differentiate into early-procyclic forms (Roditi et al. 2016, Shaw et al. 2022). This transition is accompanied by global changes in gene expression that generate the following phenotypes: i) remodeled surface proteome; ii) altered parasite morphology; iii) cell cycle re-entry; and iv) rewired metabolism (Szoor et al. 2020). In approximately one week, the early procyclic forms differentiate into the late-procyclic form (Imhof et al. 2014). After an additional week, the fully differentiated late-procyclic cells begin to migrate through the anterior of the midgut to the proventriculus, where they initiate their transition into long dividing epimastigotes. Subsequently, an asymmetric division produces short non-dividing epimastigotes that continue to migrate to the salivary glands. Here, they attach to the epithelium

and divide. In response to an unknown stimulus, the attached epimastigotes initiate a metacyclogenesis process. This involves another asymmetric division that results in non-dividing, quiescent metacyclic trypanosomes that are released into the saliva (Dyer et al. 2013, Rotureau and Van Den Abbeele 2013). The life cycle continues when the tsetse fly takes another bloodmeal and injects the infective metacyclics into a new mammalian host. Once in the bloodstream of the host, the parasites quickly differentiate into actively dividing long slender bloodstream forms that evade the host immune system by periodically switching the monoallelic expression of a variable surface glycoprotein (Mugnier et al. 2016). When parasites reach high densities and the stumpy induction factor accumulates in the bloodstream, these long slender forms differentiate into growth-arrested, short stumpy forms (Rojas and Matthews 2019). A signaling cascade that leads to the maturation of these transmission-competent parasites is triggered by oligopeptides that interact with a *T. brucei* G protein coupled receptor-like protein (Rojas et al. 2019).

1.2. The nutrients present in the host environments dictate mitochondrial metabolism

T. brucei parasites are able to rapidly alter their metabolism in response to environmental changes and differentiation cues. Many of these adaptations are related to mitochondrial metabolic pathways involved in amino acid and carbohydrate metabolism that are linked to ATP production. This flexibility is utilized during programmed developmental progression as the parasite encounters microenvironments within the two hosts that vary widely in nutrient composition (Smith et al. 2017). This is the case when trypanosomes are transmitted from the glucose-rich bloodstream of their mammalian host to the glucose-poor and amino acid-rich tissues of the tsetse fly. Consequently, the bloodstream parasites generate the majority of their cellular ATP by aerobic glycolysis, while the insect-dwelling parasites use mitochondrial oxidative phosphorylation to produce ATP. Detailed comparative studies of the two most commonly cultured life cycle stages, the procyclic and bloodstream forms, define how the core metabolic pathways differ between these two developmental stages (Michels et al. 2021). However, the molecular mechanisms controlling the functional remodeling of the organelle are still largely unknown. Fortunately, proteomic, transcriptomic and metabolomic approaches recently applied to the majority of all *T. brucei* developmental stages obtained *in vitro* or *in vivo* allow us to propose distinct metabolic adaptations for the long slender bloodstream forms, short stumpy forms, early and late procyclic forms, epimastigotes, and metacyclic parasites (Christiano et al. 2017, Savage et al. 2016, Kolev et al. 2012, Naguleswaran et al. 2021, Dolezelova et al. 2020). Therefore, the compilation of these datasets provides a rough blueprint for the progression of mitochondrial remodeling during *T. brucei* programmed development (Figure 1).

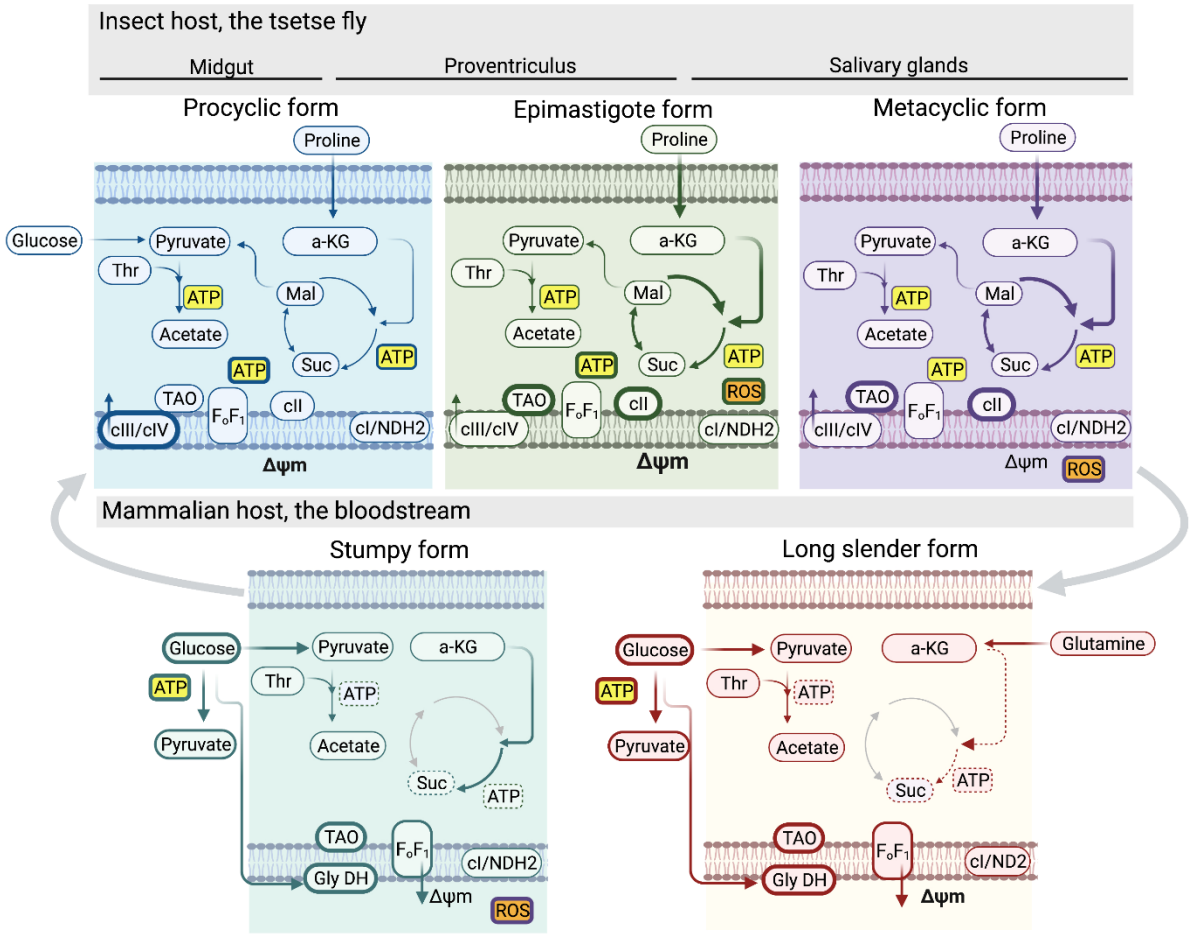

Figure 1. **Schematic representation of the mitochondrial metabolic pathways remodeled during the *T. brucei* life cycle.**

The flux of various metabolic pathways is depicted with arrows of various thicknesses depending on the activity of the respective metabolic pathway (i.e. thicker lines indicated higher rates of activity). Dashed lines indicate predicted enzymatic steps and metabolites for which direct evidence is lacking. α-KG, α-ketoglutarate; ΔΨm, mitochondrial membrane potential; cI, complex I; cII, complex II; cIII, complex III; cIV, complex IV; F_oF_1, F_oF_1-ATP synthase; mal, malate; NDH2, alternative dehydrogenase; ROS, reactive oxygen species; suc, succinate, thr, threnonine; TAO, Trypanosoma alternative oxidase. Created with BioRender.com

2. Unique features of the *T. brucei* electron transport chain

T. brucei possesses a uniquely equipped electron transport chain that allows for significant flexibility when encountering various nutrient supplies throughout its life cycle. In addition to the canonical electron transport chain complexes I, II, III and IV (Acestor et al. 2011), these parasites

encode for alternative enzymes that also contribute to the electron entry and exit from the electron transport chain (type II alternative dehydrogenase (NDH2) and Trypanosoma alternative oxidase, (TAO)) (Fang and Beattie 2003, Chaudhuri et al. 1998). NDH2 and TAO are functionally similar to complexes I and IV in that they respectively accept electrons from NADH and pass them to the terminal electron acceptor oxygen. However, these enzymes are not able to pump protons across the inner mitochondrial membrane (Chaudhuri et al. 2006, Fang and Beattie 2002). In this respect, respiration can be uncoupled from the generation of a proton motive force across the mitochondrial inner membrane.

In *T. brucei* cultured procyclic forms, the mitochondrial membrane potential is largely generated from the proton-pumping activities of the electron transport chain complexes III and IV (Horvath et al. 2005, Verner et al. 2011). Through oxidative phosphorylation, this proton motive force is coupled with the activity of the F_oF_1-ATP synthase to generate chemical energy in the form of ATP (Zikova et al. 2009). The expansive mitochondrion observed in procyclic forms is a reticulated organelle rich in mitochondrial inner membrane protrusions called cristae (Verner et al. 2015, Bily et al. 2021). It is within these pockets of typical aerobic mitochondrion that a favorable microenvironment is created to support the efficient production of ATP via oxidative phosphorylation (Mannella 2020).

However, it has long been known that trypanosomes undergo a striking remodeling of their electron transport chain during parasite development. In 1965, Keith Vickerman made the surprising discovery that the bloodstream mitochondrion lacks cytochrome pigments. Since the activity of complexes III and IV depends on these cofactors to generate a proton motive force, the essential mitochondrial membrane potential is maintained by the reverse activity of the F_oF_1-ATP synthase (Nolan and Voorheis 1992, Schnaufer et al. 2005). This is a very rare feature among aerobic eukaryotes since it requires a constant source of ATP to maintain this prolonged activity (Chinopoulos and Adam-Vizi 2010).

Soon after, it became apparent that the bloodstream forms respire at very high rates via a cyanide-insensitive alternative oxidase linked to the mitochondrial FAD-dependent glycerol-3-phosphate dehydrogenase (Opperdoes et al. 1977, Grant and Sargent 1960, Clarkson et al. 1989). Since the specific identity of these enzymes was unknown at the time, they were collectively referred to as a glycerol-3-phosphate oxidase in the original work of the 1960s and 1970s. Finally, in 2002, the last of the *T. brucei* electron transport chain peculiarities was identified with the discovery of an FMN-containing alternative dehydrogenase NDH2 (Fang and Beattie 2002). With all of these modifications, it is not surprising that the bloodstream mitochondrion has a greatly reduced morphology with few distinct cristae (Bily et al. 2021).

2.1. **Molecular entities feeding the electron transport chain**

In totality, the *T. brucei* electron transport chain contains five enzymes that communicate with the ubiquinone pool in the inner mitochondrial membrane: Complex I (NADH:ubiquinone dehydrogenase), alternative type II dehydrogenase (NDH2), FAD-dependent glycerol-3-phosphate dehydrogenase, complex II (succinate dehydrogenase) (Acestor et al. 2011) and proline dehydrogenase (discussed further in *Section 4*).

2.1.1. NADH:ubiquinone dehydrogenase (complex I)

T. brucei complex I is the largest of the electron transport chain complexes, containing at least 46 subunits encoded by both the nuclear and mitochondrial genomes (Acestor et al. 2011). In a typical eukaryotic cell, this complex has three physiological functions: i) the transfer of electrons from the reduced cofactor NADH to ubiquinone; ii) translocating protons to the intermembrane space to contribute to the mitochondrial membrane potential; iii) and under certain conditions, the production of superoxide, a type of ROS. While potentially harmful, superoxide is quickly converted to hydrogen peroxide by a mitochondrial superoxide dismutase. When produced in low amounts, the membrane permeable hydrogen peroxide is involved in cellular signal transduction pathways (Sies 2017).

In trypanosomes, the biological significance of complex I is still unclear despite considerable efforts (Duarte and Tomas 2014). In procyclic cells, complex I does not appear to contribute significantly to electron transfer from NADH or to proton translocation. For example, RNAi silencing of some complex I subunits resulted in only a slight decrease in the specific NADH:ubiquinone oxidoreductase activity and no decrease in the mitochondrial membrane potential (Verner et al. 2011). In a similar fashion, the knock-out of complex I subunits in the bloodstream form did not alter NADH:ubiquinone activity, calling into question the role of complex I in these life cycle forms (Surve et al. 2012).

Intriguingly, it is conceivable that complex I activities are required in other understudied *T. brucei* developmental life stages. In particular, it was demonstrated that short stumpy bloodstream cells had increased NAD diaphorase activity staining and a mitochondrial membrane potential sensitive to high concentrations of the complex I inhibitor rotenone (Vickerman 1985, Bienen et al. 1991). However, the treatment of this life cycle stage with azide recently demonstrated that the mitochondrial membrane potential is not generated by NADH oxidation but by the hydrolysis of ATP by the F_oF_1-ATP synthase (Dewar et al. 2018).

Finally, the programmed development of insect parasites into epimastigotes and metacyclics could reveal the necessity of complex I. Recently, it was documented that there is an increase in NADH-producing metabolic pathways and an increased mitochondrial membrane potential in

epimastigotes produced *in vitro* (Dolezelova et al. 2020). If these phenotypes are indeed due to complex I activity, this contribution to the mitochondrial membrane potential might be required to compensate for the decrease in complexes III and IV activity (discussed further in *Section 2.2.1*). Alternatively, the essential function of complex I could be the production of ROS signaling molecules during the differentiation of insect life cycle forms, as elevated levels of mitochondrial superoxide were also detected in the epimastigotes (Dolezelova et al. 2020). The insect forms differentiation *in vitro* or *in vivo* of knockout cell lines lacking key functional complex I subunits will be essential to prove if this hypothesis is correct. The unresolved question of why considerable energy is spent for the biogenesis of this large electron transport chain enzyme remains one of the most interesting topics in the field.

2.1.2. Alternative dehydrogenase, NDH2

In addition to complex I, *T. brucei* encodes the alternative type II NADH dehydrogenase, NDH2. This enzyme consists of a single rotenone-insensitive polypeptide that catalyzes the transfer of two electrons from NADH to ubiquinone. Therefore, it provides an alternative route in the electron transport chain compared to complex I. However, NDH2 activity is not coupled with proton-pumping (Fang and Beattie 2002). Furthermore, unlike complex I, NDH2 is important for procyclic cell growth because its activity contributes to the proton motive force, albeit indirectly via the ubiquinone/ubiquinol pool linked to complexes III and IV (Verner et al. 2013). Meanwhile, the inducible NDH2 knockdown in bloodstream parasites revealed a strong reduction in growth only when complex I was absent (Surve et al. 2016). This suggests that the two activities function in the mitochondrial matrix and that they can compensate for each other. Consequently, NDH2 was proposed to be involved in maintaining the mitochondrial NAD^+/NADH balance. This is important for several metabolic processes, including the vital production of mitochondrial acetate (Surve et al. 2016) (*Section 7*). However, one must keep in mind that the membrane topology of NDH2 remains unresolved, as another study reported that NDH2 faces the intermembrane space and affects the cellular NAD^+/NADH balance (Verner et al. 2013). Given its central role in mitochondrial metabolism, NDH2 remains largely unexplored. Therefore, deciphering the NDH2 physiological functions during parasite differentiation is an exciting avenue to pursue.

2.1.3. FAD-dependent glycerol-3-phosphate dehydrogenase

A striking feature of the *T. brucei* electron transport chain is the presence of an FAD-dependent glycerol-3-phosphate dehydrogenase, an inner mitochondrial membrane enzyme with an active site accessible to substrates entering the mitochondrial intermembrane space from the cytosol (Opperdoes et al. 1977). This enzyme is involved in the glycerol-3-phosphate:dihydroxyacetone phosphate shuttle that connects the mitochondrion with glycosomes, peroxisome-derived organelles that contain the majority of enzymes required for glycolysis (Haanstra et al. 2016).

Mitochondrial glycerol-3-phosphate dehydrogenase oxidizes glycerol-3-phosphate to dihydroxyacetone phosphate and then donates the resulting electrons to ubiquinone. In this way, it maintains the glycosomal NAD^+/NADH redox balance and allows for a high glycolytic flux, a typical feature of the bloodstream trypanosomes (Albert et al. 2005). Consequently, this enzyme is crucial for bloodstream cells that are completely dependent on glucose oxidation (Skodova et al. 2013).

Interestingly, trypanosomes can also utilize glycerol as a carbon source (Ryley 1956). Recently, it was demonstrated that cultured procyclic and bloodstream trypanosomes grown in elevated glycerol with low levels of glucose can proliferate by using glycerol for gluconeogenesis (Kovarova et al. 2018, Allmann et al. 2021, Pineda et al. 2018, Wargnies et al. 2018, Bringaud et al. 2021). Glycerol oxidation is entirely dependent on the activity of the mitochondrial glycerol-3-phosphate dehydrogenase (Pineda et al. 2018). Glycerol metabolism might by physiologically relevant for the bloodstream form parasites to colonize the host adipose tissue, a major extravascular parasite niche (Trindade et al. 2016), but this premise requires further studies. Moreover, it remains unclear why insect forms would need to metabolize glycerol, although this metabolite prevents differentiation from early to late procyclic forms (Vassella et al. 2000). Therefore, glycerol-3-phosphate dehydrogenase may be important for the development of early procyclic form and its activity could help to maintain the early procyclic population in the tsetse midgut when glucose and possibly glycerol are still available as nutrients (Naguleswaran et al. 2021).

2.1.4. Succinate dehydrogenase (complex II)

Last but not least, canonical complex II (succinate dehydrogenase) is the only electron transport chain enzyme directly involved in the tricarboxylic acid (TCA) cycle reaction. By oxidizing succinate to fumarate, it supplies electrons to the ubiquinone pool. As we will discuss later, this complex plays a prominent role in the insect forms as it is directly involved in the oxidative metabolism of proline to its major end product, alanine (Coustou et al. 2008). Since its abundance and activity increase markedly during the development of insect forms, it can be surmised that complex II activity is also important for these stages including metacyclic parasites (Dolezelova et al. 2020, Christiano et al. 2017). In contrast, this complex does not appear to be essential for the bloodstream form parasites (Alkhaldi et al. 2016), even though its presence would retain mitochondrial plasticity as the parasite colonizes extravascular host niches comprised of various nutrients.

2.2. **From ubiquinol to oxygen**

Trypanosomes are able to oxidize ubiquinol by two independent pathways: i) via the cytochrome-mediated pathway consisting of complexes III (ubiquinol:cytochrome c oxidoreductase, cytochrome bc1 complex) and IV (cytochrome c oxidase) and ii) via Trypanosoma alternative oxidase, TAO. Possessing these two pathways gives trypanosomes an amazing flexibility to regulate the route in which electrons flow to oxygen and thereby uncouple respiration from oxidative phosphorylation and divert electrons from the ROS-producing complex III.

2.2.1. Ubiquinol:cytochrome c oxidoreductase and cytochrome c oxidase (complexes III and IV)

In a typical eukaryotic cell complex III catalyzes the transfer of electrons from ubiquinol to cytochrome c. Complex IV then accepts electrons from the reduced cytochrome c and donates them to the molecular oxygen. This energetic "downhill" transfer of electrons from ubiquinol to oxygen is used to generate the proton motive force across the mitochondrial inner membrane.

In cultured procyclic form parasites, complexes III and IV are major producers of the mitochondrial membrane potential (Horvath et al., 2005). However, there is a strong reduction in the abundance of complexes III and IV as metacyclics develop (Dolezelova et al. 2020, Naguleswaran et al. 2021). This leads to a decrease in the mitochondrial membrane potential and possibly to lower ATP production by oxidative phosphorylation. Interestingly, in eukaryotes low levels of ATP (and high AMP levels) lead to the activation of AMP-activated kinase, a major energy sensor that down-regulates ATP-consuming metabolic pathways such as protein biosynthesis required for cell proliferation (Herzig and Shaw 2018). This most likely occurs during the differentiation of epimastigotes into the quiescent metacyclic cells, as *T. brucei* AMP-activated kinase has been identified as a positive regulator during insect forms differentiation (Toh et al. 2021).

The activities of complexes III and IV are completely absent in both the long slender and the short stumpy bloodstream forms of the parasite. The expression of individual complex III and IV subunits is evidently triggered early in the differentiation to procyclics, perhaps even when the stumpy forms first encounter the environment of the fly`s midgut after a bloodmeal (Naguleswaran et al. 2021).

2.2.2. Trypanosoma alternative oxidase (TAO)

TAO is a di-iron enzyme with ubiquinol oxidase activity associated with the matrix leaflet of the inner mitochondrial enzyme. It catalyzes the reduction of oxygen to water without contributing to energy conservation since this complex is not capable of proton pumping (Chaudhuri et al. 2006). While it is expressed throughout the life cycle of the parasite, TAO expression levels are

developmentally regulated, with the highest levels observed in the long slender bloodstream form (Dejung et al. 2016).

In cultured procyclic forms, TAO contributes about 20% of total respiration (Gnipova et al. 2012). However, the expression of TAO is sensitive to changes in mitochondrial bioenergetics. This is evident with the upregulation of TAO expression when there is a partial inhibition of oxidative phosphorylation that results in a transient membrane hyperpolarization. This response indicates a flexibility to redirect electrons from the ROS-generating complex III, potentially mitigating the deleterious effects of high ROS concentrations (Hierro-Yap et al. 2021). A similar attribute is observed during the differentiation of insect forms. Here the alternative oxidase is strongly upregulated in the salivary gland epimastigotes, which corresponds to the steady reduction of complexes III and IV mentioned above (Naguleswaran et al. 2021). Upon the development of metacyclics, TAO is now responsible for 80% of total cellular respiration (Dolezelova et al. 2020). The upregulation of TAO seems to be one of the hallmarks of programmed *T. brucei* development in the tsetse fly. Therefore, identifying the molecular mechanism employed to regulate TAO expression would reveal a major determinant that drives mitochondrial remodeling during the differentiation of insect forms.

Meanwhile, the bloodstream form depends entirely on the activity of TAO because it is linked with the activity of mitochondrial glycerol-3-phosphate dehydrogenase and therefore with glycolysis. The presence of TAO in this system results in the production of two net ATP from each glucose molecule consumed. The significance of TAO is highlighted when its activity becomes impaired and the oxidation of glucose leads to the formation of equimolar amounts of glycerol and pyruvate with only one ATP produced. This reduced ATP yield severely affects the growth of the parasite and eventually results in cell death (Helfert et al. 2001). This direct link between TAO activity and glycolytic flux provides mitochondria with the ability to regulate cell metabolism. For example, high intramitochondrial ATP content inhibits the activity of TAO and decreases cellular respiration and ATP levels (Luevano-Martinez et al. 2020, Hierro-Yap et al. 2021). Therefore, an imbalance of ATP within the mitochondrion of the parasite may affect glycolysis and cellular ATP production.

3. F_oF_1-ATP synthase – to produce or to consume ATP?

Mitochondrial F_oF_1-ATP synthases are rotary machines that allow protons from the mitochondrial intermembrane space to move down their concentration gradient and return to the mitochondrial matrix. The energy released during this process is harnessed by this enzyme to generate ATP (Walker 2013). Biochemically, however, this enzyme is capable of both the synthesis and hydrolysis of ATP. When the mitochondrial physiology is altered in response to changing environments, it can dictate a reversal of the ATP synthase rotation. This results in the hydrolysis

of ATP, which is coupled to proton translocation into the intermembrane space. In this capacity, the enzyme contributes to the mitochondrial membrane potential. However, under aerobic conditions, the enzyme almost always functions in the direction of ATP synthesis (Campanella et al. 2009).

The Trypanosoma F_oF_1-ATP synthase exhibits several peculiarities that include its diverged subunit composition, the unique structure of the F_1 moiety and the regulation of its activity, which differs markedly between the insect and mammalian forms (Gahura et al. 2021a, Montgomery et al. 2018, Panicucci et al. 2017). In procyclic trypanosomes, F_oF_1-ATP synthase acts true to its name and generates ATP by oxidative phosphorylation (Zikova et al. 2009). This activity is required for *T. brucei* development in the fly vector since parasites with a completely disrupted F_oF_1-ATP synthase are unable to fully colonize the midgut of the tsetse fly (Dewar et al. 2022). During the development of epimastigotes and metacyclics, the complex remains stable in its abundance (Dolezelova et al. 2020), but its contribution to the total ATP pool is unknown. As the parasite progresses through the insect vector, the changes in the mitochondrial physiology may even dictate that the F_oF_1-ATP synthase reverses its function and begins consuming ATP.

The *T. brucei* differentiation from metacyclic parasites into long slender bloodstream cells is underlined by a striking regression in the morphology of the mitochondrion, which includes a reduction in the size and number of cristae (Kolev et al. 2012, Bily et al. 2021). In aerobic eukaryotes, the mitochondrial F_oF_1-ATP synthase dimers play a key role in cristae biogenesis as they associate into rows of different lengths and generate the inner-membrane curvature essential for the efficient energy conversion of the oxidative phosphorylation pathway (Kuhlbrandt 2019). This relationship between F_oF_1-ATP synthase and the mitochondrial ultrastructure remodeling during differentiation of the parasite is intriguing. Indeed, the disruption of cultured procyclic *T. brucei* F_oF_1-ATP synthase dimers into monomers results in aberrant cristae morphology and less efficient ATP production by oxidative phosphorylation (Gahura et al. 2021b).

The bloodstream form of *T. brucei* is an excellent example of the obligatory dependence on the reverse mode of the F_oF_1-ATP synthase in eukaryotes (Schnaufer et al. 2005, Subrtova et al. 2015). Normally, ATP hydrolysis by the F_oF_1-ATP synthase is a rare phenomenon, typically only observed under harsh conditions such as sudden hypoxia or anoxia. This allows the generation of a modest mitochondrial membrane potential at the expense of ATP, which promotes short-term survival (Chinopoulos 2011). However, even under these conditions, the hydrolytic activity of the complex is regulated by a conserved inhibitory factor 1 (Pullman and Monroy 1963). This peptide acts as a safety mechanism to prevent the futile depletion of cellular ATP (Garcia-Bermudez and Cuezva 2016). Interestingly, the bloodstream form effectively down-regulates expression of this peptide in order to fully exploit the reverse activity of the F_oF_1-ATP synthase to maintain the vital

mitochondrial membrane potential (Panicucci et al. 2017, Subrtova et al. 2015). Similar to the long slender bloodstream form, short stumpy cells also maintain the mitochondrial membrane potential using F_oF_1-ATP synthase (Dewar et al. 2018). With the recent advancements detailing the *T. brucei* F_oF_1-ATP synthase structure and function (Gahura et al. 2021a), it is now possible to gain a better understanding of the regulation of the enzyme activity and the role of the complex in shaping the inner mitochondrial membrane during parasite differentiation.

4. Electron transport chain requires cardiolipin, a mitochondrion-specific phospholipid

In eukaryotes, optimal function of the electron transport chain and oxidative phosphorylation depends on the presence of cardiolipin, a phospholipid synthesized in the mitochondria and located exclusively in the mitochondrial inner membrane (Maguire et al. 2017, Ren et al. 2014). Cardiolipin is a phospholipid consisting of two phosphatidic acid units linked by a glycerol backbone (Houtkooper and Vaz 2008). At a physiological pH, this phospholipid carries two negative charges due to its ionized phosphate groups. This property allows it to serve as a proton trap that contributes to the proton motive force driving oxidative phosphorylation (Haiens and Dencher 2002). It also promotes the assembly of electron transport chain complexes into higher order assemblies and stabilizes the dimeric structure of the F_oF_1-ATP synthase (Zhang et al. 2005, Pfeiffer et al. 2003) . All these characteristics contribute to its role in mitochondrial biogenesis and dynamics, including proper cristae formation (Paradies et al. 2019).

In the cultured procyclic form, disruption of cardiolipin synthesis resulted in the destabilization of the electron transport chain complexes III and IV, abnormal mitochondrial morphology and cell death (Serricchio and Butikofer 2012, Schadeli et al. 2019). In the bloodstream form, cardiolipin deficiency primarily results in decreased ATP levels, a lower rate of respiration and the accumulation of glycerol and glycerol-3-phosphate (Serricchio et al. 2021). These observed phenotypes most likely reflect the impairment of the mitochondrial glycerol-3-phosphate dehydrogenase, which functions in a cardiolipin-dependent manner in other organisms (Beleznai and Jancsik 1989). All this leads to a decrease in the mitochondrial membrane potential, resulting in the death of the parasite (Serricchio et al. 2021). Notably, the Trypanosoma cardiolipin is synthesized exclusively by a bacterial-type cardiolipin synthase that is absent in the mammalian host (Serricchio and Butikofer 2012, Gottier et al. 2017). Given the importance of cardiolipin synthesis and its role in several fundamental cellular processes, the *T. brucei* cardiolipin synthesis pathway could be exploited as a potential drug target in these parasites.

5. **Proline oxidation fuels oxidative phosphorylation in the insect forms**

Proline appears to be the main energy source for all insect forms of *T. brucei* parasites, since it is a plentiful amino acid in the tsetse fly. In fact, the fly uses proline as the preferred energy reserve for driving flight muscles and for lactation during intrauterine larvigenesis. The insect forms of the parasite utilize the abundance of proline in the surroundings by actively importing it through amino acid transporters localized in the plasma membrane (Haindrich et al. 2021). Proline is oxidized within the mitochondrion via the intermediate glutamate into three different end metabolites: alanine, succinate and acetate (Coustou et al. 2008). Oxidation of proline to glutamate is catalyzed by two mitochondrial enzymes, FAD-dependent proline dehydrogenase and pyrroline-5-carboxylate dehydrogenase (Figure 2, metabolic pathways in dark purple). Mitochondrial proline dehydrogenases are membrane bound enzymes that donate electrons directly to ubiquinone (Paes et al. 2013). In trypanosomes, oxidation of proline to glutamate is required for the successful colonization of the tsetse midgut, as procyclic cells with suppressed pyrroline-5-carboxylate dehydrogenase expression were unable to establish a midgut infection (Mantilla et al. 2017). One of the most important contributions of this pathway is the donation of electrons to the electron transport chain, which supports ATP production by oxidative phosphorylation. Electrons are supplied either directly to ubiquinone by the membrane-bound proline dehydrogenase or indirectly via reduced NADH molecules generated by pyrroline-5-carboxylate dehydrogenase. In the latter scenario, the NADH is subsequently oxidized by complex I and/or NDH2 (Marchese et al. 2020, Bringaud et al. 2012).

Proline-induced ATP production by oxidative phosphorylation appears to be required primarily for parasite migration and the infection of subsequent tsetse tissues, but not for the initial midgut infection *per se* (Dewar et al. 2022). Trypanosomes with a reduced capacity for oxidative phosphorylation were able to differentiate from stumpy forms to early procyclics and initiate a midgut infection, although a motility defect impaired the ability of the parasite to fully colonize the midgut (Dewar et al. 2022). The observed viability of these early procyclics is perhaps due to the utilization of glucose to provide the sufficient cellular ATP levels required to initiate the infection (Naguleswaran et al. 2021). In addition, glycolysis in the early procyclic form is associated with a phenomenon called social motility, which involves the induction of pH taxis toward a more alkaline pH. This process is likely biologically relevant during the fly transmission because of the greater differences between the pH of the midgut and proventriculus (Shaw et al. 2022, Imhof et al. 2014).

There are several lines of evidence that indicate a higher cellular demand for proline oxidation during the transition from procyclic cells to epimastigotes: i) elevated expression of proline dehydrogenase and pyrroline-5-carboxylate dehydrogenase; ii) increased expression of proline-

alanine transporters (Naguleswaran et al. 2021); iii) significantly enhanced cellular respiration in the presence of proline (Dolezelova et al. 2020). The reason for this metabolic remodeling can include an increased need for ATP production by both oxidative and substrate-level phosphorylation or the increased production of various intermediate metabolites. Both of these metabolic pathways rely on mitochondrial dehydrogenases, whose activity depends on Ca^{2+} ions (Huang and Docampo 2018, Huang et al. 2013). These ions are imported into the mitochondrion via the mitochondrial calcium uniporter, one of most upregulated mitochondrial protein complexes during insect form differentiation (Dolezelova et al. 2020).

The elevated mitochondrial activity in the epimastigotes might be related to enhanced levels of ROS (e.g. mitochondrial superoxide and H_2O_2), signaling molecules that positively influence the differentiation of epimastigotes to metacyclics (Dolezelova et al. 2020). Importantly, overexpression of proline dehydrogenase in the insect form of *Trypanosoma cruzi*, a related trypanosomatid parasite, also leads to increased mitochondrial functions producing increased oxygen consumption and H_2O_2 levels. These attributes correlated with a more efficient differentiation of the parasite to metacyclic trypomastigotes *in vitro* and within the insect vector. These outcomes provide a link between mitochondrial metabolism and efficient progression through trypanosoma development (Mantilla et al. 2021).

Since *T. brucei* is auxotrophic for proline, this amino acid is taken up by a high affinity transporter and utilized in proteosynthesis (Johnston et al. 2019) in the bloodstream forms. However, they do not catabolize proline, which is reflected by the substantial decrease in the abundance of the enzymes involved in proline oxidation (Lamour et al. 2005). While the short stumpy form preadapts to life in the tsetse vector by increasing the mRNA levels of various mitochondrial enzymes, the expression of the proline transporters appears to be induced only after the stumpy cells enter the midgut of the fly (Naguleswaran et al. 2018, Dejung et al. 2016).

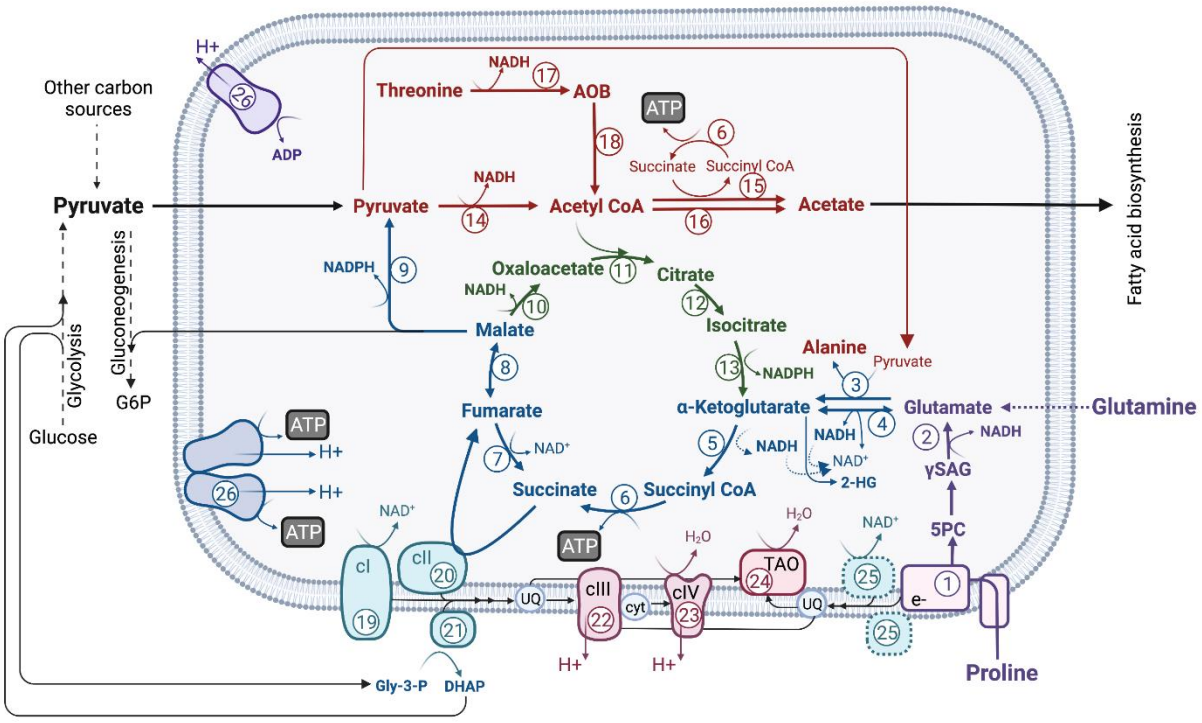

Figure 2. Schematic representation of the *T. brucei* mitochondrial metabolic pathways discussed in this review. 1, proline dehydrogenase; **2,** pyrroline-5-carboxylate dehydrogenase; 3, alanine transaminase; 4, glutamate dehydrogenase; 5, α-ketoglutarate dehydrogenase; 6, succinyl-CoA synthetase; 7, fumarate reductase; 8, fumarase; 9, malic enzyme; 10, malate dehydrogenase; 11, citrate synthase; 12, aconitase; 13, isocitrate dehydrogenase; 14, pyruvate dehydrogenase; 15, acetate:succinate coenzyme A transferase; 16, acetyl-coenzyme A thioesterase; 17, threonine dehydrogenase; 18, 2-amino-3-ketobutyrate Coenzyme A lyase; 19, NADH:ubiquinone dehydrogenase (complex I); 20, succinate dehydrogenase (complex II); 21, glycerol-3-phosphate dehydrogenase; 22, ubiquinol:cytochrome c oxidoreductase (complex III); 23, cytochrome *c* oxidase (complex IV); 24, alternative oxidase (TAO); 25, alternative dehydrogenase (NDH2); 26, F_oF_1-ATP synthase; 5PC, pyrroline-5-carboxylate; 2-HG, 2-hydroxyglutarate; γSAG, γ-glutamyl semialdehyde; NAD(P), nicotinamide adenine dinucleotide (phosphate); UQ, ubiquinone. Dotted lines indicate predicted enzymatic steps and metabolites for which there is no direct experimental evidence. Dashed lines indicate metabolic pathways consisting of multiple enzymatic steps. Created with BioRender.com

6. Glutamate-derived α-ketoglutarate enters the TCA cycle for metabolite biosynthesis and energy conversion

In the insect forms, the oxidation of proline leads to glutamate, which can be further converted to α-ketoglutarate by two independent reactions: i) the oxidative deamination of glutamate by glutamate dehydrogenase or ii) a transamination process catalyzed by alanine transaminase that transfers an amino group from glutamate to pyruvate and generates alanine and α-ketoglutarate (Spitznagel et al. 2009). α-ketoglutarate functions as the main gateway into the TCA cycle. This connects proline catabolism with the additional generation of reducing agents (NADH and $FADH_2$) that contribute to energy conversion. Entering the TCA cycle in the oxidative direction, α-ketoglutarate is further metabolized to succinate via a reaction that produces ATP by succinyl-CoA synthetase (Bochud-Allemann and Schneider 2002). This substrate-level phosphorylation may contribute significantly to the cellular ATP pool due to the very high consumption rate of α-ketoglutarate in the insect forms (15 μmol/h/mg of protein, approximately 15 times higher than glucose in these cells) (Villafraz et al. 2021). The ability to generate high levels of ATP through substrate-level phosphorylation may allow the parasite to tolerate reduced levels of oxidative phosphorylation when encountering sudden hypoxic conditions or a highly oxidative environment.

The succinate produced by succinyl-CoA synthetase can then either be excreted as an end metabolite or further oxidized by the electron transport chain complex II (succinate dehydrogenase). By continuing around the TCA cycle, succinate is further oxidized to fumarate and then malate (Figure 2, metabolic pathways in blue). At this junction, malate faces three different options: i) it can continue in the TCA cycle (*Section 6*); ii) it can be converted to pyruvate by the action of mitochondrial NADP-dependent malic enzyme (*Section 7*); iii) it can be exported to the cytosol. The cytosolic malate can be converted to pyruvate by the cytosolic malic enzyme. Both, cytosolic malate and pyruvate serve as precursors for gluconeogenesis through two phosphoenolpyruvate-producing enzymes: glycosomal phosphoenolpyruvate carboxykinase and pyruvate phosphate dikinase. This process is essential for the development of insect life cycle forms *in vitro* and *in vivo* (Wargnies et al. 2018) as it generates glucose-6-phosphate, an essential precursor for the pentose phosphate pathway and nucleotide sugar biosynthesis (Kovarova and Barrett 2016).

Recently, insect form trypanosomes were shown to consume and metabolize not only proline, but also other metabolic intermediates such as succinate, alanine, pyruvate, malate and α-ketoglutarate (Villafraz et al. 2021). This may be physiologically relevant during early procyclic differentiation when glucose becomes scarce and the parasites have not yet completed the switch to proline oxidation. The ability to recycle glucose-derived pyruvate, succinate and alanine for additional energy reserves could prove critical during the rewiring from glycolysis to proline oxidation.

Intriguingly, these metabolic intermediates might also be released by a symbiotic and commensal bacteria inhabiting the tsetse midgut. *In vitro* experiments in the presence of a physiological relevant amount of proline (1-2 mM) demonstrated that the TCA cycle intermediates (succinate, malate and α-ketoglutarate) stimulated the growth rate of the cultured procyclic form. Moreover, α-ketoglutarate was specifically shown to be required for epimastigote replication (Villafraz et al. 2021). These observations further support the need of epimastigotes to increase their consumption rate of various carbon sources during development to meet increased energy demands. Perhaps this is to offset the consequences of rewiring the electron transport chain to TAO, an enzyme that does not contribute to the mitochondrial membrane potential and therefore energy conversion. Although metacyclic cells are cell-cycle arrested with both attenuated translation and low ATP levels, they retain high levels of the enzymes involved in the oxidation of glutamate to succinate, malate and pyruvate. Presumably, these catabolic pathways remain active to maintain some baseline level of metabolism required for metacyclic viability (Dolezelova et al. 2020, Christiano et al. 2017).

Bloodstream parasites were thought to exclusively metabolize glucose to meet their energy and metabolic needs, until direct evidence was obtained that bloodstream forms also take up and metabolize threonine (*Section 7*) and glutamine (Mazet et al. 2013, Johnston et al. 2019, Creek et al. 2015). Glutamine, serving as a key amino donor, is actually consumed in large quantities by the long slender bloodstream form. Evidence for glutamine catabolism came from the detection of glutamine-derived succinate (Johnston et al. 2019). This pathway first converts glutamine into α-ketoglutarate, which is further metabolized to succinate by α-ketoglutarate dehydrogenase and succinyl-CoA synthetase. Although the expression of these two enzymes is lower in the bloodstream cells compared to the cultured procyclic form (Dejung et al. 2016), mitochondrial substrate-level phosphorylation through this portion of the TCA cycle could provide a source of intramitochondrial ATP. Possibly, this ATP could complement the glycolytically generated ATP that is required to power the reverse operation of the F_oF_1-ATP synthase.

As the insect-transmissible stage, short stumpy forms are pre-adapted to survive in the low glucose conditions of the tsetse fly midgut. Therefore, compared to the long slender bloodstream forms, there is increased expression of a few mitochondrial proteins involved in substrate-level phosphorylation, such as α-ketoglutarate dehydrogenase, succinyl-CoA synthetase and the putative α-ketoglutarate transporter MCP12 (Colasante et al. 2018) (Dejung et al. 2016). Consequently, the short stumpy forms, but not long slender bloodstream cells, respire and maintain their motility *in vitro* with α-ketoglutarate as the sole carbon source (Vickerman 1965, Bienen et al. 1993). This suggests that ATP is generated intramitochondrially by substrate-level phosphorylation.

In summary, the enzymatic steps of the TCA cycle that generate succinate from α-ketoglutarate seem to be active throughout *T. brucei* development, but their abundance and importance vary between the distinct life cycle forms.

7. The conundrum of the TCA cycle

In *T. brucei*, it appears that the TCA cycle does not normally complete a full turn that results in the oxidation of acetyl-CoA to CO_2, even though all the enzymes of the TCA cycle are encoded by the genome (van Weelden et al. 2003, van Hellemond et al. 2005). A case in point, virtually all acetyl-CoA produced in the mitochondrion is converted to acetate instead of entering the TCA cycle (Van Hellemond et al. 1998, Millerioux et al. 2012). Perhaps to necessitate this divergent use of acetyl-CoA, citrate synthase, aconitase and isocitrate dehydrogenase have low specific activities compared with the other TCA cycle enzymes (Durieux et al. 1991). This implies that the flux through this section of the TCA cycle may be very low. However, a recent metabolomic study using ^{13}C-enriched carbon sources has shown that procyclic cells grown in the presence of proline (2mM) and high concentrations of malate (10 mM) are able to metabolize malate and produce α-ketoglutarate via the oxidative branch of the TCA cycle. This observation clearly indicates that procyclic cells can utilize the entire TCA cycle when specific metabolites reach sufficient concentrations (Villafraz et al. 2021).

If this portion of the TCA cycle is available to the parasite, it is alluring to speculate when this pathway becomes an integral part of the mitochondrial physiology. The reactions from malate to α-ketoglutarate do not seem to be important for ATP production in the procyclic forms (Figure 2, metabolic pathways highlighted in green). Instead, these enzymatic reactions might serve to generate metabolites that can be consumed in other metabolic pathways. For example, during the conversion of isocitrate to α-ketoglutarate, the *T. brucei* mitochondrial isocitrate dehydrogenase 2 generates reduced NADPH (Leroux et al. 2011). NADPH serves as a primary source of electrons for NADPH-dependent trypanothione-based redox metabolism that controls redox signaling (Ebersoll et al. 2020). Interestingly, the TCA enzymes citrate synthase, aconitase and isocitrate dehydrogenase are strongly up-regulated during early differentiation in the tsetse fly (Naguleswaran et al. 2021, Naguleswaran et al. 2018). Furthermore, these enzymes are also some of the most upregulated mitochondrial enzymes during the *in vitro* differentiation of procyclic forms to epimastigotes. Intriguingly, the mitochondrial citrate transporter is also upregulated (Dolezelova et al. 2020). However, unlike most eukaryotes, the exported cytosolic citrate does not serve as a precursor of lipogenic acetyl-CoA for *de novo* fatty acid biosynthesis in *T. brucei* (Riviere et al. 2009). Therefore, the dually localized aconitase residing in the cytosol could convert this citrate to isocitrate. If this isocitrate is then transported into the glycosomes, it can act as a substrate for the glycosomal isocitrate dehydrogenase 2, which has dual coenzyme specificity for

NADH and NADPH. Utilizing isocitrate in the glycosomes might support an expanded number of possible metabolic pathways (gluconeogenesis, redox reactions) (Wang et al. 2017).

Altogether, these recent advances suggest that this branch of the TCA cycle may be required for the proper development of insect forms. Since the differentiation is underlined by enhanced levels of mitochondrial and cellular ROS (Dolezelova et al. 2020), it is possible that the *raison d´être* of this branch of the oxidative TCA cycle is the generation of NADPH cofactors by the activity of mitochondrial and glycosomal NAD(P)H-dependent isocitrate dehydrogenases. The production of these cofactors could support the trypanothione-based detoxification of hydroperoxides and help cope with the altered redox conditions (Krauth-Siegel and Comini 2008).

Meanwhile, there is no evidence that the long slender bloodstream form requires these enzymes. In fact, they are strongly downregulated in this developmental stage. However, in the short stumpy forms, these enzymes are upregulated at the RNA level, probably as a pre-adaptation for transmission to the fly (Naguleswaran et al. 2021). Interestingly, it has been known for quite some time that the development from short stumpy forms to the procyclic stage was found to be initiated by a combination of a temperature drop and the addition of the TCA cycle intermediates: citrate and/or cis-aconitate (Engstler and Boshart 2004). While it may be tempting to suggest that the mechanism of triggered differentiation is related to the activity of the TCA cycle, it is known that the citrate and/or cis-aconitate signal is transmitted via the binding to PIP39, a protein phosphatase. This consequentially triggers a phosphorylation cascade (Szoor et al. 2020) and induces metabolic reprogramming during the differentiation of short stumpy parasites into procyclic cells.

8. Mitochondrial acetate as a key metabolite for the cytosolic fatty acid synthesis

In typical aerobic mitochondria, acetyl-CoA would be completely oxidized in the TCA cycle to CO_2. However, in *T. brucei*, this metabolite is converted to acetate by the acetate:succinate coenzyme A transferase/succinyl-CoA synthetase (ASCT/SCS) cycle that generates ATP (Riviere et al. 2004). Interestingly, this fermentative reaction coupled to substrate-level phosphorylation typically provides a source of ATP to organisms that live predominantly under microaerophilic (or anaerobic) conditions (Bringaud et al. 2010). The presence of this pathway in a fully aerobic organism such as *T. brucei* is exceptional. Importantly, it provides additional flexibility for ATP production in the mitochondrion. However, trypanosomes can also uncouple acetate production from ATP generation by employing acetyl-coenzyme A thioesterase, an enzyme capable of producing acetate from acetyl-CoA (Millerioux et al. 2012) (Figure 2, metabolic pathways in red). The interplay between these two parallel acetate synthesis pathways in the mitochondrion remains to be determined.

In the procyclic form, most of the produced acetate is excreted from the mitochondrion as a metabolic end product. In the cytosol, some of this acetate is converted to acetyl-CoA by the cytosolic enzyme acetyl-CoA synthetase. Unlike all other aerobic eukaryotes studied to date, trypanosomes do not use the citrate/malate shuttle to export mitochondrial acetyl group equivalents to the cytosol for lipid biosynthesis. Instead, these parasites utilize acetate to produce cytosolic acetyl-CoA, which serves as a substrate for *de novo* fatty acid synthesis (Millerioux et al. 2013, Riviere et al. 2009).

Acetate production is essential for both the insect and mammalian life cycle stages (Riviere et al. 2009, Mazet et al. 2013). In the bloodstream form stage, threonine and glucose-derived pyruvate are interchangeable substrates for acetate production. *In vitro* functional studies demonstrated that pyruvate dehydrogenase is only essential in the absence of threonine in the medium. Furthermore, only a double mutant of both the pyruvate and threonine dehydrogenase caused a strong reduction in the parasite growth rate (Mazet et al. 2013). However, under *in vivo* conditions, the pyruvate-derived acetate metabolic pathway seems to be more physiologically relevant, since the mitochondrial pyruvate transporter is essential for the virulency of bloodstream cells in a mouse model (Stafkova et al. 2016). This argues for a vital role of pyruvate-derived acetate for the parasite.

Although the production of acetate is undoubtedly important, the ATP produced by the ASCT/SCS cycle is intriguing because the bloodstream form mitochondrion has long been considered to be strictly an ATP consuming organelle. However, the high glycolytic flux (9 µmol/hour/mg, approximately 10-fold higher than in procyclics) of the bloodstream form results in substantial amounts of pyruvate. Approximately 5% of this metabolite is imported into the mitochondrion and converted to acetate. Altogether, this suggests that the ASCT/SCS cycle could contribute significantly to intramitochondrial ATP production. However, the silencing of the ASCT hardly affected the growth of these cells (Mochizuki et al. 2020). Ongoing research is attempting to determine all the possible sources for intramitochondrial ATP production, whether it is imported from the cytosol via the ATP/ADP carrier or generated in the organelle by substrate-level phosphorylation resulting from the oxidation of pyruvate or α-ketoglutarate. An intramitochondrial ATP source could provide the parasite with the flexibility to maintain the essential mitochondrial membrane potential when colonizing nutritionally different extravascular niches (e.g. nervous system, skin and adipose tissue).

9. Maintenance of the mitochondrial NADH/NAD+: an unresolved issue

Mitochondrial membranes are not permeable to NADH, so the NADH/NAD^+ balance must be maintained within the organelle. NAD^+ is an important cofactor for numerous mitochondrial dehydrogenases, for example the pyruvate and threonine dehydrogenases that are involved in the

essential production of acetate. Without the possibility of efficient reoxidation, the mitochondrial metabolism would come to a standstill. In addition to the electron transport chain NADH:ubiquinone dehydrogenases (i.e. complex I and NDH2 - *Sections 2.1.1. and 2.1.2.*), trypanosomes implement several substrate level reactions capable of reoxidizing NADH. For example, NADH is consumed when α-ketoglutarate is reduced to either glutamate by glutamate dehydrogenase or to 2-hydroxyglutarate. It has been suggested that the latter reaction is catalyzed by the promiscuous action of an NADH-dependent malate dehydrogenase, but this needs to be further characterized (Villafraz et al. 2021). *In vitro* labeling studies indicate that these two NADH oxidization reactions allow for a very high rate of α-ketoglutarate consumption in procyclic forms since equal amounts of α-ketoglutarate were either oxidized to create succinyl-CoA or reduced to form either glutamate or 2-hydroxyglutarate (Villafraz et al. 2021). Another way to maintain the mitochondrial NAD^+/NADH balance is through the NAD^+ regenerating activity of the reductive branch of the TCA cycle, which consists of fumarase and fumarate reductase. These subsequent reactions have been shown to be highly active in the procyclic form when glucose or malate is present (Coustou et al. 2005, Villafraz et al. 2021). However, the rates at which all these NADH-consuming reactions occur, their contribution to mitochondrial NADH oxidation activity and their importance to parasite differentiation *in vivo* remain to be determined.

10. The *T. brucei* mitochondrion and its role in cellular signaling

An important by-product of the metabolic and bioenergetic functions of a typical aerobic mitochondrion are the molecular signals emanating from the organelle that can be decoded by the nucleus. It is now generally accepted that mitochondria communicate their biosynthetic and bioenergetic fitness to the rest of the cell and that this retrograde signaling can influence cell fate (Chandel 2014). Recent studies with mammalian cells have revealed two primary signal transduction pathways: the generation of ROS (e.g superoxide and hydrogen peroxide) and the excretion of TCA cycle intermediate metabolites (e.g., citrate, succinate, and α-ketoglutarate). These mitochondria-generated molecules influence a wide range of cellular biological processes that include epigenetics, metabolic reprogramming, immune responses, proliferation, adaptation, and differentiation (Martinez-Reyes and Chandel 2020, Sies and Jones 2020). However, the molecular details of these processes remain poorly understood.

It is quite plausible that the striking changes in mitochondrial activities during Trypanosoma differentiation are not mere consequences of environmental changes, but that these changes may also reinforce life cycle stage transitions. For example, the *in vivo* development of the bloodstream form to the quiescent stumpy form was accompanied by higher levels of cellular ROS levels (Saldivia et al. 2016). Similarly, the differentiation of insect forms is also accompanied by increased signaling molecules in the form of mitochondrial superoxide and cellular hydrogen

peroxide. Notably, the efficiency of parasite differentiation to quiescent metacyclics was severely impaired when the increased ROS concentrations were reduced through the heterologous expression of a *Crithidia fasciculata* catalase, a ROS scavenger.

ROS are usually associated with their harmful properties because they damage DNA, lipids, and proteins when they are produced in large quantities (Brand 2020). However, when produced in small amounts, they can act as signals by inducing the reversible oxidation of cysteines contained within redox-sensitive proteins. These post-translational modifications affect the activity, localization, and protein-protein interactions of these target proteins. For example, AMP-activated kinase, a master metabolic regulator, is activated by H_2O_2 oxidation (Zmijewski et al. 2010). Additionally, the activation of this kinase is also sensitive to changes in the AMP/ATP ratio as already discussed in section 2.2.1. Silencing of the AMP-activated kinase complex had a strong effect on metacyclogenesis *in vitro*, indicating an essential role in parasite differentiation (Toh et al. 2021). Moreover, the activation of AMP-activated kinase is also required during the transition from proliferative bloodstream forms to quiescent short stumpy cells (Saldivia et al. 2016).

The striking mitochondrial repurposing during programmed *T. brucei* development coincides with elevated levels of ROS and the increased abundance of TCA intermediates. Therefore, this model provides a unique opportunity to investigate the role of mitochondria and mitochondrial signaling in cellular differentiation.

11. **Asphyxiating trypanosomes: the electron transport chain as a drug target**

It is becoming apparent that the bloodstream form mitochondrion is more complex and active than previously thought. Actually, the differences between the procyclic and bloodstream organelles are more quantitative than qualitative (Zikova et al. 2017). The unexplored mitochondrial pathways may represent promising targets for chemotherapeutics (Pedra-Rezende et al. 2022).

The *T. brucei* mitochondrion was long considered not to be an attractive drug target due to its reputation of being a relatively dormant organelle in the bloodstream stages. The lone exception has been the mitochondrial trypanosomal alternative oxidase, TAO. As discussed earlier (*Section 2.2.2*), TAO is critical for maintaining the glycosomal NAD^+/NADH balance and thus high glycolytic flux. Despite initial doubts that the inhibition of TAO would be sufficient to kill the parasite *in vivo* due to the continued anaerobic production of one ATP per molecule of glucose, cultured trypanosomes exposed to TAO inhibitors are unable to survive longer than 24 hours (Helfert et al. 2001). In addition, these inhibitors effectively cleared a *T. brucei* mouse infection (Helfert et al. 2001, Yabu et al. 2003). Importantly, TAO meets most of the requirements for a druggable target: 1) its activity is essential for the parasite, 2) it is absent in the mammalian host, 3) its activity can be inhibited by small compounds and 4) there is no redundancy in this metabolic

pathway. While several potent inhibitors of this enzyme have been identified, unfortunately, none of them are close to clinical trials (Menzies et al. 2018). One of the most promising seems to be ascofuranone, a biologically active natural product that shows high efficacy against *T. vivax*, one of the etiological agents of animal trypanosomiases (Yabu et al. 2006). Now that the crystal structure of this enzyme is finally available, there is renewed optimism that more effective inhibitors can be identified (Shiba et al. 2013).

Proof that the *T. brucei* mitochondrion and its activities are druggable is supported by the evidence that certain potent chemotherapeutics accumulate inside the parasite mitochondrion (Alkhaldi et al. 2016, Lanteri et al. 2008). These include several drugs commonly used for the treatment of Animal African Trypanosomiases, such as diminazine aceturate, isometamidium, phenantridine, and ethidium bromide. While the exact modes of action are unknown for these therapeutics, the import of these positively-charged molecules depends on the mitochondrial membrane potential. This point is further underscored in the observations that drug resistant parasites identified in the laboratory and in nature have often found ways to reduce their mitochondrial membrane potential (Eze et al. 2016, Gould and Schnaufer 2014, Carruthers et al. 2021). This has the effect to limit the mitochondrial import of these compounds and thus prevent them from interacting with their mitochondrial targets.

12. Concluding remarks and future perspectives

In this review, I have discussed the metabolic functions of mitochondria as bioenergetic powerhouses, biosynthetic centers, and signaling organelles. I have also addressed the importance of these functions in the five major stages of the *T. brucei* life cycle (Figure 1). However, much remains to be elucidated about the multifaceted contribution of mitochondria to the differentiation of the parasite and its ability to successfully colonize different environments in the tsetse fly and the mammalian host.

Key topics of interest include:

1. **Mitochondria as signaling organelles driving cellular differentiation.** It is now generally accepted that changes in mitochondrial bioenergetic and biosynthetic fitness are communicated to the rest of the cell via signals released from mitochondria in the form of ROS and TCA cycle intermediates (citrate, succinate, fumarate, α-ketoglutarate). ROS act directly on various redox-sensitive proteins and induce reversible oxidations of cysteine thiols. For example, ROS-induced reversible oxidation of ribosomal proteins triggers attenuation of cytosolic translation in yeast (Topf et al. 2018). Interestingly, attenuation of cytosolic translation is a hallmark of cells entering the quiescent state (e.g. metacylics). In mammalian cells, TCA cycle

intermediates directly affect the activity of Fe(ii) and α-ketoglutarate dioxygenases, including hydroxylases, DNA demethylases, and histone demethylases. Acetyl-CoA is required for epigenetic modification such as histone acetylation (Martinez-Reyes and Chandel 2020). *T. brucei* provides a unique opportunity to study these phenomena because of the major metabolic reprogramming of their single mitochondrion during programmed development.

2. **Role of AMP-activated kinase in the differentiation of quiescent life cycle forms.** Recent studies have shown that the AMP-activated kinase, the master regulator of cellular energy homeostasis may be involved in differentiation from replicative stages (e.g., epimastigotes, bloodstream form) to quiescent forms (metacyclics, stumpy form) (Saldivia et al. 2016, Toh et al. 2021). Future studies may reveal a direct link between the activation of this kinase and the observed metabolic changes. Furthermore, the identification of downstream targets of the *T. brucei* AMP-activated kinase would provide insight into the components that may control the programmed development of transmission-competent quiescent parasites.
3. **Mapping of essential mitochondrial metabolic pathways of the bloodstream form parasites in the mammalian host.** The mitochondrion of the mammalian form is hardly a dormant organelle. However, its physiological contributions, which are critical for the infection of various mammalian tissues (e.g., bloodstream, skin, adipose tissue, nervous system), remain to be determined. Research on this topic will reveal new strategies for disease intervention, provide insights into the mechanism of drug resistance and have implications for host-parasite interactions.
4. **Mitochondrial metabolism and metabolic reprogramming of *T. congolense* life cycle forms.** While decades of research on *T. brucei* have made this parasite a model organism for trypanosomatids, knowledge of the biology of *T. congolense*, the causative agent of African Animal Trypanosomiasis, is inadequate because of the limited ability to make genetic modifications. This has now been overcome, allowing important questions about the biology of the parasite to be addressed, including the fact that the mitochondrial metabolism of the bloodstream form of *T. congolense* appears to be more complex and developed than that of *T. brucei* (Awuah-Mensah et al. 2021, Steketee et al. 2021). Furthermore, *T. congolense* is capable of undergoing the insect form differentiation process in culture without requiring any genetic manipulation, unlike *T. brucei* (Coustou et al. 2010, Gibson et al. 2017, Kolev et al. 2012). This provides a clear opportunity to incorporate more advanced applications such as genome-wide functional screens to address some of the fundamental questions of parasite biology. These newly introduced tools will greatly aid our efforts to combat animal diseases caused by this parasite.
5. **Unresolved peculiarities of the *T. brucei* electron transport chain.** Despite many years of research and considerable effort to understand the bioenergetic properties of the *T. brucei*

mitochondrion, the most fundamental questions regarding the presence and activity of complex I, localization of NDH2, regulation of TAO and maintenance of mitochondrial redox balance remain unanswered. The advent of powerful genetic, physiological and structural approaches to the study of mitochondrial functions is likely to lead to important discoveries in the coming years.

6. **The role of F_oF_1-ATP synthase dimers in cristae remodeling during the transition from insect to mammalian form.** The F_oF_1-ATP synthase dimer rows are a common feature of mitochondrial cristae, which exhibit extremely high variability in ultrastructure between species. *T. brucei* provides a unique opportunity to study the role of these arrays in cristae structure and mitochondrial bioenergetics because of the striking transition from the highly branched, cristae-containing and ATP-producing mitochondrion of the insect form to a streamlined, tubular, cristae-reduced and ATP-consuming organelle of the bloodstream form. These studies should be possible now that the high-resolution structure of the dimeric ATP synthase of *T. brucei* is available (Gahura et al. 2021b).

13.References

Acestor, N., Zikova, A., Dalley, R. A., Anupama, A., Panigrahi, A. K. & Stuart, K. D. 2011. Trypanosoma brucei mitochondrial respiratome: composition and organization in procyclic form. *Mol Cell Proteomics,* **10:**M110 006908.

Albert, M. A., Haanstra, J. R., Hannaert, V., Van Roy, J., Opperdoes, F. R., Bakker, B. M. & Michels, P. A. 2005. Experimental and in silico analyses of glycolytic flux control in bloodstream form Trypanosoma brucei. *J Biol Chem,* **280:**28306-15.

Alkhaldi, A. A., Martinek, J., Panicucci, B., Dardonville, C., Zikova, A. & de Koning, H. P. 2016. Trypanocidal action of bisphosphonium salts through a mitochondrial target in bloodstream form Trypanosoma brucei. *Int J Parasitol Drugs Drug Resist,* **6:**23-34.

Allmann, S., Wargnies, M., Plazolles, N., Cahoreau, E., Biran, M., Morand, P., Pineda, E., Kulyk, H., Asencio, C., Villafraz, O., Riviere, L., Tetaud, E., Rotureau, B., Mourier, A., Portais, J. C. & Bringaud, F. 2021. Glycerol suppresses glucose consumption in trypanosomes through metabolic contest. *PLoS Biol,* **19:**e3001359.

Aphasizheva, I., Alfonzo, J., Carnes, J., Cestari, I., Cruz-Reyes, J., Goringer, H. U., Hajduk, S., Lukes, J., Madison-Antenucci, S., Maslov, D. A., McDermott, S. M., Ochsenreiter, T., Read, L. K., Salavati, R., Schnaufer, A., Schneider, A., Simpson, L., Stuart, K., Yurchenko, V., Zhou, Z. H., Zikova, A., Zhang, L., Zimmer, S. & Aphasizhev, R. 2020. Lexis and

Grammar of Mitochondrial RNA Processing in Trypanosomes. *Trends Parasitol,* **36:**337-355.

Assefa, S. & Shibeshi, W. 2018. Drug resistance in African animal trypanosomes: A review. . *African Journal of Microbiology Research,* **12:**380-386.

Awuah-Mensah, G., McDonald, J., Steketee, P. C., Autheman, D., Whipple, S., D'Archivio, S., Brandt, C., Clare, S., Harcourt, K., Wright, G. J., Morrison, L. J., Gadelha, C. & Wickstead, B. 2021. Reliable, scalable functional genetics in bloodstream-form Trypanosoma congolense in vitro and in vivo. *PLoS Pathog,* **17:**e1009224.

Beleznai, Z. & Jancsik, V. 1989. Role of Cardiolipin in the Functioning of Mitochondrial L-Glycerol-3-Phosphate Dehydrogenase. *Biochemical and Biophysical Research Communications,* **159:**132-139.

Bienen, E. J., Maturi, R. K., Pollakis, G. & Clarkson, A. B., Jr. 1993. Non-cytochrome mediated mitochondrial ATP production in bloodstream form Trypanosoma brucei brucei. *Eur J Biochem,* **216:**75-80.

Bienen, E. J., Saric, M., Pollakis, G., Grady, R. W. & Clarkson, A. B., Jr. 1991. Mitochondrial development in Trypanosoma brucei brucei transitional bloodstream forms. *Mol Biochem Parasitol,* **45:**185-92.

Bily, T., Sheikh, S., Mallet, A., Bastin, P., Perez-Morga, D., Lukes, J. & Hashimi, H. 2021. Ultrastructural Changes of the Mitochondrion During the Life Cycle of Trypanosoma brucei. *J Eukaryot Microbiol,* **68:**e12846.

Bochud-Allemann, N. & Schneider, A. 2002. Mitochondrial substrate level phosphorylation is essential for growth of procyclic Trypanosoma brucei. *J Biol Chem,* **277:**32849-54.

Brand, M. D. 2020. Riding the tiger - physiological and pathological effects of superoxide and hydrogen peroxide generated in the mitochondrial matrix. *Crit Rev Biochem Mol Biol,* **55:**592-661.

Bringaud, F., Barrett, M. P. & Zilberstein, D. 2012. Multiple roles of proline transport and metabolism in trypanosomatids. *Frontiers in Bioscience-Landmark,* **17:**349-374.

Bringaud, F., Ebikeme, C. & Boshart, M. 2010. Acetate and succinate production in amoebae, helminths, diplomonads, trichomonads and trypanosomatids: common and diverse metabolic strategies used by parasitic lower eukaryotes. *Parasitology,* **137:**1315-31.

Bringaud, F., Plazolles, N., Pineda, E., Asencio, C., Villafraz, O., Millerioux, Y., Riviere, L. & Tetaud, E. 2021. Glycerol, a possible new player in the biology of trypanosomes. *PLoS Pathog,* **17:**e1010035.

Campanella, M., Parker, N., Tan, C. H., Hall, A. M. & Duchen, M. R. 2009. IF(1): setting the pace of the F(1)F(o)-ATP synthase. *Trends Biochem Sci,* **34:**343-50.

Carruthers, L. V., Munday, J. C., Ebiloma, G. U., Steketee, P., Jayaraman, S., Campagnaro, G. D., Ungogo, M. A., Lemgruber, L., Donachie, A. M., Rowan, T. G., Peter, R., Morrison, L. J., Barrett, M. P. & De Koning, H. P. 2021. Diminazene resistance in Trypanosoma congolense is not caused by reduced transport capacity but associated with reduced mitochondrial membrane potential. *Mol Microbiol*.

Chandel, N. S. 2014. Mitochondria as signaling organelles. *BMC Biol,* **12:**34.

Chaudhuri, M., Ajayi, W. & Hill, G. C. 1998. Biochemical and molecular properties of the Trypanosoma brucei alternative oxidase. *Mol Biochem Parasitol,* **95:**53-68.

Chaudhuri, M., Ott, R. D. & Hill, G. C. 2006. Trypanosome alternative oxidase: from molecule to function. *Trends Parasitol,* **22:**484-91.

Chinopoulos, C. 2011. Mitochondrial consumption of cytosolic ATP: Not so fast. *Febs Letters,* **585:**1255-1259.

Chinopoulos, C. & Adam-Vizi, V. 2010. Mitochondria as ATP consumers in cellular pathology. *Biochim Biophys Acta,* **1802:**221-7.

Christiano, R., Kolev, N. G., Shi, H., Ullu, E., Walther, T. C. & Tschudi, C. 2017. The proteome and transcriptome of the infectious metacyclic form of Trypanosoma brucei define quiescent cells primed for mammalian invasion. *Mol Microbiol,* **106:**74-92.

Clarkson, A. B., Jr., Bienen, E. J., Pollakis, G. & Grady, R. W. 1989. Respiration of bloodstream forms of the parasite Trypanosoma brucei brucei is dependent on a plant-like alternative oxidase. *J Biol Chem,* **264:**17770-6.

Colasante, C., Zheng, F., Kemp, C. & Voncken, F. 2018. A plant-like mitochondrial carrier family protein facilitates mitochondrial transport of di- and tricarboxylates in Trypanosoma brucei. *Mol Biochem Parasitol,* **221:**36-51.

Coustou, V., Guegan, F., Plazolles, N. & Baltz, T. 2010. Complete in vitro life cycle of Trypanosoma congolense: development of genetic tools. *PLoS Negl Trop Dis,* **4:**e618.

Coustou, V., Besteiro, S., Riviere, L., Biran, M., Biteau, N., Franconi, J. M., Boshart, M., Baltz, T. & Bringaud, F. 2005. A mitochondrial NADH-dependent fumarate reductase involved

in the production of succinate excreted by procyclic Trypanosoma brucei. *J Biol Chem,* **280:**16559-70.

Coustou, V., Biran, M., Breton, M., Guegan, F., Riviere, L., Plazolles, N., Nolan, D., Barrett, M. P., Franconi, J. M. & Bringaud, F. 2008. Glucose-induced remodeling of intermediary and energy metabolism in procyclic Trypanosoma brucei. *J Biol Chem,* **283:**16342-54.

Creek, D. J., Mazet, M., Achcar, F., Anderson, J., Kim, D. H., Kamour, R., Morand, P., Millerioux, Y., Biran, M., Kerkhoven, E. J., Chokkathukalam, A., Weidt, S. K., Burgess, K. E., Breitling, R., Watson, D. G., Bringaud, F. & Barrett, M. P. 2015. Probing the metabolic network in bloodstream-form Trypanosoma brucei using untargeted metabolomics with stable isotope labelled glucose. *PLoS Pathog,* **11:**e1004689.

Dejung, M., Subota, I., Bucerius, F., Dindar, G., Freiwald, A., Engstler, M., Boshart, M., Butter, F. & Janzen, C. J. 2016. Quantitative Proteomics Uncovers Novel Factors Involved in Developmental Differentiation of Trypanosoma brucei. *PLoS Pathog,* **12:**e1005439.

Dewar, C. E., MacGregor, P., Cooper, S., Gould, M. K., Matthews, K. R., Savill, N. J. & Schnaufer, A. 2018. Mitochondrial DNA is critical for longevity and metabolism of transmission stage Trypanosoma brucei. *PLoS Pathog,* **14:**e1007195.

Dewar, C. E., Casas-Sanchez, A., Dieme, C., Crouzols, A., Haines, L. R., Acosta-Serrano, A., Rotureau, B. & Schnaufer, A. 2022. Oxidative Phosphorylation Is Required for Powering Motility and Development of the Sleeping Sickness Parasite Trypanosoma brucei in the Tsetse Fly Vector. *mBio***:**e0235721.

Dolezelova, E., Kunzova, M., Dejung, M., Levin, M., Panicucci, B., Regnault, C., Janzen, C. J., Barrett, M. P., Butter, F. & Zikova, A. 2020. Cell-based and multi-omics profiling reveals dynamic metabolic repurposing of mitochondria to drive developmental progression of Trypanosoma brucei. *PLoS Biol,* **18:**e3000741.

Duarte, M. & Tomas, A. M. 2014. The mitochondrial complex I of trypanosomatids--an overview of current knowledge. *J Bioenerg Biomembr,* **46:**299-311.

Durieux, P. O., Schutz, P., Brun, R. & Kohler, P. 1991. Alterations in Krebs cycle enzyme activities and carbohydrate catabolism in two strains of Trypanosoma brucei during in vitro differentiation of their bloodstream to procyclic stages. *Mol Biochem Parasitol,* **45:**19-27.

Dyer, N. A., Rose, C., Ejeh, N. O. & Acosta-Serrano, A. 2013. Flying tryps: survival and maturation of trypanosomes in tsetse flies. *Trends Parasitol,* **29:**188-96.

Ebersoll, S., Bogacz, M., Gunter, L. M., Dick, T. P. & Krauth-Siegel, R. L. 2020. A tryparedoxin-coupled biosensor reveals a mitochondrial trypanothione metabolism in trypanosomes. *Elife*, **9**.

Engstler, M. & Boshart, M. 2004. Cold shock and regulation of surface protein trafficking convey sensitization to inducers of stage differentiation in Trypanosoma brucei. *Genes Dev*, **18:**2798-811.

Eze, A. A., Gould, M. K., Munday, J. C., Tagoe, D. N., Stelmanis, V., Schnaufer, A. & De Koning, H. P. 2016. Reduced Mitochondrial Membrane Potential Is a Late Adaptation of Trypanosoma brucei brucei to Isometamidium Preceded by Mutations in the gamma Subunit of the F1Fo-ATPase. *PLoS Negl Trop Dis*, **10:**e0004791.

Fang, J. & Beattie, D. S. 2003. Identification of a gene encoding a 54 kDa alternative NADH dehydrogenase in Trypanosoma brucei. *Mol Biochem Parasitol*, **127:**73-7.

Fang, J. & Beattie, D. S. 2002. Novel FMN-containing rotenone-insensitive NADH dehydrogenase from Trypanosoma brucei mitochondria: isolation and characterization. *Biochemistry*, **41:**3065-72.

Gahura, O., Hierro-Yap, C. & Zikova, A. 2021a. Redesigned and reversed: architectural and functional oddities of the trypanosomal ATP synthase. *Parasitology*, **148:**1151-1160.

Gahura, O., Mühleip, A., Hierro-Yap, C., Panicucci, B., Jain, M., Hollaus, D., Slapničková, M., Zíková, A. & Amunts, A. 2021b. An ancestral interaction module promotes oligomerization in divergent mitochondrial ATP synthases. *bioRxiv***:**2021.10.10.463820.

Garcia-Bermudez, J. & Cuezva, J. M. 2016. The ATPase Inhibitory Factor 1 (IF1): A master regulator of energy metabolism and of cell survival. *Biochimica Et Biophysica Acta-Bioenergetics*, **1857:**1167-1182.

Gibson, W., Kay, C. & Peacock, L. 2017. Trypanosoma congolense: Molecular Toolkit and Resources for Studying a Major Livestock Pathogen and Model Trypanosome. *Adv Parasitol*, **98:**283-309.

Gnipova, A., Panicucci, B., Paris, Z., Verner, Z., Horvath, A., Lukes, J. & Zikova, A. 2012. Disparate phenotypic effects from the knockdown of various Trypanosoma brucei cytochrome c oxidase subunits. *Mol Biochem Parasitol*, **184:**90-8.

Gottier, P., Serricchio, M., Vitale, R., Corcelli, A. & Butikofer, P. 2017. Cross-species complementation of bacterial- and eukaryotic-type cardiolipin synthases. *Microb Cell*, **4:**376-383.

Gould, M. K. & Schnaufer, A. 2014. Independence from Kinetoplast DNA maintenance and expression is associated with multidrug resistance in Trypanosoma brucei in vitro. *Antimicrob Agents Chemother,* **58:**2925-8.

Grant, P. T. & Sargent, J. R. 1960. Properties of L-alpha-glycerophosphate oxidase and its role in the respiration of Trypanosoma rhodesiense. *Biochem J,* **76:**229-37.

Haanstra, J. R., Gonzalez-Marcano, E. B., Gualdron-Lopez, M. & Michels, P. A. M. 2016. Biogenesis, maintenance and dynamics of glycosomes in trypanosomatid parasites. *Biochimica Et Biophysica Acta-Molecular Cell Research,* **1863:**1038-1048.

Haiens, T. H. & Dencher, N. A. 2002. Cardiolipin: a proton trap for oxidative phosphorylation. *Febs Letters,* **528:**35-39.

Haindrich, A. C., Ernst, V., Naguleswaran, A., Oliveres, Q. F., Roditi, I. & Rentsch, D. 2021. Nutrient availability regulates proline/alanine transporters in Trypanosoma brucei. *J Biol Chem,* **296:**100566.

Helfert, S., Estevez, A. M., Bakker, B., Michels, P. & Clayton, C. 2001. Roles of triosephosphate isomerase and aerobic metabolism in Trypanosoma brucei. *Biochem J,* **357:**117-25.

Herzig, S. & Shaw, R. J. 2018. AMPK: guardian of metabolism and mitochondrial homeostasis. *Nat Rev Mol Cell Biol,* **19:**121-135.

Hierro-Yap, C., Subrtova, K., Gahura, O., Panicucci, B., Dewar, C., Chinopoulos, C., Schnaufer, A. & Zikova, A. 2021. Bioenergetic consequences of FoF1-ATP synthase/ATPase deficiency in two life cycle stages of Trypanosoma brucei. *J Biol Chem,* **296:**100357.

Horn, D. 2022. A profile of research on the parasitic trypanosomatids and the diseases they cause. *PLoS Negl Trop Dis,* **16:**e0010040.

Horvath, A., Horakova, E., Dunajcikova, P., Verner, Z., Pravdova, E., Slapetova, I., Cuninkova, L. & Lukes, J. 2005. Downregulation of the nuclear-encoded subunits of the complexes III and IV disrupts their respective complexes but not complex I in procyclic Trypanosoma brucei. *Mol Microbiol,* **58:**116-30.

Houtkooper, R. H. & Vaz, F. M. 2008. Cardiolipin, the heart of mitochondrial metabolism. *Cellular and Molecular Life Sciences,* **65:**2493-2506.

Huang, G. & Docampo, R. 2018. The Mitochondrial Ca(2+) Uniporter Complex (MCUC) of Trypanosoma brucei Is a Hetero-oligomer That Contains Novel Subunits Essential for Ca(2+) Uptake. *MBio,* **9**.

Huang, G., Vercesi, A. E. & Docampo, R. 2013. Essential regulation of cell bioenergetics in Trypanosoma brucei by the mitochondrial calcium uniporter. *Nat Commun,* **4:**2865.

Imhof, S., Knusel, S., Gunasekera, K., Vu, X. L. & Roditi, I. 2014. Social motility of African trypanosomes is a property of a distinct life-cycle stage that occurs early in tsetse fly transmission. *PLoS Pathog,* **10:**e1004493.

Johnston, K., Kim, D. H., Kerkhoven, E. J., Burchmore, R., Barrett, M. P. & Achcar, F. 2019. Mapping the metabolism of five amino acids in bloodstream form Trypanosoma brucei using U-C-13-labelled substrates and LC-MS. *Bioscience Reports,* **39**.

Kolev, N. G., Ramey-Butler, K., Cross, G. A. M., Ullu, E. & Tschudi, C. 2012. Developmental Progression to Infectivity in Trypanosoma brucei Triggered by an RNA-Binding Protein. *Science,* **338:**1352-1353.

Kovarova, J. & Barrett, M. P. 2016. The Pentose Phosphate Pathway in Parasitic Trypanosomatids. *Trends Parasitol,* **32:**622-634.

Kovarova, J., Nagar, R., Faria, J., Ferguson, M. A. J., Barrett, M. P. & Horn, D. 2018. Gluconeogenesis using glycerol as a substrate in bloodstream-form Trypanosoma brucei. *PLoS Pathog,* **14:**e1007475.

Krauth-Siegel, R. L. & Comini, M. A. 2008. Redox control in trypanosomatids, parasitic protozoa with trypanothione-based thiol metabolism. *Biochim Biophys Acta,* **1780:**1236-48.

Kuhlbrandt, W. 2019. Structure and Mechanisms of F-Type ATP Synthases. *Annu Rev Biochem,* **88:**515-549.

Lamour, N., Riviere, L., Coustou, V., Coombs, G. H., Barrett, M. P. & Bringaud, F. 2005. Proline metabolism in procyclic Trypanosoma brucei is down-regulated in the presence of glucose. *J Biol Chem,* **280:**11902-10.

Lanteri, C. A., Tidwell, R. R. & Meshnick, S. R. 2008. The mitochondrion is a site of trypanocidal action of the aromatic diamidine DB75 in bloodstream forms of Trypanosoma brucei. *Antimicrob Agents Chemother,* **52:**875-82.

Leroux, A. E., Maugeri, D. A., Cazzulo, J. J. & Nowicki, C. 2011. Functional characterization of NADP-dependent isocitrate dehydrogenase isozymes from Trypanosoma cruzi. *Mol Biochem Parasitol,* **177:**61-4.

Luevano-Martinez, L. A., Girard, R. M. B. M., Alencar, M. B. & Silber, A. M. 2020. ATP regulates the activity of an alternative oxidase in Trypanosoma brucei. *Febs Letters,* **594:**2150-2158.

Lukes, J. & Basu, S. 2015. Fe/S protein biogenesis in trypanosomes - A review. *Biochim Biophys Acta*, **1853:**1481-92.

Maguire, J. J., Tyurina, Y. Y., Mohammadyani, D., Kapralov, A. A., Anthonymuthu, T. S., Qu, F., Amoscato, A. A., Sparvero, L. J., Tyurin, V. A., Planas-Iglesias, J., He, R. R., Klein-Seetharaman, J., Bayir, H. & Kagan, V. E. 2017. Known unknowns of cardiolipin signaling: The best is yet to come. *Biochimica Et Biophysica Acta-Molecular and Cell Biology of Lipids*, **1862:**8-24.

Mannella, C. A. 2020. Consequences of Folding the Mitochondrial Inner Membrane. *Front Physiol*, **11:**536.

Mantilla, B. S., Paes-Vieira, L., de Almeida Dias, F., Calderano, S. G., Elias, M. C., Cosentino-Gomes, D., Oliveira, P. L., Meyer-Fernandes, J. R. & Silber, A. M. 2021. Higher expression of proline dehydrogenase altered mitochondrial function and increased Trypanosoma cruzi differentiation in vitro and in the insect vector. *Biochem J*, **478:**3891-3903.

Mantilla, B. S., Marchese, L., Casas-Sanchez, A., Dyer, N. A., Ejeh, N., Biran, M., Bringaud, F., Lehane, M. J., Acosta-Serrano, A. & Silber, A. M. 2017. Proline Metabolism is Essential for Trypanosoma brucei brucei Survival in the Tsetse Vector. *PLoS Pathog*, **13:**e1006158.

Marchese, L., Olavarria, K., Mantilla, B. S., Avila, C. C., Souza, R. O. O., Damasceno, F. S., Elias, M. C. & Silber, A. M. 2020. Trypanosoma cruzi synthesizes proline via a Delta(1)-pyrroline-5-carboxylate reductase whose activity is fine-tuned by NADPH cytosolic pools. *Biochemical Journal*, **477:**1827-1845.

Martinez-Reyes, I. & Chandel, N. S. 2020. Mitochondrial TCA cycle metabolites control physiology and disease. *Nat Commun*, **11:**102.

Mazet, M., Morand, P., Biran, M., Bouyssou, G., Courtois, P., Daulouede, S., Millerioux, Y., Franconi, J. M., Vincendeau, P., Moreau, P. & Bringaud, F. 2013. Revisiting the central metabolism of the bloodstream forms of Trypanosoma brucei: production of acetate in the mitochondrion is essential for parasite viability. *PLoS Negl Trop Dis*, **7:**e2587.

Menzies, S. K., Tulloch, L. B., Florence, G. J. & Smith, T. K. 2018. The trypanosome alternative oxidase: a potential drug target? *Parasitology*, **145:**175-183.

Michels, P. A. M., Villafraz, O., Pineda, E., Alencar, M. B., Caceres, A. J., Silber, A. M. & Bringaud, F. 2021. Carbohydrate metabolism in trypanosomatids: New insights revealing novel complexity, diversity and species-unique features. *Exp Parasitol*, **224:**108102.

Millerioux, Y., Ebikeme, C., Biran, M., Morand, P., Bouyssou, G., Vincent, I. M., Mazet, M., Riviere, L., Franconi, J. M., Burchmore, R. J., Moreau, P., Barrett, M. P. & Bringaud, F. 2013. The threonine degradation pathway of the Trypanosoma brucei procyclic form: the main carbon source for lipid biosynthesis is under metabolic control. *Mol Microbiol,* **90:**114-29.

Millerioux, Y., Morand, P., Biran, M., Mazet, M., Moreau, P., Wargnies, M., Ebikeme, C., Deramchia, K., Gales, L., Portais, J. C., Boshart, M., Franconi, J. M. & Bringaud, F. 2012. ATP synthesis-coupled and -uncoupled acetate production from acetyl-CoA by mitochondrial acetate:succinate CoA-transferase and acetyl-CoA thioesterase in Trypanosoma. *J Biol Chem,* **287:**17186-97.

Mochizuki, K., Inaoka, D. K., Mazet, M., Shiba, T., Fukuda, K., Kurasawa, H., Millerioux, Y., Boshart, M., Balogun, E. O., Harada, S., Hirayama, K., Bringaud, F. & Kita, K. 2020. The ASCT/SCS cycle fuels mitochondrial ATP and acetate production in Trypanosoma brucei. *Biochimica Et Biophysica Acta-Bioenergetics,* **1861**.

Montgomery, M. G., Gahura, O., Leslie, A. G. W., Zikova, A. & Walker, J. E. 2018. ATP synthase from Trypanosoma brucei has an elaborated canonical F1-domain and conventional catalytic sites. *Proc Natl Acad Sci U S A,* **115:**2102-2107.

Mugnier, M. R., Stebbins, C. E. & Papavasiliou, F. N. 2016. Masters of Disguise: Antigenic Variation and the VSG Coat in Trypanosoma brucei. *Plos Pathogens,* **12**.

Naguleswaran, A., Doiron, N. & Roditi, I. 2018. RNA-Seq analysis validates the use of culture-derived Trypanosoma brucei and provides new markers for mammalian and insect life-cycle stages. *BMC Genomics,* **19:**227.

Naguleswaran, A., Fernandes, P., Bevkal, S., Rehmann, R., Nicholson, P. & Roditi, I. 2021. Developmental changes and metabolic reprogramming during establishment of infection and progression of Trypanosoma brucei brucei through its insect host. *PLoS Negl Trop Dis,* **15:**e0009504.

Nolan, D. P. & Voorheis, H. P. 1992. The mitochondrion in bloodstream forms of Trypanosoma brucei is energized by the electrogenic pumping of protons catalysed by the F1F0-ATPase. *Eur J Biochem,* **209:**207-16.

Opperdoes, F. R., Borst, P., Bakker, S. & Leene, W. 1977. Localization of glycerol-3-phosphate oxidase in the mitochondrion and particulate NAD+-linked glycerol-3-phosphate dehydrogenase in the microbodies of the bloodstream form to Trypanosoma brucei. *Eur J Biochem,* **76:**29-39.

Paes, L. S., Suarez Mantilla, B., Zimbres, F. M., Pral, E. M., Diogo de Melo, P., Tahara, E. B., Kowaltowski, A. J., Elias, M. C. & Silber, A. M. 2013. Proline dehydrogenase regulates redox state and respiratory metabolism in Trypanosoma cruzi. *PLoS One,* **8:**e69419.

Panicucci, B., Gahura, O. & Zikova, A. 2017. Trypanosoma brucei TbIF1 inhibits the essential F1-ATPase in the infectious form of the parasite. *PLoS Negl Trop Dis,* **11:**e0005552.

Paradies, G., Paradies, V., Ruggiero, F. M. & Petrosillo, G. 2019. Role of Cardiolipin in Mitochondrial Function and Dynamics in Health and Disease: Molecular and Pharmacological Aspects. *Cells,* **8**.

Pedra-Rezende, Y., Bombaca, A. C. S. & Menna-Barreto, R. F. S. 2022. Is the mitochondrion a promising drug target in trypanosomatids? *Mem Inst Oswaldo Cruz,* **117:**e210379.

Pfeiffer, K., Gohil, V., Stuart, R. A., Hunte, C., Brandt, U., Greenberg, M. L. & Schagger, H. 2003. Cardiolipin stabilizes respiratory chain supercomplexes. *J Biol Chem,* **278:**52873-80.

Pineda, E., Thonnus, M., Mazet, M., Mourier, A., Cahoreau, E., Kulyk, H., Dupuy, J. W., Biran, M., Masante, C., Allmann, S., Riviere, L., Rotureau, B., Portais, J. C. & Bringaud, F. 2018. Glycerol supports growth of the Trypanosoma brucei bloodstream forms in the absence of glucose: Analysis of metabolic adaptations on glycerol-rich conditions. *PLoS Pathog,* **14:**e1007412.

Pullman, M. E. & Monroy, G. C. 1963. A Naturally Occurring Inhibitor of Mitochondrial Adenosine Triphosphatase. *J Biol Chem,* **238:**3762-9.

Ren, M. D., Phoon, C. K. L. & Schlame, M. 2014. Metabolism and function of mitochondrial cardiolipin. *Progress in Lipid Research,* **55:**1-16.

Riviere, L., Moreau, P., Allmann, S., Hahn, M., Biran, M., Plazolles, N., Franconi, J. M., Boshart, M. & Bringaud, F. 2009. Acetate produced in the mitochondrion is the essential precursor for lipid biosynthesis in procyclic trypanosomes. *Proc Natl Acad Sci U S A,* **106:**12694-9.

Riviere, L., van Weelden, S. W., Glass, P., Vegh, P., Coustou, V., Biran, M., van Hellemond, J. J., Bringaud, F., Tielens, A. G. & Boshart, M. 2004. Acetyl:succinate CoA-transferase in procyclic Trypanosoma brucei. Gene identification and role in carbohydrate metabolism. *J Biol Chem,* **279:**45337-46.

Roditi, I., Schumann, G. & Naguleswaran, A. 2016. Environmental sensing by African trypanosomes. *Curr Opin Microbiol,* **32:**26-30.

Rojas, F. & Matthews, K. R. 2019. Quorum sensing in African trypanosomes. *Curr Opin Microbiol,* **52:**124-129.

Rojas, F., Silvester, E., Young, J., Milne, R., Tettey, M., Houston, D. R., Walkinshaw, M. D., Perez-Pi, I., Auer, M., Denton, H., Smith, T. K., Thompson, J. & Matthews, K. R. 2019. Oligopeptide Signaling through TbGPR89 Drives Trypanosome Quorum Sensing. *Cell,* **176:**306-317 e16.

Rotureau, B. & Van Den Abbeele, J. 2013. Through the dark continent: African trypanosome development in the tsetse fly. *Front Cell Infect Microbiol,* **3:**53.

Ryley, J. F. 1956. Studies on the metabolism of the Protozoa. 7. Comparative carbohydrate metabolism of eleven species of trypanosome. *Biochem J,* **62:**215-22.

Saldivia, M., Ceballos-Perez, G., Bart, J. M. & Navarro, M. 2016. The AMPKalpha1 Pathway Positively Regulates the Developmental Transition from Proliferation to Quiescence in Trypanosoma brucei. *Cell Rep,* **17:**660-670.

Savage, A. F., Kolev, N. G., Franklin, J. B., Vigneron, A., Aksoy, S. & Tschudi, C. 2016. Transcriptome Profiling of Trypanosoma brucei Development in the Tsetse Fly Vector Glossina morsitans. *PLoS One,* **11:**e0168877.

Schadeli, D., Serricchio, M., Ben Hamidane, H., Loffreda, A., Hemphill, A., Beneke, T., Gluenz, E., Graumann, J. & Butikofer, P. 2019. Cardiolipin depletion-induced changes in the Trypanosoma brucei proteome. *FASEB J,* **33:**13161-13175.

Schnaufer, A., Clark-Walker, G. D., Steinberg, A. G. & Stuart, K. 2005. The F1-ATP synthase complex in bloodstream stage trypanosomes has an unusual and essential function. *EMBO J,* **24:**4029-40.

Schneider, A. 2020. Evolution of mitochondrial protein import - lessons from trypanosomes. *Biol Chem,* **401:**663-676.

Schneider, A. & Ochsenreiter, T. 2018. Failure is not an option - mitochondrial genome segregation in trypanosomes. *Journal of Cell Science,* **131**.

Serricchio, M. & Butikofer, P. 2012. An essential bacterial-type cardiolipin synthase mediates cardiolipin formation in a eukaryote. *Proc Natl Acad Sci U S A,* **109:**E954-61.

Serricchio, M., Hierro-Yap, C., Schadeli, D., Ben Hamidane, H., Hemphill, A., Graumann, J., Zikova, A. & Butikofer, P. 2021. Depletion of cardiolipin induces major changes in energy metabolism in Trypanosoma brucei bloodstream forms. *FASEB J,* **35:**e21176.

Shaw, S., Knusel, S., Abbuhl, D., Naguleswaran, A., Etzensperger, R., Benninger, M. & Roditi, I. 2022. Cyclic AMP signalling and glucose metabolism mediate pH taxis by African trypanosomes. *Nat Commun,* **13:**603.

Shiba, T., Kido, Y., Sakamoto, K., Inaoka, D. K., Tsuge, C., Tatsumi, R., Takahashi, G., Balogun, E. O., Nara, T., Aoki, T., Honma, T., Tanaka, A., Inoue, M., Matsuoka, S., Saimoto, H., Moore, A. L., Harada, S. & Kita, K. 2013. Structure of the trypanosome cyanide-insensitive alternative oxidase. *Proc Natl Acad Sci U S A,* **110:**4580-5.

Sies, H. 2017. Hydrogen peroxide as a central redox signaling molecule in physiological oxidative stress: Oxidative eustress. *Redox Biol,* **11:**613-619.

Sies, H. & Jones, D. P. 2020. Reactive oxygen species (ROS) as pleiotropic physiological signalling agents. *Nat Rev Mol Cell Biol,* **21:**363-383.

Skodova, I., Verner, Z., Bringaud, F., Fabian, P., Lukes, J. & Horvath, A. 2013. Characterization of Two Mitochondrial Flavin Adenine Dinucleotide-Dependent Glycerol-3-Phosphate Dehydrogenases in Trypanosoma brucei. *Eukaryotic Cell,* **12:**1664-1673.

Smith, T. K., Bringaud, F., Nolan, D. P. & Figueiredo, L. M. 2017. Metabolic reprogramming during the Trypanosoma brucei life cycle. *F1000Res,* **6**.

Spitznagel, D., Ebikeme, C., Biran, M., Nic a' Bhaird, N., Bringaud, F., Henehan, G. T. & Nolan, D. P. 2009. Alanine aminotransferase of Trypanosoma brucei--a key role in proline metabolism in procyclic life forms. *FEBS J,* **276:**7187-99.

Stafkova, J., Mach, J., Biran, M., Verner, Z., Bringaud, F. & Tachezy, J. 2016. Mitochondrial pyruvate carrier in Trypanosoma brucei. *Mol Microbiol,* **100:**442-56.

Steketee, P. C., Dickie, E. A., Iremonger, J., Crouch, K., Paxton, E., Jayaraman, S., Alfituri, O. A., Awuah-Mensah, G., Ritchie, R., Schnaufer, A., Rowan, T., de Koning, H. P., Gadelha, C., Wickstead, B., Barrett, M. P. & Morrison, L. J. 2021. Divergent metabolism between Trypanosoma congolense and Trypanosoma brucei results in differential sensitivity to metabolic inhibition. *PLoS Pathog,* **17:**e1009734.

Subrtova, K., Panicucci, B. & Zikova, A. 2015. ATPaseTb2, a Unique Membrane-bound FoF1-ATPase Component, Is Essential in Bloodstream and Dyskinetoplastic Trypanosomes. *PLoS Pathog,* **11:**e1004660.

Surve, S., Heestand, M., Panicucci, B., Schnaufer, A. & Parsons, M. 2012. Enigmatic presence of mitochondrial complex I in Trypanosoma brucei bloodstream forms. *Eukaryot Cell,* **11:**183-93.

Surve, S. V., Jensen, B. C., Heestand, M., Mazet, M., Smith, T. K., Bringaud, F., Parsons, M. & Schnaufer, A. 2016. NADH dehydrogenase of Trypanosoma brucei is important for efficient acetate production in bloodstream forms. *Mol Biochem Parasitol*.

Szoor, B., Silvester, E. & Matthews, K. R. 2020. A Leap Into the Unknown - Early Events in African Trypanosome Transmission. *Trends Parasitol,* **36:**266-278.

Toh, J. Y., Nkouawa, A., Sanchez, S. R., Shi, H., Kolev, N. G. & Tschudi, C. 2021. Identification of positive and negative regulators in the stepwise developmental progression towards infectivity in Trypanosoma brucei. *Sci Rep,* **11:**5755.

Topf, U., Suppanz, I., Samluk, L., Wrobel, L., Boser, A., Sakowska, P., Knapp, B., Pietrzyk, M. K., Chacinska, A. & Warscheid, B. 2018. Quantitative proteomics identifies redox switches for global translation modulation by mitochondrially produced reactive oxygen species. *Nat Commun,* **9:**324.

Trindade, S., Rijo-Ferreira, F., Carvalho, T., Pinto-Neves, D., Guegan, F., Aresta-Branco, F., Bento, F., Young, S. A., Pinto, A., Van Den Abbeele, J., Ribeiro, R. M., Dias, S., Smith, T. K. & Figueiredo, L. M. 2016. Trypanosoma brucei Parasites Occupy and Functionally Adapt to the Adipose Tissue in Mice. *Cell Host Microbe,* **19:**837-48.

Van Hellemond, J. J., Opperdoes, F. R. & Tielens, A. G. M. 1998. Trypanosomatidae produce acetate via a mitochondrial acetate : succinate CoA transferase. *Proceedings of the National Academy of Sciences of the United States of America,* **95:**3036-3041.

van Hellemond, J. J., Opperdoes, F. R. & Tielens, A. G. 2005. The extraordinary mitochondrion and unusual citric acid cycle in Trypanosoma brucei. *Biochem Soc Trans,* **33:**967-71.

van Weelden, S. W., Fast, B., Vogt, A., van der Meer, P., Saas, J., van Hellemond, J. J., Tielens, A. G. & Boshart, M. 2003. Procyclic Trypanosoma brucei do not use Krebs cycle activity for energy generation. *J Biol Chem,* **278:**12854-63.

Vassella, E., Den Abbeele, J. V., Butikofer, P., Renggli, C. K., Furger, A., Brun, R. & Roditi, I. 2000. A major surface glycoprotein of trypanosoma brucei is expressed transiently during development and can be regulated post-transcriptionally by glycerol or hypoxia. *Genes Dev,* **14:**615-26.

Verner, Z., Cermakova, P., Skodova, I., Kriegova, E., Horvath, A. & Lukes, J. 2011. Complex I (NADH:ubiquinone oxidoreductase) is active in but non-essential for procyclic Trypanosoma brucei. *Mol Biochem Parasitol,* **175:**196-200.

Verner, Z., Skodova, I., Polakova, S., Durisova-Benkovicova, V., Horvath, A. & Lukes, J. 2013. Alternative NADH dehydrogenase (NDH2): intermembrane-space-facing counterpart of mitochondrial complex I in the procyclic Trypanosoma brucei. *Parasitology,* **140:**328-337.

Verner, Z., Basu, S., Benz, C., Dixit, S., Dobakova, E., Faktorova, D., Hashimi, H., Horakova, E., Huang, Z., Paris, Z., Pena-Diaz, P., Ridlon, L., Tyc, J., Wildridge, D., Zikova, A. & Lukes,

J. 2015. Malleable Mitochondrion of Trypanosoma brucei. *Int Rev Cell Mol Biol,* **315:**73-151.

Vickerman, K. 1965. Polymorphism and mitochondrial activity in sleeping sickness trypanosomes. *Nature,* **208:**762-6.

Vickerman, K. 1985. Developmental cycles and biology of pathogenic trypanosomes. *Br Med Bull,* **41:**105-14.

Villafraz, O., Biran, M., Pineda, E., Plazolles, N., Cahoreau, E., Souza, R. O. O., Thonnus, M., Allmann, S., Tetaud, E., Riviere, L., Silber, A. M., Barrett, M. P., Zikova, A., Boshart, M., Portais, J. C. & Bringaud, F. 2021. Procyclic trypanosomes recycle glucose catabolites and TCA cycle intermediates to stimulate growth in the presence of physiological amounts of proline. *Plos Pathogens,* **17**.

Walker, J. E. 2013. The ATP synthase: the understood, the uncertain and the unknown. *Biochem Soc Trans,* **41:**1-16.

Walsh, B. & Hill, K. L. 2021. Right place, right time: Environmental sensing and signal transduction directs cellular differentiation and motility in Trypanosoma brucei. *Mol Microbiol*.

Wang, X., Inaoka, D. K., Shiba, T., Balogun, E. O., Allmann, S., Watanabe, Y. I., Boshart, M., Kita, K. & Harada, S. 2017. Expression, purification, and crystallization of type 1 isocitrate dehydrogenase from Trypanosoma brucei brucei. *Protein Expr Purif,* **138:**56-62.

Wargnies, M., Bertiaux, E., Cahoreau, E., Ziebart, N., Crouzols, A., Morand, P., Biran, M., Allmann, S., Hubert, J., Villafraz, O., Millerioux, Y., Plazolles, N., Asencio, C., Riviere, L., Rotureau, B., Boshart, M., Portais, J. C. & Bringaud, F. 2018. Gluconeogenesis is essential for trypanosome development in the tsetse fly vector. *PLoS Pathog,* **14:**e1007502.

Yabu, Y., Suzuki, T., Nihei, C., Minagawa, N., Hosokawa, T., Nagai, K., Kita, K. & Ohta, N. 2006. Chemotherapeutic efficacy of ascofuranone in Trypanosoma vivax-infected mice without glycerol. *Parasitol Int,* **55:**39-43.

Yabu, Y., Yoshida, A., Suzuki, T., Nihei, C., Kawai, K., Minagawa, N., Hosokawa, T., Nagai, K., Kita, K. & Ohta, N. 2003. The efficacy of ascofuranone in a consecutive treatment on Trypanosoma brucei brucei in mice. *Parasitol Int,* **52:**155-64.

Zhang, M., Mileykovskaya, E. & Dowhan, W. 2005. Cardiolipin is essential for organization of complexes III and IV into a supercomplex in intact yeast mitochondria. *J Biol Chem,* **280:**29403-8.

Zikova, A., Schnaufer, A., Dalley, R. A., Panigrahi, A. K. & Stuart, K. D. 2009. The F(0)F(1)-ATP synthase complex contains novel subunits and is essential for procyclic Trypanosoma brucei. *PLoS Pathog,* **5:**e1000436.

Zikova, A., Verner, Z., Nenarokova, A., Michels, P. A. M. & Lukes, J. 2017. A paradigm shift: The mitoproteomes of procyclic and bloodstream Trypanosoma brucei are comparably complex. *PLoS Pathog,* **13:**e1006679.

Zmijewski, J. W., Banerjee, S., Bae, H., Friggeri, A., Lazarowski, E. R. & Abraham, E. 2010. Exposure to hydrogen peroxide induces oxidation and activation of AMP-activated protein kinase. *J Biol Chem*, **285:**33154-33164.

14. Summary of articles in the thesis

This habilitation thesis comprises a portion of my scientific accomplishments focused on the multifaceted roles of the *T. brucei mitochondrion* and its involvement in the bioenergetics of the parasite during development in both hosts. These include 13 primary research papers, 1 review paper, and 1 preprint. They are all included as appendices to the thesis. Two reviews are mentioned in the thesis but are not included due to their length (Verner et al., 2015) or limited current relevance to the topic presented (Aphasizheva et al., 2020).

The research papers are arranged in alphabetical order by the first author.

* corresponding author

- Acestor N, **Zíková A**, Dalley RA, Anupama A, Panigrahi AK, Stuart KD (2011). *Trypanosoma brucei* mitochondrial respiratome: composition and organization in procyclic form. **Mol Cell Proteomics** 10(9):M110.006908. *Shared first co-authorship. A seminal paper from my postdoctoral stay describing the novel composition of mitochondrial electron transport chain complexes involved in respiration (=respiratome) of T. brucei.*

- Alkhaldi AA, Martinek J, Panicucci B, Dardonville C, **Zíková A***, de Koning HP* (2016). Trypanocidal action of bisphosphonium salts through a mitochondrial target in bloodstream form Trypanosoma brucei. **International Journal for Parasitology: Drugs and Drug Resistance** 6: 23 -34. *This fruitful collaboration with the De Koning laboratory led to a proposed mode of action for promising drug candidates that concentrate in the mitochondria and act on ATPase activity. Here I am a co-corresponding author, as most of the key figures demonstrating the mode of action were generated by the J. Martinek, a MSc student in our lab.*

- Doleželová E, Kunzová M, Dejung M, Levin M, Panicucci B, Regnault C, Janzen C, Barrett M, Butter F, **Zíková A*.** (2020). Cell-based and multi-omics profiling reveals dynamic metabolic repurposing of mitochondria to drive developmental progression of *Trypanosoma brucei*. **PLoS Biol.** 10;18(6):e3000741. *Using a genetically modified T. brucei cell line that can undergo cellular differentiation in vitro, we unraveled a surprising mitochondrial metabolic repurposing that occurs throughout the differentiation of the previously enigmatic tsetse life cycle forms. Most of the data presented was performed by our experienced post-doc Eva Doleželová and our PhD student Michaela Kunzová, while the -omics data were acquired with our expert collaborators.*

- Gahura O, Hierro Yap C, **Zíková A*** (2021). Redesigned and reversed: architectural and functional oddities of the trypanosomal ATP synthase. **Parasitology**. 8:1-41. *An invited review to comprehensively summarize our achievements regarding the unique attributes of T. brucei F_oF_1 ATP synthase, its structure, function and regulation.*

- Gahura O, Muhleip A, Hierro-Yap C, Panicucci B, Jain M, Slapnickova M, **Zíková A***, Amunts A* (2022). An ancestral interaction module promotes oligomerization in divergent mitochondrion ATP synthases. **bioRxiv** 2021.10.10.463820. *Groundbreaking work resulting from amazing collaboration with Alexey Amunt's lab. Here we resolved the cryo-structure EM of the entire ATP synthase dimer from the insect form of Trypanosoma brucei. This it allowed us to propose the ancestral arrangement of mitochondrial ATP synthase oligomers that lay the foundation for their evolution. The manuscript has been recently resubmitted to Nat. Communication after minor revisions.*

- Gnipová A, Panicucci B, Paris Z, Verner V, Horváth A, Lukeš J, **Zíková A*** (2012). Disparate phenotypic effects from the knockdown of various Trypanosoma brucei cytochrome c oxidase subunits. Mol Biochem Parasitol. 184: 90 – 98. *One of the first papers from my laboratory describing the role of three hypothetical components of the complex IV in the mitochondrial bioenergetics of procyclic T. brucei cells. We are able to assign these proteins as genuine and indispensable subunits for the assembly and activity of cytochrome c oxidase, an essential component of the respiratory chain in these parasites.*

- Hierro-Yap C, Šubrtová K, Gahura O, Panicucci B, Dewar C, Chinopoulos C, Schnaufer A, **Zíková A*** (2021). Bioenergetic consequences of F_oF_1-ATP synthase/ATPase deficiency in two life cycle stages of *Trypanosoma brucei.* **J Biol Chem**. 1:100357. *A first-author publication of our very talented PhD student who performed the majority of the experiments. It explains in significant detail the diametrically opposed bioenergetic consequences of FoF1 ATP synthase loss in two T. brucei life cycle stages that differ strikingly in their mitochondrial metabolism.*

- Montgomery MG[#], Gahura O[#], Leslie AGW, **Zíková A,** Walker JE* (2018). ATP synthase from *Trypanosoma brucei* has an elaborated canonical F(1)-domain and conventional catalytic sites. **Proc Natl Acad Sci U S A.** 27;115(9):2102-2107. *This was the culmination of our 5-year long collaboration with the Walker lab. While the structure of the F_1 headpiece at the atomic level demonstrates that the mechanism for ATP synthesis is largely conserved, there are several unique features (addition of w novel subunit p18, cleavage of subunit alpha) that are being further explored in our lab. Our post-doc Ondřej Gahura spent more than a year growing trypanosoma cultures and purifying the F_1 complex before spending months in Cambridge setting up the crystallization trials. He was also involved in the model building. #-shared first co-authorship*

- Panicucci B, Gahura O, **Zíková A*** (2017). Trypanosoma brucei TbIF1 inhibits the essential F1-ATPase in the infectious form of the parasite. **Plos Negl Trop Dis.** 11(4):e0005552. *In addition to the structure and function of the F_oF_1-ATP synthase, we also explored if the unique ATPase activity of this enzyme during the infectious life cycle of the parasite could be a drug target. Therefore, we examined the characteristics of the endogenous T. brucei ATPase inhibitory*

peptide, IF1. This paper was performed solely by our lab. It required an extensive genome search to identify the putative IF1, whose protein expression was demonstrated to be tightly regulated between life cycles. Even though ectopic expression of IF1 in the infectious stage of the parasite was severely limited, its induction proved lethal, thus validating F_OF_1 ATPase as a drug target.

- Serricchio M, Hierro-Yap C, Schädeli D, Ben Hamidane H, Hemphill A, Graumann J, **Zíková A*,** Bütikofer P* (2020). Depletion of cardiolipin induces major changes in energy metabolism in Trypanosoma brucei bloodstream forms. **FASEB J**. 35:e21176. *A fruitful collaboration with Peter Butikofer lab that resulted in a functional study of cardiolipin role in the mitochondrion of the T. brucei bloodstream form. This is the first study showing the effects of cardiolipin loss in mitochondria lacking the canonical electron transport chain. My PhD student was directly involved in this project.*

- Šubrtová K, Panicucci B, **Zíková A*** (2015). ATPaseTb2, a unique membrane-bound FoF1-ATPase component, is essential in bloodstream and dyskinetoplastic trypanosomes**. PLoS Pathog.** 11(2):e1004660. *This was our first significant publication in the field of mitochondrial bioenergetics and it was solely produced by our first PhD student in the lab. At the time, this was the first evidence that a novel T. brucei ATP synthase subunit functioned within the peripheral stalk. This has now been further confirmed by our cryoEM structure of the complete enzyme. In addition, this work demonstrated that membrane attachment of the F_oF_1-ATP synthase is crucial for cells lacking a mitochondrial genome.*

- **Zíková A***, Verner Z, Nenarokova A, Michels PAM, Lukeš J (2017). A paradigm shift: The mitoproteomes of procyclic and bloodstream Trypanosoma brucei are comparably complex. **PLoS Pathog.** 2017 13(12):e1006679. *Mitochondrial pathways were previously left unexplored for drug discovery because of the long-standing dogma of a dormant mitochondrion within the infectious life stage of the parasite. I challenged this view by comparing the mitoproteomes between the insect and mammalian life stages and demonstrating that the mitochondria are similar regarding their protein complexity. This hypothesis is being expanded in my lab by functional studies indicating that bloodstream form T. brucei mitochondria can be ATP producing organelles, supplying the F_oF_1 ATPase with substrate to maintain the mitochondrial membrane potential.*

- **Zíková A**, Schnaufer A, Dalley RA, Panigrahi AK, Stuart KD (2009). The FoF1 synthase complex contains novel subunits and is essential for procyclic *Trypanosoma brucei*. **PLOS Pathogens** 5:e10000436. *My first author paper from my postdoctoral stay in which I purified mitochondrial FoF1 ATP synthase and analyzed its composition. This work formed the basis for*

my future studies on this essential complex, which has a unique composition and role for T. brucei parasites.

15. Attached publications

The following is an attachment of print publications.

Trypanosoma brucei Mitochondrial Respiratome: Composition and Organization in Procyclic Form*[S]

Nathalie Acestor‡, Alena Zíková‡§**, Rachel A. Dalley‡, Atashi Anupama‡, Aswini K. Panigrahi‡¶, and Kenneth D. Stuart‡‖**

The mitochondrial respiratory chain is comprised of four different protein complexes (I–IV), which are responsible for electron transport and generation of proton gradient in the mitochondrial intermembrane space. This proton gradient is then used by F_oF_1-ATP synthase (complex V) to produce ATP by oxidative phosphorylation. In this study, the respiratory complexes I, II, and III were affinity purified from *Trypanosoma brucei* procyclic form cells and their composition was determined by mass spectrometry. The results along with those that we previously reported for complexes IV and V showed that the respiratome of *Trypanosoma* is divergent because many of its proteins are unique to this group of organisms. The studies also identified two mitochondrial subunit proteins of respiratory complex IV that are encoded by edited RNAs. Proteomics data from analyses of complexes purified using numerous tagged component proteins in each of the five complexes were used to generate the first predicted protein-protein interaction network of the *Trypanosoma brucei* respiratory chain. These results provide the first comprehensive insight into the unique composition of the respiratory complexes in *Trypanosoma brucei*, an early diverged eukaryotic pathogen. *Molecular & Cellular Proteomics 10: 10.1074/mcp.M110.006908, 1–14, 2011.*

Mitochondria are dynamic organelles essential for cellular life, death, and differentiation of virtually every eukaryotic cell. They house systems for energy production through oxidative phosphorylation, synthesis of key metabolites, and iron-sulfur cluster assembly. The oxidative phoshorylation system of eukaryotic mitochondria comprises five major complexes located in the mitochondrial (mt)[1] inner membrane, and often abbreviated as mt complexes I–V. The redox energy of the substrates NADH and succinate is first converted into an electrochemical proton potential across the inner mt membrane by respiratory complexes I (NADH:ubiquinone reductase), II (SDH, succinate:ubiquinone reductase), III (bc_1, ubiquinone:cytochrome *c* reductase), and IV (cytochrome *c* oxidase). The electrochemical proton potential is then used by complex V (F_oF_1-ATP synthase) to synthesize ATP from ADP and inorganic phosphate, a mechanism that has essentially remained unchanged from bacteria to human (1). However, parasitic organisms have exploited unique energy metabolic pathways by adapting to their natural host habitats (2). Indeed, the respiratory systems of parasites typically show greater diversity in electron transfer pathways than those of their host, and *Trypanosoma brucei* is no exception to this rule (3).

T. brucei, the causative agent of human African trypanosomiasis (HAT), or sleeping sickness, is a blood-borne pathogenic parasite transmitted by tsetse flies. It has a complex life cycle that alternates between the bloodstream forms (BF) in the mammalian host and several stages in the insect vector starting with the procyclic form (PF) in the midgut. During *T. brucei* differentiation between the distinct life-cycle stages, the mitochondrion undergoes morphological and functional changes, and the parasite switches its energy metabolism from amino acid to glucose oxidation (4). BF cells, which live in sugar-rich environment, use energy metabolism predominantly through the glycolytic pathway (5). They contain no cytochrome-mediated respiratory chain and they possess a unique electron transport chain in the mitochondria, the glycerol-3-phosphate dehydrogenase and the salicyl hydroxamic acid (SHAM)-sensitive alternative oxidase, which is known as the trypanosome alternative oxidase (TAO) (6). Despite the absence of complete cytochrome-containing complexes III and IV in BF trypanosomes, a mt membrane potential is maintained and involves the hydrolytic activity of the F_oF_1-ATP synthase complex (7). Conversely, PF cells are dependent on the cytochrome-containing respiratory chain and ATP

From the ‡Seattle Biomedical Research Institute, Seattle, WA 98109, §Biology Center, Institute of Parasitology, University of South Bohemia, České Budějovice, Czech Republic, ¶King Abdullah University of Science and Technology, Thuwal, Kingdom of Saudi Arabia

Received December 2, 2010, and in revised form, May 18, 2011
Published, MCP Papers in Press, May 24, 2011, DOI 10.1074/mcp.M110.006908

[1] The abbreviations used are: mt, mitochondrial; BNE, Blue Native Electrophoresis; hrCNE, high resolution Clear Native Electrophoresis; mAb, monoclonal antibody; LC-MS/MS, liquid chromatography tandem mass spectrometry; OGDC, 2-oxoglutarate dehydrogenase complex; PF, procyclic form; TAP, tandem affinity purification; *T. brucei*, *Trypanosoma brucei*.

generated by conventional function of the F_oF_1-ATP synthase complex for their energy production (8, 9). The branched electron-transport chain contains four complexes that donate electrons to the ubiquinone pool, two NADH:ubiquinone oxidoreductases (complex I and a rotenone-insensitive enzyme), complex II, and glycerol-3-phosphate dehydrogenase. Reduced ubiquinol can be reoxidized by the transfer of electron to either the TAO, which does not translocate protons, or to the cytochrome-containing complexes III and IV that produce a proton motive force by translocation of protons and thus create essential membrane potential (10).

Although the *T. brucei* genome has been sequenced (11), little information is available on the subunit composition of mt complexes I–V based on similarity searches. However, some respiratory complexes have been partially characterized in other trypanosomatids such as *Crithidia fasciculata*, *T. cruzi*, and *Leishmania tarentolae* (12–15). In recent studies, we have determined the protein composition of complexes IV and V, and part of complex I purified from mitochondria of *T. brucei* PF cells (8, 16, 17, 25). These analyses revealed the uniqueness of respiratory complexes in trypanosomes, where large numbers of component proteins have no homologs outside of the Kinetoplastida.

In this study, we focus on the comprehensive characterization of all respiratory complexes in *T. brucei*, collectively termed the respiratome. We report the composition of complexes II and III from PF cells, and extend the characterization of complex I by identifying additional protein constituents. This included the identification of two subunits of the respiratory complex IV, both encoded by mt edited RNAs. We also present a predicted protein-protein interaction network of the respiratome, which was generated using proteomics data collected from numerous tagged proteins in each of the complexes I–V. Our results provide a comprehensive insight into the unique composition of the respiratory complexes in one of the life-cycle stages of *T. brucei*.

EXPERIMENTAL PROCEDURES

Cell Growth—*T. brucei* PF cells IsTat 1.7a were grown *in vitro* at 27 °C in SDM-79 media containing hemin (7.5 mg/ml) and 10% (v/v) fetal bovine serum to a density of 1–2 × 10^7 cells/ml. PF *T. brucei* strain 29.13 (18), which contains integrated genes for T7 polymerase and the tetracycline repressor, was grown in the presence of G418 (15 μg/ml) and hygromycin (25 μg/ml). The cells were harvested by centrifugation at 6000 × *g* for 10 min at 4 °C.

Tandem Affinity Purification (TAP)-tagged Cell Lines—To create constructs for the inducible expression of TAP tagged proteins in *T. brucei*, the open reading frames of interest were PCR amplified from the genomic DNA of *T. brucei* strain Lister 427. A detailed list of all tagged proteins and primers used to amplify the selected open reading frames is provided in the supplemental material. The PCR products were cloned into pGEM-T easy vector, digested with BamHI or BglII and HindIII enzymes, and ligated into the pLEW79-MHT vector (19, 20). The plasmids were linearized with NotI enzyme, transfected into PF *T. brucei* 29.13 cell line, phleomycin-resistant clones were selected, and checked for tetracycline-regulated expression. The transgenic PF cell lines expressing a TAP-tagged protein were supplemented with 2.5 μg/ml phleomycin.

Sample Preparation for Native Electrophoresis—Mt vesicles were isolated from IsTat 1.7a cells by hypotonic lysis followed by density gradient flotation in 20–35% linear Percoll gradients (21). The enriched vesicles were solubilized by adding *n*-dodecyl-β-D-maltoside corresponding to *n*-dodecyl-β-D-maltoside/protein ratio of 2 (g/g) and incubated on ice for 30 min. Insoluble material was removed by centrifugation at full speed in a microcentrifuge for 30 min at 4 °C.

Blue Native Electrophoresis (BNE) and High-resolution Clear Native Electrophoresis (hrCNE)—For BNE, 100 μg of mt lysate was supplemented with a 5% (w/v) stock solution of Coomassie Blue G-250 in 500 mM 6-aminohexanoic acid and analyzed on a 3–12% acrylamide gradient gel (8) using 50 mM Tricine, 15 mM Bis-Tris, pH 7.0, 0.02% Coomassie Blue G-250 as cathode buffer, and 50 mM Bis-Tris, pH 7.0 as anode buffer. For hrCNE (22), 100 μg of mt lysate was supplemented with 50% glycerol, 0.1% Ponceau S, and analyzed on a 4–13% acrylamide gradient gel using 50 mM Tricine, 7.5 mM imidazole, pH 7.0, 0.05% deoxycholate as cathode buffer, and 25 mM imidazole, pH 7.0 as anode buffer. All the native gels were run at 4°C at 100 V until the dye marker approached the gel front.

In-gel Catalytic Activity Assays—Following electrophoresis, complex I–V bands were visualized by activity staining as previously described (22). Briefly, to visualize complex I activity, the gel was incubated in 100 mM Tris-HCl, 0.1 mg/ml NADH, and 2.5 mg/ml nitrotetrazolium blue, pH 7.4. To visualize complex II activity, the gel was incubated in 50 mM phosphate buffer, 20 mM sodium succinate, 0.2 mM phenazine methasulfate, 2.5 mg/ml nitrotetrazolium blue, pH 7.4. For complex III, the gel was incubated in 50 mM phosphate buffer, pH 7.2 and 0.05% 3,3′-diaminobenzidine tetrahydrochloride; and the specificity of the reaction was demonstrated using 2 mM antimycin A. For complex IV, the gel was incubated in 50 mM phosphate buffer, pH 7.2, 0.05% 3,3′-diaminobenzidine tetrahydrochloride and 50 μM horse heart cytochrome *c*. Reactions were carried out at room temperature by slow agitation overnight and stopped by fixing the gels in 45% methanol and 10% acetic acid. Complex V was visualized as previously reported (8).

Native Western Blot Analysis for Complex I and III—Following electrophoresis, the native gels were transferred onto an Immobilon membrane overnight at 20 V at 4°C. The membranes were then blocked with Odyssey® Blocking Buffer, probed with mAb52 (1:10), which recognize a native epitope of subcomplex Iα (16) or with rabbit polyclonal antibodies against *T. brucei* apocytochrome c_1 (apoc_1) (1:1000) (23) to detect complex III. IRDye680 conjugated goat anti-rabbit (LiCor 926–32221) and IRDye800 conjugated goat anti-mouse (Rockland 610–132-121) were used as secondary antibodies at 1:15,000. Protein signal was detected by Odyssey™ Infrared Imaging System (LI-COR Biosciences, Lincoln, NE) using one-color fluorescence detection at 700 or 800 nm and analyzed with Odyssey version 3.0 software.

Tandem Affinity Purification of Tagged Complexes—TAP-tagged proteins were expressed by induction with tetracycline (100 ng/ml of culture) for 48 h and 500 ml of cells were harvested by centrifugation at a density of ~2 × 10^7 cells/ml. Tagged complexes were purified from cell lysates by two methods as previously described (8, 16). Briefly, in method 1 (M1) the harvested cells were lysed by 1% Triton-X 100 and the tagged complexes were isolated by IgG affinity chromatography. The bound complexes were eluted by TEV protease cleavage and fractionated on 10–30% glycerol gradients by centrifugation for 5 h at 38,000 rpm at 4 °C in Beckman Ultracentrifuge (SW40 Ti swinging bucket rotor). The sedimentation profiles of the tagged complexes were monitored by Western blot analyses using anti-His_6 mAb. Peak reactive fractions were pooled and further purified by calmodulin affinity chromatography. In method 2, the tagged

complexes were purified from cells lysed with 0.25% Nonidet P-40, cleared by low speed centrifugation and the supernatant was further treated with 1.25% Nonidet P-40 and cleared by high speed centrifugation. The tagged complexes were isolated by sequential IgG and calmodulin affinity columns.

Immunofluorescence Assay—Subcellular localizations of the expressed tagged proteins within the cell were determined by immunofluorescent assay using anti *c*-myc antibody (Sigma) as described (16). Colocalization analysis was performed using mAb 78 against mt heat shock protein 70 (16) coupled with Texas® Red-X conjugated secondary antibody (Invitrogen).

Protein Identification—We prepared and analyzed the samples by gel-based and gel-free approaches as described previously by us (16, 24, 25). Briefly, proteins in gel pieces were reduced with 10 mM dithiotreitol at 56 °C for 30 min, and alkylated with 55 mM iodoacetamide at room temperature for 45 min, and digested with sequencing-grade modified trypsin (Promega, Madison, WI) at 37 °C overnight; and the resulting peptides were extracted. The TAP tag-purified protein samples were precipitated with 6 volumes of acetone, and the proteins were denatured with 8 M urea, 1 mM dithiotreitol; diluted 1:4, and digested in-solution with trypsin. The resulting peptides were purified using C_{18} beads (Magnetic Dynabeads RPC18, Invitrogen). The peptides from gel pieces or complex mixtures were fractionated by nanoflow liquid chromatography using a 10-cm-long × 75-μm-inner diameter C_{18} capillary column and analyzed on line by electrospray ionization tandem mass spectrometry using a linear trap quadrupole mass spectrometer (Thermo Electron). The bound peptides were eluted from the C_{18} column at a flow rate of 200 nl/min with a 45-min linear gradient of 5–40% acetonitrile in 0.4% acetic acid followed by a 5-min linear gradient of 40–80% acetonitrile in 0.4% acetic acid.

Xcalibur 1.4 SR1 version software was used to collect MS data, and the mass range for the MS scan was *m/z* 400–1400. The tandem MS (MS/MS) data of the five most intense ions were collected sequentially following each MS scan using the dynamic exclusion parameter, where a specific ion was sequenced only twice and was excluded from the list for 45 s. The MS data were analyzed against *T. brucei* v4.0 predicted protein sequence database (11), which contains 9211 protein entries and additionally 18 predicted protein sequence from mt encoded edited and unedited RNAs, and bovine serum albumin, immunoglobulin heavy and light chains and keratin sequences. The peak list generation and search against database were carried out using SEQUEST module of Bioworks 3.1, cluster version SR1 (parameters: molecular weight range, 400–3500; mass tolerance, 1.0 Da; group scan, 25; minimum ion count, 15; no enzyme was specified during the search; no fixed modification was set for any of the amino acids, but differential modification for "M" and "C" were set at 15.994 and 57.000 Da, respectively). The output from SEQUEST search was filtered and compiled using PeptideProphet and ProteinProphet programs (26, 27). Our error rate of protein assignment is less than 1% as determined by comparing the proteomic data with six-frame translated *T. brucei* genomic sequence database that included 271,892 polypeptide entries STOP codon to-STOP codon (25). The data set presented here includes only the doubly tryptic peptides that have a minimum peptide identification probability of 0.9 and have a minimum SEQUEST X correlation value of 1.5 for +1 ions, 1.8 for +2 ions, and 2.5 for +3 ions. We excluded any peptide containing more than one missed trypsin cleavage site in the sequence. Proteins containing these peptides and with minimum identification probability of 0.9 were considered positive. All except one protein presented here was identified with two or more peptide matches and with a protein identification probability of ≥0.95. They all are unique proteins. For the protein identified with only one peptide match the MS/MS spectra and relevant scores are provided in supplemental Table S2 and supplemental Fig. S1.

Sequence Analysis—The probable functions of the proteins were assigned based on GeneDB annotation and for proteins with unknown function possible motifs and/or domains were searched in InterPro (http://www.ebi.ac.uk/Tools/InterProScan/), Pfam (http://pfam.sanger.ac.uk/) and NCBI CDD (http://www.ncbi.nlm.nih.gov/Structure/cdd/wrpsb.cgi) databases. The protein transmembrane topology was predicted using the TMHMM 2.0 program (http://www.cbs.dtu.dk/services/TMHMM).

Prediction of Protein-Protein Interactions—The composition of each complex was assessed by tagging multiple proteins individually as described above and by performing multiple MS analyses of each sample. The .out files (SEQUEST output) were compiled and filtered using the DTASelect program (28) to identify proteins in each analysis. Proteins identified with at least two tryptic peptides and with minimum peptide and protein identification probability of ≥0.9 were included in the list except for known non-mt proteins and highly abundant mt protein that are often seen in various TAP-tag experiments (17). The .raw files were converted to mzXML format and the Census program (29) was used to determine the spectral count of each of the peptides. For each individual protein, the number of spectra per peptide was calculated (sum of spectral count of all peptides respective to the protein/number of unique peptides). The relative ratio of spectra per peptide to bait protein (tagged protein) was calculated by dividing spectra per peptide value of each individual protein identified in the TAP-tag experiment by the spectra per peptide value of tagged protein. We used the Cytoscape software (http://www.cytoscape.org) to predict protein-protein interaction networks where a target protein was linked to bait protein if it had relative ratio of ≥1.0. A value of ≥1.25 was considered as high-confidence interactions.

RESULTS

In-gel Activity Staining of T. brucei mt Respiratory Complexes—Native electrophoresis and subsequent in-gel catalytic activity assays were used for visualization of respiratory chain complexes I–V (Figs. 1*A–C*). MS analyses were carried out on gel slices to assess the presence of the component protein(s) of complexes in the respective stained gel bands. Numerous proteins were identified in each gel slice (supplemental Table S1), some of which included known components of respiratory complexes. The large majority of the proteins that were detected are not part of the respective respiratory complexes, which likely reflects the complexity of the mt lysate samples and comigration of large complexes in native gels. However, some of these proteins, especially those with unknown functions, may be associated with their respective respiratory complexes.

NADH dehydrogenase activity revealed two stained bands (Fig. 1*A*). One band was in the well of the gel, suggesting that some material was not solubilized, very high molecular weight complexes and/or highly hydrophobic membrane-bound protein complexes that did not enter the gradient separation gel. The other band was observed at an apparent molecular weight of 1 MDa. MS analyses of the gel slice containing the ~1 MDa NADH dehydrogenase activity band predominantly identified Tb11.01.1740, Tb11.47.0004, Tb11.01.3550, and Tb11.01.8470 (supplemental Table S1), four proteins described as components of the 2-oxoglutarate dehydrogenase complex (OGDC) (16). Although the theoretical molecular mass of the bovine complex I was reported as 980 kDa (30),

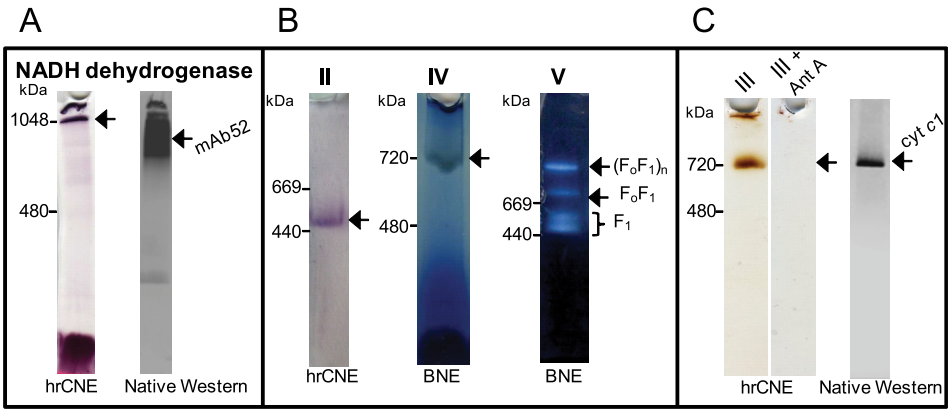

FIG. 1. **In-gel activity staining of *T. brucei* mt respiratory complexes separated by hrCNE and BNE.** Mt lysate was fractionated by hrCNE and BNE PAGE, and stained for (*A*) NADH dehydrogenase activity. The hrCNE gel was subsequently blotted and probed with mAb52, which recognizes a native epitope of the oxidoreductase complex (16). (*B*) Activity of complexes II, IV and V, and (*C*) activity of complex III in the absence and presence of antimycin A (Ant A). The hrCNE gel was also blotted and probed with polyclonal antibodies specific to the $apoc_1$ subunit of complex III. Arrows mark the major stained band in each case. The sizes of high molecular weight standards are indicated on the *left*.

only ten proteins out of the 30 nuclear-encoded subunits that were either predicted (31) or identified as part of the oxidoreductase complex (16, 25) were identified in this gel slice (supplemental Table S1, band 2). However, it was previously reported that *T. brucei* complex I has a mass of ~600 kDa (9, 32), thus we analyzed the entire lane of the native gel by MS including the well (supplemental Table S1, bands 1–10). MS analyses of the ~ 1 MDa to ~ 700 kDa region identified a total of 20 proteins out of the 30 subunits assigned to complex I (supplemental Table S1, bands 3 and 4). Western analysis using mAb52, which recognizes a native epitope in the oxidoreductase complex that corresponds to subcomplex Iα ((16) and this work) recognized the same region of the gel (Fig. 1*A*). These results suggest that NADH dehydrogenase activity staining reported earlier as complex I activity (9, 32) may not only be specific for complex I in PF cells, but it is also likely because of OGDC.

The complex II in-gel activity assay resembled the NADH dehydrogenase activity assay except that succinate rather than NADH was used as electron donor (Fig. 1*B*). MS analyses of the ~500 kDa reactive gel band identified Tb09.160.4380, Tb927.8.6580, and Tb927.8.3380, the three known core components of *T. brucei* SDH complex (supplemental Table S1), indicating that the stained band corresponds to *T. brucei* complex II. Specific in-gel complex IV staining revealed a band of an apparent molecular mass of ~ 700 kDa (Fig. 1*B*), and MS analyses identified 15 known subunits of complex IV (supplemental Table S1 and (17)). Complex V was stained by an ATP hydrolysis assay that can identify holo-F_oF_1 complex and catalytically active F_1 moiety as previously described in our study of *T. brucei* ATP synthase complex (Fig. 1*B* and (8)).

For the in-gel staining of complex III, we applied the method described previously for bovine heart complex III, in which 3,3′-diaminobenzidine tetrahydrochloride is used to stain complex III heme specifically (22). MS analyses of the gel slice containing the ~720 kDa activity band (Fig. 1*C*) identified two known subunits of complex III; Tb927.8.1890 and Tb09.211.4700 (supplemental Table S1). The specificity of the catalytic activity was further demonstrated by incubating the mt lysates with 2 mM antimycin A, a specific inhibitor of complex III before hrCNE electrophoresis (Fig. 1*C*). Upon inhibition with antimycin A, the ~720 kDa activity band was no longer visible, and only residual activities remained visible in the well, thus supporting that the stained band corresponds to complex III. Furthermore, native Western analysis with antibodies against $apoc_1$ (33), a core component of complex III, confirmed the size of the native complex III (Fig. 1*C*).

In summary, we visualized under native conditions the *T. brucei* mt respiratory complexes II–V by activity staining using the characteristic enzyme activities associated with each complex. The primary observed NADH dehydrogenase activity is most likely because of OGDC, however, *T. brucei* complex I was detected using a specific monoclonal antibody.

Identification of Mitochondrial-encoded Subunits of Respiratory Chain Complexes—The mt genome of *T. brucei*, like that of most other organisms, encodes subunits of the respiratory complexes, such as apocytochrome *b* (complex III), cytochrome *c* oxidase subunits I (COI), II (COII), and III (COIII), and subunit A6 of ATP synthase (34). To date, apocytochrome *b* and COI from *Leishmania tarentolae* are the only proteins identified that are translated from edited mRNAs (35–37), which are the processed RNA products of kinetoplastid mt DNA (kDNA). Liquid chromatography (LC)-MS/MS analyses of the ~1 MDa to ~700 kDa region (Fig. 1*A*) identified three unique peptides that match to the COII subunit of complex IV (Fig. 2 and supplemental Table S1) and COIII, another subunit of complex IV was identified by a single tryptic peptide in the gel slice containing the ~720 kDa activity band (Fig. 1*C*) (Fig. 2, supplemental Table S2 and supplemental Fig. S1). Fig. 2 shows the amino acid

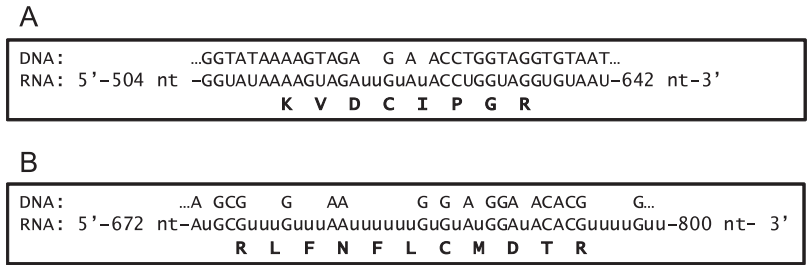

FIG. 2. **Identification of the mitochondrial encoded subunits COII and COIII.** A portion of the gene (DNA), edited mRNA (RNA) and amino acid sequence of the peptides identified by MS that match an edited region of (*A*) COII and of (*B*) COIII from *T. brucei*. The uridylate residues inserted by RNA editing are shown in lowercase. nt, nucleotide.

sequence of a tryptic peptide that matches the edited region of COII (Fig. 2*A*), and another peptide sequence that matches an edited region of COIII (Fig. 2*B*). Hence, peptides from two mt encoded-protein subunits of complex IV and their edited mRNAs were detected.

Tagged Respiratory Complexes—The data obtained by MS analyses from the gel slices as described above did not allow us to specifically determine the composition of complexes I–III. Therefore, we purified these complexes from *T. brucei* PF cells by tandem affinity purification (TAP) using two previously published methods (M1 and M2) (8, 16), and analyzed the protein composition by LC-MS/MS. The mt localization of almost all tagged proteins was confirmed by immunofluorescence analysis using anti-*myc* Ab (anti-tag), indicating that the tags as well as over-expression did not alter the mt localization (supplemental Fig. S2).

NADH Dehydrogenase Complex and Subunit Composition—Complex I is the largest and least understood complex of the respiratory chain. Mammalian complex I consists of ~46 different subunits that are assembled into a ~1 MDa structure. The subunit composition and general topology of complex I has been defined through its dissection into three subcomplexes (Iα + λ, Iβ, and Iγ) (38). The *T. brucei* genome database contains seven mt encoded and 12 nuclear encoded genes with homology to eukaryotic subunits (Table I). To purify complex I from *T. brucei*, Tb10.61.1790 (NDUFA6), Tb11.01.0640 (NDUFA13), Tb10.05.0070 (NDUFA9), Tb11.47.0017 (NDUFS7), Tb09.244.4620 (NDUFA9), and Tb10.70.3150 (NDUFA5) subunits of the subcomplex Iα + γ as well as Tb11.01.7460 (NDUFB9), a subunit of the subcomplex Iβ were tagged resulting in generation of TAP100, TAP205, TAP204, TAP206, TAP081, TAP203, and TAP157 cell lines, respectively (Table I). Unfortunately, we were not able to tag any subunits of subcomplex Iγ because it contains mt encoded subunits and methodology for expression of these subunits is not yet available. Purification of intact complex I was not observed potentially because of its instability during lysis and purification. MS analyses of the TAP100, TAP081, TAP203, and TAP157 purified complexes yielded two separate sets of proteins, of which many were annotated as hypothetical (supplemental Table S3). TAP204, TAP205, and TAP206 were not incorporated into the complex I because only the tagged proteins were identified by MS analyses (supplemental Table S3). Given that these proteins are predicted to be subunits of complex I (25, 31), most likely the tag interfered with the folding of the tagged protein or with its integration into the complex. To assess the validity of the association of the hypothetical [novel] proteins identified by MS analyses, three additional proteins associated with subcomplexes Iα + λ Tb927.2.4380 (TAP096), Tb09.160.5260 (TAP055 (16)), Tb927.7.7330 (TAP054), and one protein associated with subcomplex Iβ Tb11.01.7090 (TAP151) were also TAP-tagged. The SDS-PAGE of the subcomplexes Iα and Iβ (Figs. 3*A* and *B*) showed similar protein profiles for their respective subcomplexes, which differed mainly with respect to the abundance and position of the tagged bait as detected by Western blot analysis (data not shown). All of the most prominent gel bands in subcomplex Iα+λ were individually analyzed by MS and the respective proteins were identified (Fig. 3*A* and supplemental Table S3). Twenty four proteins were identified in this subcomplex. The most prominent bands in TAP151 purifications were also analyzed by MS and twelve proteins were identified in this subcomplex (Fig. 3B). These twelve proteins were also identified in TAP157 purification with the exception of NDUFAB1 and Tb09.160.0390 (supplemental Table S3). In addition, five other proteins were identified in at least two samples of the subcomplex Iα+λ (Tb11.01.8630, Tb10.70.3150, Tb09.244.2620, Tb927.1.730, Tb927.6.1410) and three more proteins (Tb11.01.7460, Tb11.02.2070, Tb927.8.5560) in subcomplex β when the SDS-PAGE step was omitted and samples were directly submitted to trypsin cleavage and LC-MS/MS analysis (supplemental Table S3).These proteins are most likely associated with the Iα+λ and β sub-complexes although their affinity of association and relative concentration (stoichiometry) may be lower compared with the proteins identified by gel-band analysis. These results suggest that subcomplexes Iα + γ and Iβ were purified, each subcomplex contains at least 32 and 15 subunits, respectively and they had no overlapping composition except for NDUFAB1 (Tb927.3.860) subunit, which was identified in both subcomplexes. All twelve nuclear-encoded proteins that have similarity to the eukaryotic complex I subunits as predicted by genome and proteome analysis (25, 31) have been identified in our TAP-tag complex purifications. However, we were not able to identify the seven mt encoded subunits ND1, ND3, ND4, ND5, ND7, ND8, and ND9 most likely because of their high hydrophobicity and properties such as few tryptic cleavage sites and

TABLE I

Trypanosoma brucei complex I subunits

√ indicates that only proteins identified in at least two experiments and by at least two unique tryptic peptides are shown. ND, protein has not been detected by MS. TAPProteins used as baits.

Protein_Id[d]	Genome[f]/Proteome analysis[g]	Complex I Subcomplex Iα[h]	Complex I Subcomplex Iβ[i]	Domains/Motifs[e]	Homology with human/bovine proteins
Nuclear encoded					
Tb10.05.0070TAP204	√	√	ND	NADH-ubiquinone oxidoreductase complex I subunit	NDUFA9/39-kDa
Tb10.389.1140	√	√	ND	NADH-ubiquinone oxidoreductase, 75kDa 2Fe-2S ferredoxin-like	NDUFS1/75-kDa
Tb10.61.1790TAP100	√	√	ND	NADH-ubiquinone oxidoreductase, subunit B14	NDUFA6/B14
Tb11.01.0640TAP205	√	√	ND	NADH-ubiquinone oxidoreductase, subunit B16.6	NDUFA13/B16.6
Tb11.01.7460TAP157	√	ND	√	NADH-ubiquinone oxidoreductase, subunit NI2M	NDUFB9/B22
Tb11.01.8630	√	√	ND	NADH-ubiquinone oxidoreductase, subunit B8	NDUFA2/B8
Tb11.47.0017TAP206	√	√	ND	NADH-ubiquinone oxidoreductase, subunit NdhK	NDUFS7/PSST
Tb927.3.860	√	√	√	Acyl carrier protein	NDUFAB1/SDAP
Tb927.5.450	√	√	ND	NADH-ubiquinone oxidoreductase, 51 kDa	NDUFV1/51-kDa
Tb927.7.6350	√	√	ND	NADH-ubiquinone oxidoreductase, 24 kDa	NDUFV2/24-kDa
Tb09.160.0760	√	√	ND	Alpha/beta-Hydrolases	
[a]Tb09.160.5260TAP055	√	√	ND	2-enoyl thioester reductase	Trans-2-enoyl-CoA reductase
[a]Tb927.7.7410	√	√	ND	2-enoyl thioester reductase	Trans-2-enoyl-CoA reductase
Tb09.211.0330	√	√	ND	Heat shock protein DnaJ	DnaJ homolog
Tb09.244.2620TAP081	√	√	ND	NADB_Rossman super family, NDUFA9_like_SDR_a	
Tb09.244.2670	√	√	ND		
Tb10.6k15.3040	√	√	ND	Vacuolar H+-ATPase V1 sector, subunit C	
Tb10.70.3150TAP203	√	√	ND	NADH-ubiquinone oxidoreductase, 13 kDa-B subunit	NDUFA5/B13
Tb10.70.5510	√	√	ND	Adrenodoxin reductase, putative; ferredoxin	Adrenodoxin oxidoreductase; ferredoxin
Tb11.01.5480	√	√	ND		
[b]Tb11.01.7480	√	√	ND	Manganese and iron superoxide dismutase	Superoxide dismutase
[b]Tb927.5.3350	√	√	ND	Manganese and iron superoxide dismutase	Superoxide dismutase
Tb11.02.4810	√	√	ND	Phosphoenolpyruvate carboxykinase	
Tb927.1.730	√	√	ND	NB-ARC domain	
Tb927.2.4380TAP096	√	√	ND		
Tb927.3.3660	√	√	ND		
Tb927.6.1410	√	√	ND		
[c]Tb927.6.2010	√	√	ND	Acyl-CoA synthetase-like	Acyl-CoA synthetase
[c]Tb11.02.2070	√	ND	√	Acyl-CoA synthetase-like	Acyl-CoA synthetase
Tb927.7.7330TAP054	√	√	ND		
Tb927.8.4250	√	√	ND	Tetratricopeptide repeat	Tetratricopeptide repeat
Tb11.02.1020	√	√	ND		
Tb09.160.0390[g]	√	ND	√	Flavoprotein monooxygenase	Kynurenine 3-monooxygenase
Tb09.160.4910	√	ND	√	Flavoprotein monooxygenase	Kynurenine 3-monooxygenase
Tb09.211.1280	√	√	ND		
Tb09.211.2780	ND	ND	√		
Tb09.244.2840	√	ND	√		
Tb10.70.6930	√	ND	√		
Tb11.01.1690	√	ND	√		
Tb11.01.7090TAP151	√	ND	√	Complex1 LYR	LYR motif
Tb927.2.1680	√	√	ND	Cyclophilin-type peptidyl-prolyl cis-trans isomerase	Peptidyl-prolyl cis-trans isomerase
Tb927.4.4300	√	ND	√	SET domain	
Tb927.4.440	√	ND	√		
Tb927.7.3910	√	ND	√	P-loop containing nucleoside triphosphate hydrolases	
Tb927.8.2530	√	ND	√	Cytochrome C oxidase copper chaperone	

TABLE I—*continued*

Protein_Id[d]	Genome[f]/Proteome analysis[g]	Complex I Subcomplex Iα[h]	Complex I Subcomplex Iβ[i]	Domains/Motifs[e]	Homology with human/bovine proteins
Tb927.8.5560	√	ND	√	S-adenosyl-L-methionine-dependent methyltransferases	Methyltransferase
Mitochondrial encoded					
M94286	ND	ND	ND	36 kDa subunit 1	ND1/Chain1
AAA20887	ND	ND	ND	18 kDa CR5/G5 cryptogene	ND3/Chain3
AAB59224	ND	ND	ND	52 kDa subunit 4	ND4/Chain4
P04540	ND	ND	ND	71 kDa subunit 5	ND5/Chain5
P21301	ND	ND	ND	45 kDa 4Fe-FS protein	ND7/49kDa
gi 552291 gb AAA91499.1	ND	ND	ND	17 kDa subunit 8	ND8/TYKY
gi 162166 gb AAA03749.1	ND	ND	ND	14 kDa subunit 9	ND9/30kDa
Plant origin					
Tb11.02.5070	√	ND	ND	33 kDa plant 2	
Tb927.4.4980	ND	ND	ND	18 kDa plant 6	

[a, b, and c] Protein pairs with sequence homology.

[d] GeneDB accession number (http://www.genedb.org) or GeneBank (http://www.ncbi.nlm.nih.gov/GenBank/index.html) for the mitochondrially encoded polypeptides.

[e] All proteins have orthologs in *T. cruzi* and *L. major*.

[f] [31].

[g] [25] and native gel analysis (this study).

[h] Proteins identified in pull-downs with mAb 52, 63, 69 [16] and/or TAP054, TAP055 [16],TAP081,TAP096, TAP100, TAP203, TAP204, TAP205 and TAP206 affinity purification.

[i] Proteins identified in TAP151 and TAP157 affinity purification.

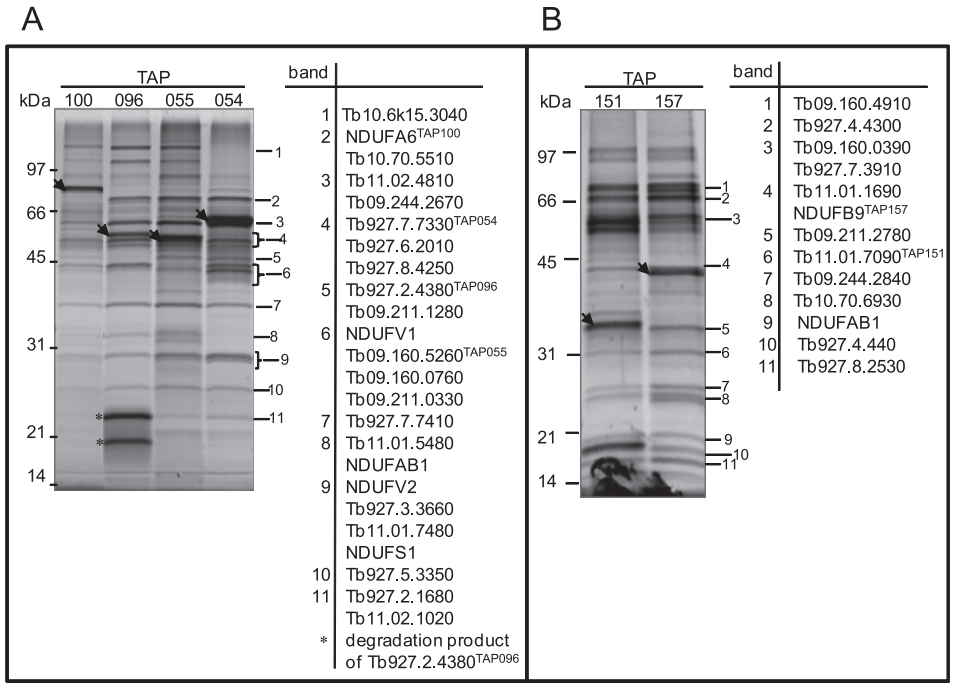

FIG. 3. **TAP tag purified *T. brucei* NADH:ubiquinone dehydrogenase complex.** *A*, TAP100, TAP096, TAP055 and TAP054 complexes were purified and separated on a 10–14.5% polyacrylamide Tris-glycine gel and stained with Sypro Ruby. The listed proteins were identified in the bands shown with corresponding numbers. The sizes of the protein marker are indicated. The position of tagged proteins is indicated by arrowheads. *B*, TAP151 and TAP157 complexes were purified and separated on a 10–14.5% and labeled as in A.

resulting cysteine rich peptides or not present in PFs (see discussion). Analysis of peptide sequences generated *in silico* indicated only six peptides has high probability of being detected by the MS approach taken in this study (data not shown). Also we were not able to identify in our purifications the two proteins that share identity with subunits of plant complex I ((31) and Table I), suggesting that these proteins may not be part of *T. brucei* complex I. Of all 46 proteins identified in purified complex I (subcomplexes Iα+λ and Iβ combined), 24 are currently annotated as hypothetical in the GeneDB database. Several of the latter possess domains/motifs that are indicative of possible function(s) in oxidoreduc-

TABLE II

Trypanosoma brucei complex II subunits. Only proteins identified in at least two experiments and by at least two unique tryptic peptides are shown. [TAP]Proteins used as baits

Protein_ID[a]	Homolog/Domain[b]	Shotgun approach[c]	TAP Tag	Ortholog in T. cruzi[d]
Tb927.8.6580[TAP106]	SDH1	√	√	SDH1
Tb09.160.4380[TAP105]	$SDH2_C$	√	√	$SDH2_C$
Tb927.8.3380[TAP120]	$SDH2_N$	√	√	$SDH2_N$
Tb927.2.4700		√	√	SDH8
Tb927.8.5640		√	√	SDH6
Tb10.70.4500		√	√	SDH9
Tb927.6.4130		√	√	SDH3
Tb927.7.3590		√	√	
Tb927.8.1490	DUF1674 (domain of unknown function)	√	√	

[a] GeneDB accession number (http://www.genedb.org).
[b] All proteins have orthologs in *L. major*.
[c] [25] and native gel analysis (this study).
[d] [15].

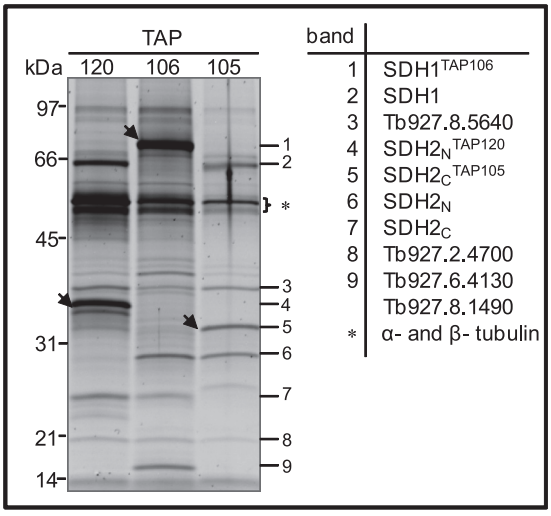

FIG. 4. **TAP tag purified *T. brucei* SDH Complex.** Sypro Ruby-stained SDS-PAGE protein profile of complexes, which were purified using TAP120, TAP106 and TAP105. The proteins identified by MS analysis of the corresponding band are shown and the position of tagged proteins is indicated by arrowheads. The asterisk indicates α- and β- tubulin.

tase processes (Table I). All together, we found that the *T. brucei* complex I is purified as two subcomplexes, and composed of at least 46 subunits (Table I).

SDH Complex and Subunit Composition—The large flavoprotein subunit Tb927.8.6580 (SDH1) and the smaller iron-sulfur subunit that is heterodimeric in Trypanosomatids (39) Tb927.8.3380, $SDH2_N$; Tb09.160.4380, $SDH2_C$ were tagged resulting in generation of TAP106, TAP120, and TAP105 cell lines (Table II). All visible gel bands (Fig. 4) were individually analyzed by MS and the respective proteins SDH1, $SDH2_N$, $SDH2_C$, and four hypothetical proteins Tb927.8.5640, Tb927.2.4700, Tb927.6.4130, and Tb927.8.1490, were identified in all three tagged complexes with at least two peptides (Fig. 4 and supplemental Table S4). In addition, two other proteins (Tb927.7.3590 and Tb10.70.4500) were identified in all three purifications when the SDS-PAGE step was omitted (supplemental Table S4).

In mammalian and bacterial mitochondria, SDH1 and SDH2 are anchored to the inner mt membrane by two small hydrophobic subunits, SDH3 and SDH4, which are required for electron transfer and ubiquinone reduction. These two subunits were not identified in the genome of the *T. brucei* by BLAST search suggesting that they may be highly diverged in sequence. However, two hypothetical proteins (Tb927.2.4700 and Tb927.7.3590) out of the nine proteins that were found associated with complex II possess predicted transmembrane domains and are similar in size to SDH3 and SDH4 (supplemental Table S4). This implies that they may play a role in electron transfer and perhaps function similar to SDH3 and SDH4 subunits, however direct comparison with these proteins did not reveal any predicted structural or motif similarity. In summary, we assigned nine proteins with high confidence to *T. brucei* SDH complex (Table II). This suggests that the complexity of the *T. brucei* complex is similar to that in *T. cruzi*, which is comprised of six hydrophobic and six hydrophilic subunits (15).

bc_1 Complex and Subunit Composition—In trypanosomatids, as in other eukaryotes, the bc_1 complex contains three subunits with active redox centers: the mt encoded cytochrome *b*, and the two nuclear encoded proteins, Tb927.8.1890 (cytochrome c_1) and the Rieske iron-sulfur protein (Tb09.211.4700, ISP). The latter two were tagged resulting in generation of TAP059 and TAP021 cell lines (Table III). Because the members of the mt processing peptidase family have been shown to be core subunits of complex III, as in yeast and mammals (40), Tb11.02.1480 the *T. brucei* homolog of the α-MMP was also tagged (TAP066). All visible gel bands (Fig. 5 and supplemental Table S5) were individually analyzed by MS and the respective proteins cytochrome c_1, ISP, α-MMP and Tb927.5.1060 (β-MMP) were identified in both purifications. Surprisingly, cytochrome c_1 was not detected by MS analysis in the purified TAP021 samples although,

TABLE III

Trypanosoma brucei complex III subunits. Only proteins identified in at least two experiments and by at least two unique tryptic peptides are shown. [TAP]Proteins used as baits

Protein_ID[a]	Homolog/Domain[b]	Shotgun approach[c]	TAP Tag
Nuclear encoded			
Tb09.211.4700[TAP021]	ISP	√	√
Tb927.8.1890[TAP059]	Cytochrome c_1	√	√
Tb11.02.1480[TAP066]	α-MMP	√	√
Tb927.5.1060	β-MMP	√	√
Tb10.70.2970[d]	Cytochrome bd ubiquinol oxidase, 14kDa subunit	√	√
Tb11.01.7900		√	√
Mitochondrial encoded			
AAA32115	apocytochrome *b*	ND	ND

[a] GeneDB accession number (http://www.genedb.org) or GeneBank (http://www.ncbi.nlm.nih.gov/GenBank/index.html) for the mitochondrially encoded polypeptide.

[b] All proteins have orthologs in *L. major* and in *T. cruzi*.

[c] [25] and native gel analysis (this study).

[d] Only identified in TAP066.

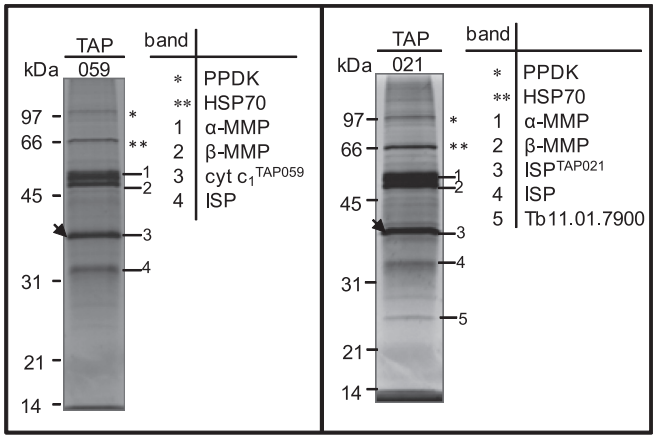

FIG. 5. **TAP tag purified *T. brucei* cytochrome bc_1 complex.** SYPRO Ruby-stained SDS-PAGE gels of TAP059 and TAP021 purifications. The proteins identified by MS analysis of the corresponding bands are indicated. The position of tagged proteins is indicated by arrowheads. PPDK, pyruvate phosphate dikinase; HSP70, heat shock 70 kDa protein.

detected when tagged itself (TAP059). Perhaps the TAP-tag interferes with the binding of cytochrome c_1 with ISP protein. The additional ISP band in TAP021 (Fig. 5) is probably a product of proteolysis of the tagged protein because two bands were also detected by Western blot analysis (data not shown). Tb11.01.7900 has been identified in gel band analysis in TAP021 and TAP066 purifications as well as in TAP059 purification when the SDS-PAGE step was omitted (Fig. 5 and supplemental Table S5). In addition, two other annotated hypothetical proteins (Tb11.01.8225 and Tb10.70.2970) were identified only in TAP066 purification (data not shown and supplemental Table S5). Although Tb10.70.2970 has been identified only in one TAP purification, we assigned it to complex III based on its ubiquinol-cytochrome *c* reductase domain and its 28% sequence identity to the *Saccharomyces cerevisiae* Qcr7p subunit, which has a role in the assembly of bc_1 complex (41). All together we were able to assign six proteins to the *T. brucei* complex III with high confidence (Table III).

Besides the respiratory complexes described above, *T. brucei* mitochondrion contains a branched electron transport chain that is composed of the mt FAD-linked glycerol-3-phosphate dehydrogenase (Tb927.1.1130) and alternative oxidase TAO (Tb10.6k15.3640) (Fig. 6*A*). Moreover, an alternative rotenone-insensitive NADH dehydrogenase (Tb10.6k15.0960), which also occurs in plants and fungi, was characterized in *T. brucei* cells (42). All three enzymes are predicted to work as single proteins; however, these predictions have not been experimentally verified. Thus, all three proteins were tagged resulting in TAP208, TAP207, and TAP210 cell lines respectively, and TAP-purified samples were then subjected to SDS-PAGE fractionation and to LC-MS/MS analyses (Fig. 6*B*). SyproRuby-stained gel and MS data showed that alternative dehydrogenase and glycerol-3-phosphate dehydrogenase were purified as single protein since except typical contamination arising from α- and β-tubulin, only the bait protein was identified by MS. In TAP207 two protein bands were apparent on SDS-PAGE gel (Fig. 6*B*), the higher one corresponding to the tagged version of the TAO and the second one representing the endogenous protein, suggesting that this enzyme exists as a dimer or multimer.

Protein-Protein Interaction Map—The acquired MS data from TAP-tag purified multiprotein complexes was used to predict a protein-protein interaction network of the respiratome (Fig. 7). The bold lines in Fig. 7 indicate high confidence predicted direct-interactions between the indicated proteins, and dotted lines indicate additional proteins pulled-down by the bait (tagged protein). As described above, complex I exists as multiple subunits, and results from the interaction map suggest Tb927.3.860 (NDUFAB1) interacts with Tb11.01.7090 and connects subcomplex Iα and Iβ. Six addi-

A

GeneDB ID	Annotation	TAP
Tb10.6k15.3640	Alternative oxidase (TAO)	207
Tb10.6k15.0960	Alternative dehydrogenase	210
Tb927.1.1130	Glycerol-3-phosphate dehydrogenase	208

B

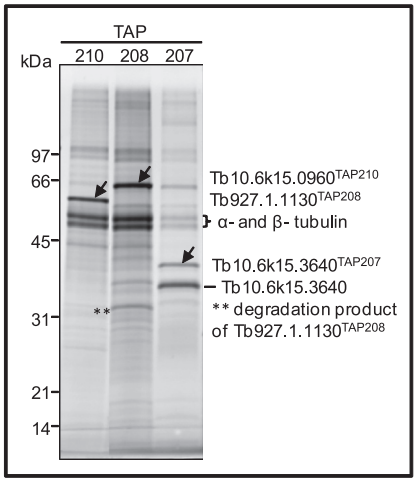

FIG. 6. **TAP tag purified *T. brucei* glycerol-3-phosphate dehydrogenase, alternative dehydrogenase and alternative oxidase.** *A*, Annotated and tagged enzymes. *B*, Sypro Ruby staining of TAP-tag purified proteins. The arrowheads indicate the tagged proteins that were identified by MS analysis. The sizes of the protein marker are indicated on *left*.

tional proteins (Tb10.70.1520, Tb11.02.0290, Tb10.v4.0045, Tb09.211.1600, Tb927.8.6960, and Tb927.5.3300) with unknown function were identified in complex I map that did not match our criteria of being identified in two separate TAP-tag experiments (Fig. 7), thus they are not included as bona-fide components of complex I in Table I. However, these are possible components of complex I or other complex(es) that may associate with complex I. Similarly, a number of proteins that did not match our criteria were identified in complex III, IV, and V map (Fig. 7). We also identified two components of complex III (Tb09.211.4700 and Tb11.01.7900) in purified subcomplex Iα. Similarly, four components of complex V (Tb927.7.7420/7430, α; Tb927.3.1380, β; Tb10.100.0070, γ; and Tb11.02.4120) were identified in complex IV preparation, and a potential new component of complex V Tb927.2.5930 was identified by this analysis as we included additional TAP-tag data than published earlier (8). We also found "MIX" protein (Tb927.5.3040) associated with components of complex IV, which we previously reported (17). These results identify the possible linking partners between the five respiratory complexes. However, the interactions have not yet been identified from genuine reciprocal interactions between the different subunits, thus further experimental evidence is required for validating these predictions especially as spurious association of proteins or highly abundant mt proteins may result in erroneous prediction. Overall, aggregate data may be useful for identifying component compositions of multi-protein complexes, where data from multiple TAP-tags and multiple MS runs are available.

DISCUSSION

The composition of the respiratory complexes was explored using native gel electrophoresis combined with in-gel activity staining, Western blot analysis and TAP-tag complex purification coupled with MS analysis. Respiratory complexes I, II, and III were purified using multiple tagged subunits and protein assignments were made based on the results from several purifications. In addition, the aggregate spectral counts of identified peptides from the TAP-tag studies were used to generate a preliminary protein-protein interaction map of the respiratory complexes. The interactions are consistent with the known structure of the respiratory complexes, *e.g.* complex I organized in subcomplexes, association of "MIX" protein with complex IV (17).The interaction map is consistent with our finding that RNAi knockdown of Tb10.70.7760 in complex V, resulted in the loss of the F_oF_1 complex interactions that contains the interactor, but the F_1 moiety was retained (8). Also, we report the first evidence of MS identification of mt proteins encoded by edited RNAs in *T. brucei*. Two tryptic peptides match edited region of COII and COIII, indicating that translated products from fully edited mRNA were detected. The results suggest that electrophoresis under native conditions might avoid the loss of these highly hydrophobic subunits, which have a tendency to aggregate and precipitate when in SDS (13, 33).

Successful activity staining of the respiratory complex II and III helped to estimate the native size of these complexes which range from ~450 to ~720 kDa. Complex II is an integral membrane protein complex involved in both the Krebs cycle and the respiratory electron transport chain. The total molecular mass of SDH complex is calculated to be ~220 kDa if it contained equimolar amounts of subunits. However, the activity band detected in hrCNE gel runs at ~450 kDa which may suggest that complex II exists as a homodimer. It is also possible that the complex is a monomer but migrates at a higher size in native gel because of the effect of salt, detergent etc. Nevertheless dimeric complex II has been reported for *T. cruzi* (15). Among the 12 subunits that compose *T. cruzi* complex II, our TAP tag analyses did not identify the ortholog of SDH4, SDH5 and SDH11, whereas we identified two other subunits of *T. brucei* complex II that are not present in the *T. cruzi* complex (Table II). Moreover, we identified the ortholog of SDH7 and SDH10 but they did not match our criteria of being identified in two separate TAP-tag experiments and/or by more than one peptide (supplemental Table S4). The homologs of the membrane bound subunits SDH3 and SDH4 are difficult to identify with conventional BLAST programs due to their highly diverged sequence. However, their putative homologs were identified in *T. cruzi* purified complex II based on the presence of quinone/heme binding motifs (15). The ortholog of *T. cruzi* SDH3 was identified in our preparation,

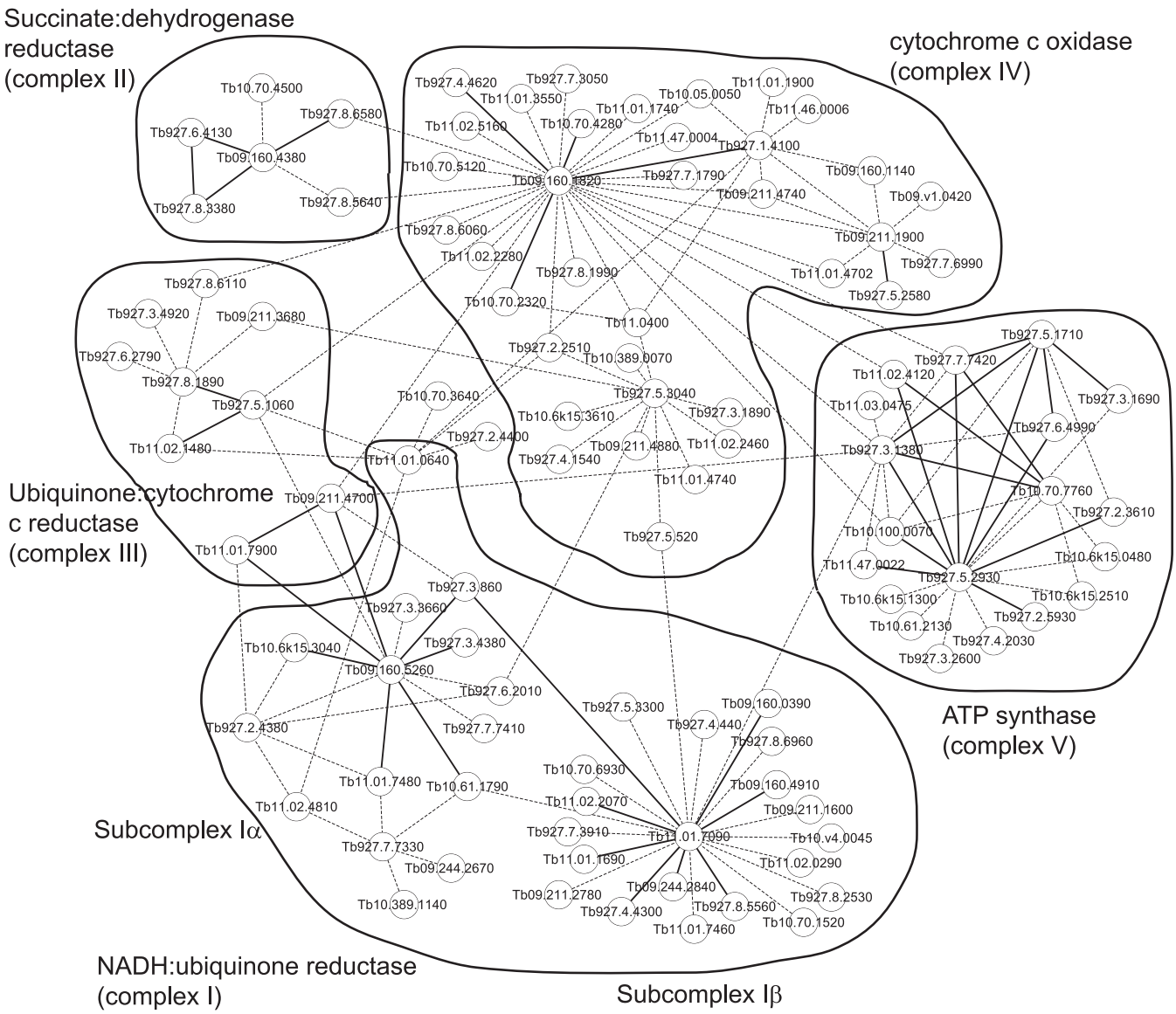

FIG. 7. **Predicted protein-protein interaction network of the *T. brucei* respiratome.** This Cytoscape graphical representation shows probable interactions within each respiratory complexes I-V and within the respiratome. The bold line indicates high confidence potential direct-interaction between the indicated proteins, and dotted line indicates additional proteins that were pulled-down by the bait.

but it appears that this protein (Tb927.6.4130) does not have a predicted transmembrane domain in *T. brucei* (supplemental Table S4). The supramolecular organization of *T. brucei* complex II resembles the *T. cruzi* complex, but is divergent from the *S. cerevisiae* and mammalian SDH complex structure, indicating that trypanosomatid SDH complex contains additional non-catalytic subunits as it was previously suggested for plant complex II (43).

In *S. cerevisiae*, mutation in any one of the four genes leads to the loss of complex II function and the inability of *S. cerevisiae* to grow by respiration (reviewed in (44)). In contrast, *T. brucei* RNAi knockdown of the core subunits of complex II resulted in a complete loss of oxidative phosphorylation in response to succinate, but were conditionally lethal only in the absence of glucose (45, 46). Our functional analysis of the core subunits by RNAi showed that the complex II is not essential for the growth of *T. brucei* cells even in the absence of glucose (supplemental Fig. S3 and data not shown). These results suggest that *Trypanosoma* complex II is not the main entrance for electrons into the respiratory chain in PF cells.

bc_1 complex (complex III) is typically a structurally dimeric protein complex. In yeast and in bovine mitochondria, it exists in association with one and two copies of complex IV (47, 48). The total mass of the six proteins identified in this study is 237 kDa (supplemental Table S5), but it migrates at ~720 kDa indicating that *T. brucei* complex III could similarly form a multimer. The same size band (~720kDa) is observed for

cytochrome *c* oxidase activity, which has a predicted monomer size of ~360 kDa (17). Hence, the stained band may correspond to the bc_1-cytochrome *c* oxidase heteromultimeric-supercomplex as described in yeast (48). A bc_1-cytochrome *c* oxidase supercomplex is also suggested by MS analyses of the ~720 kDa activity band that revealed five core components of complex IV (supplemental Table 1). Nevertheless, this possible association does not appear to be essential for the structural integrity of either complex because repression of components of either complex that result in the loss of one complex do not result in the loss of the other complex (9).

Purified complexes III from *Crithidia fasciculate* (13, 33) and *L. tarentolae* (14) consist of ten and eleven subunits, respectively. Whereas only six subunits were found in the complex purified from *T. brucei*. This suggests a differential composition of complex III among trypanosomatids, or nonspecific association of other proteins with *Leishmania* and *Crithidia* complexes. It is also possible that the protein components identified in TAP purified complex III in this analysis are the more stably associated proteins. Other proteins that correspond to those seen in the other species may not be stably associated with the complex, but may have similar functions *in vivo*.

Although hrCNE combined with NADH:NTB reductase was successfully applied for the detection of bovine complex I (22), we found that the *T. brucei* NADH dehydrogenase activity stained band corresponded primarily to OGDC. In *T. brucei*, dihydrolipoyl dehydrogenase, one of the four subunits of OGDC is shared between OGDC and the pyruvate dehydrogenase complex (16). Its activity was detected using the same approach in mammalian mitochondria, implying that this assay is not specific for complex I activity (49). Furthermore, using a nongradient BNE method, both complex I and dihydrolipoyl dehydrogenase protein were detected simultaneously on the same gel (50), suggesting that the gel-based method used to separate mt respiratory complexes could be critical. Moreover, *Trypanosoma* subcomplex Iα and OGDC cosediment in glycerol gradients (16), implying that the native size of both complexes might be very similar and their respective activities may overlap in native gel. However, MS analysis revealed the presence of OGDC rather than *T. brucei* complex I in the NADH activity band, suggesting that the activity of complex I cannot be readily detected in this system. These results may imply that complex I has a limited activity and role in NADH reoxidation in culture-grown PF cells. This assumption is further supported by a novel finding that complex I is not essential for the growth of PF cells (51). Thus it is plausible to hypothesize that most of the mitochondrially generated NADH is regenerated in PFs by an alternative dehydrogenase which is also localized in the inner membrane (52). In addition, it has been reported that deletions in the ND4, ND5, and ND7 genes that encode for complex I mt subunits occurring in natural mutants of *T. cruzi* have no consequence to the mt redox state, indicating that complex I can have limited function in NADH oxidation in this species (53).

In general, complex I is composed of 14 subunits in prokaryotes and up to 46 subunits in eukaryotes. Yet, only 19 subunits of *Trypanosoma* complex I were found to have some degree of homology to these subunits based on homology search (25, 31). Out of these 19 subunits, all 12 nuclear-encoded ones were identified in our purified complexes, however none of the seven mt encoded subunits were detected by MS possibly due to the characteristics of these proteins, making their peptide identification by routine mass spectrometry analysis difficult. Moreover, some of these subunits may be present at very low abundance/absent in PF as they are preferentially edited in BF cells (54).

Previous purification of the hydrophilic subcomplex I$\alpha+\lambda$ of complex I suggested that *T. brucei* complex I is a unique multifunctional complex in trypanosomes that is involved not only in respiration but also in fatty acid synthesis (16). Our high confidence interaction map (Fig. 7) shows Tb11.02.2070, a long-chain-fatty acid-CoA ligase protein to be associated with subcomplex Iβ. In addition, the acyl carrier protein (NDUFAB1) that links subcomplex Iα with Iβ has homology to two acyl carrier proteins (ACPM1 and ACPM2) of *Yarrowia lipolytica*, which play roles in mitochondrial fatty acid metabolism as well as complex I assembly (55). Two flavoprotein monooxygenases were also identified as subunits of complex I. The members of the flavoprotein monooxygenases are usually involved in the microbial degradation of aromatic compounds, in biosynthesis of ubiquinone, and in detoxification of drugs and other xenobiotics (56). Thus, presence of such proteins reinforce that the complex I in trypanosomes is multifunctional.

Overall, this study characterized the composition of respiratory complexes I, II and III, identified not only the predicted subunits but also novel complex-associated proteins. These results expand our knowledge of the unique mt respiratory machinery in these early diverged parasitic protozoa. We also created a protein-protein interaction network of the respiratome. Although, we have not validated our prediction network, it provides a framework and candidates for downstream analyses.

Acknowledgments—We thank Yuko Ogata for help with mass spectrometry; Steve L. Hajduk (University of Georgia, Athens) for the apoc_1 antibody.

* This work was supported by National Institutes of Health grant AI065935 to KS. AZ received support from grant 204/09/P563 from the Grant Agency of the Czech Republic. Research was conducted using equipment made possible by support from the Economic Development Administration - US Department of Commerce and the M.J. Murdock Charitable Trust.

** These authors contributed equally to this work.

[S] This article contains supplemental Figs. S1 to S3 and Tables S1 to S5.

‖ To whom correspondence should be addressed: Seattle Biomedical Research Institute, 307 Westlake Ave N, Suite 500, Seattle, WA 98109-5219. Tel.: +1 206-256-7316; Fax: +1 206-256-7229; E-mail: ken.stuart@seattlebiomed.org.

REFERENCES

1. von Ballmoos, C., Cook, G. M., and Dimroth, P. (2008) Unique rotary ATP synthase and its biological diversity. *Annu. Rev. Biophys.* **37,** 43–64
2. Tielens, A. G., Rotte, C., van Hellemond, J. J., and Martin, W. (2002) Mitochondria as we don't know them. *Trends Biochem. Sci.* **27,** 564–572
3. Tielens, A. G., and van Hellemond, J. J. (2009) Surprising variety in energy metabolism within Trypanosomatidae. *Trends Parasitol.* **25,** 482–490
4. Vickerman, K. (1985) Developmental cycles and biology of pathogenic trypanosomes. *Br. Med. Bull.* **41,** 105–114
5. Bienen, E. J., Maturi, R. K., Pollakis, G., and Clarkson, A. B., Jr. (1993) Non-cytochrome mediated mitochondrial ATP production in bloodstream form *Trypanosoma brucei brucei. Eur. J. Biochem.* **216,** 75–80
6. Chaudhuri, M., Ott, R. D., and Hill, G. C. (2006) Trypanosome alternative oxidase: from molecule to function. *Trends Parasitol.* **22,** 484–491
7. Schnaufer, A., Clark-Walker, G. D., Steinberg, A. G., and Stuart, K. (2005) The F(1)-ATP synthase complex in bloodstream stage trypanosomes has an unusual and essential function. *EMBO J.* **24,** 4029–4040
8. Ziková, A., Schnaufer, A., Dalley, R. A., Panigrahi, A. K., and Stuart, K. D. (2009) The F(0)F(1)-ATP synthase complex contains novel subunits and is essential for procyclic *Trypanosoma brucei. PLoS Pathog.* **5,** e1000436
9. Horváth, A., Horakova, E., Dunajciková, P., Verner, Z., Pravdová, E., Slapetová, I., Cuninková, L., and Lukes, J. (2005) Downregulation of the nuclear-encoded subunits of the complexes III and IV disrupts their respective complexes but not complex I in procyclic *Trypanosoma brucei. Mol. Microbiol.* **58,** 116–130
10. Besteiro, S., Barrett, M. P., Rivière, L., and Bringaud, F. (2005) Energy generation in insect stages of *Trypanosoma brucei:* metabolism in flux. *Trends Parasitol.* **21,** 185–191
11. Berriman, M., Ghedin, E., Hertz-Fowler, C., Blandin, G., Lennard, N. J., Renauld, H., Bartholomeu, D., Caler, E., Hamlin, N., Haas, B., Böhme, U., Harris, B. R., Hannick, L., Barrell, B., Donelson, J., Hall, N., Fraser, C. M., Melville, S. E., El-Sayed, N., Shallom, J., Aslett, M., Hou, L., Atkin, B., Barron, A. J., Bringaud, F., Brooks, K., Cherevach, I., Chillingworth, T., Churcher, C., Clark, L. N., Corton, C. H., Cronin, A., Davies, R., Doggett, J., Djikeng, A., Feldblyum, T., Fraser, A., Goodhead, I., Hance, Z., Harper, A. D., Hauser, H., Hostetler, J., Jagels, K., Johnson, D., Johnson, J., Jones, C., Kerhornou, A., Koo, H., Larke, N., Larkin, C., Leech, V., Line, A., MacLeod, A., Mooney, P., Moule, S., Mungall, K., Norbertczak, H., Ormond, D., Pai, G., Peterson, J., Quail, M. A., Rajandream, M. A., Reitter, C., Sanders, M., Schobel, S., Sharp, S., Simmonds, M., Simpson, A. J., Tallon, L., Turner, C. M., Tait, A., Tivey, A., Van Aken, S., Walker, D., Wanless, D., White, B., White, O., Whitehead, S., Wortman, J., Barry, J. D., Fairlamb, A. H., Field, M. C., Gull, K., Landfear, S., Marcello, L., Martin, D. M., Opperdoes, F., Ullu, E., Whickstead, B., Alsmark, C., Arrowsmith, C., Carrington, M., Embley, T. M., Ivens, A., Lord, A., Morgan, G. M., Peacock, C. S., Rabbinowitsch, E., Salzberg, S., Wang, S., Woodward, J., and Adams, M. D. (2005) The genome of the African trypanosome, *Trypanosoma brucei. Science* **309,** 416–422
12. Speijer, D., Muijsers, A. O., Dekker, H., de, Haan, A., Breek, C. K., Albracht, S. P., and Benne, R. (1996) Purification and characterization of cytochrome c oxidase from the insect trypanosomatid *Crithidia fasciculata. Mol. Biochem. Parasitol.* **79,** 47–59
13. Speijer, D., Breek, C. K., Muijsers, A. O., Hartog, A. F., Berden, J. A., Albracht, S. P., Samyn, B., Van Beeumen, J., and Benne, R. (1997) Characterization of the respiratory chain from cultured *Crithidia fasciculata. Mol. Biochem. Parasitol.* **85,** 171–186
14. Horváth, A., Berry, E. A., Huang, L. S., and Maslov, D. A. (2000) Leishmania tarentolae: a parallel isolation of cytochrome bc(1) and cytochrome c oxidase. *Exp. Parasitol.* **96,** 160–167
15. Morales, J., Mogi, T., Mineki, S., Takashima, E., Mineki, R., Hirawake, H., Sakamoto, K., Omura, S., and Kita, K. (2009) Novel mitochondrial complex II isolated from *Trypanosoma cruzi* is composed of 12 peptides including a heterodimeric Ip subunit. *J. Biol. Chem.* **284,** 7255–7263
16. Panigrahi, A. K., Ziková, A., Dalley, R. A., Acestor, N., Ogata, Y., Anupama, A., Myler, P. J., and Stuart, K. D. (2008) Mitochondrial complexes in *Trypanosoma brucei*: a novel complex and a unique oxidoreductase complex. *Mol. Cell. Proteomics* **7,** 534–545
17. Ziková, A., Panigrahi, A. K., Uboldi, A. D., Dalley, R. A., Handman, E., and Stuart, K. (2008) Structural and functional association of *Trypanosoma brucei* MIX protein with cytochrome c oxidase complex. *Eukaryot Cell* **7,** 1994–2003
18. Wirtz, E., Leal, S., Ochatt, C., and Cross, G. A. M. (1999) A tightly regulated inducible expression system for conditional gene knock-outs and dominant-negative genetics in *Trypanosoma brucei. Mol. Biochem. Parasitol.* **99,** 89–101
19. Jensen, B. C., Kifer, C. T., Brekken, D. L., Randall, A. C., Wang, Q., Drees, B. L., and Parsons, M. (2007) Characterization of protein kinase CK2 from *Trypanosoma brucei. Mol. Biochem. Parasitol.* **151,** 28–40
20. Panigrahi, A. K., Schnaufer, A., Ernst, N. L., Wang, B., Carmean, N., Salavati, R., and Stuart, K. (2003) Identification of novel components of *Trypanosoma brucei* editosomes. *RNA.* **9,** 484–492
21. Panigrahi, A. K., Schnaufer, A., and Stuart, K. D. (2007) Isolation and Compositional Analysis of Trypanosomatid Editosomes, In: Gott, J. M. (ed), *Methods in Enzymology*, Vol 424 Ed., pp. 3–24, Elsevier Inc.
22. Wittig, I., Karas, M., and Schägger, H. (2007) High resolution clear native electrophoresis for in-gel functional assays and fluorescence studies of membrane protein complexes. *Mol. Cell Proteomics.* **6,** 1215–1225
23. Priest, J. W., and Hajduk, S. L. (2003) Trypanosoma brucei cytochrome c1 is imported into mitochondria along an unusual pathway. *J. Biol. Chem.* **278,** 15084–15094
24. Ziková, A., Panigrahi, A. K., Dalley, R. A., Acestor, N., Anupama, A., Ogata, Y., Myler, P. J., and Stuart, K. (2008) Trypanosoma brucei mitochondrial ribosomes: affinity purification and component identification by mass spectrometry. *Mol. Cell Proteomics* **7,** 1286–1296
25. Panigrahi, A. K., Ogata, Y., Ziková, A., Anupama, A., Dalley, R. A., Acestor, N., Myler, P. J., and Stuart, K. D. (2009) A comprehensive analysis of *Trypanosoma brucei* mitochondrial proteome. *Proteomics* **9,** 434–450
26. Keller, A., Nesvizhskii, A. I., Kolker, E., and Aebersold, R. (2002) Empirical statistical model to estimate the accuracy of peptide identifications made by MS/MS and database search. *Anal. Chem.* **74,** 5383–5392
27. Nesvizhskii, A. I., Keller, A., Kolker, E., and Aebersold, R. (2003) A statistical model for identifying proteins by tandem mass spectrometry. *Anal. Chem.* **75,** 4646–4658
28. Tabb, D. L., McDonald, W. H., and Yates, J. R., 3rd (2002) DTASelect and Contrast: tools for assembling and comparing protein identifications from shotgun proteomics. *J Proteome. Res.* **1,** 21–26
29. Park, S. K., Venable, J. D., Xu, T., and Yates, J. R., 3rd (2008) A quantitative analysis software tool for mass spectrometry-based proteomics. *Nat Methods.* **5,** 319–322
30. Carroll, J., Fearnley, I. M., Shannon, R. J., Hirst, J., and Walker, J. E. (2003) Analysis of the subunit composition of complex I from bovine heart mitochondria. *Mol Cell Proteomics.* **2,** 117–126
31. Opperdoes, F. R., and Michels, P. A. (2008) Complex I of Trypanosomatidae: does it exist? *Trends Parasitol.* **24,** 310–317
32. Fang, J., Wang, Y., and Beattie, D. S. (2001) Isolation and characterization of complex I, rotenone-sensitive NADH: ubiquinone oxidoreductase, from the procyclic forms of *Trypanosoma brucei. Eur. J. Biochem.* **268,** 3075–3082
33. Priest, J. W., and Hajduk, S. L. (1992) Cytochrome *c* reductase purified from *Crithidia fasciculata* contains an atypical cytochrome c_1. *J. Biol. Chem.* **267,** 20188–20195
34. Stuart, K., and Feagin, J. E. (1992) Mitochondrial DNA of kinetoplastids. *Int. Rev. Cytol.* **141,** 65–88
35. Horváth, A., Berry, E. A., and Maslov, D. A. (2000) Translation of the edited mRNA for cytochrome b in trypanosome mitochondria. *Science.* **287,** 1639–1640
36. Horvath, A., Kingan, T. G., and Maslov, D. A. (2000) Detection of the mitochondrially encoded cytochrome c oxidase subunit I in the trypanosomatid protozoan *Leishmania tarentolae. Evidence for translation of unedited mRNA in the kinetoplast. J. Biol. Chem.* **275,** 17160–17165
37. Hashimi, H., Benkovicová, V., Cermaková, P., Lai, D. H., Horváth, A., and Lukes, J. (2010) The assembly of F(1)F(O)-ATP synthase is disrupted upon interference of RNA editing in *Trypanosoma brucei. Int. J Parasitol.* **40,** 45–54
38. Lazarou, M., Thorburn, D. R., Ryan, M. T., and McKenzie, M. (2009) Assembly of mitochondrial complex I and defects in disease. *Biochim. Biophys. Acta* **1793,** 78–88

39. Gawryluk, R. M., and Gray, M. W. A split and rearranged nuclear gene encoding the iron-sulfur subunit of mitochondrial succinate dehydrogenase in Euglenozoa. *BMC Res. Notes.* 2: 16:16, 2009
40. Iwata, S., Lee, J. W., Okada, K., Lee, J. K., Iwata, M., Rasmussen, B., Link, T. A., Ramaswamy, S., and Jap, B. K. (1998) Complete structure of the 11-subunit bovine mitochondrial cytochrome bc1 complex. *Science* **281,** 64–71
41. Hemrika, W., De, Jong, M., Berden, J. A., and Grivell, L. A. (1994) The C-terminus of the 14-kDa subunit of ubiquinol-cytochrome-c oxidoreductase of the yeast *Saccharomyces cerevisiae* is involved in the assembly of a functional enzyme. *Eur. J Biochem.* **220,** 569–576
42. Fang, J., and Beattie, D. S. (2002) Novel FMN-containing rotenone-insensitive NADH dehydrogenase from *Trypanosoma brucei* mitochondria: isolation and characterization. *Biochemistry* **41,** 3065–3072
43. Millar, A. H., Eubel, H., Jänsch, L., Kruft, V., Heazlewood, J. L., and Braun, H. P. (2004) Mitochondrial cytochrome c oxidase and succinate dehydrogenase complexes contain plant specific subunits. *Plant Mol. Biol.* **56,** 77–90
44. Lemire, B. D., and Oyedotun, K. S. (2002) The *Saccharomyces cerevisiae* mitochondrial succinate:ubiquinone oxidoreductase. *Biochim. Biophys. Acta* **1553,** 102–116
45. Bochud-Allemann, N., and Schneider, A. (2002) Mitochondrial substrate level phosphorylation is essential for growth of procyclic *Trypanosoma brucei. J. Biol. Chem.* **277,** 32849–32854
46. Coustou, V., Biran, M., Breton, M., Guegan, F., Rivière, L., Plazolles, N., Nolan, D., Barrett, M. P., Franconi, J. M., and Bringaud, F. (2008) Glucose-induced remodeling of intermediary and energy metabolism in procyclic *Trypanosoma brucei. J. Biol. Chem.* **283,** 16342–16354
47. Schägger, H., and Pfeiffer, K. (2000) Supercomplexes in the respiratory chains of yeast and mammalian mitochondria. *EMBO J.* **19,** 1777–1783
48. Cruciat, C. M., Brunner, S., Baumann, F., Neupert, W., and Stuart, R. A. (2000) The cytochrome bc1 and cytochrome c oxidase complexes associate to form a single supracomplex in yeast mitochondria. *J. Biol. Chem.* **275,** 18093–18098
49. Yan, L. J., Yang, S. H., Shu, H., Prokai, L., and Forster, M. J. (2007) Histochemical staining and quantification of dihydrolipoamide dehydrogenase diaphorase activity using blue native PAGE. *Electrophoresis* **28,** 1036–1045
50. Yan, L. J., and Forster, M. J. (2009) Resolving mitochondrial protein complexes using nongradient blue native polyacrylamide gel electrophoresis. *Anal. Biochem.* **389,** 143–149
51. Verner, Z., Cermakova, P., Skodova, I., Kriegova, E., Horvath, A., and Lukes, J. (2010) Complex I (NADH:ubiquinone oxidoreductase) is active in but non-essential for procyclic *Trypanosoma brucei. Mol. Biochem. Parasitol.* doi:10.1016/j.molbiopara.2010.11.003
52. Fang, J., and Beattie, D. S. (2003) Alternative oxidase present in procyclic *Trypanosoma brucei* may act to lower the mitochondrial production of superoxide. *Arch. Biochem. Biophys.* **414,** 294–302
53. Carranza, J. C., Kowaltowski, A. J., Mendonca, M. A., de Oliveira, T. C., Gadelha, F. R., and Zingales, B. (2009) Mitochondrial bioenergetics and redox state are unaltered in *Trypanosoma cruzi* isolates with compromised mitochondrial complex I subunit genes. *J. Bioenerg. Biomembr.* **41,** 299–308
54. Corell, R. A., Myler, P. J., and Stuart, K. (1994) Trypanosoma brucei mitochondrial gene CR4 encodes an extensively edited mRNA with completely edited sequence only in the bloodstream forms. *Mol. Biochem. Parasitol.* **64,** 65–74
55. Dobrynin, K., Abdrakhmanova, A., Richers, S., Hunte, C., Kerscher, S., and Brandt, U. (2010) Characterization of two different acyl carrier proteins in complex I from *Yarrowia lipolytica. Biochim. Biophys Acta* **1797,** 152–159
56. van Berkel, W. J., Kamerbeek, N. M., and Fraaije, M. W. (2006) Flavoprotein monooxygenases, a diverse class of oxidative biocatalysts. *J. Biotechnol.* **124,** 670–689

In order to cite this article properly, please include all of the following information: Acestor, N., Zíková, A., Dalley, R. A., Anupama, A., Panigrahi, A. K., and Stuart, K. D. (2011) *Trypanosoma brucei* Mitochondrial Respiratome: Composition and Organization in Procyclic Form. *Mol. Cell. Proteomics* 10(9):M110.006908. DOI: 10.1074/mcp.M110.006908.

International Journal for Parasitology: Drugs and Drug Resistance 6 (2016) 23–34

Contents lists available at ScienceDirect

International Journal for Parasitology: Drugs and Drug Resistance

journal homepage: www.elsevier.com/locate/ijppaw

Trypanocidal action of bisphosphonium salts through a mitochondrial target in bloodstream form *Trypanosoma brucei*

Abdulsalam A.M. Alkhaldi [a, 1, 2], Jan Martinek [b, 1], Brian Panicucci [b], Christophe Dardonville [c], Alena Zíková [b, **], Harry P. de Koning [a, *]

[a] Institute of Infection, Immunity and Inflammation, College of Medical, Veterinary and Life Sciences, University of Glasgow, Glasgow, United Kingdom
[b] Institute of Parasitology, Biology Centre & Faculty of Science, University of South Bohemia, České Budějovice, Czech Republic
[c] Instituto de Química Médica, IQM–CSIC, Juan de la Cierva 3, E-28006 Madrid, Spain

ARTICLE INFO

Article history:
Received 15 October 2015
Received in revised form
3 December 2015
Accepted 7 December 2015
Available online 11 December 2015

Keywords:
Trypanosoma brucei
Mitochondrion
FoF1 ATPase
Succinate dehydrogenase
Phosphonium salt
SDH complex

ABSTRACT

Lipophilic bisphosphonium salts are among the most promising antiprotozoal leads currently under investigation. As part of their preclinical evaluation we here report on their mode of action against African trypanosomes, the etiological agents of sleeping sickness. The bisphosphonium compounds CD38 and AHI-9 exhibited rapid inhibition of *Trypanosoma brucei* growth, apparently the result of cell cycle arrest that blocked the replication of mitochondrial DNA, contained in the kinetoplast, thereby preventing the initiation of S-phase. Incubation with either compound led to a rapid reduction in mitochondrial membrane potential, and ATP levels decreased by approximately 50% within 1 h. Between 4 and 8 h, cellular calcium levels increased, consistent with release from the depolarized mitochondria. Within the mitochondria, the Succinate Dehydrogenase complex (SDH) was investigated as a target for bisphosphonium salts, but while its subunit 1 (SDH1) was present at low levels in the bloodstream form trypanosomes, the assembled complex was hardly detectable. RNAi knockdown of the SDH1 subunit produced no growth phenotype, either in bloodstream or in the procyclic (insect) forms and we conclude that in trypanosomes SDH is not the target for bisphosphonium salts. Instead, the compounds inhibited ATP production in intact mitochondria, as well as the purified F_1 ATPase, to a level that was similar to 1 mM azide. Co-incubation with azide and bisphosphonium compounds did not inhibit ATPase activity more than either product alone. The results show that, in *T. brucei*, bisphosphonium compounds do not principally act on succinate dehydrogenase but on the mitochondrial F_oF_1 ATPase.

1. Introduction

African trypanosomes are responsible for a spectrum of important human and veterinary diseases south of the Sahara, transmitted by various tsetse fly species. *Trypanosoma brucei gambiense* causes a chronic but fatal human African trypanosomiasis (HAT, or sleeping sickness) in Western and Central Africa, whereas *T. b. rhodesiense* causes a much more acute illness in Eastern and Southern Africa (Brun et al., 2010); both forms of the disease are considered almost invariably fatal if left untreated. Whereas transmission of *T. b. gambiense* appears to be almost exclusively anthroponotic, *T. b. rhodesiense* is a zoonotic parasite, with many wild and domestic animals, particularly cattle, acting as reservoirs (Welburn et al., 2001). In addition, *Trypanosoma congolense*, *T. b. brucei*, *Trypanosoma evansi* and *Trypanosoma vivax* cause animal African trypanosomiasis (AAT), inflicting a terrible burden on agriculture in the tsetse belt and, for the latter two species, also in areas far beyond the testse habitat including the Indian subcontinent and South America (Desquesnes et al., 2013; Osório et al., 2008; Swallow, 1999).

While vector control in conjunction with extensive surveillance can have highly significant local impact on the disease burden, there is no realistic prospect of a vaccine (La Greca and Magez,

* Corresponding author. Institute of Infection, Immunity and Inflammation, College of Medical, Veterinary and Life Sciences, University of Glasgow, 120 University Place, Glasgow G12 8TA, United Kingdom.
** Corresponding author. Institute of Parasitology, Biology Centre & Faculty of Science, University of South Bohemia, České Budějovice 37005, Czech Republic.
E-mail addresses: azikova@paru.cas.cz (A. Zíková), Harry.de-Koning@glasgow.ac.uk (H.P. de Koning).
[1] These authors contributed equally.
[2] Present address: Department of Biology, College of Science, Aljouf University, Sakaka, Saudi Arabia.

http://dx.doi.org/10.1016/j.ijpddr.2015.12.002

2011) and chemotherapy is practically the only option in most areas (Delespaux and de Koning, 2007; Jannin and Cattand, 2004). However, few drugs currently exist for either HAT or AAT, and these are old, suffer from severe side-effects and/or resistance, and are usually only effective against certain (sub) species or stages of the disease (Brun et al., 2010; Delespaux and de Koning, 2007). New therapeutic agents are therefore urgently necessary, preferably active against all African trypanosome species, and against both stages of the human disease. One promising lead is the class of benzyltriphenylphosphonium compounds that displays highly potent activity against rodent models of *T. b. rhodesiense* (Kinnamon et al., 1979), *Trypanosoma cruzi* (Kinnamon et al., 1977) and *Leishmania donovani* (Hanson et al., 1977) infections. Moreover, a large series of bisphosphonium salts were shown to possess strong anti-leishmanial (Luque-Ortega et al., 2010) and trypanocidal (Dardonville et al., 2015; Taladriz et al., 2012) activity in vitro. Many of these compounds showed high selectivity against the kinetoplastid parasites relative to human cell lines and, importantly, displayed no cross-resistance with existing trypanocides such as diamidines and melaminophenyl arsenicals (Taladriz et al., 2012).

The triphenylphosphonium (TPP) moiety has been used extensively as a vehicle to deliver drugs to mitochondrial targets (Cairns et al., 2015; Cortes et al., 2015; Smith et al., 2011). Among many applications, TPP has been used to deliver functional probes (Cairns et al., 2015), antioxidants (Kelso et al., 2001; Teixeira et al., 2012), anti-cancer drugs (Jara et al., 2014), and even liposomes (Benein et al., 2015) to mitochondria. TPP-linked natural compounds botulin and betulinic acid showed in vitro and in vivo activity against *Schistosoma mansoni* (Spivak et al., 2014). Crucially, TPP-mediated mitochondrial targeting appears to be generally safe, as a double-blind, placebo controlled study with human volunteers found no evidence of side-effects of the TPP-coupled antioxidant MitoQ over a 12-month period (Snow et al., 2010).

The mitochondrial accumulation of TPP-coupled drugs is driven by the strong inside-negative potential across the inner membrane of the mitochondrion. TPP, being a lipophilic cation with a highly dispersed charge is believed to diffuse freely across the inner membrane and be highly concentrated in the mitochondrial matrix, to an extent determined by the mitochondrial membrane potential Ψm and the plasma membrane potential V_m, as described by the Nernst equation (Cairns et al., 2015). Consistent with the extensive TPP literature, Luque-Ortega et al. showed that the anti-leishmanial TPP analogues targeted the parasite's mitochondrion, and proposed their principal action to be the inhibition of the succinate dehydrogenase complex (complex II) (Luque-Ortega et al., 2010). However, similar compounds also had strong activity against bloodstream form (BF) *T. brucei* (Dardonville et al., 2015; Taladriz et al., 2012), which has a much less elaborate mitochondrial metabolism, lacking for instance much of the Krebs cycle, and the cytochrome-dependent respiratory chain (Tielens and van Hellemond, 2009). Transfer of electrons to oxygen is instead mediated by a plant-like alternative oxidase (Chaudhuri et al., 1998) and the mitochondrial membrane potential is maintained by the F_oF_1 ATPase pumping protons from the mitochondrial matrix (Nolan and Voorheis, 1992; Schnaufer et al., 2005). We thus investigated whether the succinate dehydrogenase complex is expressed in BF *T. brucei*, and whether this might be the primary target for the trypanocidal activity of triphenylphosphonium salts and their analogues. We selected two compounds with strong trypanocidal activity (Taladriz et al., 2012) to represent the main two classes of aliphatic and aromatic bisphosphonium salts (Fig. 1).

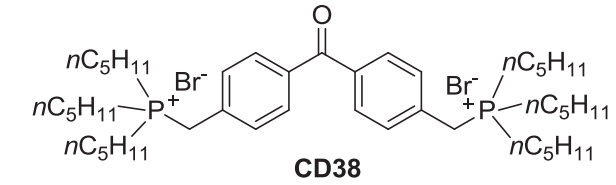

CD38

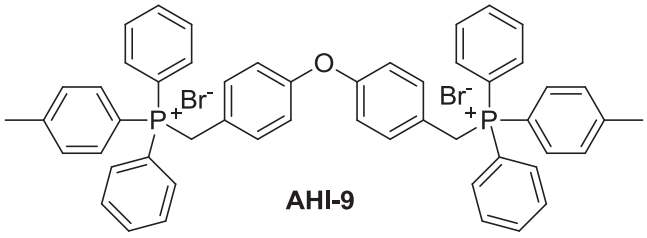

AHI-9

Fig. 1. Benzophenone-derived bisphosphonium salts used in this study.

2. Materials and methods

2.1. Effect of bisphosphonium compounds on growth of BF T. brucei

The effects of AHI-9 and CD38 on growth of BF *Trypanosoma brucei brucei* strain Lister 427 were investigated by incubating cultures under standard conditions (HMI-9/10% FBS; 37 °C, 5% CO_2) in the presence or absence of 0.1 μM, 0.3 μM or 1 μM test compound for up to 72 h. Samples were taken in triplicate at the following times (h) after initiation of the experiment: 0, 4, 8, 12, 24, 28, 32, 36, 48, 52, 56, 60, 72. Cell density in the samples was determined using a haemocytometer. Compounds CD38 and AHI-9 were synthesized as reported previously (Luque-Ortega et al., 2010; Taladriz et al., 2012).

2.2. Determination of trypanocidal action using the Alamar blue assay

Fifty percent effective concentrations (EC_{50}) were determined using the fluorescence viability indicator dye Alamar Blue (resazurin sodium salt, Sigma), exactly as described (Gould et al., 2013, 2008). Serial doubling dilutions of test compounds were prepared over two rows of a 96-well plate, leaving the last well without added drug as a control, before the addition of an equal volume of cell suspension to each well. Final cell density in each well was 10^5 BF *T. brucei* per mL. The plates were incubated for 48 h (37 °C, 5% CO_2) before the addition of 20 μL resazurin solution (125 μg/mL in PBS pH7.4) per well and incubation for a further 24 h. Fluorescence was determined using a FLUOstar Optima (BMG Labtech, Durham, NC, USA) with excitation wavelength set at 544 nm and emission at 620 nm. Data were plotted to a sigmoid curve with variable slope using Prism 5.0 (GraphPad, San Diego, CA).

2.3. Assessing cell cycle progression in T. brucei

2.3.1. DAPI staining

Nuclei and kinetoplasts were visualized using the fluorescent dye 4,6-diamidino-2-phenylindole (DAPI) on BF trypanosomes after fixation. 50 μL of cells at ~5 × 10^5 cells/mL were spread onto a glass microscope slide, left to air dry and fixed in methanol overnight at −20 °C. The slides were rehydrated with 1 mL of PBS for 10 min, which was allowed to evaporate (but not to completely dry). 50 μL of PBS containing 1 μg/mL DAPI and 1% of 1,4-diazabicyclo [2.2.2] octane (DAPCO) was added to the slides and

spread by coverslip. Slides were observed under UV light on a Zeiss Axioplan microscope using a Hamamatso digital camera and Openlab software. 500 cells were recorded for each sample, and scored for DNA configuration into the following groups: 1N1K, 1N2K, 2N2K (Early) and 2N2K (Late) (N, nucleus; K, kinetoplast; 'Early' no ingression furrow; 'Late', cell division started with clear ingression furrow). The effect of test compounds on DNA configuration was determined at 0, 8, 12, 16 and 24 h; untreated cultures served as control.

2.3.2. Flow cytometry

DNA content of BF trypanosomes was measured by flow cytometry using the fluorescent dye propidium iodide (PI), as described (Hammarton et al., 2003; Ibrahim et al., 2011). Briefly, 1 mL of cell suspension at 10^6 cells/mL was transferred at each time point into microfuge tubes and centrifuged at 2500 rpm for 10 min at 4 °C, then resuspended and fixed in 1 mL of 70% methanol and 30% PBS and left at 4 °C overnight. The samples were washed twice with 1 mL of PBS and subsequently resuspended in 1 mL PBS containing propidium iodide and RNase A (both at 10 μg/mL), and incubated at 37 °C for 45 min while protected from light. Samples were analysed by Becton Dickinson FACSCalibur using the FL2-Area detector and CellQuest software. ModFit LT software was used to quantify the flow cytometry results.

2.4. Measuring intracellular calcium in BF T. brucei

Intracellular calcium levels were measured using the Screen Quest™ Fluo-8 Calcium Kit (ABD Bioquest, Sunnyvale, CA). *T. b. brucei* of strain Lister 427 were grown in HMI-9/FCS in vented flasks incubated (37 °C/5% CO_2 for 48 h) and harvested by centrifugation (2500 × *g*, 10 min at 4 °C), resuspended to a final density of 4×10^6 cells/mL and divided into aliquots for determination at 0, 4, 8, 12 h of exposure to test compounds (in HMI-9/FCS, 37 °C/5% CO_2). At an appropriate interval before the start of the measurement, aliquots of this culture were transferred to centrifuge tubes, centrifuged (10 min, 2500 *g*) and resuspended in the Fluo-8 dye-loading solution at exactly 4×10^6 cells/mL and further incubated at 37 °C for 30 min. The cells were then washed twice with assay buffer to remove any extracellular dye-loading solution. 90 μL of cell suspension was added to each well of a black-bottomed 96-well plate, and subsequently 10 μL of test compound at 10 × concentration was added (except for the 0 min recording); 10 μM calcium ionophore A23187 (Sigma) was used as a positive control and 10 μL buffer was added to a well that served as drug-free control. The plate was then incubated in a FLUOstar OPTIMA fluorimeter at 37 °C, and the fluorescence was observed for 10 min using cycles of 4 s.

2.5. Mitochondrial membrane potential of BF T. brucei

2.5.1. Analysis of drug-treated cells

The mitochondrial membrane potential of treated and untreated cells was assessed by using Tetramethylrhodamine ethyl ester (TMRE) (Denninger et al., 2007; Figarella et al., 2006). The cell density was adjusted to 10^6 cells/mL with and without test compounds for the start of the experiment. 1 mL of sample was transferred at each time point into a microfuge tube and centrifuged at 2500 rpm for 10 min at 4 °C, and was then resuspended in 1 mL PBS containing 25 nM of TMRE, and cells were incubated at 37 °C for 30 min. Valinomycin (100 nM) and troglitazone (10 μM) were used as controls, as they are known to induce mitochondrial membrane depolarization and hyperpolarization, respectively (Denninger et al., 2007). All samples were analysed by flow cytometry using a FL2-heigth detector and CellQuest software. Mitochondrial membrane potential was expressed as the percentage of cells displaying fluorescence higher than 100 artificial units, which was calibrated at exactly 50% for the no-drug control sample of the zero incubation time point, as described (Ibrahim et al., 2011).

2.5.2. Analysis of RNAi cell lines

Cells in the exponential growth phase were stained with 60 nM of TMRE for 30 min at 37 °C. Cells were pelleted (1300 × *g*, 10 min, RT), resuspended in 2 mL of PBS (pH 7.4) and immediately analysed by flow cytometry (BD FACS Canto II Instrument). For each sample, 10,000 events were collected. Treatment with the protonophore FCCP (20 μM) was used as a control for mitochondrial membrane depolarization. Data were evaluated using BD FACSDiva (BD Company) software.

2.6. Plasmid construction, transfection, cell growth and RNAi induction

To create the SDH1 (Tb927.8.6580) RNAi construct, a 485 bp fragment was PCR amplified from *T. brucei* strain 427 genomic DNA with the following oligonucleotides: FW: GAT GGA TCC CTC TGG GCT TCG TGC CGC AA, REV: GGA AAG CTT TGC CAC GAC AAC AGC CGT CC utilizing the respective *Bam*HI and *Hind*III restriction sites inherent in the primers (underlined). The digested amplicon was then cloned into the p2T7-177 plasmid (Wickstead et al., 2002). This plasmid was used for transfection of PF *T. brucei* Lister 427 29.13 and BF Lister 427 single marker (SM) *T. brucei* cells that are transgenic for the T7 RNA polymerase and the tetracyclin (tet) repressor (Wirtz et al., 1999). PF 29.13 cells were grown in vitro at 27 °C in SDM79 medium containing hemin (7.5 mg/mL), hygromycin (25 μg/mL), G-418 (10 μg/mL) and 10% foetal bovine serum. BF SM cells were grown in vitro at 37 °C in HMI-9 medium containing G-418 (2.5 μg/mL) and 10% foetal bovine serum. After the transfection, both cell lines were selected using phleomycin (2.5 μg/mL). The inducible expression of double-stranded RNA was triggered by the addition of 1 μg/mL tetracycline to the medium. Growth curves were generated by measuring the cell density of tet-treated and untreated cultures using the Z2 cell counter (Beckman Coulter Inc.). Throughout the experiment, PF and BF cultures were split daily to ensure they continuously maintained an exponential growth phase of 10^6 - 10^7 cells/mL and 10^5–10^6 cells/mL, respectively.

2.7. Electrophoresis and western blot analysis

Crude mitochondrial fraction was isolated as described previously (Koreny et al., 2012; Subrtova et al., 2015) and the mitochondria were lysed using digitonin at detergent:protein ratio of 4 mg:1 mg. High resolution clear native (hrCN) PAGE analysis was performed by fractionating 50 μg of mitochondrial lysate on a 3–12% clear native (CN) PAGE gel followed by a protein transfer onto a nitrocellulose membrane. Protein samples from mitochondrial lysates were also separated on SDS PAGE gels and blotted onto a PVDF membrane. Both membranes were incubated with a specific SDH1 peptide antibody (1:1000) (Koreny et al., 2012), followed by an incubation with a secondary HRP-conjugated anti-rabbit antibody (1:2000, BioRad). The specific reaction was visualized using the Clarity™ Western ECl Substrate (Biorad) on a ChemiDoc instrument (BioRad).

2.8. Succinate:ubiquinone reductase (SQR) activity assay

The specific SQR activity was measured in a crude mitochondrial preparation (15μg) in 1 mL of SDH buffer (25 mM K2HPO4, pH 7.2, 5 mM MgCl2, 20 mM sodium succinate) containing specific inhibitors of respiratory complexes III and IV (0.0002% antimycin,

2 mM KCN) and 50μM DCIP (2,6-dichlorophenolindophenol (Sigma)), which acts as the electron acceptor. The reaction was started by adding 65 μM coenzyme Q2. The unit of succinate–dehydrogenase activity (U) is defined as an amount of enzyme in 1 mg of kinetoplastid proteins, which causes the conversion of 1 nmol of DCIP in 1 min, as monitored at 600 nm (Birch-Machin and Turnbull, 2001).

2.9. F_1-ATPase purification

Mitochondrial vesicles were purified as described previously (Acestor et al., 2011). Afterwards they were resuspended in buffer A (0.25 M sucrose, 50 mM Tris–HCl pH 8, 1 mM DTT) and the suspension was sonicated on power 8.5 for 3 × 40 s, with an incubation on ice of 1 min between sonications to prevent heating the sample. The samples were further sonicated for 10 15-s bursts, again left on ice for 1 min between the sonications (Sonicator 3000, Misonix, 19 mm probe, 250 W). The submitochondrial particles were then pelleted overnight in a SW60Ti rotor at 52,000 g at 4 °C.

The SMP pellet was resuspended in buffer B (0.25 M sucrose, 50 mM Tris HCl pH 8.0, 1 mM DTT, 4 mM EDTA, 2 mM ADP). Chloroform, saturated with 2 M Tris–HCl pH 8.5, was added to the pellet and then vigorously shaken for 20 s followed by immediate centrifugation for 5 min at 8500 rpm at room temperature. The top (light brown) layer was taken, leaving the middle (dark brown) and the bottom (chloroform containing) layers behind. The F_1 depleted SMPs and residual chloroform were removed by centrifugation in a SW28 rotor at 27,000 rpm for 30 min at room temperature, using chloroform resistant polyallomer tubes. The F_1-ATPase containing supernatant was carefully removed to avoid any chloroform contamination, blown with nitrogen for 15 min to remove all traces of chloroform. The F_1-ATPase was filtered, concentrated down to 750 μl and loaded on a Superdex 200 10/300 GL. The F_1-ATPase was purified on a FPLC using a specific F_1-column buffer (20 mM Tris pH 8.5, 200 mM NaCl, 1 mM DTT, 4 mM EDTA, 1 mM ADP, 0.002% PMSF).

2.10. ATPase activity measurements

The amount of ATP hydrolysis in a crude mitochondrial preparation or by affinity purified F_1 ATPase was measured by ATP regenerating assay (Pullman et al., 1960) that couples the hydrolysis of ATP with the oxidation of NADH. Crude mitochondrial lysates (15 μg) or purified F_1 ATPase (0.7 μg) were incubated with different concentrations (5–200 μM) of CD38 and AHI-9 for 5 min after which the mix was transferred to a 1-mL UV cuvette containing an ATPase buffer (50 mM Tris, pH 8, 50 mM KCl, 2 mM $MgSO_4$, 200 μM NADH, 1 mM phosphoenol pyruvate, 5 μL of lactate dehydrogenase (Sigma) and 9 μL of pyruvate kinase (Sigma)). The reaction was then initiated by adding 2 mM MgATP (from 100× solution of 400 mM Tris, 200 mM $MgSO_4$, 200 mM ATP) and the change of absorbance at 340 nm was measured for 5 min. Azide (1 mM) was used as a known inhibitor of F_1 ATPase activity (Bowler et al., 2006). Specific ATPase activity of mitochondrial lysate or of purified F_1 ATPase was calculated from the amount of NADH oxidized in 1 min, and normalised to the amount of the protein in the sample.

2.11. ATP production

ATP production in digitonin-extracted mitochondria was measured following a protocol described previously (Allemann and Schneider, 2000). Briefly, crude mitochondrial fractions from the RNAi knockdown cell lines were obtained by digitonin extraction (Tan et al., 2002). ATP production in these samples was induced by the addition of 67 μM ADP and 5 mM of succinate. The mitochondrial preparations were preincubated for 10 min on ice with the inhibitors malonate (6.7 mM) and atractyloside (33 μg/mL). The concentration of ATP was determined by a luminometer (Orion II, Berthold detection systems) using the CLS I ATP bioluminescence assay kit (Roche Applied Science).

2.12. Surface plasmon resonance (SPR)

SPR experiments were performed at 25 °C with a Biacore X100 apparatus (GE Healthcare, Biacore AB, Uppsala, Sweden) in MES buffer (10 mM 2-(N-morpholino)ethanesulfonic acid, 1 mM EDTA, 100 mM NaCl, 0.005% surfactant P20, pH 6.25). The 5′-biotin labelled DNA hairpins 5′-CGAATTCGTCTCCGAATTCG-3′ and 5′-CGCGCGCGTTTTCGCGCGCG-3′ (the loop is underlined) were purchased from Sigma–Aldrich with HPLC purification. The SPR measurements were carried out as described (Rios Martinez et al., 2014).

3. Results

3.1. Actions of bisphosphonium compounds on T. brucei growth and cell cycle

We investigated the actions of two bisphosphonium compounds on bloodstream form (BF) *T. b. brucei*. The compounds CD38 and AHI-9 were selected as (i) displaying sub-micromolar activity against the parasite, (ii) possessing >300-fold in vitro selectivity with a human cell line and (iii) representing the two main classes of phosphonium trypanocides, possessing either linear saturated aliphatic substituents (*n*-pentyl; CD38) or aromatic substituents (phenyl and 3-methylphenyl; AHI-9) on the phosphonium moiety (Taladriz et al., 2012).

Both compounds were confirmed to be active against *T. brucei*, with sub-micromolar activity against BF cells and about an order of magnitude less activity against the procyclic forms (PF) (Table 1). At concentrations up to the EC_{50} values the compounds caused delayed growth rather than cell death and even at concentrations several fold above EC_{50} (1 μM) the initial effect appeared to be immediate (CD38) or slightly delayed (AHI9) growth arrest, followed by cell death 16–24 h later (Fig. 2). We thus investigated whether the compounds induced cell cycle arrest in a specific phase of the cycle, using flow cytometry to measure the DNA content in single cells of the population. As expected, we found that untreated control cells were less prone to enter S-phase when the culture entered the late log-phase of growth, leading to a small increase in G1-phase cells after 16 h; the proportion of G1-phase cells had initially decreased as the culture progressed from stationary to early log phase; the proportion of cells in S-phase steadily declined during late log phase (Fig. 3A). Similar effects, but much more pronounced and at much lower cell densities, were observed in the cultures treated with CD38 or AHI-9: both displayed a steep decline in S-phase cells after 8 h, accompanied by a significant increase in G1-phase cells (Fig. 3A, B), although the cultures were in virtual growth arrest and at comparatively low density (Fig. 3C). We thus

Table 1
EC_{50} values for CD38 and AHI-9 compounds against BF427 and PF427 *T. brucei* cells.

	EC_{50} CD38 [μM]	EC_{50} AHI-9 [μM]
T. brucei BF427	0.52 ± 0.038	0.14 ± 0.016
T. brucei PF427	3.54 ± 0.14	1.19 ± 0.08
P value	0.00003	0.00004

The values represent the average and SEM of three independent determinations. The P value given is of an unpaired Student's t-test comparing the EC_{50} values for BF and PF trypanosomes.

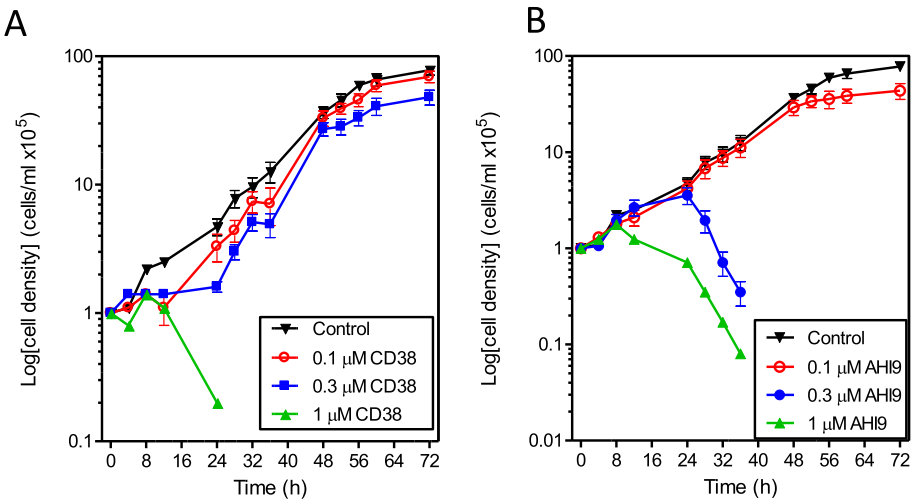

Fig. 2. Effect of different concentrations of two bisphosphonium compounds on the growth of BF *T. brucei brucei* over 72 h. Cell cultures were seeded at 10^5 cells/mL. Microscopic cell counts were performed in triplicate using a haemocytometer at various time points as indicated. The results shown are the average of three independent determinations; error bars depict standard errors.

conclude that bisphosphonium compounds prevent trypanosomes from entering the cell cycle and initiating DNA synthesis.

CD38 also caused a highly significant decrease in cells in the first stages of trypanosomal cell division, i.e. with 1 nucleus and 2 kinetoplasts (1N2K), or with 2 of each (2N2K) but no cleavage furrow initiated (2N2K-Early), after 8 h of treatment; the percentage of cells in all stages of division (IN2K, 2N2K) continued to decline sharply with the exposure time (Fig. 3D), as no new cells entered the cell division cycle. This experiment showed that bisphosphonium-treated cells were unable to replicate kinetoplast DNA and/or initiate kinetoplast division. It was not possible to reliably distinguish between the two possibilities, although we did not observe increased DAPI fluorescence associated with the kinetoplast (i.e. kDNA content) after CD38 treatment (not shown); however, it is uncertain whether this would have been sufficiently unambiguous. However, it has previously been reported that CD38 does not bind directly to a poly(dA.dT)$_2$ DNA polymer (Dardonville et al., 2006), and we here follow that up with SPR measurements of CD38 and AHI-9 binding to two other DNA. Neither compound showed measurable binding to the CGAATTCG oligonucleotide, and only CD38 interacted, weakly, with the CGCGCGCG sequence, with a K_D of 7.0×10^{-6} M (Supplementary Fig. S1). This seems inconsistent with a direct action on kinetoplast replication by kDNA binding.

3.2. The mitochondrion as a target for the trypanocidal activity of bisphosphonium salts

It has been reported that CD38 elicits anti-leishmanial activity by inhibiting the succinate dehydrogenase complex (also known as complex II) in the *L. donovani* mitochondrion (Luque-Ortega et al., 2010), and a mitochondrial target would be consistent with the observed phenotype of being unable to initiate kinetoplast division (above).

Incubation of BF *T. brucei* with CD38 or AHI-9 for 4 h, at concentrations close to their respective EC_{50} values, caused a dose-dependent reduction of the mitochondrial membrane potential Ψm (Fig. 4A). At 0.7 μM bisphosphonium compound, small effects were observed after just 30 min ($P < 0.05$ for CD38) and much more dramatic reductions were seen after 4 h of exposure ($P < 0.001$ for both compounds) until the mitochondrial membranes appeared to be almost fully depolarized (Fig. 4B). This was accompanied by a similar drop in cellular ATP levels, which was highly significantly different from control ($P < 0.01$) and was statistically identical to treatment with the F_1F_o ATPase inhibitor oligomycin after 1 h. This level of cellular ATP remained essentially constant for at least 12 h of treatment with either of the test compounds (Fig. 4C). The decrease of cellular ATP is in agreement with the observed redirection of glycolysis to 1 molecule of glycerol and 1 molecule of pyruvate due to Ψm dissipation (see the discussion). Another cellular effect was that after four hours of incubation with CD38 or AHI-9 the level of free intracellular Ca^{2+} started to increase (Fig. 4D), which was consistent with the depolarized mitochondria being unable to maintain their capacity as calcium reservoir (Huang et al., 2013).

3.3. Assessment of succinate dehydrogenase as a potential target for bisphosphonium compounds in T. brucei

Because the target of bisphosphonium salts in *L. donovani* cells was suggested to be the succinate dehydrogenase (SDH) complex (Luque-Ortega et al., 2010), we explored, in both PF and BF *T. brucei*, its steady state protein level, the assembly of the complex, and whether its depletion elicits a reduced growth rate. First, we determined the steady state levels of a specific subunit of the SDH complex, SDH1, which contains the cofactor FAD and is responsible for the electron entry into the complex. When mitochondrial lysate was fractionated on a TGX stain-free precast gel followed by western blot analysis using anti-SDH1 antibody, the correct size band for SDH1 (66 kDa) was detected. The highest level of expression is seen in PF cells and much lower amounts of SDH1 subunit are detected in BF cells (Fig. 5A, upper panel). Equal loading of protein samples was verified by UV detection of proteins (Fig. 5A, lower panel). Independently-generated mitochondrial samples were analysed repeatedly with similar results, confirming the relatively low intensity of the SDH1 signal in BF cells compared to PF, and clearly show a much lower steady-state SDH1 protein level in the former life cycle stage.

To gain better insight about the significance of the function of the SDH complex in PF and BF cells, the level of assembled SDH complex was analysed by high resolution clear native (hrCNE) PAGE. The expected band of ~500 kDa (Acestor et al., 2011) is prominent in the PF sample, but only a very faint band is detected in BF mitochondrial lysate (Fig. 5B), which correlates well with the

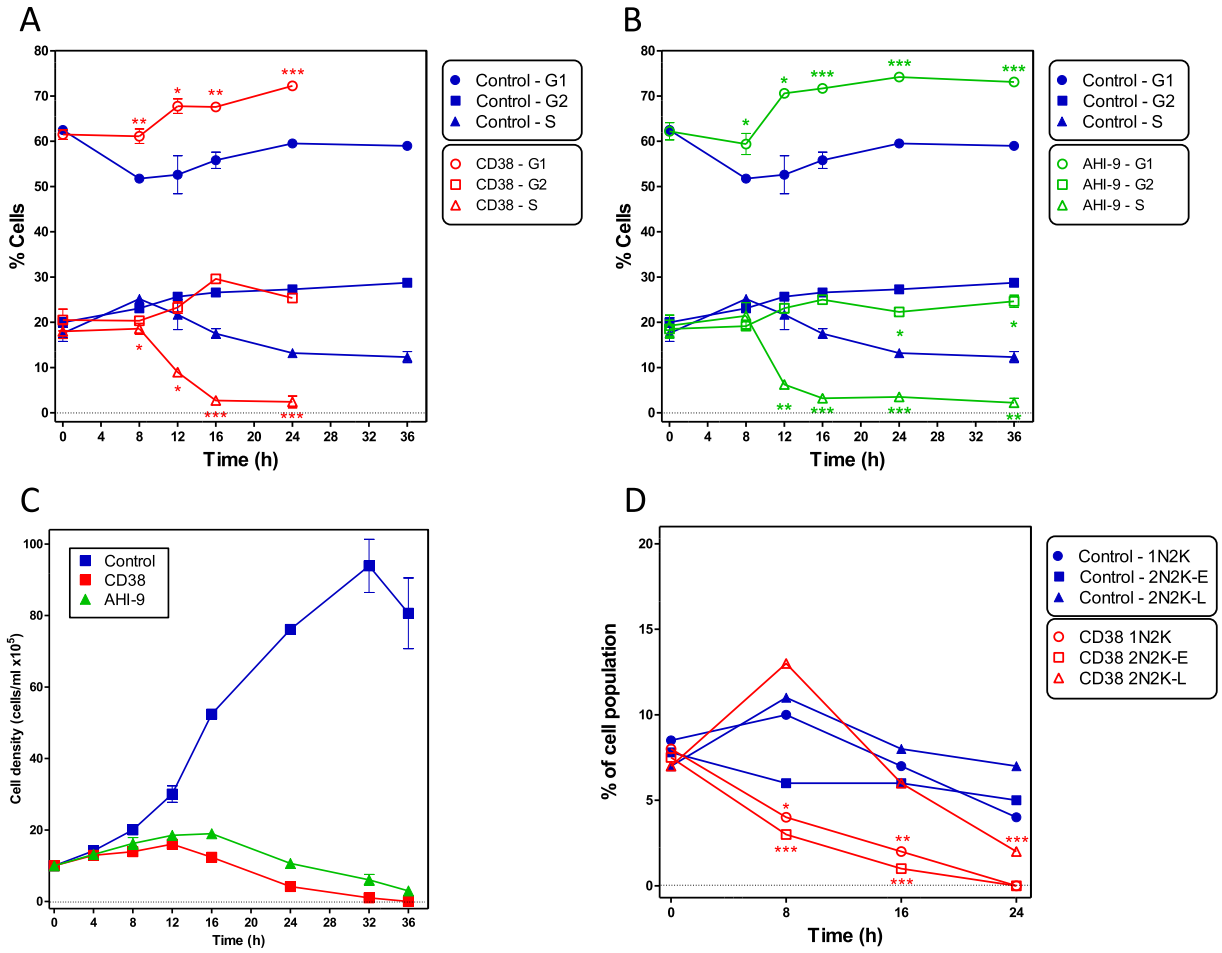

Fig. 3. Cell cycle analysis of BF *T. b. brucei*. (A) Control culture grown under standard conditions (blue closed symbols) or in the presence of 0.7 μM CD38 analysed for DNA content (red open symbols). Percentages of cells in each cell cycle stage were determined after staining of the permeabilised cells with propidium iodide, followed by flow cytometry. The data was further analysed by using the ModFit LT software to accurately separate and quantity the different peaks. (B) Identical culture grown in parallel but in the presence of 0.7 μM AHI-9 (green open symbols). The same control data as in panel A is shown for easy comparison. Panel C shows the cell densities of the cultures in panels A and B during this experiment, measured by using microscopic cell counts, performed in triplicate, using a haemocytometer. The results shown in panel A–C are the average of three independent experiments. Error bars depict standard errors, when not shown fall into the symbol. Statistical significance was determined using Student's unpaired T-test against the corresponding control group (*P < 0.05, **P < 0.01, ***P < 0.001). D. Percentage of the *T. brucei* population in each stage of the cell division cycle, with and without incubation with 0.7 μM CD38 over 24 h, as determined by fluorescence microscopy after staining with DAPI. For each culture, about 500 cells were counted and scored in terms of nuclei and kinetoplasts. N = nuclei, K = kinetoplasts, E = early stage of division, L = late stage of division (furrow ingression). Significant differences from the drug free control were calculated by using the Chi-squared test. (For interpretation of the references to colour in this figure legend, the reader is referred to the web version of this article.)

relative steady state levels of SDH1 in the respective life stages of *T. brucei*. Interestingly, two bands were detected in the PF sample, suggesting that the complex may form higher molecular weight aggregates, or associate with another macromolecular structure, as suggested by Kovarova et al. for the mammalian complex II (Kovarova et al., 2013).

The activity of the SDH complex can be followed spectrophotometrically as a change in the absorbance of DCIP, with electrons flowing from succinate to DCIP via ubiquinone Q_2. Each cell line was also incubated with the specific SDH inhibitor malonate to verify that only this specific activity was detected. The succinate-ubiquinone reductase (SQR) activity measured in BF cells corresponded to only 7% of the activity of SQR measured in PF cells (Table 2). These data closely correspond with the relative steady state protein levels of SDH complex (see above), and confirm that the SDH complex is much more abundant and is thus likely to play a more important role in the mitochondria of PF than BF cells.

It has been shown that the SDH complex possesses an essential function in PF *T. brucei* (strain EATRO1125) when grown in the absence of glucose, while its function was unimportant for cells grown in the presence of glucose (Coustou et al., 2008). Nevertheless, both tested compounds exert a cytotoxic effect for PF 427 Lister strain *T. brucei* grown in the presence of glucose (Table 1). To address whether the SDH complex is essential for the viability of this specific strain of *T. brucei*, and under the specific conditions used in our study, a cell line expressing RNAi targeting the SDH1 subunit was generated. When PF SDH1 RNAi cells were grown in glucose-rich media, no significant difference in growth of non-induced and tetracycline-induced RNA cells was observed. (Fig. 5C) confirming that the SDH complex is not essential for PF cells under glucose-rich growth conditions. To test whether the SDH complex is important for the viability of BF *T. brucei* cells, the BF SDH RNAi cell line was examined upon induction with tetracycline. Importantly, there was no growth phenotype at all (Fig. 5D). To verify successful depletion of SDH1 protein in the PF and BF RNAi induced cell lines, a western blot analysis was performed with the specific SDH1 antibody. In PF RNAi tetracycline-induced cells a band of the appropriate size had disappeared after 1 day, but a band of somewhat lower apparent weight remained unchanged (Fig. 5E). In order to confirm that the upper band was specific for SDH1, the

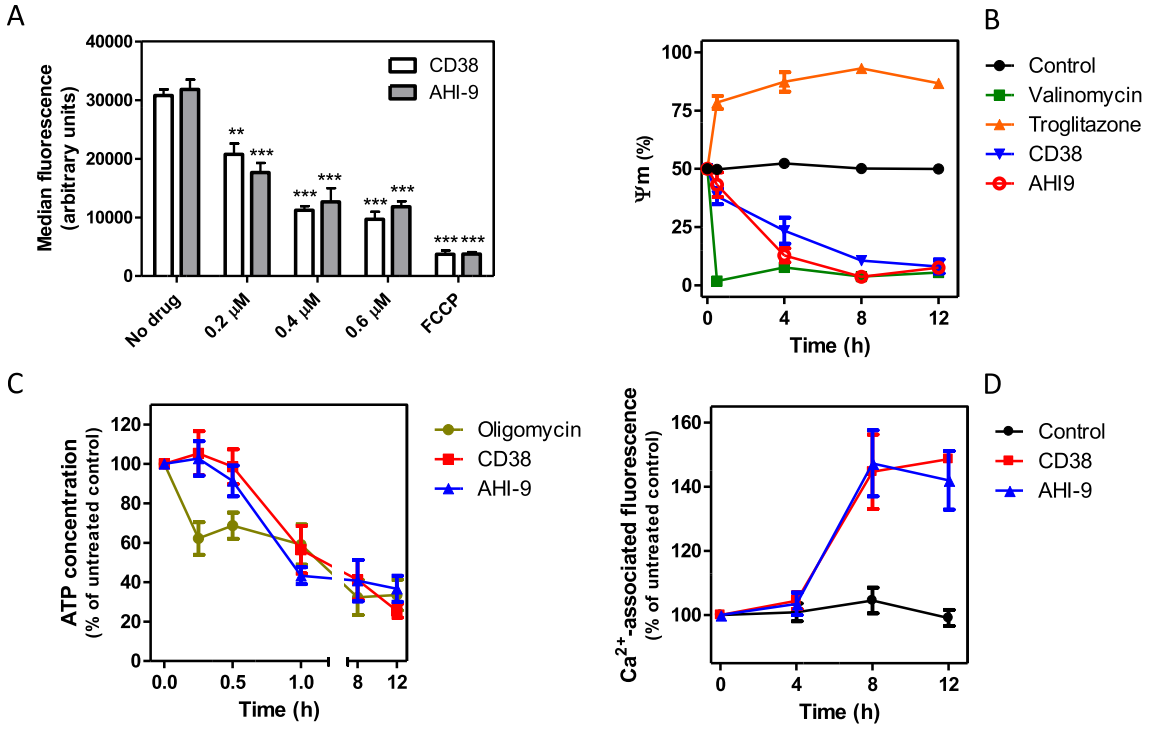

Fig. 4. Effects of bisphosphonium compounds on mitochondrial functionality in live BF trypanosomes. (A) Dose-dependency of effect of CD38 and AHI-9 on mitochondrial membrane potential Ψm after four hours of exposure, measured by flow cytometry using the indicator fluorophore TMRE. Data are the triplicate and SEM of three independent experiments. Statistical significance was determined using an unpaired Student's t-test: **, $P < 0.01$; ***, $P < 0.001$. (B) Effects of 0.7 μM CD38 and AHI-9 on Ψm over a period of 8 h, using 0.1 μM valinomycin and 10 μM troglitazone as controls for membrane depolarisation and hyperpolarisation, respectively. Data are the triplicate and SEM of three independent experiments. Statistically significant differences were observed for CD38 ($P < 0.05$, 30 min; $P < 0.01$, 4 h; $P < 0.001$, 8 and 12 h) and for AHI-9 ($P < 0.001$ for 4, 8 and 12 h). (C) The effects of 0.7 μM CD38 or AHI-9 on the total cellular ATP content. Oligomycin (2 μg/mL) was used as positive control and was significantly different from untreated controls at all time points ($P < 0.01$) whereas the bisphosphonium compounds only induced significantly reduced ATP levels at 60 min ($P < 0.01$). All data are the average and SEM of 3–4 independent experiments. (D) Assessment of intracellular calcium levels using the Fluo-8 indicator dye. Data are presented as percentage of the fluorescence level at time = 0 h for the untreated control cells. Fluorescence was significantly increased after treatment with 0.7 μM CD38 ($P < 0.05$, 8 h; $P < 0.01$, 12 h) or AHI-9 (($P < 0.05$, 8 and 12 h). Average and SEM of three independent experiments.

tetracycline was washed out from the media (Fig. 5E, -tet samples) which led to the reappearance of the upper band within 48 h. In BF SDH1 RNAi cells, a single distinct band of the expected size was observed in non-induced cells (N), but this band was undetectable after just 24 h of RNAi induction (Fig. 5F). Furthermore, the specific SQR activity of SDH complex in PF RNAi SDH1 cell line was decreased by 62% after 1 day of RNAi induction, and almost completely absent by day 3 (Table 3).

The mitochondrial membrane potential in BF cells is maintained exclusively by the hydrolytic activity of the F_oF_1 ATPase complex (Schnaufer et al., 2005; Subrtova et al., 2015), while in PF cells the proton motive force is generated by the respiratory chain complexes (Gnipova et al., 2012; Horvath et al., 2005). In order to determine whether the depletion of SDH complex has any effect on the mitochondrial membrane potential in PF cells, the electrochemical gradient was measured using a flow cytometry analysis with the dye TMRE that accumulates only in charged mitochondria. The membrane potential remained unchanged after even 5 days of RNAi induction (Fig. 5G) indicating that the SDH complex does not significantly contribute to Ψm in PF *T. brucei* cells.

3.4. The effects of bisphosphonium compounds on mitochondrial ATPases

The reductions in Ψm and cellular ATP levels are the early effects seen after the treatment of *T. brucei* with bisphosphonium compounds (see above). However, we here show that, in *T. brucei*, the SDH complex is not essential and does not contribute to the membrane potential. It seems therefore unlikely that the principal trypanocidal activity of bisphosphonium salts would be on this complex and we thus explored other potential mitochondrial targets - in particular, the F_oF_1 ATPase complex that maintains Ψm in BF cells.

First, in vitro ATPase assays were performed using a purified mitochondrial fraction, which was lysed by digitonin. The prepared lysed mitochondrion-enriched fractions from PF cells were treated with various concentrations of CD38 (Fig. 6A) or AHI-9 (Fig. 6B). Since there are many ATPases in these samples, the fractions were also treated with the F_1-ATPase inhibitor azide. Typically, 1 mM azide inhibits 30–40% of all measured ATP hydrolysis activity in such samples (Zikova et al., 2009). Increasing concentrations of either drug elicited a similar (CD38) or identical (AHI-9) level of inhibition as the azide control, albeit at much higher concentrations than their measured EC_{50} values. These inflated concentrations might be an artifact of the in vitro assay performed on lysed instead of intact and charged mitochondria, as the latter would be able to concentrate the drugs, driven by Ψm. Importantly, the same level of inhibition was observed when the crude mitochondria were treated with azide together with a bisphosphonium salt, indicating that the inhibitions were not additive and both inhibitors were therefore acting on the same target. Furthermore, the enzymatic activity was more strongly affected by AHI-9, which typically has a stronger effect on trypanosome cells than CD38.

To further evaluate the mechanism of action of bisphosphonium salts, we determined whether these compounds also affect the rate of ATP synthesis by F_oF_1-ATP synthase. This experimental set-up

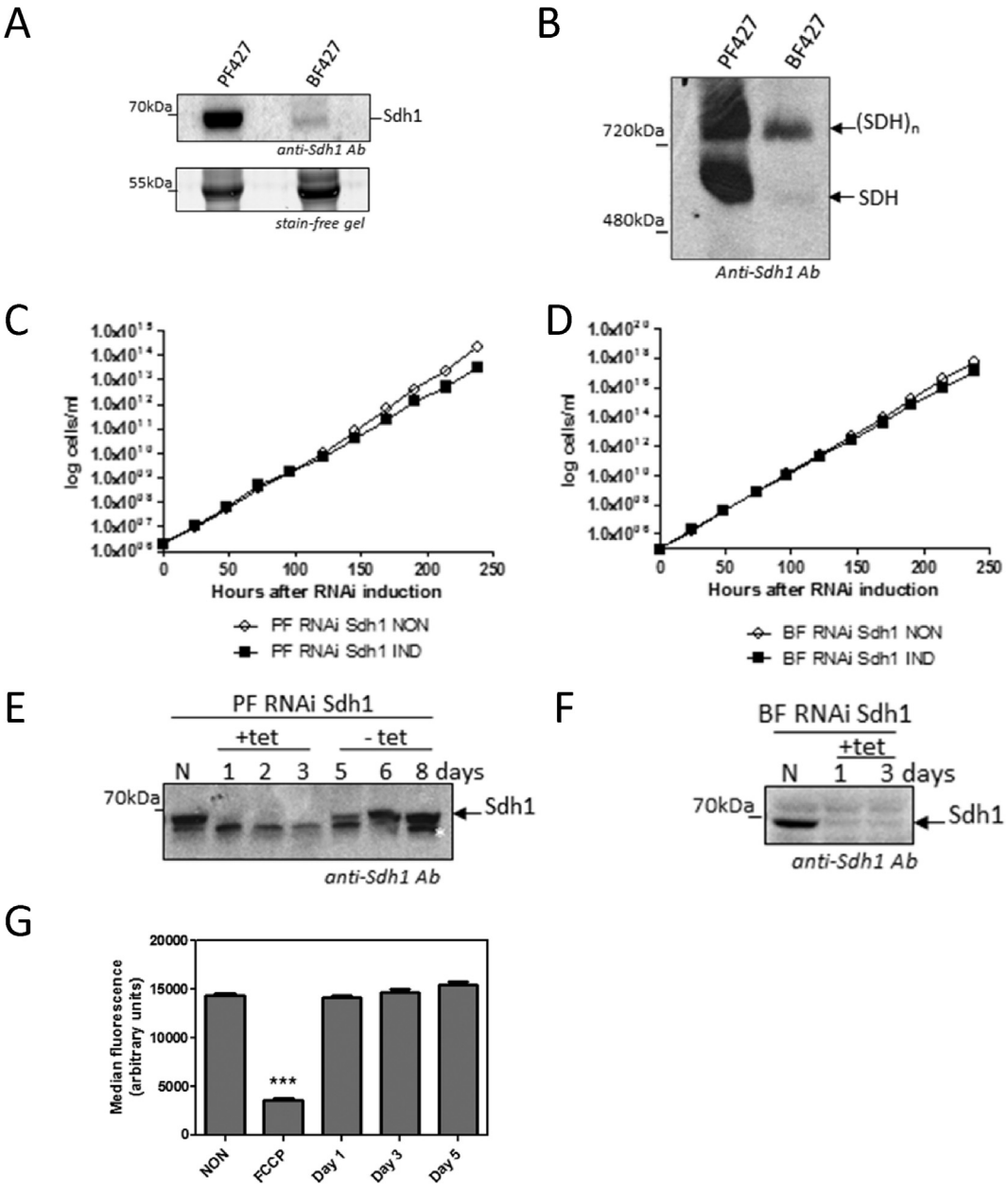

Fig. 5. Abundance and essentiality of SDH complex in PF and BF cells. A. Steady state abundance of SDH1 subunit in PF and BF cells. Mitochondria were isolated from equal numbers of cells from *T. brucei* PF and BF. For each sample 50 μg of protein was loaded onto a BioRad TGX stain-free precast gel. After transfer to a PVDF membrane, the blot was probed with a rabbit antibody raised against a peptide of *T. brucei* SDH1. The 50 kDa unknown protein visualized using UV light served as a loading control. B. Relative levels of assembled SDH complex in PF and BF cells. For each sample 50 μg of mitochondrial protein was loaded onto a high resolution clear native (hrCN) PAGE, which was blotted and probed with the anti-SDH1 peptide antibody. C. Growth curve of the PF SDH1 RNAi cell line. PF 29.13 cells were transfected with a linearized p2T7-177 vector containing a 485bp fragment of the SDH1 cds. The resulting clonal transfectants were then analysed for a growth phenotype when RNAi was induced with 1 μg/mL tetracycline. These growth curves are representative of several clones. NON, non-induced cells; IND, induced cells. D. Growth curve of BF SDH1 RNAi. BF *T. brucei* SM cells were transfected with the same p2T7-177 plasmid and the growth curve analysis was performed as in C. E. Western blot analysis of PF SDH1 RNAi cells. Whole cell lysates made from equal amounts of cells after the indicated of tetracycline induction, and loaded onto a 12% SDS PAGE gel. After transfer, the PVDF membrane was probed with the anti-SDH1 antibody. To confirm that the upper of the two bands was specific for SDH1, the tetracycline was washed out (-tet) and the reappearance of the upper band was observed within 48 h (-tet, day 5). F. Western blot analysis of BF SDH1 RNAi cells. Mitochondrial lysate from noninduced (N) cells and cells induced by tetracycline (+tet) for 1 and 3 days were analysed. G. Mitochondrial membrane potential in PF *T. brucei* expressing RNAi against SDH1. Units indicated are arbitrary units of TMRE-associated fluorescence. NON, non-induced RNAi cells; Day 1, Day 3, Day 5, signifies the time in days after RNAi induction. The protonophore FCCP was included as a positive control to indicate the level of fluorescence in cells with depolarised mitochondrial membranes; fluorescence in FCCP-treated cells was highly significantly different from all other test groups. ***, $P < 0.001$, unpaired Student's t-test, $n = 5$.

relies on a complete and functional oxidative phosphorylation pathway and is performed with intact, charged mitochondria isolated from PF cells (Allemann and Schneider, 2000). Malonate and atractyloside are used as positive controls, as the former inhibits the succinate dehydrogenase complex (i.e. the entry of the electrons), and the latter inhibits the ATP/ADP carrier (i.e. the supplier of the substrate). Not surprisingly, the results indicated that both CD38 and AHI-9 dose-dependently inhibited ATP production in intact *T. brucei* mitochondria, with concentrations similar to the measured EC_{50} values moderately inhibitory and higher concentrations inhibiting ATP production almost completely (Fig. 7). While this assay does not rule out succinate dehydrogenase as a

Table 2
SQR activity in intact PF427 and BF427 *Trypanosoma brucei*.

Cells	SDH specific activity (U[a]/mg) ± SEM[b]	% of PF activity	% of effect of malonate
PF 427	1.2 ± 0.011	100	100
PF 427 + mal	0.21 ± 0.006		17
BF 427	0.084 ± 0.007	7	100
BF 427 + mal	0.0381 ± 0.002		45

SQR activity in PF and BF *T. brucei* cells was measured spectrophotometrically as described in the methods section, in the presence or absence of 1 mM malonate (mal).
[a] The unit (U) of SQR is defined as the amount of enzyme required for the conversion of 1 nmol of 2,6-dichlorophenolindophenol/min/mg of mitochondrial proteins.
[b] Each measurement was performed in triplicate.

Table 3
SQR activity in PF RNAi SDH1 noninduced (N) and tetracycline induced (+tet) cells in the presence of absence of malonate (mal).

Cells	SDH specific activity (U[a]/mg) ± SEM[b]	% of 29–13 activity	% of RNAi N activity
PF 29-13	0.658 ± 0.021	100	
PF 29-13 + mal	0.156 ± 0.004	24	
PF RNAi Sdh1 N	0.497 ± 0.005		100
PF RNAi Sdh1 N/+mal	0.107 ± 0.008		22
PF RNAi Sdh1 1d +tet	0.19 ± 0.0046		38
PF RNAi Sdh1 3d +tet	0.08 ± 0.005		16

[a] The unit (U) of SQR is defined as an amount of enzyme required for conversion of 1 nmol of 2,6-dichlorophenolindophenol/min/mg of mitochondrial proteins.
[b] Each measurement was performed in triplicate.

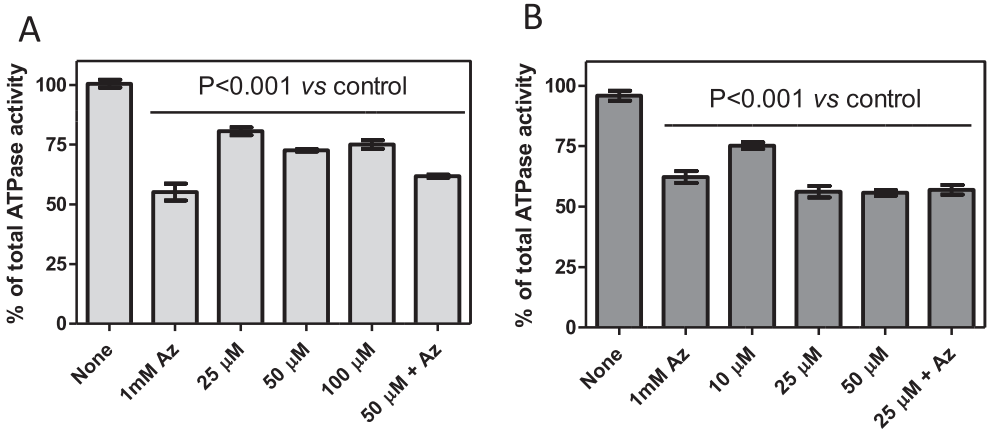

Fig. 6. ATPase activity of mitochondrion-enriched fractions of PF427 treated with CD38 (A) and AHI-9 (B). Approximately 15 μg of hypotonically isolated mitochondria were incubated with the indicated test compounds for 5 min and then transferred to ATPase assay buffer. Changes in NADH absorbance were monitored at 340 nm for 5 min. Specific ATPase activity from mitochondrial lysates was calculated from the amount of oxidized NADH per minute, and related to the amount of total protein. The specific ATPase activity in the non-induced sample was set at 100%. Assays were performed in triplicate. Error bars depict standard errors of the mean. Statistical significance was determined using Student's unpaired T-test.

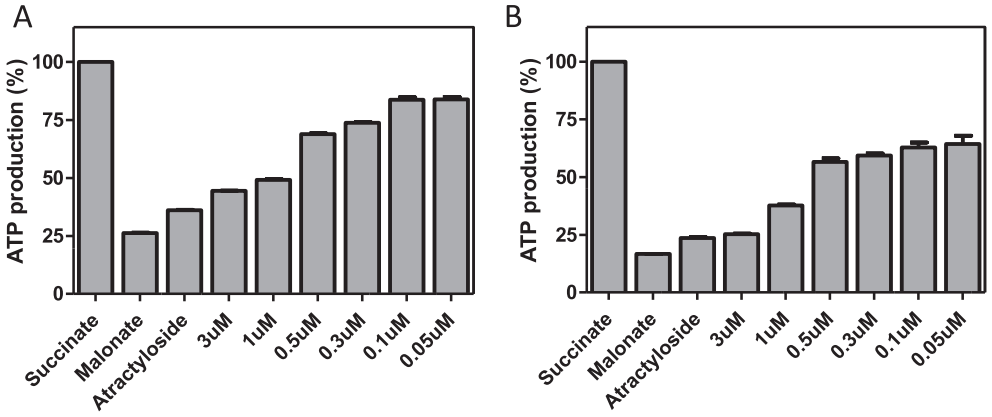

Fig. 7. Effect of CD38 (A) and AHI-9 (B) treatment on ATP production in PF mitochondria. Crude mitochondrial preparations were obtained by digitonin extraction and ATP production in untreated and treated samples was measured using succinate as a substrate. Malonate, specific inhibitor of succinate dehydrogenase was used to inhibit ATP production by oxidative phosphorylation and atractyloside was used to inhibit import of ADP into mitochondria. ATP production in untreated mitochondria was set to 100%. The bars represent means expressed as percentages from three independent RNAi inductions. Error bars are SEM.

potential target, the dose-dependency shows unambiguously that an active mitochondrial Ψm is important to these in vitro assays, as the test compounds were much more active than on mitochondrial lysates.

Since the effects on total mitochondrial ATP hydrolytic and ATP synthetic activities were indicative of specific inhibition of the F_oF_1 ATP synthase/ATPase, we repeated the assay on highly purified F_1-ATPase, and observed a similar dose dependency of inhibition as above on the lysed mitochondrial fractions, i.e. less potent than in intact and charged mitochondria. In this experiment, azide inhibits almost 100% of the activity of the purified F_1-ATPase, confirming the purity of the sample. The increasing concentrations of the bisphosphonium test compounds reduced the ATP hydrolysis activity in a linear manner. Once again, AHI-9 displayed a significantly higher level of inhibition than CD38. In fact, 200 μM AHI-9 inactivated F_1-ATPase almost to the same extent as azide (Fig. 8). We conclude that inhibition of the F_1-ATPase is at a minimum an important contributing factor in the mechanism of action of bisphosphonium compounds on *T. brucei*.

4. Discussion

The phosphonium salts were discovered as potent chemotherapeutics against *Trypanosoma cruzi* and *T. b. rhodesiense* in the late 1970s (Kinnamon et al., 1977, 1979). Thirty years later benzophenone-derived bisphosphonium salts were synthesized showing much higher potency against *Leishmania* parasites. Some of these phosphonium derivatives act as lipophilic cations with enhanced hydrophobicity that allow them to cross biological membranes and accumulate in organelles with a strong electrochemical gradient, e.g. mitochondria. Interestingly, in mammalian cells, these lipophilic phosphonium ions are being developed to deliver antioxidants or anti-cancer drugs to mitochondria as they pass easily through the lipid bilayers. Because of their disperse charged the electrochemical gradient drives their accumulation into the mitochondrial matrix concentrating them as high as 100–500 fold (Murphy, 2008).

The nature of the trypanocidal activity of these compounds has not been determined yet, but in *L. donovani* some bisphosphonium compounds including CD38 were shown to have a negative impact on proper mitochondrial function (Luque-Ortega et al., 2010). Upon treatment with a low drug concentration (0.7 μM) the mitochondria were swollen, the mitochondrial Ψm was significantly decreased, the oxygen consumption rate, using succinate as a substrate, was affected, and the cellular ATP levels were reduced. These results would suggest that the drug was either affecting a component of the oxidative phosphorylation pathway, or was acting as a kind of ionophore or charge carrier, depolarizing the mitochondrial membrane. The study proposed that in *L. donovani* the bisphosphonium compounds act through inhibition of the respiratory complex II, succinate dehydrogenase (Luque-Ortega et al., 2010).

While the available data certainly suggest that CD38 might be able to inhibit succinate dehydrogenase in *Leishmania*, it seems unlikely that this would be the mode of action for bisphosphonium drugs in *T. brucei*. Since metabolic activities of BF mitochondria are largely repressed with the exception of lipid metabolism (Guler et al., 2008), ion homeostasis (Nolan and Voorheis, 1992), calcium signalling (Huang et al., 2013; Vercesi et al., 1992), FeS cluster assembly (Kovarova et al., 2014) and acetate production for de novo lipid biosynthesis (Mazet et al., 2013), it is generally assumed that succinate dehydrogenase complex is largely inactive and unimportant for these cells. Therefore, we decided to investigate how bisphosphonium salts interact with the unique metabolism of BF trypanosomes.

We found that adding CD38 and AHI-9, at concentrations close to their trypanocidal EC_{50} values, into the *T. brucei* culture prevents the initiation and replication of kDNA, reduces cellular ATP levels, and depolarizes the mitochondrial membrane potential within a few hours of treatment; this was immediately followed by increased cytosolic Ca^{2+} levels. All these phenotypic changes point also to a mitochondrial target, although not necessarily to succinate dehydrogenase. Succinate dehydrogenase does not directly contribute to the membrane potential by pumping protons, as it passes its electrons to ubiquinone. Moreover, we show that in BF it is not essential, as RNAi knockdown presented no growth phenotype, and indeed succinate dehydrogenase is barely present as an assembled complex in this life-cycle stage. Furthermore, the succinate dehydrogenase complex is also not essential for PF *T. brucei* grown under high glucose conditions (this work and (Coustou et al., 2008)) and does not contribute to the mitochondrial membrane potential – yet, both of the tested drugs have a strong effect against PF cells (EC_{50} values in single digit μM range) and decreased the mitochondrial Ψm. We thus conclude that, in trypanosomes, inhibition of succinate dehydrogenase is not mode of action of the bisphosphonium compounds.

Interestingly, the potent trypanocidal diamidine DB75 induces a similar phenotype in BF cells, as its treatment collapses the mitochondrial Ψm and inhibits glucose-dependent cellular respiration, apparently through inhibition of the hydrolytic function of F_oF_1 ATPase (Lanteri et al., 2008), which, in BF cells, employs its reverse function in order to maintain the mitochondrial Ψm (Schnaufer

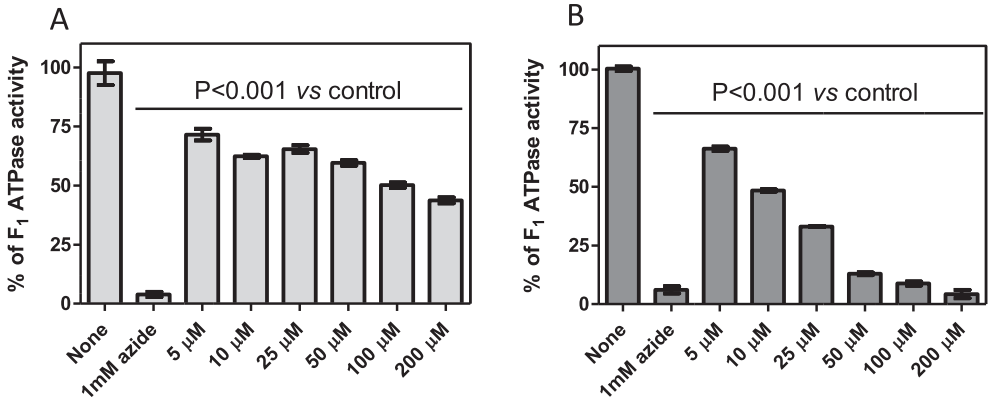

Fig. 8. Activity of *T. brucei* purified F_1-ATPase treated with CD38 (A) and AHI-9 (B). ATPase activity was measured as described in the legend to Fig. 6, in triplicate. Error bars depict standard errors of mean.

et al., 2005; Subrtova et al., 2015). These actions of DB75 certainly overlap with those of the specific F_oF_1 ATPase inhibitor oligomycin, which decreases mitochondrial membrane potential, inhibits oxygen consumption and reduces cellular ATP levels by 50% (Nolan and Voorheis, 1992). We observed similarly reduced cellular ATP levels upon treatment with the bisphosphonium compounds CD38 and AHI-9. The observed reduction in ATP is consistent with inhibition of the F_oF_1 complex, which is followed by immediate mitochondrial membrane depolarization, as in BF cells respiration through alternative oxidase is sensitive to Ψm dissipation (Miller and Klein, 1980). The membrane depolarization in turn results in the loss of the glycerol-3-phosphate shuttle and the subsequent redirection of glycolysis to 1 molecule of glycerol and 1 molecular of pyruvate. Thus, pyruvate production falls by 50% upon oligomycin treatment (Nolan and Voorheis, 1992) and only 1 molecule of ATP is made from 1 molecule of glucose. Similarly, we report an approximately 50% reduction in cellular ATP concentration upon treatment with bisphosphonium drugs.

Moreover, our data strongly suggest that bisphosphonium salts CD38 and AHI-9 inhibit the hydrolytic activity of the F_oF_1 ATPase in vitro. Inhibition assays, performed on mitochondrial lysates from PF cells and on highly purified F_1-ATPase, showed highly significant inhibition of ATPase activity to similar levels as achieved with 1 mM azide. AHI-9, particularly, inhibited the isolated F_1 ATPase almost completely. Furthermore, a combination of azide plus CD38 or AHI-9 did not result in additional inhibition of ATPase activity compared to either drug separately, suggesting that no other mitochondrial ATPases play a significant role in the observed phenotype.

Interestingly, all the biochemical analyses performed revealed a greater sensitivity to AHI-9 than to CD38, which correlates nicely with the almost 4-fold lower EC_{50} value for the former compound. It should be noted that the in vitro assay, which measured ATPase activity in lysates, required concentration of the compounds that are considerably higher than the EC_{50} values, as the lipophilic cations greatly concentrate in the mitochondrion (Murphy, 2008), because Ψm creates a negative charge in the matrix. This assumption is completely consistent with our results from the ATP production assay, which utilizes intact and charged mitochondria from PF cells. In this assay, ATP production was inhibited by the bisphosphonium compounds at the concentration similar to EC_{50} values.

The reduction in cellular ATP levels may be the immediate cause of the observed failure in initiating the S-phase of the cell cycle (DNA synthesis). Trypanosomatid kDNA is a highly organized structure composed of thousands of minicircles and tens of maxicircles (Liu et al., 2005). To ensure that daughter cells receive completely identical kDNA networks, the replication process is highly synchronized with nuclear replication followed by cell division (Jensen and Englund, 2012). kDNA replication relies on ATP and hundreds of mitochondrial proteins (Beck et al., 2013), which are imported to mitochondria via the Ψm-dependent TIM machinery (Williams et al., 2008). Thus it is plausible to speculate that a lack of ATP and decrease of Ψm will interfere with proper initiation of kDNA replication and result in cell cycle arrest. Similar results were observed upon RNAi knock-down of the ATP/ADP carrier in PF *T. brucei* cells, in which reduced ATP levels led to failure of the overall cell division machinery (Gnipova et al., 2015). In contrast, a direct inhibition by bisphosphonium salts of kDNA replication, segregation and maintenance as their primary mode of action is far less likely, as (i) these compounds have a poor affinity to DNA as shown previously (Dardonville et al., 2006) and in this study, (ii) CD38 and AHI-9 cause a decrease in Ψm in *T. brucei* cells that lack mitochondrial DNA (Gould, Schnaufer and De Koning, unpublished), and (iii) interference with kDNA replication, either by RNAi or drug treatment, usually leads to complete loss of kDNA (Bruhn et al., 2011; Hiltensperger et al., 2012; Tyc et al., 2015).

In conclusion, our data strongly suggest that bisphosphonium compounds CD38 and AHI-9 primarily act on trypanosomes through inhibition of the F_1-ATPase although additional mitochondrial targets cannot be excluded.

Acknowledgements

The assistance of Dr Laura Lagartera with the SPR experiments (DNA binding) is gratefully acknowledged.

This work was funded by the Czech Republic Ministry of Education ERC CZ grant LL1205, and EMBO Installation grant 1965 (both to AZ); AAMA was funded by a studentship from the Government of Saudi Arabia (Ref. JFU008).

Appendix A. Supplementary data

Supplementary data related to this article can be found at http://dx.doi.org/10.1016/j.ijpddr.2015.12.002.

Authorship contributions

Participated in research design: Panicucci, Dardonville, Zíková, De Koning.

Conducted experiments: Alkhaldi, Martinek, Panicucci, Dardonville.

Contributed new reagents or analytic tools: Dardonville.

Performed data analysis: Alkhaldi, Martinek, Panicucci, Zíková, De Koning.

Wrote or contributed to the writing of the manuscript: Zíková, De Koning.

References

Acestor, N., Zikova, A., Dalley, R.A., Anupama, A., Panigrahi, A.K., Stuart, K.D., 2011. *Trypanosoma brucei* mitochondrial respiratome: composition and organization in procyclic form. Mol. Cell Proteom. 10. M110 006908.

Allemann, N., Schneider, A., 2000. ATP production in isolated mitochondria of procyclic *Trypanosoma brucei*. Mol. Biochem. Parasitol. 111, 87–94.

Beck, K., Acestor, N., Schulfer, A., Anupama, A., Carnes, J., Panigrahi, A.K., Stuart, K., 2013. *Trypanosoma brucei* Tb927.2.6100 is an essential protein associated with kinetoplast DNA. Eukaryot. Cell 12, 970–978.

Benein, P., Almuteri, M.A., Mehanna, A.S., D'Souza, G.G., 2015. Synthesis of triphenylphosphonium phospholipid conjugates for the preparation of mitochondriotropic liposomes. Methods Mol. Biol. 1265, 51–57.

Birch-Machin, M.A., Turnbull, D.M., 2001. Assaying mitochondrial respiratory complex activity in mitochondria isolated from human cells and tissues. Methods Cell Biol. 65, 97–117.

Bowler, M.W., Montgomery, M.G., Leslie, A.G., Walker, J.E., 2006. How azide inhibits ATP hydrolysis by the F-ATPases. Proc. Natl. Acad. Sci. U. S. A. 103, 8646–8649.

Bruhn, D.F., Sammartino, M.P., Klingbeil, M.M., 2011. Three mitochondrial DNA polymerases are essential for kinetoplast DNA replication and survival of bloodstream form *Trypanosoma brucei*. Eukaryot. Cell 10, 734–743.

Brun, R., Blum, J., Chappuis, F., Burri, C., 2010. Human African trypanosomiasis. Lancet 375, 148–159.

Cairns, A.G., McQuaker, S.J., Murphy, M.P., Hartley, R.C., 2015. Targeting mitochondria with small molecules: the preparation of MitoB and MitoP as exomarkers of mitochondrial hydrogen peroxide. Methods Mol. Biol. 1265, 25–50.

Chaudhuri, M., Ajayi, W., Hill, G.C., 1998. Biochemical and molecular properties of the *Trypanosoma brucei* alternative oxidase. Mol. Biochem. Parasitol. 95, 53–68.

Cortes, L.A., Castro, L., Pesce, B., Maya, J.D., Ferreira, J., Castro-Castillo, V., Parra, E., Jara, J.A., Lopez-Munoz, R., 2015. Novel gallate triphenylphosphonium derivatives with potent antichagasic activity. PLoS One 10, e0136852.

Coustou, V., Biran, M., Breton, M., Guegan, F., Riviere, L., Plazolles, N., Nolan, D., Barrett, M.P., Franconi, J.M., Bringaud, F., 2008. Glucose-induced remodeling of intermediary and energy metabolism in procyclic *Trypanosoma brucei*. J. Biol. Chem. 283, 16342–16354.

Dardonville, C., Alkhaldi, A.A., De Koning, H.P., 2015. SAR studies of diphenyl cationic trypanocides: superior activity of phosphonium over ammonium salts. ACS Med. Chem. Lett. 6, 151–155.

Dardonville, C., Barrett, M.P., Brun, R., Kaiser, M., Tanious, F., Wilson, W.D., 2006. DNA binding affinity of bisguanidine and bis(2-aminoimidazoline) derivatives with in vivo antitrypanosomal activity. J. Med. Chem. 49, 3748–3752.

Delespaux, V., de Koning, H.P., 2007. Drugs and drug resistance in African

trypanosomiasis. Drug Resist. Updates 10, 30–50.
Denninger, V., Figarella, K., Schonfeld, C., Brems, S., Busold, C., Lang, F., Hoheisel, J., Duszenko, M., 2007. Troglitazone induces differentiation in *Trypanosoma brucei*. Exp. Cell Res. 313, 1805–1819.
Desquesnes, M., Dargantes, A., Lai, D.H., Lun, Z.R., Holzmuller, P., Jittapalapong, S., 2013. *Trypanosoma evansi* and surra: a review and perspectives on transmission, epidemiology and control, impact, and zoonotic aspects. Biomed. Res. Int. 321237.
Figarella, K., Uzcategui, N.L., Beck, A., Schoenfeld, C., Kubata, B.K., Lang, F., Duszenko, M., 2006. Prostaglandin-induced programmed cell death in *Trypanosoma brucei* involves oxidative stress. Cell Death Differ. 13, 1802–1814.
Gnipova, A., Panicucci, B., Paris, Z., Verner, Z., Horvath, A., Lukes, J., Zikova, A., 2012. Disparate phenotypic effects from the knockdown of various *Trypanosoma brucei* cytochrome c oxidase subunits. Mol. Biochem. Parasitol. 184, 90–98.
Gnipova, A., Subrtova, K., Panicucci, B., Horvath, A., Lukes, J., Zikova, A., 2015. The ADP/ATP carrier and its relationship to OXPHOS in an ancestral protist *Trypanosoma brucei*. Eukaryot. Cell 14, 297–310.
Gould, M.K., Bachmaier, S., Ali, J.A., Alsford, S., Tagoe, D.N., Munday, J.C., Schnaufer, A.C., Horn, D., Boshart, M., de Koning, H.P., 2013. Cyclic AMP effectors in African trypanosomes revealed by genome-scale RNA interference library screening for resistance to the phosphodiesterase inhibitor CpdA. Antimicrob. Agents Chemother. 57, 4882–4893.
Gould, M.K., Vu, X.L., Seebeck, T., de Koning, H.P., 2008. Propidium iodide-based methods for monitoring drug action in the kinetoplastidae: comparison with the Alamar Blue assay. Anal. Biochem. 382, 87–93.
Guler, J.L., Kriegova, E., Smith, T.K., Lukes, J., Englund, P.T., 2008. Mitochondrial fatty acid synthesis is required for normal mitochondrial morphology and function in *Trypanosoma brucei*. Mol. Microbiol. 67, 1125–1142.
Hammarton, T.C., Mottram, J.C., Doerig, C., 2003. The cell cycle of parasitic protozoa: potential for chemotherapeutic exploitation. Prog. Cell Cycle Res. 5, 91–101.
Hanson, W.L., Chapman Jr., W.L., Kinnamon, K.E., 1977. Testing of drugs for anti-leishmanial activity in golden hamsters infected with *Leishmania donovani*. Int. J. Parasitol. 7, 443–447.
Hiltensperger, G., Jones, N.G., Niedermeier, S., Stich, A., Kaiser, M., Jung, J., Puhl, S., Damme, A., Braunschweig, H., Meinel, L., Engstler, M., Holzgrabe, U., 2012. Synthesis and structure-activity relationships of new quinolone-type molecules against *Trypanosoma brucei*. J. Med. Chem. 55, 2538–2548.
Horvath, A., Horakova, E., Dunajcikova, P., Verner, Z., Pravdova, E., Slapetova, I., Cuninkova, L., Lukes, J., 2005. Downregulation of the nuclear-encoded subunits of the complexes III and IV disrupts their respective complexes but not complex I in procyclic *Trypanosoma brucei*. Mol. Microbiol. 58, 116–130.
Huang, G., Vercesi, A.E., Docampo, R., 2013. Essential regulation of cell bioenergetics in *Trypanosoma brucei* by the mitochondrial calcium uniporter. Nat. Commun. 4, 2865.
Ibrahim, H.M., Al-Salabi, M.I., El Sabbagh, N., Quashie, N.B., Alkhaldi, A.A., Escale, R., Smith, T.K., Vial, H.J., de Koning, H.P., 2011. Symmetrical choline-derived dications display strong anti-kinetoplastid activity. J. Antimicrob. Chemother. 66, 111–125.
Jannin, J., Cattand, P., 2004. Treatment and control of human African trypanosomiasis. Curr. Opin. Infect. Dis. 17, 565–571.
Jara, J.A., Castro-Castillo, V., Saavedra-Olavarria, J., Peredo, L., Pavanni, M., Jana, F., Letelier, M.E., Parra, E., Becker, M.I., Morello, A., Kemmerling, U., Maya, J.D., Ferreira, J., 2014. Antiproliferative and uncoupling effects of delocalized, lipophilic, cationic gallic acid derivatives on cancer cell lines. Validation in vivo in singenic mice. J. Med. Chem. 57, 2440–2454.
Jensen, R.E., Englund, P.T., 2012. Network news: the replication of kinetoplast DNA. Annu. Rev. Microbiol. 66, 473–491.
Kelso, G.F., Porteous, C.M., Coulter, C.V., Hughes, G., Porteous, W.K., Ledgerwood, E.C., Smith, R.A., Murphy, M.P., 2001. Selective targeting of a redox-active ubiquinone to mitochondria within cells: antioxidant and antiapoptotic properties. J. Biol. Chem. 276, 4588–4596.
Kinnamon, K.E., Steck, E.A., Hanson, W.L., Chapman Jr., W.L., 1977. In search of anti-*Trypanosoma cruzi* drugs: new leads from a mouse model. J. Med. Chem. 20, 741–744.
Kinnamon, K.E., Steck, E.A., Rane, D.S., 1979. A new chemical series active against African trypanosomes: benzyltriphenylphosphonium salts. J. Med. Chem. 22, 452–455.
Koreny, L., Sobotka, R., Kovarova, J., Gnipova, A., Flegontov, P., Horvath, A., Obornik, M., Ayala, F.J., Lukes, J., 2012. Aerobic kinetoplastid flagellate Phytomonas does not require heme for viability. Proc. Natl. Acad. Sci. U. S. A. 109, 3808–3813.
Kovarova, J., Horakova, E., Changmai, P., Vancova, M., Lukes, J., 2014. Mitochondrial and nucleolar localization of cysteine desulfurase Nfs and the scaffold protein Isu in *Trypanosoma brucei*. Eukaryot. Cell 13, 353–362.
Kovarova, N., Mracek, T., Nuskova, H., Holzerova, E., Vrbacky, M., Pecina, P., Hejzlarova, K., Kluckova, K., Rohlena, J., Neuzil, J., Houstek, J., 2013. High molecular weight forms of mammalian respiratory chain complex II. PLoS One 8, e71869.
La Greca, F., Magez, S., 2011. Vaccination against trypanosomiasis: can it be done or is the trypanosome truly the ultimate immune destroyer and escape artist? Hum. Vaccines 7, 1225–1233.
Lanteri, C.A., Tidwell, R.R., Meshnick, S.R., 2008. The mitochondrion is a site of trypanocidal action of the aromatic diamidine DB75 in bloodstream forms of *Trypanosoma brucei*. Antimicrob. Agents Chemother. 52, 875–882.
Liu, B., Liu, Y., Motyka, S.A., Agbo, E.E., Englund, P.T., 2005. Fellowship of the rings: the replication of kinetoplast DNA. Trends Parasitol. 21, 363–369.
Luque-Ortega, J.R., Reuther, P., Rivas, L., Dardonville, C., 2010. New benzophenone-derived bisphosphonium salts as leishmanicidal leads targeting mitochondria through inhibition of respiratory complex II. J. Med. Chem. 53, 1788–1798.
Mazet, M., Morand, P., Biran, M., Bouyssou, G., Courtois, P., Daulouede, S., Millerioux, Y., Franconi, J.M., Vincendeau, P., Moreau, P., Bringaud, F., 2013. Revisiting the central metabolism of the bloodstream forms of *Trypanosoma brucei*: production of acetate in the mitochondrion is essential for parasite viability. PLoS Negl. Trop. Dis. 7, e2587.
Miller, P.G., Klein, R.A., 1980. Effects of oligomycin on glucose utilization and calcium transport in African trypanosomes. J. General Microbiol. 116, 391–396.
Murphy, M.P., 2008. Targeting lipophilic cations to mitochondria. Biochim. Biophys. Acta 1777, 1028–1031.
Nolan, D.P., Voorheis, H.P., 1992. The mitochondrion in bloodstream forms of *Trypanosoma brucei* is energized by the electrogenic pumping of protons catalysed by the F1F0-ATPase. Eur. J. Biochem. 209, 207–216.
Osório, A.L., Madruga, C.R., Desquesnes, M., Soares, C.O., Ribeiro, L.R., Costa, S.C., 2008. *Trypanosoma (Duttonella) vivax*: its biology, epidemiology, pathogenesis, and introduction in the New World – a review. Mem. Inst. Oswaldo Cruz 103, 1–13.
Pullman, M.E., Penefsky, H.S., Datta, A., Racker, E., 1960. Partial resolution of the enzymes catalyzing oxidative phosphorylation. I. Purification and properties of soluble dinitrophenol-stimulated adenosine triphosphatase. J. Biol. Chem. 235, 3322–3329.
Rios Martinez, C.H., Lagartera, L., Kaiser, M., Dardonville, C., 2014. Antiprotozoal activity and DNA binding of N-substituted N-phenylbenzamide and 1,3-diphenylurea bisguanidines. Eur. J. Med. Chem. 81, 481–491.
Schnaufer, A., Clark-Walker, G.D., Steinberg, A.G., Stuart, K., 2005. The F1-ATP synthase complex in bloodstream stage trypanosomes has an unusual and essential function. EMBO J. 24, 4029–4040.
Smith, R.A., Hartley, R.C., Murphy, M.P., 2011. Mitochondria-targeted small molecule therapeutics and probes. Antioxid. Redox Signal 15, 3021–3038.
Snow, B.J., Rolfe, F.L., Lockhart, M.M., Frampton, C.M., O'Sullivan, J.D., Fung, V., Smith, R.A., Murphy, M.P., Taylor, K.M., Protect Study, G., 2010. A double-blind, placebo-controlled study to assess the mitochondria-targeted antioxidant MitoQ as a disease-modifying therapy in Parkinson's disease. Mov. Disord. 25, 1670–1674.
Spivak, A.Y., Keiser, J., Vargas, M., Gubaidullin, R.R., Nedopekina, D.A., Shakurova, E.R., Khalitova, R.R., Odinokov, V.N., 2014. Synthesis and activity of new triphenylphosphonium derivatives of betulin and betulinic acid against Schistosoma mansoni in vitro and in vivo. Bioorg. Med. Chem. 22, 6297–6304.
Subrtova, K., Panicucci, B., Zikova, A., 2015. ATPaseTb2, a unique membrane-bound FoF1-ATPase component, is essential in bloodstream and dyskinetoplastic trypanosomes. PLoS Pathog. 11, e1004660.
Swallow, B.M., 1999. Impacts of Trypanosomiasis on African Agriculture. Food and Agriculture Organization of the United Nations, Rome.
Taladriz, A., Healy, A., Flores Perez, E.J., Herrero Garcia, V., Rios Martinez, C., Alkhaldi, A.A., Eze, A.A., Kaiser, M., de Koning, H.P., Chana, A., Dardonville, C., 2012. Synthesis and structure-activity analysis of new phosphonium salts with potent activity against African trypanosomes. J. Med. Chem. 55, 2606–2622.
Tan, T.H., Bochud-Allemann, N., Horn, E.K., Schneider, A., 2002. Eukaryotic-type elongator tRNAMet of *Trypanosoma brucei* becomes formylated after import into mitochondria. Proc. Natl. Acad. Sci. U. S. A. 99, 1152–1157.
Teixeira, J., Soares, P., Benfeito, S., Gaspar, A., Garrido, J., Murphy, M.P., Borges, F., 2012. Rational discovery and development of a mitochondria-targeted antioxidant based on cinnamic acid scaffold. Free Radic. Res. 46, 600–611.
Tielens, A.G., van Hellemond, J.J., 2009. Surprising variety in energy metabolism within Trypanosomatidae. Trends Parasitol. 25, 482–490.
Tyc, J., Klingbeil, M.M., Lukes, J., 2015. Mitochondrial heat shock protein machinery hsp70/hsp40 is indispensable for proper mitochondrial DNA maintenance and replication. mBio 6.
Vercesi, A.E., Docampo, R., Moreno, S.N., 1992. Energization-dependent Ca2+ accumulation in *Trypanosoma brucei* bloodstream and procyclic trypomastigotes mitochondria. Mol. Biochem. Parasitol. 56, 251–257.
Welburn, S.C., Picozzi, K., Fevre, E.M., Coleman, P.G., Odiit, M., Carrington, M., Maudlin, I., 2001. Identification of human-infective trypanosomes in animal reservoir of sleeping sickness in Uganda by means of serum-resistance-associated (SRA) gene. Lancet 358, 2017–2019.
Wickstead, B., Ersfeld, K., Gull, K., 2002. Targeting of a tetracycline-inducible expression system to the transcriptionally silent minichromosomes of *Trypanosoma brucei*. Mol. Biochem. Parasitol. 125, 211–216.
Williams, S., Saha, L., Singha, U.K., Chaudhuri, M., 2008. *Trypanosoma brucei*: differential requirement of membrane potential for import of proteins into mitochondria in two developmental stages. Exp. Parasitol. 118, 420–433.
Wirtz, E., Leal, S., Ochatt, C., Cross, G.A., 1999. A tightly regulated inducible expression system for conditional gene knock-outs and dominant-negative genetics in *Trypanosoma brucei*. Mol. Biochem. Parasitol. 99, 89–101.
Zikova, A., Schnaufer, A., Dalley, R.A., Panigrahi, A.K., Stuart, K.D., 2009. The F(0)F(1)-ATP synthase complex contains novel subunits and is essential for procyclic *Trypanosoma brucei*. PLoS Pathog. 5, e1000436.

PLOS BIOLOGY

METHODS AND RESOURCES

Cell-based and multi-omics profiling reveals dynamic metabolic repurposing of mitochondria to drive developmental progression of *Trypanosoma brucei*

Eva Doleželová[1], Michaela Kunzová[1,2], Mario Dejung[3☯], Michal Levin[3☯], Brian Panicucci[1], Clément Regnault[4], Christian J. Janzen[5], Michael P. Barrett[4], Falk Butter[3], Alena Zíková[1,2]*

1 Institute of Parasitology, Biology Centre, Czech Academy of Sciences, Ceske Budejovice, Czech Republic, **2** Faculty of Science, University of South Bohemia, Ceske Budejovice, Czech Republic, **3** Institute of Molecular Biology (IMB), Mainz, Germany, **4** Welcome Centre for Integrative Parasitology, Institute of Infection, Immunity and Inflammation, Glasgow Polyomics, College of Medical, Veterinary and Life Sciences, University of Glasgow, Glasgow, United Kingdom, **5** Department of Cell and Developmental Biology, Biocenter, University Wuerzburg, Wuerzburg, Germany

☯ These authors contributed equally to this work.
* azikova@paru.cas.cz

Citation: Doleželová E, Kunzová M, Dejung M, Levin M, Panicucci B, Regnault C, et al. (2020) Cell-based and multi-omics profiling reveals dynamic metabolic repurposing of mitochondria to drive developmental progression of *Trypanosoma brucei*. PLoS Biol 18(6): e3000741. https://doi.org/10.1371/journal.pbio.3000741

Academic Editor: André Schneider, Universitat Bern, SWITZERLAND

Received: December 4, 2019

Accepted: May 27, 2020

Published: June 10, 2020

Peer Review History: PLOS recognizes the benefits of transparency in the peer review process; therefore, we enable the publication of all of the content of peer review and author responses alongside final, published articles. The editorial history of this article is available here: https://doi.org/10.1371/journal.pbio.3000741

Data Availability Statement: All relevant data are within the paper and in S1 Data file. Transcriptomic data are available at https://www.ncbi.nlm.nih.gov/

Abstract

Mitochondrial metabolic remodeling is a hallmark of the *Trypanosoma brucei* digenetic life cycle because the insect stage utilizes a cost-effective oxidative phosphorylation (OxPhos) to generate ATP, while bloodstream cells switch to aerobic glycolysis. Due to difficulties in acquiring enough parasites from the tsetse fly vector, the dynamics of the parasite's metabolic rewiring in the vector have remained obscure. Here, we took advantage of in vitro–induced differentiation to follow changes at the RNA, protein, and metabolite levels. This multi-omics and cell-based profiling showed an immediate redirection of electron flow from the cytochrome-mediated pathway to an alternative oxidase (AOX), an increase in proline consumption, elevated activity of complex II, and certain tricarboxylic acid (TCA) cycle enzymes, which led to mitochondrial membrane hyperpolarization and increased reactive oxygen species (ROS) levels. Interestingly, these ROS molecules appear to act as signaling molecules driving developmental progression because ectopic expression of catalase, a ROS scavenger, halted the in vitro–induced differentiation. Our results provide insights into the mechanisms of the parasite's mitochondrial rewiring and reinforce the emerging concept that mitochondria act as signaling organelles through release of ROS to drive cellular differentiation.

Introduction

In most eukaryotic cells, energy metabolism is an interplay between two energy production pathways to generate ATP: an efficient mitochondrial oxidative phosphorylation (OxPhos)

geo/query/acc.cgi?acc=GSE140796. Proteomic data are available at the ProteomeXchange Consortium via the PRIDE, with the dataset identifier PXD016370. Metabolomic data are available at MetaboLights database with identifier MTBLS1390.

Funding: This work was supported by grants from the Grant Agency of the Czech Republic (17-22248S) and by the ERD fund (No. CZ.02.1.01/0.0/0.0/16_019/0000759), both to AZ, as well as by Grant Agency of the University of South Bohemia (GAJU 080/2020/P) to MK. MPB is funded as part of the Wellcome Trust core grant to the Wellcome Trust Centre for Integrative Parasitology (WCIP) - 104111/Z/14/Z. The funders had no role in study design, data collection and analysis, decision to publish, or preparation of the manuscript.

Competing interests: The authors have declared that no competing interests exist.

Abbreviations: AAC, ATP/ADP carrier; ACL, ATP-dependent citrate lyase; AOX, alternative oxidase; BARP, brucei alanine-rich protein; BNE, blue-native electrophoresis; BPS, bathophenanthroline disulphonic acid; BSF, bloodstream form; CS, citrate synthase; DCF, 2′,7′-dichlorofluorescein; DDA, data-dependent acquisition; ETC, electron transport chain; EP, procyclin rich in Glu-Pro repeats; FAD, flavin adenine dinucleotide; FBPase, fructose bisphosphatase; FBS, fetal bovine serum; FCCP, carbonyl cyanide-4-phenylhydrazone; GLM, generalized linear model; GO, Gene Ontology; GPEET, procyclin rich in Gly-Pro-Glu-Glu-Thr repeats; hrCNE, high-resolution clear-native electrophoresis; hsp70, heat shock protein 70; H_2DCFHDA, 2′,7′-dichlorofluorescein diacetate; IDH, isocitrate dehydrogenase; IF1, inhibitory peptide 1; k, kinetoplast; KCN, potassium cyanide; kDNA, kinetoplast DNA; LC-MS, liquid chromatography–mass spectrometry; LFQ, label-free quantification; mAb, monoclonal antibody; MCU, mitochondrial calcium uniporter; mVSG, metacyclic-like variable surface glycoprotein; n, nucleus; NGS, next generation sequencing; OxPhos, oxidative phosphorylation; p, posterior end; pAb, polyclonal antibody; PBS, phosphate-buffered saline; PCA, principal component analysis; PCF, procyclic form; PiC, phosphate carrier; RBP6, RNA binding protein 6; $RBP6^{OE}$, RBP6 overexpressing; RET, reverse electron transfer; ROS, reactive oxygen species; SBPase, sedoheptulose-1,7-bisphosphatase; SCoAS, succinyl Co-A synthetase; SDS, sodium dodecyl sulfate; SHAM, salicylhydroxamic acid; SOD, superoxide dismutase; TCA, tricarboxylic acid; THT, *Trypanosoma brucei* hexose transporter; TMRE, tetramethyl rhodamine ethyl ester.

and an ancient glycolytic pathway. A "textbook-like" aerobic eukaryotic cell relies mainly on cost-effective OxPhos to fulfill cellular requirements for ATP. Exceptions apply to some rapidly proliferating cells, e.g., some cancer cells exploit high rates of fermentative glycolysis, irrespective of oxygen availability [1]. Oncogenic metabolic reprogramming from OxPhos to glycolysis allows the malignant cell to fulfill a great demand for synthesis of nucleotides and amino acids, the building blocks of DNA and proteins, respectively, to promote tumor growth and progression [2]. Metabolic rewiring to aerobic glycolysis also drives the activation of macrophages to a pro-inflammatory phenotype in response to infection. This phenotypic switch involves suppressed OxPhos, disruption of the tricarboxylic acid (TCA) cycle, reactive oxygen species (ROS) production, and accumulation of succinate [3]. The factors that underlie the striking metabolic changes during the aforementioned cellular processes are not fully understood. However, multiple lines of evidence implicate alterations in mitochondrial function that lead to the release of signal molecules to drive cell differentiation. Prominent examples of these signals are ROS and certain metabolic intermediates (e.g., succinate, citrate, and itaconate) with the ability to affect gene expression at the global level via posttranslational mechanisms [4–6]. This demonstrates how mitochondrial plasticity and metabolic remodeling are crucial for cells to respond to various signals to acquire new functions.

A quintessential example of metabolic remodeling is represented by metabolic changes underlying the life cycle of a digenetic mammalian parasite, *Trypanosoma brucei* [7]. This parasite of medical and veterinary importance needs to make crucial adaptations to new environments, including different temperatures and nutrients, as it alternates between an insect vector, the tsetse fly, and a mammalian host [8]. Dictated by the availability of nutrients in the midgut of the tsetse fly, the insect procyclic form (PCF) accumulates and metabolizes amino acids, including proline and threonine, using an incomplete TCA cycle, which leads to the production of different metabolic intermediates as well as ATP by substrate-level phosphorylation [9,10]. The cells respire through a canonical cytochrome-containing electron transport chain (ETC), which generates a mitochondrial membrane potential ($\Delta\psi m$) that powers the F_oF_1-ATP synthase [11,12]. The full activity of the parasite's mitochondrion is reflected by its highly branched, reticulated structure that intertwines the whole cell. Bloodstream form (BSF), by contrast, inhabits glucose-rich blood of the mammalian host, and the majority of its ATP is produced by a highly active glycolytic pathway, the redox balance of which is maintained by a glycosomal glycerol-3-phosphate/dihydroxyacetone phosphate shuttle via mitochondrial flavin adenine dinucleotide (FAD)-dependent glycerol-3-phosphate dehydrogenase and alternative oxidase (AOX) [13,14]. In the absence of ETC complexes III and IV, the $\Delta\psi m$ is generated by ATP hydrolysis through the F_oF_1-ATP synthase complex operating in its reverse mode [15,16]. Structurally, the BSF mitochondrion is a simple tubular organelle lacking recognizable invaginations. Over the past 25 years, we have acquired extensive knowledge of PCF and BSF metabolism due to the availability of axenic cultures [17,18]. However, the molecular mechanisms underlying the dramatic metabolic remodeling that occurs during differentiation, including signals and signal transduction pathways, are elusive. This lack of knowledge is mainly due to difficulties in characterizing parasites undergoing differentiation from one life cycle stage to another in the tsetse fly [19].

Upon entry into a tsetse fly during a blood meal, the tsetse-primed (stumpy form) subpopulation of the BSF trypanosomes responds to two major signals: lower temperature and the presence of metabolites (e.g., *cis*-aconitate, citrate) to trigger differentiation to the PCF morphotype [20]. Once the PCF cells establish infection in the tsetse midgut, the parasites migrate to the ectoperitrophic space by crossing the acellular peritrophic membrane and re-enter the alimentary canal at the proventriculus as elongated trypomastigotes [21]. These cells differentiate to short epimastigotes through an asymmetric division that produces one long and one

short daughter. The short epimastigotes are believed to colonize salivary glands, where they fully differentiate to attached epimastigotes. Early during infection, these attached morphotypes divide symmetrically into identical progeny and colonize salivary glands. Later, the epimastigote cells undergo asymmetric division, producing a daughter cell of the metacyclic type. These cells are released to the lumen and are ready to be transmitted during the next blood meal to establish infection in a new mammalian host [22–24]. Until recently, the tsetse morphotypes were not available in culture, restricting our knowledge about their metabolism and signaling pathways underlying their complex developmental program.

The discovery that overexpression of a single RNA binding protein 6 (RBP6) induced differentiation of PCF cells to epimastigotes and further to infective metacyclics [25,26] offered a simplified route to dissect differentiation-related events. Using this system, we report here a multi-omics and cell-based profiling to describe the metabolic alterations that accompany in vitro–induced differentiation. We provide a series of publicly available multi-omics datasets that will be of high relevance to the community interested in exciting aspects of *Trypanosoma* biology and biological data integration. Moreover, our data show dynamic metabolic remodeling of mitochondria from cytochrome-mediated respiration to AOX, followed by increased $\Delta\psi m$ and ROS production to drive the developmental progression of *T. brucei* tsetse life cycle stages.

Results

Establishment of RBP6^{OE} cell line

For the study reported here, we took advantage of an in vitro differentiation system based on the inducible expression of RBP6 in the *T. brucei* Lister 427 (29–13) strain [25]. As with published data, we observed a time-dependent appearance of epimastigotes, and then metacyclic cells (Fig 1A) in RBP6 overexpressing (RBP6^{OE}) trypanosomes adapted to no-glucose medium SDM-80 supplemented with N-acetyl glucosamine. The life cycle stages were determined by means of the stage-specific morphology based on shape and cell size, as well as the relative position of the kinetoplast to the nucleus. While the mitochondrial DNA called kinetoplast (kDNA) in PCF is posterior to the nucleus, during epimastigote maturation, it migrates to the opposite side of the nucleus, where it is found in its close proximity or at the anterior part of the cell. The metacyclic trypomastigotes are typically smaller than PCF and epimastigotes, and are characterized by the kinetoplast occupying the very end of the rounded posterior tip (Fig 1A). Furthermore, there are well-characterized differences at the level of the parasite surface molecules. The procyclic trypomastigotes are covered with a glycoprotein coat composed mainly of procyclins rich in Gly-Pro-Glu-Glu-Thr repeats (GPEET procyclin) and procyclins rich in Glu-Pro repeats (EP procyclin) [27], whereas mature epimastigote forms have a coat consisting of glycosylphosphatidyl inositol-anchored proteins, brucei alanine-rich proteins (BARPs) [28].

After the RBP6 overexpression (RBP6^{OE}), a cell was considered an epimastigote form if the kDNA was found juxtanuclear or at the anterior end of the nucleus. We also measured the distance between the nucleus and kDNA for each time point and detected a significant shift toward the nucleus at day 2 upon RBP6^{OE} (Fig 1B). Immunofluorescence analysis showed that at day 2, procyclic as well as epimastigote cells express procyclin on their surface (Fig 1C), while later during development, RBP6^{OE} cells expressed BARP (Fig 1D). A metacyclic cell was defined by a smaller size, having the kinetoplast in close proximity to the plasma membrane, and by uptake of fluorescein-labeled dextran due to metacyclic cells' up-regulated endocytosis [25] (Fig 1A). On day two after the RBP6 induction, the cell culture contained mainly epimastigotes (procyclin positive), and metacyclics were first detected on day 4. By day six, the culture

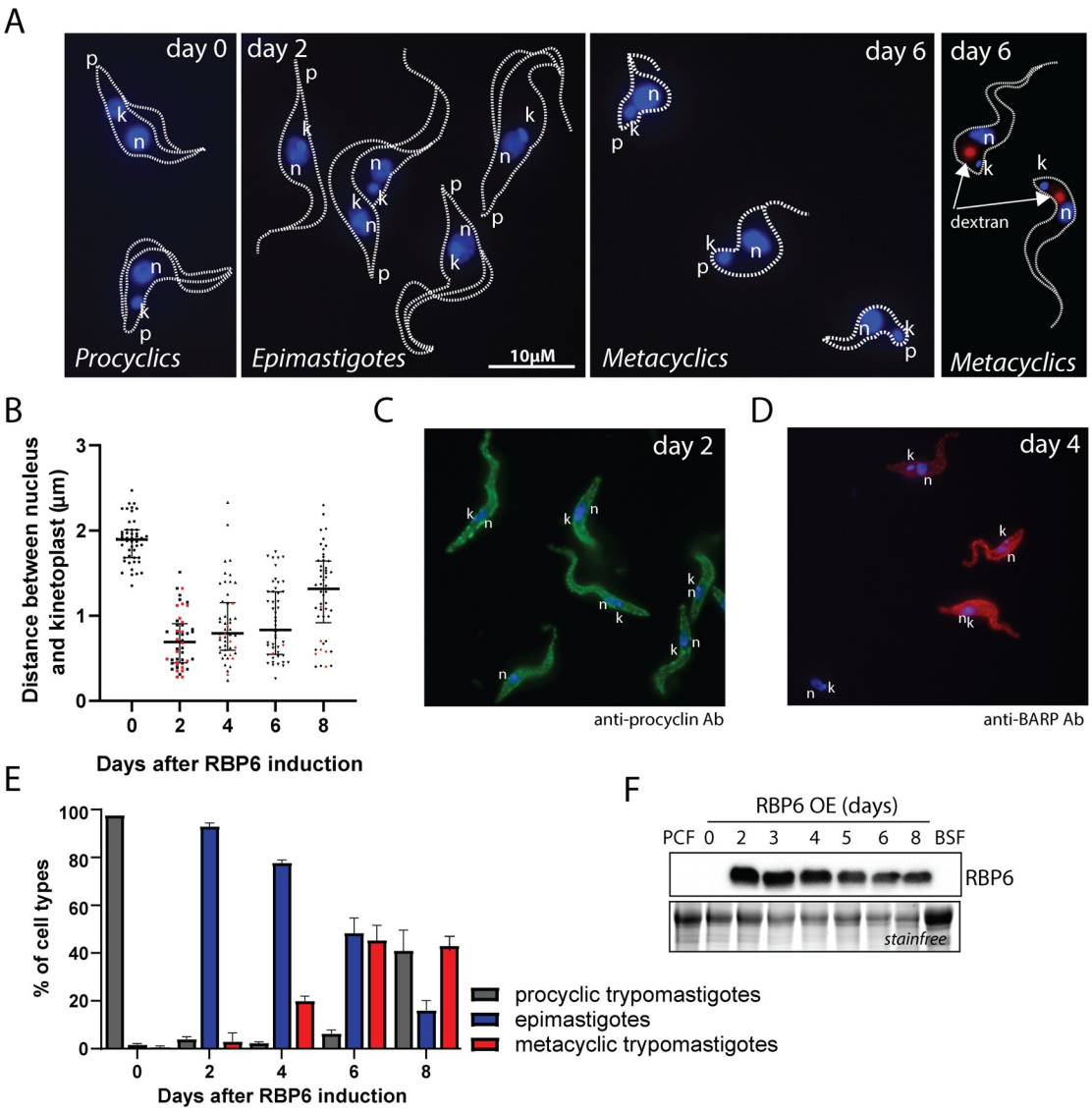

Fig 1. RBP6-induced differentiation of PCF *T. brucei* cells in the absence of glucose. (A) Imaging of procyclic, epimastigote, and metacyclic forms. Cells were characterized by means of morphological features such as shape, size, and the relative position of the kinetoplast to the nucleus, as well as by internalization of fluorescently labeled dextran. DNA was visualized by DAPI staining. (B) Quantification of the intracelullar distance between kDNA and nucleus. For each day, 50 cells were used for measurements. The red dots indicate cells with anterior localization of their kDNA. (C) Immunofluorescence analysis of RBP6^{OE} cells at day 2 using anti-procyclin antibody. (D) Immunofluorescence analysis of RBP6^{OE} cells at day 4 using anti-BARP antibody. (E) Time line for the appearance of epimastigotes and metacyclic cells upon induction of RBP6^{OE}. (F) Western blot analysis of whole-cell lysates from RBP6^{OE} cells. Underlying data plotted in panels B and E are provided in S1 Data. Ab, antibody; BARP, brucei alanine-rich protein; BSF, bloodstream form; k, kinetoplast (mitochondrial DNA); kDNA, kinetoplast DNA; n, nucleus; p, posterior end; PCF, procyclic form; RBP6, RNA binding protein 6.

https://doi.org/10.1371/journal.pbio.3000741.g001

contained epimastigotes (mainly BARP positive) and the metacyclic form constituted approximately 50% of the total number of parasites (Fig 1E). On day 8, the culture comprised a mixture of nondividing metacyclics and epimastigotes, which were being overgrown by an emerging population of procyclin-positive procyclic-like cells. These cells may represent dedifferentiating cells or else a population of procyclic cells that did not respond to RBP6 overexpression. RBP6 overexpression was verified by western blot (Fig 1F).

Time-course transcriptomes and proteomes of RBP6^{OE} trypanosomes

To determine global changes to the transcriptome and proteome across the in vitro–induced developmental progression of RBP6^{OE} cells, we applied RNA-Seq and label-free quantitative proteomic analyses (Fig 2A).

RNA was extracted from cells induced for 0, 2, 3, 4, 6, and 8 days and processed using polyA-enrichment for sequencing on an Illumina NextSeq 500 platform. Our analysis of the transcriptomes is based on four biological replicates for each time point. The principal component analysis (PCA) showed a clear difference between the uninduced cells at day 0 and the later stages (S1 Fig). Furthermore, the transcriptomic analysis revealed significant (corrected *P* value <0.05) differential expression for 3,439 transcripts/genes during the RBP6-induced development (S1 Table). For example, at day 2 post-RBP6^{OE}, 1,221 transcripts were up-regulated and 1,588 transcripts were down-regulated when compared to the uninduced cells (Fig 2A), indicating a global change in transcript expression. First, we analyzed the expression profile of well-known surface molecule markers for early and late PCF (GPEET and EP procyclins, respectively) [29], mature epimastigotes (BARPs) [27], and infectious metacyclics, which express metacyclic-like variable surface glycoproteins (mVSGs) [30]. The GPEET transcript was highly down-regulated, while the procyclin EP transcripts and BARP transcripts were up-regulated immediately at day 2 following RBP6 induction. As expected, high levels of metacyclic specific mVSG transcripts were detected later during the differentiation process, namely at days 6 and 8 (Fig 2B). The presence of mRNAs for the three types of surface molecules at days 6 and 8 after the RBP6^{OE} confirms the mixture of various life cycle stages (Fig 1E).

To identify groups of genes that followed similar trends, we performed time-course expression profiling based on K-medoids clustering and selected four clusters based on optimum average silhouette within the distance matrix (Fig 2C, S2 Table). Cluster 1 grouped genes being slowly down-regulated after RBP6 induction. Gene Ontology (GO) term analysis of this cluster indicated enrichment for genes involved in translation. This observation reflects the fact that metacyclic trypanosomes are metabolically quiescent, arrested in G1/G0 with repressed mRNA translation [26]. Cluster 2 is characteristic of genes being steadily up-regulated during developmental progression. Interestingly, GO annotation highlighted genes involved in signal transduction, regulation, and protein modification. Cluster 3 comprises genes being immediately down-regulated over the time-course experiments and contains genes involved in the regulation of gene expression, biosynthetic processes, and RNA processing. Cluster 4 shows fast up-regulation upon RBP6 induction, and it includes genes involved in oxidoreduction metabolic processes linked to the mitochondrion, such as transcripts for TCA cycle or proline degradation enzymes (Fig 2D, S2 Table).

Because transcriptomic data are available for several time-points of RBP6^{OE} cells grown in the presence of glucose as well as for monomorphic populations of in vitro–differentiated metacyclics [26,31], we compared our time-course data with these previously published datasets to benchmark developmental progression in our experiments. The RBP6^{OE} time-course transcriptomes have high correlation coefficients (0.99) (S2 Fig, S3 Table) and become increasingly similar to metacyclic samples (S3 Fig).

For the proteomic analysis, we performed label-free quantitative mass spectrometry for the same time points as for the transcriptomes. Each time point consists of quadruplicate samples, measured with a 4-hour liquid chromatography (LC) gradient on a high-resolution mass spectrometer, and data were analyzed by MaxLFQ [32] (Fig 2A). We quantified 5,227 protein groups with a minimum of 2 peptides (1 unique) and present in at least two out of four replicates, covering differences in expression levels of three orders of magnitude (S4 Fig, S4 Table). PCA showed that replicates of the same time points clustered closely together, demonstrating

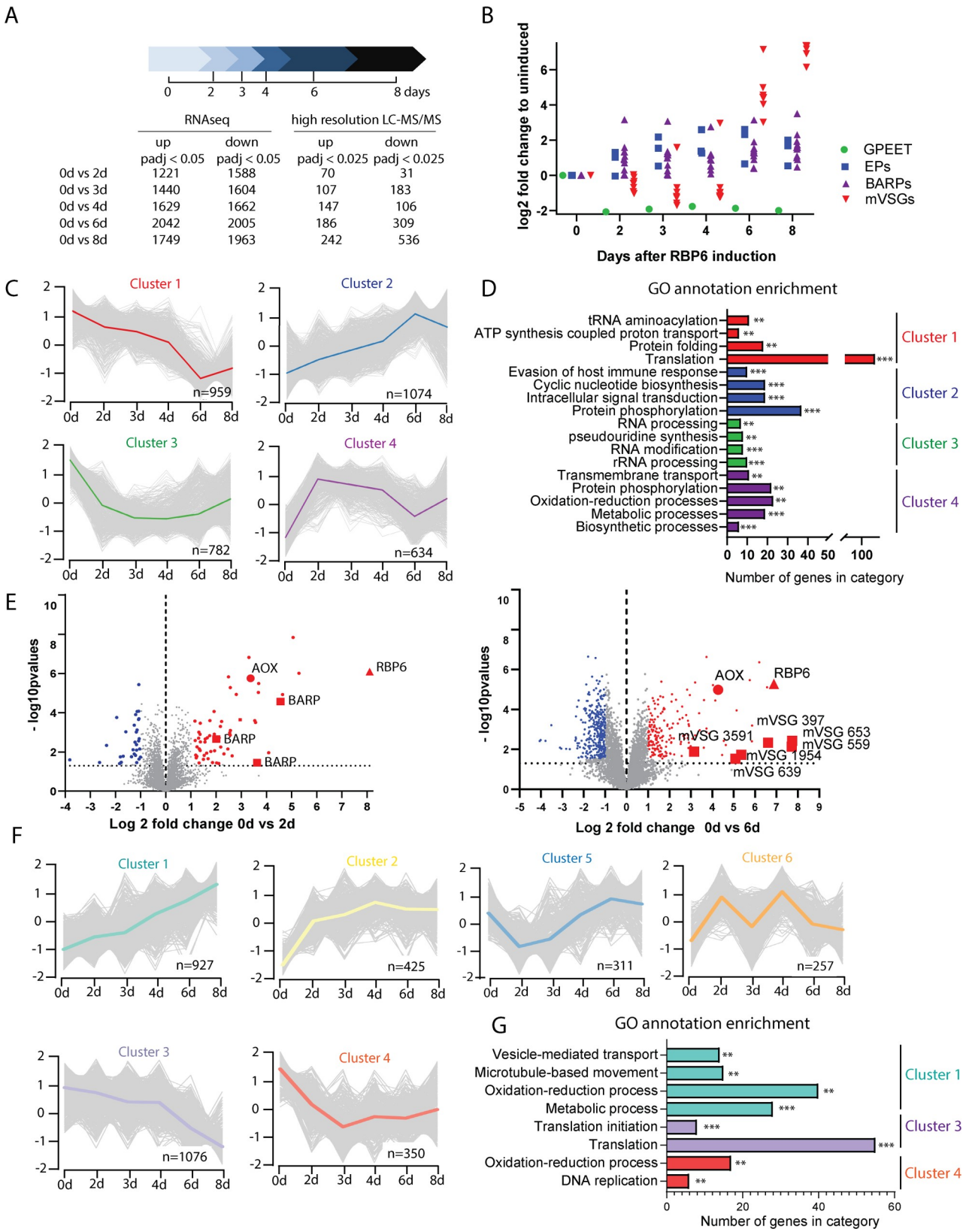

Fig 2. RBP6^{OE} differentiation transcriptome and proteome. (A) Scheme of the differentiation process and the experimental time points. The RBP6-induced cells were harvested and analyzed by RNA-Seq and label-free quantitative mass spectrometry at different time points, as indicated. The

table contains an overview of the number of differentially expressed transcripts and proteins. (B) Gene expression profile of transcripts encoding surface glycoproteins GPEET (Tb927.6.510), BARP (Tb927.5.15530, Tb927.5.15550, Tb927.5.15560, Tb927.5.15600, Tb927.5.15590), and *T. brucei* 427 mVSG (Tb427_000106600.1, Tb427_000524500.1, Tb427_000173600.1, Tb427_000288600.1, Tb427_000304300.1, Tb427_000108300.1, Tb427_000627000.1, Tb427_000615900.1). (C) Time-course expression profiling of transcriptomic data based on K-medoids clustering. (D) Gene Ontology (GO) term analysis applied to all four transcriptomics clusters. Significant levels are depicted as follows $^{**}P < 0.01$, $^{***}P < 0.0001$. (E) Volcano plots showing a comparison of protein expression levels (5,227 protein groups) between day 0 and day 2 (left panel) or day 6 (right panel) upon RBP6 induction. Log2 fold change values of averaged LFQ intensities from quadruplicate experiments are plotted against the respective −log10-transformed *P* values. Significantly down-regulated proteins are depicted in blue, while significantly up-regulated proteins are depicted in red. RBP6, AOX, and surface glycoproteins BARP (day 2) and metacyclic (m)VSGs (day 6) are highlighted. (F) Time-course expression profiling of proteomic data based on K-medoids clustering. (G) GO term analysis of Clusters 1, 3, and 4 showing a significant enrichment. $^{**}P < 0.01$, $^{***}P < 0.001$. Underlying data plotted in panel B are provided in S1 Data. AOX, alternative oxidase; BARP, brucei alanine-rich protein; EP, procyclin rich in Glu-Pro repeats; GO, Gene Ontology; GPEET, procyclin rich in Gly-Pro-Glu-Glu-Thr repeats; k, kinetoplast; LC-MS/MS, liquid chromatography tandem mass spectrometry; LFQ, label-free quantification; mVSG, metacyclic-like variable surface glycoprotein; n, nucleus; RBP6, RNA binding protein 6.

https://doi.org/10.1371/journal.pbio.3000741.g002

minimal experimental variation (S5 Fig). In fact, the separation of the time course is more clearly discernable at the proteome level than the transcriptome level (S1 Fig), indicating that posttranscriptional processes prevail in the progression towards metacyclics. The changes at the proteome level were relatively slow in emerging, because at day 2 only 31 proteins were significantly down-regulated (log2 fold change <-1, *P* value <0.025), while 70 proteins were significantly up-regulated (log2 fold change >1, *P* value <0.025). Among these proteins, RBP6 was detected together with BARPs and AOX (Fig 2E left panel, S4 Table). At day six, 495 proteins were differentially expressed, with mVSG glycoproteins being the most up-regulated entities detected (Fig 2E right panel, S4 Table).

To assess proteome remodeling systematically, we performed K-medoids clustering of the expression profiles across time and obtained six different clusters (Fig 2F), which were further analyzed for GO annotation enrichments (Fig 2G, S5 Table). Cluster 1 includes proteins that are being up-regulated during the developmental progression and, in agreement with the transcriptomic cluster 4, which exhibits a similar trend, it contains enzymes involved in energy metabolism in addition to proteins responsible for microtubule-based movement and vesicle-mediated transport. Cluster 3 is characterized by proteins being steadily down-regulated and contains mainly proteins involved in translation and translation initiation. Cluster 4 is enriched for proteins involved in DNA replication, DNA binding, and oxidation-reduction processes (S5 Table). Unfortunately, GO annotation analysis of clusters 2, 5, and 6 did not reveal any statistically significant enrichment. Cluster 2 comprises of proteins, which are being steadily up-regulated. Clusters 5 and 6 contain proteins with fluctuating expression (Fig 2F, S5 Table).

Proteomics suggest mitochondrial metabolic alterations in proline oxidation pathway and TCA cycle over the *T. brucei* differentiation pathway towards metacyclogenesis

The remodeling of the energy metabolic pathways is a hallmark of *T. brucei* life cycle development. In the absence of glucose, PCF parasites metabolize proline in fully competent mitochondria, gluconeogenesis feeds the pentose phosphate pathway, and ATP is provided by OxPhos. In contrast, BSF cells generate the majority of cellular ATP by glycolysis, have a rudimentary mitochondrion, TCA cycle enzyme activities are barely detectable, and functional cytochrome *c*–mediated ETC is absent. An alternative truncated ETC involving glycerol-3-phosphate dehydrogenase and AOX sustains glycosomal redox balance, with oxygen being the electron sink [7,14].

To gain insight into the proposed rewiring from OxPhos to aerobic glycolysis, we checked the expression profile of glycolytic enzymes, subunits of respiratory chain complexes I, II, III,

and IV, the F_oF_1-ATP synthase, and TCA cycle enzymes over the induced differentiation pathway (Fig 3, S6 Fig). Some of the complex I subunits displayed only a slight increase, while the abundance of the F_oF_1-ATP synthase (complex V) subunits was largely unaffected (S6 Fig). Complex III and IV subunits showed slow but progressive down-regulation (S6 Fig). This detected trend would suggest that during the developmental progression, the cells maintain PCF-like mitochondrial metabolism, with the exception of the BSF final oxidase AOX, the expression of which was strongly elevated (Fig 3A) as cells progressed toward the bloodstream infective metacyclic form. Interestingly, expression of all 15 subunits of complex II was strongly up-regulated immediately at day two after RBP6 induction (Fig 3A). Because complex II is part of the TCA cycle, we examined other TCA cycle enzymes. Citrate synthase (CS), aconitase, and mitochondrial isocitrate dehydrogenase (IDH) also showed strong up-regulation (Fig 3A). Both proline transporters and mitochondrial dehydrogenases involved in proline catabolism were up-regulated, suggesting an unexpected spike in proline consumption during differentiation (Fig 3A). Interestingly, expression of the BSF-specific high-affinity proline transporter (Tb927.8.7610) was steadily up-regulated during differentiation. The activity of mitochondrial dehydrogenases is dependent on Ca^{2+} ions, which are imported into the mitochondrion via a heterooligomeric mitochondrial calcium uniporter (MCU) [33,34]. Changes in expression in three out of four known MCU subunits were among the most notable features in our proteomic data, showing 6-fold up-regulation at day 6 following RBP6 induction (Fig 3A). Because the cells were grown in the absence of glucose, we assessed the expression profiles of gluconeogenetic enzymes. Interestingly, the majority of these were down-regulated or not affected except for sedoheptulose-1,7-bisphosphatase (SBPase) and fructose bisphosphatase (FBPase), the expression of which was up-regulated. Other enzymes involved in glucose metabolism were only mildly affected, including members of the pentose phosphate pathway. Noteworthy, the expression of *T*. *brucei* hexose transporters THT1 and THT2 were differentially altered. The PCF transporter, THT2, with low capacity and high affinity, showed a moderate down-regulation, while the high-capacity BSF transporter, THT1, was up-regulated later during the differentiation process, reaching >6-fold change at day 8 following RBP6 induction (Fig 3A), consistent with preadaptation for re-entry to the glucose-rich environment of the mammalian bloodstream. To validate our MS proteomic results, we performed western blot analysis for selected mitochondrial proteins with available antibodies and also included whole-cell lysate from in vitro cultured BSF cells (Fig 3B). As expected, we detected no significant changes in protein levels of the F_1-ATPase subunit beta, the ATP/ADP carrier (AAC), the phosphate carrier (PiC), or mitochondrial heat shock protein 70 (mitochondrial hsp70). We observed lower abundance of subunits of complexes IV and III, trCOIV, and Rieske. As measured by proteomics, aconitase, pyruvate dehydrogenase, subunit I of complex II (SDH66), succinyl-CoA synthetase (SCoAS; subunit beta), and AOX were up-regulated over the time course of developmental progression. To summarize the acquired data, Fig 4 highlights changes in enzymatic pathways during the in vitro–induced metacyclogenesis and proposes that the $RBP6^{OE}$ cells maintain their PCF-like mitochondrion, with the exception of AOX expression, and remarkably up-regulate proline catabolism and some TCA cycle enzymes.

Electrons entering the ETC are preferentially channeled to AOX as trypanosomes progress towards metacyclogenesis

To probe the changes in mitochondrial bioenergetics induced by differential expression of key bioenergetic enzymes, we first checked cellular respiration in live cells in medium without any carbon sources. The resting respiration was unchanged in $RBP6^{OE}$ cells (Fig 5A). Adding

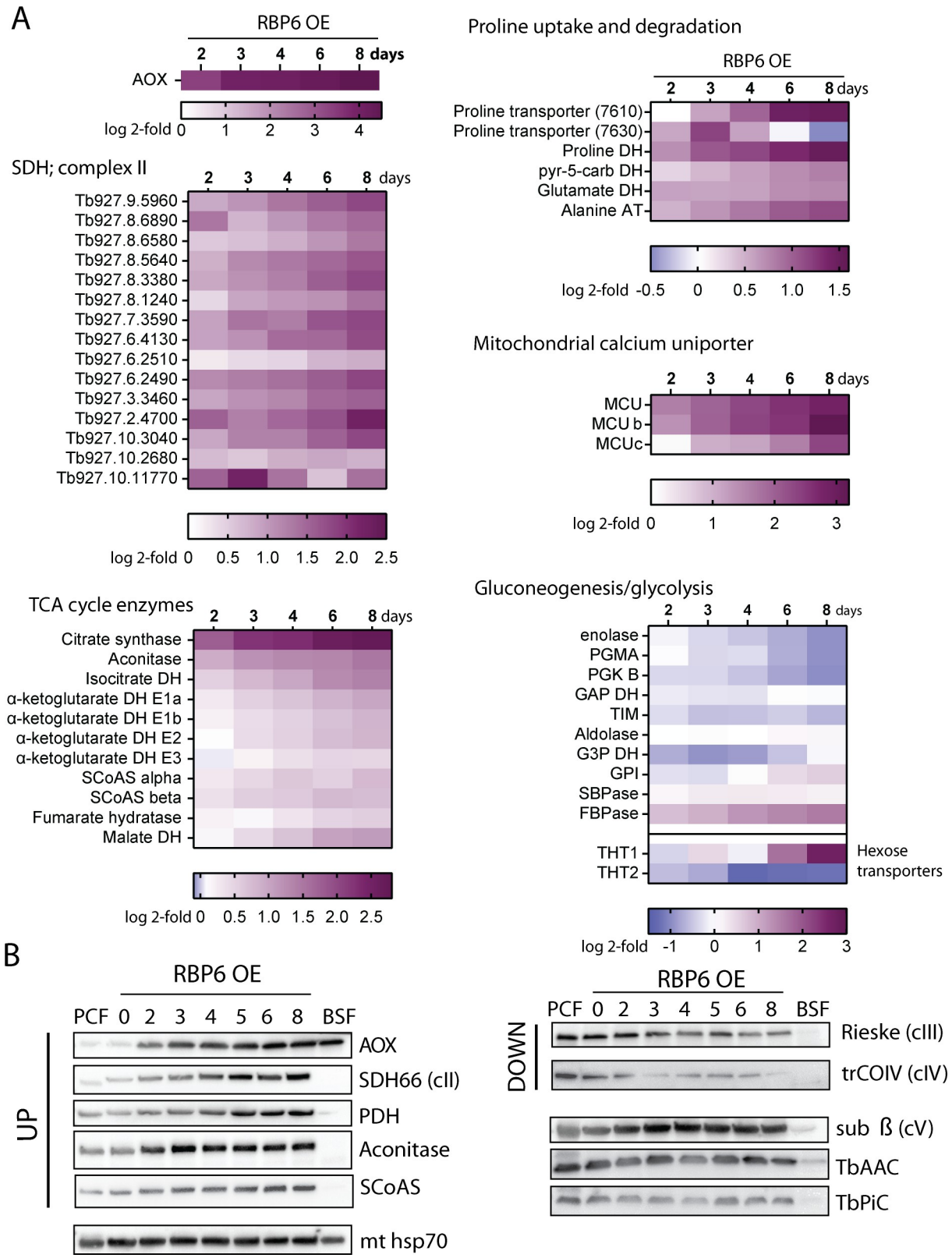

Fig 3. Major changes in protein abundance during RBP6 overexpression. (A) Heatmaps showing log2 fold change of average LFQ intensities of selected proteins identified in induced samples compared to uninduced. The color key differs for each map and is always located below the heatmap. (B) Western blot analyses of whole-cell lysates from RBP6^{OE} cells undergoing differentiation using a panel of various antibodies.

Mitochondrial (mt) hsp70 serves as a loading control because its expression remains constant. AOX, alternative oxidase; AT, aminotransferase; BSF, bloodstream form; DH, dehydrogenase; FBPase, fructose 1,6-bisphosphatase; GAP DH, glyceraldehyde-3-phosphate dehydrogenase; G3P DH, glycerol-3-phosphate dehydrogenase; hsp70, heat shock protein 70; LFQ, label-free quantification; PCF, procyclic form; PDH, pyruvate dehydrogenase; PGK, phosphoglycerate kinase; PGMA, phosphoglycerate mutase; pyr-5-carb DH, pyrroline-5 carboxylate dehydrogenase; RBP6, RNA binding protein 6; SBPase, sedoheptulose 1,7-bisphosphatase; SCoAS, succinyl CoA synthetase; SDH, succinate dehydrogenase; TIM, triose-phosphate isomerase.

https://doi.org/10.1371/journal.pbio.3000741.g003

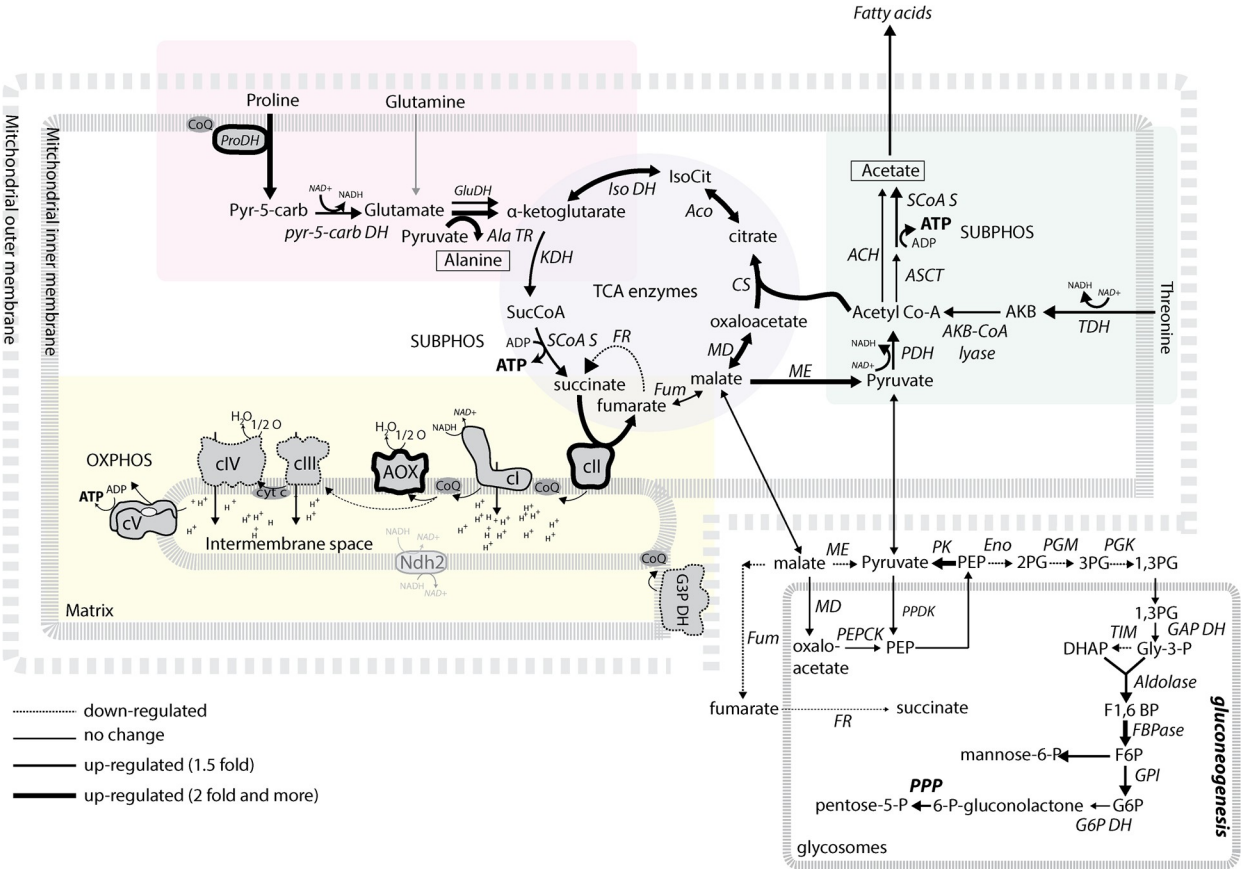

Fig 4. Schematic representation of changes in selected mitochondrial and glycosomal pathways. Enzymatic steps are represented by arrows with different thicknesses, depending on the observed abundance change of the respective protein at day 6 upon RBP6 induction. Dashed lines indicate steps that were down-regulated. Alternative dehydrogenase with unresolved orientation is in gray. The metabolic end products are highlighted by black lines. ACH, acetyl-CoA thioesterase; Aco, aconitase; AKB–CoA lyase, 2-amino-3-ketobutyrate Coenzyme A lyase; Ala TR, alanine aminotransferase; AOX, alternative oxidase; ASCT, acetate:succinate CoA-transferase; cI, complex I, NADH:ubiquinone oxidoreductase; cII, succinate dehydrogenase; cIII, complex III, ubiquinol:cytochrome *c* reductase; cIV, complex IV, cytochrome *c* oxidase; cV, F_oF_1-ATP synthase; CS, citrate synthase; DHAP, dihydroxyacetone phosphate; Eno, enolase; FBPase, fructose 1,6-bisphosphatase; FR, fumarate reductase; Fum, fumarase; F1,6 BP, fructose 1,6 bisphosphate; F6P, fructose-6-phosphate; GAPDH, glyceraldehyde-3-phosphate dehydrogenase; Glu DH, glutamate dehydrogenase; Gly-3-P, glycerol-3-phosphate; GPI, glucose-6-phosphate isomerase; G3P DH, glycerol-3-phosphate dehydrogenase; G6P, glucose-6-phosphate; G6P DH, glucose-6-phosphate dehydrogenase; Iso DH, isocitrate dehydrogenase; IsoCit, isocitrate; KDH, α-ketoglutarate dehydrogenase; MD, malate dehydrogenase; ME, malic enzyme; OXPHOS, oxidative phosphorylation; PDH, pyruvate dehydrogenase; PEP, phosphoenolpyruvate; PEPCK, phosphoenolpyruvate carboxykinase; PG, phosphoglycerate; PGK, phosphoglycerate kinase; PGM, phosphoglycerate mutase; PK, pyruvate kinase; PPDK, pyruvate, phosphate dikinase; PPP, pentose phosphate pathway; Pro DH, proline dehydrogenase; pyr-5-carb, pyrroline-2-carboxylate; pyr-5-carb DH, pyrroline-5 carboxylate dehydrogenase; RBP6, RNA binding protein 6; SUBPHOS, substrate phosphorylation; SCoAS, succinyl-Coenzyme A synthetase; SucCoA, succinyl-CoA; TDH, threonine dehydrogenase; TIM, triose-phosphate isomerase.

https://doi.org/10.1371/journal.pbio.3000741.g004

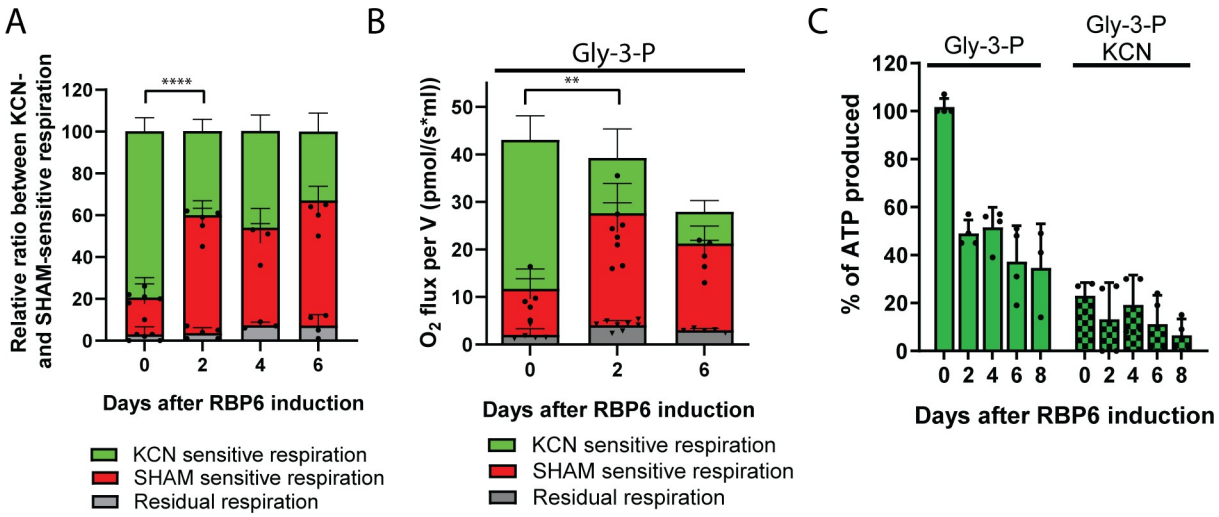

Fig 5. RBP6^{OE} cells respire predominantly via AOX. (A) The resting respiration of cells undergoing RBP6-induced differentiation was measured using the O2k-oxygraph. The ratio of complex IV–and AOX-mediated respiration was determined using KCN, a potent inhibitor of complex IV, and SHAM, a potent inhibitor of AOX. Individual values shown as dots (mean ± SD, $n = 3–5$), $^{****}P < 0.0001$. (B) Glycerol-3-phosphate stimulated respiration in live cells. The proportion of complex IV–and AOX-mediated respiration was determined as in (A). Individual values shown as dots (mean ± SD, $n = 5–8$), $^{**}P < 0.01$. (C) In vitro ATP production was measured in digitonin-extracted mitochondria. The OxPhos pathway was triggered by the addition of ADP and glycerol-3-P. Treatment with 1 mM KCN serves as a control. Individual values shown as dots (mean ± SD, $n = 3–4$). Underlying data plotted in panels (A), (B), and (C) are provided in S1 Data. AOX, alternative oxidase; Gly-3-P, glycerol-3-phosphate; KCN, potassium cyanide; OxPhos, oxidative phosphorylation; RBP6, RNA binding protein 6; SHAM, salicylhydroxamic acid.

https://doi.org/10.1371/journal.pbio.3000741.g005

potassium cyanide (KCN), an inhibitor of cytochrome *c* oxidase, showed that this final oxidase is responsible for approximately 80% of oxygen consumption in uninduced cells (Fig 5A, S7 Fig). The increased expression of AOX at day 2 following RBP6 induction caused preferential redirection of the electrons from the canonical cytochrome *c*–mediated pathway to this enzyme. The induced respiration by glycerol 3-phosphate, a substrate for glycerol-3-phosphate dehydrogenase that passes electrons to ubiquinone, also showed preferential oxidation of ubiquinol by AOX during RBP6^{OE} (Fig 5B). This rewiring of electron flow resulted in less ATP being produced by OxPhos in digitonin-permeabilized cells in the presence of glycerol 3-phosphate as substrate (Fig 5C), likely because AOX is not linked to the generation of $\Delta\psi m$ while electron transfer from ubiquinol to oxygen via complexes III and IV generates $\Delta\psi m$.

To assess if the electrons are preferentially channeled to AOX or this rewiring is a consequence of decreased levels of complexes III and IV, we performed blue-native electrophoresis (BNE) followed by western blotting and activity staining, which is specific for the complexes in question (Fig 6) [11]. At day 2 of RBP6^{OE}, no drastic changes in abundance or activity of the complexes III and IV were detected, suggesting that the reduced ubiquinol molecules are preferentially oxidized by AOX, which competes effectively with the cIII/cIV pathway. Furthermore, the in-gel activity assay shows that both complexes III and IV are active throughout the induced development. The western blot analysis of the same samples indicates that the assembly of the complexes is visibly affected at day 6, most likely due to decreased expression of individual subunits (S6 Fig). In agreement with proteomics data illustrating expression profiles of individual subunits of complexes II (Fig 3A) and V (S6 Fig), Fig 6 shows increased activity and abundance of complex II, while complex V remains largely unaffected during the time course of the experiment.

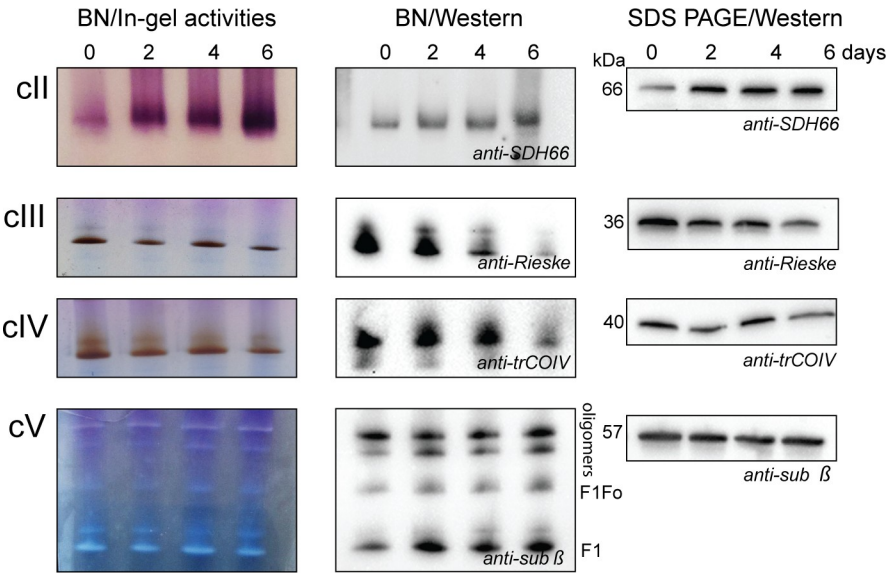

Fig 6. RBP6^{OE}-induced changes in levels and activities of ETC complexes and F_oF_1-ATP synthase. In-gel activity staining and western blot analysis of respiratory complexes II, III, and IV and F_oF_1-ATP synthase (complex V, cV). Mitochondrial preparations were solubilized using dodecyl maltoside and the same amount of the protein samples was separated on NativePAGE 3%–12% Bis-Tris protein gels followed by in-gel activity staining specific for individual complexes (left panels) or by western blot analysis using specific antibodies (middle panels). Mitochondrial lysates were also evaluated by SDS-PAGE and western blot analysis for individual subunits of complexes II, III, IV, and V (right panels). ETC, electron transport chain; RBP6, RNA binding protein 6.

https://doi.org/10.1371/journal.pbio.3000741.g006

RBP6 overexpression induces changes in mitochondrial metabolic pathways that lead to increased mitochondrial membrane potential (Δψm)

In our classical view of the PCF mitochondrion, Δψm is maintained by the activity of complexes III and IV [35,36]. Fig 7A shows that Δψm measured in live cells by FACS is significantly increased during the RBP6 induction (Fig 7A). However, in agreement with the electron rewiring to AOX, the detected Δψm was less sensitive to KCN treatment, suggesting that complex IV contributes less to the overall Δψm during in vitro–induced differentiation (Fig 7B). Interestingly, in other eukaryotic systems, during sudden anoxia or induced complex IV dysfunction, the Δψm collapses rapidly and F_oF_1-ATP synthase maintains the Δψm for a short period by reversing its activity [37]. The F_oF_1-ATP synthase hydrolytic activity is regulated by inhibitory peptide 1 (IF1) [38], which is expressed in PCF cells and prevents the reversal of F_oF_1-ATP synthase and thus ATP depletion upon complex IV inhibition [39]. Fig 7C reveals that *T. brucei* IF1 (TbIF1) expression is down-regulated during the RBP6 overexpression. We therefore measured the ability of the mitochondrial proton pumps, complexes III and IV, to generate the Δψm. Utilizing safranine O dye, the RBP6^{OE} digitonin-permeabilized cells were allowed to establish Δψm in the presence of succinate as the only electron donor. Upon the addition of KCN, the rate of mitochondrial membrane depolarization was a little bit slower in RBP6^{OE}-induced cells compared to uninduced, while a combined treatment of KCN and oligomycin, an inhibitor of F_oF_1-ATP synthase, depolarized the mitochondrial membranes at the same rate. These results suggest that decreased expression of TbIF1 allows the reversal of F_oF_1-ATP synthase to partially maintain Δψm upon inhibition of complex IV in permeabilized cells (Fig 7D). But as the overall Δψm measured in live cells was not sensitive to oligomycin (Fig 7E), the contribution of F_oF_1-ATP synthase to the total Δψm is most likely negligible. In fact, the oligomycin treatment caused hyperpolarization of mitochondrial inner

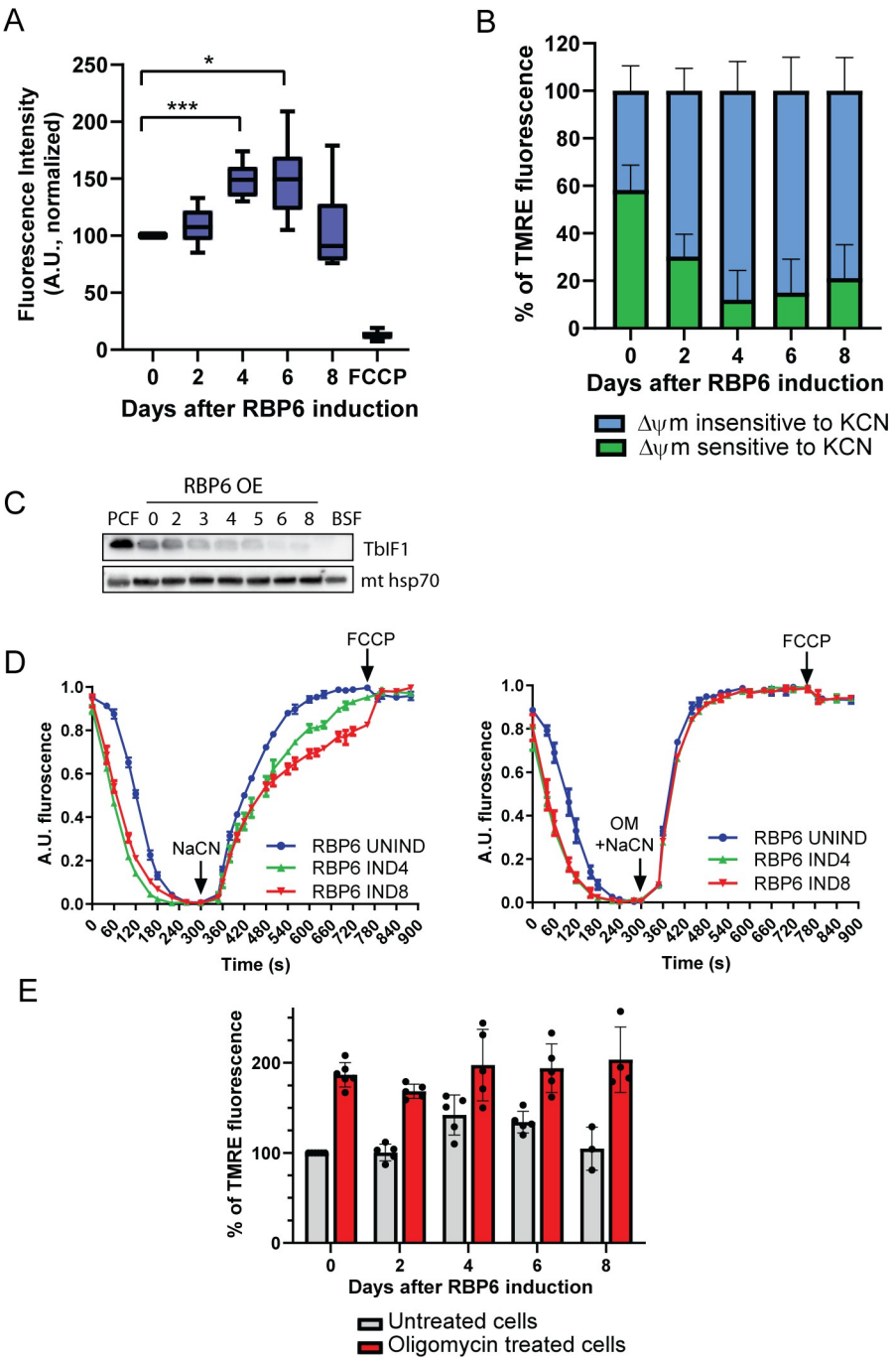

Fig 7. Mitochondrial membrane potential (Δψm) is increased during RBP6^{OE}. (A) The Δψm of RBP6^{OE} cells post induction was measured by flow cytometry using TMRE. A protonophore FCCP serves as a control for membrane depolarization (mean ± SD, $n = 6–10$) $^{*}P < 0.05$, $^{***}P < 0.001$. (B) The proportion of Δψm that is generated by complex IV was established by treating the cells with KCN (0.5 mM) in the presence of TMRE for 30 minutes before the analysis. The graph shows a proportion of KCN-sensitive Δψm to the total Δψm measured in each individual sample (mean ± SD, $n = 5$). (C) Western blot analysis of F_oF_1-ATPase inhibitory factor TbIF1 during RBP6^{OE}. Mitochondrial (mt) hsp70 serves as a loading control. (D) The in situ dissipation of the Δψm in response to chemical inhibition of complex IV by 1 mM NaCN was measured using safranine O dye in RBP6^{OE} uninduced (UNIND) cells and cells induced for 4 and 6 days. The reaction was initiated with digitonin; OM, oligomycin (2.5 μg/mL), and FCCP (5 μM) were added when indicated (mean ± SD, $n = 3$). (E) The Δψm of RBP6^{OE} cells that were treated (red columns) or not with oligomycin (2.5 μg/mL). Individual values shown as dots (mean ± SD, $n = 3–6$). Underlying data plotted in panels A, B, D, and E are provided in S1 Data. BSF, bloodstream cell; FCCP, carbonyl cyanide-4-phenylhydrazone;

KCN, potassium cyanide; PCF, procyclic cell; RBP6, RNA binding protein 6; TbIF1, *T. brucei* inhibitory peptide 1; TMRE, tetramethyl rhodamine ethyl ester.

https://doi.org/10.1371/journal.pbio.3000741.g007

membrane in uninduced as well as in RBP6^{OE}-induced cells (Fig 7E), implying that F_oF_1-ATP synthase functions in its forward mode allowing protons to re-enter the mitochondrial matrix to synthesize ATP.

Because the total Δψm is not sensitive to oligomycin and it is less sensitive to KCN, the Δψm during RBP6^{OE} can be partially maintained by complex I, which contributes to Δψm by coupling NADH oxidation with reduction of ubiquinone [40]. The role of complex I in trypanosome mitochondria remains enigmatic because functional studies are hampered by its lack of sensitivity to rotenone, a typical inhibitor of the mitochondrial complex I [41]. Nevertheless, this complex is fully assembled and active, albeit not essential, in procyclic trypanosomes [40]. Proteomics data suggest a significant increase in proline consumption, possibly leading to high levels of reduced NADH and thus higher activity of complex I. This is confirmed by highly enhanced respiration of live cells in the presence of 5 mM proline simulating the growth conditions immediately at day 2 upon RBP6 induction (Fig 8A). The measured increase in oxygen consumption was fully salicylhydroxamic acid (SHAM)-sensitive, suggesting that the majority of electrons is passed to oxygen via AOX (Fig 8A). Similarly, Fig 8B shows an increased succinate-stimulated respiration in digitonin-permeabilized cells, most likely because of elevated abundance and activity of complex II, the succinate dehydrogenase (Fig 6). Interestingly in both cases, we did not observe a dramatic decrease in cytochrome *c*–mediated respiration, suggesting that in the presence of a plentiful carbon source, the canonical pathway maintains its capacity during parasite differentiation. Indeed, in a digitonin-extracted mitochondrial sample, succinate was able to stimulate ATP production via OxPhos (Fig 8C). Because proline consumption is significantly increased during differentiation, one would expect that the oxidation of α-ketoglutarate through the reactions of the TCA cycle will lead to more ATP being produced by substrate phosphorylation pathways, which is integral to the TCA cycle (Fig 4). This pathway uses SCoAS and it is induced by α-ketoglutarate in vitro [42]. Interestingly, α-ketoglutarate did not significantly stimulate ATP production by substrate phosphorylation during the RBP6-induced differentiation (Fig 8D). This observation opens a possibility of α-ketoglutarate entering the reductive branch of the TCA cycle, leading to production of citrate, a phenomenon described in human cells with OxPhos dysfunction [43] (Fig 4). Last but not least, the steady-state cellular levels of ATP were progressively decreased (Fig 8E), indicating a higher need for ATP and consistent with increased ADP/ATP ratio during differentiation (Fig 8F).

Metabolomic profiling during RBP6^{OE} differentiation

To get further insights into the metabolic changes induced by RBP6 overexpression, we undertook a global metabolomics analysis for the RBP6^{OE} cell line (S6 Table). In agreement with earlier observations, the levels of proline, glutamate, and glutamine were decreased, confirming that proline and glutamine consumption pathways are elevated by day 2 following RBP6 induction (Fig 9A). Possibly due to the high activity of mitochondrial dehydrogenases involved in these pathways, the levels of NADH and thiamine, an essential cofactor for various mitochondrial dehydrogenases, were up-regulated. Accumulation of alanine, the ultimate end product of proline metabolism was detected. Other intracellular amino acids were unchanged or showed non-statistically significant changes with the exception of tyrosine, leucine/isoleucine, and tryptophan (as well as its derivatives 5-hydroxy-L-tryptophan, indole, and quinolinate), the levels of which were up-regulated (Fig 9A). Notably, a comparison of volcano plots

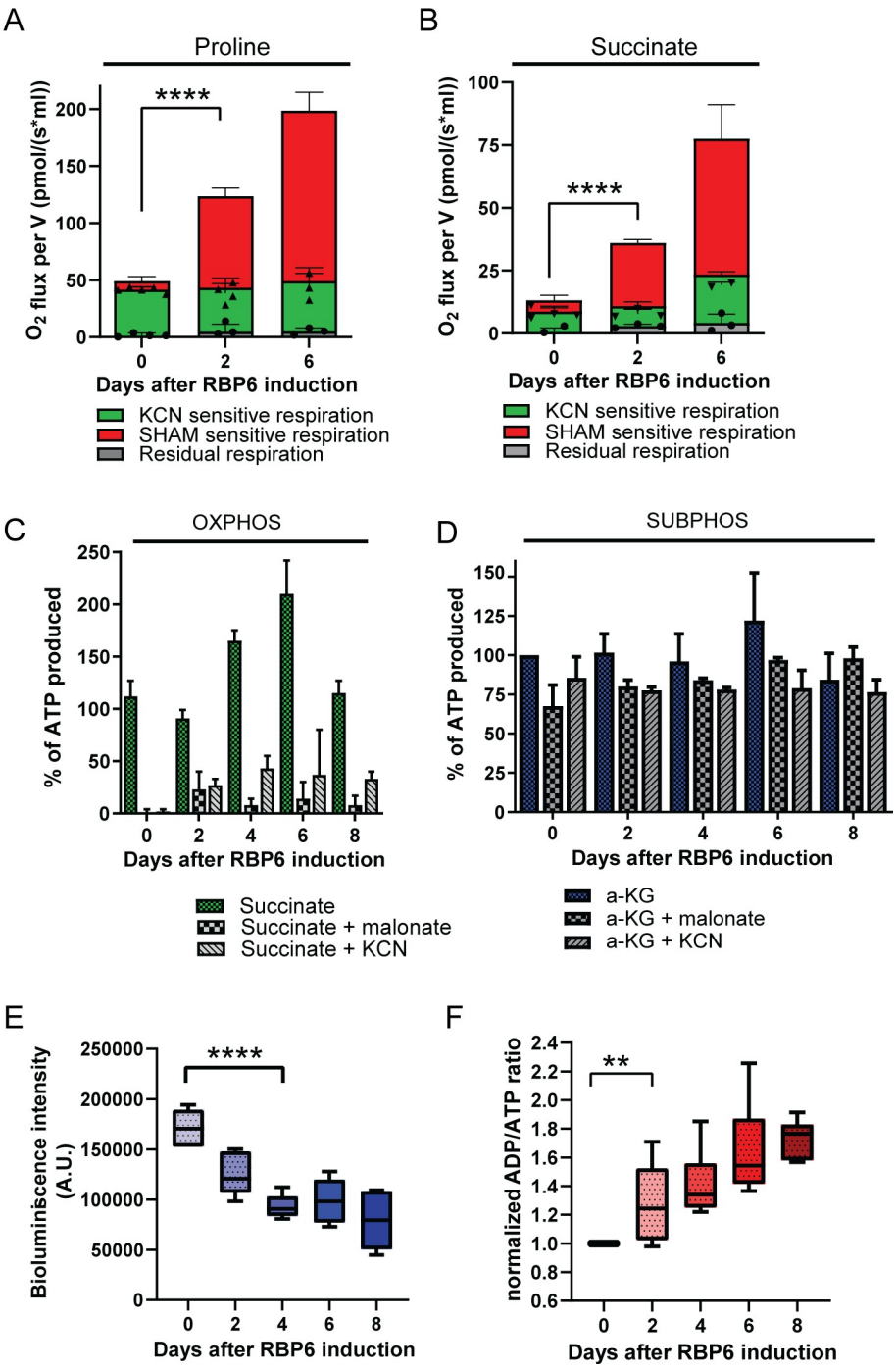

Fig 8. Changes in cellular respiration and mitochondrial ATP production in RBP6^{OE} cells. (A, B) Oxygen consumption rates in the presence of 5 mM proline (A) or 5 mM succinate (B) in live or digitonin-permeabilized cells, respectively. Respiration via AOX was monitored in the presence of KCN (0.5 mM). Individual values shown as dots (means ± SD, $n = 3–5$). $^{****}P < 0.0001$. (C, D) The in vitro ATP production by oxidative or substrate phosphorylation (OXPHOS, SUBPHOS) measured in digitonin-extracted mitochondria from uninduced and RBP6-induced cells. The phosphorylation pathways are triggered by the addition of ADP and by succinate (C) or α-ketoglutarate (a-KG, D). Malonate (mal.) and KCN, specific inhibitors of succinate dehydrogenase and complex IV are used to inhibit ATP production by OXPHOS. The levels of ATP production in mitochondria isolated from uninduced RBP6^{OE} cells are established as the reference and set to 100% (means ± SD, $n = 2–4$). (E) Cellular ATP content in RBP6^{OE} cells. (means ± SD, $n = 6$, $^{****}P < 0.0001$). (F) Relative ADP/ATP ratios of RBP6^{OE} cells. The ADP/ATP ratio in uninduced RBP6^{OE} cells (between 1.75 and 6.01) is established as a reference and set to 1. In *T. brucei*, ADP/ATP ratio reaches

unusually high levels, as also reported elsewhere [44]. The measured values are shown in S1 Data (means ± SD, $n = 6–10$, $^{**}P < 0.01$). Underlying data plotted in panels A, B, C, D, E, and F are provided in S1 Data. AOX, alternative oxidase; KCN, potassium cyanide; OXPHOS, oxidative phosphorylation; RBP6, RNA binding protein 6; SHAM, salicylhydroxamic acid; SUBPHOS, substrate phosphorylation.

https://doi.org/10.1371/journal.pbio.3000741.g008

generated from data acquired on days 2 and 8 after RBP6 induction suggests an overall accumulation of metabolites (Fig 9B). Gluconeogenesis-related intermediates were mainly unchanged, with the exception of glyceraldehyde 3-phosphate, levels of which were down-regulated (Fig 9C). Nucleotide metabolism was altered with purine-based metabolites being increased. Phosphorylated nucleotides were generally slightly down-regulated (Fig 9D). Among the most striking alterations was an accumulation of several TCA cycle intermediates including malate and citrate (Fig 9E). Interestingly, the molecules crucial for energy storage,

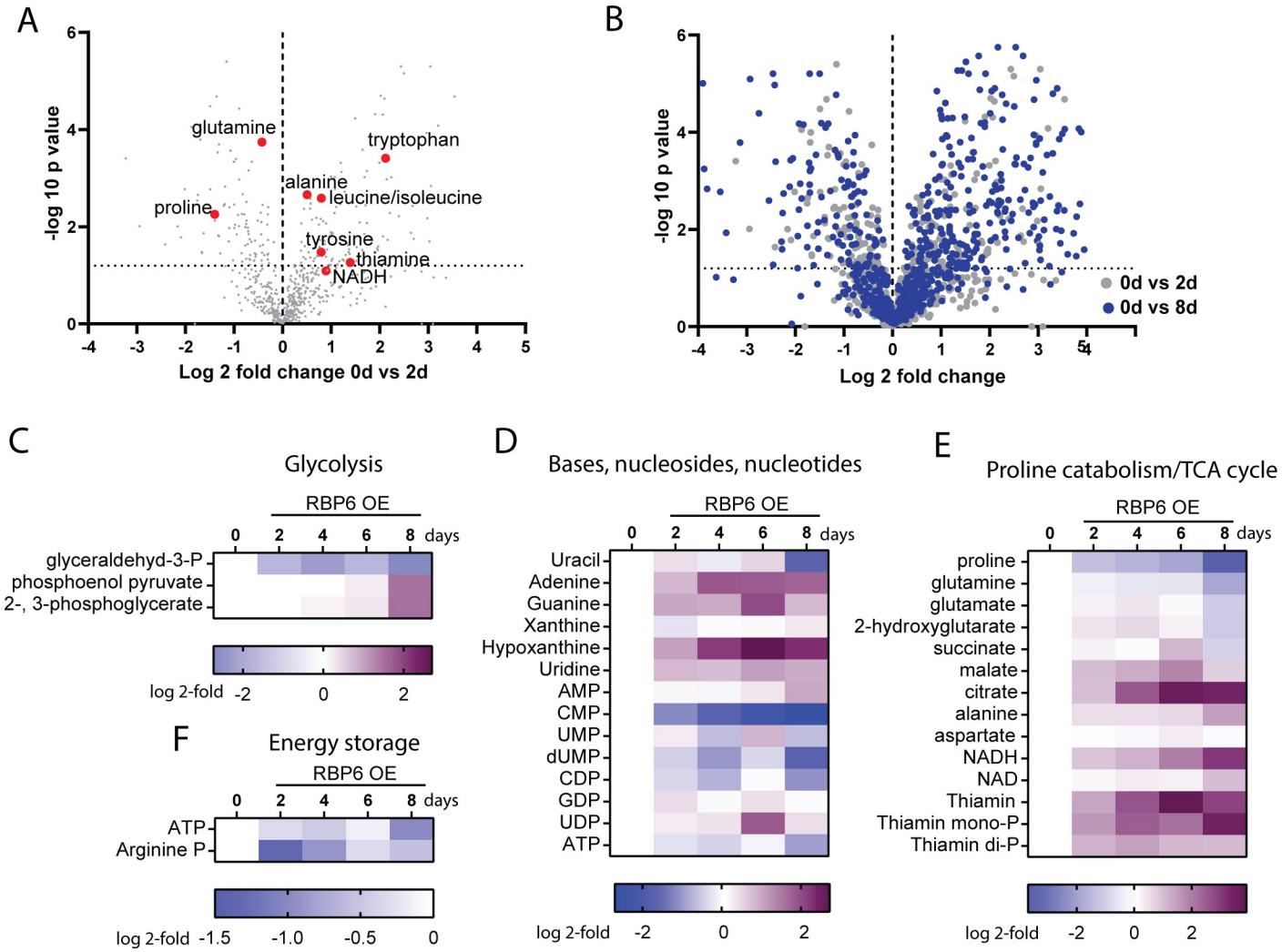

Fig 9. Metabolomics profiling of RBP6^{OE} cells. (A) Volcano plot showing the full metabolome (698 metabolites) analyzed at day 0 and day 2 upon RBP6 induction. Log2 fold change values of the average of mean peak area from quadruplicate experiments are plotted against the respective –log10 transformed *P* values. Few key metabolites are highlighted. (B) Volcano plot showing the full metabolome analyzed at day 2 (gray) and 8 (blue) upon RBP6 induction compared to day 0. Log2 fold change values of the average of mean peak area from quadruplicate experiments are plotted against the respective –log10 transformed *P* values. (D, E, F) Heatmaps showing log2 fold change of average of mean peak area of selected metabolites identified in induced samples compared to uninduced (day 0). The color key differs for each map and is always located below the heatmap. Heatmaps were generated with GraphPad prism 8.2.0. RBP6, RNA binding protein 6; TCA, tricarboxylic acid.

https://doi.org/10.1371/journal.pbio.3000741.g009

ATP and arginine phosphate, were progressively diminished (Fig 9F). While other changes in metabolite levels across the trypanosome metabolome were detected, no clear trends showing activation or repression of other specific metabolic pathways upon RBP6^{OE} were noted. The full metabolomics dataset can be found in S6 Table and all liquid chromatography–mass spectrometry (LC-MS) data files were deposited in MetaboLights (study identifier MTBLS1390). In summary, the identified changes in the parasite metabolome are consistent with suggested increased activities in mitochondrial dehydrogenases involved in proline consumption and TCA cycle enzymes (Fig 3A and Fig 4).

Repurposing of the mitochondrion to a ROS-producing signaling organelle

Notably, the levels of glutathione were diminished while the levels of its oxidized product glutathione disulfide were amplified 8-fold at day 8 following RBP6 overexpression (Fig 10A). This was accompanied by a significant 2.2-fold decrease in the levels of the trypanosomatid-specific thiol-based antioxidant ovothiol A at day 2 post expression, and levels were further depleted throughout the time course (S6 Table). The levels of L-cystathionine were also found to be decreased after day 4 following RBP6 overexpression (S6 Table). The latter is an intermediate in the biosynthesis of L-cysteine (not detected in a dataset), and it was reported that enhanced activities of cysteine synthase and cystathionine β-synthase possess a beneficial effect on *Leishmania braziliensis* survival under oxidative stress [45]. The other trypanosomatid-specific derivative of glutathione, trypanothione, was not detected in its reduced form using the LC-MS platform, but its oxidized form, trypanothione disulfide, was annotated in the dataset and was not found to have significantly altered levels across the time course of RBP6^{OE}. The increasing abundance of oxidized glutathione is suggestive of mild oxidative stress during developmental progression. We therefore surveyed changes in the expression levels of proteins involved in redox metabolism and, except for putative mitochondrial thioredoxin (Tb927.7.5780), we did not detect any major changes (S8 Fig).

We then analyzed intramitochondrial and intracellular ROS levels (Fig 10B). Interestingly, levels of mitochondrial ROS were elevated immediately after RBP6 induction, while overall cellular ROS were up-regulated only at later time points. ROS molecules, when produced in small concentration, are considered as signaling molecules with the ability to change cell fate and drive cellular differentiation [6]. Excited by the idea that the metabolic repurposing of the mitochondria during the developmental progression leads to the production of signaling molecules, we sought to investigate whether ROS elimination would halt the in vitro–induced differentiation. We took advantage of the fact that *T. brucei* genome lacks catalase, a natural and very potent scavenger of ROS molecules [46]. We introduced the catalase gene from a related organism, *Crithidia fasciculata*, into the *T. brucei* genome under the control of a tetracycline-inducible system. The tetracycline-induced expression and cytosolic localization of the catalase in RBP6^{OE} catalase transduced cells (RBP6^{OE}_catalase) were verified by western blot analysis (Fig 10C, inset), and activity was verified visually by a simple assay using live cells, which produced oxygen upon exposure to H_2O_2 (S1 Video). An indicator of successful RBP6-induced differentiation is a delay in growth in the first four days post induction, followed by entry into a growth-arrested stationary phase (Fig 10C, red line). Importantly, cells expressing catalase maintained continuous growth (Fig 10C, blue line), and the differentiation kinetics, scored by cell morphology analyses, showed that while the RBP6^{OE}_catalase cell line developed epimastigote-like cells after two days, it completely failed to differentiate to metacyclic forms. The fraction of epimastigote-like cells never reached the same proportion as in RBP6^{OE} cells and was eventually overtaken by proliferative procyclics (Fig 10D). Western blot analysis showed that both cell lines expressed RBP6 protein to similar levels (Fig 10E). The major differences were

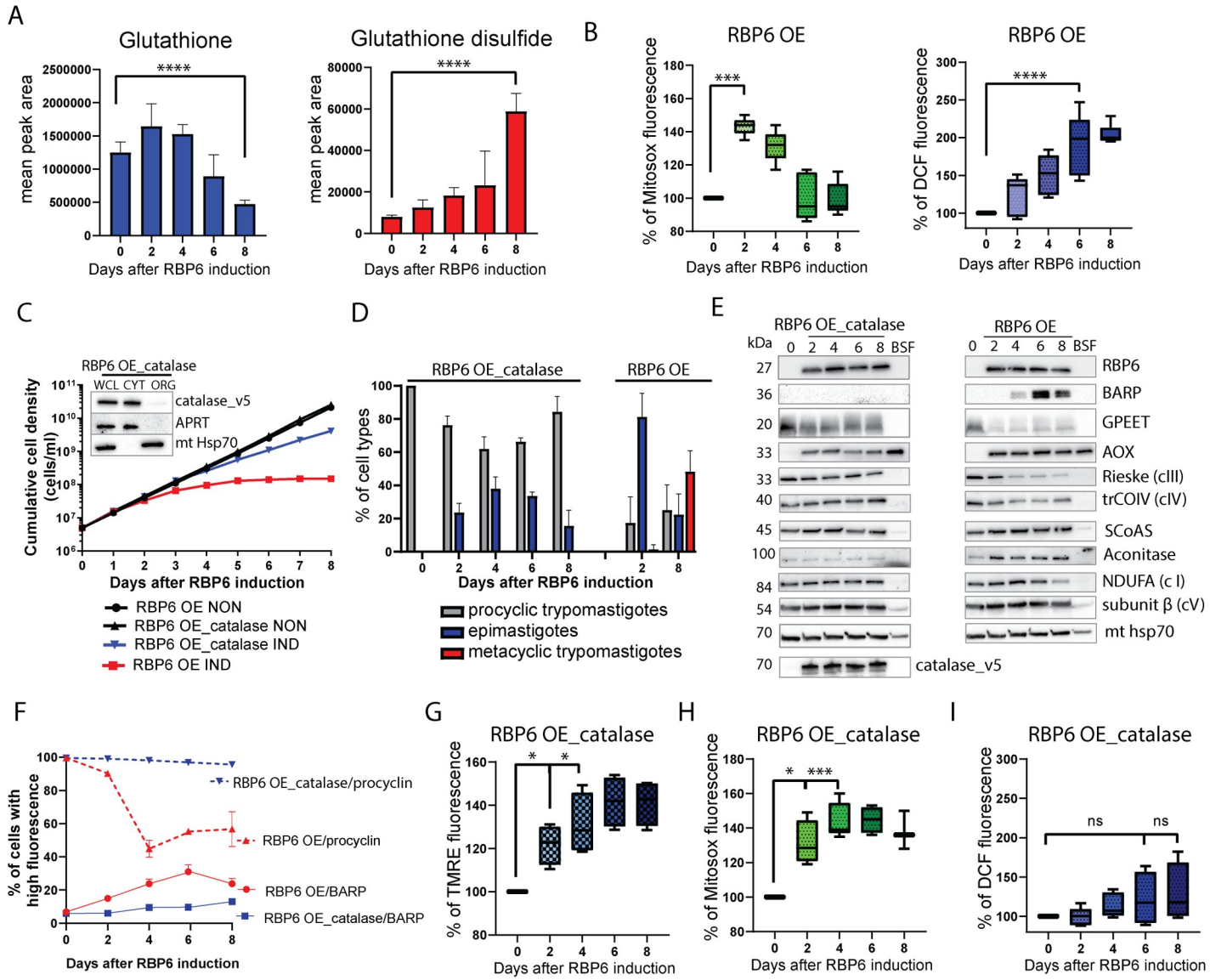

Fig 10. Elevated ROS generated during the differentiation of *T. brucei* are crucial for driving forward RBP6-induced differentiation. (A) Metabolites glutathione and glutathione disulfide as detected by LC-MS analyses. The size of the bars represents the total abundance of the metabolite (mean ± SD, $n = 4$, $^{***}P < 0.001$). (B) Mitochondrial and cellular ROS detection reagents (MitoSox and H_2DCFDA, respectively) were quantified by FACS (means ± SD, $n = 5$, $^{***}P < 0.001$, $^{****}P < 0.0001$). (C) Representative growth curves of RBP6^{OE} and RBP6^{OE}_catalase cells induced by tetracycline. Total number of experiments $n = 5$. The inset shows subcellular localization of v5-tagged catalase in RBP6^{OE}_catalase cells induced for 48 hours. Immunoblots were labeled with anti-v5, anti-adenosine phosphoribosyl transferase (APRT), and anti-mt hsp70 antibodies to visualize catalase, cytosolic APRT, and mitochondrial localized hsp70, respectively. (D) Time line for the appearance of epimastigotes and metacyclic cells upon induction of RBP6^{OE} and RBP6^{OE}_catalase. Total number of experiments $n = 3$. (E) Western blot analysis of whole-cell lysates from RBP6^{OE} and RBP6^{OE}_catalase cells using available antibodies. (F) FACS analyses of RBP6^{OE} and RBP6^{OE}_catalase cells treated with 5 mM bathophenanthroline disulphonic acid (BPS) and labeled with polyclonal anti-BARP and anti-procyclin antibodies. (G) The Δψm of RBP6^{OE}_catalase cells post induction measured by flow cytometry using TMRE (means ± SD, $n = 4$), $^{*}P < 0.05$. (H) Mitochondrial ROS detection reagent MitoSox in RBP6^{OE}_catalase cells quantified by FACS (means ± SD, $n = 5$), $^{*}P < 0.05$, $^{***}P < 0.001$. (I) Cellular ROS detection reagent H_2DCFDA in RBP6^{OE}_catalase cells quantified by FACS (means ± SD, $n = 5$). Underlying data plotted in panels A, B, C, D, F, G, H, and I are provided in S1 Data. AOX, alternative oxidase; APRT, adenine phosphoribosyl transferase; BARP, brucei alanine-rich protein; CYT, cytosol; hsp70, heat shock protein 70; H_2DCFDA, 2′,7′-dichlorofluorescin diacetate; LC-MS, liquid chromatography–mass spectrometry; ns, statistically not significant; ORG, organellar fraction; RBP6, RNA binding protein 6; ROS, reactive oxygen species; SCoAS, succinyl Co-A synthetase; TMRE, tetramethyl rhodamine ethyl ester; WCL, whole-cell lysate.

https://doi.org/10.1371/journal.pbio.3000741.g010

seen in the expression of surface glycoproteins, GPEET and BARP. Overexpression of catalase during the RBP6^{OE} interfered with the programmed destabilization of GPEET, whose expression in vivo is controlled by the activity of mitochondrial enzymes [47]. BARP protein, a

hallmark molecule for the surface of salivary gland epimastigotes, however, was not detected in RBP6^{OE}_catalase cells (Fig 10E). These results suggest that the expression of catalase blocks the differentiation earlier than the transition from BARP-positive mature epimastigotes to metacyclic forms. The steady expression of the procyclin-containing coat in RBP6^{OE}_catalase cells was confirmed by flow cytometry analysis (Fig 10F). The changes in the expression of mitochondrial proteins were also detected, when RBP6^{OE}_catalase cells are compared to RBP6^{OE} cells. In RBP6^{OE}_catalase cells, in contrast to RBP6^{OE} cells, the expression of trCOIV and Rieske was not decreased and we did not detect changes in the expression of SCoAS and aconitase (Fig 10E). Similarly to the RBP6^{OE} cells, the $\Delta\psi$m was elevated in the RBP6^{OE}_catalase cells (Fig 10G), as was mitochondrial ROS production (Fig 10H). Cytosolic catalase, however, scavenged cytosolic ROS because no statistically significant increase in ROS measured by 2′,7′-dichlorofluorescein (DCF) was detected (Fig 10I).

In summary, our data suggest that RBP6 expression induces differentiation to epimastigote cells, accompanied by significant changes in mitochondrial metabolism. These alterations lead to increased production of ROS molecules, the levels of which seem to be important for efficient differentiation towards metacyclogenesis. Our results provide insights into the mechanisms of the parasite's mitochondrial rewiring and reinforce the emerging concept that mitochondria act as signaling organelles through the release of ROS to drive cellular differentiation.

Discussion

Our knowledge of molecular mechanisms driving metabolic rewiring of the *T. brucei* mitochondrion from a fully competent organelle capable of OxPhos to its metabolically reduced ATP-consuming version is limited. Until recently, investigations of the developmental program inside of the tsetse [19] required fly infections and laborious dissections [48]. This void has been partially overcome by introducing an in vitro differentiation system based on induced overexpression of the RBP6 protein [25]. Compared to this study, we achieved faster differentiation (higher levels of metacyclics at day 6 versus day 10) and higher efficacy (50% of metacyclics versus 32%) by growing the RBP6^{OE} cells in SDM-80 medium supplemented with a fetal bovine serum (FBS), which contains proline, not glucose, as the energy source. To prevent uptake of residual glucose molecules from the FBS, the RBP6^{OE} cells were grown in the presence of N-acetyl glucosamine (a non-transported glucose analog that binds the transporter). Because the efficacy of differentiation correlates with the expression of RBP6 [25], our results suggest that the absence of glucose increases RBP6 expression in vitro, and possibly RBP6 gene expression is controlled by environmental stimuli, as reported for other genes such as GPEET [27]. Proline and glutamine are the major amino acids in the haemolymph of the tsetse fly. In PCF mitochondria, proline is oxidized by several enzymatic reactions to α-ketoglutarate, a key anaplerotic substrate of the TCA cycle, preceding further metabolism to succinate and alanine [49]. Upon the RBP6 induction, we detected lower levels of proline and glutamate, which may suggest a higher consumption rate, with a concomitant increase in expression of enzymes involved in their catabolism and in the levels of the catabolic end product, alanine. Given that alanine is the predominant building block of the parasite's dynamic surface coat composed of BARP, the parasite might be satisfying its higher need for this amino acid. Interestingly, low alanine levels were detected in RNA interference-silenced Δ-pyrroline-5-carboxylate dehydrogenase (TbP5CDH) cells, which were incompetent in the efficient establishment of infection in the tsetse fly [50]. Higher activities of mitochondrial dehydrogenases together with the α-ketoglutarate entry to the TCA cycle should boost mitochondrial ATP production to support a higher need for cellular energy currency, which might be required for the energy-costly

reorganization of the kinetoplast from the posterior to the anterior side and back during the differentiation to epimastigotes and metacyclics [22]. In agreement with the proposed higher energy demand, we measured decreased steady-state levels of cellular ATP and arginine-phosphate with increased levels of ADP/ATP ratio.

Enzymatic activities of all TCA cycle enzymes have been detected in PCF trypanosomes [51], but direct experimental evidence revealed that the parasite does not use the full cycle but rather its partial reactions [52]. The metabolite α-ketoglutarate can be metabolized via pyruvate to alanine or acetate or just partially oxidized to malate, which is then diverted to feed gluconeogenesis, a process essential for in vivo development in the tsetse fly [53]. Four canonical TCA cycle enzymes, malate dehydrogenase, CS, aconitase, and IDH seem to have no metabolic role in trypanosomes grown either in glucose or proline/threonine [54,55]. Strikingly, all of these enzymes were strongly up-regulated during the RBP6 overexpression, with CS being the most affected (increased in expression by 3.5 to 6.5 times during the differentiation). Another remarkable observation was an up-regulation of a putative mitochondrial citrate transporter (Tb927.9.4310; S8 Fig) and high levels of intracellular citrate. This intermediate TCA cycle metabolite can be produced from either threonine-derived acetyl-CoA or by reductive carboxylation of α-ketoglutarate involving a reversal of NADP-dependent IDH and aconitase. In mammalian cells, the bifurcation of the TCA cycle to its reductive branch responds to a high α-ketoglutarate/citrate ratio and is crucial for the provision of lipogenic citrate during hypoxia, aglycemia, or when mitochondrial respiration is impaired. Citrate is then transported to the cytosol, where it is converted to lipogenic acetyl-CoA by the action of cytosolic ATP-dependent citrate lyase (ACL) [43,56]. *T. brucei* does not synthesize lipids from citrate-derived acetyl-CoA; instead, the parasite uses mitochondrial acetate for further lipogenesis and cholesterolgenesis [57]. Therefore, it is unlikely that citrate accumulation would yield a higher fatty acid synthesis. Instead, citrate can be converted to isocitrate by action of cytosolic aconitase [58] and further oxidized to α-ketoglutarate by glycosomal NAD/NADP-dependent IDH [59] to maintain NAD(P)H redox balance. Reduced NADPH is also critical for oxidative stress defense.

ROS (e.g., superoxide and H_2O_2) are important regulators of cellular homeostasis and play an essential role in cellular stress signaling, cell survival, differentiation, proliferation, and oncogenic transformation [5,6,60]. The ETC is thought to be the main source of mitochondrial ROS in a process that can be triggered by increased respiratory rate, changes in Δψm, and dysfunctional ETC complexes. ETC complexes I, II, and III contain sites wherein electrons can prematurely reduce oxygen, resulting in the formation of superoxide, which can be further converted to H_2O_2 by superoxide dismutases (SODs). In RBP6^{OE} cells, a significant increase in mitochondrial ROS production coincides with elevated expression of AOX and with rechanneling of electrons entering ETC to this oxidase. This observation, interestingly, contradicts the available literature on AOX expression in other systems. For example, the introduction of *Ciona intestinalis* AOX into mammalian cells with severe mitochondrial dysfunction minimized ROS production by bypassing complexes III and IV [61,62], re-activating the electron flow and thereby maintaining redox homeostasis for TCA cycle activity [63].

As electrons are redirected away from complex III, during RBP6^{OE}, complex I is the prominent candidate for the observed ROS production. Although the abundance of this complex was not affected by RBP6 overexpression, its activity should be increased because of the elevated levels of NADH-producing enzymes involved in proline oxidation. Complex I can produce ROS at the entrance flavin mononucleotide site in a manner dependent on the NAD^+/NADH ratio, independently of the coenzyme Q (CoQ) pool status [64], or by reverse electron transfer (RET) driven by succinate oxidation, substantial Δψm, and highly reduced CoQ pool [65]. While during the in vitro–induced differentiation, we observed conditions that could

support RET, without further studies defining the CoQ redox poise, the role of complex I in ROS production during $RBP6^{OE}$ will remain elusive.

ROS molecules also play an important role in the differentiation of the *T*. *brucei*–related parasite *Leishmania* [66]. Following infection of mammalian macrophages, *Leishmania* promastigotes differentiate to amastigotes. Intriguingly, ROS-generating drug menadione or H_2O_2 alone triggered promastigote differentiation to fully infective amastigote [66]. Here, we show that ROS molecules produced during the RBP6 overexpression are important for the completion of the developmental program, as overexpression of cytosolic catalase hindered the in vitro–induced differentiation. In vivo, catalase expression also impeded the ability of *T*. *brucei* to establish infection in the midgut of the tsetse fly [67]. The ROS-induced signal transduction pathway likely takes place in the cytosol, because only the cytosolic ROS levels were decreased to the original values upon the catalase induction. H_2O_2 molecules are prominent candidates for ROS signaling as they are long-lived, membrane-permeable, and induce reversible oxidation of thiols present in redox-sensitive proteins [68]. At the cellular level, in yeast, mitochondrion-induced H_2O_2 signal was shown to attenuate global protein synthesis by modulating the redox status of proteins involved in translation [69]. Intriguingly, translational attenuation is a hallmark of *T*. *brucei* metacyclic cells, which are quiescent (arrested in G1/G0 phase [26]). Multiple kinases and phosphatases are also susceptible to cysteine oxidation, with activity controlled by redox signals. ROS-induced activation of AMP-activated kinase alpha, for example, is important in inducing quiescence in stumpy BSF trypanosomes [70], and inactivation of *T*. *brucei* tyrosine phosphatase TbPTP1 is important for in vitro–induced differentiation of the bloodstream stumpy forms to PCF [71].

In summary, we have provided a global transcriptomic, proteomic, and metabolomic study of *T*. *brucei* cells undergoing an 8-day-long in vitro differentiation to metacyclic cells. Even though $RBP6^{OE}$ is genetically induced and thus an artificial route to the differentiation of the midgut PCF trypomastigote, our–omics and functional data constitute a unique set of resources to facilitate further interrogation of intrinsic and extrinsic signaling pathways to gain deeper insights into the differentiation processes underlying not only rewiring of mitochondrial metabolism and its consequences but also changes in gene expression of surface proteins, kDNA repositioning, and mitochondrial cristae remodeling.

Material and methods

RNA preparation, RNA-Seq, read processing, and data analysis

Total RNA was isolated from *T*. *brucei* at different stages (1×10^8 cells/replicate) using the miRNeasy Kit (Qiagen, Germany) according to the manufacturer's protocol. An additional DNase1 digestion step was performed to ensure that the samples were not contaminated with genomic DNA. RNA purity was assessed using the Agilent 2100 Bioanalyzer (Agilent Technologies, Santa Clara, CA). Next generation sequencing (NGS) library prep was performed with TruSeq Strand-Specific mRNA Library Prep with PolyA-Selection following Illuminas standard protocol. Libraries were profiled using the High Sensitivity DNA Kit on a 2100 Bioanalyzer and quantified using the Qubit dsDNA HS Assay Kit, in a Qubit 2.0 Fluorometer (Life technologies). Libraries were sequenced on an Illumina NextSeq 500 in the Genomics Core Facility at the Institute of Molecular Biology, Mainz, Germany. The RNA-Seq measurement yielded on average 11.1 M single reads of 75 nt per sample. We assessed the quality of the sequenced reads with fastqc [72] and dupRadar (https://doi.org/10.1186/s12859-016-1276-2). Spliced-leader sequences (CAATATAGTACAGAAACTGTTCTAATAATAGCGTTAGTT) were removed from the reads using cutadapt (https://doi.org/10.14806/ej.17.1.200) and then mapped to the *T*. *brucei* 11 megabase chromosomes (TriTrypDB version 36) using STAR

version 2.5.2b (https://doi.org/10.1093/bioinformatics/bts635), allowing up to 2 mismatches, a minimum intron length of 21, and keeping only uniquely aligned reads (on average, 75.1% of all reads). We then counted reads per gene using featureCounts (https://doi.org/10.1093/bioinformatics/btt656) from the subread package version 1.5.1 with default parameters and using the gene models provided by TriTrypDB version 36. For the differential expression analysis, we used R version 3.4.3 (http://www.R-project.org/) and DESeq2 version 1.18.1 (https://doi.org/10.1186/s13059-014-0550-8) to normalize, transform, and model the data. The counts were fitted to a Negative Binomial generalized linear model (GLM), and the Wald significance test was used to determine the differentially expressed genes between control and knockdown samples. Finally, RPKM values were calculated per gene using the library size-normalized FPM (robust counts per million mapped fragments) values from DESeq2. We applied automatic independent filtering to avoid testing genes, which were poor candidates of being differentially expressed (maximizes the number of adjusted *P* values less than alpha = 0.1). Differentially expressed mRNAs were identified using a threshold of Benjamini-Hochberg–corrected *P* values <0.05. GO enrichment analyses were performed using GO Term annotations TriTrypDB-36_TbruceiLister427_GO.gaf from TriTrypDB version 36 and Fisher's exact test. For the comparison to the transcriptome data of the previously published dataset of procyclic and metacyclic forms of *T. brucei* [26,31], the respective RNA-Seq raw data files were downloaded from SRA (Bioproject PRJNA381952) and processed exactly as described above for our data.

Mass spectrometry sample preparation, MS measurement, and proteomics data analysis

T. brucei at different stages (1×10^8 cells/replicate) were washed three times in 10 mL of phosphate-buffered saline (PBS) and lysed in 6% sodium dodecyl sulfate (SDS), 300 mM DTT, and 150 mM Tris-HCl (pH 6.8), 30% glycerol, and 0.02% Bromophenol Blue. Samples were loaded on a NOVEX NuPage 4%–12% gradient gel (Thermo Fisher Scientific, Waltham, MA), run for 10 minutes at 180 V, and stained with Coommassie G250. Each lane was cut and the minced gel pieces were transferred to an Eppendorf tube for destaining with 50% ethanol/50 mM ABC buffer pH 8.0. The gel pieces were dried and subsequently reduced (10 mM DTT/50 mM ABC buffer pH 8.0), alkylated (55 mM iodoacetamide/50 mM ABC buffer pH 8.0), and digested with 1 μg trypsin overnight at 37˚C. The tryptic peptides were eluted from the gel pieces with pure acetonitrile and stored on a StageTip [73].

The proteomic measurement was performed on a Q Exactive Plus mass spectrometer (Thermo Fisher Scientific, Waltham, MA) with an online-mounted C18-packed capillary column (New Objective, Woburn, MA) by eluting along a 225-minute gradient of 2% to 40% acetonitrile using an EasyLC 1000 uHPLC system (Thermo Fisher Scientific, Waltham, MA). The mass spectrometer was operated with a top10 data-dependent acquisition (DDA) mode.

Data analysis was performed in MaxQuant [74] version 1.5.2.8 using the tritrypDB-43_TbruceiLister427_2018_AnnotatedProteins database (16,869 entries) and standard settings, except activating the match between run feature and the label-free quantification (LFQ) algorithm. Protein groups marked as contaminants, reverse entries, and only identified by site were removed prior to bioinformatics analysis, as well as protein groups with less than 2 peptides (minimum 1 unique). Additional information like gene names and descriptions were extracted from the fasta header and attached to the individual protein groups. Additionally, we identified the best ortholog to Tb927 by using the inparanoid algorithm [75]. Imputation of missing values was performed using a beta distribution within 0.2 and 2.5 percentile of measured values for individual replicates separately. PCA plot was created using R package ggbiplot-0.55; the heatmap was produced by heatmap.2 command from gplots-3.0.1.1 package.

Clustering was performed using the pamk function from fpc-2.2–1 package with "usepam" deactivated and a "krange" between 5 and 9. The algorithm performs a partitioning around medoids clustering of large datasets, with the optimal number of clusters estimated by optimum average silhouette width. GO enrichment was performed using Fisher's Exact Test, and *P* values were corrected using the Benjamini-Hochberg method.

Trypanosome culture conditions and generation of cell lines

T. brucei PCF cells strains 29.13, transgenic for T7 RNA polymerase and the tetracycline repressor [76], were grown in vitro at 27˚C in SDM-80 medium containing hemin (7.5 mg/mL) and 10% FBS. The pLew100v5 vector for RBP6 expression (a kind gift from Prof. Tschudi) was linearized with NotI enzyme and transfected into the 29.13 cell line. RBP6^{OE} cells were adapted to grow in SDM-80 medium containing no glucose and further supplemented with 50 mM N-acetyl glucose-amine to block uptake of residual glucose molecules from 10% FBS. The induction of ectopically expressed RBP6 protein was triggered by the addition of 10 μg/mL of tetracycline into the medium. Cell densities were measured using the Z2 Cell Counter (Beckman Coulter, Brea, CA). Throughout the analyses, cells were maintained in the exponential mid-log growth phase (between 2×10^6 and 1×10^7 cells/mL). The RBP6^{OE}_catalase cell line was generated using pT7v5 plasmid containing a *C. fasciculata* catalase ORF sequence (cCAT TriTrypDB gene ID = CFAC1_250006200) [67]. The pT7v5_catalase plasmid was linearized with NotI and transfected into RBP6^{OE} cells. The activity of the catalase was detected using a simple visual activity test. A total of 5×10^7 parasites were resuspended in 100 μL of PBS and placed on a microscopic slide. A volume of 20 μL of 3% H_2O_2 was added to the cells, mixed, and the formation of oxygen (bubbles formation) was monitored by eye.

Isolation of mitochondrial vesicles, BNE, and high-resolution clear-native PAGE

BNE of mitochondria lysed with dodecylmaltoside, followed by in-gel activity staining, was adapted from published protocols [11]. Briefly, the mitochondrial vesicles from 5×10^8 cells were isolated by hypotonic cell lysis, and mitochondria were resuspended in a buffer (750 mM aminocaproic acid, 50 mM Bis-Tris, 0.5 mM EDTA pH 7.0, supplemented with the complete EDTA-free protease inhibitor cocktail [Roche, Basel, Switzerland]) and lysed for one hour on ice with 2% dodecylmaltosid. The samples were spun down at 16,000*g* for 30 minutes and the cleared lysate protein concentrations were determined by a BCA assay. Mitochondrial lysate (20 μg) was mixed with a loading dye (50 mM ACA, 0.5% [w/v] Coomassie Brilliant Blue G-250). After electrophoresis (3 hours, 150 V, 4˚C), the resolved mitochondrial lysates were transferred onto a PVDF membrane and probed with selected antibodies, or the native gels were directly used for in-gel activity staining of the respiratory complexes. Specific staining of complex III was achieved by incubating the gel in complex III assay buffer (1 mg/mL of 3,3′ diaminobenzidine, 50 mM sodium phosphate pH 7.4, 75 mg/mL sucrose) by slow agitation overnight. Complex IV staining was achieved using a reaction buffer (50 mM phosphate buffer pH 7.4, 1 mg/mL 3,3′diaminobenzidine, 24 U/mL catalase, 1 mg/mL cytochrome *c*, 75 mg/mL sucrose) overnight. Complex V was visualized using ATPase reaction buffer (35 mM Tris-HCl pH 8.0, 270 mM glycine, 19 mM $MgSO_4$, 0.3% [w/v] $Pb(NO_3)_2$, 11 mM ATP) for overnight incubation by slow agitation. Mitochondrial samples for complex II detection were treated with loading dye (0.1% Ponceau-S, 50% glycerol) and they were run on 3%–12% gradient high-resolution clear-native gels (hrCNE). Specific staining was achieved by incubating the gel in staining solution: 5 mM Tris HCl 7.4, 20 mM sodium succinate, 0.2 mM phenazine methasulfate, and 2.5 mg/mL nitrotetrazolium blue chloride.

SDS-PAGE and western blot

Protein samples were separated on SDS-PAGE, blotted onto a PVDF membrane (Thermo Fisher Scientific, Waltham, MA), and probed with the appropriate monoclonal antibody (mAb) or polyclonal antibody (pAb). This was followed by incubation with a secondary HRP-conjugated anti-rabbit or anti-mouse antibody (1:2,000, BioRad). Proteins were visualized using the Pierce ECL system on a ChemiDoc instrument ((BioRad, Hercules, CA)). The PageRuler prestained protein standard (Fermentas, Vilnius, Lithuania) was used to determine the size of the detected bands. Several antibodies (anti-Rieske, anti-trCOIV, anti-SCoAS, anti-aconitase, and anti-NDUFA) were prepared for the purpose of this study. The open reading frames of the respective genes without their predicted mitochondrial localization signal were cloned into the *E. coli* expression plasmid, pSKB3. The proteins were overexpressed in BL21 *Escherichia coli* cells and purified under native or denatured conditions. Antigens were sent to Davids Biotechnologie (Regensburg, Germany) for pAb production. Primary antibodies used in this study were as follows: mAb anti-mitochondrial hsp70 (1:2,000) [77], pAb anti-RBP6 (1:5,000, a generous gift from Prof. Tschudi), pAb anti-BARP and GPEET (1:2,000, 1:1,000, respectively, a generous gift from Prof. Roditi), mAb AOX (1:100) (a generous gift from Prof. Chaudhuri), mAb41-PDH (1:100) [77], pAb anti-Rieske (1:1,000, commercially produced for the purpose of this study), pAb trCoIV (1:1,000, commercially produced for the purpose of this study), pAb anti-subunit beta, F_1-ATPase (1:2,000) [78], pAb anti-SCoAS (1:1,000, commercially produced for the purpose of this study), pAb anti-aconitase (1:2,000, commercially produced for the purpose of this study), pAb anti-AAC (1:2,000) [79], anti-SDH1 [80], pAb anti-TbIF1 [39], pAb anti-PiC (1:500) [79], pAb anti-NDUFA (1:1,000, commercially produced for the purpose of this study).

Cellular ROS, mitochondrial ROS, and mitochondrial membrane potential (Δψm) measurements

The cellular and mitochondrial ROS levels were determined using the 2′,7′-dichlorofluorescein diacetate (H_2DCFHDA) and MitoSOX Red Mitochondrial Superoxide dyes (Thermo Fisher Scientific Waltham, MA), respectively. Cells in the exponential growth phase were treated with 10 μM H_2DCFHDA or with 5 μM MitoSOX for 30 minutes at 27˚C. A total of 1×10^7 cells were pelleted (1,300*g*, 10 minutes, RT), washed with 1 mL of PBS (pH 7.4), resuspended in 2 mL of PBS, and immediately analyzed by flow cytometry (BD FACS Canto II Instrument, BD Biosciences, San Jose, CA). The Δψm was determined using the red-fluorescent stain tetramethylrhodamine ethyl ester TMRE (Thermo Fisher Scientific Waltham, MA). Cells in the exponential growth phase were stained with 60 nM of the dye for 30 minutes at 27˚C. Cells were pelleted (1,300*g*, 10 minutes, RT), resuspended in 2 mL of PBS (pH 7.4), and immediately analyzed by flow cytometry (BD FACS Canto II Instrument). Treatment with the protonophore FCCP (20 μM) was used as a control for mitochondrial membrane depolarization. To evaluate the effect of oligomycin and KCN on Δψm, the cells were incubated with 2.5 ug/mL of oligomycin or 0.5 mM of KCN in the presence of TMRE for 30 minutes at 27˚C. For all samples, 10,000 events were collected. Data were evaluated using BD FACSDiva software (BD Biosciences, San Jose, CA).

In situ Δψm measurement

Estimation of the Δψm in situ was performed spectrofluorometrically using the indicating dye safranine O (Sigma-Aldrich, St. Louis, MO). *T. brucei* PCF cells (2×10^7 cells/mL) were resuspended in a reaction buffer containing the following: 200 mM sucrose, 10 mM HEPES-Na

(pH 7.0), 2 mM succinate, 1 mM $MgCl_2$, and 1 mM EGTA. The reaction was induced with digitonin (40 μM), while NaCN (1 mM) and FCCP (5 μM) were injected at specific time points throughout the assay. Changes in the amount of fluorescence over time were detected on an Infinite M200 microplate reader (TECAN) (excitation = 496 nm; emission = 586 nm). Values were normalized according to the following equation: normalized $(E_i) = E_i - E_{min}/E_{max} - E_{min}$ (E_{min} − the minimum value for variable E, E_{max} − the maximum value for variable E).

Measurement of oxygen consumption

The oxygen consumption rate was assessed at 27˚C using 2×10^7 cells per Oroboros O2K oxygraph chamber. The endogenous respiration of cells, as well as the substrate-induced respiration, were measured in MiR05 medium (Oroboros, Innsbruck, Austria). The following respiratory substrates were used: 10 mM succinate, 5 mM proline, or 10 mM glycerol-3-phosphate. The SHAM-sensitive respiration was determined by injecting 250 μM SHAM, while the KCN sensitive respiration was assessed with 1 mM KCN. If needed, the cells were permeabilized with 4 ug of digitonin (Sigma-Aldrich, St. Louis, MO).

ATP production assay

ATP production was measured as described [42]. Briefly, crude mitochondrial fractions from the $RBP6^{OE}$ cells were obtained by digitonin extraction. ATP production in these samples was induced by the addition of 5 mM of indicated substrates (succinate, α-ketoglutarate, and glycerol 3-phosphate) and 67 μM ADP. The mitochondrial preparations were preincubated for 10 minutes on ice with the inhibitor malonate (6.7 mM) or KCN (1 mM). The concentration of ATP was determined by a luminometer (Orion II; Berthold Detection Systems, Pforzheim, Germany) using the ATP Bioluminescence assay kit CLS II (Roche Applied Science, Basel, Switzerland).

Cell morphology and immunofluorescence assay

For the immunofluorescence assay, the cells were first treated with 5 mM bathophenanthroline disulphonic acid (BPS), a metalloprotease inhibitor, to stabilize the surface proteins 24 hours prior harvesting [28]. Then, cells were harvested and fixed in 3.7% formaldehyde/PBS for 10 minutes at room temperature. The cell suspension was applied to the polylysine-coated coverslip (Sigma-Aldrich, St. Louis, MO). Then, the coverslips were incubated with primary pAb anti-procyclin (1:400) and anti-BARP (1:400) followed by incubation with Alexa Fluor 488–conjugated goat anti-rabbit secondary antibody. To detect metacyclic cells, the RBP6-induced cells (5×10^6) were resuspended in 80 μL media and supplemented with 20 μL of Dextran, Alexa Fluor 568; 10,000 Mw (Thermo Fisher Scientific Waltham, MA). After 1 hour, the cells were fixed by formaldehyde, applied to the polylysine-coated coverslip. The coverslips were then mounted on a glass slide with ProLong Gold Antifade Mountant (Thermo Fisher Scientific Waltham, MA). Images were taken with the fluorescent microscope (Axioplan 2 imaging Universal microscope, Zeiss, Oberkochen, Germany) with a CCD camera (Olympus DP73). To determine cells by their morphology, 100 cells were counted and assigned to a certain cell type based on their size, shape, position of the kinetoplast relative to the nucleus, and position of the kinetoplast relative to the posterior end of the cell (S1 Data).

Flow cytometry analysis

The 2×10^7 cells were treated with 5 mM BPS, harvested (1,500*g*, 10 minutes, RT), and resuspended in 200 μL of 1× PBS pH 7.4. The cells were fixed by the addition of 7.4% formaldehyde

in 1× PBS pH 7.4 for 15 minutes at RT. Subsequently, the cells were washed 3 times in 1× PBS, labeled with polyclonal rabbit anti-BARP (1:400) and anti-procyclin (1:400) in 1% BSA for 1 hour at RT, followed by staining with Alexa Fluor 488–conjugated goat α-rabbit (1:400) antibody in 1% BSA. Samples were then washed, resuspended in 1 mL of 1× PBS pH 7.4 and analyzed by flow cytometry. Data were evaluated using BD FACSDiva software.

LC-MS metabolomic analysis

For the LC-MS metabolomic analysis, the sample extraction was performed as described previously [81,82]. Briefly, 5×10^7 cells were used for each sample. Cells were rapidly cooled in a dry ice/ethanol bath to 4˚C, centrifuged at 1,300*g*, 4˚C for 10 minutes, washed with 1× PBS, and resuspended in extraction solvent (chloroform:methanol:water, 1:3:1 volume ratio). Following shaking for 1 hour at 4˚C, samples were centrifuged at 16,000*g* at 4˚C for 10 minutes, and the supernatant was collected and stored at −80˚C. The analysis was performed using separation on 150 × 4.6 mm ZIC-pHILIC (Merck, Kenilworth, NJ) on Dionex UltiMate 3000 RSLC (Thermo Fisher Scientific Waltham, MA) followed by mass detection on an Orbitrap Fusion mass spectrometer (Thermo Fisher Scientific Waltham, MA) at Glasgow Polyomics.

Statistical analysis

The number of replicates, controls, and statistical tests are in accordance with published studies employing comparable techniques and are generally accepted in the field. Statistical differences were analyzed with Prism software (version 8.2.1, GraphPad software). Comparisons of two groups were calculated with two-tailed paired *t* test. A *P* value of less than 0.05 was considered statistically significant. Quantitative mass spectrometry experiments were performed in four biological replicates.

Supporting information

S1 Fig. PCA shows high reproducibility of replicates and consecutive progression of RBP6^{OE}-induced differentiation that can be described by the first two components, PC1 and PC2. PCA, principal component analysis; RBP6, RNA binding protein 6.
(TIF)

S2 Fig. RBP6^{OE} transcriptomes highly correlate with the published time course of RBP6 induction [31]. The genes with fold change larger than 2 or smaller than 0.5 (with Benjamini-Hochberg–corrected *P* values smaller than 0.05) are highlighted in red. RBP6, RNA binding protein 6.
(PDF)

S3 Fig. RBP6^{OE} transcriptomes become increasingly more similar to pure metacyclics [26]. The Pearson correlation values reflect the similarity of the transcriptomes of the respective time points to the two trypomastigote types—procyclic and metacyclic forms. RBP6, RNA binding protein 6.
(PNG)

S4 Fig. Differentiation proteomics. The heatmap encompassing 5,227 z-scored LFQ quantified protein groups illustrates significant proteome remodeling during RBP6-induced differentiation. LFQ, label-free quantification; RBP6, RNA binding protein 6.
(PDF)

S5 Fig. Differentiation proteomics. PCA of the proteomic samples shows the reproducibility of replicates. PCA, principal component analysis.
(PDF)

S6 Fig. Heatmap showing log2 fold change of average LFQ intensities of all complex I, III, IV, and V subunits identified in RBP6-induced samples compared to uninduced (day 0). The color key differs for each map and is always located below the heatmap. LFQ, label-free quantification; RBP6, RNA binding protein 6.
(JPG)

S7 Fig. Oxygen consumption rates in live RBP6^{OE} cells in the absence of substrate. The black lines show a decreasing concentration of oxygen in the buffer (left y-axis), while the red line shows O_2 flux per cell (right y-axis). Inhibition of AOX-mediated respiration was induced by addition of SHAM. The addition of KCN inhibited respiration via complex IV. AOX, alternative oxidase; KCN, potassium cyanide; RBP6, RNA binding protein 6; SHAM, salicylhydroxamic acid.
(PDF)

S8 Fig. Heatmap showing log2 fold change of average LFQ intensities of selected proteins involved in redox metabolism and mitochondrial carrier proteins identified in RBP6-induced samples compared to uninduced (day 0). The color key differs for each map and is located below the heatmap. LFQ, label-free quantification; RBP6, RNA binding protein 6.
(PDF)

S1 Table. RNA-Seq results for RBP6^{OE} cells undergoing differentiation. Sheet 1 contains gene IDs for *T. brucei* strain 427 (https://tritrypdb.org/tritrypdb/), their respective best orthologs from *T. brucei* strain 927, and RPKM values for each sample. The experiment was performed in quadruplicates for time points 0, 2, 3, 4, 6, and 8 days upon RBP6 induction. Analyses using R version 3.4.3 and DESeq2 version 1.18.1 were used to identify differentially expressed mRNAs, which were identified using a threshold of Benjamini-Hochberg–corrected *P* values <0.05. RBP6, RNA binding protein 6; RPKM, reads per kilobase of transcript, per million mapped reads.
(XLSX)

S2 Table. Cluster assignment—transcriptomics. Gene IDs belonging to four different clusters from time-course expression profiling based on K-medoids. GO enrichment analyses performed using GO Term annotations TriTrypDB-36_TbruceiLister427_GO.gaf from TriTrypDB version 36 and Fisher's exact test. GO, Gene Ontology.
(XLSX)

S3 Table. Comparison of RNA-Seq data of RBP6^{OE} cells (time points 0, 2, 3, 4, and 6 days) with the time course of RBP6 induction published in [31]. Sheets contains gene IDs for *T. brucei* strain 427 (https://tritrypdb.org/tritrypdb/), their respective best orthologs from *T. brucei* strain 927, log2 fold change, Benjamini-Hochberg–corrected *P* values, and RPKM values for each sample. RBP6, RNA binding protein 6; RPKM, reads per kilobase of transcript, per million mapped reads.
(XLSX)

S4 Table. Proteomic analysis of RBP6^{OE} cells undergoing differentiation. Sheet 1 contains Tb427 and Tb927 gene IDs and descriptions for 5,227 protein groups identified by a minimum of 2 peptides (1 unique) and present in at least two out of four replicates. Other sheets contain protein groups differentially expressed (log2 fold change <-1, log2 fold change >1). RBP6,

RNA binding protein 6.
(XLSX)

S5 Table. Cluster assignment—proteomics. Gene IDs belonging to six different clusters from time-course expression profiling based on K-medoids. GO enrichment analyses performed using GO Term annotations TriTrypDB-36_TbruceiLister427_GO.gaf from TriTrypDB version 36 and Fisher's exact test. GO, Gene Ontology.
(XLSX)

S6 Table. Metabolomic analysis of RBP6^{OE} cells undergoing differentiation. LC-MS metabolomic data. LC-MS, liquid chromatography–mass spectrometry; RBP6, RNA binding protein 6.
(XLSX)

S1 Video. In vivo measurements of the catalase activity. The activity of the catalase was detected using a simple visual activity test. A total of 5×10^7 parasites were resuspended in 100 μL of PBS and placed on a microscopic slide. A total of 20 μL of 3% H_2O_2 was added to the cells, mixed, and the formation of oxygen (bubbles formation) was monitored visually. PBS, phosphate-buffered saline.
(MP4)

S1 Data. All experimental data used to generate graphs of this manuscript.
(XLSX)

S1 Raw Images. Original images supporting blot results reported in Figs 1, 3, 6, 7 and 10.
(PDF)

Acknowledgments

We thank Martina Slapničková, Jasmin Cartano, and Anja Freiwald for technical assistance.

Author Contributions

Conceptualization: Eva Doleželová, Brian Panicucci, Christian J. Janzen, Alena Zíková.

Data curation: Eva Doleželová, Michaela Kunzová, Mario Dejung, Michal Levin, Brian Panicucci, Clément Regnault, Christian J. Janzen, Michael P. Barrett, Falk Butter, Alena Zíková.

Formal analysis: Mario Dejung, Michal Levin, Clément Regnault, Christian J. Janzen, Michael P. Barrett, Falk Butter, Alena Zíková.

Funding acquisition: Michael P. Barrett, Falk Butter, Alena Zíková.

Investigation: Eva Doleželová, Michaela Kunzová, Brian Panicucci.

Resources: Michael P. Barrett, Falk Butter, Alena Zíková.

Supervision: Alena Zíková.

Validation: Eva Doleželová, Alena Zíková.

Visualization: Alena Zíková.

Writing – original draft: Mario Dejung, Michal Levin, Michael P. Barrett, Falk Butter, Alena Zíková.

Writing – review & editing: Mario Dejung, Michael P. Barrett, Falk Butter, Alena Zíková.

References

1. Zheng J. Energy metabolism of cancer: Glycolysis versus oxidative phosphorylation (Review). Oncology letters. 2012; 4(6):1151–7. Epub 2012/12/12. https://doi.org/10.3892/ol.2012.928 PMID: 23226794; PubMed Central PMCID: PMC3506713.
2. Vander Heiden MG, Cantley LC, Thompson CB. Understanding the Warburg effect: the metabolic requirements of cell proliferation. Science. 2009; 324(5930):1029–33. Epub 2009/05/23. https://doi.org/10.1126/science.1160809 PMID: 19460998; PubMed Central PMCID: PMC2849637.
3. Mills EL, Kelly B, Logan A, Costa ASH, Varma M, Bryant CE, et al. Succinate Dehydrogenase Supports Metabolic Repurposing of Mitochondria to Drive Inflammatory Macrophages. Cell. 2016; 167(2):457–70 e13. Epub 2016/09/27. https://doi.org/10.1016/j.cell.2016.08.064 PMID: 27667687; PubMed Central PMCID: PMC5863951.
4. Murphy MP, O'Neill LAJ. Krebs Cycle Reimagined: The Emerging Roles of Succinate and Itaconate as Signal Transducers. Cell. 2018; 174(4):780–4. Epub 2018/08/11. https://doi.org/10.1016/j.cell.2018.07.030 PMID: 30096309.
5. Tretter L, Patocs A, Chinopoulos C. Succinate, an intermediate in metabolism, signal transduction, ROS, hypoxia, and tumorigenesis. Biochim Biophys Acta. 2016; 1857(8):1086–101. Epub 2016/03/15. https://doi.org/10.1016/j.bbabio.2016.03.012 PMID: 26971832.
6. Hamanaka RB, Chandel NS. Mitochondrial reactive oxygen species regulate cellular signaling and dictate biological outcomes. Trends Biochem Sci. 2010; 35(9):505–13. Epub 2010/05/01. https://doi.org/10.1016/j.tibs.2010.04.002 PMID: 20430626; PubMed Central PMCID: PMC2933303.
7. Smith TK, Bringaud F, Nolan DP, Figueiredo LM. Metabolic reprogramming during the Trypanosoma brucei life cycle. F1000Research. 2017; 6. Epub 2017/06/20. https://doi.org/10.12688/f1000research.10342.2 PMID: 28620452; PubMed Central PMCID: PMC5461901.
8. Roditi I, Schumann G, Naguleswaran A. Environmental sensing by African trypanosomes. Curr Opin Microbiol. 2016; 32:26–30. Epub 2016/05/01. https://doi.org/10.1016/j.mib.2016.04.011 PMID: 27131101.
9. Bochud-Allemann N, Schneider A. Mitochondrial substrate level phosphorylation is essential for growth of procyclic Trypanosoma brucei. J Biol Chem. 2002; 277(36):32849–54. Epub 2002/07/04. https://doi.org/10.1074/jbc.M205776200 [pii]. PMID: 12095995.
10. van Hellemond JJ, Opperdoes FR, Tielens AG. The extraordinary mitochondrion and unusual citric acid cycle in Trypanosoma brucei. Biochem Soc Trans. 2005; 33(Pt 5):967–71. Epub 2005/10/26. https://doi.org/10.1042/BST20050967 PMID: 16246022.
11. Acestor N, Zikova A, Dalley RA, Anupama A, Panigrahi AK, Stuart KD. Trypanosoma brucei mitochondrial respiratome: composition and organization in procyclic form. Mol Cell Proteomics. 2011; 10(9):M110 006908. Epub 2011/05/26. M110.006908 [pii] https://doi.org/10.1074/mcp.M110.006908 PMID: 21610103; PubMed Central PMCID: PMC3186196.
12. Zikova A, Schnaufer A, Dalley RA, Panigrahi AK, Stuart KD. The F(0)F(1)-ATP synthase complex contains novel subunits and is essential for procyclic Trypanosoma brucei. PLoS Pathog. 2009; 5(5):e1000436. Epub 2009/05/14. https://doi.org/10.1371/journal.ppat.1000436 PMID: 19436713; PubMed Central PMCID: PMC2674945.
13. Guerra DG, Decottignies A, Bakker BM, Michels PA. The mitochondrial FAD-dependent glycerol-3-phosphate dehydrogenase of Trypanosomatidae and the glycosomal redox balance of insect stages of Trypanosoma brucei and Leishmania spp. Mol Biochem Parasitol. 2006; 149(2):155–69. Epub 2006/06/30. https://doi.org/10.1016/j.molbiopara.2006.05.006 PMID: 16806528.
14. Zikova A, Verner Z, Nenarokova A, Michels PAM, Lukes J. A paradigm shift: The mitoproteomes of procyclic and bloodstream Trypanosoma brucei are comparably complex. PLoS Pathog. 2017; 13(12):e1006679. Epub 2017/12/22. https://doi.org/10.1371/journal.ppat.1006679 PMID: 29267392; PubMed Central PMCID: PMC5739487.
15. Schnaufer A, Clark-Walker GD, Steinberg AG, Stuart K. The F1-ATP synthase complex in bloodstream stage trypanosomes has an unusual and essential function. EMBO J. 2005; 24(23):4029–40. Epub 2005/11/05. 7600862 [pii] https://doi.org/10.1038/sj.emboj.7600862 PMID: 16270030; PubMed Central PMCID: PMC1356303.
16. Subrtova K, Panicucci B, Zikova A. ATPaseTb2, a Unique Membrane-bound FoF1-ATPase Component, Is Essential in Bloodstream and Dyskinetoplastic Trypanosomes. PLoS Pathog. 2015; 11(2):e1004660. Epub 2015/02/26. https://doi.org/10.1371/journal.ppat.1004660 PMID: 25714685.
17. Matthews KR. 25 years of African trypanosome research: From description to molecular dissection and new drug discovery. Mol Biochem Parasitol. 2015; 200(1–2):30–40. Epub 2015/03/05. https://doi.org/10.1016/j.molbiopara.2015.01.006 PMID: 25736427; PubMed Central PMCID: PMC4509711.

18. Naguleswaran A, Doiron N, Roditi I. RNA-Seq analysis validates the use of culture-derived Trypanosoma brucei and provides new markers for mammalian and insect life-cycle stages. BMC Genomics. 2018; 19(1):227. Epub 2018/04/03. https://doi.org/10.1186/s12864-018-4600-6 PMID: 29606092; PubMed Central PMCID: PMC5879877.

19. Sharma R, Gluenz E, Peacock L, Gibson W, Gull K, Carrington M. The heart of darkness: growth and form of Trypanosoma brucei in the tsetse fly. Trends Parasitol. 2009; 25(11):517–24. Epub 2009/09/15. https://doi.org/10.1016/j.pt.2009.08.001 PMID: 19747880; PubMed Central PMCID: PMC3770903.

20. Dean S, Marchetti R, Kirk K, Matthews KR. A surface transporter family conveys the trypanosome differentiation signal. Nature. 2009; 459(7244):213–7. Epub 2009/05/16. https://doi.org/10.1038/nature07997 PMID: 19444208; PubMed Central PMCID: PMC2685892.

21. Rose C, Casas-Sanchez A, Dyer NA, Solorzano C, Beckett AJ, Middlehurst B, et al. Trypanosoma brucei colonizes the tsetse gut via an immature peritrophic matrix in the proventriculus. Nature microbiology. 2020. Epub 2020/04/22. https://doi.org/10.1038/s41564-020-0707-z PMID: 32313202.

22. Rotureau B, Van Den Abbeele J. Through the dark continent: African trypanosome development in the tsetse fly. Frontiers in cellular and infection microbiology. 2013; 3:53. Epub 2013/09/26. https://doi.org/10.3389/fcimb.2013.00053 PMID: 24066283; PubMed Central PMCID: PMC3776139.

23. Dyer NA, Rose C, Ejeh NO, Acosta-Serrano A. Flying tryps: survival and maturation of trypanosomes in tsetse flies. Trends Parasitol. 2013; 29(4):188–96. Epub 2013/03/20. https://doi.org/10.1016/j.pt.2013.02.003 PMID: 23507033.

24. Rotureau B, Subota I, Buisson J, Bastin P. A new asymmetric division contributes to the continuous production of infective trypanosomes in the tsetse fly. Development. 2012; 139(10):1842–50. Epub 2012/04/12. https://doi.org/10.1242/dev.072611 PMID: 22491946.

25. Kolev NG, Ramey-Butler K, Cross GAM, Ullu E, Tschudi C. Developmental Progression to Infectivity in Trypanosoma brucei Triggered by an RNA-Binding Protein. Science. 2012; 338(6112):1352–3. https://doi.org/10.1126/science.1229641 ISI:000311991200069. PMID: 23224556

26. Christiano R, Kolev NG, Shi H, Ullu E, Walther TC, Tschudi C. The proteome and transcriptome of the infectious metacyclic form of Trypanosoma brucei define quiescent cells primed for mammalian invasion. Mol Microbiol. 2017; 106(1):74–92. Epub 2017/07/26. https://doi.org/10.1111/mmi.13754 PMID: 28742275; PubMed Central PMCID: PMC5607103.

27. Vassella E, Den Abbeele JV, Butikofer P, Renggli CK, Furger A, Brun R, et al. A major surface glycoprotein of trypanosoma brucei is expressed transiently during development and can be regulated post-transcriptionally by glycerol or hypoxia. Genes Dev. 2000; 14(5):615–26. Epub 2000/03/16. PMID: 10716949; PubMed Central PMCID: PMC316419.

28. Urwyler S, Studer E, Renggli CK, Roditi I. A family of stage-specific alanine-rich proteins on the surface of epimastigote forms of Trypanosoma brucei. Mol Microbiol. 2007; 63(1):218–28. Epub 2007/01/19. https://doi.org/10.1111/j.1365-2958.2006.05492.x PMID: 17229212.

29. Knusel S, Roditi I. Insights into the regulation of GPEET procyclin during differentiation from early to late procyclic forms of Trypanosoma brucei. Mol Biochem Parasitol. 2013; 191(2):66–74. Epub 2013/10/01. https://doi.org/10.1016/j.molbiopara.2013.09.004 PMID: 24076427.

30. Vigneron A, O'Neill MB, Weiss BL, Savage AF, Campbell OC, Kamhawi S, et al. Single-cell RNA sequencing of Trypanosoma brucei from tsetse salivary glands unveils metacyclogenesis and identifies potential transmission blocking antigens. Proc Natl Acad Sci U S A. 2020; 117(5):2613–21. Epub 2020/01/23. https://doi.org/10.1073/pnas.1914423117 PMID: 31964820; PubMed Central PMCID: PMC7007551.

31. Shi H, Butler K, Tschudi C. A single-point mutation in the RNA-binding protein 6 generates Trypanosoma brucei metacyclics that are able to progress to bloodstream forms in vitro. Mol Biochem Parasitol. 2018; 224:50–6. Epub 2018/07/29. https://doi.org/10.1016/j.molbiopara.2018.07.011 PMID: 30055184; PubMed Central PMCID: PMC6147148.

32. Cox J, Hein MY, Luber CA, Paron I, Nagaraj N, Mann M. Accurate proteome-wide label-free quantification by delayed normalization and maximal peptide ratio extraction, termed MaxLFQ. Mol Cell Proteomics. 2014; 13(9):2513–26. Epub 2014/06/20. https://doi.org/10.1074/mcp.M113.031591 PMID: 24942700; PubMed Central PMCID: PMC4159666.

33. Huang G, Vercesi AE, Docampo R. Essential regulation of cell bioenergetics in Trypanosoma brucei by the mitochondrial calcium uniporter. Nature communications. 2013; 4:2865. Epub 2013/12/07. https://doi.org/10.1038/ncomms3865 PMID: 24305511; PubMed Central PMCID: PMC3868461.

34. Huang G, Docampo R. The Mitochondrial Ca(2+) Uniporter Complex (MCUC) of Trypanosoma brucei Is a Hetero-oligomer That Contains Novel Subunits Essential for Ca(2+) Uptake. mBio. 2018; 9(5). Epub 2018/09/20. https://doi.org/10.1128/mBio.01700-18 PMID: 30228243; PubMed Central PMCID: PMC6143741.

35. Gnipova A, Panicucci B, Paris Z, Verner Z, Horvath A, Lukes J, et al. Disparate phenotypic effects from the knockdown of various Trypanosoma brucei cytochrome c oxidase subunits. Mol Biochem Parasitol. 2012; 184(2):90–8. Epub 2012/05/10. https://doi.org/10.1016/j.molbiopara.2012.04.013 PMID: 22569586.

36. Horvath A, Horakova E, Dunajcikova P, Verner Z, Pravdova E, Slapetova I, et al. Downregulation of the nuclear-encoded subunits of the complexes III and IV disrupts their respective complexes but not complex I in procyclic Trypanosoma brucei. Mol Microbiol. 2005; 58(1):116–30. Epub 2005/09/17. MMI4813 [pii] https://doi.org/10.1111/j.1365-2958.2005.04813.x PMID: 16164553.

37. Chinopoulos C, Adam-Vizi V. Mitochondria as ATP consumers in cellular pathology. Biochim Biophys Acta. 2010; 1802(1):221–7. Epub 2009/09/01. https://doi.org/10.1016/j.bbadis.2009.08.008 PMID: 19715757.

38. Campanella M, Casswell E, Chong S, Farah Z, Wieckowski MR, Abramov AY, et al. Regulation of mitochondrial structure and function by the F1Fo-ATPase inhibitor protein, IF1. Cell Metab. 2008; 8(1):13–25. Epub 2008/07/02. S1550-4131(08)00172-1 [pii] https://doi.org/10.1016/j.cmet.2008.06.001 PMID: 18590689.

39. Panicucci B, Gahura O, Zikova A. Trypanosoma brucei TbIF1 inhibits the essential F1-ATPase in the infectious form of the parasite. PLoS Negl Trop Dis. 2017; 11(4):e0005552. Epub 2017/04/18. https://doi.org/10.1371/journal.pntd.0005552 PMID: 28414727; PubMed Central PMCID: PMC5407850.

40. Verner Z, Cermakova P, Skodova I, Kriegova E, Horvath A, Lukes J. Complex I (NADH:ubiquinone oxidoreductase) is active in but non-essential for procyclic Trypanosoma brucei. Mol Biochem Parasitol. 2011; 175(2):196–200. Epub 2010/11/16. S0166-6851(10)00280-X [pii] https://doi.org/10.1016/j.molbiopara.2010.11.003 PMID: 21074578.

41. Opperdoes FR, Michels PA. Complex I of Trypanosomatidae: does it exist? Trends Parasitol. 2008; 24(7):310–7. Epub 2008/06/07. S1471-4922(08)00135-9 [pii] https://doi.org/10.1016/j.pt.2008.03.013 PMID: 18534909.

42. Allemann N, Schneider A. ATP production in isolated mitochondria of procyclic Trypanosoma brucei. Mol Biochem Parasitol. 2000; 111(1):87–94. Epub 2000/11/23. S0166-6851(00)00303-0 [pii]. https://doi.org/10.1016/s0166-6851(00)00303-0 PMID: 11087919.

43. Chen Q, Kirk K, Shurubor YI, Zhao D, Arreguin AJ, Shahi I, et al. Rewiring of Glutamine Metabolism Is a Bioenergetic Adaptation of Human Cells with Mitochondrial DNA Mutations. Cell Metab. 2018; 27(5):1007–25 e5. Epub 2018/04/17. https://doi.org/10.1016/j.cmet.2018.03.002 PMID: 29657030; PubMed Central PMCID: PMC5932217.

44. Li FJ, Xu ZS, Soo AD, Lun ZR, He CY. ATP-driven and AMPK-independent autophagy in an early branching eukaryotic parasite. Autophagy. 2017; 13(4):715–29. Epub 2017/01/26. https://doi.org/10.1080/15548627.2017.1280218 PMID: 28121493; PubMed Central PMCID: PMC5388219.

45. Romero I, Tellez J, Romanha AJ, Steindel M, Grisard EC. Upregulation of Cysteine Synthase and Cystathionine beta-Synthase Contributes to Leishmania braziliensis Survival under Oxidative Stress. Antimicrob Agents Chemother. 2015; 59(8):4770–81. Epub 2015/06/03. https://doi.org/10.1128/AAC.04880-14 PMID: 26033728; PubMed Central PMCID: PMC4505290.

46. Kraeva N, Horakova E, Kostygov AY, Koreny L, Butenko A, Yurchenko V, et al. Catalase in Leishmaniinae: With me or against me? Infect Genet Evol. 2017; 50:121–7. Epub 2016/07/07. https://doi.org/10.1016/j.meegid.2016.06.054 PMID: 27381333.

47. Vassella E, Probst M, Schneider A, Studer E, Renggli CK, Roditi I. Expression of a major surface protein of Trypanosoma brucei insect forms is controlled by the activity of mitochondrial enzymes. Mol Biol Cell. 2004; 15(9):3986–93. Epub 2004/06/18. https://doi.org/10.1091/mbc.e04-04-0341 PMID: 15201340; PubMed Central PMCID: PMC515333.

48. Savage AF, Kolev NG, Franklin JB, Vigneron A, Aksoy S, Tschudi C. Transcriptome Profiling of Trypanosoma brucei Development in the Tsetse Fly Vector Glossina morsitans. PLoS ONE. 2016; 11(12):e0168877. Epub 2016/12/22. https://doi.org/10.1371/journal.pone.0168877 PMID: 28002435; PubMed Central PMCID: PMC5176191.

49. Lamour N, Riviere L, Coustou V, Coombs GH, Barrett MP, Bringaud F. Proline metabolism in procyclic Trypanosoma brucei is down-regulated in the presence of glucose. J Biol Chem. 2005; 280(12):11902–10. Epub 2005/01/25. https://doi.org/10.1074/jbc.M414274200 PMID: 15665328.

50. Mantilla BS, Marchese L, Casas-Sanchez A, Dyer NA, Ejeh N, Biran M, et al. Proline Metabolism is Essential for Trypanosoma brucei brucei Survival in the Tsetse Vector. PLoS Pathog. 2017; 13(1):e1006158. Epub 2017/01/24. https://doi.org/10.1371/journal.ppat.1006158 PMID: 28114403; PubMed Central PMCID: PMC5289646.

51. Durieux PO, Schutz P, Brun R, Kohler P. Alterations in Krebs cycle enzyme activities and carbohydrate catabolism in two strains of Trypanosoma brucei during in vitro differentiation of their bloodstream to

procyclic stages. Mol Biochem Parasitol. 1991; 45(1):19–27. Epub 1991/03/01. https://doi.org/10.1016/0166-6851(91)90023-y PMID: 1904988.

52. van Weelden SW, van Hellemond JJ, Opperdoes FR, Tielens AG. New functions for parts of the Krebs cycle in procyclic Trypanosoma brucei, a cycle not operating as a cycle. J Biol Chem. 2005; 280 (13):12451–60. Epub 2005/01/14. https://doi.org/10.1074/jbc.M412447200 PMID: 15647263.

53. Wargnies M, Bertiaux E, Cahoreau E, Ziebart N, Crouzols A, Morand P, et al. Gluconeogenesis is essential for trypanosome development in the tsetse fly vector. PLoS Pathog. 2018; 14(12):e1007502. Epub 2018/12/18. https://doi.org/10.1371/journal.ppat.1007502 PMID: 30557412; PubMed Central PMCID: PMC6312356.

54. Bringaud F, Riviere L, Coustou V. Energy metabolism of trypanosomatids: adaptation to available carbon sources. Mol Biochem Parasitol. 2006; 149(1):1–9. Epub 2006/05/10. S0166-6851(06)00115-0 [pii] https://doi.org/10.1016/j.molbiopara.2006.03.017 PMID: 16682088.

55. Tielens AG, van Hellemond JJ. Surprising variety in energy metabolism within Trypanosomatidae. Trends Parasitol. 2009; 25(10):482–90. Epub 2009/09/15. https://doi.org/10.1016/j.pt.2009.07.007 PMID: 19748317.

56. Fendt SM, Bell EL, Keibler MA, Olenchock BA, Mayers JR, Wasylenko TM, et al. Reductive glutamine metabolism is a function of the alpha-ketoglutarate to citrate ratio in cells. Nature communications. 2013; 4:2236. Epub 2013/08/01. https://doi.org/10.1038/ncomms3236 PMID: 23900562; PubMed Central PMCID: PMC3934748.

57. Riviere L, Moreau P, Allmann S, Hahn M, Biran M, Plazolles N, et al. Acetate produced in the mitochondrion is the essential precursor for lipid biosynthesis in procyclic trypanosomes. Proc Natl Acad Sci U S A. 2009; 106(31):12694–9. Epub 2009/07/25. https://doi.org/10.1073/pnas.0903355106 PMID: 19625628; PubMed Central PMCID: PMC2722340.

58. Saas J, Ziegelbauer K, von Haeseler A, Fast B, Boshart M. A developmentally regulated aconitase related to iron-regulatory protein-1 is localized in the cytoplasm and in the mitochondrion of Trypanosoma brucei. J Biol Chem. 2000; 275(4):2745–55. Epub 2000/01/25. https://doi.org/10.1074/jbc.275.4.2745 PMID: 10644738.

59. Wang X, Inaoka DK, Shiba T, Balogun EO, Allmann S, Watanabe YI, et al. Expression, purification, and crystallization of type 1 isocitrate dehydrogenase from Trypanosoma brucei brucei. Protein Expr Purif. 2017; 138:56–62. Epub 2017/06/24. https://doi.org/10.1016/j.pep.2017.06.011 PMID: 28642005.

60. Bahat A, Gross A. Mitochondrial plasticity in cell fate regulation. J Biol Chem. 2019; 294(38):13852–63. Epub 2019/08/07. https://doi.org/10.1074/jbc.REV118.000828 PMID: 31383739; PubMed Central PMCID: PMC6755789.

61. Han S, Chandel NS. There Is No Smoke without Mitochondria. Am J Respir Cell Mol Biol. 2019; 60 (5):489–91. Epub 2018/11/02. https://doi.org/10.1165/rcmb.2018-0348ED PMID: 30383397; PubMed Central PMCID: PMC6503615.

62. Dogan SA, Cerutti R, Beninca C, Brea-Calvo G, Jacobs HT, Zeviani M, et al. Perturbed Redox Signaling Exacerbates a Mitochondrial Myopathy. Cell Metab. 2018. Epub 2018/08/21. https://doi.org/10.1016/j.cmet.2018.07.012 PMID: 30122554.

63. Martinez-Reyes I, Diebold LP, Kong H, Schieber M, Huang H, Hensley CT, et al. TCA Cycle and Mitochondrial Membrane Potential Are Necessary for Diverse Biological Functions. Mol Cell. 2016; 61 (2):199–209. Epub 2016/01/05. https://doi.org/10.1016/j.molcel.2015.12.002 PMID: 26725009; PubMed Central PMCID: PMC4724312.

64. Pryde KR, Hirst J. Superoxide is produced by the reduced flavin in mitochondrial complex I: a single, unified mechanism that applies during both forward and reverse electron transfer. J Biol Chem. 2011; 286(20):18056–65. Epub 2011/03/12. M110.186841 [pii] https://doi.org/10.1074/jbc.M110.186841 PMID: 21393237; PubMed Central PMCID: PMC3093879.

65. Robb EL, Hall AR, Prime TA, Eaton S, Szibor M, Viscomi C, et al. Control of mitochondrial superoxide production by reverse electron transport at complex I. J Biol Chem. 2018; 293(25):9869–79. Epub 2018/05/11. https://doi.org/10.1074/jbc.RA118.003647 PMID: 29743240; PubMed Central PMCID: PMC6016480.

66. Mittra B, Cortez M, Haydock A, Ramasamy G, Myler PJ, Andrews NW. Iron uptake controls the generation of Leishmania infective forms through regulation of ROS levels. The Journal of experimental medicine. 2013; 210(2):401–16. Epub 2013/02/06. https://doi.org/10.1084/jem.20121368 PMID: 23382545; PubMed Central PMCID: PMC3570109.

67. Horakova E, Faktorova D, Kraeva N, Kaur B, Van Den Abbeele J, Yurchenko V, et al. Catalase compromises the development of the insect and mammalian stages of Trypanosoma brucei. FEBS J. 2020; 287(5):964–77. Epub 2019/10/09. https://doi.org/10.1111/febs.15083 PMID: 31593329.

68. van der Reest J, Lilla S, Zheng L, Zanivan S, Gottlieb E. Proteome-wide analysis of cysteine oxidation reveals metabolic sensitivity to redox stress. Nature communications. 2018; 9(1):1581. Epub 2018/04/

22. https://doi.org/10.1038/s41467-018-04003-3 PMID: 29679077; PubMed Central PMCID: PMC5910380.

69. Topf U, Suppanz I, Samluk L, Wrobel L, Boser A, Sakowska P, et al. Quantitative proteomics identifies redox switches for global translation modulation by mitochondrially produced reactive oxygen species. Nature communications. 2018; 9(1):324. Epub 2018/01/24. https://doi.org/10.1038/s41467-017-02694-8 PMID: 29358734; PubMed Central PMCID: PMC5778013.

70. Saldivia M, Ceballos-Perez G, Bart JM, Navarro M. The AMPKalpha1 Pathway Positively Regulates the Developmental Transition from Proliferation to Quiescence in Trypanosoma brucei. Cell reports. 2016; 17(3):660–70. Epub 2016/10/13. https://doi.org/10.1016/j.celrep.2016.09.041 PMID: 27732844; PubMed Central PMCID: PMC5074416.

71. Szoor B, Ruberto I, Burchmore R, Matthews KR. A novel phosphatase cascade regulates differentiation in Trypanosoma brucei via a glycosomal signaling pathway. Genes Dev. 2010; 24(12):1306–16. Epub 2010/06/17. https://doi.org/10.1101/gad.570310 PMID: 20551176; PubMed Central PMCID: PMC2885665.

72. Wingett SW, Andrews S. FastQ Screen: A tool for multi-genome mapping and quality control. F1000Research. 2018; 7:1338. Epub 2018/09/29. https://doi.org/10.12688/f1000research.15931.2 PMID: 30254741; PubMed Central PMCID: PMC6124377.

73. Rappsilber J, Mann M. Analysis of the topology of protein complexes using cross-linking and mass spectrometry. CSH protocols. 2007; 2007:pdb prot4594. Epub 2007/01/01. https://doi.org/10.1101/pdb.prot4594 PMID: 21357017.

74. Cox J, Mann M. MaxQuant enables high peptide identification rates, individualized p.p.b.-range mass accuracies and proteome-wide protein quantification. Nat Biotechnol. 2008; 26(12):1367–72. Epub 2008/11/26. https://doi.org/10.1038/nbt.1511 PMID: 19029910.

75. Ostlund G, Schmitt T, Forslund K, Kostler T, Messina DN, Roopra S, et al. InParanoid 7: new algorithms and tools for eukaryotic orthology analysis. Nucleic Acids Res. 2010; 38(Database issue):D196–203. Epub 2009/11/07. https://doi.org/10.1093/nar/gkp931 PMID: 19892828; PubMed Central PMCID: PMC2808972.

76. Wirtz E, Leal S, Ochatt C, Cross GA. A tightly regulated inducible expression system for conditional gene knock-outs and dominant-negative genetics in Trypanosoma brucei. Mol Biochem Parasitol. 1999; 99(1):89–101. Epub 1999/04/24. S016668519900002X [pii]. https://doi.org/10.1016/s0166-6851(99)00002-x PMID: 10215027.

77. Panigrahi AK, Zikova A, Dalley RA, Acestor N, Ogata Y, Anupama A, et al. Mitochondrial complexes in Trypanosoma brucei: a novel complex and a unique oxidoreductase complex. Mol Cell Proteomics. 2008; 7(3):534–45. Epub 2007/12/13. M700430-MCP200 [pii] https://doi.org/10.1074/mcp.M700430-MCP200 PMID: 18073385.

78. Gahura O, Subrtova K, Vachova H, Panicucci B, Fearnley IM, Harbour ME, et al. The F1 -ATPase from Trypanosoma brucei is elaborated by three copies of an additional p18-subunit. FEBS J. 2018; 285(3):614–28. Epub 2017/12/17. https://doi.org/10.1111/febs.14364 PMID: 29247468.

79. Gnipova A, Subrtova K, Panicucci B, Horvath A, Lukes J, Zikova A. The ADP/ATP carrier and its relationship to OXPHOS in an ancestral protist, Trypanosoma brucei. Eukaryot Cell. 2015. Epub 2015/01/27. https://doi.org/10.1128/EC.00238-14 PMID: 25616281.

80. Koreny L, Sobotka R, Kovarova J, Gnipova A, Flegontov P, Horvath A, et al. Aerobic kinetoplastid flagellate Phytomonas does not require heme for viability. Proc Natl Acad Sci U S A. 2012. Epub 2012/02/23. https://doi.org/10.1073/pnas.1201089109 PMID: 22355128.

81. Kovarova J, Nagar R, Faria J, Ferguson MAJ, Barrett MP, Horn D. Gluconeogenesis using glycerol as a substrate in bloodstream-form Trypanosoma brucei. PLoS Pathog. 2018; 14(12):e1007475. Epub 2018/12/28. https://doi.org/10.1371/journal.ppat.1007475 PMID: 30589893; PubMed Central PMCID: PMC6307712.

82. Creek DJ, Mazet M, Achcar F, Anderson J, Kim DH, Kamour R, et al. Probing the metabolic network in bloodstream-form Trypanosoma brucei using untargeted metabolomics with stable isotope labelled glucose. PLoS Pathog. 2015; 11(3):e1004689. Epub 2015/03/17. https://doi.org/10.1371/journal.ppat.1004689 PMID: 25775470; PubMed Central PMCID: PMC4361558.

Parasitology

cambridge.org/par

Redesigned and reversed: architectural and functional oddities of the trypanosomal ATP synthase

Ondřej Gahura[1], Carolina Hierro-Yap[1,2] and Alena Zíková[1,2]

[1]Biology Centre, Czech Academy of Sciences, Branišovská 31, České Budějovice, 37005, Czech Republic and [2]Faculty of Science, University of South Bohemia, Branišovská 31, České Budějovice, 37005, Czech Republic

Review

Cite this article: Gahura O, Hierro-Yap C, Zíková A (2021). Redesigned and reversed: architectural and functional oddities of the trypanosomal ATP synthase. *Parasitology* **148**, 1151–1160. https://doi.org/10.1017/S0031182021000202

Received: 29 November 2020
Revised: 23 January 2021
Accepted: 26 January 2021
First published online: 8 February 2021

Key words:
ATP synthase; cryo-EM; mitochondria; mitochondrial membrane potential; oxidative phosphorylation

Author for correspondence:
Alena Zíková, E-mail: azikova@paru.cas.cz

Abstract

Mitochondrial F-type adenosine triphosphate (ATP) synthases are commonly introduced as highly conserved membrane-embedded rotary machines generating the majority of cellular ATP. This simplified view neglects recently revealed striking compositional diversity of the enzyme and the fact that in specific life stages of some parasites, the physiological role of the enzyme is to maintain the mitochondrial membrane potential at the expense of ATP rather than to produce ATP. In addition, mitochondrial ATP synthases contribute indirectly to the organelle's other functions because they belong to major determinants of submitochondrial morphology. Here, we review current knowledge about the trypanosomal ATP synthase composition and architecture in the context of recent advances in the structural characterization of counterpart enzymes from several eukaryotic supergroups. We also discuss the physiological function of mitochondrial ATP synthases in three trypanosomatid parasites, *Trypanosoma cruzi*, *Trypanosoma brucei* and *Leishmania*, with a focus on their disease-causing life cycle stages. We highlight the reversed proton-pumping role of the ATP synthase in the *T. brucei* bloodstream form, the enzyme's potential link to the regulation of parasite's glycolysis and its role in generating mitochondrial membrane potential in the absence of mitochondrial DNA.

Introduction

F-type adenosine triphosphate (ATP) synthases (also called F-ATPases of F_1F_0-ATPases) are bidirectional turbine-like enzymes coupling ATP synthesis or hydrolysis with proton translocation through biological membranes in bacteria and their endosymbiotic descendants, mitochondria and chloroplasts (for recent reviews see Junge and Nelson, 2015; Walker, 2017; Kuhlbrandt, 2019). When operating in the forward mode, ATP synthases utilize the proton motive force to produce ATP and thus represent fundamental constituents of the oxidative phosphorylation pathway. In the reverse mode, they act as ATP-consuming proton pumps contributing to the generation of electrochemical membrane potential. Bacteria employ both modes depending on the species and growth conditions (Cotter and Hill, 2003). By contrast, mitochondrial ATP synthases in most aerobic eukaryotes function as a major source of cellular ATP and the reversal of their activity is a manifestation of pathophysiological conditions (Campanella *et al.*, 2009). Unlike the monomeric bacterial and chloroplastic counterparts, all mitochondrial ATP synthases characterized so far occur in dimers (Arnold *et al.*, 1998; Dudkina *et al.*, 2005). The wide phylogenetic distribution of the ATP synthase dimers suggests that the enzyme's dimerization is a common feature of all aerobic eukaryotes with oxidative phosphorylation and was possibly present already in the last eukaryotic common ancestor. Dimerization of ATP synthases induces curvature of the inner mitochondrial membrane (Dudkina *et al.*, 2006; Davies *et al.*, 2012) and the intrinsic propensity of dimers to self-assemble into rows facilitates membrane shaping and governs cristae formation (Anselmi *et al.*, 2018; Blum *et al.*, 2019). Spatial separation of ATP synthases and electron transport chain (ETC) complexes on rims and flat regions of cristae, respectively, creates a local proton concentration gradient in cristae lumen, enhancing oxidative phosphorylation (Davies *et al.*, 2011). Therefore, apart from the enzymatic function, ATP synthases affect mitochondrial physiology by aiding in the determination of submitochondrial ultrastructure.

In *Trypanosoma brucei*, a medically relevant digenetic parasite, the mitochondrial ATP synthase exhibits a 2-fold deviation from its counterparts from traditional model organisms. First, its architecture differs markedly from canonical ATP synthases. Second, its role switches during the parasite's life cycle, from being an ATP producer in the insect form to an ATP consumer maintaining the vital mitochondrial membrane potential in the mammalian bloodstream form (BSF). This switch is associated with major rearrangement of mitochondrial morphology, possibly involving altered ATP synthase oligomerization. Unlike in *T. brucei*, in *Trypanosoma cruzi* and *Leishmania*, ATP synthase acts true to its name and participates in the oxidative phosphorylation providing ATP in all life forms of the parasite. In the first part of this review, we discuss the recent progress in our understanding of ATP synthase architecture based on structural characterization of enzymes from various eukaryotic supergroups

with a focus on trypanosomal ATP synthase complex. In the second part, we summarize our knowledge of the ATP synthase importance for the disease-causing forms of medically relevant trypanosomatid parasites.

Unexpected diversity of mitochondrial ATP synthases

Structural studies of mitochondrial ATP synthases have been key for the understanding of molecular mechanisms of ATP synthesis. The seminal research on the structure of the matrix-facing soluble F_1-ATPase subcomplex isolated from the bovine heart (Abrahams *et al.*, 1994) initiated two decades of dominance of X-ray crystallography in the field. Numerous crystal structures of subcomplexes of bovine and yeast ATP synthases provided atomic models of the enzyme's rotor and the extrinsic part of the peripheral stalk, and revealed the mechanism of the conversion of the rotational force into the cyclic catalysis of ATP formation (reviewed in Junge and Nelson, 2015; Walker, 2017). Due to the striking similarity of the blueprints for bacterial and opisthokontal mitochondrial F-type ATP synthases and their fundamental role in cellular energetics, it was assumed that the mitochondrial enzymes do not differ substantially between eukaryotic lineages. However, only the advance of cryo-electron microscopy (cryo-EM) techniques in the last few years allowed researchers to build atomic models of complete mitochondrial ATP synthases not only from conventional model organisms [mammals (Gu *et al.*, 2019; Pinke *et al.*, 2020; Spikes *et al.*, 2020) and *Saccharomyces cerevisiae* (Guo *et al.*, 2017)], but also from protists representing other eukaryotic phyla [*Polytomella* (Murphy *et al.*, 2019), *Euglena* (Muhleip *et al.*, 2019), *Tetrahymena* (Flygaard *et al.*, 2020) and *Toxoplasma* (Mühleip *et al.*, 2021)]. From the mechanistic point of view, structures revealed by cryo-EM elucidated how the proton motive force across biological membranes is converted into the torque of the enzyme's rotor (Klusch *et al.*, 2017; Hahn *et al.*, 2018) and how the symmetry mismatch of the rotor and catalytic subcomplexes is compensated by the flexibility of the peripheral stalk (Sobti *et al.*, 2019). From the evolutionary perspective, the structures demonstrated that although the functional core is universally conserved in all F-type ATP synthases, peripheral parts and the dimerization interface of mitochondrial ATP synthases have diverged substantially among eukaryotic lineages. Notably, cryo-EM structures not only allowed identification of novel lineage-specific components, but in some species also revealed conserved subunits, which had not been previously identified by traditional homology searches using known genomes and proteomes (Fig. 1).

All F-type ATP synthases are composed of two subcomplexes, the membrane-embedded F_0 and the soluble F_1, connected by a rotary central stalk and a stationary peripheral stalk (Fig. 2). The globular F_1 subcomplex, also referred to as F_1-ATPase, is a pseudo-symmetrical assembly of three heterodimers of α- and β-subunits organized around single γ-subunit, the main constituent of the central stalk. The functional core of F_0 consists of the a-subunit and a ring of several identical c-subunits (c-ring), providing together a path for protons across the membrane. Proton translocation drives the rotation of the c-ring and the tightly attached central stalk. The torque of the asymmetric γ-subunit induces cyclic conformational changes of three active sites on the interfaces of α- and β-subunits, resulting in the stepwise binding of ADP and phosphate, their condensation into ATP, and its release, emptying the nucleotide binding site for the next catalytic cycle (Abrahams *et al.*, 1994). The $(\alpha\beta)_3$-hexamer is prevented from rotation by interaction with the oligomycin sensitivity-conferring protein (OSCP), the uppermost constituent of the extrinsic part of the peripheral stalk.

The entire F_1-ATPase consisting of subunits α_3, β_3, γ, δ and ε (stoichiometry of subunits indicated by the subscripts), OSCP and both proton translocating components (a-subunit and c-ring) are present in all reported mitochondrial ATP synthases. The rest of the enzyme is markedly less conserved (Fig. 2). The highest diversity is observed in the soluble part of the peripheral stalk and in the lumenal and peripheral F_0 regions, often composed of lineage-specific subunits or lineage-specific extensions of conserved proteins. Subunits involved in the anchoring of the peripheral stalk to the membrane and in clamping the a-subunit to the c-ring (b, d, e, f, g, i/j, k and 8), originally identified in opisthokonts, appear to be conserved in several other eukaryotic groups (Fig. 1). In many cases, their proposed homology is based largely on tertiary and quaternary structure resemblances revealed by cryo-EM. Low sequence similarity precludes identification of the respective homologs in lineages without structurally characterized ATP synthases. Although dimerization is a general hallmark of all reported mitochondrial ATP synthases, subunits constituting the dimer interface differ between eukaryotic lineages, likely due to divergent evolution. Consequently, the shape of dimers and topography of oligomeric assemblies vary in the characterized enzymes, which is reflected in diverse cristae morphology (Fig. 1; Dudkina *et al.*, 2010; Davies *et al.*, 2012; Muhleip *et al.*, 2016; Muhleip *et al.*, 2017; Mühleip *et al.*, 2021).

Unique structural features of ATP synthases in Trypanosomatida

The knowledge about the architecture of mitochondrial ATP synthases in Trypanosomatida, a group of protozoan parasites with monoxenous or dixenous life cycles, is based mostly on studies performed with cultured insect trypomastigotes of *T. brucei*. The composition of the mitochondrial ATP synthase in these cells was determined by mass spectrometry (MS) identification of proteins co-immunoprecipitated with F_1 and tandem affinity purified using TAP-tagged conserved or newly identified subunits as baits. These biochemical analyses complemented by a comprehensive genome search revealed 23 subunits (Zikova *et al.*, 2009), including the a-subunit detected by MS later (Skodova-Sverakova *et al.*, 2015). Characterization of the trypanosomal F_1-ATPase released by chloroform from mitochondrial membrane fragments and purified by two-step chromatography (Gahura and Zikova, 2019) showed that the catalytic subcomplex contains three copies of the euglenozoan-specific p18-subunit in addition to the universally conserved subunits α, β, γ, δ and ε (Gahura *et al.*, 2018*b*). The F_1-ATPase structure determined by X-ray crystallography further revealed that each copy of p18-subunit, an α-helical protein with three pentatricopeptide repeats, associates peripherally with one of the three α chains (Fig. 3A), and does not contribute directly to the catalytic mechanism (Montgomery *et al.*, 2018). Although the atomic structure did not explain the function of p18, the elaboration of the F_1 head in Euglenozoa by this additional subunit is extraordinary, because the $\alpha_3\beta_3\gamma$ subcomplex is invariant in all other known F-type ATP synthases. In addition, the α-subunit was found to be proteolytically cleaved at two sites separated by eight amino acid residues, producing two fragments α_{1-127} and $\alpha_{135-560}$, both stably associated with the complex. The split of α-subunit into two parts was also demonstrated in other euglenozoan protists *Crithidia fasciculata* (Speijer *et al.*, 1997), *Leishmania tarentolae* (Nelson *et al.*, 2004) and *Euglena gracilis* (Sathish Yadav *et al.*, 2017). The structure of the trypanosomal F_1-ATPase showed that the cleavage occurs at the region corresponding to a loop on the surface of F_1-ATPases from other organisms and splits the N-terminal β-barrel domain from the rest of the protein (Montgomery *et al.*, 2018; Fig. 3A and B). Nevertheless, the architecture of the entire $(\alpha\beta)_3$-headpiece, including the nucleotide binding pockets, is highly similar to

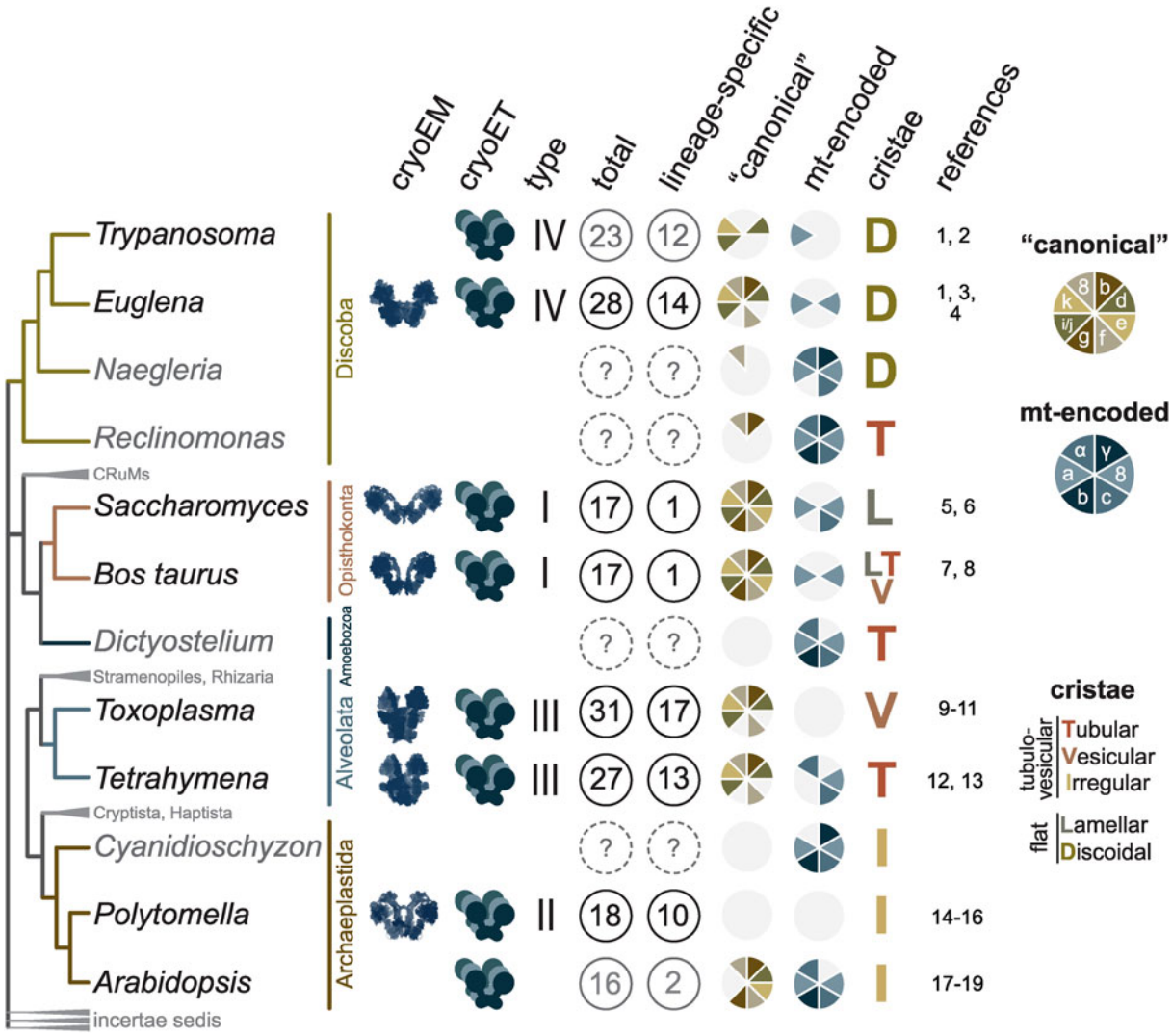

Fig. 1. Structural diversity of mitochondrial ATP synthases mapped on the phylogenetic tree of eukaryotes. The figure summarizes structural and proteomic studies of mitochondrial ATP synthases. The phylogenetic tree is based on Burki *et al.* (2020). Organisms with ATP synthases with atomic models obtained by single particle cryo-EM, visualized by cryo-ET (see first two columns) or characterized by MS, and several relative species were included. Major groups without experimental data are shown in small font. Numbers of subunits showed in grey are based on proteomic characterization of purified complexes without available single particle cryo-EM analysis and might be revised in future. 'Canonical' subunits are proteins originally identified in opisthokonts, which have divergent homologs in other lineages. Categorization of ATP synthases in types I to IV is based on Kuhlbrandt (2019). Cristae morphology is adopted from Panek *et al.* (2020). The numbered references are following: [1] (Muhleip *et al.*, 2017), [2] (Zikova *et al.*, 2009), [3] (Muhleip *et al.*, 2019), [4] (Sathish Yadav *et al.*, 2017), [5] (Davies *et al.*, 2012), [6] (Guo *et al.*, 2017), [7] (Davies *et al.*, 2011), [8] (Spikes *et al.*, 2020), [9] (Mühleip *et al.*, 2021), [10] (Salunke *et al.*, 2018), [11] (Huet *et al.*, 2018), [12] (Flygaard *et al.*, 2020), [13] (Muhleip *et al.*, 2016), [14] (Blum *et al.*, 2019), [15] (Murphy *et al.*, 2019), [16] (Vazquez-Acevedo *et al.*, 2006), [17] (Klodmann *et al.*, 2011), [18] (Bultema *et al.*, 2009), [19] (Senkler *et al.*, 2017).

the prototypical bovine F_1-ATPase (Bowler *et al.*, 2007) and the biological relevance of the α-subunit cleavage remains unclear.

So far, there is no available structure of a complete ATP synthase from any trypanosomatid species. However, low-resolution structures obtained by subtomogram averaging documented general morphological similarity between ATP synthase dimers from *T. brucei* and *E. gracilis*, a representative of euglenids, a lineage closely related to kinetoplastids (Muhleip *et al.*, 2017). An atomic model of dimeric ATP synthase from *E. gracilis* has recently been determined by cryo-EM (Muhleip *et al.*, 2019). Apart from the universally conserved components of mitochondrial ATP synthases (α, β, γ, δ, ε, a, c and OSCP), the *E. gracilis* enzyme contains seven subunits with previously recognized homology (Sathish Yadav *et al.*, 2017) to proteins found in the complex from *T. brucei* (Zikova *et al.*, 2009). To get a deeper insight into the trypanosomal ATP synthase structure, we performed systematic pairwise sequence comparison of all remaining subunits in the complex from *E. gracilis* with all non-conserved trypanosomal ATP synthase components, and propose homology of four additional protein pairs, which exhibit >20% sequence identity (Fig. 3C). Overall, 19 of 23 subunits of the trypanosomal ATP synthase have homologs found in the structure from *E. gracilis*. Taken together, although the ATP synthases from *E. gracilis* and *T. brucei* are not compositionally identical, it is conceivable to assume that the structural features shaped by the conserved subunits are shared between the two species (Fig. 3C), and possibly among Euglenozoa in general.

The peripheral stalk in euglenozoan ATP synthases differs markedly from other lineages. The universally conserved OSCP features a long and partially flexible C-terminal extension, which bridges the core of the protein on the top of F_1 with ATPTB2, a highly divergent and extended homolog of the d-subunit from opisthokontal ATP synthases anchoring the peripheral stalk to the membrane. The interaction of ATPTB2 with the extension of OSCP is clamped between two laterally positioned lineage-specific globular proteins ATPTB3 and ATPTB4 on one side and one copy of p18 on the other side. The contacts of the peripheral stalk with p18 contribute to the immobilization

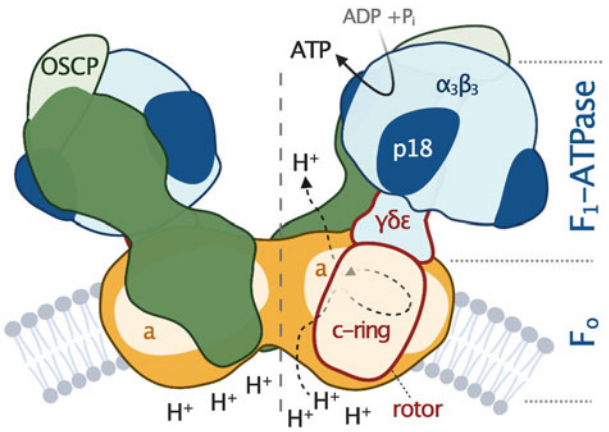

Fig. 2. Schematic depiction of euglenozoan mitochondrial ATP synthase in the ATP production mode. The F_1-ATPase, peripheral stalk and membrane-embedded part are shown in shades of blue, green and orange, respectively. Subunits identified in all reported mitochondrial ATP synthases are pale. The dark green and dark orange regions are composed of conserved and lineage-specific subunits. The p18 subunit is restricted to Euglenozoa. The rotor is outlined in red.

of the $(\alpha\beta)_3$-hexamer (Fig. 3D). However, the reinforcement of the interaction between the F_1 head and the peripheral stalk is unlikely the only role of p18, because the protein is essential for the integrity of the F_1-ATPase (Gahura *et al.*, 2018*b*), in contrast to the peripheral stalk components OSCP (Hierro-Yap *et al.*, 2021) and ATPTB2/d-subunit (Subrtova *et al.*, 2015). In *E. gracilis*, the extensions of OSCP and d-subunit compensate for the reduction of the b-subunit, the major constituent of the peripheral stalk in bacteria and mitochondria of mammals and yeast. Sequence comparison did not reveal a homolog of the b-subunit in the ATP synthase of *T. brucei*, suggesting that it might be further reduced or completely absent in Trypanosomatida.

In all reported F-type ATP synthases, the proton channel-forming a-subunit contains two horizontal membrane-embedded helices H5 and H6, which are directly involved in proton translocation (Guo *et al.*, 2017; Murphy *et al.*, 2019). In mammals (Spikes *et al.*, 2020) and yeast (Guo *et al.*, 2017) the two helices are lined by a series of six parallel transmembrane helices, contributed by one helix of each of subunits b, f, 8, i/j and k, and by a transmembrane helix of the a-subunit itself. The same configuration is observed in *E. gracilis* (Fig. 3E), suggesting the conservancy of the contributing subunits. Although the ATP synthase in *T. brucei* contains homologs of *E. gracilis* subunits k and i/j, the homologs of subunits b, f and 8 were not identified. The dimer interface of the ATP synthase in *E. gracilis* is formed largely by subunits ATPEG1 and ATPEG2 without discernible homology outside Euglenozoa, but with apparent homologs in Trypanosomatida (called ATPTB9 and ATPTB8 in *T. brucei*; Perez *et al.*, 2014; Fig. 3C and F). The presence of these two proteins in *T. brucei* together with the fact that the dimers from both species arrange into short left-handed helices, as showed by cryo-electron tomography (cryo-ET; Muhleip *et al.*, 2017), strongly suggests that the dimerization is mediated by the same elements. The dimer in *E. gracilis* is further stabilized by a homotypic interaction of extensions of d-subunit adopting a ferredoxin-like fold on the matrix side of the membrane. This extension is specific to euglenids and the interaction is therefore completely missing in *T. brucei*, possibly explaining the poor stability of its ATP synthase dimers (our observation). Notably, the dimer interface in *Euglena* contains several ordered phospholipid molecules, predominantly cardiolipins (Muhleip *et al.*, 2019; Fig. 3F). Molecules of cardiolipin are presumably integrated also in the trypanosomal ATP synthase, as cardiolipin plays a vital role in the stability of the complex (Serricchio *et al.*, 2020).

Role of the ATP synthase in trypanosomatid parasites

The function of the ATP synthase in trypanosomatid parasites depends on the species and their life cycle stage. Digenetic trypanosomatid parasites (e.g. *T. brucei*, *T. cruzi* and *Leishmania*) possess a complex life cycle as they alternate between the insect vector and a mammalian host. In humans, they cause dreadful diseases (African trypanosomiasis, Chagas disease and leishmaniases). The scarcity of effective treatments and weak vaccine prospects drive an ongoing urgent need to identify new therapeutic targets. Considering the ATP synthase's central position in energy metabolism and its structural and compositional divergence from the mammalian counterpart, one may consider this complex as a promising drug target. The feasibility of targeting the ATP synthase is underscored by the recent approval of bedaquiline, a specific F-ATP synthase inhibitor that blocks the c-ring rotation, to treat multi-drug resistant tuberculosis (Preiss *et al.*, 2015). Whereas the function of the ATP synthase in *T. brucei* parasites is well understood, the exact role of the ATP synthase and its requirement for virulence and survival of *Leishmania* and *T. cruzi* parasites are not well defined yet.

Role of the ATP synthase in intracellular amastigotes of Leishmania *and* T. cruzi *parasites*

Leishmania parasites infect a mammalian host when an infected sand fly takes a blood meal. The promastigote form is released to the skin and is rapidly internalized by macrophages. Inside the macrophages, promastigotes differentiate to aflagellated and non-motile amastigotes, which multiply in the acidic environment of the phagolysosome-like parasitophorous vacuole, whose exact metabolic content has not been determined yet. The environment most likely offers a wide range of carbon sources (sugars, amino acids and fatty acids) for the parasite to salvage due to macrophage polarization to the M2 state, which exhibits increased oxidative metabolism and promotes *Leishmania* parasites growth (Saunders and McConville, 2020). Despite this seemingly plentiful environment, intracellular amastigotes do not proliferate rapidly (Kloehn *et al.*, 2015), but rather activate a stringent metabolic response, a protective mechanism to confer resistance to multiple cellular stresses (oxidative, nutritional and pH). This programmed response is associated with reduced rates of glucose uptake and with low metabolic activity to possibly minimize reactive oxygen species (ROS)-sensitive processes and to lessen the levels of endogenously generated ROS (McConville *et al.*, 2015). The glucose-sparing metabolism of the intracellular amastigotes questions the importance of oxidative phosphorylation, and hence ATP production by the ATP synthase, for the parasite. Nevertheless, amastigotes show increased reliance on mitochondrial metabolism, including tricarboxylic acid (TCA) cycle and fatty acid β-oxidation (Saunders *et al.*, 2014). These pathways generate reduced electron carriers NADH and $FADH_2$ that are reoxidized by the ETC coupled to ATP synthase (Dey *et al.*, 2010; Saunders *et al.*, 2014). The ablation of aconitase, a TCA cycle enzyme, cytochrome *c* oxidase, or ATP synthase is predicted to be lethal by an *in silico*-generated model of the metabolic network (Subramanian *et al.*, 2015). Indeed, the inhibition of ATP synthase by the cell-permeable antimicrobial peptide histatin 5 arrests of *Leishmania* amastigotes' growth (Luque-Ortega *et al.*, 2008). Nevertheless, to prove that oxidative phosphorylation is critical for the *Leishmania* amastigote forms, further studies are necessary (Fig. 4).

Trypanosoma cruzi parasites are transmitted to humans by a blood-sucking triatomine bug through contact with its infected feces. In the skin wound, metacyclic trypomastigotes invade various types of cells, escape the lysosome-derived parasitophorous vacuole and establish infection in the host cell cytoplasm as

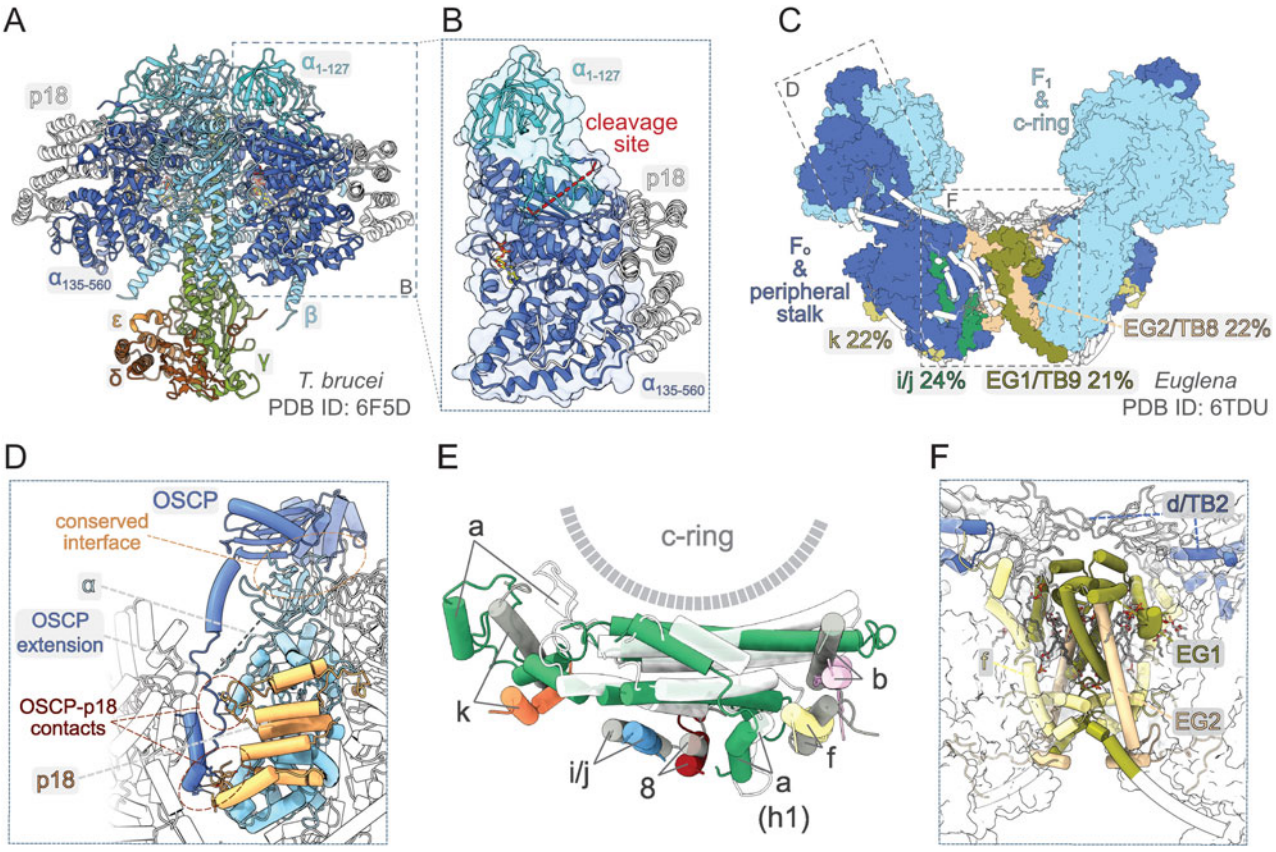

Fig. 3. Structural traits of euglenozoan mitochondrial ATP synthases. (A) Structure of F_1-ATPase from *Trypanosoma brucei* determined by X-ray crystallography (Montgomery *et al*., 2018). (B) The α-subunit in euglenozoans is split by proteolytic cleavage at two sites. The euglenozoan-specific subunit p18 associates with the C-terminal fragment $\alpha_{135–560}$ and does not contact any other F_1 component. (C) Structure of the ATP synthase dimer from *Euglena gracilis* (Muhleip *et al*., 2019). Elements with and without homology in *T. brucei* are shown in surface and white cartoon representation, respectively. F_1-ATPase and c-ring are in pale blue. Subunits with newly proposed homology between *Euglena* and *Trypanosoma* are coloured individually and labelled with names used in both species (Perez *et al*., 2014; Muhleip *et al*., 2019). The sequence identities of respective homolog pairs are shown. All other peripheral stalk and F_0 subunits are in dark blue. (D) Interaction of the peripheral stalk with F_1-ATPase. The canonical interaction interface and lineage-specific contacts between OSCP and p18 are shown. (E) Superposition of the a-subunit and adjacent conserved transmembrane helices from *E. gracilis* (subunits coloured individually) and bovine [a-subunit white, all other subunits in grey; PDB ID 6ZPO (Spikes *et al*., 2020)] ATP synthase. (F) Dimer interface of the ATP synthase in *E. gracilis*. Subunits involved in inter-monomer contacts are shown in cartoon representation. Regions that are present in *T. brucei* counterparts based on homology modelling with Swiss model (Waterhouse *et al*., 2018) are coloured individually and *Euglena*-specific elements are in white. All other subunits are shown as transparent surfaces. Ordered lipids (cardiolipins and phosphatidylcholines or phosphatidylethanolamines) localizing to the dimer interface are shown as sticks.

intracellular amastigotes (de Souza *et al*., 2010). During *T. cruzi* trypomastigotes' transition to amastigotes, there is a dramatic shift from sugar-based metabolism to catabolism of amino and fatty acids manifested by repression of glucose transporters and increased levels of TCA cycle enzymes and proteins involved in fatty acid oxidation and oxidative phosphorylation. The oxidative metabolism of amino and fatty acids suggests a crucial role for oxidative phosphorylation to generate ATP (Atwood *et al*., 2005; Silber *et al*., 2009; Li *et al*., 2016; Shah-Simpson *et al*., 2016). This is further supported by the identification of highly selective compounds (i.e. GNF7686 and ELQ271) that target complex III and inhibit the growth of intracellular amastigotes in a dose-dependent manner (Khare *et al*., 2015).

After several rounds of intracellular replication, amastigotes differentiate to trypomastigotes, which are released from the cell by its rupture. Extracellular trypomastigotes disseminate and infect other cells or they are ingested by the triatomine bug to conclude the life cycle. Interestingly, the extracellular bloodstream trypomastigotes switch back to glycolysis to meet their energy demands but still employ ETC complexes to maintain the mitochondrial membrane potential. Moreover, disproportional changes in expression of ETC complexes II, III and IV create a bottleneck forcing electrons to prematurely reduce molecules of oxygen and generate significant levels of ROS (Goncalves *et al*., 2011). This induced production of ROS probably provides a redox-mediated pre-conditioning to evoke protection against host-induced oxidative challenge once the parasite enters the cell again. In this particular case, the ETC linked to ATP synthase also serves as an adaptive process allowing parasites to survive redox challenges imposed by the host. Presumably, inhibition of the ATP synthase would cause a decrease in ATP levels, which by itself can be lethal, but it would also further increase the already elevated ROS levels. Although there is evidence that the oxidative environment stimulates the parasite's growth and ROS are critical for successful infection of *T. cruzi* in various cell types (Paiva and Bozza, 2014), very high levels of ROS reverse this favourable effect and are harmful for the parasite (Goes *et al*., 2016). Therefore, an additive effect of endogenous and exogenous ROS bursts may induce deleterious changes resulting in parasites' elimination by oxidative damage (Fig. 4).

Despite some evidence that mitochondrial ETC and ATP synthase might be essential entities for the clinically relevant infectious stages of *Leishmania* and *T. cruzi* parasites, the knowledge of the mitochondrial energy metabolism in these parasites remains largely incomplete.

The F-ATPase in the bloodstream form of T. brucei

The disease-causing form of *T. brucei* is an extracellular parasite inhabiting various niches of its mammalian host, including the bloodstream, adipose tissue, skin or central nervous system

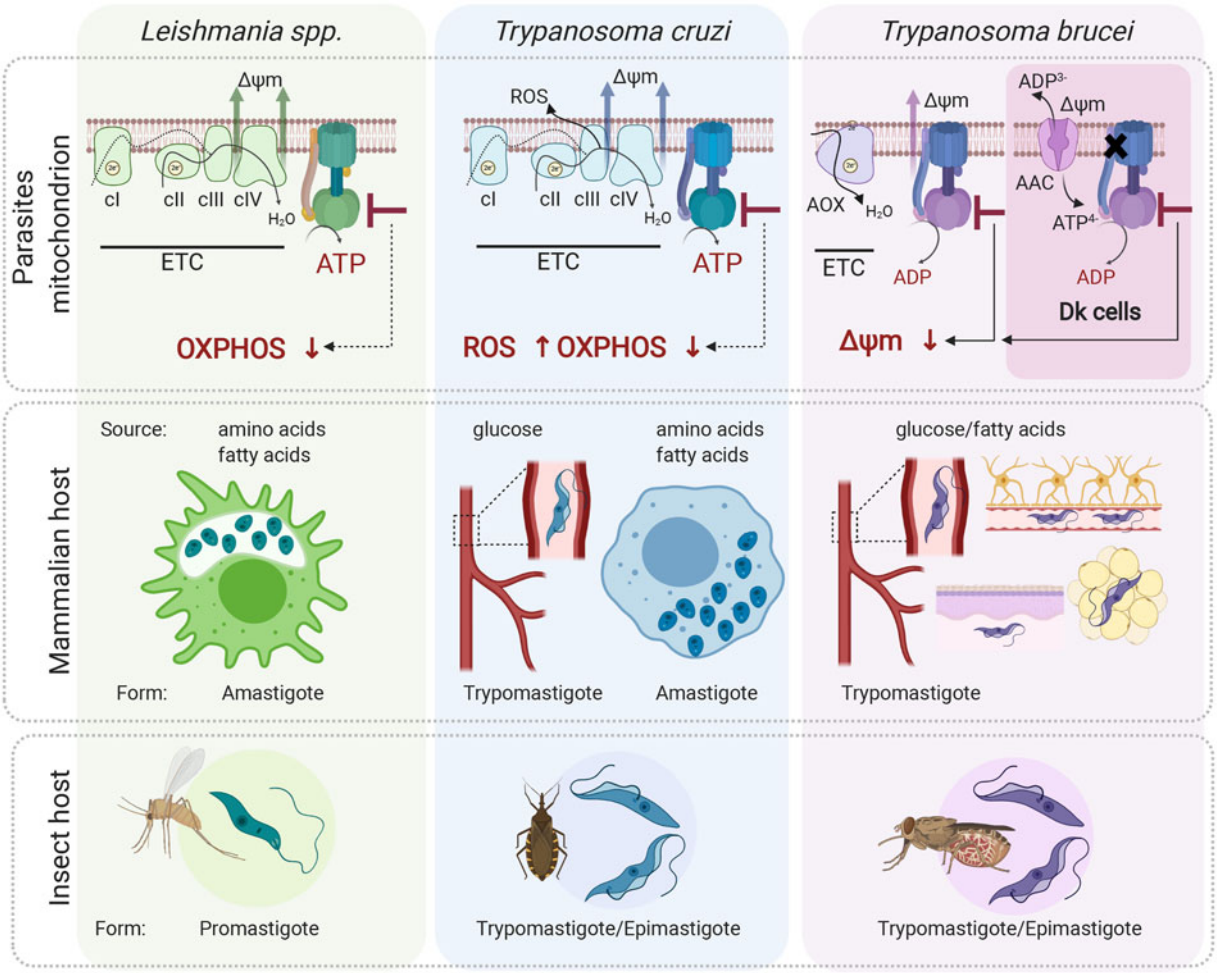

Fig. 4. Role of the mitochondrial ATP synthase in *Leishmania*, *Trypanosoma cruzi* and *T. brucei* disease-causing life cycle stages. In the mammalian host, *Leishmania* parasites proliferate in macrophages as intracellular amastigotes, while *T. cruzi* parasites exist in two different forms; as intracellular amastigotes of various mammalian cells and as extracellular trypomastigotes in the host bloodstream. In these life forms, ATP synthase is involved in oxidative phosphorylation and generates ATP. Its inhibition is predicted to cause a depletion of cellular ATP levels. Interestingly, in *T. cruzi* trypomastigotes, the ATP synthase inhibition would also lead to increased levels of ROS due to differential expression of ETC complexes III and IV. *Trypanosoma brucei* parasites proliferate in the mammalian bloodstream but also invade interstitial spaces of various tissues such as brain, adipose tissue and skin. Importantly, *T. brucei* ATP synthase works in reverse and maintains mitochondrial membrane potential ($\Delta\psi_m$) even in trypanosomes lacking mitochondrial DNA. These Dk parasites employ vestigial ATP synthase coupled to ATP/ADP carrier (AAC) to generate $\Delta\psi_m$ electrogenically. Inhibition of F-ATPase in both forms leads to dissipation of $\Delta\psi_m$ and cell death. All three aforementioned parasites (except for Dk *T. brucei*) possess a digenetic life cycle involving insect vectors, namely sand fly for *Leishmania*, triatomine bug for *T. cruzi* and tsetse fly for *T. brucei* transmission. Figure created with Biorender.com.

(Silva Pereira *et al.*, 2019). Since these environments offer different nutrients, the BSF mitochondrion maintains its complexity and plasticity despite its largely reduced size compared to the insect stage organelle (Zikova *et al.*, 2017). Uniquely, the parasite's mitochondrion employs ATP synthase as an ATP-consuming proton pump (Fig. 4).

The discovery of the oligomycin-sensitive F-ATP synthase in BSF by Opperdoes *et al.* (1977), elicited the curiosity of scientists, who back then considered the BSF mitochondrion a vestigial organelle with no obvious role in cellular metabolism. Seeking if this 'promitochondrion' possesses mitochondrial membrane potential, Nolan and Voorheis reported the existence of electrochemical gradients in BSF trypanosomes, documented by the accumulation of the radiolabelled lipophilic cation methyltriphenylphosphonium. One year after, the same authors reported that oligomycin caused a collapse of the mitochondrial membrane potential identical in magnitude to that achieved by the proton uncoupler FCCP, concluding that in BSF cells, the nature of the mitochondrial electrical gradient was exclusively attributable to the proton-pumping activity, or reverse mode, of the ATP synthase (Nolan and Voorheis, 1992). In more than 10 years, RNA interference silencing of two F_1-ATPase subunits further corroborated the previous findings and confirmed the unusual and essential function of this enzyme for the survival of BSF trypanosomes (Schnaufer *et al.*, 2005; Brown *et al.*, 2006).

The role of the F-ATPase in BSF *T. brucei* strikingly contrasts with that of other eukaryotes, where the reverse operation of the ATP synthase is a rare and short-term phenomenon associated with hypoxia or anoxia. For example, under ischaemic conditions in mammalian tissues, respiration is halted and the ATP synthase reverses in response to decreased mitochondrial membrane potential, partially compensating for its loss by utilizing ATP produced by glycolysis. To limit the detrimental depletion of cellular ATP caused by an ATP-consuming F-ATP synthase (Rouslin *et al.*, 1986; Jennings *et al.*, 1991; St-Pierre *et al.*, 2000), the activity of this enzyme is regulated by a short naturally occurring protein, the inhibitory factor 1 (IF1) (Pullman and Monroy, 1963; Walker, 1994). IF1 specifically inhibits the ATPase activity with no effect on ATP synthesis (Pullman and Monroy, 1963; Asami *et al.*, 1970), although some authors propose an inhibitory effect of IF1 on both ATP synthase modes (Harris *et al.*, 1979; Schwerzmann and Pedersen, 1981;

Formentini *et al.*, 2012; Garcia-Bermudez and Cuezva, 2016). IF1 has also been implicated in cristae biogenesis, dimerization of the ATP synthase and metabolic reprogramming of cancer cells (Campanella *et al.*, 2009). This regulatory protein has been identified in *T. brucei* (TbIF1) and related trypanosomatid parasites. In *T. brucei* the expression of TbIF1 is tightly regulated throughout the life cycle as it is expressed only in the insect stages, but not in BSF (Panicucci *et al.*, 2017). In *T. cruzi* and *Leishmania* parasites, regulation of IF1 expression is reflected in its slight upregulation in the mammalian intracellular stages compared to the respective insect stages in agreement with increased mitochondrial activity of *T. cruzi* and *Leishmania* amastigotes (Li *et al.*, 2016; Inbar *et al.*, 2017). As in other organisms, TbIF1 inhibits the hydrolytic but not the synthetic activity of the mitochondrial ATP synthase *in vitro* (Panicucci *et al.*, 2017; Gahura *et al.*, 2018*a*). The artificial expression of TbIF1 is lethal for BSF trypanosomes, due to the abolishment of the mitochondrial membrane potential (Panicucci *et al.*, 2017).

In addition to its role in the maintenance of mitochondrial membrane potential, a functional F-ATPase is also required by BSF parasites to prevent the intramitochondrial accumulation of ATP. Elevated ATP levels lead to inhibition of the alternative oxidase, the only terminal oxidase in BSF parasites, and consequently to a reduced respiration rate (Luevano-Martinez *et al.*, 2020). This represents a novel and unique role of the F-ATPase connecting this enzyme to the regulation of the glycolytic pathway, which is intimately linked to respiration *via* the alternative oxidase (Bakker *et al.*, 1999). Despite these fundamental roles, BSF trypanosomes can withstand a loss of approximately 90% of the membrane-bound F-ATPase complexes with no obvious deleterious effect on their viability in culture nor on the mitochondrial membrane potential in live cells (Hierro-Yap *et al.*, 2021). We speculate that the long-term tolerance of reduced levels of F-ATPase complexes might be favourable for the emergence of trypanosomes lacking mitochondrial genome, as it might provide the time frame for the parasites to gain key nuclear mutation(s) in the F-ATPase that enable(s) generation of mitochondrial membrane potential in the absence of mitochondrial-encoded a-subunit.

The vestigial F-ATPase in trypanosomes without mitochondrial genome

The mitochondrial DNA of trypanosomatids, which is arranged in a distinct submitochondrial structure termed kinetoplast (hence kinetoplast DNA, kDNA), encodes mostly for the components of the oxidative phosphorylation pathway, key for the survival of *T. brucei*'s insect stages (Stuart, 1983; Schnaufer *et al.*, 2002). In BSF trypanosomes, which do not carry out oxidative phosphorylation, kDNA is indispensable due to the requirement of the F-ATP synthase a-subunit involved in proton translocation across the inner mitochondrial membrane. To synthesize the a-subunit, BSF mitochondria express additional two kDNA-encoded proteins, uS3m and uS12m, core components of mitochondrial ribosomes (Ramrath *et al.*, 2018). However, there are BSF trypanosomes that partially or completely lack their kDNA and they are referred to as dyskinetoplastic (Dk) subspecies (Agbe and Yielding, 1995). The Dk trypanosomes thriving in nature, *T. brucei evansi* (Hoare, 1937) and *T. brucei equiperdum* (Tobie, 1951), cause surra and dourine, respectively, devastating diseases that affect a broad range of domestic and wild animals in Africa, Asia and South America (Brun *et al.*, 1998). Stable kDNA-deficient strains can also be generated artificially using compounds targeting the kDNA network, such as ethidium bromide or acriflavine (Stuart, 1971; Riou *et al.*, 1980; Riou and Benard, 1980). Although Dk trypanosomes were thought to be locked in the long slender BSF stage, the absence of kDNA does not impair their differentiation into the stumpy form, a transmission pre-adapted stage with partially activated mitochondrial functions. However, the absence of kDNA does reduce the lifespan of the stumpy form (Dewar *et al.*, 2018), hampering their differentiation into the procyclic form (Timms *et al.*, 2002). Therefore, Dk trypanosomes are transmitted between hosts during sexual intercourse or mechanically *via* blood-sucking insects or vampire bats (Brun *et al.*, 1998), which facilitated their spread outside the area of the tsetse fly belt (Lun and Desser, 1995).

Because the ATP synthase a-subunit is absent in Dk trypanosomes, the molecular mechanism for the generation of mitochondrial membrane potential is analogous to that of mammalian ρ^0 cells and yeast *petite* mutants, both of which lack mitochondrial genome. The mechanism involves ATP hydrolysis by the vestigial ATP synthase, which provides the substrate for the electrogenic exchange of mitochondrial ADP^{3-} for cytosolic ATP^{4-} by the ATP/ADP carrier (AAC). Accordingly, oligomycin, an inhibitor that blocks the c-ring rotation, has virtually no effect on the growth of *T. b. evansi* (Schnaufer *et al.*, 2005). Moreover, Dk strains contain one of several point mutations in the nuclear-encoded subunits of the F_1-ATPase, most often the L262P or A273P substitutions in the γ-subunit (Lai *et al.*, 2008; Dean *et al.*, 2013). These substitutions are sufficient to allow the loss of kDNA and enable the generation of mitochondrial membrane potential in an F_0-independent manner, perhaps by enhancing the hydrolytic activity of the F_1-ATPase (Dean *et al.*, 2013).

The functional independence from the F_0 section led to the long-standing belief that the F_1 moiety exists as a soluble entity detached from the inner mitochondrial membrane in Dk trypanosomes (Schnaufer *et al.*, 2005; Jensen *et al.*, 2008). However, the finding that the silenced expression of the peripheral stalk subunit ATPTB2/d-subunit slowed the growth of Dk trypanosomes *in vitro* (Subrtova *et al.*, 2015) indicates that the complex might be attached to the membrane. Considering the presence of a membrane-bound F-ATP synthase in cells devoid of mitochondrial genome in other organisms (Wittig *et al.*, 2010; He *et al.*, 2017), it is likely that the vestigial F-ATPase in Dk trypanosomes also remains associated with the membrane to increase the spatial proximity between the AAC and the F_1-ATPase, and ensure an efficient exchange of substrates between the two entities.

Perspectives

Although many architectural features of ATP synthase from *Euglena* can be extrapolated to Trypanosomatida, a high-resolution cryo-EM structure of a trypanosomatid ATP synthase will be necessary for an unbiased and complete description of the enzyme in this parasitic lineage. Such research will reveal structural divergency, predominantly in the membrane-embedded part of the enzyme, as suggested by the absence of apparent homologs of some conserved ATP synthase subunits in *T. brucei* (Fig. 1). If several rotational states of the enzyme are characterized, the study would explain how the apparently flexible peripheral stalk immobilizes the catalytic subcomplex and what is the contribution of its unprecedented contacts with the F_1-ATPase (Fig. 3D). An atomic model of trypanosomal ATP synthase could also reveal details with potential relevance to structure-based drug development. For example, the IF1-F_1-ATPase interaction interface can be exploited by peptidomimetics to develop inhibitors selective for ATP hydrolytic activity of the enzyme. In the insect stage of *T. brucei*, the dimers of ATP synthase contribute to the shaping of the inner mitochondrial membrane by assembling into short helices on the rims of discoidal cristae (Muhleip *et al.*, 2017). However, it is not clear how the dimers

arrange in the BSF cells, which exhibit reduced complexity of mitochondrial ultrastructure. The understanding of the molecular mechanisms of membrane reshaping during the *T. brucei* life cycle, which can now be mimicked *in vitro* (Kolev *et al.*, 2012; Dolezelova *et al.*, 2020), will further illuminate the principles underlying mitochondrial dynamics in eukaryotes in general. Furthermore, recent data suggested interaction of the ATP synthase complex with mitochondrial calcium uniporter complex, AAC and phosphate carrier (Huang and Docampo, 2020). Further studies scrutinizing this putative megacomplex may reveal ATP synthase regulation by Ca^{2+} and strengthen the importance of the functional interplay between ATP synthase and both carriers in BSF and Dk cells. Considering our detailed knowledge of ATP synthase's role in *T. brucei* parasites, it is surprising that very little is known about its function in medically important parasites, *Leishmania* and *T. cruzi*. Although this gap is caused most likely by the fact that these parasites are less amenable to genetic manipulation, this can now be overcome by using subgenomic CRISPR/Cas9 libraries to dissect the role of oxidative phosphorylation complexes in different life cycle forms of these parasites. This will lead to a better understanding of the parasites' metabolic flexibility and capacity, ultimately advancing our efforts to target mitochondrial essential metabolic pathways for drug development.

Financial support. This study was supported by the Czech Science Foundation (18-17529S) and ERD fund and Ministry of Education, Youth and Sports (CZ.02.1.01/0.0/0.0/16_019/0000759).

Conflict of interest. The authors declare no competing interests.

References

Abrahams JP, Leslie AG, Lutter R and Walker JE (1994) Structure at 2.8 Å resolution of F_1-ATPase from bovine heart mitochondria. *Nature* **370**, 621–628.

Agbe A and Yielding KL (1995) Kinetoplasts play an important role in the drug responses of *Trypanosoma brucei*. *Journal of Parasitology* **81**, 968–973.

Anselmi C, Davies KM and Faraldo-Gomez JD (2018) Mitochondrial ATP synthase dimers spontaneously associate due to a long-range membrane-induced force. *The Journal of General Physiology* **150**, 763–770.

Arnold I, Pfeiffer K, Neupert W, Stuart RA and Schagger H (1998) Yeast mitochondrial F_1F_o-ATP synthase exists as a dimer: identification of three dimer-specific subunits. *The EMBO Journal* **17**, 7170–7178.

Asami K, Juniti K and Ernster L (1970) Possible regulatory function of a mitochondrial ATPase inhibitor in respiratory chain-linked energy transfer. *Biochimica et Biophysica Acta* **205**, 307–311.

Atwood JA III, Weatherly DB, Minning TA, Bundy B, Cavola C, Opperdoes FR, Orlando R and Tarleton RL (2005). The *Trypanosoma cruzi* proteome. *Science*, **309**, 473-476.

Bakker BM, Michels PA, Opperdoes FR and Westerhoff HV (1999) What controls glycolysis in bloodstream form *Trypanosoma brucei*? *Journal of Biological Chemistry* **274**, 14551–14559.

Blum TB, Hahn A, Meier T, Davies KM and Kühlbrandt W (2019) Dimers of mitochondrial ATP synthase induce membrane curvature and self-assemble into rows. *Proceedings of the National Academy of Sciences* **116**, 4250–4255.

Bowler MW, Montgomery MG, Leslie AG and Walker JE (2007) Ground state structure of F_1-ATPase from bovine heart mitochondria at 1.9 Å resolution. *Journal of Biological Chemistry* **282**, 14238–14242.

Brown SV, Hosking P, Li J and Williams N (2006) ATP synthase is responsible for maintaining mitochondrial membrane potential in bloodstream form *Trypanosoma brucei*. *Eukaryotic Cell* **5**, 45–53.

Brun R, Hecker H and Lun ZR (1998) *Trypanosoma evansi* and *T. equiperdum*: distribution, biology, treatment and phylogenetic relationship (a review). *Veterinary Parasitology* **79**, 95–107.

Bultema JB, Braun HP, Boekema EJ and Kouril R (2009) Megacomplex organization of the oxidative phosphorylation system by structural analysis of respiratory supercomplexes from potato. *Biochimica et Biophysica Acta* **1787**, 60–67.

Burki F, Roger AJ, Brown MW and Simpson AGB (2020) The new tree of eukaryotes. *Trends in Ecology & Evolution* **35**, 43–55.

Campanella M, Parker N, Tan CH, Hall AM and Duchen MR (2009) IF1: setting the pace of the F_1F_o-ATP synthase. *Trends in Biochemical Sciences* **34**, 343–350.

Cotter PD and Hill C (2003) Surviving the acid test: responses of gram-positive bacteria to low pH. *Microbiology and Molecular Biology Reviews* **67**, 429–453.

Davies KM, Strauss M, Daum B, Kief JH, Osiewacz HD, Rycovska A, Zickermann V and Kuhlbrandt W (2011) Macromolecular organization of ATP synthase and complex I in whole mitochondria. *Proceedings of the National Academy of Sciences* **108**, 14121–14126.

Davies KM, Anselmi C, Wittig I, Faraldo-Gomez JD and Kuhlbrandt W (2012) Structure of the yeast F_1F_o-ATP synthase dimer and its role in shaping the mitochondrial cristae. *Proceedings of the National Academy of Sciences* **109**, 13602–13607.

Dean S, Gould MK, Dewar CE and Schnaufer AC (2013) Single point mutations in ATP synthase compensate for mitochondrial genome loss in trypanosomes. *Proceedings of the National Academy of Sciences* **110**, 14741–14746.

de Souza W, de Carvalho TM and Barrias ES (2010) Review on *Trypanosoma cruzi*: host cell interaction. *International Journal of Cell Biology* **2010**, 295394.

Dewar CE, MacGregor P, Cooper S, Gould MK, Matthews KR, Savill NJ and Schnaufer A (2018) Mitochondrial DNA is critical for longevity and metabolism of transmission stage *Trypanosoma brucei*. *PLoS Pathogens* **14**, e1007195.

Dey R, Meneses C, Salotra P, Kamhawi S, Nakhasi HL and Duncan R (2010) Characterization of a *Leishmania* stage-specific mitochondrial membrane protein that enhances the activity of cytochrome c oxidase and its role in virulence. *Molecular Microbiology* **77**, 399–414.

Dolezelova E, Kunzova M, Dejung M, Levin M, Panicucci B, Regnault C, Janzen CJ, Barrett MP, Butter F and Zikova A (2020) Cell-based and multi-omics profiling reveals dynamic metabolic repurposing of mitochondria to drive developmental progression of *Trypanosoma brucei*. *PLoS Biology* **18**, e3000741.

Dudkina NV, Heinemeyer J, Keegstra W, Boekema EJ and Braun HP (2005) Structure of dimeric ATP synthase from mitochondria: an angular association of monomers induces the strong curvature of the inner membrane. *FEBS Letters* **579**, 5769–5772.

Dudkina NV, Sunderhaus S, Braun HP and Boekema EJ (2006) Characterization of dimeric ATP synthase and cristae membrane ultrastructure from *Saccharomyces* and *Polytomella* mitochondria. *FEBS Letters* **580**, 3427–3432.

Dudkina NV, Oostergetel GT, Lewejohann D, Braun HP and Boekema EJ (2010) Row-like organization of ATP synthase in intact mitochondria determined by cryo-electron tomography. *Biochimica et Biophysica Acta* **1797**, 272–277.

Flygaard RK, Mühleip A, Tobiasson V and Amunts A (2020) Type III ATP synthase is a symmetry-deviated dimer that induces membrane curvature through tetramerization. *Nature Communications* **11**, 1–11.

Formentini L, Sanchez-Arago M, Sanchez-Cenizo L and Cuezva JM (2012) The mitochondrial ATPase inhibitory factor 1 triggers a ROS-mediated retrograde prosurvival and proliferative response. *Molecular Cell* **45**, 731–742.

Gahura O and Zikova A (2019) Isolation of F_1-ATPase from the parasitic protist *Trypanosoma brucei*. *Journal of Visualized Experiments* **143**, e58334. doi: 10.3791/58334

Gahura O, Panicucci B, Vachova H, Walker JE and Zikova A (2018a) Inhibition of F_1-ATPase from *Trypanosoma brucei* by its regulatory protein inhibitor TbIF1. *The FEBS Journal* **285**, 4413–4423.

Gahura O, Subrtova K, Vachova H, Panicucci B, Fearnley IM, Harbour ME, Walker JE and Zikova A (2018b) The F_1-ATPase from *Trypanosoma brucei* is elaborated by three copies of an additional p18-subunit. *The FEBS Journal* **285**, 614–628.

Garcia-Bermudez J and Cuezva JM (2016) The ATPase inhibitory factor 1 (IF1): a master regulator of energy metabolism and of cell survival. *Biochimica et Biophysica Acta* **1857**, 1167–1182.

Goes GR, Rocha PS, Diniz AR, Aguiar PH, Machado CR and Vieira LQ (2016) *Trypanosoma cruzi* needs a signal provided by reactive oxygen species to infect macrophages. *PLoS Neglected Tropical Diseases* **10**, e0004555.

Goncalves RL, Barreto RF, Polycarpo CR, Gadelha FR, Castro SL and Oliveira MF (2011) A comparative assessment of mitochondrial function

in epimastigotes and bloodstream trypomastigotes of *Trypanosoma cruzi*. *Journal of Bioenergetics and Biomembranes* **43**, 651–661.

Gu J, Zhang L, Zong S, Guo R, Liu T, Yi J, Wang P, Zhuo W and Yang M (2019) Cryo-EM structure of the mammalian ATP synthase tetramer bound with inhibitory protein IF1. *Science* **364**, 1068–1075.

Guo H, Bueler SA and Rubinstein JL (2017) Atomic model for the dimeric F_o region of mitochondrial ATP synthase. *Science* **358**, 936–940.

Hahn A, Vonck J, Mills DJ, Meier T and Kuhlbrandt W (2018) Structure, mechanism, and regulation of the chloroplast ATP synthase. *Science* **360**, eaat4318.

Harris DA, von Tscharner V and Radda GK (1979) The ATPase inhibitor protein in oxidative phosphorylation. The rate-limiting factor to phosphorylation in submitochondrial particles. *Biochimica et Biophysica Acta* **548**, 72–84.

He J, Carroll J, Ding S, Fearnley IM and Walker JE (2017) Permeability transition in human mitochondria persists in the absence of peripheral stalk subunits of ATP synthase. *Proceedings of the National Academy of Sciences* **114**, 9086–9091.

Hierro-Yap C, Subrtová K, Gahura O, Panicucci B, Dewar C, Chinopoulos C, Schnaufer A and Zikova A (2021) Bioenergetic consequences of F_oF_1-ATP synthase/ATPase deficiency in two life cycle stages of *Trypanosoma brucei*. *Journal of Biological Chemistry* **1**, 100357. doi: 10.1016/j.jbc.2021.100357.

Hoare CABSCJ (1937) Spontaneous occurrence of strains of *Trypanosoma evansi* devoid of kinetonucleus. *Parasitology* **29**, 43–56.

Huang G and Docampo R (2020) The mitochondrial calcium uniporter interacts with subunit c of the ATP synthase of trypanosomes and humans. *mBio* **11**, e00168–20.

Huet D, Rajendran E, van Dooren GG and Lourido S (2018) Identification of cryptic subunits from an apicomplexan ATP synthase. *eLife* **7**, e38097.

Inbar E, Hughitt VK, Dillon LA, Ghosh K, El-Sayed NM and Sacks DL (2017) The transcriptome of *Leishmania major* developmental stages in their natural sand fly vector. *mBio* **8**, e00029–17.

Jennings RB, Reimer KA and Steenbergen C (1991) Effect of inhibition of the mitochondrial ATPase on net myocardial ATP in total ischemia. *Journal of Molecular and Cellular Cardiology* **23**, 1383–1395.

Jensen RE, Simpson L and Englund PT (2008) What happens when *Trypanosoma brucei* leaves Africa. *Trends in Parasitology* **24**, 428–431.

Junge W and Nelson N (2015) ATP synthase. *Annual Reviews of Biochemistry* **84**, 631–657.

Khare S, Roach SL, Barnes SW, Hoepfner D, Walker JR, Chatterjee AK, Neitz RJ, Arkin MR, McNamara CW, Ballard J, Lai Y, Fu Y, Molteni V, Yeh V, McKerrow JH, Glynne RJ and Supek F (2015) Utilizing chemical genomics to identify cytochrome b as a novel drug target for Chagas disease. *PLoS Pathogens* **11**, e1005058.

Klodmann J, Senkler M, Rode C and Braun HP (2011) Defining the protein complex proteome of plant mitochondria. *Plant Physiology* **157**, 587–598.

Kloehn J, Saunders EC, O'Callaghan S, Dagley MJ and McConville MJ (2015) Characterization of metabolically quiescent *Leishmania* parasites in murine lesions using heavy water labeling. *PLoS Pathogens* **11**, e1004683.

Klusch N, Murphy BJ, Mills DJ, Yildiz O and Kuhlbrandt W (2017) Structural basis of proton translocation and force generation in mitochondrial ATP synthase. *eLife* **6**, e33274.

Kolev NG, Ramey-Butler K, Cross GA, Ullu E and Tschudi C (2012) Developmental progression to infectivity in *Trypanosoma brucei* triggered by an RNA-binding protein. *Science* **338**, 1352–1353.

Kuhlbrandt W (2019) Structure and mechanisms of F-type ATP synthases. *Annual Reviews of Biochemistry* **88**, 515–549.

Lai DH, Hashimi H, Lun ZR, Ayala FJ and Lukes J (2008) Adaptations of *Trypanosoma brucei* to gradual loss of kinetoplast DNA: *Trypanosoma equiperdum* and *Trypanosoma evansi* are petite mutants of *T. brucei*. *Proceedings of the National Academy of Sciences* **105**, 1999–2004.

Li Y, Shah-Simpson S, Okrah K, Belew AT, Choi J, Caradonna KL, Padmanabhan P, Ndegwa DM, Temanni MR, Corrada Bravo H, El-Sayed NM and Burleigh BA (2016) Transcriptome remodeling in *Trypanosoma cruzi* and human cells during intracellular infection. *PLoS Pathogens* **12**, e1005511.

Luevano-Martinez LA, Girard R, Alencar MB and Silber AM (2020) ATP Regulates the activity of an alternative oxidase in *Trypanosoma brucei*. *FEBS Letters* **594**, 2150–2158.

Lun ZR and Desser SS (1995) Is the broad range of hosts and geographical distribution of *Trypanosoma evansi* attributable to the loss of maxicircle kinetoplast DNA? *Parasitology Today* **11**, 131–133.

Luque-Ortega JR, van't Hof W, Veerman EC, Saugar JM and Rivas L (2008) Human antimicrobial peptide histatin 5 is a cell-penetrating peptide targeting mitochondrial ATP synthesis in *Leishmania*. *The FASEB Journal* **22**, 1817–1828.

McConville MJ, Saunders EC, Kloehn J and Dagley MJ (2015) *Leishmania* carbon metabolism in the macrophage phagolysosome- feast or famine? *F1000Research* **4**, 938.

Montgomery MG, Gahura O, Leslie AGW, Zikova A and Walker JE (2018) ATP Synthase from *Trypanosoma brucei* has an elaborated canonical F_1-domain and conventional catalytic sites. *Proceedings of the National Academy of Sciences* **115**, 2102–2107.

Muhleip AW, Joos F, Wigge C, Frangakis AS, Kuhlbrandt W and Davies KM (2016) Helical arrays of U-shaped ATP synthase dimers form tubular cristae in ciliate mitochondria. *Proceedings of the National Academy of Sciences* **113**, 8442–8447.

Muhleip AW, Dewar CE, Schnaufer A, Kuhlbrandt W and Davies KM (2017) *In situ* structure of trypanosomal ATP synthase dimer reveals a unique arrangement of catalytic subunits. *Proceedings of the National Academy of Sciences* **114**, 992–997.

Muhleip A, McComas SE and Amunts A (2019) Structure of a mitochondrial ATP synthase with bound native cardiolipin. *eLife* **8**, e51179.

Mühleip A, Kock Flygaard R, Ovciarikova J, Lacombe A, Fernandes P, Sheiner L and Amunts A (2021) ATP Synthase hexamer assemblies shape cristae of *Toxoplasma* mitochondria. *Nature Communications* **12**, 1–13.

Murphy BJ, Klusch N, Langer J, Mills DJ, Yildiz O and Kuhlbrandt W (2019) Rotary substates of mitochondrial ATP synthase reveal the basis of flexible F_1–F_o coupling. *Science* **364**, eaaw9128.

Nelson RE, Aphasizheva I, Falick AM, Nebohacova M and Simpson L (2004) The I-complex in *Leishmania tarentolae* is an uniquely-structured F_1-ATPase. *Molecular and Biochemical Parasitology* **135**, 221–224.

Nolan DP and Voorheis HP (1992) The mitochondrion in bloodstream forms of *Trypanosoma brucei* is energized by the electrogenic pumping of protons catalysed by the F_1F_o-ATPase. *European Journal of Biochemistry* **209**, 207–216.

Opperdoes FR, Borst P and Spits H (1977) Particle-bound enzymes in the bloodstream form of *Trypanosoma brucei*. *European Journal of Biochemistry* **76**, 21–28.

Paiva CN and Bozza MT (2014) Are reactive oxygen species always detrimental to pathogens? *Antioxidants & Redox Signaling* **20**, 1000–1037.

Panek T, Elias M, Vancova M, Lukes J and Hashimi H (2020) Returning to the fold for lessons in mitochondrial Crista diversity and evolution. *Current Biology* **30**, R575–R588.

Panicucci B, Gahura O and Zikova A (2017) *Trypanosoma brucei* TbIF1 inhibits the essential F_1-ATPase in the infectious form of the parasite. *PLoS Neglected Tropical Diseases* **11**, e0005552.

Perez E, Lapaille M, Degand H, Cilibrasi L, Villavicencio-Queijeiro A, Morsomme P, Gonzalez-Halphen D, Field MC, Remacle C, Baurain D and Cardol P (2014) The mitochondrial respiratory chain of the secondary green alga *Euglena gracilis* shares many additional subunits with parasitic Trypanosomatidae. *Mitochondrion* **19**, 338–349.

Pinke G, Zhou L and Sazanov LA (2020) Cryo-EM structure of the entire mammalian F-type ATP synthase. *Nature Structural & Molecular Biology* **27**, 1077–1085.

Preiss L, Langer JD, Yildiz O, Eckhardt-Strelau L, Guillemont JE, Koul A and Meier T (2015) Structure of the mycobacterial ATP synthase F_o rotor ring in complex with the anti-TB drug bedaquiline. *Science Advances* **1**, e1500106.

Pullman ME and Monroy GC (1963) A naturally occurring inhibitor of mitochondrial adenosine triphosphatase. *Journal of Biological Chemistry* **238**, 3762–3769.

Ramrath DJF, Niemann M, Leibundgut M, Bieri P, Prange C, Horn EK, Leitner A, Boehringer D, Schneider A and Ban N (2018) Evolutionary shift toward protein-based architecture in trypanosomal mitochondrial ribosomes. *Science* **362**, eaau7735.

Riou G and Benard J (1980) Berenil induces the complete loss of kinetoblast DNA sequences in *Trypanosoma equiperdum*. *Biochemical and Biophysical Research Communications* **96**, 350–354.

Riou GF, Belnat P and Benard J (1980) Complete loss of kinetoplast DNA sequences induced by ethidium bromide or by acriflavine in *Trypanosoma equiperdum*. *Journal of Biological Chemistry* **255**, 5141–5144.

Rouslin W, Erickson JL and Solaro RJ (1986) Effects of oligomycin and acidosis on rates of ATP depletion in ischemic heart muscle. *American Journal of Physiology* **250**, H503–H508.

Salunke R, Mourier T, Banerjee M, Pain A and Shanmugam D (2018) Highly diverged novel subunit composition of apicomplexan F-type ATP synthase identified from *Toxoplasma gondii*. *PLoS Biology* **16**, e2006128.

Sathish Yadav KN, Miranda-Astudillo HV, Colina-Tenorio L, Bouillenne F, Degand H, Morsomme P, Gonzalez-Halphen D, Boekema EJ and Cardol P (2017) Atypical composition and structure of the mitochondrial dimeric ATP synthase from *Euglena gracilis*. *Biochimica et Biophysica Acta* **1858**, 267–275.

Saunders EC and McConville MJ (2020) Immunometabolism of *Leishmania* granulomas. *Immunology and Cell Biology* **98**, 832–844.

Saunders EC, Ng WW, Kloehn J, Chambers JM, Ng M and McConville MJ (2014) Induction of a stringent metabolic response in intracellular stages of *Leishmania mexicana* leads to increased dependence on mitochondrial metabolism. *PLoS Pathogens* **10**, e1003888.

Schnaufer A, Domingo GJ and Stuart K (2002) Natural and induced dyskinetoplastic trypanosomatids: how to live without mitochondrial DNA. *International Journal of Parasitology* **32**, 1071–1084.

Schnaufer A, Clark-Walker GD, Steinberg AG and Stuart K (2005) The F_1-ATP synthase complex in bloodstream stage trypanosomes has an unusual and essential function. *The EMBO Journal* **24**, 4029–4040.

Schwerzmann K and Pedersen PL (1981) Proton-adenosine triphosphatase complex of rat liver mitochondria: effect of energy state on its interaction with the adenosine triphosphatase inhibitory peptide. *Biochemistry* **20**, 6305–6311.

Senkler J, Senkler M, Eubel H, Hildebrandt T, Lengwenus C, Schertl P, Schwarzlander M, Wagner S, Wittig I and Braun HP (2017) The mitochondrial complexome of *Arabidopsis thaliana*. *The Plant Journal* **89**, 1079–1092.

Serricchio M, Hierro-Yap C, Schadeli D, Ben Hamidane H, Hemphill A, Graumann J, Zikova A and Butikofer P (2020) Depletion of cardiolipin induces major changes in energy metabolism in *Trypanosoma brucei* bloodstream forms. *The FASEB Journal* 1–16.

Shah-Simpson S, Pereira CF, Dumoulin PC, Caradonna KL and Burleigh BA (2016) Bioenergetic profiling of *Trypanosoma cruzi* life stages using seahorse extracellular flux technology. *Molecular and Biochemical Parasitology* **208**, 91–95.

Silber AM, Tonelli RR, Lopes CG, Cunha-e-Silva N, Torrecilhas AC, Schumacher RI, Colli W and Alves MJ (2009) Glucose uptake in the mammalian stages of *Trypanosoma cruzi*. *Molecular and Biochemical Parasitology* **168**, 102–108.

Silva Pereira S, Trindade S, De Niz M and Figueiredo LM (2019) Tissue tropism in parasitic diseases. *Open Biology* **9**, 190036.

Skodova-Sverakova I, Horvath A and Maslov DA (2015) Identification of the mitochondrially encoded subunit 6 of F_1F_o ATPase in *Trypanosoma brucei*. *Molecular and Biochemical Parasitology* **201**, 135–138.

Sobti M, Ishmukhametov R, Bouwer JC, Ayer A, Suarna C, Smith NJ, Christie M, Stocker R, Duncan TM and Stewart AG (2019) Cryo-EM reveals distinct conformations of *E. coli* ATP synthase on exposure to ATP. *eLife* **8**, e43864.

Speijer D, Breek CK, Muijsers AO, Hartog AF, Berden JA, Albracht SP, Samyn B, Van Beeumen J and Benne R (1997) Characterization of the respiratory chain from cultured *Crithidia fasciculata*. *Molecular and Biochemical Parasitology* **85**, 171–186.

Spikes TE, Montgomery MG and Walker JE (2020) Structure of the dimeric ATP synthase from bovine mitochondria. *Proceedings of the National Academy of Sciences* **117**, 23519–23526.

St-Pierre J, Brand MD and Boutilier RG (2000) Mitochondria as ATP consumers: cellular treason in anoxia. *Proceedings of the National Academy of Sciences* **97**, 8670–8674.

Stuart KD (1971) Evidence for the retention of kinetoplast DNA in an acriflavine-induced dyskinetoplastic strain of *Trypanosoma brucei* which replicates the altered central element of the kinetoplast. *Journal of Cell Biology* **49**, 189–195.

Stuart K (1983) Mitochondrial DNA of an African trypanosome. *Journal of Cellular Biochemistry* **23**, 13–26.

Subramanian A, Jhawar J and Sarkar RR (2015) Dissecting *Leishmania infantum* energy metabolism – a systems perspective. *PLoS ONE* **10**, e0137976.

Subrtova K, Panicucci B and Zikova A (2015) ATPasetb2, a unique membrane-bound F_oF_1-ATPase component, is essential in bloodstream and dyskinetoplastic trypanosomes. *PLoS Pathogens* **11**, e1004660.

Timms MW, van Deursen FJ, Hendriks EF and Matthews KR (2002) Mitochondrial development during life cycle differentiation of African trypanosomes: evidence for a kinetoplast-dependent differentiation control point. *Molecular Biology of the Cell* **13**, 3747–3759.

Tobie EJ (1951) Loss of the kinetoplast in a strain of *Trypanosoma equiperdum*. *Transactions of the American Microscopical Society* **70**, 251–254.

Vazquez-Acevedo M, Cardol P, Cano-Estrada A, Lapaille M, Remacle C and Gonzalez-Halphen D (2006) The mitochondrial ATP synthase of chlorophycean algae contains eight subunits of unknown origin involved in the formation of an atypical stator-stalk and in the dimerization of the complex. *Journal of Bioenergetics and Biomembranes* **38**, 271–282.

Walker JE (1994) The regulation of catalysis in ATP synthase. *Current Opinion in Structural Biology* **4**, 912–918.

Walker JE (2017) Structure, mechanism and regulation of ATP synthases. In Wikstrom M (ed.), *Mechanisms of Primary Energy Transduction in Biology*. Cambridge, UK: The Royal Society of Chemistry, pp. 338–373.

Waterhouse A, Bertoni M, Bienert S, Studer G, Tauriello G, Gumienny R, Heer FT, de Beer TAP, Rempfer C, Bordoli L, Lepore R and Schwede T (2018) Swiss-model: homology modelling of protein structures and complexes. *Nucleic Acids Research* **46**, W296–W303.

Wittig I, Meyer B, Heide H, Steger M, Bleier L, Wumaier Z, Karas M and Schagger H (2010) Assembly and oligomerization of human ATP synthase lacking mitochondrial subunits a and A6L. *Biochimica et Biophysica Acta* **1797**, 1004–1011.

Zikova A, Schnaufer A, Dalley RA, Panigrahi AK and Stuart KD (2009) The F_oF_1-ATP synthase complex contains novel subunits and is essential for procyclic *Trypanosoma brucei*. *PLoS Pathogens* **5**, e1000436.

Zikova A, Verner Z, Nenarokova A, Michels PAM and Lukes J (2017) A paradigm shift: the mitoproteomes of procyclic and bloodstream *Trypanosoma brucei* are comparably complex. *PLoS Pathogens* **13**, e1006679.

An ancestral interaction module promotes oligomerization in divergent mitochondrial ATP synthases

Ondřej Gahura[1,†], Alexander Mühleip[2,†], Carolina Hierro-Yap[1,3], Brian Panicucci[1], Minal Jain[1,3], David Hollaus[3], Martina Slapničková[1], Alena Zíková[1,3,*], Alexey Amunts[2,*]

[1]Institute of Parasitology, Biology Centre CAS, Ceske Budejovice, Czech Republic
[2]Science for Life Laboratory, Department of Biochemistry and Biophysics, Stockholm University, 17165 Solna, Sweden
[3]Faculty of Science, University of South Bohemia, Ceske Budejovice, Czech Republic

[*] Correspondence to: azikova@paru.cas.cz; amunts@scilifelab.se
[†] These authors contributed equally to this work.

Abstract

Mitochondrial ATP synthase forms stable dimers arranged into oligomeric assemblies that generate the inner-membrane curvature essential for efficient energy conversion. Here, we report cryo-EM structures of the intact ATP synthase dimer from *Trypanosoma brucei* in ten different rotational states. The model consists of 25 subunits, including nine lineage-specific, as well as 36 lipids. The rotary mechanism is influenced by the divergent peripheral stalk, conferring a greater conformational flexibility. Proton transfer in the lumenal half-channel occurs via a chain of five ordered water molecules. The dimerization interface is formed by subunit-*g* that is critical for interactions but not for the catalytic activity. Although overall dimer architecture varies among eukaryotes, we find that subunit-*g* together with subunit-*e* form an ancestral oligomerization motif, which is shared between the trypanosomal and mammalian lineages. Therefore, our data defines the subunit-*g/e* module as a structural component determining ATP synthase oligomeric assemblies.

Mitochondrial ATP synthase consists of the soluble F_1 and membrane-bound F_o subcomplexes, and occurs in dimers that assemble into oligomers to induce the formation of inner-membrane folds, called cristae. The cristae are the sites for oxidative phosphorylation and energy conversion in eukaryotic cells. Dissociation of ATP synthase dimers into monomers results in the loss of native cristae architecture and impairs mitochondrial function[1,2]. While cristae morphology varies substantially between organisms from different lineages, ranging from flat lamellar in opisthokonts to coiled tubular in ciliates and discoidal in euglenozoans[3], the mitochondrial ATP synthase dimers represent a universal occurrence to maintain the membrane shape[4].

ATP synthase dimers of variable size and architecture, classified into types I to IV have recently been resolved by high-resolution cryo-EM studies. In the structure of the type-I ATP synthase dimer from mammals, the monomers are only weakly associated[5,6], and in yeast insertions in the membrane subunits form tighter contacts[7]. The structure of the type-II ATP synthase dimer from the alga *Polytomella* sp. showed that the dimer interface is formed by phylum-specific components[8]. The type-III ATP synthase dimer from the ciliate *Tetrahymena* thermophila is characterized by parallel rotary axes, and a substoichiometric subunit, as well as multiple lipids were identified at the dimer interface, while additional protein components that tie the monomers together are distributed between the matrix, transmembrane, and lumenal regions[9]. The structure of the type-IV ATP synthase with native lipids from *Euglena gracilis* also showed that specific protein-lipid interactions contribute to the dimerization, and that the central and peripheral stalks interact with each other directly[10]. Finally, a unique apicomplexan ATP synthase dimerizes via 11 parasite-specific components that contribute ~7000 $Å^2$ buried surface area[11], and unlike all other ATP synthases, that assemble into rows, it associates in higher oligomeric states of pentagonal pyramids in the curved apical membrane regions. Together, the available structural data suggest a diversity of oligomerization, and it remains unknown whether common elements mediating these interactions exist or whether dimerization of ATP synthase occurred independently and multiple times in evolution[4].

The ATP synthase of *Trypanosoma brucei*, a representative of kinetoplastids and an established medically important model organism causing the sleeping sickness, is highly divergent, exemplified by the pyramid-shaped F_1 head containing a phylum specific subunit[12,13]. The dimers are sensitive to the lack of cardiolipin[14] and form short left-handed helical segments that extend across the membrane ridge of the discoidal cristae[15]. Uniquely among aerobic eukaryotes, the mammalian life cycle stage of *T. brucei* utilizes the reverse mode of ATP synthase, using the enzyme as a proton pump to maintain mitochondrial membrane potential at the expense of ATP[16,17]. In contrast, the insect stages of the parasite employ the ATP-producing forward mode of the enzyme[18,19].

Given the conservation of the core subunits, the different nature of oligomerization and the ability to test structural hypotheses biochemically, we reasoned that investigation of the *T. brucei* ATP synthase structure and function would provide the missing evolutionary link to understand how the monomers interact to form physiological dimers. Here, we address this question by combining structural, functional and evolutionary analysis of the *T. brucei* ATP synthase dimer.

Results

Cryo-EM structure of the *T. brucei* ATP synthase

We purified ATP synthase dimers from cultured *T. brucei* procyclic trypomastigotes by affinity chromatography with a recombinant natural protein inhibitor $TbIF_1$[20], and subjected the sample to cryo-EM analysis (Extended Data Fig. 1 and 2). Using masked refinements, maps were obtained for the membrane region, the rotor, and the peripheral stalk. To describe the conformational space of the *T. brucei* ATP synthase, we resolved ten distinct rotary substates, which were refined to 3.5-4.3 Å resolution. Finally, particles with both monomers in rotational state 1 were selected, and the consensus structure of the dimer was refined to 3.2 Å resolution (Extended Data Table 1, Extended Data Figs. 2&3).

Unlike the wide-angle architecture of dimers found in animals and fungi, the *T. brucei* ATP synthase displays an angle of 60° between the two F_1/*c*-ring subcomplexes. The model of the *T. brucei* ATP synthase includes all 25 different subunits, nine of which are lineage-specific (Fig. 1a, Supplementary Video 1, Extended Data Fig. 4). We named the subunits according to the previously proposed nomenclature[21-23] (Extended Data Table 2). In addition, we identified and modeled 36 bound phospholipids, including 24 cardiolipins (Extended Data Fig. 5). Both detergents used during purification, n-dodecyl β-D-maltoside (β-DDM) and glyco-diosgenin (GDN) are also resolved in the periphery of the membrane region (Extended Data Fig. 6).

In the catalytic region, F_1 is augmented by three copies of subunit p18, each bound to subunit-α[12,13]. Our structure shows that p18 is involved in the unusual attachment of F_1 to the peripheral stalk. The membrane region includes eight conserved F_o subunits (*b*, *d*, *f*, 8, *i/j*, *k*, *e*, and *g*) arranged around the central proton translocator subunit-*a*. We identified those subunits based on the structural similarity and matching topology to their yeast counterparts (Fig. 2). For subunit-*b*, a single transmembrane helix superimposes well with *b*H1 from yeast and anchors the newly identified subunit-*e* and -*g* to the F_o (Fig. 2a,b). In yeast and bovine ATP synthases *b*H1 and transmembrane helices of subunits-*e* and -*g* are arranged in the same way as in our structure and contribute to a characteristic wedge in the membrane domain[5]. The long helix *b*H2, which constitutes the central part of the peripheral stalk in other organisms is absent in *T. brucei* (Fig. 2c). No alternative subunit-*b*[24] is found in our structure.

The membrane region contains a peripheral subcomplex, formed primarily by the phylum-specific ATPTB1,6,12 and ATPEG3 (Fig. 1b). It is separated from the conserved core by a membrane-intrinsic cavity, in which nine bound cardiolipins are resolved (Fig. 1c), and the C-terminus of ATPTB12 interacts with the lumenal β-barrel of the c_{10}-ring. The β-barrel, which has previously been reported also in the ATP synthase from *E. gracilis*[10], extends from the c_{10}-ring approximately 15 Å to the lumen (Fig. 1a and Extended Data Fig. 7). The cavity of the decameric *c*-ring contains density consistent with disordered lipids, as observed in other ATP synthases[5,6,7], and in addition near the matrix side, 10 $Arg66_c$ residues coordinate a ligand density, which is consistent with a pyrimidine ribonucleoside triphosphate (Fig. 1d). We assign this density as uridine-triphosphate (UTP), due to its large requirement in the mitochondrial RNA metabolism of African trypanosomes being a substrate for post-transcriptional RNA editing[25], and addition of poly-uridine tails to gRNAs and rRNAs[26,27], as well as due to low abundance of cytidine triphosphate (CTP)[28]. The nucleotide base is inserted between two

Arg82$_c$ residues, whereas the triphosphate region is coordinated by another five Arg82$_c$ residues, with Tyr79$_\delta$ and Asn76$_\delta$ providing asymmetric coordination contacts. The presence of a nucleotide inside the *c*-ring is surprising, given the recent reports of phospholipids inside the *c*-rings in mammals[5,6] and ciliates[9], indicating that a range of different ligands can provide structural scaffolding.

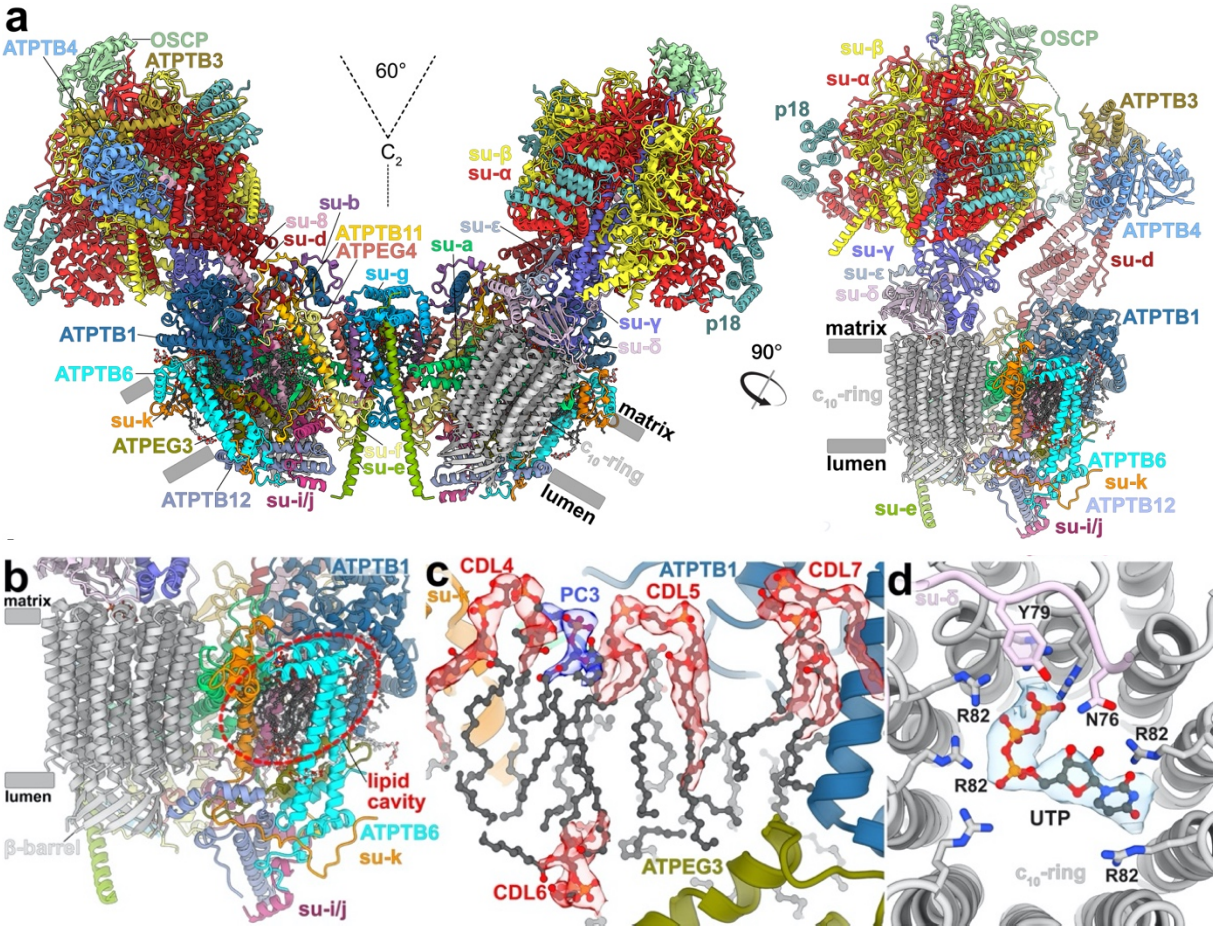

Fig. 1: The *T. brucei* ATP synthase structure with lipids and ligands.

a, Front and side views of the composite model with both monomers in rotational state 1. The two F$_1$/*c*$_{10}$-ring complexes, each augmented by three copies of the phylum-specific p18 subunit, are tied together at a 60°-angle. The membrane-bound F$_o$ region displays a unique architecture and is composed of both conserved and phylum-specific subunits. **b**, Side view of the F$_o$ region showing the lumenal interaction of the ten-stranded β-barrel of the *c*-ring (grey) with ATPTB12 (pale blue). The lipid-filled peripheral F$_o$ cavity is indicated. **c**, Close-up view of the bound lipids within the peripheral F$_o$ cavity with cryo-EM density shown. **d**, Top view into the decameric *c*-ring with a bound pyrimidine ribonucleoside triphosphate, assigned as UTP, although not experimentally detected. Map density shown in transparent blue, interacting residues shown.

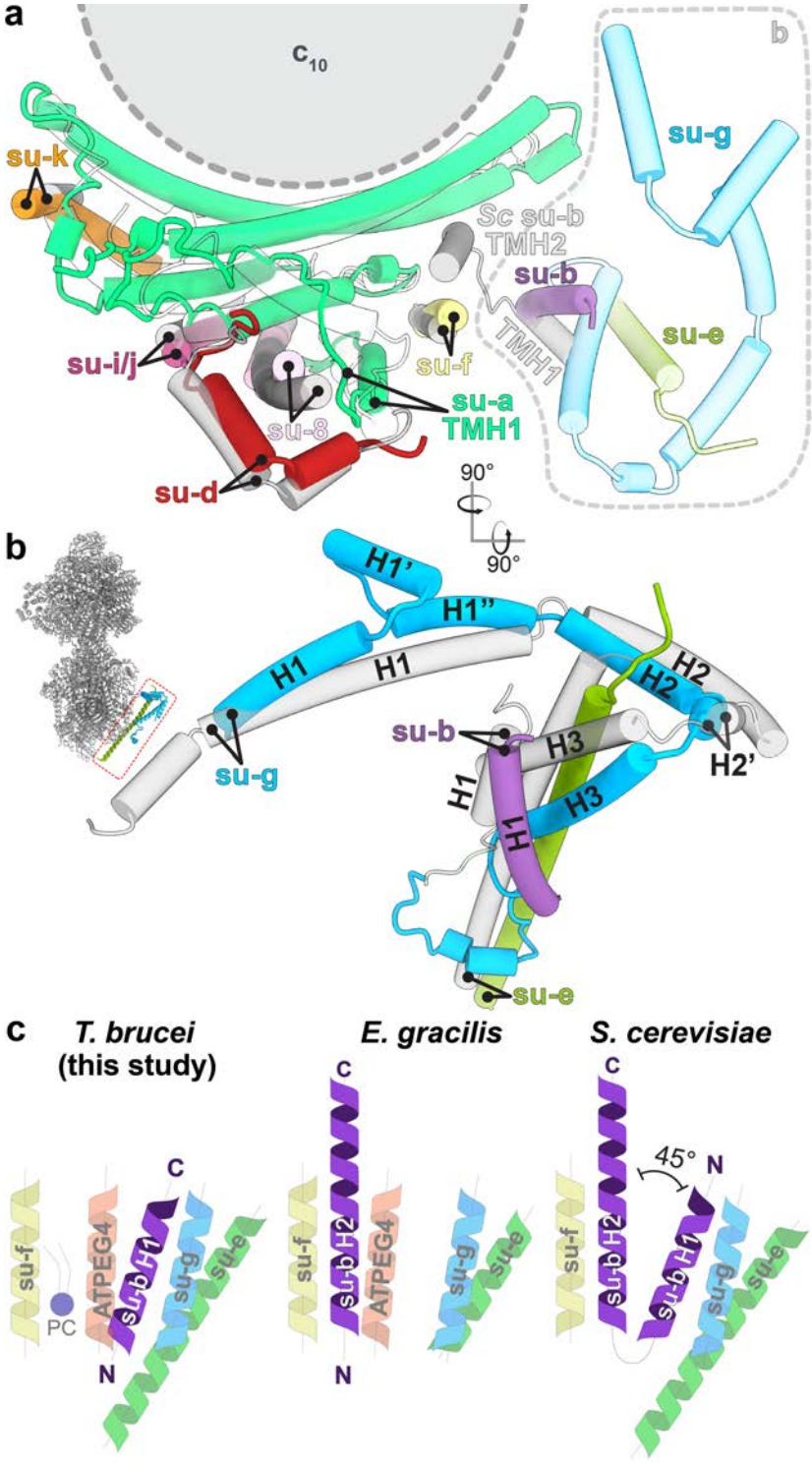

Fig. 2: Identification of conserved F_o subunits.

a, Top view of the membrane region with *T. brucei* subunits (colored) overlaid with *S. cerevisiae* structure (gray transparent). Close structural superposition and matching topology allowed the assignment of conserved subunits based on matching topology and location. **b**, Superposition of subunits-*b*, -*e* and -*g* with their *S. cerevisiae* counterparts (PDB 6B2Z) confirms their identity. **c**, Schematic representation of transmembrane helices of subunit-*b* and adjacent subunits in *T. brucei*, *E. gracilis* (PDB 6TDV)[10] and *S. cerevisiae* (PDB 6B2Z)[7] ATP synthases. PC – phosphatidylcholine.

Peripheral stalk flexibility and distinct rotational states

The trypanosomal peripheral stalk displays a markedly different architecture compared to its yeast and mammalian counterparts. In the opisthokont complexes, the peripheral stalk is organized around the long *b*H2, which extends from the membrane ~15 nm into the matrix and attaches to OSCP at the top of F_1[5,7]. By contrast, *T. brucei* lacks the canonical *b*H2 and instead, helices 5-7 of divergent subunit-*d* and the C-terminal helix of extended subunit-*8* bind to a C-terminal extension of OSCP at the apical part of the peripheral stalk (Fig. 3a). The interaction between OSCP and subunit-*d* and -*8* is stabilized by soluble ATPTB3 and ATPTB4. The peripheral stalk is rooted to the membrane subcomplex by a transmembrane helix of subunit-*8*, wrapped on the matrix side by helices 8-11 of subunit-*d*. Apart from the canonical contacts at the top of F_1, the peripheral stalk is attached to the F_1 via a euglenozoa-specific C-terminal extension of OSCP, which contains a disordered linker and a terminal helix hairpin extending between the F_1-bound p18 and subunits -*d* and -*8* of the peripheral stalk (Fig. 3a, Supplementary Videos 2,3). Another interaction of F_1 with the peripheral stalk occurs between the stacked C-terminal helices of subunit-β and -*d* (Fig. 3b), the latter of which structurally belongs to F_1 and is connected to the peripheral stalk via a flexible linker.

To assess whether the unusual peripheral stalk architecture influences the rotary mechanism, we analysed 10 classes representing different rotational states. The three main states (1-3) result from three ~120° rotation steps of the rotor relatively to the static F_o. In all classes F_1 is in a similar conformation, corresponding to the catalytic dwell, observed previously also in the crystal structure of *T. brucei* F_1-ATPase[13]. In accordance with the ~120° rotation of the central stalk, the conformations and nucleotide occupancy of the catalytic interfaces of the individual $\alpha\beta$ dimers differ between the main states, showing ADP and ATP in the "loose" and "tight" closed conformations, respectively, and empty nucleotide binding site in the "open" conformation. We identified five (1a-1e), four (2a-2d) and one (3) classes of the respective main states. The rotor positions of the rotational states 1a, 2a and 3 are related by steps of 117°, 136° and 107°, respectively. Throughout all the identified substeps of the rotational state 1 (classes 1a to 1e) the rotor turns by ~33°, which corresponds approximately to the advancement by one subunit-*c* of the c_{10}-ring (Fig. 3c). While rotating along with the rotor, the F_1 headpiece lags behind, advancing by only ~13°. During the following transition from 1e to 2a, the rotor advances by ~84°, whereas the F_1 headpiece rotates ~22° in the opposite direction (Fig. 3d). This generates a counter-directional torque between the two motors, which is consistent with a power-stroke mechanism. This counter-directional torque may occur in all three main rotational state transitions. However, it was observed only in the main state 1, because it was captured in more substeps than the remaining two states, presumably as a consequence of the symmetry mismatch between the decameric *c*-ring and the $\alpha_3\beta_3$ hexamer[29]. Within the four classes of the state 2 the rotor advances by 23° and F_1 returns close to its position observed in class 1a, where it is found also in the only observed class of the state 3. Albeit with small differences in step size, this mechanism is consistent with a previous observation in the *Polytomella* ATP synthase[8]. However, due to its large, rigid peripheral stalk, the *Polytomella* ATP synthase mainly displays rotational substeps, whereas the *Trypanosoma* F_1 also displays a tilting motion of ~8° revealed by rotary states 1a and 1b (Fig. 3e, Supplementary Video 2). The previously reported hinge motion between the N- and C-terminal domains of OSCP[8] is not

found in our structures, instead, the conformational changes of the F_1/c_{10}-ring subcomplex are accommodated by a 5° bending of the apical part of the peripheral stalk. (Fig. 3e, Supplementary Videos 2,3). Together, the structural data indicate that the divergent peripheral stalk attachment confers greater conformational flexibility to the *T. brucei* ATP synthase.

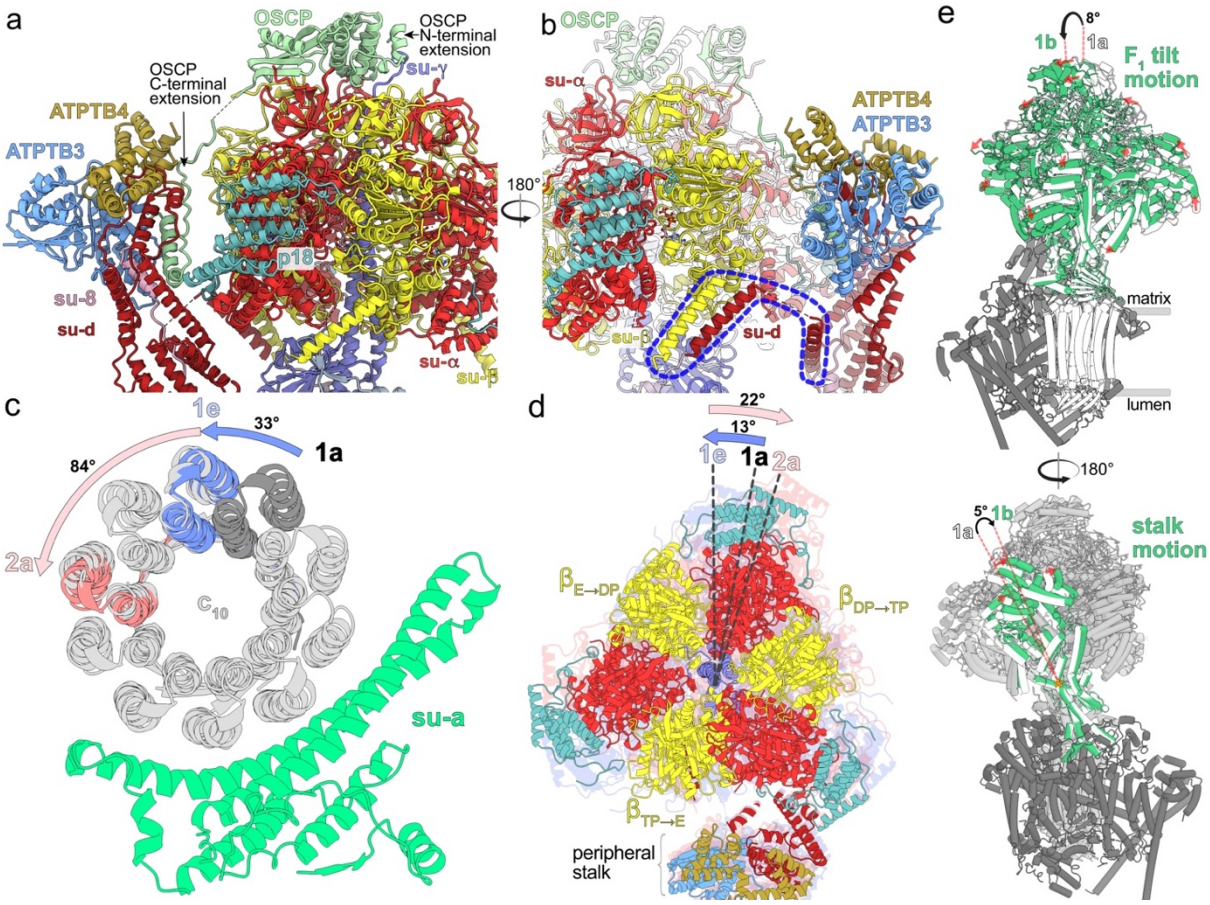

Fig. 3: A divergent peripheral stalk allows high flexibility during rotary catalysis. a, N-terminal OSCP extension provides a permanent central stalk attachment, while the C-terminal extension provides a phylum-specific attachment to the divergent peripheral stalk. **b**, The C-terminal helices of subunits -*β* and -*d* provide a permanent F_1 attachment. **c**, Substeps of the *c*-ring during transition from rotational state 1 to 2. **d**, F_1 motion accommodating steps shown in (c). After advancing along with the rotor to state 1e, the F_1 rotates in the opposite direction when transitioning to state 2a. **e**, Tilting motion of F_1 and accommodating bending of the peripheral stalk.

Lumenal proton half-channel is insulated by a lipid and contains ordered water molecules

The mechanism of proton translocation involves sequential protonation of E102 of subunits-*c*, rotation of the c_{10}-ring with neutralized E102*c* exposed to the phospholipid bilayer, and release of protons on the other side of the membrane. The sites of proton binding and release are separated by the conserved R146 contributed by the horizontal helix H5 of subunit-*a* and are accessible from the cristae lumen and mitochondrial matrix by aqueous half-channels (Fig. 4a). Together, R146 and the adjacent N209 coordinate a pair of water molecules in between helices

H5 and H6 (Fig. 4b). A similar coordination has been observed in the *Polytomella* ATP synthase[8]. The coordination of water likely restricts the R146 to rotamers that extend towards the *c*-ring, with which it is thought to interact.

In our structure, the lumenal half-channel, which displays a local resolution of 2.55 Å (Extended Data Fig. 3), is filled with a network of resolved water densities, ending in a chain of five ordered water molecules (W1-W5; Fig. 4c,d,e). The presence of ordered water molecules in the aqueous channel is consistent with a Grotthuss-type mechanism for proton transfer, which would not require long-distance diffusion of water molecules[5]. However, because some distances between the observed water molecules are too large for direct hydrogen bonding, proton transfer may involve both coordinated and disordered water molecules. The distance of 7 Å between the last resolved water (W1) and D202$_a$, the conserved residue that is thought to transfer protons to the *c*-ring, is too long for direct proton transfer. Instead, it may occur via the adjacent H155$_a$. Therefore, our structure resolves individual elements participating in proton transport (Fig. 4d,e).

The lumenal proton half-channel in the mammalian[5,6] and apicomplexan[11] ATP synthase is lined by the transmembrane part of *b*H2, which is absent in *T. brucei*. Instead, the position of *b*H2 is occupied by a fully ordered phosphatidylcholine in our structure (PC1; Fig. 4a,c). Therefore, a bound lipid replaces a proteinaceous element in the proton path.

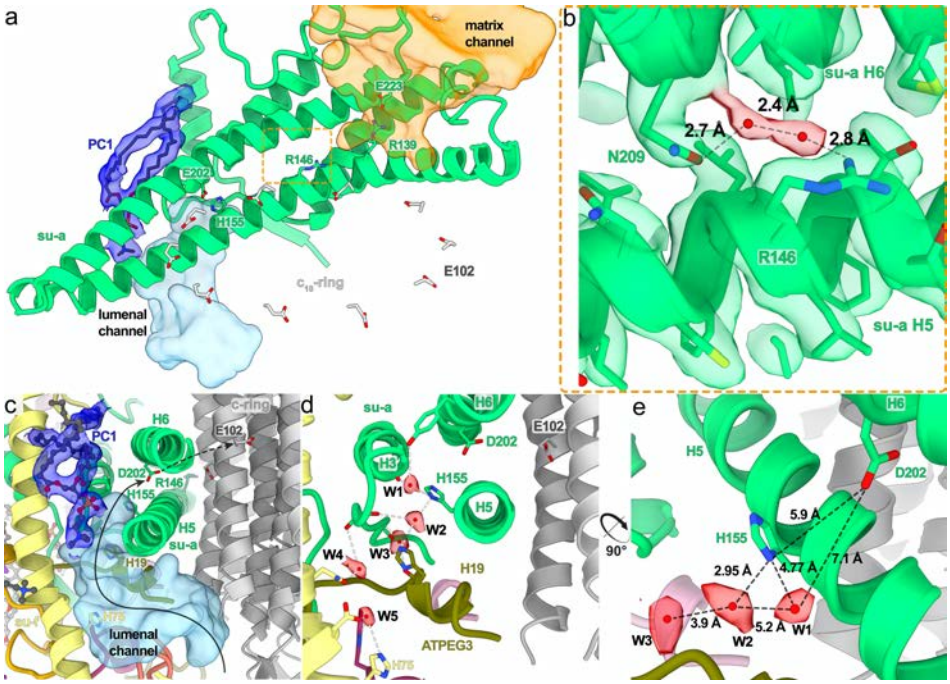

Fig. 4: The lumenal half-channel contains ordered water molecules and is confined by an F_o-bound lipid. a, Subunit-*a* (green) with the matrix (orange) and lumenal (light blue) channels, and an ordered phosphatidylcholine (PC1; blue). E102 of the c_{10}-ring shown in grey. **b**, Close-up view of the highly conserved R146$_a$ and N209$_a$, which coordinate two water molecules between helices H5-6$_a$. **c**, Sideview of the lumenal channel with proton pathway (light blue) and confining phosphatidylcholine (blue). **d**, Chain of ordered water molecules in the lumenal channel. Distances between the W1-W5 (red) are 5.2, 3.9, 7.3 and 4.8 Å, respectively. **e**, The ordered waters extend to H155$_a$, which likely mediates the transfer of protons to D202$_a$.

Subunit-*g* facilitates assembly of different ATP synthase oligomers

Despite sharing a set of conserved F_o subunits, the *T. brucei* ATP synthase dimer displays a markedly different dimer architecture compared to previously determined structures. First, its dimerization interface of 3,600 Å^2 is smaller than that of the *E. gracilis* type-IV (10,000 Å^2) and the *T. thermophila* type-III ATP synthases (16,000 Å^2). Second, unlike mammalian and fungal ATP synthase, in which the peripheral stalks extend in the plane defined by the two rotary axes, in our structure the monomers are rotated such that the peripheral stalks are offset laterally on the opposite sides of the plane. Due to the rotated monomers, this architecture is associated with a specific dimerization interface, where two subunit-*g* copies interact homotypically on the C_2 symmetry axis (Fig. 5a, Supplementary Video 1). Both copies of H1-2_g extend horizontally along the matrix side of the membrane, clamping against each other (Fig. 5c,e). This facilitates formation of contacts between an associated transmembrane helix of subunit-*e* with the neighbouring monomer via subunit-*a'* in the membrane, and -*f*' in the lumen, thereby further contributing to the interface (Fig. 5b). Thus, the ATP synthase dimer is assembled via the subunit-*e/g* module. The C-terminal part of the subunit-*e* helix extends into the lumen, towards the ten-stranded β-barrel of the *c*-ring (Extended Data Fig. 7a). The terminal 23 residues are disordered with poorly resolved density connecting to the detergent plug of the *c*-ring β-barrel (Extended Data Fig. 7b). This resembles the lumenal C-terminus of subunit-*e* in the bovine structure[5], indicating a conserved interaction with the *c*-ring. In mammals, a mechanism, in which retraction of subunit-*e* upon calcium exposure pulls out the lipid plug and induces disassembly of the c-ring, which triggers permeability transition pore (PTP) opening, has been proposed[6].

The *e/g* module is held together by four bound cardiolipins in the matrix leaflet, anchoring it to the remaining F_o region (Fig. 5c). The head groups of the lipids are coordinated by polar and charged residues with their acyl chains filling a central cavity in the membrane region at the dimer interface (Fig 5c, Extended Data Fig. 5f). Cardiolipin binding has previously been reported to be obligatory for dimerization in secondary transporters[30] and the depletion of cardiolipin synthase resulted in reduced levels of ATP synthase in bloodstream trypanosomes[14].

Interestingly, for yeasts, early blue native gel electrophoresis[31] and subtomogram averaging studies[2] suggested subunit-*g* as potentially dimer-mediating, however the *e/g* modules are located laterally opposed on either side of the dimer long axis, in the periphery of the complex, ~8.5 nm apart from each other. Because the *e/g* modules do not interact directly within the yeast ATP synthase dimer, they have been proposed to serve as membrane-bending elements, whereas the major dimer contacts are formed by subunit-*a* and -*i/j*[7]. In mammals, the *e/g* module occupies the same position as in yeasts, forming the interaction between two diagonal monomers in a tetramer[5,6,32], as well as between parallel dimers[33]. The comparison with our structure shows that the overall organization of the intra-dimeric trypanosomal and inter-dimeric mammalian *e/g* module is structurally similar (Fig. 5d). Furthermore, kinetoplastid parasites and mammals share conserved GXXXG motifs in subunit-*e*[34] and -*g* (Extended Data Fig. 8), which allow close interaction of their transmembrane helices (Fig. 5e), providing further evidence for subunit homology. However, while the mammalian ATP synthase dimers are arranged perpendicularly to the long axis of their rows along the edge of cristae[35], the

T. brucei dimers on the rims of discoidal cristae are inclined ~45º to the row axis[15]. Therefore, the *e/g* module occupies equivalent positions in the rows of both evolutionary distant groups (Fig. 5f and reference 33).

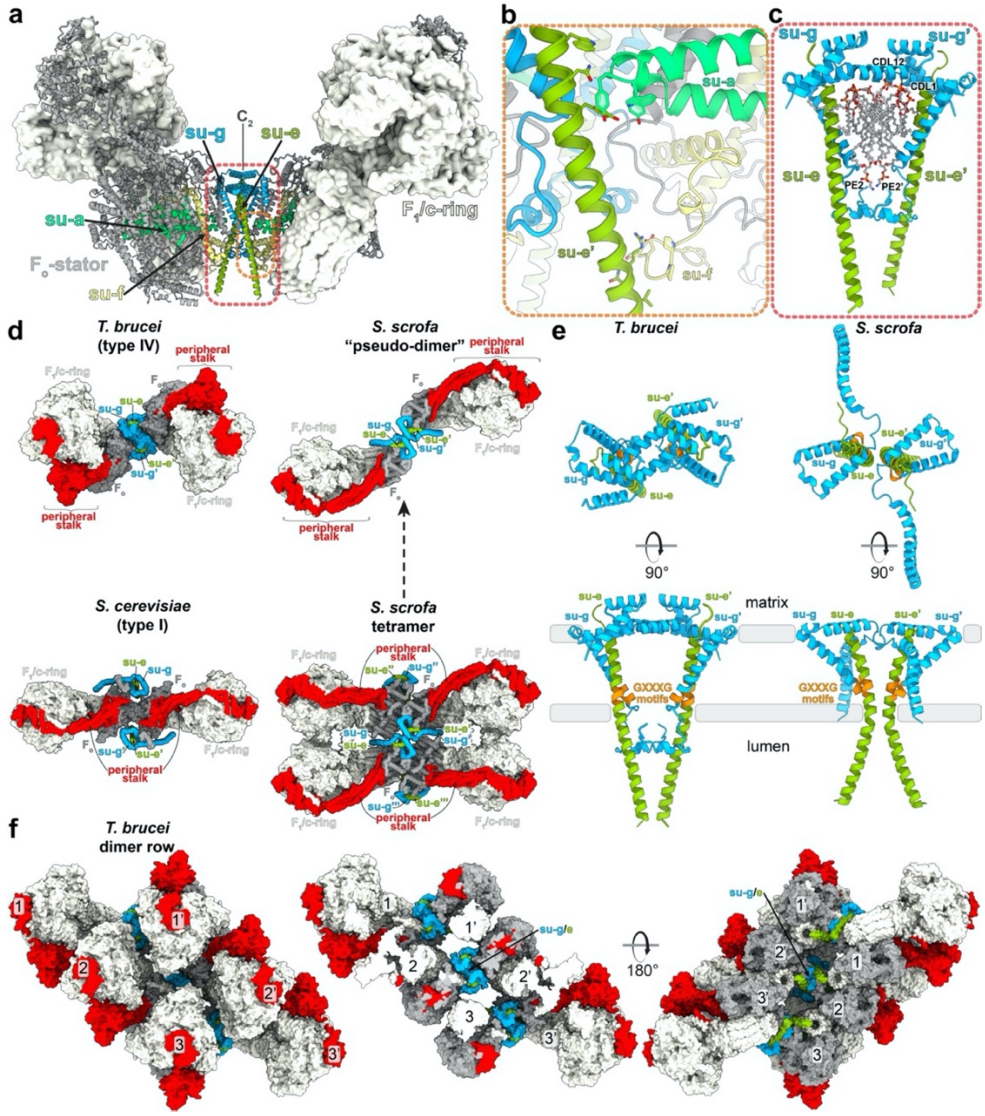

Fig. 5: The homotypic dimerization motif of subunit-*g* generates a conserved oligomerization module. a, Side view with dimerising subunits colored. **b,c**, The dimer interface is constituted by (b) subunit-*e'* contacting subunit-*a* in the membrane and subunit-*f* in the lumen, (c) subunits *e* and *g* from both monomers forming a subcomplex with bound lipids. **d**, Subunit-*g* and -*e* form a dimerization motif in the trypanosomal (type-IV) ATP synthase dimer (this study), the same structural element forms the oligomerization motif in the porcine ATP synthase tetramer. The structural similarity of the pseudo-dimer (i.e., two diagonal monomers from adjacent dimers) in the porcine structure with the trypanosomal dimer suggests that type I and IV ATP synthase dimers have evolved through divergence from a common ancestor. **e**, The dimeric subunit-*e/g* structures are conserved in pig (PDB 6ZNA) and *T. brucei* (this work) and contain a conserved GXXXG motif (orange) mediating interaction of transmembrane helices. **f**, Models of the ATP synthase dimers fitted into subtomogram averages of short oligomers[15]: matrix view, left; cut-through, middle, lumenal view, right (EMD-3560).

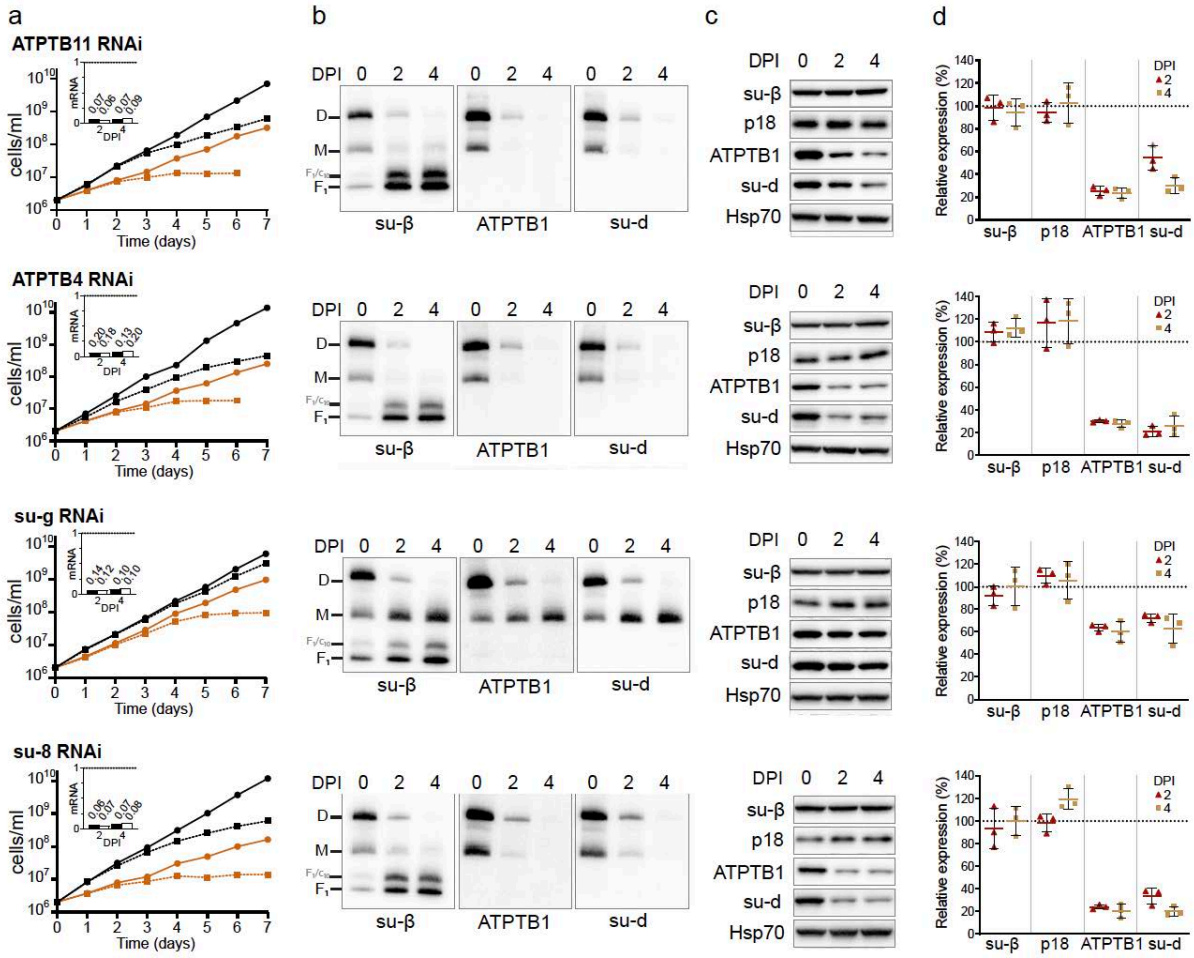

Fig. 6: RNAi knockdown of subunit-*g* results in monomerization of ATP synthase. a, Growth curves of non-induced (solid lines) and tetracycline-induced (dashed lines) RNAi cell lines grown in the presence (black) or absence (brown) of glucose. The insets show relative levels of the respective target mRNA at indicated days post-induction (DPI) normalized to the levels of 18S rRNA (black bars) or β-tubulin (white bars). **b**, Immunoblots of mitochondrial lysates from indicated RNAi cell lines resolved by BN-PAGE probed with antibodies against indicated ATP synthase subunits. **c**, Representative immunoblots of whole cell lysates from indicated RNAi cell lines probed with indicated antibodies. **d**, Quantification of three replicates of immunoblots in (c). Values were normalized to the signal of the loading control Hsp70 and to non-induced cells. Plots show means with standard deviations (SD).

Subunit-*g* retains the dimer but is not essential for the catalytic monomer

To validate structural insights, we knocked down each individual F_o subunit by inducible RNA interference (RNAi). All target mRNAs dropped to 5-20 % of their original levels after two and four days of induction (Fig. 6a and Extended Data Fig. 9a). Western blot analysis of whole-cell lysates resolved by denaturing electrophoresis revealed decreased levels of F_o subunits ATPB1 and *-d* suggesting that the integrity of the F_o moiety depends on the presence of other F_o subunits (Fig. 6c,d). Immunoblotting of mitochondrial complexes resolved by blue native polyacrylamide gel electrophoresis (BN-PAGE) with antibodies against F_1 and F_o subunits revealed a strong decrease or nearly complete loss of dimeric and monomeric forms of ATP synthases four days after induction of RNAi of most subunits (*b*, *e*, *f*, *i/j*, *k*, 8, ATPTB3, ATPTB4, ATPTB6, ATPTB11, ATPTB12, ATPEG3 and ATPEG4), documenting an increased instability of the enzyme or defects in its assembly. Simultaneous accumulation in F_1-ATPase, as observed by BN-PAGE, demonstrated that the catalytic moiety remains intact after the disruption of the peripheral stalk or the membrane subcomplex (Fig. 6b,c,d and Extended Data Fig. 9b).

In contrast to the other targeted F_o subunits, the downregulation of subunit-*g* with RNAi resulted in a specific loss of dimeric complexes with concomitant accumulation of monomers (Fig. 6b), indicating that it is required for dimerization, but not for the assembly and stability of the monomeric F_1F_o ATP synthase units. Transmission electron microscopy of thin cell sections revealed that the ATP synthase monomerization in the subunit-g^{RNAi} cell line had the same effect on mitochondrial ultrastructure as nearly complete loss of monomers and dimers upon knockdown of subunit-8. Both cell lines exhibited decreased cristae counts and aberrant cristae morphology (Fig. 7a,b), including the appearance of round shapes reminiscent of structures detected upon deletion of subunit-*g* or *-e* in *Saccharomyces cerevisiae*[1]. These results indicate that monomerization prevents the trypanosomal ATP synthase from assembling into short helical rows on the rims of the discoidal cristae[15], as has been reported for impaired oligomerization in counterparts from other eukaryotes[2,36].

Despite the altered mitochondrial ultrastructure, the subunit-g^{RNAi} cells showed only a very mild growth phenotype, in contrast to all other RNAi cell lines that exhibited steadily slowed growth from day three to four after the RNAi induction (Fig. 7a, Extended Data Fig. 9a). This is consistent with the growth defects observed after the ablation of F_o subunit ATPTB1[19] and F_1 subunits-α and p18[12]. Thus, the monomerization of ATP synthase upon subunit-*g* ablation had only a negligible effect on the fitness of trypanosomes cultured in glucose-rich medium, in which ATP production by substrate level phosphorylation partially compensates for compromised oxidative phosphorylation[37].

Measurement of oligomycin-sensitive ATP-dependent mitochondrial membrane polarization by safranin O assay in permeabilized cells showed that the proton pumping activity of the ATP synthase in the induced subunit-g^{RNAi} cells is negligibly affected, demonstrating that the monomerized enzyme is catalytically functional. By contrast, RNAi downregulation of subunit-8, ATPTB4 and ATPTB11, and ATPTB1 resulted in a strong decline of the mitochondrial membrane polarization capacity, consistent with the loss of both monomeric and dimeric ATP synthase forms (Fig. 7c). Accordingly, knockdown of the same subunits resulted in inability to produce ATP by oxidative phosphorylation (Fig. 7d). However, upon subunit-*g*

ablation the ATP production was affected only partially, confirming that the monomerized ATP synthase remains catalytically active. The ~50 % drop in ATP production of subunit-g^{RNAi} cells can be attributed to the decreased oxidative phosphorylation efficiency due to the impaired cristae morphology. Indeed, when cells were cultured in the absence of glucose, enforcing the need for oxidative phosphorylation, knockdown of subunit-*g* results in a growth arrest, albeit one to two days later than knockdown of all other tested subunits (Fig. 6a). The data show that dimerization is critical when oxidative phosphorylation is the predominant source of ATP.

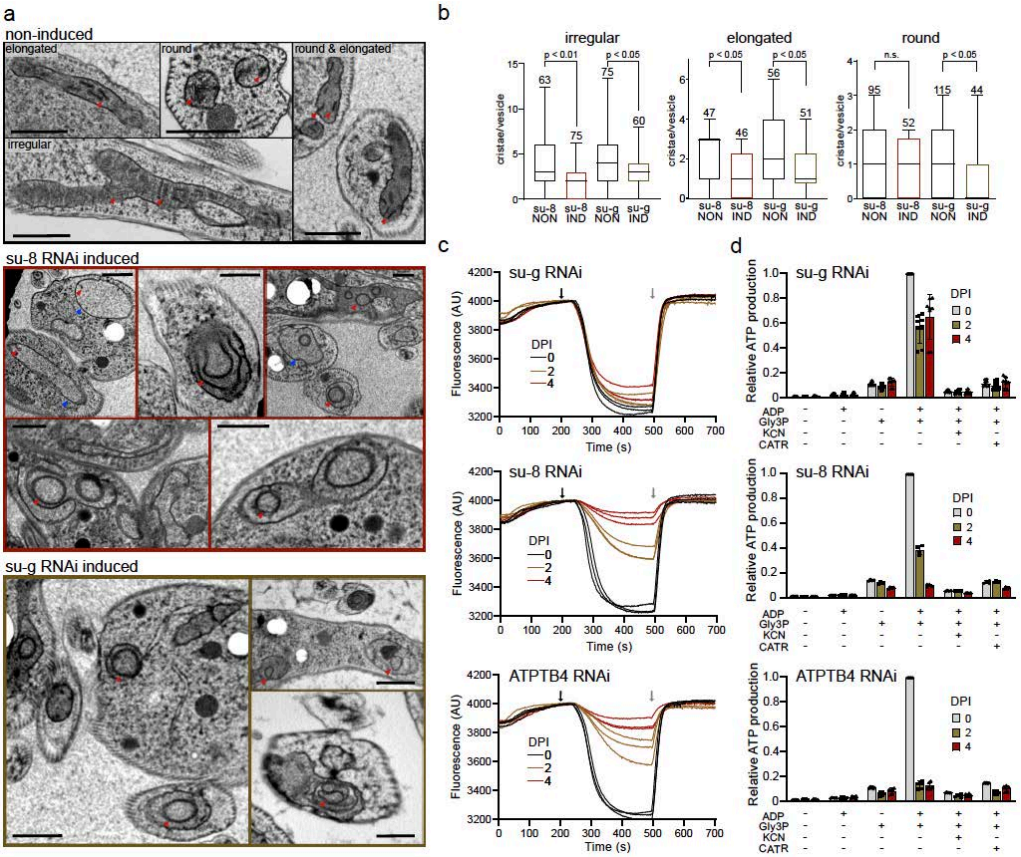

Fig. 7: Monomerization of ATP synthase by subunit-*g* knockdown results in aberrant mitochondrial ultrastructure but does not abolish catalytic activity. a, Transmission electron micrographs of sections of non-induced or 4 days induced RNAi cell lines. Mitochondrial membranes and cristae are marked with blue and red arrowheads, respectively. Top panel shows examples of irregular, elongated and round cross-sections of mitochondria quantified in (b). **b**, Cristae numbers per vesicle from indicated induced (IND) or non-induced (NON) cell lines counted separately in irregular, elongated and round mitochondrial cross-section. Boxes and whiskers show 25th to 75th and 5th to 95th percentiles, respectively. The numbers of analysed cross-sections are indicated for each data point. Unpaired t-test, p-values are shown. **c**, Mitochondrial membrane polarization capacity of non-induced or RNAi-induced cell lines two and four DPI measured by Safranine O. Black and gray arrow indicate addition of ATP and oligomycin, respectively. **d**, ATP production in permeabilized non-induced (0) or RNAi-induced cells 2 and 4 DPI in the presence of indicated substrates and inhibitors. The graphs show individual values, means (bars) and SD (error bars) of at least four replicates. *Gly3P*, DL-glycerol phosphate; *KCN*, potassium cyanide; *CATR*, carboxyatractyloside

Discussion

Our structure of the mitochondrial ATP synthase dimer from the mammalian parasite *T. brucei* offers new insight into the mechanism of membrane shaping, rotary catalysis, and proton transfer. Considering that trypanosomes belong to an evolutionarily divergent group of Kinetoplastida, the ATP synthase dimer has several interesting features that differ from other dimer structures. The subunit-*b* found in bacterial and other mitochondrial F-type ATP synthases appears to be highly reduced to a single transmembrane helix *b*H1. The long *b*H2, which constitutes the central part of the peripheral stalk in other organisms, and is also involved in the composition of the lumenal proton half-channel, is completely absent in *T. brucei*. Interestingly, the position of *b*H2 in the proton half channel is occupied by a fully ordered phosphatidylcholine molecule that replaces a well-conserved proteinaceous element in the proton path. However, this replacement is not a common trait of all type-IV ATP synthases, because subunit-*b* in *Euglena gracilis* contains the canonical bH2 but lacks bH1[10]. Thus, while subunit-*b* is conserved in Euglenozoa, the lineages of *T. brucei* and *E. gracilis* retained its different non-overlapping structural elements (Fig. 2c). Lack of *b*H2 in *T. brucei* also affects composition of the peripheral stalk in which the divergent subunit-*d* and subunit-*8* binds directly to a C-terminal extension of OSCP, indicating a remodeled peripheral stalk architecture. The peripheral stalk contacts the F_1 headpiece at several positions conferring greater conformational flexibility to the ATP synthase.

Using the structural and functional data, we also identified a conserved structural element of the ATP synthase that is responsible for its multimerization. Particularly, subunit-*g* is required for the dimerization, but dispensable for the assembly of the F_1F_o monomers. Although the monomerized enzyme is catalytically competent, the inability to form dimers results in defective cristae structure, and consequently leads to compromised oxidative phosphorylation and cease of proliferation. The cristae-shaping properties of mitochondrial ATP synthase dimers are critical for sufficient ATP production by oxidative phosphorylation, but not for other mitochondrial functions, as demonstrated by the lack of growth phenotype of subunit-g^{RNAi} cells in the presence of glucose. Thus, trypanosomal subunit-*g* depletion strain represents an experimental tool to assess the roles of the enzyme's primary catalytic function and mitochondria-specific membrane-shaping activity, highlighting the importance of the latter for oxidative phosphorylation.

Based on our data and previously published structures, we propose an ancestral state with double rows of ATP synthase monomers connected by *e/g* modules longitudinally and by other F_o subunits transversally. During the course of evolution, different pairs of adjacent ATP synthase monomer units formed stable dimers in individual lineages (Fig. 8). This gave rise to the highly divergent type-I and type-IV ATP synthase dimers with subunit-*e/g* modules serving either as oligomerization or dimerization motives, respectively. Because trypanosomes belong to the deep-branching eukaryotic supergroup Discoba, the proposed arrangement might have been present in the last eukaryotic common ancestor. Although sequence similarity of subunit-*g* is low and restricted to the single transmembrane helix, we found homologs of subunit-*g* in addition to Opisthokonta and Discoba also in Archaeplastida and Amoebozoa, which represent other eukaryotic supergroups, thus supporting the ancestral role in oligomerization (Extended Data Fig. 8). Taken together, our analysis reveals that mitochondrial ATP synthases that

display markedly diverged architecture share the ancestral structural module that promotes oligomerization.

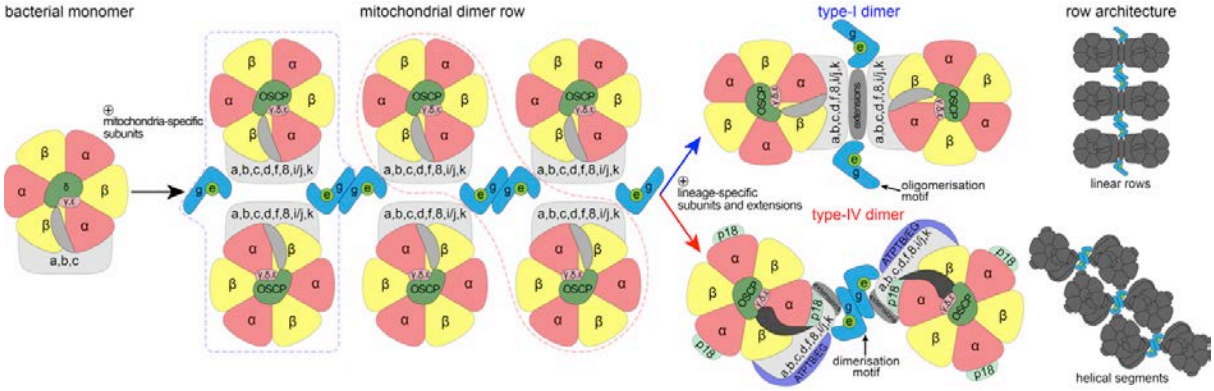

Fig. 8: The subunit-*e/g* module is an ancestral oligomerization motif of ATP synthase. Schematic model of the evolution of type-I and IV ATP synthases. Mitochondrial ATP synthases are derived from a monomeric complex of proteobacterial origin. In a mitochondrial ancestor, acquisition of mitochondria-specific subunits, including the subunit-*e/g* module resulted in the assembly of ATP synthase double rows, the structural basis for cristae biogenesis. Through divergence, different ATP synthase architectures evolved, with the subunit-*e/g* module functioning as an oligomerization (type I) or dimerization (type IV) motif, resulting in distinct row assemblies between mitochondrial lineages.

Materials and Methods

Cell culture and isolation of mitochondria

T. brucei procyclic strains were cultured in SDM-79 medium supplemented with 10% (v/v) fetal bovine serum. For growth curves in glucose-free conditions, cells were grown in SDM-80 medium with 10 % dialysed FBS. RNAi cell lines were grown in presence of 2.5 µg/ml phleomycin and 1 µg/ml puromycin. For ATP synthase purification, mitochondria were isolated from the Lister strain 427. Typically, $1.5x10^{11}$ cells were harvested, washed in 20 mM sodium phosphate buffer pH 7.9 with 150 mM NaCl and 20 mM glucose, resuspended in hypotonic buffer 1 mM Tris-HCl pH 8.0, 1 mM EDTA, and disrupted by 10 strokes in a 40-ml Dounce homogenizer. The lysis was stopped by immediate addition of sucrose to 0.25 M. Crude mitochondria were pelleted (15 min at 16,000 xg, 4°C), resuspended in 20 mM Tris-HCl pH 8.0, 250 mM sucrose, 5 mM $MgCl_2$, 0.3 mM $CaCl_2$ and treated with 5 µg/ml DNase I. After 60 min on ice, one volume of the STE buffer (20 mM Tris-HCl pH 8.0, 250 mM sucrose, 2 mM EDTA) was added and mitochondria were pelleted (15 min at 16000 xg, 4°C). The pellet was resuspended in 60% (v/v) Percoll in STE and loaded on six linear 10-35% Percoll gradients in STE in polycarbonate tubes for SW28 rotor (Beckman). Gradients were centrifuged for 1 h at 24,000 rpm, 4°C. The middle phase containing mitochondrial vesicles (15-20 ml per tube) was collected, washed four times in the STE buffer, and pellets were snap-frozen in liquid nitrogen and stored at -80°C.

456 Plasmid construction and generation of RNAi cell lines

457 To downregulate ATP synthase subunits by RNAi, DNA fragments corresponding to
458 individual target sequences were amplified by PCR from Lister 427 strain genomic DNA using
459 forward and reverse primers extended with restriction sites *Xho*I&*Kpn*I and *Xba*I&*Bam*HI,
460 respectively (Extended Data Table 3). Each fragment was inserted into the multiple cloning
461 sites 1 and 2 of pAZ0055 vector, derived from pRP$^{HYG-iSL}$ (courtesy of Sam Alsford) by
462 replacement of hygromycine resistance gene with phleomycine resistance gene, with restriction
463 enzymes *Kpn*I/*Bam*HI and *Xho*I/*Xba*I, respectively. Resulting constructs with tetracycline
464 inducible T7 polymerase driven RNAi cassettes were linearized with *Not*I and transfected into
465 a cell line derived from the Lister strain 427 by integration of the SmOx construct for
466 expression of T7 polymerase and the tetracycline repressor[38] into the β-tubulin locus. RNAi
467 was induced in selected semi-clonal populations by addition of 1 μg/ml tetracycline and the
468 downregulation of target mRNAs was verified by quantitative RT-PCR 2 and 4 days post
469 induction. The total RNA isolated by an RNeasy Mini Kit (Qiagen) was treated with 2 μg of
470 DNase I, and then reverse transcribed to cDNA with TaqMan Reverse Transcription kit
471 (Applied Biosciences). qPCR reactions were set with Light Cycler 480 SYBR Green I Master
472 mix (Roche), 2 μl of cDNA and 0.3 μM primers (Extended Data Table 3), and run on
473 LightCycler 480 (Roche). Relative expression of target genes was calculated using - ΔΔCt
474 method with 18S rRNA or β-tubulin as endogenous reference genes and normalized to
475 noninduced cells.

476

477 Denaturing and blue native polyacrylamide electrophoresis and immunoblotting

478 Whole cell lysates for denaturing sodium dodecyl sulphate polyacrylamide electrophoresis
479 (SDS-PAGE) were prepared from cells resuspended in PBS buffer (10 mM phosphate buffer,
480 130 mM NaCl, pH 7.3) by addition of 3x Laemmli buffer (150 mM Tris pH 6.8, 300 mM 1,4-
481 dithiothreitol, 6% (w/v) SDS, 30% (w/v) glycerol, 0.02% (w/v) bromophenol blue) to final
482 concentration of $1x10^7$ cells in 30 μl. The lysates were boiled at 97ºC for 10 min and stored at
483 -20ºC. For immunoblotting, lysates from $3x10^6$ cells were separated on 4-20 % gradient Tris-
484 glycine polyacrylamide gels (BioRad 4568094), electroblotted onto a PVDF membrane (Pierce
485 88518), and probed with respective antibodies (Extended Data Table 4). Membranes were
486 incubated with the Clarity Western ECL substrate (BioRad 1705060EM) and
487 chemiluminescence was detected on a ChemiDoc instrument (BioRad). Band intensities were
488 quantified densitometrically using the ImageLab software. The levels of individual subunits
489 were normalized to the signal of mtHsp70.

490 Blue native PAGE (BN-PAGE) was performed as described earlier[12] with following
491 modifications. Crude mitochondrial vesicles from 2.5 x 10^8 cells were resuspended in 40 μl of
492 Solubilization buffer A (2 mM ε-aminocaproic acid (ACA), 1 mM EDTA, 50 mM NaCl, 50
493 mM Bis-Tris/HCl, pH 7.0) and solubilized with 2% (w/v) dodecylmaltoside (β-DDM) for 1 h
494 on ice. Lysates were cleared at 16,000 g for 30 min at 4ºC and their protein concentration was
495 estimated using bicinchoninic acid assay. For each time point, a volume of mitochondrial lysate
496 corresponding to 4 μg of total protein was mixed with 1.5 μl of loading dye (500 mM ACA,
497 5% (w/v) Coomassie Brilliant Blue G-250) and 5% (w/v) glycerol and with 1 M ACA until a

final volume of 20 µl/well, and resolved on a native PAGE 3-12% Bis-Tris gel (Invitrogen). After the electrophoresis (3 h, 140 V, 4°C), proteins were transferred by electroblotting onto a PVDF membrane (2 h, 100 V, 4ºC, stirring), followed by immunodetection with an appropriate antibody (Extended Data Table 4).

Mitochondrial membrane polarization measurement

The capacity to polarize mitochondrial membrane was determined fluorometrically employing safranin O dye (Sigma S2255) in permeabilized cells. For each sample, $2x10^7$ cells were harvested and washed with ANT buffer (8 mM KCl, 110 mM K-gluconate, 10 mM NaCl, 10 mM free-acid Hepes, 10 mM K_2HPO_4, 0.015 mM EGTA potassium salt, 10 mM mannitol, 0.5 mg/ml fatty acid-free BSA, 1.5 mM $MgCl_2$, pH 7.25). The cells were permeabilized by 8 µM digitonin in 2 ml of ANT buffer containing 5 µM safranin O. Fluorescence was recorded for 700 s in a Hitachi F-7100 spectrofluorimeter (Hitachi High Technologies) at a 5-Hz acquisition rate, using 495 nm and 585 nm excitation and emission wavelengths, respectively. 1 mM ATP (PanReac AppliChem A1348,0025) and 10 µg/ml oligomycin (Sigma O4876) were added after 230 s and 500 s, respectively. Final addition of the uncoupler SF 6847 (250 nM; Enzo Life Sciences BML-EI215-0050) served as a control for maximal depolarization. All experiments were performed at room temperature and constant stirring.

ATP production assay

ATP production in digitonin-isolated mitochondria was performed as described previously[39]. Briefly, $1x10^8$ cells per time point were lysed in SoTE buffer (600 mM sorbitol, 2 mM EDTA, 20 mM Tris-HCl, pH 7.75) containing 0.015% (w/v) digitonin for 5 min on ice. After centrifugation (3 min, 4,000 g, 4ºC), the soluble cytosolic fraction was discarded and the organellar pellet was resuspended in 75 µl of ATP production assay buffer (600 mM sorbitol, 10 mM $MgSO_4$, 15 mM potassium phosphate buffer pH 7.4, 20 mM Tris-HCl pH 7.4, 2.5 mg/ml fatty acid-free BSA). ATP production was induced by addition of 20 mM DL-glycerol phosphate (sodium salt) and 67 µM ADP. Control samples were preincubated with the inhibitors potassium cyanide (1 mM) and carboxyatractyloside (6.5 µM) for 10 min at room temperature. After 30 min at room temperature, the reaction was stopped by addition of 1.5 µl of 70% perchloric acid. The concentration of ATP was estimated using the Roche ATP Bioluminescence Assay Kit HS II in a Tecan Spark plate reader. The luminescence values of the RNAi induced samples were normalized to that of the corresponding noninduced sample.

Thin sectioning and transmission electron microscopy

The samples were centrifuged and pellet was transferred to the specimen carriers which were completed with 20% BSA and immediately frozen using high pressure freezer Leica EM ICE (Leica Microsystems). Freeze substitution was performed in the presence of 2% osmium tetroxide diluted in 100% acetone at -90°C. After 96 h, specimens were warmed to -20°C at a slope 5 °C/h. After the next 24 h, the temperature was increased to 3°C (3°C/h). At room temperature, samples were washed in acetone and infiltrated with 25%, 50%, 75%

acetone/resin EMbed 812 (EMS) mixture 1 h at each step. Finally, samples were infiltrated in 100% resin and polymerized at 60°C for 48h. Ultrathin sections (70 nm) were cut using a diamond knife, placed on copper grids and stained with uranyl acetate and lead citrate. TEM micrographs were taken with Mega View III camera (SIS) using a JEOL 1010 TEM operating at an accelerating voltage of 80 kV.

Purification of *T. brucei* ATP synthase dimers

Mitochondria from $3x10^{11}$ cells were lysed by 1 % (w/v) β-DDM in 60 ml of 20 mM Bis-tris propane pH 8.0 with 10 % glycerol and EDTA-free Complete protease inhibitors (Roche) for 20 min at 4ºC. The lysate was cleared by centrifugation at 30,000 xg for 20 min at 4ºC and adjusted to pH 6.8 by drop-wise addition of 1 M 3-(N-morpholino) propanesulfonic acid pH 5.9. Recombinant $TbIF_1$ without dimerization region, whose affinity to F_1-ATPase was increased by N-terminal truncation and substitution of tyrosine 36 with tryptophan[20], with a C-terminal glutathione S-transferase (GST) tag ($TbIF_1$(9-64)-Y36W-GST) was added in approximately 10-fold molar excess over the estimated content of ATP synthase. Binding of $TbIF_1$ was facilitated by addition of neutralized 2 mM ATP with 4 mM magnesium sulphate. After 5 min, sodium chloride was added to 100 mM, the lysate was filtered through a 0.2 µm syringe filter and immediately loaded on 5 ml GSTrap HP column (Cytiva) equilibrated in 20 mM Bis-Tris-Propane pH 6.8 binding buffer containing 0.1 % (w/v) glyco-diosgenin (GDN; Avanti Polar Lipids), 10 % (v/v) glycerol, 100 mM sodium chloride, 1 mM tris(2-carboxyethyl)phosphine (TCEP), 1 mM ATP, 2 mM magnesium sulphate, 15 µg/ml cardiolipin, 50 µg/ml 1-palmitoyl-2-oleoyl-sn-glycero-3-phosphocholine (POPC), 25 µg/ml 1-palmitoyl-2-oleoyl-sn-glycero-3-phosphoethanolamine (POPE) and 10 µg/ml 1-palmitoyl-2-oleoyl-sn-glycero-3-[phospho-rac-(1-glycerol)] (POPG). All phospholipids were purchased from Avanti Polar Lipids (catalog numbers 840012C, 850457C, 850757C and 840757, respectively). ATP synthase was eluted with a gradient of 20 mM reduced glutathione in Tris pH 8.0 buffer containing the same components as the binding buffer. Fractions containing ATP synthase were pooled and concentrated to 150 µl on Vivaspin centrifugal concentrator with 30 kDa molecular weight cut-off. The sample was fractionated by size exclusion chromatography on a Superose 6 Increase 3.2/300 GL column (Cytiva) equilibrated in a buffer containing 20 mM Tris pH 8.0, 100 mM sodium chloride, 2 mM magnesium chloride, 0.1 % (w/v) GDN, 3.75 µg/ml cardiolipin, 12.5 µg/ml POPC, 6.25 µg/ml POPE and 2.5 µg/ml POPG at 0.03 ml/min. Fractions corresponding to ATP synthase were pooled, supplemented with 0.05% (w/v) β-DDM that we and others experimentally found to better preserve dimer assemblies in cryo-EM[40], and concentrated to 50 µl.

Preparation of cryo-EM grids and data collection

Samples were vitrified on glow-discharged Quantifoil R1.2/1.3 Au 300-mesh grids after blotting for 3 sec, followed by plunging into liquid ethane using a Vitrobot Mark IV. 5,199 movies were collected using EPU 1.9 on a Titan Krios (ThermoFisher Scientific) operated at 300 kV at a nominal magnification of 165 kx (0.83 Å/pixel) with a Quantum K2 camera

(Gatan) using a slit width of 20 eV. Data was collected with an exposure rate of 3.6 electrons/px/s, a total exposure of 33 electrons/Å^2 and 20 frames per movie.

Image processing

Image processing was performed within the Scipion 2 framework[41], using RELION-3.0 unless specified otherwise. Movies were motion-corrected using the RELION implementation of the MotionCor2. 294,054 particles were initially picked using reference-based picking in Gautomatch (http://www.mrc-lmb.cam.ac.uk/kzhang/Gautomatch) and Contrast-transfer function parameters were using GCTF[42]. Subsequent image processing was performed in RELION-3.0 and 2D and 3D classification was used to select 100,605 particles, which were then extracted in an unbinned 560-pixel box (Fig. S1). An initial model of the ATP synthase dimer was obtained using *de novo* 3D model generation. Using masked refinement with applied C_2 symmetry, a 2.7-Å structure of the membrane region was obtained following per-particle CTF refinement and Bayesian polishing. Following C_2-symmetry expansion and signal subtraction of one monomer, a 3.7 Å map of the peripheral stalk was obtained. Using 3D classification (T=100) of aligned particles, with a mask on the F_1/*c*-ring region, 10 different rotational substates were then separated and maps at 3.5-4.3 Å resolution were obtained using 3D refinement. The authors note that the number of classes identified in this study likely reflects the limited number of particles, rather than the complete conformational space of the complex. By combining particles from all states belonging to main rotational state 1, a 3.7-Å map of the rotor and a 3.2-Å consensus map of the complete ATP synthase dimer with both rotors in main rotational state 1 were obtained.

Model building, refinement and data visualization

An initial atomic model of the static F_o membrane region was built automatically using Bucaneer[43]. Subunits were subsequently assigned directly from the cryo-EM map, 15 of them corresponding to previously identified *T. brucei* ATP synthase subunits[21], while three subunits (ATPTB14, ATPEG3, ATPEG4) were newly identified using BLAST searches. Manual model building was performed in *Coot* using the *T. brucei* F_1 (PDB 6F5D)[13] and homology models[44] of the *E. gracilis* OSCP and *c*-ring (PDB 6TDU)[10] as starting models. Ligands were manually fitted to the map and restraints were generated by the GRADE server (http://grade.globalphasing.org). Cardiolipins were assigned based on the presence of a characteristic elongated density branched on both termini, corresponding to two phosphatidyl groups linked by the central glycerol bridge. Monophosphatidyl lipids were assigned based on their headgroup densities. Characteristic tetrahedral shapes of densities of choline groups served to distinguish phosphatidylcholines from elongated phosphatidylethanolamine head groups (Extended Data Figure 5g,h). Real-space refinement was performed in PHENIX using auto-sharpened, local-resolution-filtered maps of the membrane region, peripheral stalk tip, *c*-ring/central stalk and F_1F_o monomers in different rotational states, respectively, using secondary structure restraints. Model statistics were generated using MolProbity[45] and EMRinger[46] Finally, the respective refined models were combined into a composite ATP synthase dimer model and real-space refined against the local-resolution-filtered consensus ATP synthase dimer map with both monomers in rotational state 1, applying reference

restraints. Figures of the structures were prepared using ChimeraX[47], the proton half-channels were traced using HOLLOW[48].

Data availability

The atomic coordinates have been deposited in the Protein Data Bank (PDB) and are available under the accession codes: XXXX (membrane-region), XXXX (peripheral stalk), XXXX (rotor), XXXX (F1Fo dimer), XXXX (rotational state 1a), XXXX (rotational state 1b), XXXX (rotational state 1c), XXXX (rotational state 1d), XXXX (rotational state 1e), XXXX (rotational state 2a), XXXX (rotational state 2b), XXXX (rotational state 2c), XXXX (rotational state 2d), XXXX (rotational state 3). The local resolution filtered cryo-EM maps, half maps, masks and FSC-curves have been deposited in the Electron Microscopy Data Bank with the accession codes: EMD-XXXX (membrane-region), EMD-XXXX (peripheral stalk), EMD-XXXX (rotor), EMD-XXXX (F_1F_o dimer), EMD-XXXX (rotational state 1a), EMD-XXXX (rotational state 1b), EMD-XXXX (rotational state 1c), EMD-XXXX (rotational state 1d), EMD-XXXX (rotational state 1e), EMD-XXXX (rotational state 2a), EMD-XXXX (rotational state 2b), EMD-XXXX (rotational state 2c), EMD-XXXX (rotational state 2d), EMD-XXXX (rotational state 3). Source data are provided with this paper.

Acknowledgements

We are grateful to Sir John E. Walker and Martin G. Montgomery for invaluable assistance with ATP synthase purification in the initial stage of the project. We acknowledge cryo-electron microscopy and tomography core facility of CIISB, Instruct-CZ Centre, supported by MEYS CR (LM2018127). This work was supported by the Czech Science Foundation grants number 18-17529S to A.Z. and 20-04150Y to O.G. and by European Regional Development Fund (ERDF) and Ministry of Education, Youth and Sport (MEYS) project CZ.02.1.01/0.0/0.0/16_019/0000759 to A.Z., Swedish Foundation for Strategic Research (FFL15:0325), Ragnar Söderberg Foundation (M44/16), European Research Council (ERC-2018-StG-805230), Knut and Alice Wallenberg Foundation (2018.0080), and EMBO Young Investigator Programme to A.A.

Author contributions

A.Z. and A.A. conceived and designed the work. O.G. prepared the sample for cryo-EM. O.G. and A.M. performed initial screening. A.M. processed the cryo-EM data and built the model. O.G., A.M. and A.A. analyzed the structure. B.P., C.H.Y., M.J., M.S., O.G. and A.Z. performed biochemical analysis. O.G., A.M., A.A. and A.Z. interpreted the data. O.G., A.M., A.A. and A.Z. wrote and revised the manuscript. All authors contributed to the analysis and approved the final version of the manuscript.

Competing interests

The authors declare no competing interests.

References

1. Paumard, P. et al. The ATP synthase is involved in generating mitochondrial cristae morphology. *EMBO J* **21**, 221-30 (2002).
2. Davies, K.M., Anselmi, C., Wittig, I., Faraldo-Gomez, J.D. & Kuhlbrandt, W. Structure of the yeast F_1F_o-ATP synthase dimer and its role in shaping the mitochondrial cristae. *Proc Natl Acad Sci U S A* **109**, 13602-7 (2012).
3. Panek, T., Elias, M., Vancova, M., Lukes, J. & Hashimi, H. Returning to the Fold for Lessons in Mitochondrial Crista Diversity and Evolution. *Curr Biol* **30**, R575-R588 (2020).
4. Kuhlbrandt, W. Structure and Mechanisms of F-Type ATP Synthases. *Annu Rev Biochem* **88**, 515-549 (2019).
5. Spikes, T.E., Montgomery, M.G. & Walker, J.E. Structure of the dimeric ATP synthase from bovine mitochondria. *Proc Natl Acad Sci U S A* **117**, 23519-23526 (2020).
6. Pinke, G., Zhou, L. & Sazanov, L.A. Cryo-EM structure of the entire mammalian F-type ATP synthase. *Nat Struct Mol Biol* **27**, 1077-1085 (2020).
7. Guo, H., Bueler, S.A. & Rubinstein, J.L. Atomic model for the dimeric F_o region of mitochondrial ATP synthase. *Science* **358**, 936-940 (2017).
8. Murphy, B.J. et al. Rotary substates of mitochondrial ATP synthase reveal the basis of flexible F_1-F_o coupling. *Science* **364**, eaaw9128 (2019).
9. Flygaard, R.K., Mühleip, A., Tobiasson, V. & Amunts, A. Type III ATP synthase is a symmetry-deviated dimer that induces membrane curvature through tetramerization. *Nature Communications* **11**, 5342 (2020).
10. Muhleip, A., McComas, S.E. & Amunts, A. Structure of a mitochondrial ATP synthase with bound native cardiolipin. *Elife* **8**, e51179 (2019).
11. Mühleip, A. et al. ATP synthase hexamer assemblies shape cristae of *Toxoplasma* mitochondria. *Nature Communications* **12**, 120 (2021).
12. Gahura, O. et al. The F_1-ATPase from *Trypanosoma brucei* is elaborated by three copies of an additional p18-subunit. *FEBS J* **285**, 614-628 (2018).
13. Montgomery, M.G., Gahura, O., Leslie, A.G.W., Zikova, A. & Walker, J.E. ATP synthase from *Trypanosoma brucei* has an elaborated canonical F_1-domain and conventional catalytic sites. *Proc Natl Acad Sci U S A* **115**, 2102-2107 (2018).
14. Serricchio, M. et al. Depletion of cardiolipin induces major changes in energy metabolism in *Trypanosoma brucei* bloodstream forms. *FASEB J **35**, 21176* (2020).
15. Muhleip, A.W., Dewar, C.E., Schnaufer, A., Kuhlbrandt, W. & Davies, K.M. In situ structure of trypanosomal ATP synthase dimer reveals a unique arrangement of catalytic subunits. *Proc Natl Acad Sci U S A* **114**, 992-997 (2017).
16. Schnaufer, A., Clark-Walker, G.D., Steinberg, A.G. & Stuart, K. The F_1-ATP synthase complex in bloodstream stage trypanosomes has an unusual and essential function. *EMBO J* **24**, 4029-40 (2005).
17. Brown, S.V., Hosking, P., Li, J. & Williams, N. ATP synthase is responsible for maintaining mitochondrial membrane potential in bloodstream form *Trypanosoma brucei*. *Eukaryot Cell* **5**, 45-53 (2006).

18. Gahura, O., Hierro-Yap, C. & Zikova, A. Redesigned and reversed: Architectural and functional oddities of the trypanosomal ATP synthase. *Parasitology* **148**, 1151-1160 (2021).
19. Hierro-Yap, C. et al. Bioenergetic consequences of F_oF_1-ATP synthase/ATPase deficiency in two life cycle stages of *Trypanosoma brucei*. *J Biol Chem* **296**, 100357 (2021).
20. Gahura, O., Panicucci, B., Vachova, H., Walker, J.E. & Zikova, A. Inhibition of F_1-ATPase from *Trypanosoma brucei* by its regulatory protein inhibitor TbIF1. *FEBS J* **285**, 4413-4423 (2018).
21. Zikova, A., Schnaufer, A., Dalley, R.A., Panigrahi, A.K. & Stuart, K.D. The F(0)F(1)-ATP synthase complex contains novel subunits and is essential for procyclic *Trypanosoma brucei*. *PLoS Pathog* **5**, e1000436 (2009).
22. Perez, E. et al. The mitochondrial respiratory chain of the secondary green alga *Euglena gracilis* shares many additional subunits with parasitic Trypanosomatidae. *Mitochondrion* **19 Pt B**, 338-49 (2014).
23. Sathish Yadav, K.N. et al. Atypical composition and structure of the mitochondrial dimeric ATP synthase from *Euglena gracilis*. *Biochim Biophys Acta* **1858**, 267-275 (2017).
24. Dewar, C.E., Oeljeklaus, S., Wenger, C., Warscheid, B. and Schneider, A. Characterisation of a highly diverged mitochondrial ATP synthase F_o subunit in *Trypanosoma brucei*. *J Biol Chem.* Epub ahead of print, 101829 (2022)
25. Aphasizheva, I. et al. Lexis and Grammar of Mitochondrial RNA Processing in Trypanosomes. *Trends Parasitol* **36**, 337-355 (2020).
26. Blum, B., Bakalara, N. & Simpson, L. A model for RNA editing in kinetoplastid mitochondria: "guide" RNA molecules transcribed from maxicircle DNA provide the edited information. *Cell* **60**, 189-98 (1990).
27. Adler, B.K., Harris, M.E., Bertrand, K.I. & Hajduk, S.L. Modification of *Trypanosoma brucei* mitochondrial rRNA by posttranscriptional 3' polyuridine tail formation. *Mol Cell Biol* **11**, 5878-84 (1991).
28. Hofer, A., Steverding, D., Chabes, A., Brun, R. & Thelander, L. *Trypanosoma brucei* CTP synthetase: a target for the treatment of African sleeping sickness. *Proc Natl Acad Sci U S A* **98**, 6412-6 (2001).
29. Sobti, M., Walshe, J.L., Wu, D. *et al.* Cryo-EM structures provide insight into how *E. coli* F_1F_o ATP synthase accommodates symmetry mismatch. *Nat Commun* **11,** 2615 (2020). https://doi.org/10.1038/s41467-020-16387-2
30. Gupta, K. et al. The role of interfacial lipids in stabilizing membrane protein oligomers. *Nature* **541**, 421-424 (2017).
31. Arnold, I., Pfeiffer, K., Neupert, W., Stuart, R.A. & Schagger, H. Yeast mitochondrial F_1F_o-ATP synthase exists as a dimer: identification of three dimer-specific subunits. *EMBO J* **17**, 7170-8 (1998).
32. Gu, J. et al. Cryo-EM structure of the mammalian ATP synthase tetramer bound with inhibitory protein IF1. *Science* **364**, 1068-1075 (2019).

33. Spikes, T.E., Montgomery, M.G. & Walker, J.E. Interface mobility between monomers in dimeric bovine ATP synthase participates in the ultrastructure of inner mitochondrial membranes. *Proc Natl Acad Sci U S A* **118**, e2021012118 (2021).
34. Cadena, L.R. et al. Mitochondrial contact site and cristae organization system and F_1F_o-ATP synthase crosstalk is a fundamental property of mitochondrial cristae. *mSphere* **6**, e0032721 (2021).
35. Davies, K.M. et al. Macromolecular organization of ATP synthase and complex I in whole mitochondria. *Proc Natl Acad Sci U S A* **108**, 14121-6 (2011).
36. Blum, T.B., Hahn, A., Meier, T., Davies, K.M. & Kühlbrandt, W. Dimers of mitochondrial ATP synthase induce membrane curvature and self-assemble into rows. *Proc Natl Acad Sci U S A* **116**, 4250-4255 (2019).
37. Bochud-Allemann, N. & Schneider, A. Mitochondrial substrate level phosphorylation is essential for growth of procyclic *Trypanosoma brucei*. *J Biol Chem* **277**, 32849-54 (2002).
38. Poon, S.K., Peacock, L., Gibson, W., Gull, K. & Kelly, S. A modular and optimized single marker system for generating *Trypanosoma brucei* cell lines expressing T7 RNA polymerase and the tetracycline repressor. *Open Biol* **2**, 110037 (2012).
39. Allemann, N. & Schneider, A. ATP production in isolated mitochondria of procyclic Trypanosoma brucei. *Mol Biochem Parasitol* **111**, 87-94 (2000).
40. Aibara, S., Dienemann, C., & Cramer, P.. Structure of an inactive RNA polymerase II dimer. *Nucleic Acids Research*, gkab783 (2021).
41. de la Rosa-Trevin, J.M. et al. Scipion: A software framework toward integration, reproducibility and validation in 3D electron microscopy. *J Struct Biol* **195**, 93-9 (2016).
42. Zhang, K. Gctf: Real-time CTF determination and correction. *J Struct Biol* **193**, 1-12 (2016).
43. Cowtan, K. The Buccaneer software for automated model building. 1. Tracing protein chains. *Acta Crystallogr D Biol Crystallogr* **62**, 1002-11 (2006).
44. Waterhouse, A. et al. SWISS-MODEL: homology modelling of protein structures and complexes. *Nucleic Acids Res* **46**, W296-W303 (2018).
45. Williams, C.J., Headd, J.J., Moriarty, N.W., Prisant, M.G., Videau, L.L., Deis, L.N., Verma, V., Keedy, D.A., Hintze, B.J., Chen, V.B. and Jain, S. MolProbity: More and better reference data for improved all-atom structure validation. *Protein Science*, **27**, 293-315 (2018).
46. Barad, B.A., Echols, N., Wang, R.Y.R., Cheng, Y., DiMaio, F., Adams, P.D. and Fraser, J.S. EMRinger: side chain–directed model and map validation for 3D cryo-electron microscopy. *Nature methods*, **12**, 943-946 (2015).
47. Goddard, T.D. et al. UCSF ChimeraX: Meeting modern challenges in visualization and analysis. *Protein Sci* **27**, 14-25 (2018).
48. Ho, B.K. & Gruswitz, F. HOLLOW: generating accurate representations of channel and interior surfaces in molecular structures. *BMC Struct Biol* **8**, 49 (2008).

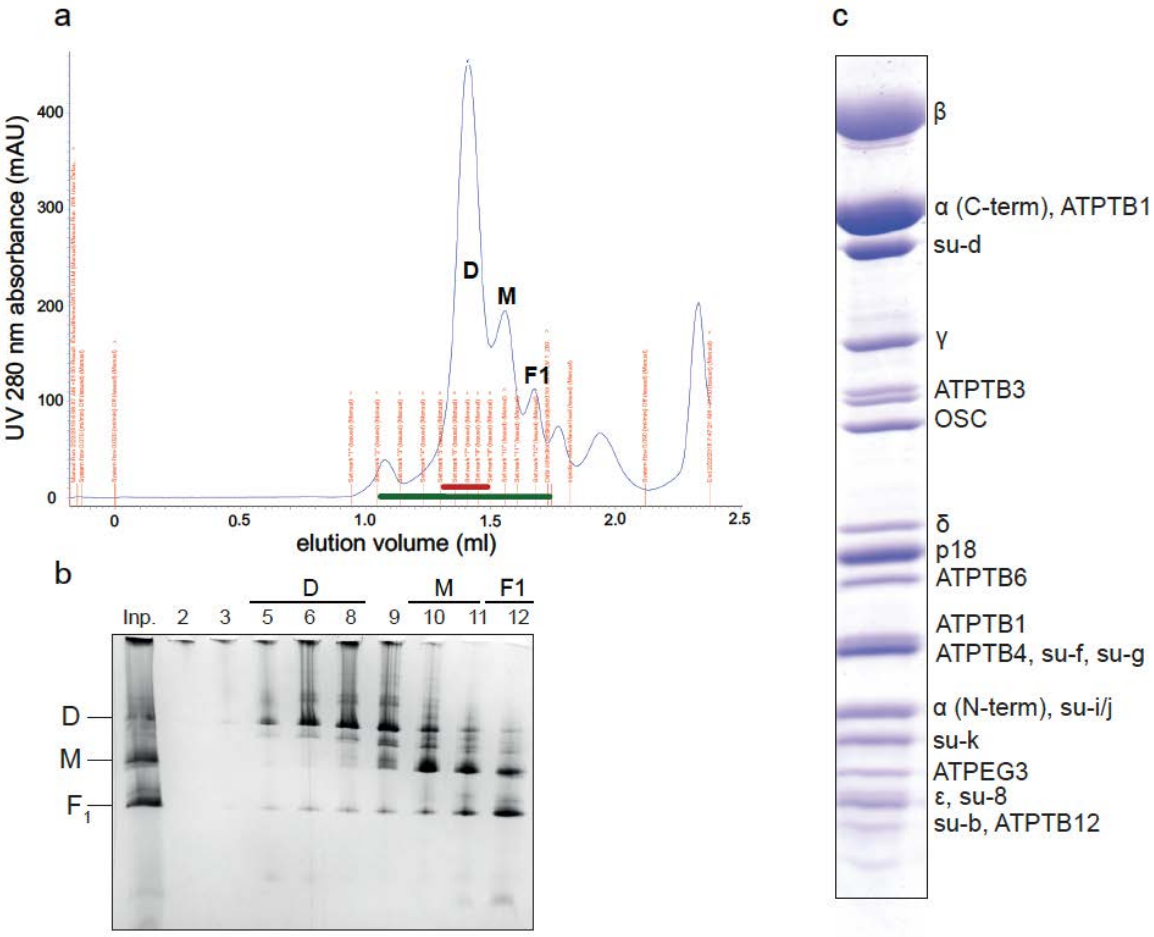

Extended Data Fig. 1 Purification of the *T. brucei* ATP synthase dimer.

a, Size exclusion chromatography trace with peaks enriched with ATP synthase dimers (D), monomers (M) and F_1-ATPase (F_1) labelled. The red bar marks the fractions for cryo-EM. **b,** Fractions from size exclusion chromatography marked with green bar in (a) resolved by native BN-PAGE. **c,** Dimer-enriched fractions resolved by SDS-PAGE stained by Coomassie blue dye. Bands are annotated based on mass spectrometry identification from excised gel pieces.

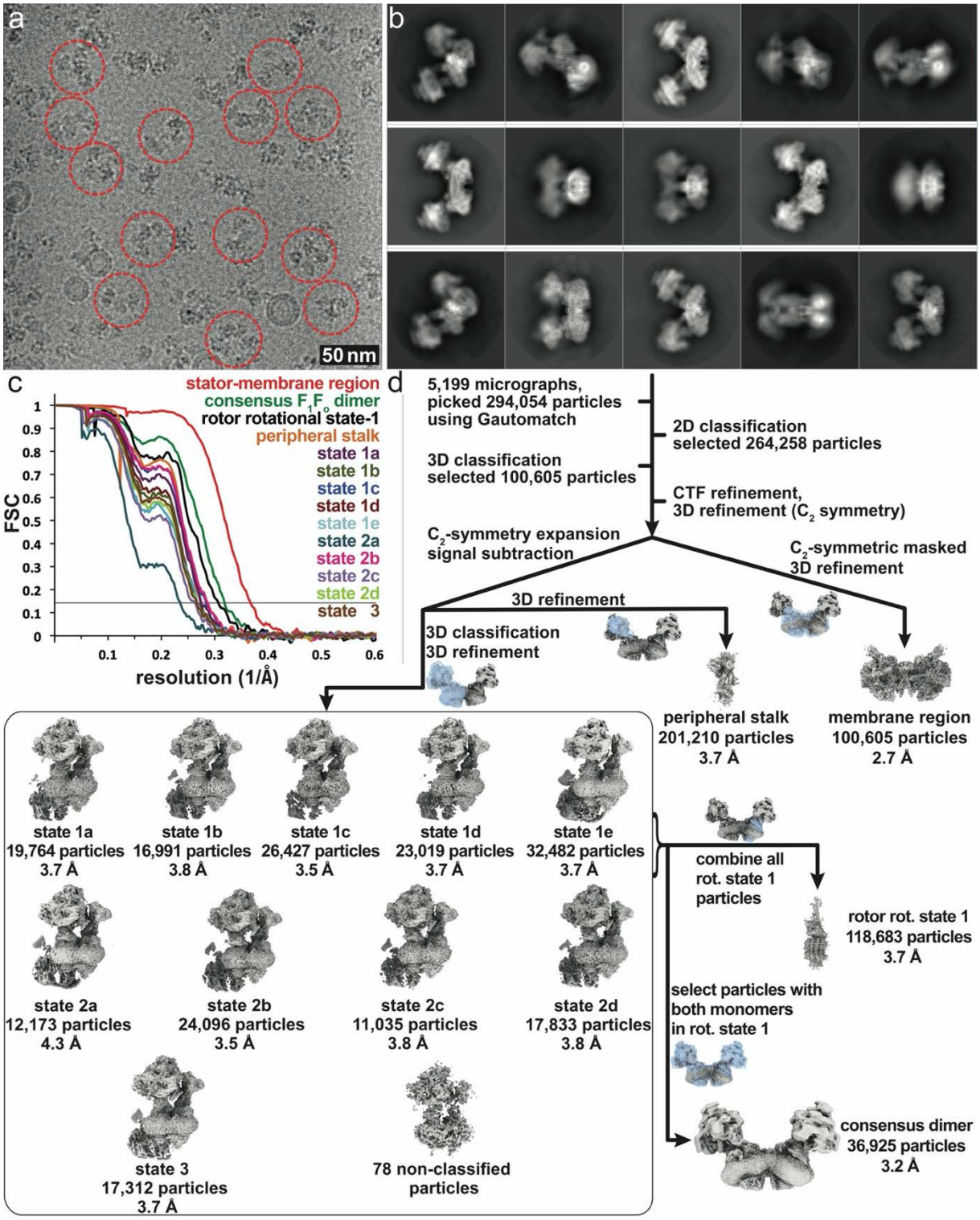

Extended Data Fig. 2 Cryo-EM data processing of the *T. brucei* ATP synthase dimer. **a**, Representative micrograph. **b**, 2D class averages. **c**, Fourier Shell Correlation (FSC) curves showing the estimated resolutions of ATP synthase maps according to the gold standard 0.143 criterion. **d**, Data processing scheme resulting in maps covering all regions of the complex, as well as 10 rotational states.

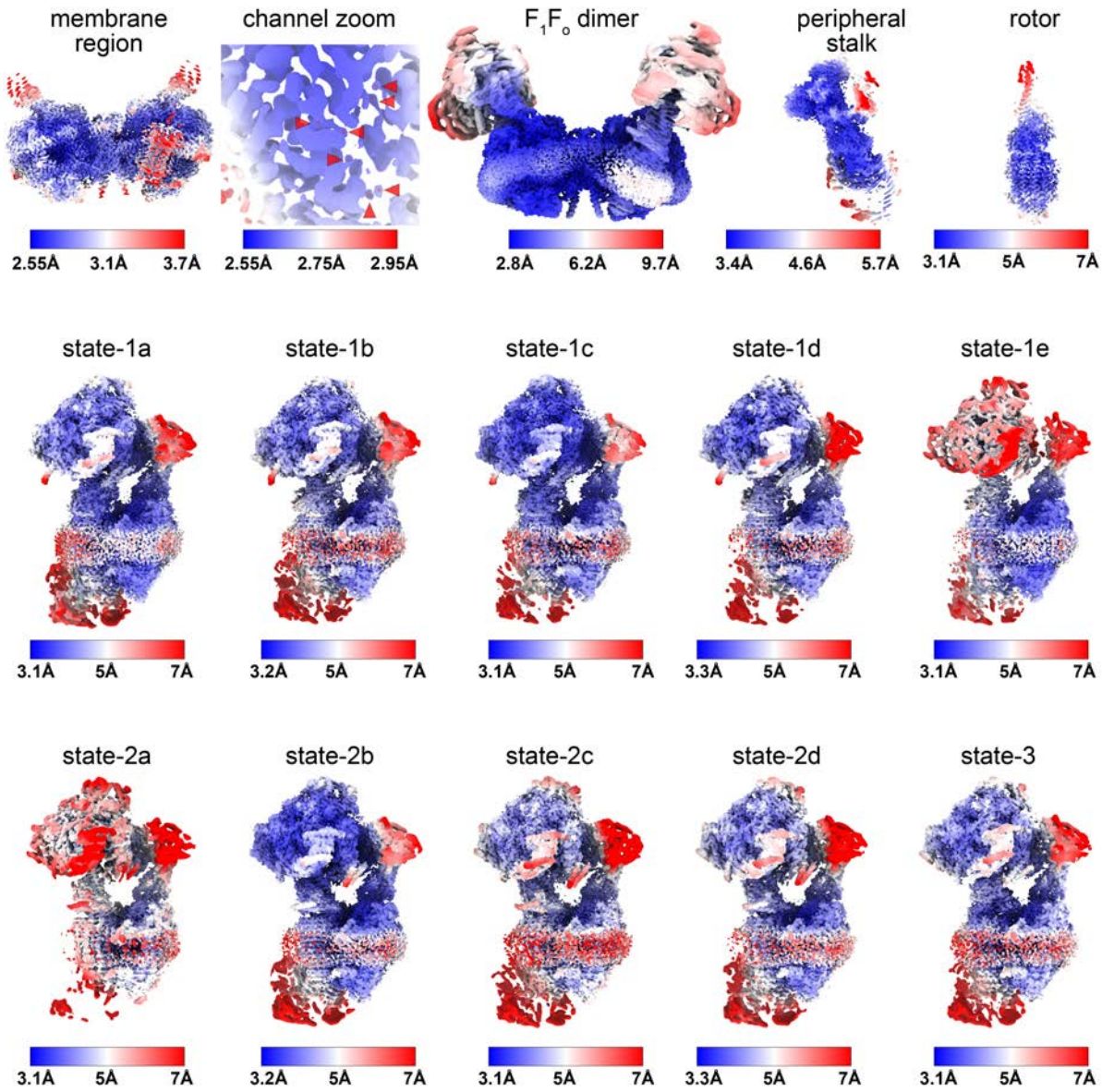

Extended Data Fig. 3 Local resolution estimation of final cryo-em maps. Local resolution estimates colored according to the respective color legends of the membrane region, F_1F_o dimer, the peripheral stalk, the rotor and all identified rotational states. A zoomed-in view of the membrane region shows that the resolution in the lumenal channel extends to 2.55 Å, allowing the assignment of water molecules.

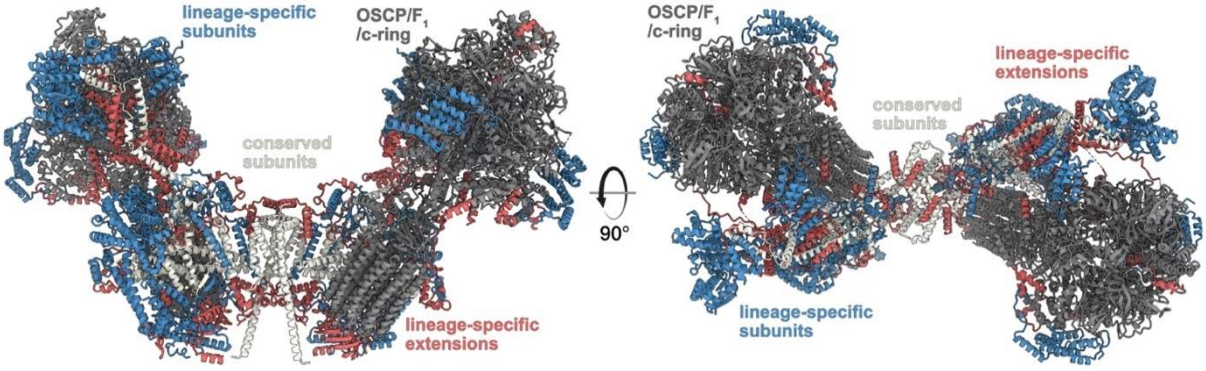

Extended Data Fig. 4 Conserved and phylum specific elements generate the *T. brucei* ATP synthase architecture.

The canonical OSCP/F_1/*c*-ring monomers (dark grey) are tied together by both conserved F_o subunits and extensions of lineage-specific subunits (red). The F_o periphery and peripheral stalk attachment are composed of lineage specific subunits (blue).

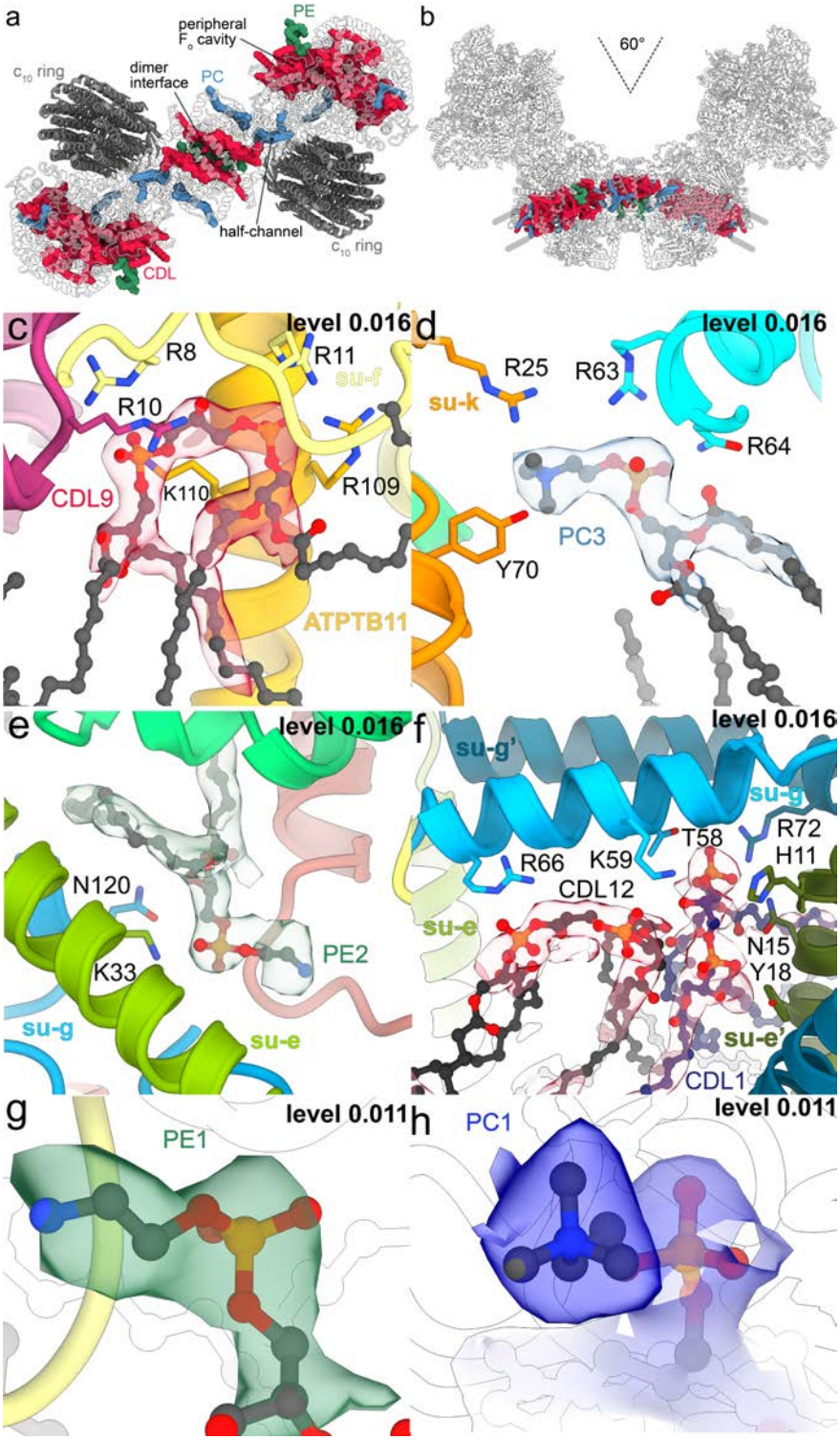

Extended Data Fig. 5 The F_o region coordinates numerous bound lipids.

a, F_o top view, cardiolipin (CDL), phosphatidylcholine (PC) and phosphatidlyethanolamine (PE) are bound at the dimer interface, the lumenal proton half-channel and the peripheral F_o cavity. **b**, The 60°-dimer angle generates a curved F_o region with phospholipids bound in an arc-shaped bilayer. **c-f**, Bound lipids with cryo-EM density and coordinating residues. **g-h,** Representative densities of headgroups of PE (g) and PC (h).

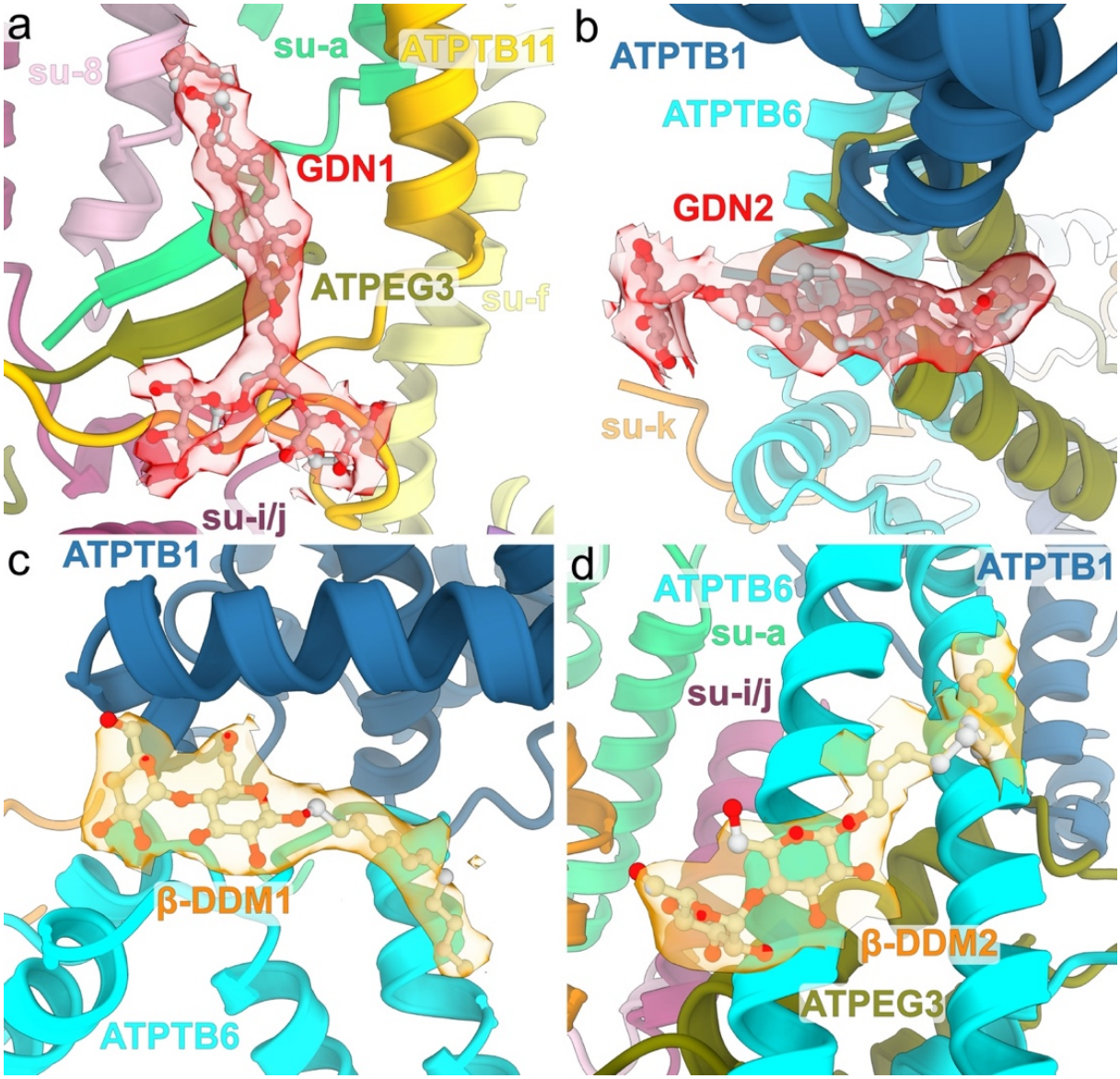

Extended Data Fig. 6 Bound detergents of the F_o region.
GDN **(a,b)** and β-DDM **(c,d)** molecules bound in the periphery of the membrane region with cryo-EM map densities shown (transparent), indicating that both glycosides are retained in the detergent micelle.

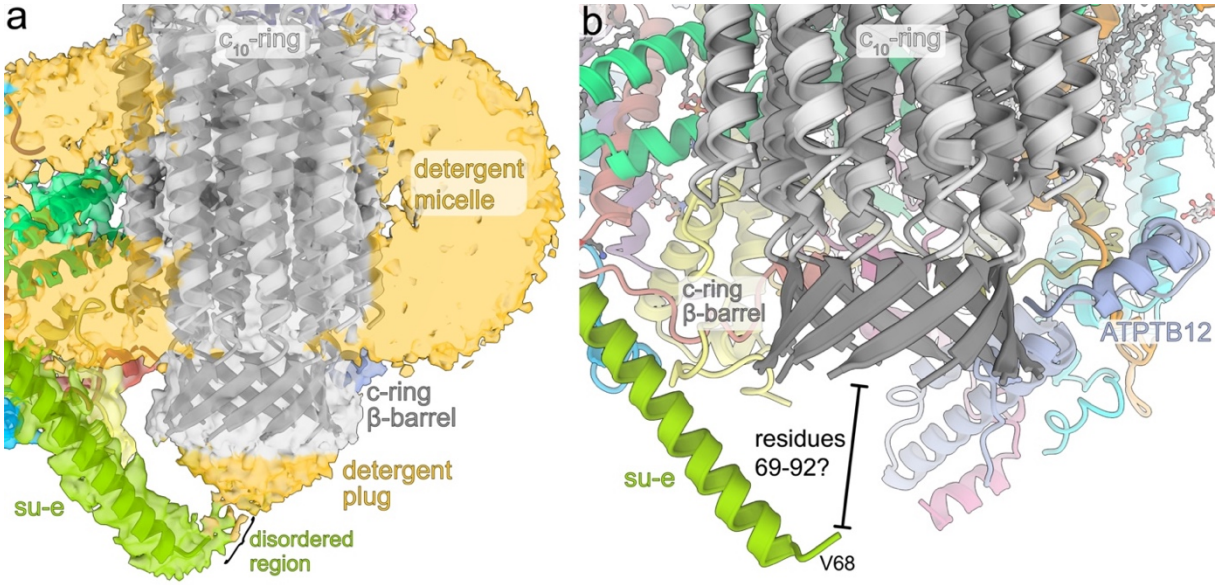

Extended Data Fig. 7 The C-terminal tail of subunit-*e* interacts with the c_{10}-ring.
a, The cryo-EM map reveals disordered detergent density of the detergent belt surrounding the membrane region as well as a detergent plug on the luminal side of the *c*-ring. **b,** The helical C-terminus of subunit-*e* extends into the lumen towards the *c*-ring. The terminal 23 residues are disordered and likely interact with the β-barrel.

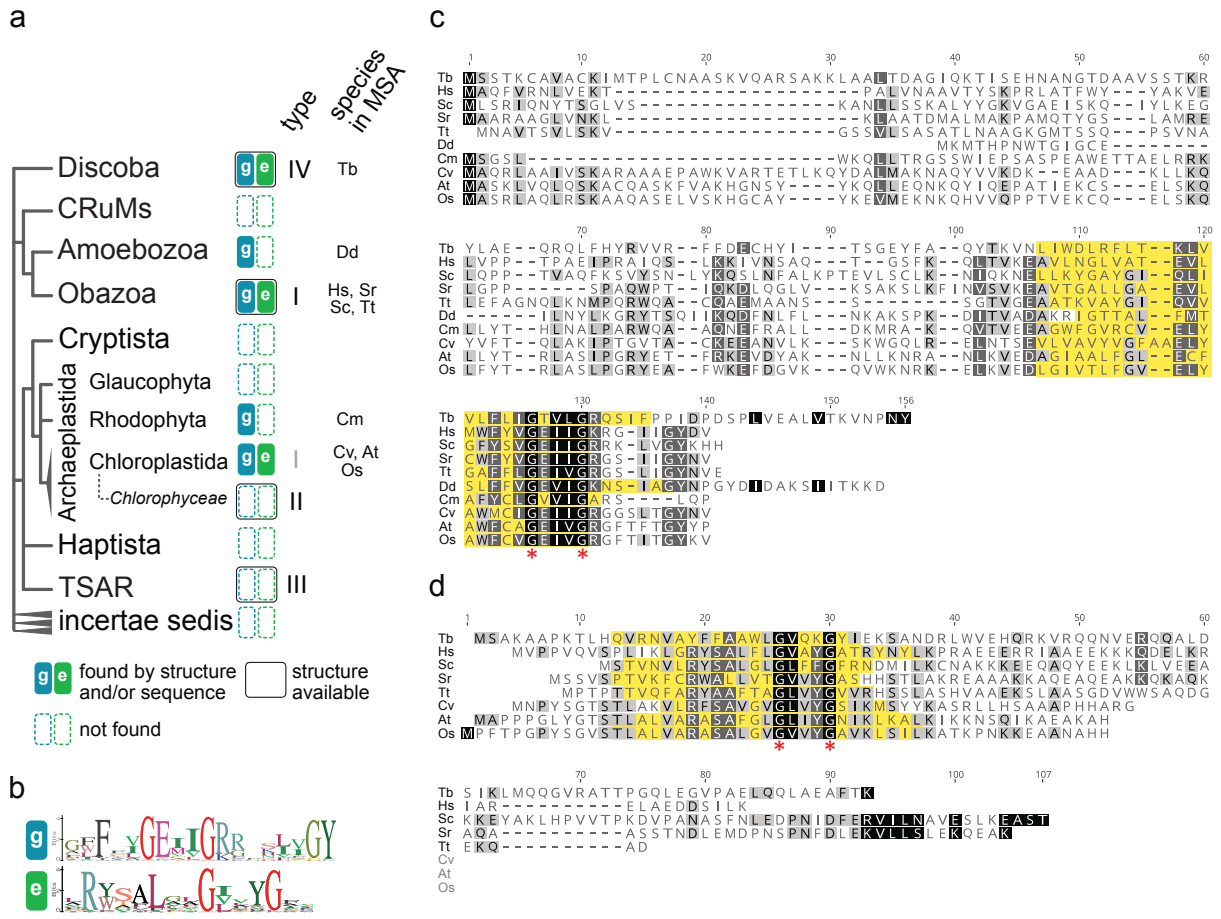

Extended Data Fig. 8 Phylogenetic distribution and sequence conservancy of subunit-*e* and -*g*.

a, Distribution of subunits *e* and *g* mapped on the phylogenetic tree of eukaryotes[3]. Homologs of subunits *e* and *g* were searched in non-redundant GenBank and UniprotKB protein databases by PSI-BLAST, and phmmer and hmmsearch[4], respectively, using individual sequences of representatives from *H. sapiens* and *T. brucei*, and in the case of hmmsearch a multiple sequence alignment (MSA) of representatives from *Homo sapiens*, *Saccharomyces cerevisiae*, *Arabidopsis thaliana* and *T. brucei*, as queries. Groups, in which at least one structure of ATP synthase is available, are marked. Abbreviations of species used in MSA in panels (c) and (d) are shown. **b**, Sequence logo of GXXXG motifs and flanking regions of subunits *e* and *g*. Hits from hmmsearch were clustered by CD-HIT Suite[5] to 50% sequence identity and MSA of representative sequences of each cluster was generated by Clustal Omega4[6]. The sequence logos were created from MSA in Geneious Prime (Biomatters Ltd.). **c**,**d**, MSA of sequences of subunits g (c) and e (d) from species representing major groups shown in (a) generated by MUSCLE[7] and visualized in Geneious Prime. The experimentally determined or predicted transmembrane regions are highlighted in yellow. Species abbreviations: Tb – *T. brucei*, Hs – *H. sapiens*, Sc – *S. cerevisiae*, Sr – *Salpingoeca rosetta*, Tt – *Thecamonas trahens*, Dd – *Dictyostelium discoideum*, Cm – *Cyanidioschyzon merolae*, Cv – *Chlorella vulgaris*, At – *Arabidopsis thaliana*, Os – *Oryza sativa*.

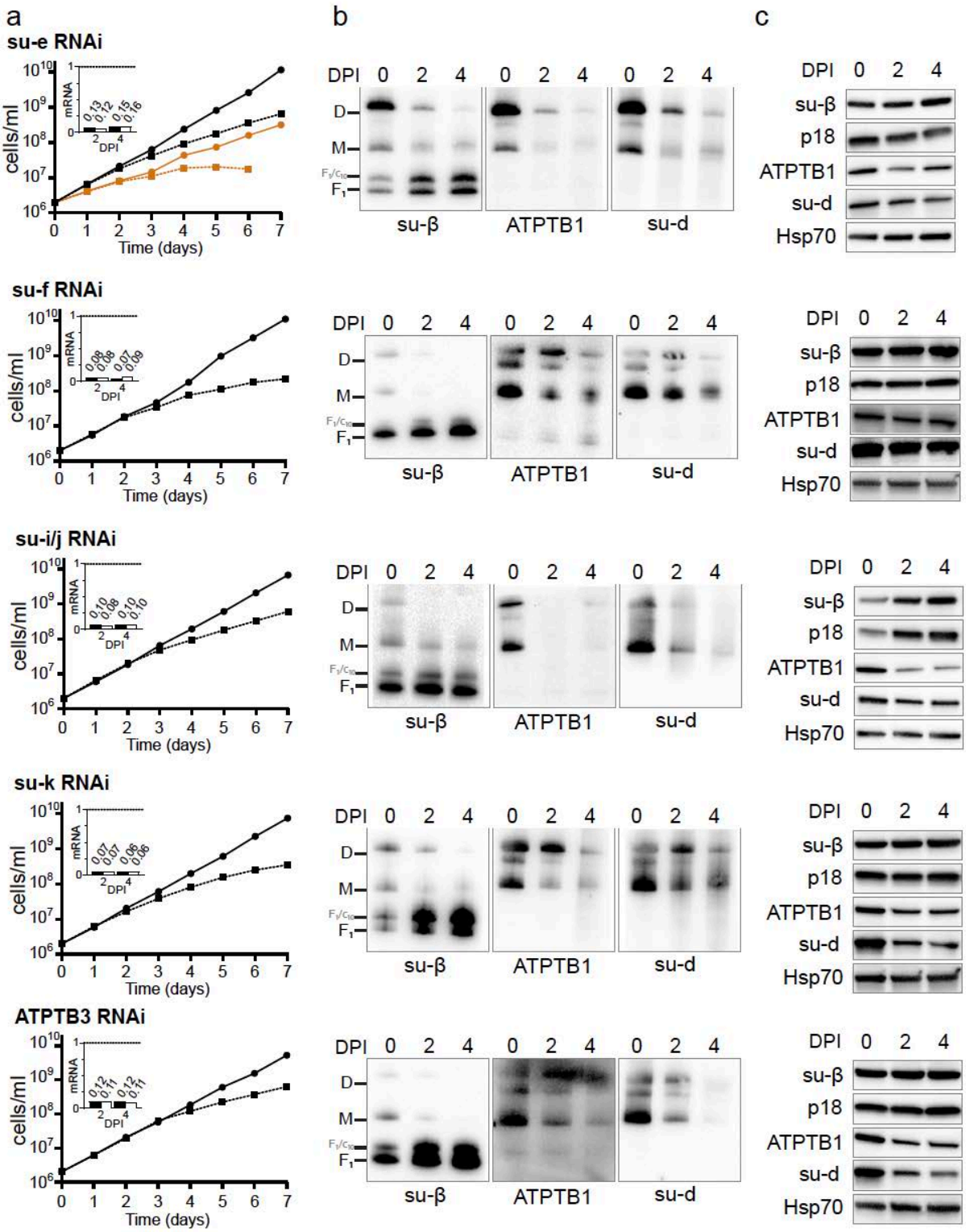

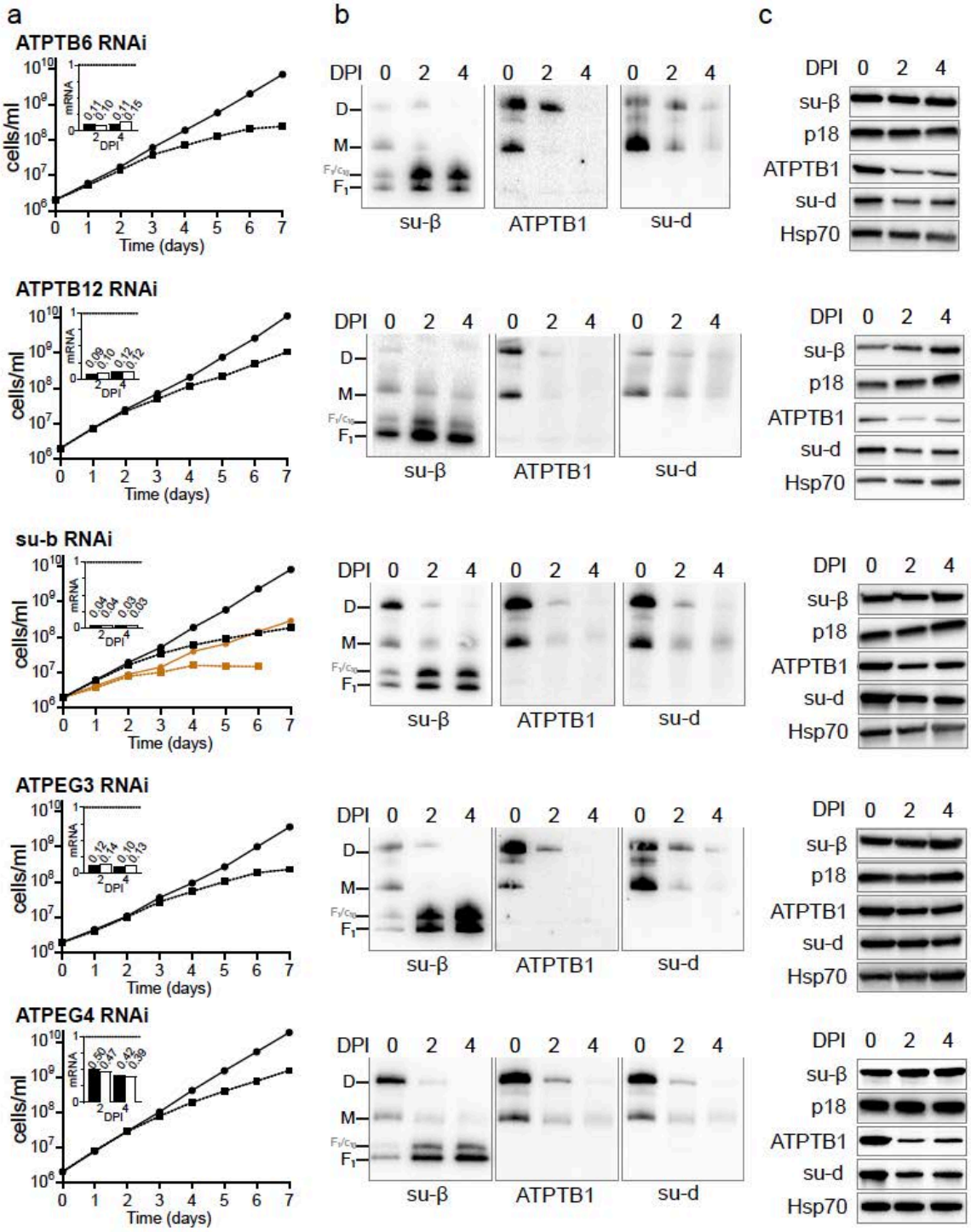

Extended Data Fig. 9 Effects of RNAi knock-down of ATP synthase subunits on viability and stability and dimerization of ATP synthase.

a, Growth curves of indicated non-induced (solid lines) and tetracycline induced (dashed lines) RNAi cells lines in the presence (black) or absence (brown) of glucose. The insets show relative levels of the respective target mRNA at indicated days post induction (DPI) normalized to the levels of 18S rRNA (black bars) or ß-tubulin (white bars). **b**, Immunoblots of mitochondrial lysates from indicated RNAi cell lines resolved by BN-PAGE probed by antibodies against indicated ATP synthase subunits. **c**, Immunoblots of whole cell lysates from indicated RNAi cell lines probed with indicated antibodies.

	Mem-brane region	Rotor	Periphe-ral stalk	F_1F_o dimer	Rot. 1a	Rot. 1b	Rot. 1c	Rot. 1d	Rot. 1e	Rot. 2a	Rot. 2b	Rot. 2c	Rot. 2d	Rot. 3
Data collection														
Microscope	Titan Krios													
Voltage (kV)	300													
Camera	K2 Summit													
Magnification	165 kx													
Exposure ($e^-/Å^2$)	33													
Defocus range (μm)	-1.6 to -3.2													
Pixel size (Å)	0.83													
Movies collected	5,199													
Frames per movie	20													
Data processing														
Initial particles	100,605 (C_2 symmetry-expanded: 201,210)													
Final no. particles	100,605	118,683	201,210	36,925	19,764	26,427	23,019	16,991	34,482	12,173	24,096	11,035	17,833	17.312
Symmetry	C_2	C_1	C_1	C_2	C_1	C_1	C_1	C_1	C_1	C_1	C_1	C_1	C_1	C_1
Map resolution (Å)	2.7	3.7	3.7	3.2	3.7	3.5	3.7	3.8	3.7	4.3	3.5	3.8	3.8	3.7
Sharpening B factor	-46.2	-74.4	-92.5	-49.8	-61.8	-61.1	-57.6	-45.6	-58.0	-73.8	-54.5	-65.2	-54.9	-61.7
EMD ID														
Model refinement statistics														
CC (map/model)	0.86	0.83	0.82	0.71	0.79	0.79	0.82	0.79	0.69	0.71	0.81	0.77	0.77	0.79
Resolution (map/model)	2.65	3.4	3.68	3.13	3.48	3.56	3.36	3.55	3.57	3.94	3.39	3.73	3.64	3.58
No. of atoms	76,690	19,669	12,083	251,552	129,568	129,568	129,568	129,568	129,568	129,563	129,563	129,563	129,563	129,566
No. of residues	4074	1285	767	15,356	7872	7872	7872	7872	7872	7872	7872	7872	7872	7872
No. of lipids	36	0	0	36	21	21	21	21	21	21	21	21	21	21
No. of ATP/ADP	0	0	0	10	5	5	5	5	5	5	5	5	5	5
No. of Mg ions	0	0	0	10	5	5	5	5	5	5	5	5	5	5
B-factor ($Å^2$)														
- protein	54.05	56.13	77.88	84.48	55.65	70.37	80.22	83.27	70.70	112,72	79.93	65.52	66.49	101.5
- ligands	50.57	58.25	-	69.94	40.99	72.29	63.18	78.43	63.76	75,25	74.47	61.79	46.55	83.68
Rotamer outliers (%)	0.44	0.40	0.31	0.22	0.42	0.09	0.18	0.26	0.58	0.18	0.27	0.48	0.42	0.39
Ramachandran (%)														
- outliers	0.00	0.00	0.00	0.01	0.001	0.003	0.004	0.01	0.003	0.01	0.00	0.04	0.04	0.04
- allowed	1.57	1.91	1.59	1.56	1.52	1.65	1.44	1.49	1.49	1.67	1.58	1.47	1.65	1.79
- favored	98.43	98.08	98.41	98.42	98.47	98.34	98.56	98.49	98.48	98.31	98.42	98.49	98.31	98.17
Clash score	1.66	2.44	2.32	2.26	2.60	2.65	2.53	2.67	2.99	2.38	2.30	2.52	2.38	3.57
MolProbity score	0.92	1.03	1.01	1.00	1.05	1.05	1.04	1.05	1.09	1.02	1.01	1.04	1.02	1.15
RMSD														
- bonds (Å)	0.004	0.004	0.02	0.003	0.003	0.003	0.004	0.003	0.003	0.002	0.003	0.003	0.003	0.003
- angles (°)	0.455	0.416	0.386	0.407	0.414	0.424	0.417	0.407	0.412	0.410	0.416	0.419	0.428	0.421
EMRinger score	5.11	3.96	1.61	2.56	3.24	2.95	3.32	2.85	3.32	1.35	2.89	2.32	2.49	2.8
PDB ID														

Extended Data Table 1. Data collection, processing, model refinement and validation statistics.

Subunit name	TriTrypDB Lister strain 427 ID	TriTrypDB TREU927 strain ID	Uniprot TREU927 strain ID	Residues	Residues built
F_1 subcomplex					
α	Tb427_070081800 Tb427_070081900	Tb927.7.7420 Tb927.7.7430	Q57TX9	584	45-151, 161-584
β	Tb427_030013500	Tb927.3.1380	Q57XX1	519	26-514
γ	Tb427_100005200	Tb927.10.180	B0Z0F6	305	2-301
δ	Tb427_060054900	Tb927.6.4990	Q586H1	182	22-182
ε	Tb427_100054600	Tb427.10.5050	N/A	75	11-75
p18	Tb427_050022900	Tb927.5.1710	Q57ZP0	188	23-188
F_o subcomplex					
OSCP	Tb427_100087100	Tb927.10.8030	Q38AG1	255	18-202, 208-255
a	mt encoded	mt encoded	P24499	231	1-231
b	Tb427_040009100	Tb927.4.720	Q580A0	105	26-105
c	Tb427_100018700 Tb427_110057900 Tb427_070019000	Tb927.10.1570 Tb927.11.5280 Tb927.7.1470	Q38C84 Q385P0 Q57WQ3	118	41-118
d	Tb427_050035800	Tb927.5.2930	Q57ZW9	370	17-325, 332-354
e	Tb427_110010200	Tb927.11.600	N/A	92	1-383
f	Tb427_030016600	Tb927.3.1690	Q57ZE2	145	2-136
g	Tb427_020016900	Tb927.2.3610	Q586X8	144	16-144
i/j	Tb427_030029400	Tb927.3.2880	Q57ZM4	104	2-104
k	Tb427_070011800	Tb927.7.840	Q57VT0	124	20-124
8	Tb427_040037300	Tb927.4.3450	Q585K5	114	29-114
ATBTB1	Tb427_100008400	Tb927.10.520	Q38CI8	396	1-383
ATPTB3	Tb427_110067400	Tb927.11.6250	Q385E4	269	2-269
ATPTB4	Tb427_100105100	Tb927.10.9830	Q389Z3	157	21-157
ATPTB6	Tb427_110017200	Tb927.11.1270	Q387C5	169	2-169
ATPTB11	Tb427_030021500	Tb927.3.2180	Q582T1	156	18-156
ATPTB12	Tb427_050037400	Tb927.5.3090	Q57Z84	101	5-100
ATPEG3	Tb427_060009300	Tb927.6.590	Q583U4	98	14-98
ATPEG4	N/A	Tb927.11.2245	N/A	62	1-62

Extended Data Table 2. Composition of *T. brucei* ATP synthase dimer.

Subunit	Primer pair sequences
Primers for amplification of RNAi cassettes	
b	TAATCTCGAGGGTACCGTTGAGTGAGGAGGAACGGG GCAGTCTAGAGGATCCTATCCCTTCCACCCACCACT
e	TAATCTCGAGGGTACCGGGAGTACAGAAGGGCTACA TAGATCTAGAGGATCCCGTGCACACCATCAGCTG
f	ATACTCGAGGGTACCGTGAGTACCGCCTTTACGC GCGTCTAGAGGATCCAGCACTGATCACCAAACTGC
g	ACTGCTCGAGGGTACCACGCGGGAATTCAAAAGACC GCGGTCTAGAGGATCCCGTTGCGGTGCTTGTCATTA
i/j	TAATCTCGAGGGTACCGAATATCCGATGCATGCCGC GCCGTCTAGAGGATCCACTTCGCTCTACTGCATGCA
k	ATTACTCGAGCCCGGGCGATCAGTGCAGGGGATTTT GCCGTCTAGAGGATCCTTTCCTCGAAAACGCACACA
8	ATGACTCGAGGGTACCGGGCTATGGTGTGGTATTATGC GACGTCTAGAGGATCCGCAGAAAACTCCCAACGACA
ATPTB3	ACTGCTCGAGGGTACCAAAGAGGAGGTGAGGTCTGC GCAGTCTAGAGGATCCCCCTAGGGTTCTTCGAAGCA
ATPTB4	CTGACTCGAGGGTACCTTCCTTTTCTGCTGCATCGG GCAGTCTAGAGGATCCCTCCTCGGGCTTCCAATTTG
ATPTB6	ACTGCTCGAGGGTACCCAACATGGCAGTATCCGGTG GCAGTCTAGAGGATCCTTATTAGTGGCGGTGGTGGT
ATPTB11	ACTGCTCGAGGGTACCGCGCTCGTCTTCTCCATTTC GCAGAAGCTTGGATCCAGGTTGGGGTGTTTAGGGAG
ATPTB12	TAATCTCGAGGGTACCGACGCCATCAAAGGAATGCC GCCGTCTAGAGGATCCAGCAGCCAACAAACAGACAA
ATPEG3	TACACTCGAGGGTACCAAACCTGAAGGCCCTCACAC GCAGTCTAGAGGATCCCTCTTTCGTGCCGCCTGATA
Primers for quantification of mRNA levels by qPCR	
b	CCAAGAGTGATGATGGCCCC CGTTTAGGGTCGCGGAAAAC
e	CAAGCCTTGCACACACTTTATG CCGCAAAGAAGTACGCCAC
f	TTTTCTACATACCGCAGCAGT TACCATTCCATGCGCGTTG
g	GCAATTGTGTGAGCTGAACG TACTGGCCGCATTGCATAAC
i/j	AGAGTAAAAGCGCGCCTACG

	CAGTTGGAAAACCGGTAGCC
k	ACACAAAACACTTCCAGCAGA CGCTATGACGGACAGGTGT
8	GCTACGGCGACTTGGTGC CGTCACCGCGTATTTGTTCA
ATPTB3	AACGTTTATATCAGCGGGCG CTGTTTTGGTCTGCACACGA
ATPTB4	CCAAACTTTGAAGCAGCGGA ATTCCTTGGATCCGCACCTT
ATPTB6	TCGGCATAGGAGAAGTAACGA GATTCGGTTTGGAACTTGCG
ATPTB11	CAACGGCCCCACATTCTC ACACCGCGGTCATTCATTG
ATPTB12	GCACTTCATTCTCCCGACTG ACATGATGTAACACCTCCGC
ATPEG3	TGGCCCCACATGACTGAAAA GGAAGTGATCCGCCGGATTT

Extended Data Table 3. List of primers used in the study.

Target	Type	Reference	Dilution SDS-PAGE	Dilution BN-PAGE
Primary antibodies				
subunit-β	rabbit polyclonal	1	1:2000	1:2000
p18	rabbit polyclonal	1	1:1000	-
ATPTB1	rabbit polyclonal	1	1:1000	1:1000
subunit-*d*	rabbit polyclonal	1	1:1000	1:500
mtHsp70	mouse monoclonal	2	1:5000	-
Secondary antibodies				
goat anti-rabbit IgG HRP conjugate		BioRad 1721019	1:2000	1:2000
goat anti-mouse IgG HRP conjugate		BioRad 1721011	1:2000	1:2000

Extended Data Table 4. List of antibodies used in the study.

Extended Data references:

1. Muhleip, A., McComas, S.E. & Amunts, A. Structure of a mitochondrial ATP synthase with bound native cardiolipin. *Elife* **8**, e51179 (2019).
2. Larkin, M.A. et al. (2007). Clustal W and Clustal X version 2.0. *Bioinformatics*, **23**, 2947-2948 (2007).
3. Burki, F., Roger, A.J., Brown, M.W. & Simpson, A.G.B. The New Tree of Eukaryotes. *Trends Ecol Evol* **35**, 43-55 (2020).
4. Protein Sequence Similarity Search. *Curr Protoc Bioinformatics* **60**, 3151-31523 (2017).
5. Huang, Y., Niu, B., Gao, Y., Fu, L. & Li, W. CD-HIT Suite: a web server for clustering and comparing biological sequences. *Bioinformatics* **26**, 680-2 (2010).
6. Sievers, F. et al. Fast, scalable generation of high-quality protein multiple sequence alignments using Clustal Omega. *Mol Syst Biol* **7**, 539 (2011).
7. Edgar, R.C. MUSCLE: multiple sequence alignment with high accuracy and high throughput. *Nucleic Acids Res* **32**, 1792-7 (2004).

Molecular & Biochemical Parasitology 184 (2012) 90–98

Contents lists available at SciVerse ScienceDirect

Molecular & Biochemical Parasitology

Disparate phenotypic effects from the knockdown of various *Trypanosoma brucei* cytochrome *c* oxidase subunits

Anna Gnipová[a,b], Brian Panicucci[a], Zdeněk Paris[a,1], Zdeněk Verner[a,c], Anton Horváth[b], Julius Lukeš[a,c], Alena Zíková[a,c,*]

[a] *Institute of Parasitology, Biology Centre, České Budějovice, Czech Republic*
[b] *Faculty of Science, Comenius University, Bratislava, Slovakia*
[c] *Faculty of Science, University of South Bohemia, České Budějovice, Czech Republic*

ARTICLE INFO

Article history:
Received 23 March 2012
Received in revised form 27 April 2012
Accepted 28 April 2012
Available online 5 May 2012

Keywords:
Trypanosoma
RNA interference
Mitochondrion
Respiratory complexes
Cytochrome *c* oxidase

ABSTRACT

The *Trypanosoma brucei* cytochrome *c* oxidase (respiratory complex IV) is a very divergent complex containing a surprisingly high number of trypanosomatid-specific subunits with unknown function. To gain insight into the functional organization of this large protein complex, the expression of three novel subunits (TbCOX VII, TbCOX X and TbCOX 6080) were down-regulated by RNA interference. We demonstrate that all three subunits are important for the proper function of complex IV and the growth of the procyclic stage of *T. brucei*. These phenotypes were manifested by the structural instability of the complex when these indispensible subunits were repressed. Furthermore, the impairment of cytochrome *c* oxidase resulted in other severe mitochondrial phenotypes, such as a decreased mitochondrial membrane potential, reduced ATP production *via* oxidative phoshorylation and redirection of oxygen consumption to the trypanosome-specific alternative oxidase, TAO. Interestingly, the inspected subunits revealed some disparate phenotypes, particularly regarding the activity of cytochrome *c* reductase (respiratory complex III). While the activity of complex III was down-regulated in RNAi induced cells for TbCOX X and TbCOX 6080, the TbCOX VII silenced cell line actually exhibited higher levels of complex III activity and elevated levels of ROS formation. This result suggests that the examined subunits may have different functional roles within complex IV of *T. brucei*, perhaps involving the ability to communicate between sequential enzymes in the respiratory chain. In summary, by characterizing the function of three hypothetical components of complex IV, we are able to assign these proteins as genuine and indispensable subunits of the procyclic *T. brucei* cytochrome *c* oxidase, an essential component of the respiratory chain in these evolutionary ancestral and medically important parasites.

1. Introduction

Trypanosoma brucei is a flagellated parasite of major medical and veterinary significance, causing Human African Trypanosomiases and nagana in cattle [1]. It is a member of Excavata, a group comprised of important human parasites, such as *Giardia*, *Trichomonas*, *Naegleria*, *T. cruzi* and *Leishmania ssp.* [2]. *T. brucei* has become a model organism for these devastating protozoa because it is amenable to all reverse genetic approaches, which include gene knock-out by homologous recombination, inducible expression systems and RNA interference (RNAi) [3]. Furthermore, *T. brucei* belongs to the class Kinetoplastida, which is named after the distinctive mitochondrial (mt) genomic structure located in its singular mitochondria. Kinetoplastida organisms are often regarded as primitive eukaryotes that have found fascinating ways to solve various problems presented to eukaryotes [4]. Thus, the pathogen *T. brucei* is now exploited for both the exploration of interesting biological processes of eukaryotic cells as well as deciphering its unique biology for future drug discovery.

The mitochondria of *T. brucei* houses several unique biological phenomena that have been extensively studied, including kinetoplast DNA structure and replication, RNA editing, and the respiratory pathway [5–8]. While all of these processes are essential, there is significant interest in the mechanism of respiration of the procyclic form (PF) of *T. brucei*, which resides in the digestive tract of its insect vector, the tse–tse fly [9]. During this life stage, the parasite can utilize its fully functional cytochrome-mediated respiratory pathway, which is comprised of a ubiquinone/ubiquinol pool, cytochrome *c* and four protein

* Corresponding author at: Biology Centre, Branišovská 31, 37005 České Budějovice, Czech Republic. Tel.: +420 387775482; fax: +420 385310388.
E-mail address: azikova@paru.cas.cz (A. Zíková).
[1] Present address: Department of Microbiology, The Ohio State University, Columbus, 43210 OH, USA.

0166-6851/$ – see front matter © 2012 Elsevier B.V. All rights reserved.
http://dx.doi.org/10.1016/j.molbiopara.2012.04.013

complexes: complex I (NADH:ubiquinone reductase), II (SDH, succinate:ubiquinone reductase), III (*bc*1, ubiquinone:cytochrome *c* reductase), and IV (cytochrome *c* oxidase). This electron transport chain transfers electrons from the reduced NADH and FADH molecules to the final electron acceptor, an oxygen molecule. Concurrently, protons are pumped across the inner mt membrane by complexes III and IV to generate the essential mt membrane potential. This electrochemical gradient is then used by the F_oF_1-ATP synthase to produce ATP by oxidative phosphorylation [10]. Interestingly, in addition to the conventional cytochrome-mediated respiratory pathway, the *T. brucei* mitochondrion utilizes a functionally distinct pathway to regenerate oxidized forms of NAD^+ molecules. This is achieved by the soluble alternative NADH dehydrogenase that passes electrons to ubiquinone [11]. These electrons can be further transferred to the plant-like alternative terminal oxidase (TAO) to reduce oxygen into water, though this process is not coupled with proton translocation [12,13]. Recently, comprehensive proteomic analyses have defined the composition of all the respiratory complexes [8], revealing the unique attributes of these macromolecular machines that consist of many protein subunits that have no homologs outside of Kinetoplastida. The most striking example of this divergence is respiratory complex IV, cytochrome *c* oxidase [14].

The cytochrome *c* oxidase complex was biochemically purified from three related trypanosomatid species *Crithidia fasciculata*, *Leishmania tarentolae* and *T. brucei*. To some extent, these purifications yielded overlapping sets of proteins, suggesting that in the trypanosomatid flagellates, the cytochrome *c* oxidase complex has at least 15 core nuclear-encoded subunits and three large mt-encoded subunits, a complexity similar to higher eukaryotic cytochrome *c* oxidases [14–16]. However, in contrast to these well conserved cytochrome *c* oxidase complexes, the *T. brucei* complex IV appears to be highly diverged, as only two of the nuclear-encoded subunits, COX VI and COX VIII, possess recognizable homology to the human subunits coxVIb and coxIV, respectively [14,17]. In addition to its core subunits, the *T. brucei* complex IV is transiently associated with an entourage of 18 proteins, most of them with unknown function [14]. While this divergence from the composition of oxidative phosphorylation complexes found in more publicized model species can be explained by the distant relationship of this ancient organism with higher eukaryotes, it is important to verify the true function of these hypothetical complex IV compatriots and begin to comprehend the alternative strategies employed by these medically important parasites.

Thus, in this study we characterized three proteins that have been shown to associate with trypanosomatid cytochrome *c* oxidase to various degrees: (i) Tb11.01.4702 (annotated as COX X in the geneDB database) was purified as a core subunit in each of the complexes isolated from *C. fasciculata*, *L. tarentolae* and *T. brucei*; (ii) Tb927.3.1410 (annotated as COX VII) is considered a core subunit in both the *C. fasciculata* and *L. tarentolae* complex, but is only transiently associated with the *T. brucei* complex; (iii) Tb927.8.6080–TbCOX 6080 (annotated as a hypothetical protein) was not detected in *C. fasciculata* or *L. tarentolae*; however, it was shown to transiently interact with the *T. brucei* complex [14,15,18]. The assignment of trypanosomatid cytochrome *c* oxidase subunits was based on the SDS-PAGE migration pattern observed for the purified subunits of the *C. fasciculata* cytochrome *c* oxidase complex. Since TbCOX VII and TbCOX X subunits show significant homology to *C. fasciculata* subunits VII and X, their nomenclature was made to acknowledge this attribute. However, the homologous *L. tarentolae* and *T. brucei* cytochrome *c* oxidase complexes do not display the same purification profiles as *C. fasciculata*. Since TbCOX 6080 subunit is not homologous to any known cytochrome *c* oxidase subunits, it was decided to use the geneDB identification number (*e.g.* Tb927.8.6080 = TbCOX 6080).

In order to explore the putative structural and functional associations of these subunits with the cytochrome *c* oxidase complex in *T. brucei*, we silenced all three genes by RNAi in the PF stage and examined the ensuing phenotypes. All three subunits are important for the structural integrity of the cytochrome *c* oxidase complex and their knockdowns caused severe phenotypes related to mt functions. Surprisingly, these subunits produced a disparate effect regarding the activity of the neighboring complex III and ROS production. These results suggest that all three subunits are genuine subunits of *T. brucei* complex IV, though they may have different functional roles, perhaps involving the ability to communicate between sequential enzymes in the respiratory chain.

2. Materials and methods

2.1. Construction of plasmids

To create the constructs for RNAi of TbCOX VII (Tb927.3.1410), TbCOX X (Tb11.01.4702) and TbCOX 6080 (Tb927.8.6080) transcripts, coding sequence (cds) fragments comprised of 486 base pairs (bp), 326 bp and 731 bp, respectively, were PCR amplified using the oligonucleotides listed below. The resulting PCR fragments were then cloned into the p2T7-177 plasmid [19] using XhoI and BamHI restriction sites (underlined).

TbCOX VII	Fw – 5′ CTCGAGCCCTTTGGTGTGTGG
	Rev – 5′ GGATCCGGCAGGAATATAGAA
TbCOX X	Fw – 5′ CTCGAGGTTGCGTGTGCTTGC
	Rev – 5′ GGATCCTACCAGCCGCGATGG
TbCOX 6080	Fw – 5′ CTCGAGCATCTAGTATGGCTG
	Rev – 5′ GGATCCATATGGGCATACCAT

2.2. Cell growth, transfection and RNAi induction

PF *T. brucei* strain 29.13 cells are transgenic for both the T7 RNA polymerase and the tetracycline (tet) repressor. Grown *in vitro* at 27 °C in SDM-79 medium containing hemin (7.5 mg/ml) and 10% fetal bovine serum, these cells were used as the parental cell line for the RNAi transfections. The RNAi plasmids containing opposing T7 promoters regulated by tet were linearized with NotI and stably transfected into the minichromosome 177 bp repeat region. The synthesis of double-stranded (ds) RNA in clonal cell lines was induced by the addition of 1 μg/ml tet to the medium. Growth curves were generated over a period of 7 days by measuring the cell density of tet treated and untreated cell cultures using the Z2 cell counter (Beckman Coulter Inc.). Throughout the experiment, cells were split daily to ensure that they remained within their exponential growth phase of 10^6–10^7 cells/ml.

2.3. Northern blot analysis

A total of 10^8 uninduced and RNAi induced exponentially growing cells were harvested at appropriate time points and the total RNA was extracted with TriReagent (MRC), according to the instructions provided by the manufacturer. The RNA samples were resolved on a 1% agarose gel and transferred to a nitrocellulose membrane. Prior to blotting, the rRNAs for each sample were stained with ethidium bromide and visualized on the AlphaImager HP gel documentation system (Cell Biosciences) as a loading control. The same cds fragments used to generate each RNAi were labeled with [α-^{32}P] dATP using the DecaLabel DNA labeling kit (Fermentas) and used as a probe. Hybridization of the probe to gene specific transcripts was performed using standard procedures, chiefly using a sodium phosphate buffer and hybridizing at 55 °C. The radioactive signal from the blots was captured on GE Healthcare storage phosphor screens and the autoradiograms were analyzed

by densitometry using the Typhoon phosphorImager and Imagequant software.

2.4. SDS-PAGE, 2D BN/Tricine SDS PAGE and Western blot analysis

Cleared whole cell or mt lysates fractionated on 12% SDS-PAGE gels were blotted onto a PVDF membrane and probed with polyclonal rabbit antibodies against *L. tarentolae* cytochrome *c* oxidase subunit IV (trCOIV) [20], *T. brucei* complex IV subunit VI (COVI) [21], or mt RNA binding protein 1 (MRP1) [22]. All of these polyclonal antibodies were used at a 1:500 dilution and the targeted proteins were visualized using the ECL system (Roche). The abundance of the immunodetected proteins was analyzed by densitometry (Image Quant™ software, GE Healthcare) and normalized to the loading control. The intensity of each band is represented as a percentage of the uninduced sample, which was set as 100%.

Two dimensional (2D) PAGE analysis was performed by first fractionating 100 μg of mt lysate on a 6% BN PAGE gel, which was then further resolved on a 10% Tricine–SDS-PAGE gel. After electrophoresis, the gel was stained with Coomassie Brilliant Blue (G-250) to visualize mt respiratory complexes or transferred onto a nitrocellulose membrane and probed with an anti-trCOIV antibody.

2.5. In vitro and in gel activity measurements of respiratory complexes

Mt vesicles from 5×10^8 cells were isolated by hypotonic cell lysis, as described previously [21], and stored as pellets at −70 °C. These mitochondria were then lysed with 2% dodecyl maltoside and the cytochrome *c* oxidase activity was determined *in vitro* by measuring the change in absorbance of cytochrome *c* as it becomes oxidized after passing its electrons to complex IV [21]. Cytochrome *c* reductase activity was determined in a similar way, this time the reduction of cytochrome *c* was measured when reduced decylubiquinone (Sigma) was added as an electron donor and complex III transferred these electrons to cytochrome *c*. In parallel, the same dodecyl maltoside lysed mitochondria samples were resolved (100 μg of protein per lane) on a 3–12% deep blue native (BN) PAGE gel and the cytochrome *c* oxidase activity was detected by an in-gel assay. The enzymatic activity of complex IV causes the native complex to be stained a dark blue as the electron acceptor 3,3′-diaminobenzidine is precipitated when it becomes reduced [23]. The enzymatic activities of complexes II and V were detected as described in [8,24].

2.6. FACS analysis of cells stained by TRME and DCFH-DA

To measure the changes in mt membrane potential, a 1 ml culture of mid-log phase cells was stained with 125 nM tetramethylrhodamine ethyl ester (TMRE, Molecular Probes) for 30 min at 27 °C. These cells were then harvested, washed with an isotonic solution suitable for flow cytometry and then analyzed for red fluorescence by a flow cytometer (BD FACSCanto II). Twenty thousand events were measured for each experiment. The data was analyzed by FACSDiva Version 6.1.3 software and the values, representing the median of red fluorescence intensity, were expressed as a percentage of the uninduced cells, which were set as 100%.

Reacting oxygen species were measured using 2′,7′-dichlorofluorescin diacetate (DCFH-DA, Sigma). DCFH-DA is a non-fluorescent dye that diffuses across the cell membrane and is retained as it becomes hydrolyzed intracellularly to form DCFH. In the presence of ROS, DCFH is rapidly oxidized to create the highly fluorescent compound, dichlorofluorescein. The uninduced and induced cells were incubated with 10 μM DCFH-DA for 30 min at 27 °C as described in [25]. The cells were then washed once with PBS-G and analyzed by FACS. Ten thousand events were measured in each experiment and the resulting data were analyzed using with Cyflogic™ software (CyFlo Ltd., Finland).

2.7. ATP production assay

ATP production was measured as described previously [26]. Briefly, a crude mt preparation from the untreated and tet treated RNAi cells was obtained by digitonin extraction. ATP production was then induced by the addition of 67 μM ADP and 5 mM of one of the substrates for the oxidative phosphorylation pathway (succinate) or for substrate phosphorylation (pyruvate and α-ketoglutarate). Specific inhibitors against succinate dehydrogenase (6.7 mM malonate) and the ADP/ATP carrier (33 μg/ml atractyloside) were preincubated with the enriched mitochondria samples for 10 min on ice to suppress oxidative phosphorylation. The resulting concentrations of ATP were determined by using the ATP Bioluminescence Assay Kit HS II (Roche) and a microplate luminometer (Orion II).

2.8. Measurement of oxygen consumption

Logarithmically growing cells were harvested, washed and resuspended in 1 ml of SDM-79 medium at a concentration of 2×10^7 cells ml^{-1}. Oxygen consumption at 27 °C was determined with a Clark-type polarographic electrode (1302 Microcathode Oxygen Electrode, Strathkelvin Instruments). The specific inhibitors, potassium cyanide (KCN) for cytochrome *c* oxidase and salicylhydroxamic acid (SHAM) for trypanosomatid alternative oxidase, were added in 2 min intervals at final concentrations of 0.1 mM and 0.03 mM, respectively. Background respiration was determined after collectively adding KCN and SHAM. This value was then subtracted from the initial rate of respiration for both uninduced and RNAi induced cells respiring without either inhibitor, resulting in a value for total cellular oxygen consumption that was set to 100%. Each sample was then treated with 0.1 mM KCN to determine the percentage of oxygen consumed by TAO. The amount of respiration produced from respiratory complex IV was conversely calculated by subtracting the percentage of TAO oxygen consumption from the initial respiration rate that was normalized for background respiration.

3. Results

3.1. Inhibition of TbCOX VII, TbCOX X and TbCOX 6080 gene expression generates significant PF T. brucei growth defects

To evaluate the functional associations of all three of the selected putative subunits of cytochrome *c* oxidase, we constructed PF *T. brucei* cell lines in which the expression of Tb927.3.1410 (TbCOX VII), Tb11.01.4702 (TbCOX X) and Tb927.8.6080 (TbCOX 6080) can be inducibly silenced using RNAi. In all cases, RNAi was administered by the p2T7-177 construct [19], which regulates the expression of double stranded RNA in a tet-dependent manner, resulting in the RNAi mediated degradation of the target mRNA. After the addition of tet into the culture medium, the growth of the TbCOX VII cell line was strongly inhibited by day 3 (Fig. 1A). Meanwhile, the growth inhibition of the RNAi induced TbCOX X and TbCOX 6080 cells was less dramatic and slightly delayed as the growth phenotype did not become apparent until after the fourth day of tet induction (Fig. 1A). While the growth phenotype was delayed slightly longer for TbCOX 6080, the doubling time of these affected cells was significantly more inhibited than those of the RNAi induced TbCOX X cells from the same time period. The efficiency of the RNAi was confirmed by Northern blot analysis using transcript specific probes, demonstrating that the mRNA for TbCOX

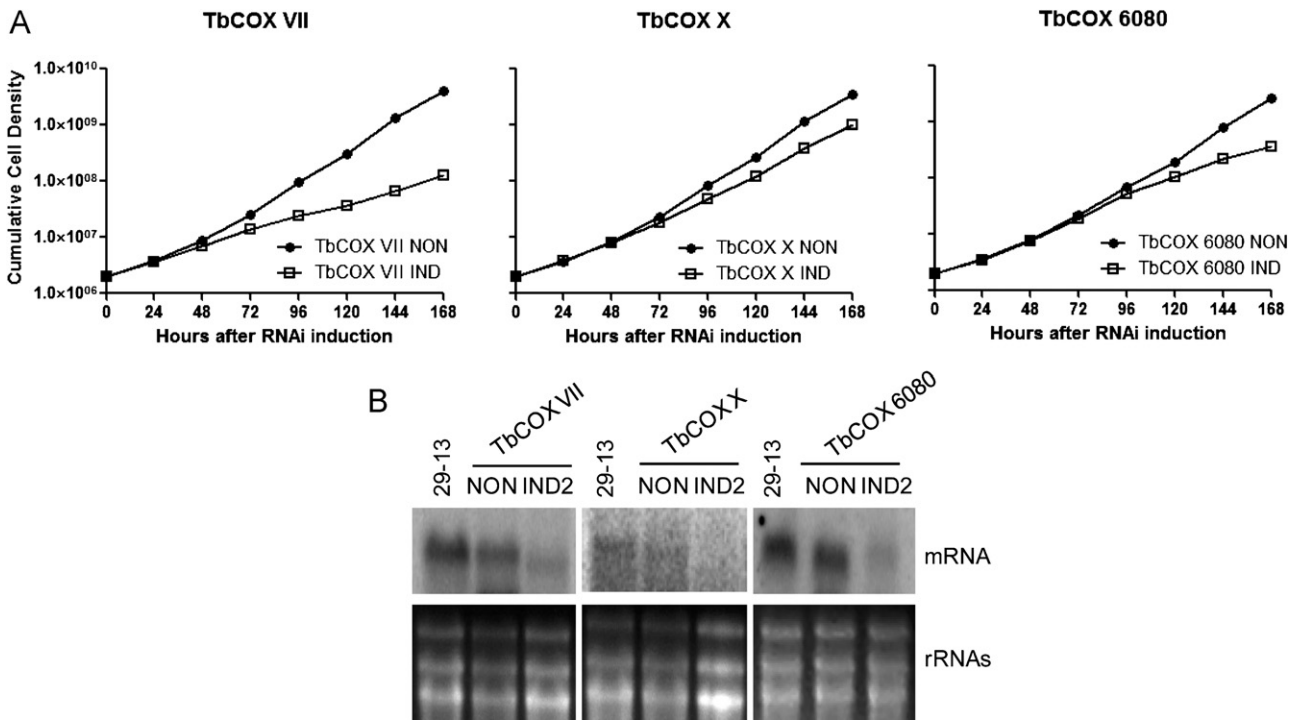

Fig. 1. Subunits TbCOX VII, TbCOX X and TbCOX 6080 are important for the *in vitro* growth of procyclic *T. brucei*. (A) Growth curves of the uninduced (NON) and tet induced (IND) TbCOX VII (left), TbCOX X (middle) and TbCOX 6080 (right) RNAi procyclic *T. brucei* cell lines. Cells were split everyday to maintain their exponential growth phase (between 10^6 and 10^7 cells/ml), thus the cumulative cell number represents the normalization of the daily cell density measurements by factoring in their dilution factor. Each graph is representative of the growth phenotype observed in three independent experiments. (B) Northern blot analysis of the corresponding mRNA (upper panel) for TbCOX VII, TbCOX X and TbCOX 6080 in the parental 29–13 cells, non-induced cells (NON) and cells 2 days upon induction of RNAi (IND2). As a loading control, the rRNAs (bottom panel) for each sample were stained with ethidium bromide and visualized with UV light.

VII, TbCOX X and TbCOX 6080 were all virtually eliminated after two days of RNAi induction (Fig. 1B). Based on the growth curve data, materials for all subsequent experiments involving TbCOX VII cells were collected on days 3 or 5 following RNAi induction, while the slightly delayed onset of the growth phenotype in the TbCOX X and TbCOX 6080 knockdown cells dictated that they be harvested at days 5 or 7 after the addition of tet.

3.2. Reduction of TbCOX VII, TbCOX X and TbCOX 6080 severely affects the function of cytochrome c oxidase

The biological function of complex IV is to transfer electrons from reduced cytochrome *c* to molecules of oxygen, while simultaneously contributing to the mt membrane potential by pumping H^+ into the inner mt membrane space. To assess if the ability of complex IV to pump protons is compromised when these putative subunits are knocked-down, we measured the mt membrane potential of uninduced and RNAi induced cells using the fluorescent probe TMRE, which accumulates in the matrix of the mitochondria when there is an active membrane potential. The analysis of all three induced RNAi cell lines revealed a decrease in fluorescence intensity (Fig. 2), which is indicative of a reduced mt membrane potential. As expected, the strongest phenotype was observed in cells with downregulated TbCOX VII, where on day 3 after RNAi induction the mt membrane potential was decreased by ~60% relative to values obtained with the uninduced cells. The five day RNAi induced TbCOX X and TbCOX 6080 cells also demonstrated a decrease in their membrane potential. However, TbCOX X was only mildly affected (~25% inhibition), whereas TbCOX 6080 was inhibited almost as significantly as TbCOX VII (~50% inhibition) (Fig. 2).

Since the capacity of complex IV to pump protons is decreased in these knockdowns, we applied a BN gel-based assay to detect the coordinated activity of the multi-subunit cytochrome *c* oxidase to transfer electrons to the artificial acceptor diaminobenzidine [21]. The mt lysates from uninduced and RNAi induced cells were fractionated on a BN gel and the cytochrome *c* oxidase activity was detected by histochemical staining (Fig. 3). The resulting dark blue activity band (~720 kDa) is in stark contrast to the faint staining of total protein seen in BN PAGE gels, as is evidenced by the intensity of the ~550 kDa band below it. In all RNAi induced cells, we observed a very strong decrease in the staining of this activity. To further corroborate this qualitative analysis, an *in vitro* assay was performed to

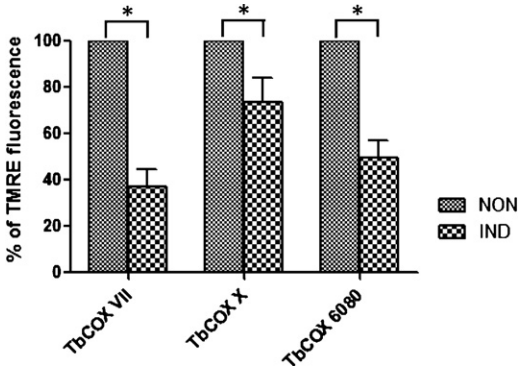

Fig. 2. Mitochondrial membrane potential is decreased following the reduction of TbCOX VII, TbCOX X and TbCOX 6080. Mt membrane potential was measured in both uninduced cells (NON, grey hatched bars) and tet induced RNAi cells (IND, black checkered bars) by flow cytometry after staining with TMRE. The fluorescence measurements for RNAi induced cells were obtained from day 3 for TbCOX VII and day 5 for TbCOX X and TbCOX 6080. The measured median values of red fluorescent intensity are represented as percentages of the uninduced sample, which was set to 100%. Data were obtained from at least three independent RNAi experiments and standard deviations are indicated. A Student's *t*-test analysis determined that the results are significant, with *P* values less than 0.05 (*).

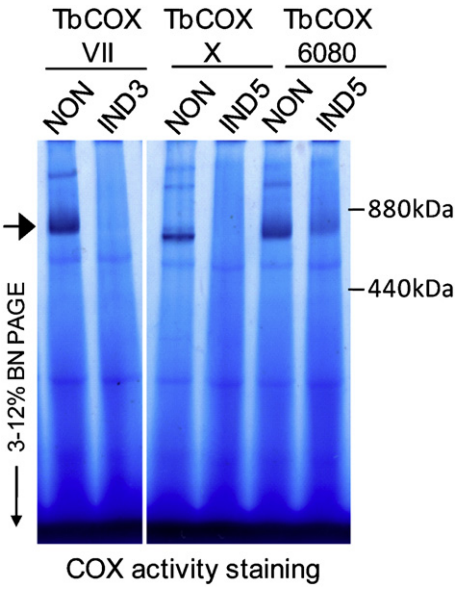

Fig. 3. Activity of the cyt *c* oxidase complex is affected upon depletion of TbCOX VII, TbCOX X and TbCOX 6080. In-gel *T. brucei* cyt *c* oxidase activity staining after the individual repression of subunits TbCOX VII (3 days after RNAi, IND3), TbCOX X and TbCOX 6080 (both 5 days after RNAi, IND5), compared to uninduced cells (NON). Mt preparations were solubilized using dodecyl maltoside and separated by 3–12% BN PAGE. The arrow points to bands visualized by the specific activity staining of cytochrome *c* oxidase, representing a complex of ~720 kDa. The sizes of high molecular weight markers (ferritin and its dimer, Sigma) are indicated on the right. This gel is representative of five independent experiments.

quantitatively measure the ability of complex IV to pass electrons to oxygen. As shown in Table 1, the specific cytochrome *c* oxidase activity was decreased by 67, 53 and 40% in TbCOX VII, TbCOX X and TbCOX 6080 RNAi induced cells, respectively, as compared to the uninduced cells. In summary, several independent assays demonstrate that both functions of cytochrome *c* oxidase, electron transfer and H^+ transport, are significantly diminished after each of the three complex IV subunits are abated.

3.3. Cytochrome c oxidase loss of function is due to the impaired structural integrity of the complex

To ascertain if the loss of cytochrome *c* oxidase activity is due to the instability of the complex, we analyzed the composition of the complex when each of the putative subunits was knocked-down. This was achieved by separating dodecyl maltoside solubilized mt lysates by 2D BN/Tricine SDS PAGE and identifying cytochrome *c* oxidase subunits based on the migration patterns observed in previous work [20,21]. The position of the largest nuclear encoded subunit, trCOIV, in the 2D BN/Tricine–SDS PAGE gel was further verified by Western blot analysis using mt lysates of uninduced and induced TbCOX VII RNAi cells (Fig. 4A, right panel). While mitochondria from uninduced cells contain several of the observable complex IV subunits, these proteins were significantly depleted or not detected at all in the same region of the gel containing the lysates of the RNAi induced cells (Fig. 4A and B, depicted area). These results suggest that the structural integrity of the cytochrome *c* oxidase complex is diminished after RNAi silencing of any of the examined subunits. Additional studies focusing on the individual components of the complex utilized specific antibodies already available against subunits trCOIV and COVI of the trypanosomatid respiratory complex IV. The steady-state abundance of these two core subunits in the total mt lysates of uninduced and RNAi induced cells was determined. As a consequence of the incomplete assembly of the cytochrome *c* oxidase complex, subunits trCOIV and COVI were drastically decreased (by 69% and 75%, respectively) in the induced TbCOX VII cells, significantly reduced (by 56% and 42%, respectively) in the cells depleted for TbCOX X and moderately depleted (by 36% and 29%, respectively) in the TbCOX 6080 induced cells (Fig. 4C). Thus, it appears that when any of these three investigated complex IV subunits are knocked-down, the stability of the complex is so severely affected that unincorporated trCOIV and COVI subunits become partially degraded.

Table 1
Functional assay for cytochrome *c* reductase and cytochrome *c* oxidase activities.

Cell line	Cytochrome *c* reductase activities (%)	Cytochrome *c* oxidase activities (%)
TbCOX VII IND 5 days	123 ± 7	33 ± 5
TbCOX X IND 7 days	28 ± 3	47 ± 13
TbCOX 6080 IND 7 days	50 ± 4	60 ± 4

All activities were measured in mt lysates prepared from at least three independent experiments as described in the Experimental procedures. Activities in the RNAi induced cells are represented as a percentage of the uninduced cells, which are set to 100%. Mean values and standard deviations are indicated.

3.4. Silencing of TbCOX VII, TbCOX X and TbCOX 6080 creates a disparate effect on the activity of cytochrome c reductase

Since the reduction of any of the three inspected complex IV subunits leads to a significantly decreased capacity of the complex to perform its normal functions, what are the implications for the rest of the respiratory chain complexes? To detect the ensuing effects of the loss of cytochrome *c* oxidase, the activities of other respiratory complexes were measured in each of the RNAi cell lines. The activities of respiratory complexes II and V were detected using BN and high resolution clear native gel electrophoresis, followed by in-gel specific activity staining. No significant differences in the activity and size of these complexes were observed (data not shown). Since no gel-based activity staining is available for the cytochrome *c* reductase complex, this activity was measured directly from mt lysates *in vitro*. Unexpectedly, the activity of this complex was slightly increased following the depletion of TbCOX VII, while it was considerably decreased in cells lacking the other two cytochrome *c* oxidase subunits, TbCOX X and TbCOX 6080 (Table 1). Since complex III is one of the major sites for reactive oxygen species (ROS) formation, its increased activity concurrent with the severe impairment of complex IV to transfer electrons, may result in higher intracellular ROS production. Therefore, it is plausible to hypothesize that a higher amount of ROS molecules will be formed in the induced TbCOX VII RNAi cell line. Indeed, on the third day of RNAi induction we detected a significant elevation of ROS molecules in this cell line (Fig. 5). However, it was not until day 5 post-tet induction that we finally observed a subtle increase in ROS production in the TbCOX 6080 cells, while no change was observed in the TbCOX X cells at this time. This result suggests that these subunits may have different complex IV functional roles in the mitochondrion of *T. brucei*, perhaps involving the cross-talk between sequential enzymes in the respiratory chain.

3.5. Diminished TbCOX VII, TbCOX X and TbCOX 6080 subunits effectively uncouples F_oF_1-ATP synthase

In PF *T. brucei*, respiratory complexes III and IV pump protons into the mt inner membrane space, resulting in a membrane potential that is then exploited by the coupled F_oF_1-ATP synthase to generate ATP by oxidative phosphorylation. Since this pathway depends on the proper function of all of the respiratory complexes, we investigated whether the generation of ATP *via* oxidative phosphorylation is affected in the complex IV RNAi induced cells. Indeed, we observed a significant decrease of ATP production by 85, 48

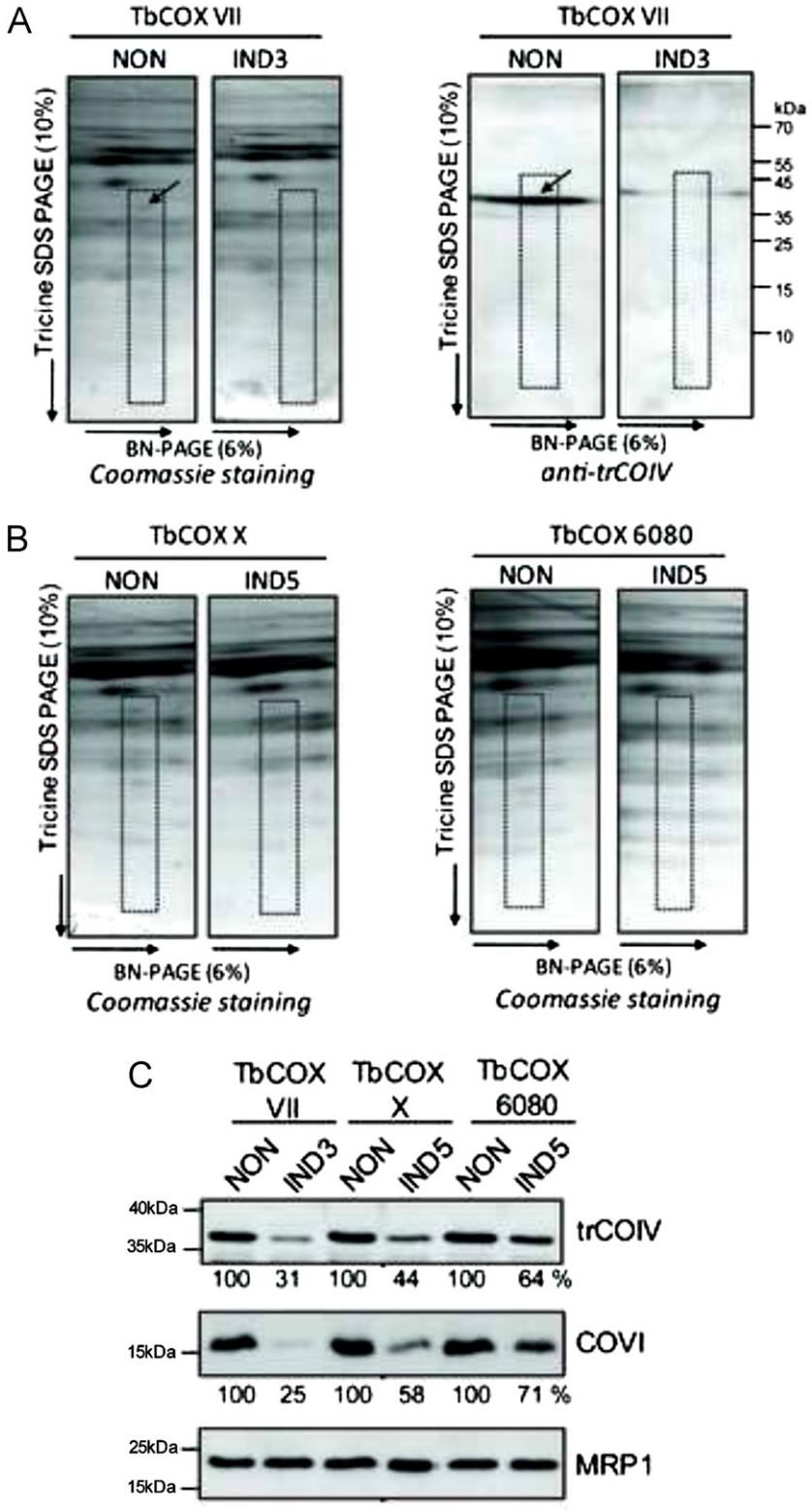

Fig. 4. Structural integrity of complex IV is affected by TbCOX VII, TbCOX X and TbCOX 6080 silencing. (A) 2D gel analysis of dodecyl maltoside-solubilized mitochondria of uninduced (NON) and day 3 induced (IND3) TbCOX VII RNAi cells. The 1st and 2nd dimensions were performed on a 6% BN gel and a 10% Tricine–SDS PAGE gel, respectively. The gel was stained with Coomassie Brilliant blue (left panel) or transferred onto a nitrocellulose membrane and probed with an anti-trCOIV antibody (right panel). The position of the largest nuclear encoded subunit, trCOIV, is indicated by an arrow. The area where the subunits of the cytochrome *c* oxidase complex migrate is indicated on the gel by a dashed box. The sizes of the molecular weight markers are indicated to the right of the Western blot. (B) 2D gel analysis of dodecyl maltoside-solubilized mitochondria of uninduced (NON) and day 5 induced (IND5) TbCOX X and TbCOX 6080 RNAi cells. The 2D BN/Tricine SDS PAGE gels were stained with Coomassie Brilliant blue. (C) Effects of TbCOX VII, TbCOX X and TbCOX 6080 RNAi on the steady-state abundance of the cytochrome *c* oxidase subunits trCOIV and COVI. Western blot analysis was performed on mt extracts obtained from uninduced RNAi cells (NON) and those induced with tet for 3 (IND3) or 5 (IND5) days. Each lane was loaded with 20 μg of total mt protein and the blots were immunodecorated with a polyclonal antibody against trCOIV or COVI. Mt RNA binding protein (MRP1) served as a loading control. The numbers depicted underneath each panel represent the abundance of immunodetected protein expressed as a percentage of the uninduced samples after normalizing to the loading control. The sizes of the molecular weight markers are indicated on the left.

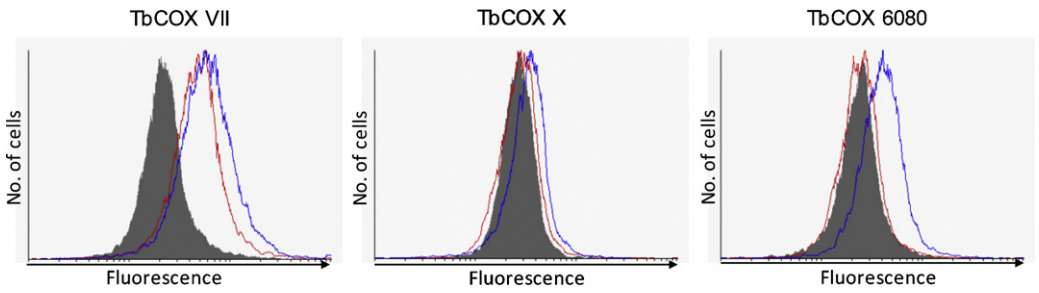

Fig. 5. ROS formation during TbCOX VII, TbCOX X and TbCOX 6080 RNAi. Measurement of intracellular reactive oxygen species in RNAi induced and uninduced cells using the ROS detection reagent DCFH-DA. Uninduced cells (shaded curve) and RNAi cells induced for 3 (red curve) or 5 (blue curve) days were analyzed by FACS analyses. The increase of the fluorescence intensity, most significantly witnessed in the TbCOX VII induced cells, corresponds to increased ROS formation that was observed in each of three independent assays. (For interpretation of the references to color in this figure caption, the reader is referred to the web version of the article.)

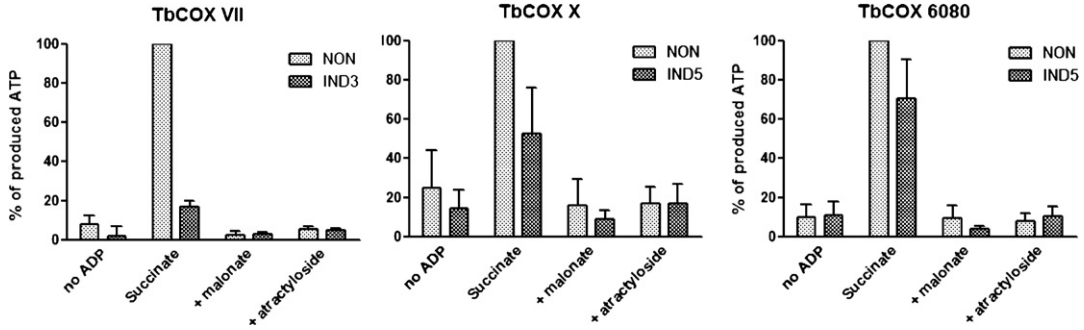

Fig. 6. ATP production by oxidative phosphorylation is severely reduced in mitochondria depleted for TbCOX VII, TbCOX X and TbCOX 6080. The *in vitro* generation of ATP was measured in digitonin-extracted mitochondria. The oxidative phosphorylation pathway was triggered by the addition of ADP and succinate. The level of ATP production in mitochondria isolated from uninduced RNAi cells stimulated with succinate without the presence of the specific inhibitors for succinate dehydrogenase (malonate) and the ADP/ATP carrier (atractyloside) was established as the reference and set to 100%. All other measurements in each panel are the mean values of each sample expressed as percentages of this reference sample, with the light grey bars representing the noninduced cells (NON) and the darker grey shaded bars representing RNAi samples induced for 3 (IND3) or 5 (IND5) days. "No ADP" serves as a control for the background production of ATP from the endogenous mt source of ADP. The data represent the average of three independent experiments and the standard deviations are indicated.

and 30% in RNAi induced TbCOX VII, TbCOX X and TbCOX 6080 cells, respectively (Fig. 6). Furthermore, this ATP synthesis was sensitive to malonate, an inhibitor of succinate dehydrogenase, and atractyloside, an inhibitor of the ATP/ADP translocator that provides the needed substrate for complex V. In addition to the oxidative phosphorylation pathway, which is triggered *in vitro* by succinate, there are two substrate phosphorylation pathways that are part of the incomplete citric acid cycle and the acetate-succinate CoA transferase/succinyl-CoA synthetase cycle [27]. While ATP generated specifically by oxidative phosphorylation was decreased in the inspected RNAi cells, neither of the substrate phosphorylation pathways were significantly affected in the RNAi interfered cells. Only a slight increase of ATP production by either substrate phosphorylation pathway was observed (data not shown). Taken together, these results show that TbCOX VII, TbCOX X and TbCOX 6080 directly affect ATP synthesis only *via* the oxidative phosphorylation pathway.

3.6. Depletion of TbCOX VII, TbCOX X and TbCOX 6080 causes a shift from cytochrome-mediated respiration to alternative oxidase

Interestingly, the mitochondrion of PF *T. brucei* cells is equipped with two oxygen-dependent terminal oxidases, namely the cytochrome *c* oxidase and TAO. Importantly, the electron flow from the cytochrome-mediated chain can be redirected to TAO when the former oxidase is disrupted. To verify this occurrence, the cells can be treated with drugs that selectively inhibit only one of these pathways, enabling one to distinguish between cytochrome *c* oxidase- and TAO-mediated oxygen consumption. After the addition of KCN, which selectively inhibits the activity of cytochrome *c* oxidase, oxygen uptake decreased by about 70% in the uninduced cells, indicating that the majority of oxygen consumption occurs through the cytochrome mediated pathway in normal PF cells. This contrasts sharply with the RNAi induced cells, where there was a less dramatic decrease of KCN-sensitive oxygen consumption observed (Fig. 7). In particular, we measured only a 15% decrease in

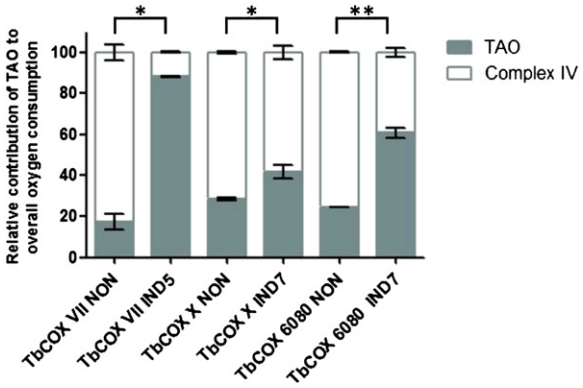

Fig. 7. Shift from cytochrome-mediated respiration to alternative oxidase respiration follows the repression of TbCOX VII, TbCOX X and TbCOX 6080. The oxygen consumption of uninduced and RNAi-induced cells incubated in SDM-79 medium at 27 °C was monitored with a Clark-type oxygen electrode. The graph depicts the percentage of total oxygen consumption by TAO. In this experiment, non-induced cells (NON) were compared with the TbCOX VII cell line induced with tet for 5 days (IND5) or the TbCOX X and TbCOX 6080 cell lines induced for 7 days (IND7). The mean and standard deviation values of three to four experiments are depicted. A Student's *t*-test analysis demonstrates that the results are significant with *P* values less than 0.05 (*) or less than 0.005 (**).

oxygen consumption when KCN was added to cells abated of TbCOX VII, which demonstrates that these cells have switched predominantly to TAO mediated respiration. A similar phenotype, although not as strong, was observed in cells with decreased TbCOX X and TbCOX 6080. These results are summarized in Fig. 7 by plotting the relative contribution to the overall cellular respiration by both the cytochrome *c* oxidase and TAO pathways. Importantly, the amount of respiration accounted for by TAO is proportional to the level of cytochrome *c* oxidase impairment produced by each of the RNAi cell lines.

4. Discussion

In this study, we presented evidence that TbCOX VII, TbCOX X and TbCOX 6080 are structurally and functionally important components of respiratory complex IV in PF *T. brucei*. This is a significant contribution to our understanding of the functional composition of a large protein complex, whose purification has revealed 15 core subunits and an additional 18 proteins not previously identified. This elaborate architecture implies that these additional proteins either directly complement the core subunits to comprise an unusual species-specific composition of cytochrome *c* oxidase or that they have transient interactions with the core complex and possess secondary functions. The increased complexity of cytochrome *c* oxidase in eukaryotes is often attributed to the increased need for regulation of this rate-limiting process in the cytochrome-mediated respiratory chain, which is even more important for this digenetic parasite whose complicated life cycle directly affects the regulation of its oxidative phosphorylation components [28,29]. However, an example of possible secondary functions is the association of cytochrome *c* oxidase with the MIX protein, which was shown to play a role in mt segregation and virulence in *L. major* [30]. This association adds further intricacy to the identification of the key functions of complex IV associated subunits and opens the possibility that cytochrome *c* oxidase is part of a larger membrane-bound multifunctional complex. Furthermore, recent studies of the individual complexes forming the electron transport chain in various protists revealed a surprisingly high number of lineage-specific subunits [24,31,32]. Therefore, the acquisition of unique components by these complexes can represent constructive neutral evolution, which might be responsible for the transformation of initially spurious associations into specialized essential functions of these subunits [33].

To gain insight into the function of the three novel complex IV candidate subunits, we prepared RNAi knockdowns for each of these subunits. While these knockdowns significantly decreased the level of the cognate RNA and the activity of cytochrome *c* oxidase, they generated phenotypes of various severity. This discrepancy could be explained by the possible difference in the turnover rate of subunits TbCOX VII, TbCOX X and TbCOX 6080; a claim currently difficult to verify in the absence of specific antibodies. Another alternative is that the built up complexity of the composition of complex IV in this protist allows for the function of TbCOX X and TbCOX 6080 to be complemented, to a limited extent, by other subunits.

Interestingly, it appears that the overall effect on the mt membrane potential most closely correlates with growth inhibition. For example, RNAi induced TbCOX X cells had significantly reduced cytochrome *c* oxidase activity *in vitro* (53%), but the mt membrane potential was only mildly affected and these cells displayed the weakest growth suppression. However, the TbCOX 6080 knockdown cells demonstrated less complex IV inactivation (40%), yet the mt membrane was more significantly decreased and the growth inhibition was more severe than the TbCOX X RNAi induced cells. This suggests that the overall viability of PF *T. brucei* grown *in vitro* is more dependent on the mt membrane potential than on the ability of cytochrome *c* oxidase to transfer electrons in the oxidative phosphorylation pathway. This observation also complies with the fact that the infectious stage of this parasite sacrifices ATP produced from glycolysis to maintain the mt membrane potential by F_oF_1 ATPase [34].

One plausible explanation why RNAi of TbCOX VII produces the most debilitating growth phenotype incorporates the regulation of the oxidative phosphorylation pathway. We observe that the activity of cytochrome *c* oxidase is decreased when any of the studied subunits are repressed. Without complex IV, the electrons flowing through complex III are not capable of completely reducing the terminal acceptor molecule, oxygen, into water. Therefore, the flow of electrons from the conventional cytochrome-mediated pathway will be diverted to the alternative terminal oxidase, TAO, as we witnessed. The branching point between these two pathways is ubiquinone, so the diminished capability of complex IV in these circumstances must be communicated back to cytochrome *c* reductase in a manner that proportionately down-regulates its activity. Indeed, when TbCOX X or TbCOX 6080 are depleted, there is a significant decrease in the activity of both complex III and IV. However, with TbCOX VII ablation, complex IV activity is severely decreased while the activity of complex III is actually increased 20%. This suggests that TbCOX VII is responsible for the signaling mechanism that allows these two sequential respiratory complexes to communicate. Therefore, this loss of function results in the uncoordinated activity of complex III, resulting in an increased flow of electrons necessary to replenish the decreased mt membrane potential. However, this could decrease the overall fitness of the cell as complex III is also responsible for superoxide production [35]. This is validated by the significant increase in ROS production detected in the TbCOX VII RNAi cell line.

The mechanism of communication between complexes III and IV may depend on physical interactions, as yeast supercomplexes consisting of cytochrome *c* reductase and cytochrome *c* oxidase have been biochemically isolated [36]. This solid state model of the respiratory complexes would enhance substrate availability and allow electron flow to occur more efficiently [37]. The in-gel activity staining of *T. brucei* complexes III and IV on BN gels both correspond to a mobility of about 720 kDa, while their predicted sizes are only 237 kDa and 360 kDa, respectively [8]. While it is possible that these activity bands simply represent multimers of each individual complex, they could also represent an intact supercomplex of both complexes III and IV. This intriguing possibility needs to be further explored as previous results indirectly suggested that complexes III and IV do not assemble into supercomplexes [21].

While TbCOX 6080 is annotated as a hypothetical protein in the geneDB database, it has significant homology to the glycerophosphoryl diester phosphodiesterases (GDPD). In eukaryotes, membrane proteins that contain the GDPD motif and activity form a large family of proteins involved in phospholipid metabolism. The role of these enzymes is to hydrolyze deacylated phospholipids to generate glycerol-3-phosphate and the corresponding alcohol, thus participating in various biological functions involving pathogenesis and host immunity in bacteria, to scavenging phosphates in plants and yeast, as well as altering levels of oxygen consumption in mammalian cells [38]. While the available data cannot exclude or confirm the possibility that TbCOX 6080 plays a role in phospholipid catabolic processes, there is already a similar example of a respiratory complex anchoring a polypeptide of fatty acid metabolism. The acyl carrier protein is an essential component of complex I [39] and it affects the rate of cytochrome-mediated respiration in *T. brucei*, independently of the function of complex I [40]. Therefore, the future investigation of TbCOX 6080 could shed light on the increasing correlation between mt membrane composition and the regulation of oxidative phosphorylation.

The mt encoded subunits I, II and III form the functional core of all mt cytochrome *c* oxidases [41], but little is known about the function of the other associated proteins. It is predicted that these nuclear-encoded supplementary complex IV components are involved in the assembly of the complex, help maintain the structural integrity, or are involved in the regulation of the enzyme. While we have been able to further validate that TbCOX VII, TbCOX X and TbCOX 6080 are functional subunits of the PF *T. brucei* cytochrome *c* oxidase complex, additional studies need to be completed to tease apart the specific functions of these proteins. It is promising that this can be accomplished in the unique *T. brucei* model organism, which displays disparate phenotypes for each of the studied subunits.

Acknowledgements

We would like to thank the members of our laboratories for their meaningful discussions. Furthermore, the work contributed by A.Z. was supported by the Grant Agency of the Academy of Sciences (KJB500960901) and the EMBO Installation Grant No. 1965. J.L. is a Fellow of the Canadian Institute of Advanced Research and his research was supported by the Grant Agency of the Czech Republic 204/09/1667 and the Praemium Academiae. In addition, the Institute of Parasitology (project Z60220518) provided valuable resources to both A.Z. and J.L. Finally, results provided by A.H. were funded by the Scientific Grant Agency of the Slovak Ministry of Education and the Academy of Sciences 1/0393/09.

References

[1] Simarro PP, Jannin J, Cattand P. Eliminating human African trypanosomiasis: where do we stand and what comes next? PLoS Medicine 2008;5:e55.
[2] Hampl V, Hug L, Leigh JW, Dacks JB, Lang BF, Simpson AG, et al. Phylogenomic analyses support the monophyly of Excavata and resolve relationships among eukaryotic supergroups. Proceedings of the National Academy of Sciences of the United States of America 2009;106:3859–64.
[3] Wirtz E, Leal S, Ochatt C, Cross GA. A tightly regulated inducible expression system for conditional gene knock-outs and dominant-negative genetics in *Trypanosoma brucei*. Molecular and Biochemical Parasitology 1999;99:89–101.
[4] Simpson AG, Stevens JR, Lukes J. The evolution and diversity of kinetoplastid flagellates. Trends in Parasitology 2006;22:168–74.
[5] Liu B, Liu Y, Motyka SA, Agbo EE, Englund PT. Fellowship of the rings: the replication of kinetoplast DNA. Trends in Parasitology 2005;21:363–9.
[6] Stuart KD, Schnaufer A, Ernst NL, Panigrahi AK. Complex management: RNA editing in trypanosomes. Trends in Biochemical Sciences 2005;30:97–105.
[7] Lukes J, Hashimi H, Zikova A. Unexplained complexity of the mitochondrial genome and transcriptome in kinetoplastid flagellates. Current Genetics 2005;48:277–99.
[8] Acestor N, Zikova A, Dalley RA, Anupama A, Panigrahi AK, Stuart KD. *Trypanosoma brucei* mitochondrial respiratome: composition and organization in procyclic form. Molecular and Cell Proteomics 2011;10:M110006908.
[9] Vickerman K. Developmental cycles and biology of pathogenic trypanosomes. British Medical Bulletin 1985;41:105–14.
[10] Besteiro S, Barrett MP, Riviere L, Bringaud F. Energy generation in insect stages of *Trypanosoma brucei*: metabolism in flux. Trends in Parasitology 2005;21:185–91.
[11] Fang J, Beattie DS. Identification of a gene encoding a 54 kDa alternative NADH dehydrogenase in *Trypanosoma brucei*. Molecular and Biochemical Parasitology 2003;127:73–7.
[12] Clarkson Jr AB, Bienen EJ, Pollakis G, Grady RW. Respiration of bloodstream forms of the parasite *Trypanosoma brucei brucei* is dependent on a plant-like alternative oxidase. Journal of Biological Chemistry 1989;264:17770–6.
[13] Chaudhuri M, Ajayi W, Hill GC. Biochemical and molecular properties of the *Trypanosoma brucei* alternative oxidase. Molecular and Biochemical Parasitology 1998;95:53–68.
[14] Zikova A, Panigrahi AK, Uboldi AD, Dalley RA, Handman E, F Stuart K. Structural and functional association of *Trypanosoma brucei* MIX protein with cytochrome c oxidase complex. Eukaryotic Cell 2008;7:1994–2003.
[15] Speijer D, Muijsers AO, Dekker H, de Haan A, Breek CK, Albracht SP, et al. Purification and characterization of cytochrome c oxidase from the insect trypanosomatid *Crithidia fasciculata*. Molecular and Biochemical Parasitology 1996;79:47–59.
[16] Horvath A, Berry EA, Huang LS, Maslov DA. *Leishmania tarentolae*: a parallel isolation of cytochrome bc(1) and cytochrome c oxidase. Experimental Parasitology 2000;96:160–7.
[17] Speijer D, Breek CK, Muijsers AO, Groenevelt PX, Dekker H, de Haan A, et al. The sequence of a small subunit of cytochrome c oxidase from *Crithidia fasciculata* which is homologous to mammalian subunit IV. FEBS Letters 1996;381:123–6.
[18] Horvath A, Kingan TG, Maslov DA. Detection of the mitochondrially encoded cytochrome c oxidase subunit I in the trypanosomatid protozoan *Leishmania tarentolae*. Evidence for translation of unedited mRNA in the kinetoplast. Journal of Biological Chemistry 2000;275:17160–5.
[19] Wickstead B, Ersfeld K, Gull K. Targeting of a tetracycline-inducible expression system to the transcriptionally silent minichromosomes of *Trypanosoma brucei*. Molecular and Biochemical Parasitology 2002;125:211–6.
[20] Maslov DA, Zikova A, Kyselova I, Lukes J. A putative novel nuclear-encoded subunit of the cytochrome c oxidase complex in trypanosomatids. Molecular and Biochemical Parasitology 2002;125:113–25.
[21] Horvath A, Horakova E, Dunajcikova P, Verner Z, Pravdova E, Slapetova I, et al. Downregulation of the nuclear-encoded subunits of the complexes III and IV disrupts their respective complexes but not complex I in procyclic *Trypanosoma brucei*. Molecular Microbiology 2005;58:116–30.
[22] Vondruskova E, van den Burg J, Zikova A, Ernst NL, Stuart K, Benne R, et al. RNA interference analyses suggest a transcript-specific regulatory role for mitochondrial RNA-binding proteins MRP1 and MRP2 in RNA editing and other RNA processing in *Trypanosoma brucei*. Journal of Biological Chemistry 2005;280:2429–38.
[23] Jung C, Higgins CM, Xu Z. Measuring the quantity and activity of mitochondrial electron transport chain complexes in tissues of central nervous system using blue native polyacrylamide gel electrophoresis. Analytical Biochemistry 2000;286:214–23.
[24] Zikova A, Schnaufer A, Dalley RA, Panigrahi AK, Stuart KD. The F(0)F(1)-ATP synthase complex contains novel subunits and is essential for procyclic *Trypanosoma brucei*. PLoS Pathogen 2009;5:e1000436.
[25] Goldshmidt H, Matas D, Kabi A, Carmi S, Hope R, Michaeli S. Persistent ER stress induces the spliced leader RNA silencing pathway (SLS), leading to programmed cell death in *Trypanosoma brucei*. PLoS Pathogen 2010;6:e1000731.
[26] Allemann N, Schneider A. ATP production in isolated mitochondria of procyclic *Trypanosoma brucei*. Molecular and Biochemical Parasitology 2000;111:87–94.
[27] Schneider A, Bouzaidi-Tiali N, Chanez AL, Bulliard L. ATP production in isolated mitochondria of procyclic *Trypanosoma brucei*. Methods of Molecular Biology 2007;372:379–87.
[28] Schnaufer A, Domingo GJ, Stuart K. Natural and induced dyskinetoplastic trypanosomatids: how to live without mitochondrial DNA. International Journal for Parasitology 2002;32:1071–84.
[29] Matthews KR. The developmental cell biology of *Trypanosoma brucei*. Journal of Cell Science 2005;118:283–90.
[30] Uboldi AD, Lueder FB, Walsh P, Spurck T, McFadden GI, Curtis J, et al. A mitochondrial protein affects cell morphology, mitochondrial segregation and virulence in Leishmania. International Journal for Parasitology 2006;36:1499–514.
[31] Lapaille M, Escobar-Ramirez A, Degand H, Baurain D, Rodriguez-Salinas E, Coosemans N, et al. Atypical subunit composition of the chlorophycean mitochondrial F1FO-ATP synthase and role of Asa7 protein in stability and oligomycin resistance of the enzyme. Molecular Biology and Evolution 2010;27:1630–44.
[32] Balabaskaran Nina P, Dudkina NV, Kane LA, van Eyk JE, Boekema EJ, Mather MW, et al. Highly divergent mitochondrial ATP synthase complexes in *Tetrahymena thermophila*. PLoS Biology 2010;8:e1000418.
[33] Doolittle WF, Lukes J, Archibald JM, Keeling PJ, Gray MW. Comment on does constructive neutral evolution play an important role in the origin of cellular complexity? Bioessays 2011;33:427–9, doi:101002/bies.201100010.
[34] Schnaufer A, Clark-Walker GD, Steinberg AG, Stuart K. The F1-ATP synthase complex in bloodstream stage trypanosomes has an unusual and essential function. EMBO Journal 2005;24:4029–40.
[35] Muller FL, Liu Y, Van Remmen H. Complex III releases superoxide to both sides of the inner mitochondrial membrane. Journal of Biological Chemistry 2004;279:49064–73.
[36] Schagger H, Pfeiffer K. Supercomplexes in the respiratory chains of yeast and mammalian mitochondria. EMBO Journal 2000;19:1777–83.
[37] Vonck J, Schafer E. Supramolecular organization of protein complexes in the mitochondrial inner membrane. Biochimica Et Biophysica Acta 2009;1793:117–24.
[38] Patton-Vogt J. Transport and metabolism of glycerophosphodiesters produced through phospholipid deacylation. Biochimica Et Biophysica Acta 2007;1771:337–42.
[39] Cronan JE, Fearnley IM, Walker JE. Mammalian mitochondria contain a soluble acyl carrier protein. FEBS Letters 2005;579:4892–6.
[40] Guler JL, Kriegova E, Smith TK, Lukes J, Englund PT. Mitochondrial fatty acid synthesis is required for normal mitochondrial morphology and function in *Trypanosoma brucei*. Molecular Microbiology 2008;67:1125–42.
[41] Cooper CE, Nicholls P, Freedman JA. Cytochrome c oxidase: structure, function, and membrane topology of the polypeptide subunits. Biochemistry and Cell Biology 1991;69:586–607.

JBC RESEARCH ARTICLE

Bioenergetic consequences of F_oF_1–ATP synthase/ATPase deficiency in two life cycle stages of *Trypanosoma brucei*

Received for publication, July 22, 2020, and in revised form, December 23, 2020 Published, Papers in Press, February 2, 2021, https://doi.org/10.1016/j.jbc.2021.100357

Carolina Hierro-Yap[1,2], Karolína Šubrtová[1,3], Ondřej Gahura[1], Brian Panicucci[1], Caroline Dewar[3], Christos Chinopoulos[4], Achim Schnaufer[3], and Alena Zíková[1,2,*]

From the [1]Institute of Parasitology, Biology Centre, Czech Academy of Sciences, Ceske Budejovice, Czech Republic; [2]Faculty of Science, University of South Bohemia, Ceske Budejovice, Czech Republic; [3]Institute of Immunology and Infection Research, University of Edinburgh, United Kingdom; [4]Department of Medical Biochemistry, Semmelweis University, Budapest, Hungary

Edited by John Denu

Mitochondrial ATP synthase is a reversible nanomotor synthesizing or hydrolyzing ATP depending on the potential across the membrane in which it is embedded. In the unicellular parasite *Trypanosoma brucei*, the direction of the complex depends on the life cycle stage of this digenetic parasite: in the midgut of the tsetse fly vector (procyclic form), the F_oF_1–ATP synthase generates ATP by oxidative phosphorylation, whereas in the mammalian bloodstream form, this complex hydrolyzes ATP and maintains mitochondrial membrane potential (ΔΨm). The trypanosome F_oF_1–ATP synthase contains numerous lineage-specific subunits whose roles remain unknown. Here, we seek to elucidate the function of the lineage-specific protein Tb1, the largest membrane-bound subunit. In procyclic form cells, Tb1 silencing resulted in a decrease of F_oF_1–ATP synthase monomers and dimers, rerouting of mitochondrial electron transfer to the alternative oxidase, reduced growth rate and cellular ATP levels, and elevated ΔΨm and total cellular reactive oxygen species levels. In bloodstream form parasites, RNAi silencing of Tb1 by ∼90% resulted in decreased F_oF_1–ATPase monomers and dimers, but it had no apparent effect on growth. The same findings were obtained by silencing of the oligomycin sensitivity-conferring protein, a conserved subunit in *T. brucei* F_oF_1–ATP synthase. However, as expected, nearly complete Tb1 or oligomycin sensitivity-conferring protein suppression was lethal because of the inability to sustain ΔΨm. The diminishment of F_oF_1–ATPase complexes was further accompanied by a decreased ADP/ATP ratio and reduced oxygen consumption *via* the alternative oxidase. Our data illuminate the often diametrically opposed bioenergetic consequences of F_oF_1–ATP synthase loss in insect *versus* mammalian forms of the parasite.

The F_oF_1–ATP synthase is a multisubunit protein complex capable of coupling ATP synthesis/hydrolysis with transmembrane proton translocation. In eukaryotes, this nanomachine is embedded in the inner mitochondrial membrane and consists of two parts, the matrix-facing F_1 and the membrane-embedded F_o. The F_1 domain, known as F_1-ATPase, is responsible for the phosphorylation of ADP to ATP, and it consists of a heterohexamer of α and β subunits and a central stalk (subunits γ, δ, and ε) that connects the $(\alpha\beta)_3$-headpiece to the F_o section. The core of the F_o section consists of a ring of c subunits that tightly interacts with subunit a, a highly hydrophobic subunit encoded by the mitochondrial genome in most eukaryotes, including trypanosomatids (1, 2). Aside from the central stalk, the interaction between the F_o and F_1 domains is mediated by the peripheral stalk, an elongated structure that immobilizes the $(\alpha\beta)_3$-headpiece during the rotation of the central rotor shaft (central stalk plus c-ring) by directly binding to subunits α and β (1). Despite the long period of evolutionary divergence of more than 2 billion years, the structure of prokaryotic and eukaryotic F_oF_1–ATP synthases is notably conserved, mainly at the level of tertiary and quaternary structures (2).

Nevertheless, in recent years, purifications and high-resolution structures of F_oF_1–ATP synthases from nonclassical model organisms revealed a wider variety in complex composition and structural organization than initially recognized (3–7). This includes the *Trypanosoma brucei brucei* F_oF_1–ATP synthase, an enzyme composed of 23 subunits, of which 14 are either lineage specific or highly divergent (8). For example, the lineage-specific subunits p18 and ATPaseTb2 (Tb2 in short) elaborate the otherwise conserved F_1 domain (9, 10) and represent one of the largest peripheral stalk subunits found in F_oF_1–ATP synthases to date (11), respectively.

The peculiarities of *T. brucei* F_oF_1–ATP synthase are not restricted only to complex composition. A remarkable feature of this complex is that its activity depends on the parasite's life cycle. The procyclic form (PCF), also known as insect midgut stage, harbors a conventional mitochondrion where the F_oF_1–ATP synthase produces ATP (forward mode) using the electrochemical gradient across the inner mitochondrial membrane generated by the proton-pumping activity of respiratory complexes III and IV (8, 12, 13). In contrast, the infectious stage of the mammalian host, termed long slender bloodstream form (BSF), lacks a cytochrome-mediated electron transport chain and respires exclusively *via* the alternative

This article contains supporting information.

* For correspondence: Alena Zíková, azikova@paru.cas.cz.

Present address for Caroline Dewar: Department of Chemistry and Biochemistry, University of Bern, Bern, Switzerland.

oxidase (AOX) pathway (14). The mitochondrial membrane potential (ΔΨm) is generated by the proton-pumping activity (reverse mode) of the F_oF_1–ATP synthase (aka F_oF_1–ATPase) complex at the expense of ATP (15, 16). Hence, *T. brucei* represents a unique eukaryotic system that allows to study both modes of the F_oF_1–ATP synthase in physiological settings and the distinct bioenergetic consequences upon the loss of either of the activities.

The reverse mode of the F_oF_1–ATP synthase complex is used by some prokaryotes (17), but it is unusual in eukaryotes, where it occurs under rare nonphysiological and stress conditions, such as hypoxia or anoxia. In these cases, the respiratory arrest and subsequent collapse of the ΔΨm causes a reversal of the F_oF_1–ATP synthase to generate a modest ΔΨm (18, 19). The reversal of F_oF_1–ATP synthase also takes place in cells lacking mitochondrial DNA, which maintain ΔΨm by an electrogenic exchange of ATP^{4-} for ADP^{3-} by the ADP/ATP carrier (AAC) coupled to ATP hydrolysis by an incomplete F_oF_1–ATPase (20–22). The depletion of ATP due to the hydrolytic activity of the F_oF_1–ATP synthase during ischemic conditions is mitigated by a unidirectional inhibitor, the inhibitory factor 1 (23). Noteworthy, in *T. brucei*, the expression of inhibitory factor 1 is tightly regulated throughout the parasite's life cycle, and its experimental expression in BSF trypanosomes results in cell death (24, 25), highlighting the indispensability of the F_oF_1–ATPase complex for BSF *T. brucei*.

ATPaseTb1 (Tb1 in short; systematic TriTrypDB.org ID Tb927.10.520) (47 kDa) is one of the 14 lineage-specific subunits and the largest F_o subunit of the *T. brucei* F_oF_1–ATP synthase complex (8) (named Tb7760 in that study, after its previous systematic TriTrypDB ID TB10.70.7760). Downregulation of Tb1 in PCF trypanosomes inhibits cell growth, destabilizes F_oF_1–ATP synthase, and affects both the ATP synthetic and hydrolytic activities of the complex (8). Here, we studied in more detail the mitochondrial phenotypes associated with the downregulation of Tb1 in PCF cells and further explore the role of this subunit, as well as that of the peripheral subunit oligomycin sensitivity-conferring protein (OSCP), in the BSF stage.

Results

Tb1 is a membrane-bound subunit of the F_o moiety

Tb1, the largest membrane-associated subunit of the *T. brucei* F_oF_1–ATP synthase, has homologs in representatives of the Euglenozoa group but appears to be absent from other eukaryotic lineages (8). In agreement with the reduced size and activity of the mitochondrion in the BSFs of *T. brucei* (26), Tb1 is less abundant in BSF cells than in PCF cells and barely detectable in the mitochondrial DNA-lacking (aka akinetoplastic) strains *T. b. brucei* Dk 164 and *Trypanosoma brucei evansi* AnTat 3/3 (Fig. 1*A*). To confirm the submitochondrial localization of Tb1 and determine how it is associated with the inner mitochondrial membrane, we performed carbonate extraction of mitochondria purified from *T. brucei* cells expressing C-terminally v5-tagged Tb1 (Fig. 1*B*). Tb1 is found exclusively in the membrane fraction, and the marker proteins, enolase, mitochondrial RNA-binding protein 1, and AAC, are detected in their expected compartments: cytosol, mitochondrial matrix, and mitochondrial membrane, respectively. This result suggests that Tb1 is an integral membrane protein. In PCF and BSF cells, Tb1 is present in fully assembled F_oF_1–ATP synthase monomers and dimers, as documented by high-resolution clear native electrophoresis (Fig. 1*C*) and sedimentation in glycerol gradient (Fig. 1*D*) followed by Western blot analyses with a specific anti-Tb1 antibody. In glycerol gradients, the Tb1 antibody detected, in addition to Tb1 migrating with the F_oF_1–ATP synthase, nonspecific bands of ~40 kDa and 42 kDa in PCF and of 55 kDa in BSF, which are identified by the asterisk (Fig. 1*D*).

Our observations that Tb1 is present in fully assembled F_oF_1–ATP synthase are in agreement with a recent cryogenic electron microscopy structure of the F_oF_1–ATP synthase dimer from *Euglena gracilis*, a closely related free-living species within the Euglenozoa group, in which Tb1 is found on the matrix side of the membrane part of the complex at the peripheral stalk base (6). We predicted the structure of *T. brucei* Tb1 using *E. gracilis* Tb1 as a template (Fig. 1*E*). The modeling showed that both Tb1 orthologs share a fold similar to the mitochondrial distribution and morphology protein 38 (Mdm38) from *Saccharomyces cerevisiae*, a protein suggested to be involved in the assembly of the mitochondrial-encoded subunit a into the F_o moiety (27). Although several algorithms predicted one transmembrane helix in Tb1, the protein does not span the inner mitochondrial membrane. Instead, the presumptive transmembrane region occurs as a HTH motif intruding into the membrane (Fig. 1*E*), and therefore, Tb1 is a monotopic membrane protein.

Silencing of Tb1 in PCF cells leads to a transient increase of ΔΨm followed by redirection of respiration toward AOX

Previously, we showed that Tb1 silencing in PCF cells leads to decreased steady-state levels of fully assembled F_oF_1–ATP synthase complexes, and, therefore, to less ATP produced by substrate-stimulated oxidative phosphorylation in digitonin-permeabilized cells (8). Here, we explored in more detail the effect of Tb1 silencing on mitochondrial physiology and bioenergetics of PCF cells. As expected, Tb1 silencing caused a progressive growth phenotype detected first at day 4 of RNAi induction (Fig. 2*A*). Western blot analysis using a specific anti-Tb1 antibody showed that Tb1 protein expression was reduced to less than 10% at day 2 of RNAi induction (Fig. 2*B*). The downregulation of Tb1 was accompanied by a decrease in the steady-state level of the peripheral stalk subunit Tb2, whereas the abundance of the F_1 moiety subunit β was not as strongly affected (Fig. 2*B*). The structural integrity and the activity of the F_oF_1–ATP synthase complex were assessed by blue native electrophoresis (BNE) followed by Western blotting and in-gel activity staining of the complex, respectively (Fig. 2*C*). Western blot analyses of native complexes showed a significant reduction of F_oF_1–ATP synthase monomers and dimers at days 2 and 4 of RNAi induction. In agreement with the steady-state

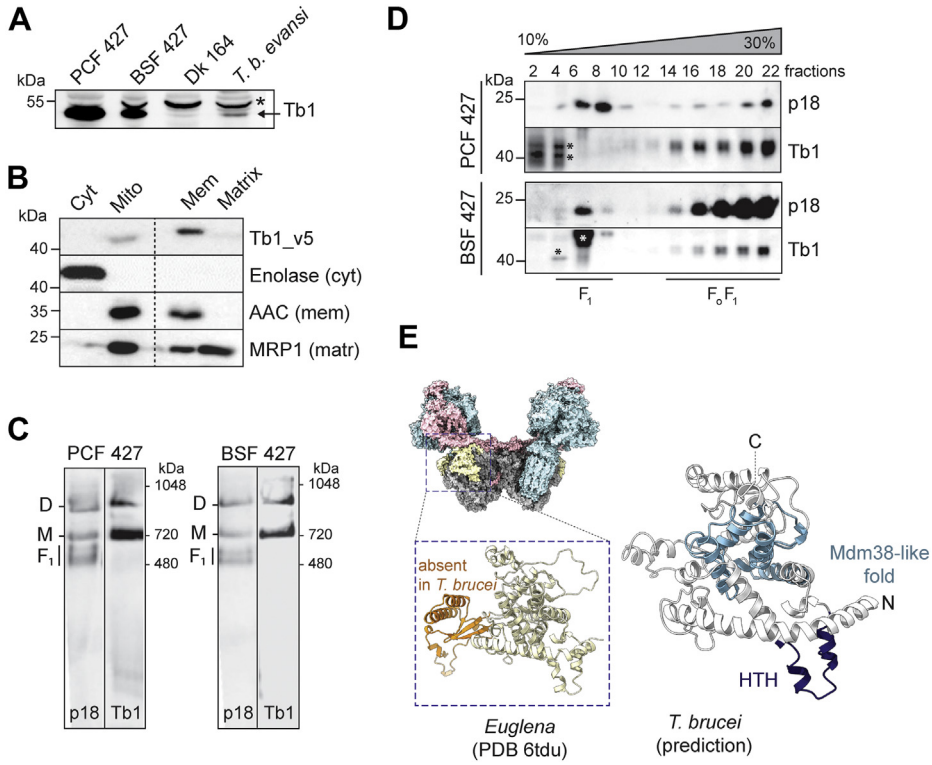

Figure 1. Tb1 is a membrane-bound F_oF_1–ATP synthase subunit. *A*, Western blot analysis of whole-cell lysates prepared from 1×10^7 *T. brucei* PCF, BSF, Dk 164, and *Trypanosoma brucei evansi* AnTat 3/3 cells probed with anti-Tb1 antibody. The laboratory-induced Dk 164 and the naturally occurring laboratory-adapted *T. b. evansi* AnTat 3/3 are BSF strains devoid of mitochondrial DNA. An *asterisk* points to a nonspecific band detected by the anti-Tb1 antibody. *B*, Western blot analysis of subcellular fractions obtained by carbonate extraction of mitochondria purified from PCF cells expressing v5-tagged Tb1 protein. Blots were probed with anti-v5 antibody, anti-enolase, anti-AAC, and anti-MRP1 antibodies to visualize Tb1, cytosolic enolase, inner mitochondrial membrane-bound AAC, and mitochondrial matrix–localized MRP1, respectively. *C*, High-resolution clear native electrophoresis of crude mitochondrial vesicles from PCF and BSF parasites. The F_1-ATPase (F_1) and the monomeric (M) and dimeric (D) forms of the complex were visualized using specific antibodies against subunits p18 and Tb1. *D*, glycerol gradient sedimentation of PCF and BSF lysed mitochondrial samples to determine the sedimentation profile of F_1– and F_oF_1–ATP synthase complexes. Glycerol gradient fractions were analyzed by SDS-PAGE followed by Western blotting using antibodies against p18 and Tb1. The p18 antibody depicts the sedimentation profile of both F_1–ATPase and the monomeric/dimeric states of the complex, whereas the Tb1 antibody detects only the monomeric/dimeric assemblies of the F_oF_1–ATP synthase. *Asterisks* represent nonspecific bands detected by the anti-Tb1 antibody. *E*, the structure of Tb1 from *Euglena* determined by cryo-EM (PDB ID 6TDU (6), *light yellow*) and the predicted structure of *T. brucei* Tb1. In the *E. gracilis* Tb1, the region absent in *T. brucei* is shown in *orange*. In the *T. brucei* Tb1, the Mdm38-like fold and the helix-turn-helix motif (HTH) intruding into the membrane are shown in *light blue* and *dark blue*, respectively. In the space-filling model of the *E. gracilis* F_oF_1–ATP synthase, the F_1–ATPase and the c-ring are *blue*, the peripheral stalk subunits are *pink*, and all other membrane subunits are *gray*. AAC, ADP/ATP carrier; BSF, bloodstream form; cryo-EM, cryogenic electron microscopy; *Cyt*, cytosol; *Matr*, mitochondrial matrix; Mdm38, mitochondrial distribution and morphology protein 38; *Mem*, mitochondrial membranes; *Mito*, mitochondria; MRP1, mitochondrial RNA binding protein 1; PCF, procyclic form; Tb1, ATPaseTb1.

levels of subunit β, the free F_1-ATPase moiety was assembled and active, and it accumulated in Tb1-silenced cells. The decreased levels of fully assembled F_oF_1–ATP synthase complexes affected ATP production by oxidative phosphorylation (8), which was reflected by a ∼25% reduction in the total cellular ATP levels (Fig. 2*D*) and by a 50% increase in the ADP/ATP ratio (Fig. 2*E*) by day 4 of RNAi induction. Suppression of Tb1 expression also caused a mild, but statistically significant, increase in ΔΨm at day 2 of RNAi induction (Fig. 2*F*), but notably, this increase was only transient. In PCF cells, the ΔΨm is maintained by the activity of respiratory complexes III and IV, passing electrons from ubiquinol to molecular oxygen. However, electrons can be rerouted to another electron acceptor, a plant-like AOX, which reduces molecular oxygen to water without proton translocation (28). By doing so, PCF cells can uncouple cellular respiration from ΔΨm generation. To test if the cells responded to the hyperpolarization detected at day 2 by rewiring the electrons toward AOX, we measured the oxygen consumption rate in the presence of potassium cyanide (KCN) and salicylhydroxamic acid (SHAM), inhibitors of complex IV and AOX, respectively. Indeed, we detected that the respiration of Tb1-silenced cells is more sensitive to SHAM compared with KCN, confirming the higher proportion of AOX-mediated respiration (Fig. 2*G*). This rerouting of electrons was accompanied by an increase in AOX expression as determined by Western blot (Fig. 2*B*). Because complex III is one of the major producers of harmful superoxide ($O_2^{\bullet -}$) molecules, an important subclass of reactive oxygen species (ROS) (29), we measured the mitochondrial concentration of $O_2^{\bullet -}$ before and after Tb1 RNAi in PCF cells (Fig. 2*H*). We found that $O_2^{\bullet -}$ decreased over time after Tb1 ablation, supporting the proposed rerouting of electrons from complexes III and IV toward AOX, perhaps as a protective mechanism against oxidative stress (30–32). Despite the lower levels of mitochondrial $O_2^{\bullet -}$, the disruption of fully assembled F_oF_1–ATP synthase induced changes in cellular physiology that ultimately led to higher levels of various cytosolic ROS molecules (*e.g.*, peroxyl, hydroxyl) as measured by

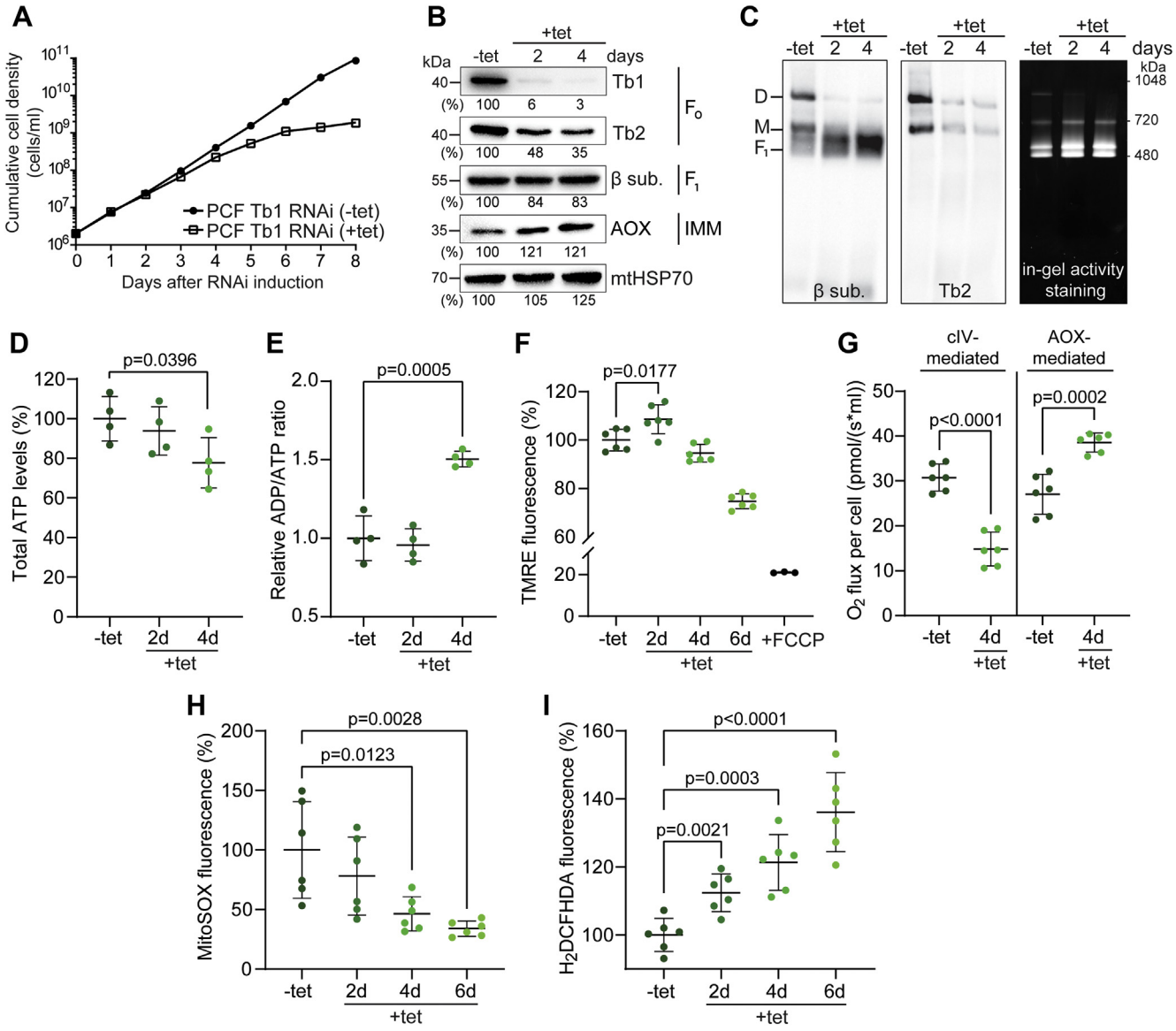

Figure 2. Loss of Tb1 in PCF cells affects the structural integrity of the F_oF_1–ATP synthase complex and induces changes in mitochondrial physiology. *A*, growth of noninduced (–tet) and Tb1 RNAi–induced (+tet) PCF cells measured for 8 days. Cumulative cell density was calculated from the cell counts adjusted by the dilution factor needed to seed the cultures at 2×10^6 cells/ml each day. *B*, Western blot analysis of PCF Tb1 RNAi trypanosomes grown in the absence (–tet) or presence (+tet) of tetracycline for 2 and 4 days. Whole-cell lysates were subjected to SDS-PAGE followed by immunostaining with antibodies against Tb1 and Tb2 (F_o moiety), subunit β (F_1 moiety), and AOX. The numbers beneath each blot represent the abundance of immunodetected protein expressed as a percentage of the noninduced sample after normalizing to the signal intensity of the mitochondrial HSP70 probing (loading control). *C*, BNE of 4 μg of DDM-lysed mitochondria from PCF Tb1 RNAi–noninduced (–tet) and PCF Tb1 RNAi–induced (+tet, 2 and 4 days) cells followed by Western blot analysis using antibodies against subunit β and Tb2 to detect free F_1 and monomeric (M) and dimeric (D) ATP synthase complexes (first two panels). BNE of 60 μg of DDM-lysed mitochondria from PCF Tb1 RNAi–noninduced (–tet) and PCF Tb1 RNAi–induced (+tet, 2 and 4 days) cells followed by in-gel staining of ATPase activity (*rightmost* panel). *D*, total cellular ATP levels of PCF Tb1 RNAi–noninduced cells (–tet) and cells induced for 2 and 4 days (+tet, 2 days and 4 days) (means ± SD, n = 4, Student's unpaired *t*-test). *E*, relative ADP/ATP ratio of PCF Tb1 RNAi–noninduced cells (–tet) and cells induced for 2 and 4 days (+tet, 2 days and 4 days) (means ± SD, n = 4, Student's unpaired *t*-test). *F*, flow cytometry analysis of TMRE-stained PCF Tb1 RNAi–noninduced cells (–tet) and cells induced for 2, 4, and 6 days (+tet, 2 days, 4 days, and 6 days) to measure ΔΨm. The addition of FCCP served as a control for mitochondrial membrane depolarization (+FCCP) (means ± SD, n = 6, Student's unpaired *t*-test). *G*, the oxygen consumption rate of PCF Tb1 RNAi live cells in the presence of glycerol-3-phosphate. After the addition of the substrate, cells were consuming oxygen at the steady rate. Injection of SHAM inhibited AOX-mediated respiration. The difference between the original values and the values after addition of SHAM is graphed as AOX-mediated respiration. Additional injection of KCN inhibited complex IV–mediated respiration and ceased the oxygen consumption of the cells. The difference between the values after SHAM addition and after KCN addition is graphed as complex IV–mediated respiration (means ± SD, n = 6, Student's unpaired *t*-test). *H* and *I*, flow cytometry analysis of MitoSOX-treated (*H*) and H_2DCFHDA-treated (*I*) PCF Tb1 RNAi–noninduced cells (–tet) and cells induced for 2, 4, and 6 days (+tet, 2 days, 4 days, and 6 days) to measure mitochondrial $O_2^{\bullet-}$ and total cellular ROS levels, respectively (means ± SD, n = 6, Student's unpaired *t*-test). ΔΨm, mitochondrial membrane potential; AOX, alternative oxidase; BNE, blue native electrophoresis; DDM, dodecylmaltoside; FCCP, carbonyl cyanide 4-(trifluoromethoxy) phenylhydrazone; H_2DCFHDA, dichlorodihydrofluorescein; KCN, potassium cyanide; $O_2^{\bullet-}$, superoxide; PCF, procyclic form; ROS, reactive oxygen species; SHAM, salicylhydroxamic acid; Tb1, ATPaseTb1; Tb2, ATPaseTb2; TMRE, tetramethylrhodamine ethyl ester.

dichlorodihydrofluorescein (H_2DCFHDA), a fluorescent ROS-sensitive dye (Fig. 2*I*). This gradual increment of oxidative stress might have contributed to the growth phenotype observed in parasites with suppressed Tb1 expression.

Stringent Tb1 silencing leads to a virtually complete loss of F_oF_1–ATPase complex in BSF parasites and mitochondrial membrane depolarization, followed by cell death

In contrast to the canonical role of the F_oF_1–ATP synthase in PCF cells, BSF cells use the reverse activity of this complex, which generates ΔΨm at the expense of ATP (15, 16). We silenced Tb1 in BSF cells by using an RNAi construct targeting the 3' region of the Tb1 ORF. This caused a decrease of Tb1 to 11% at day 2 of RNAi induction, reaching undetectable levels of the protein at day 3 (Fig. 3*A*). As expected, the BSF Tb1 3' RNAi cell line exhibited a strong growth phenotype and ceased growing entirely by day 4 of induction (Fig. 3*B*). The steady-state levels of F_1–ATPase subunits β and p18 were decreased by ∼40% at day 2, whereas the steady-state levels of the F_o-associated subunits Tb2 and OSCP dropped to ∼10% (Fig. 3*C*). Moreover, the levels of AAC were decreased by 60% (Fig. 3*C*), suggesting that disruption of the F_oF_1–ATPase might affect the stability of this transporter. As in PCF cells, Tb1 downregulation caused a strong decrease of F_oF_1–ATPase monomers and dimers while there was a simultaneous increase in free F_1 subcomplex (Fig. 3*D*, Fig. S1*A*).

Similarly, a conditional double knock-out (cDKO) of OSCP resulted in undetectable levels of OSCP at day 2 (Fig. 3*E*), which was accompanied by a strong growth phenotype (Fig. 3*F*). In this cell line, termed BSF OSCP cDKO, both OSCP alleles were replaced by drug resistance cassettes, and an ectopic copy of the OSCP gene, whose expression depends on the presence of tetracycline in the culture medium, was introduced (Fig. S2). The removal of tetracycline led to ablation of OSCP expression, reduced levels of F_1 subunits to ∼80%, and F_o subunits to ∼10% (Fig. 3*G*), as well as virtually complete loss of the monomeric and dimeric forms of the complex (Fig. 3*H*, Fig. S1*B*), by day 2 of tetracycline removal.

To investigate the effect of the F_oF_1–ATPase loss on ΔΨm, we used flow cytometry analysis of intact, live cells stained with tetramethylrhodamine ethyl ester (TMRE). In both BSF Tb1 3' RNAi and OSCP cDKO cell lines, the ΔΨm was strongly compromised at day 2 of RNAi induction and tetracycline removal, respectively (Fig. 4, *A* and *B*), preceding the observed growth defect. To corroborate these results, we determined the ability of the mitochondrion to generate ΔΨm in digitonin-permeabilized cells using safranin O dye. Control BSF Tb1 3' RNAi and OSCP cDKO cells were able to build up and retain a ΔΨm, as addition of ATP caused a decrease in safranin O fluorescence, indicating stacking of the dye within the energized organelle. This decrease was completely reversed by adding either oligomycin (Fig. 4, *C* and *D*, black lines) or carboxyatractyloside (Fig. S3, *A* and *D*, black lines), inhibitors of the F_oF_1–ATP synthase and the AAC, respectively. Subsequent addition of the uncoupler SF 6847 had no further effect on depolarization. In contrast, cells silenced for Tb1 or ablated for OSCP were unable to generate ΔΨm *in situ* (Fig. 4, *C* and *D*, red lines). No changes in fluorescence were detected when the addition of oligomycin or carboxyatractyloside preceded that of ATP (Fig. S3, *B*, *C*, *E* and *F*), confirming that the decrease in safranin O fluorescence observed in control cells indeed depends on the ATP-hydrolyzing activity of the F_oF_1–ATPase and on the ADP/ATP exchanging activity of the AAC. In summary, these measurements indicate that, in the absence of either Tb1 or OSCP, BSF cells cannot generate ΔΨm, presumably because the proton-pumping F_oF_1–ATPase is completely disrupted in these cells.

Because the activity of the F_1–ATPase is tightly connected to the cellular ADP/ATP pool (33), we measured the cellular ADP/ATP ratio in control BSF Tb1 3' RNAi and OSCP cDKO cells and in cells with diminished Tb1 and OSCP expression. The ADP/ATP ratio was already significantly decreased at day 1 (Fig. 4, *E* and *F*), the opposite of the effect observed in PCF cells (compare Fig. 2*E*), likely because of the dysfunctional F_oF_1–ATPase. Higher levels of ATP than ADP may also affect the glycolytic flux, which is directly linked to respiration *via* the mitochondrial glycerol-3-phosphate dehydrogenase (34) and/or activity of AOX (35). Indeed, decreased levels of F_oF_1–ATPase caused lower glycerol-3-phosphate–stimulated oxygen consumption in digitonin-permeabilized BSF cells depleted of Tb1 or OSCP (Fig. 4, *G* and *H*). As expected, in both samples, the measured respiration was fully inhibited by addition of SHAM.

Suppression of F_o subunits expression to ∼10% is compatible with BSF cell viability in vitro

The virtually complete ablation of either Tb1 or OSCP (Fig. 3, *A* and *E*) is lethal for BSF trypanosomes, and this is in agreement with previous studies examining F_oF_1–ATPase subunits (9, 11, 16). Surprisingly, these parasites can withstand a 90 to 95% loss of the same proteins as revealed by analysis of two different cell lines: a BSF Tb1 5' RNAi cell line, in which the dsRNA targets the 5' region of the Tb1 ORF, and a BSF OSCP RNAi cell line. In these cell lines, Tb1 and OSCP expressions were stably downregulated to 7 to 9% and 3 to 4%, respectively, over the period of 7 days of RNAi induction (Fig. 5, *A* and *B*), with no obvious effect on their growth rate (Fig. 5, *C* and *D*). The different outcomes in the viability of the BSF Tb1 RNAi cell lines might be attributed to different efficiencies of the 3' and 5' targeted RNAi probes or to their distinctive genetic backgrounds (Tb1 3' RNAi: EATRO 1125 AnTat 1.1 *versus* Tb1 5' RNAi: BSF Lister 427). However, as the same difference in viability was observed for BSF OSCP cDKO and OSCP RNAi cells, which share the same genetic background, the distinct phenotypes were most likely due to the differences in stringency of suppression. Thus, we decided to further investigate the basis for the observed differences.

Western blot analyses revealed a correlative decrease in F_o subunits in both BSF Tb1 5' and OSCP RNAi cell lines, whereas F_1 subunits stayed largely unaffected. Similar to BSF Tb1 3' RNAi cells, the expression of AOX was slightly

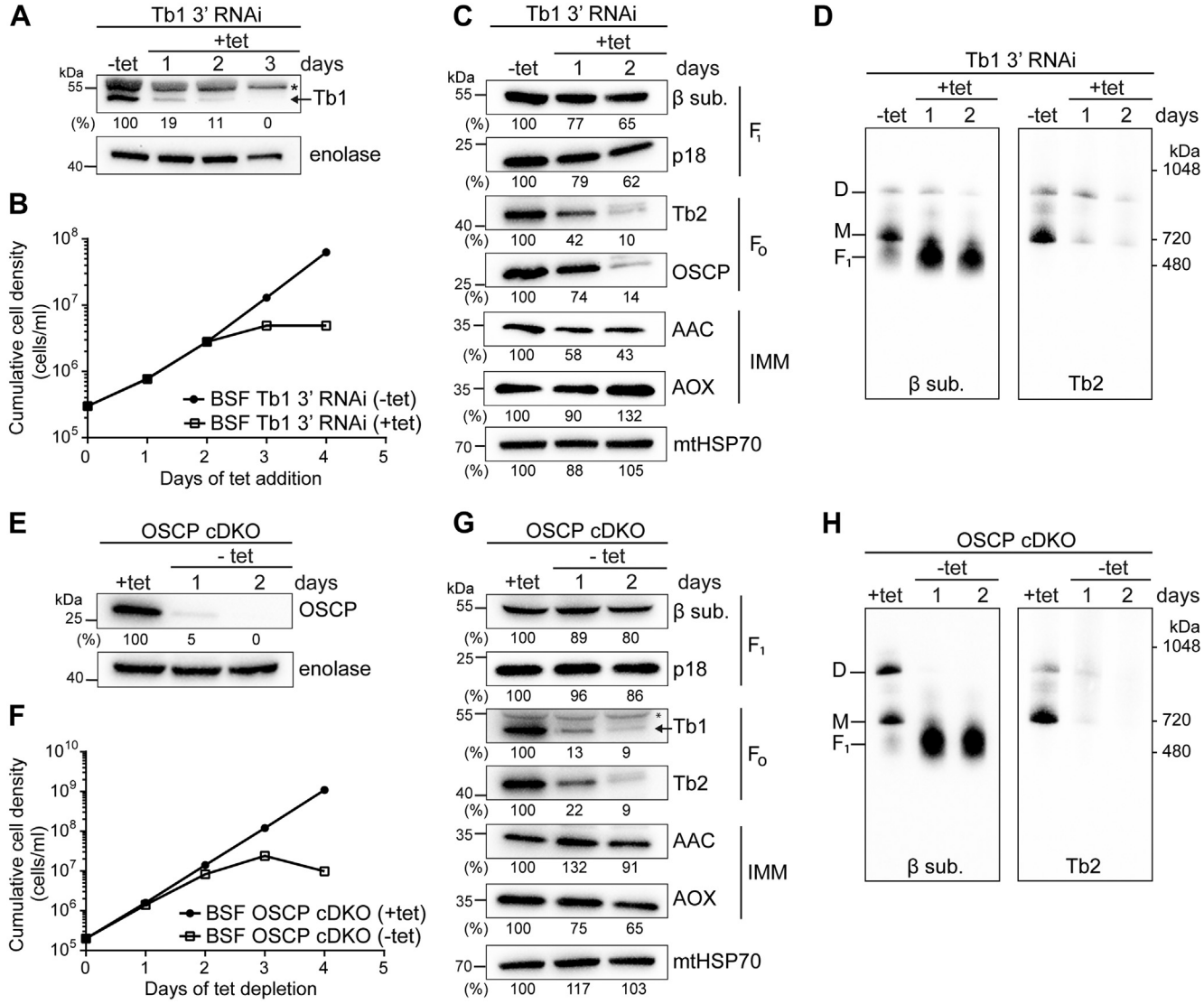

Figure 3. Virtually complete loss of F_oF_1–ATPase is lethal to BSF cells. *A*, Western blot of whole-cell lysates from BSF Tb1 3′ RNAi–noninduced (−tet) and BSF Tb1 3′ RNAi–induced (+tet, 1–3 days) cells using an antibody against Tb1. The numbers beneath the blot represent the abundance of immunodetected Tb1 expressed as a percentage of the noninduced samples after normalizing to the signal intensity of the enolase probing (loading control). An *asterisk* points to a nonspecific band detected by anti-Tb1 antibody. *B*, growth of BSF Tb1 3′ RNAi–noninduced (−tet) and BSF Tb1 3′ RNAi–induced (+tet) cells measured for 4 days. Cumulative cell density was calculated from the cell counts adjusted by the dilution factor needed to seed the cultures at 2×10^5 cells/ml each day. *C*, Western blot analysis of whole-cell lysates from BSF Tb1 3′ RNAi–noninduced (−tet) and cells induced for 1 and 2 days (+tet) using antibodies against the F_1 moiety (anti-β and anti-p18), the F_o moiety (anti-Tb2 and anti-OSCP), and inner mitochondrial membrane proteins (anti-AAC and anti-AOX). The immunoblot probed with anti-mitochondrial HSP70 antibody served as loading control. The densitometric analysis is depicted by the percentages beneath each blot and was carried out as in Figure 2*B*. *D*, BNE of 20 μg of DDM-lysed mitochondria from BSF Tb1 3′ RNAi–noninduced cells (−tet) and cells induced for 1 and 2 days (+tet) followed by Western blot analysis using antibodies to detect free F_1 (anti-subunit β) and monomeric (M) and dimeric (D) F_oF_1–ATPase complexes (anti-Tb2). *E*, Western blot of whole-cell lysates from BSF OSCP cDKO cells grown in the presence (+tet) or absence (−tet) of tetracycline for 1 and 2 days using an antibody against OSCP. The numbers beneath the blot represent the abundance of immunodetected OSCP expressed as a percentage of the +tet sample after normalizing to the signal intensity of the enolase probing (loading control). *F*, the growth curve of BSF OSCP cDKO cells cultured in the presence (+tet) or absence (−tet) of tetracycline for 4 days. Cumulative cell density was calculated as in Figure 3*B*. *G*, Western blot analysis of whole-cell lysates from BSF OSCP cDKO cells cultured in the presence (+tet) or absence (−tet) of tetracycline for 1 day and 2 days using antibodies against the F_1 moiety (anti-β and anti-p18), the F_o moiety (anti-Tb1 and anti-Tb2) and inner mitochondrial membrane proteins (anti-AAC and anti-AOX). The immunoblot probed with antimitochondrial HSP70 antibody served as the loading control. The densitometric analysis is depicted by the percentages beneath each blot and was carried out as in Figure 2*B*. The *asterisk* points to a nonspecific band detected by anti-Tb1 antibody. *H*, BNE of 20 μg of DDM-lysed mitochondria from BSF OSCP cDKO cells grown in the presence (+tet) or absence (−tet) of tetracycline for 1 day and 2 days followed by Western blot analysis using antibodies to detect free F_1 (anti-subunit β) and monomeric (M) and dimeric (D) F_oF_1–ATPase complexes (anti-Tb2). AAC, ADP/ATP carrier; AOX, alternative oxidase; BNE, blue native electrophoresis; BSF, bloodstream form; cDKO, conditional double knock-out; DDM, dodecylmaltoside; OSCP, oligomycin sensitivity-conferring protein; Tb1, ATPaseTb1; Tb2, ATPaseTb2.

upregulated, whereas the levels of AAC were halved (Fig. 5, *E* and *F*). Next, we analyzed the assembly of F_oF_1–ATPase complexes in BSF Tb1 5′ and OSCP RNAi cells by BNE. Silencing of Tb1 and OSCP induced monomer and dimer instability as F_1–ATPase subcomplexes accumulated in RNAi-induced cells, and less monomeric and dimeric forms were detected using antibodies against F_1 and F_o moieties (Fig. 5, *G* and *H*, Fig. S1, *C* and *D*), but compared with BSF Tb1 3′

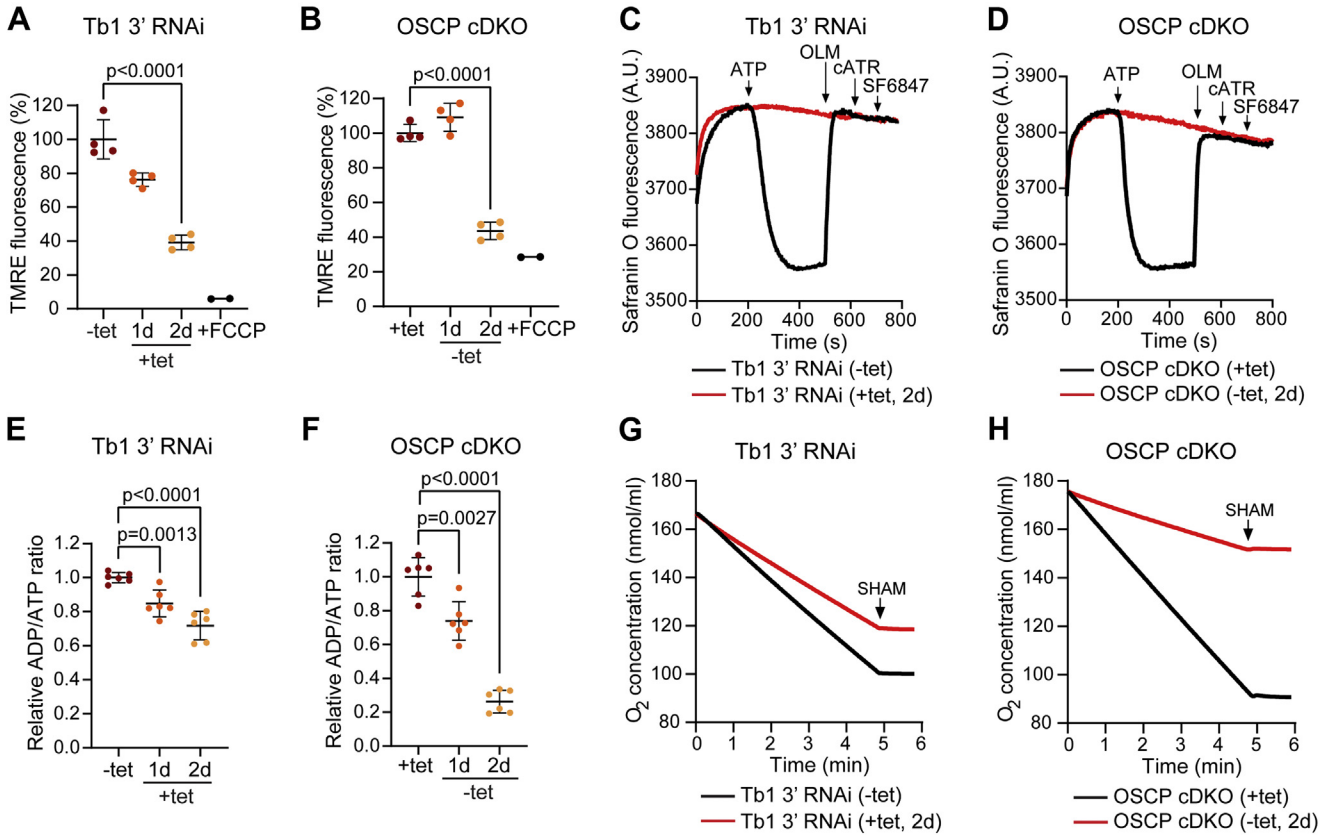

Figure 4. Virtually complete loss of F_oF_1–ATPase leads to a sudden collapse of ΔΨm, lower ADP/ATP ratio, and reduced respiration rate in BSF parasites. *A*, flow cytometry analysis of TMRE-stained BSF Tb1 3′ RNAi–noninduced cells (–tet) and cells induced for 1 day and 2 days (+tet, 1 day and 2 days) to detect changes in the ΔΨm. The addition of FCCP served as a control for mitochondrial membrane depolarization (+FCCP) (means ± SD, n = 4, Student's unpaired *t*-test). *B*, flow cytometry analysis of TMRE-stained BSF OSCP cDKO cells grown in the presence (+tet) or absence of tetracycline for 1 day and 2 days (–tet, 1 day and 2 days) to detect changes in the ΔΨm. The addition of FCCP served as a control for mitochondrial membrane depolarization (+FCCP) (means ± SD, n = 4, Student's unpaired *t*-test). *C*, mitochondrial membrane polarization detected using safranin O dye in digitonin-permeabilized BSF Tb1 3′ RNAi–noninduced cells (–tet, *black line*) and cells induced for 2 days (+tet, 2 days, *red line*) in the presence of ATP. ATP, oligomycin (OLM), carboxyatractyloside (cATR), and SF 6847, an uncoupler, were added where indicated. cATR was added after OLM to test for any further depolarization of the mitochondrial membrane due to inhibition of the AAC, whose electrogenic activity can potentially contribute in the generation of ATP-stimulated ΔΨm. *D*, mitochondrial membrane polarization detected using safranin O dye in digitonin-permeabilized BSF OSCP cDKO cells grown in the presence (+tet, *black line*) or absence of tetracycline for 2 days (–tet, 2 days, *red line*) after the addition of ATP. ATP, oligomycin (OLM), carboxyatractyloside (cATR), and SF 6847, an uncoupler, were added where indicated. cATR was added after OLM to test for any further depolarization of the mitochondrial membrane due to inhibition of the AAC, whose electrogenic activity can potentially contribute in the generation of ATP-stimulated ΔΨm. *E*, relative ADP/ATP ratio in BSF Tb1 3′ RNAi–noninduced cells (–tet) and cells induced for 1 day and 2 days (+tet, 1 day and 2 days) (means ± SD, n = 6, Student's unpaired *t*-test). *F*, relative ADP/ATP ratio in BSF OSCP cDKO cells cultured in the presence (+tet) or absence of tetracycline for 1 day and 2 days (–tet, 1 day and 2 days) (means ± SD, n = 6, Student's unpaired *t*-test). *G*, oxygen consumption rates of digitonin-permeabilized BSF Tb1 3′ RNAi–noninduced cells (–tet, *black line*) and cells induced for 2 days (+tet, 2 days, *red line*) in the presence of glycerol-3-phosphate. Respiration was arrested by the addition of SHAM where indicated. *H*, oxygen consumption rates of digitonin-permeabilized BSF OSCP cDKO cells grown in the presence (+tet, *black line*) or absence of tetracycline for 2 days (–tet, 2 days, *red line*) after addition of glycerol-3-phosphate. Respiration was arrested by addition of SHAM where indicated. ΔΨm, mitochondrial membrane potential; AAC, ADP/ATP carrier; BSF, bloodstream form; cDKO, conditional double knock-out; FCCP, carbonyl cyanide 4-(trifluoromethoxy) phenylhydrazone; OSCP, oligomycin sensitivity-conferring protein; SHAM, salicylhydroxamic acid; TMRE, tetramethylrhodamine ethyl ester.

RNAi–induced cells and OSCP cDKO cells (Fig. 3, *D* and *H*), the decrease was not as profound.

We hypothesized that the observed differences in the viability of the examined cell lines may lay in the varying amounts of remaining active F_oF_1–ATPase complexes. Therefore, we quantified and compared the changes in the steady-state levels of F_1 (β and p18) and F_o (Tb1, Tb2 and OSCP) subunits for the four BSF cell lines. At day 4 of RNAi induction, when the steady-state levels of the target proteins in BSF Tb1 5′ and OSCP RNAi cells were the lowest in their respective cell lines (Fig. 5, *A* and *B*), the steady-state levels of the tested F_o subunits remained significantly higher (25.1% ± 12.3%, means ± SD) than those in BSF Tb1 3′ RNAi and OSCP cDKO cells by day 2 of RNAi induction or tetracycline removal, respectively (9.2% ± 4.2%, means ± SD) (Fig. 5*I*). We propose that in the BSF Tb1 3′ RNAi and the OSCP cDKO cell lines, the levels of F_o subunits drop under a threshold that does not allow the parasite to assemble a sufficient amount of F_oF_1–ATPase complexes to maintain its viability. Assuming a direct relationship between the steady-state levels of individual F_o subunits and the total levels of F_oF_1 holocomplex, it would suggest that at least a 10% of assembled F_oF_1–ATPase complexes is necessary to maintain the viability of BSF *T. brucei* cells *in vitro*.

To test if the detected decrease in the levels of F_oF_1–ATPase monomers and dimers in BSF Tb1 5′ and OSCP RNAi cells affects ΔΨm, we measured TMRE fluorescence in live cells from both cell lines by flow cytometry. We did not detect

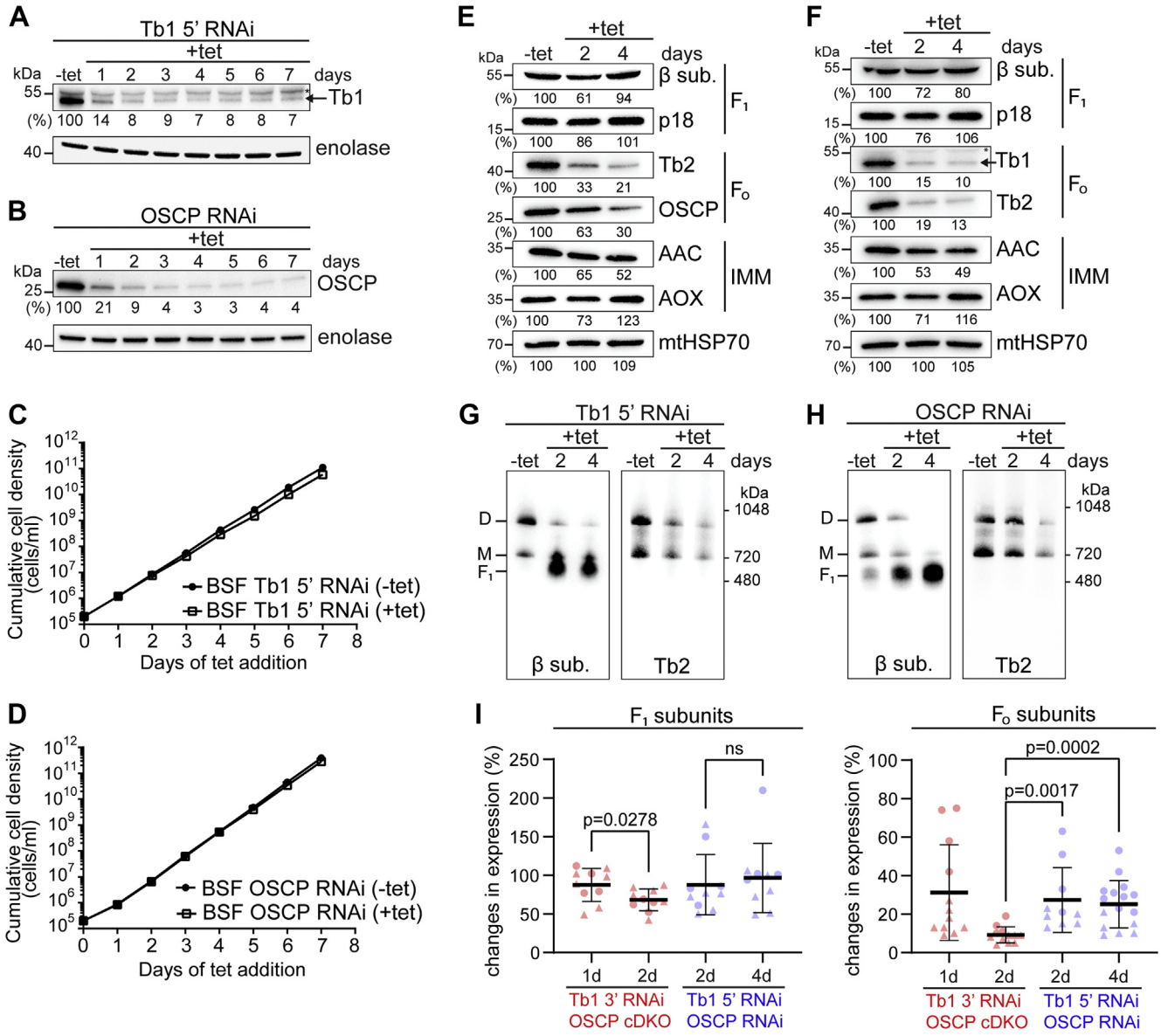

Figure 5. BSF cells are able to tolerate suppression of Tb1 and OSCP expression by 90 to 95%. *A* and *B*, Western blot analysis of whole-cell lysates from BSF Tb1 5′ RNAi (*A*) and BSF OSCP RNAi (*B*) noninduced cells (−tet) and cells induced for 1 to 7 days (+tet) using antibodies against Tb1 and OSCP, respectively. The numbers beneath the blot represent the abundance of immunodetected Tb1 (*A*) or OSCP (*B*) expressed as a percentage of the noninduced sample after normalizing to the signal intensity of the enolase probing (loading control). In Figure 5*A*, an *asterisk* points to a nonspecific band detected by anti-Tb1 antibody. *C* and *D*, growth of BSF Tb1 5′ RNAi (*C*) and BSF OSCP RNAi (*D*) noninduced (−tet) and induced (+tet) cells measured for 7 days. Cumulative cell density was calculated as in Figure 3*B*. *E* and *F*, Western blot analysis of whole-cell lysates from BSF Tb1 5′ RNAi (*E*) and BSF OSCP RNAi (*F*) noninduced cells (−tet) and cells induced for 2 and 4 days (+tet) using antibodies against the F_1 moiety (anti-β and anti-p18), the F_o moiety (anti-Tb1, anti-Tb2, and anti-OSCP), and inner mitochondrial membrane proteins (anti-AAC and anti-AOX). The immunoblots probed with anti-mitochondrial HSP70 antibody served as the loading control. The densitometric analysis is depicted by the percentages beneath each blot and was carried out as in Figure 2*B*. The *asterisk* points to a nonspecific band detected by anti-Tb1 antibody. *G* and *H*, BNE of 20 μg of DDM-lysed mitochondria from BSF Tb1 5′ RNAi (*G*) and BSF OSCP RNAi (*H*) noninduced cells (−tet) and cells induced for 2 and 4 days (+tet) followed by Western blot analysis using antibodies to detect free F_1 (anti-subunit β) and monomeric (M) and dimeric (D) F_oF_1–ATPase complexes (anti-Tb2). *I*, comparison of changes in F_1 and F_o subunit levels between BSF Tb1 3′ RNAi (*red circles*)/BSF OSCP cDKO cells (*red triangles*) and BSF Tb1 5′ RNAi (*blue circles*)/BSF OSCP RNAi (*blue triangles*) cells along the days of RNAi induction/tetracycline removal. The antibody signals of F_1 (β and p18) and F_o (Tb1, Tb2, and OSCP) subunits at days 1 and 2 of RNAi induction/tetracycline removal (BSF Tb1 3′ RNAi and OSCP cDKO cells, respectively) and at days 2 and 4 of RNAi induction (BSF Tb1 5′ and OSCP RNAi cells) were quantified and normalized as in Figure 2*B*. In both Tb1 RNAi cell lines, the plotted values of F_o subunits correspond to the quantified signals of anti-Tb2 and anti-OSCP antibodies. In the OSCP cDKO and OSCP RNAi cell lines, the plotted values of F_o subunits correspond to the quantified signals of anti-Tb1 and anti-Tb2 antibodies. The values were analyzed statistically using GraphPad Prism 8.0 software (means ± SD, n ≥ 4, Student's unpaired *t*-test). ΔΨm, mitochondrial membrane potential; AAC, ADP/ATP carrier; AOX, alternative oxidase; BSF, bloodstream form; cDKO, conditional double knock-out; *ns*, not significant; OSCP, oligomycin sensitivity-conferring protein; Tb1, ATPaseTb1.

any differences in ΔΨm between the measured time points (Fig. 6*A*). Furthermore, we assessed the ability of the F_oF_1–ATPase to polarize the mitochondrial membrane in digitonin-permeabilized BSF Tb1 5′ and OSCP RNAi cells using safranin O dye in the presence of ATP. Albeit reduced, compared with control cells (Fig. 6, *B* and *C*, Fig. S4, *A* and *D*,

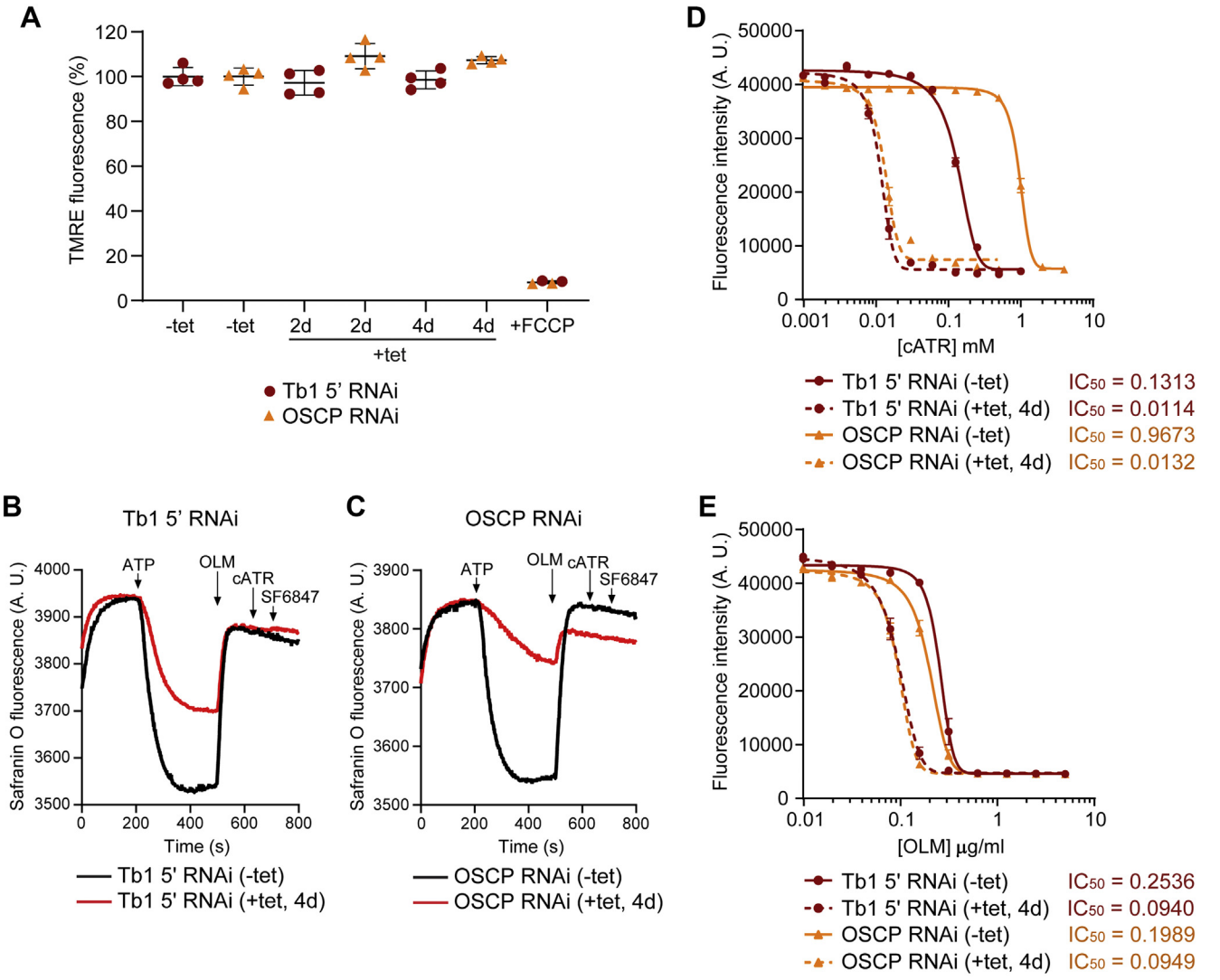

Figure 6. BSF cells with 90 to 95% reduced expression of Tb1 and OSCP have unchanged ΔΨm but are more sensitive to AAC and F_oF_1–ATPase inhibitors. *A*, flow cytometry analysis of TMRE-stained BSF Tb1 5′ RNAi (*brick-red circles*) and BSF OSCP RNAi (*orange triangles*) noninduced cells (–tet) and cells induced for 2 and 4 days (+tet, 2 days and 4 days) to detect changes in ΔΨm. The addition of FCCP served as a control for mitochondrial membrane depolarization (means ± SD, n = 4, Student's unpaired *t*-test). *B* and *C*, mitochondrial membrane polarization detected using safranin O dye in digitonin-permeabilized BSF Tb1 5′ RNAi (*B*) and BSF OSCP RNAi (*C*) noninduced cells (–tet, *black lines*) and cells induced for 4 days (+tet, 4 days, *red lines*) in the presence of ATP. ATP, oligomycin (OLM), carboxyatractyloside (cATR), and SF 6847, an uncoupler, were added where indicated. cATR was added after OLM to test for any further depolarization of the mitochondrial membrane due to inhibition of the AAC, whose electrogenic activity can potentially contribute in the generation of ATP-stimulated ΔΨm. *D* and *E*, sensitivity of BSF Tb1 5′ RNAi– and BSF OSCP RNAi–noninduced cells (–tet, *brick-red* and *orange full lines*, respectively) and cells induced for 4 days (+tet, 4 days, *brick-red* and *orange dashed lines*, respectively) to carboxyatractyloside (cATR) (*D*) and to oligomycin (OLM) (*E*) estimated by resazurin cell-viability assay. The dose–response curves were calculated using GraphPad Prism 8.0 software. The calculated IC_{50} values are shown beside the corresponding sample and are expressed in mM and in µg/ml for cATR and OLM, respectively. ΔΨm, mitochondrial membrane potential; AAC, ADP/ATP carrier; BSF, bloodstream form; FCCP, carbonyl cyanide 4-(trifluoromethoxy) phenylhydrazone; OSCP, oligomycin sensitivity-conferring protein; TMRE, tetramethylrhodamine ethyl ester.

black lines), RNAi-induced cells from both cell lines were still able to generate a ΔΨm (Fig. 6, *B* and *C*, Fig. S4, *A* and *D*, red lines). In all four cases, the inner mitochondrial membrane was fully depolarized by the addition of oligomycin (Fig. 6, *B* and *C*) or carboxyatractyloside (Fig. S4, *A* and *D*). The results were further validated by measuring safranin O fluorescence when either oligomycin or carboxyatractyloside was present before ATP addition (Fig. S4, *B*, *C*, *E* and *F*). These observations show that the F_oF_1–ATPase activity is affected in BSF Tb1 5′ and OSCP RNAi–induced cells but is not fully abolished as observed for BSF Tb1 3′ RNAi and OSCP cDKO cells (Fig. 4, *C* and *D*, Fig. S3, *A* and *D*, red lines).

The difference between the ΔΨm measured *in vivo* (by flow cytometry) and *in situ* (by safranin O) may reflect the different aspects of ΔΨm generation interrogated by these assays: the former measures the actual magnitude of ΔΨm in living cells, and the latter, the capacity of cells to generate ΔΨm. The differences observed imply that BSF cells do not use F_oF_1–ATPase complexes at full capacity to generate ΔΨm, and therefore, a significant decrease in these assemblies has no effect on their total ΔΨm and the viability of cells grown in culture. The need for the ∼10% of remaining F_oF_1–ATPase complexes (Fig. 5*I*) in the mitochondria is corroborated by increased sensitivity of BSF Tb1 5′ and OSCP

RNAi–induced cells to carboxyatractyloside (~12 and ~73 times, respectively) and to oligomycin (~2.5 and ~2.1 times, respectively) as measured by resazurin cell viability assay (Fig. 6, *D* and *E*).

In summary, our data provide insight into the distinct bioenergetic consequences of the loss of F_oF_1–ATP synthase/ATPase in PCF and BSF parasites. We showed that a decrease in the F_oF_1–ATP synthase levels in PCF cells led to lowered ATP levels and transiently increased ΔΨm, which manifested in the form of oxidative stress and slower cell growth. In BSF trypanosomes, as reported before, a full disruption of the F_oF_1–ATPase caused the loss of ΔΨm followed by cell death, but we observed that these parasites can withstand a substantial loss of the complex without an obvious effect on viability in culture.

Discussion

Tb1 is the largest membrane-associated subunit of the F_oF_1–ATP synthase in *T. brucei*. Inferring from the F_oF_1–ATP synthase structure of the related organism *E. gracilis*, Tb1 is located on the matrix side of the F_o periphery (6) and contains an Mdm38-like fold. Mdm38 is a component of the yeast mitochondrial cotranslational membrane insertion machinery, and it has been reported to assist in the assembly of the mitochondrial-encoded proton channel subunit a into the F_oF_1–ATP synthase (27). Despite the structural similarity between Mdm38 and Tb1, the former was never copurified with either electron transport chain complexes or F_oF_1–ATP synthase (27, 36, 37), whereas the latter is a *bona fide* component of the euglenozoan F_oF_1–ATP synthase (6, 8, 38). In addition, the *E. gracilis* Tb1 ortholog contacts nearly exclusively a species-specific extension of subunit a (6), suggesting that it is not involved in the incorporation of subunit a into the complex in the same way as in yeast. Based on the predicted structural conservancy of Tb1 and compositional similarity of the F_oF_1–ATP synthase in *T. brucei* and *Euglena*, it is reasonable to assume that Tb1 in *T. brucei* is located on the periphery of the dimer. Presumably, it establishes very few, or none at all, contacts with subunits involved directly in the proton translocation or dimerization of the complex. Yet, Tb1 is absolutely crucial for the F_oF_1–ATP synthase integrity (8), potentially by aiding in the stability or assembly of auxiliary F_o subunits.

Here, we silenced Tb1 subunit by RNAi with high efficiency in two cultivable forms of *T. brucei* to study phenotypes associated with F_oF_1–ATP synthase loss. In PCF cells, the severe loss of the monomeric and dimeric forms of the F_oF_1–ATP synthase after depletion of Tb1 causes a transient hyperpolarization of the inner mitochondrial membrane. This effect is then reversed by redirecting electrons from the conventional respiratory chain complexes III and IV toward AOX, as documented by the increased SHAM-sensitive respiration. The increased respiration through the AOX pathway is accompanied by a gradual but mild reduction in the ΔΨm (~25% by day 6 of RNAi induction), consistent with the fact that AOX is incapable of pumping protons across the inner mitochondrial membrane, and therefore, does not contribute to the generation of ΔΨm (28). Moreover, the increase in AOX-mediated respiration led to lowered levels of mitochondrial $O_2^{\bullet-}$, presumably produced to a large extent by complex III. The rerouting of electrons toward AOX is a phenomenon that was already reported in PCF *T. brucei* cells when complexes III and IV were downregulated (39, 40) and may reflect a protective mechanism also used by plants to cope with the increase in ROS generation associated with inhibition of the cytochrome pathway (39). Similarly, artificial expression of AOX in fruit fly and mouse cells was shown to limit mitochondrial ROS formation when respiration was inhibited by antimycin (inhibitor of complex III) or cyanide (inhibitor of complex IV) (31, 32).

Furthermore, we observed that the total cellular ATP levels decreased only by ~25% at day 4 of RNAi induction, reflecting the ability of PCF cells to rely also on ATP production through both cytosolic and mitochondrial substrate-level phosphorylation *via* the pyruvate kinase and the succinyl-CoA synthetase, respectively, when grown in glucose-rich conditions (41, 42). Although the ATP levels were reduced just ~25%, there was a 50% increase in the ADP/ATP ratio. This could be explained by the avid ATP consumption by the accumulated F_1 subcomplexes, as reflected by the in-gel staining of ATPase activity. An increased ADP/ATP ratio could also reflect a higher intracellular ATP demand, namely by processes intended to restore homeostasis. Although the increased respiration through AOX contributed to the reduction of intramitochondrial $O_2^{\bullet-}$ levels, prolonged inhibition of the oxidative phosphorylation pathway due to Tb1 downregulation led to an increase of various cytosolic ROS, causing oxidative stress. Because the synthesis of certain ROS-detoxifying molecules requires ATP (43), we hypothesize that the inability of PCF Tb1 RNAi–induced cells to cope with the increasing concentrations of cytosolic ROS might be due to the lowered levels of intracellular ATP caused by inhibition of oxidative phosphorylation.

In BSF *T. brucei*, the F_oF_1–ATP synthase complex operates in reverse mode to generate the vital ΔΨm (15, 16). Therefore, the cell death that followed the collapse of the ΔΨm in parasites fully depleted of Tb1 or OSCP was expected and is consistent with the earlier studies. Nevertheless, while Tb1 and OSCP suppression down to 3 to 10% caused a corresponding loss of F_oF_1–ATPase complexes, these BSF trypanosomes were able to thrive in culture without any obvious effect on their viability. Similarly, perturbation of mitochondrial translation in BSF cells, manifested by decreased levels of F_oF_1–ATPase due to reduced production of its mitochondrial encoded subunit a, had no effect on growth in culture (44). Moreover, the ΔΨm of BSF Tb1 5′ and OSCP RNAi–induced cells was not affected when measured by flow cytometry of live cells, but there was a significant reduction in the ability of the F_oF_1–ATPase to generate a proton gradient when estimated in permeabilized cells by safranin O assay. This phenomenon can be explained by a combination of two factors: the higher sensitivity of safranin O to changes in ΔΨm compared with TMRE (45) and a possible overcapacity of the F_oF_1–ATPase

complex in BSF trypanosomes. The overcapacity of certain enzymes has already been documented in *T. brucei*. For instance, the reduction of the maximum rate (V_{max}) of AOX reaction by 50% was predicted to have no effect on oxygen consumption (46). Taken together, our observations would suggest that although the F_oF_1–ATPase is a promising drug target, the potential drug would have to inhibit the majority of the assembled complexes to exert cytotoxic effects, although the proportion of F_oF_1–ATPase complexes that is required to sustain the viability of the parasite in the host environment might be different compared with the situation *in vitro*.

Dyskinetoplastic trypanosomes are BSF cells that partially or entirely lack their mitochondrial DNA, termed kinetoplast DNA, and consequently, the mitochondrial-encoded subunit a (47–49). Because the vestigial F-ATPase in dyskinetoplastic cells is incapable of proton pumping, it is proposed that ΔΨm is maintained by the synergistic activities of the F_1-ATPase and the electrogenic exchange of ADP for ATP mediated by the AAC (22). Unlike yeast "*petite* mutants" or mammalian ρ^0 cells, dyskinetoplastic trypanosomes are successful in nature, where they are transmitted mechanically by bloodsucking insects among a vast range of mammals or by coitus in equids (50). It is striking that in African trypanosomes of the trypanozoon group, the kinetoplast DNA loss has occurred repeatedly and does not appear to impair cell viability of the replicative stage in the mammalian bloodstream (48). The loss of kinetoplast DNA in BSF trypanosomes is most likely facilitated by the facts that (i) these cells rely only on a single mitochondrial-encoded protein, the subunit a of the F_oF_1–ATP synthase, (ii) they do not use the F_oF_1–ATP synthase for energy production, as glycolysis fulfills their ATP demands, thanks to the abundant glucose in the mammalian host's bloodstream, and (iii) these cells acquire a compensatory mutation that affects F_1–ATPase function (22). We speculate that the long-term tolerance of reduced levels of F_oF_1–ATPase, exemplified by our BSF Tb1 5' and OSCP RNAi cell lines, can provide BSF cells with a time frame to gain nuclear mutation(s) that allow ΔΨm generation in the absence of an intact F_oF_1–ATPase and consequently facilitate life without kinetoplast DNA (22). This has major implications, as a number of trypanocidal compounds, including those that constitute the currently available treatments for animal African trypanosomiasis, target the kinetoplast DNA network (51–53) and, indeed, the loss of dependence on kinetoplast DNA due to the compensatory mutations has been related to multidrug resistance in trypanosomes (54–56). Our results further highlight how the parasite's unique biology helps this species to cope with the loss of mitochondrial DNA, an event that is deleterious, or even lethal, for the majority of eukaryotes (57).

A striking phenotype exhibited by BSF Tb1 3' RNAi and OSCP cDKO trypanosomes is the reduced respiration rate upon Tb1 and OSCP depletion, respectively, as there is no direct link between the activities of AOX and the F_oF_1–ATPase. Rather, the oxygen consumption rate by AOX is a measure of glycolysis, which provides BSF trypanosomes with the majority, if not all, of the cellular ATP (34, 58). We hypothesize that disruption of the F_oF_1–ATPase complex leads to a lower consumption rate of intracellular ATP. In support of this argument, we observed a gradual reduction in the cellular ADP/ATP ratio after suppression of Tb1 or OSCP expression. A recent study showed that *T. brucei* AOX can be inhibited by a transient accumulation of intramitochondrial ATP caused by inhibition of the F_oF_1–ATPase hydrolytic activity with oligomycin (35), representing the first report proposing that the F_oF_1–ATPase activity can affect the glycolytic flux in BSF trypanosomes. Similarly, oligomycin treatment inhibits the rates of oxygen consumption and pyruvate production with a concomitant dissipation of ΔΨm when glucose is the substrate (15, 59). This effect that was originally contributed to the inhibition of glycolysis before triose phosphate oxidation (60) can now be linked to the inhibition of the F_oF_1–ATPase. According to the metabolic control theory (61), the flux control of a pathway can be exerted not solely by enzymes from the particular pathway but also by processes outside of it, such as the ATP-consuming processes. In *T. brucei*, the glycolytic flux is controlled mainly by enzymes outside of the pathway, specifically, by hexose transporters responsible for glucose uptake into the cell (62). The absence of regulation by components from the pathway is not restricted to this organism, as it was reported that overexpression of glycolytic enzymes does not exert significant control on the pathway in both yeast (63) and bacteria (64). Interestingly, a study in *Escherichia coli* demonstrated that incrementing the cytosolic ATP consumption by expression of free F_1-ATPase resulted in a 70% increase in the glycolytic rate, concluding that enzymes consuming ATP can affect the glycolytic flux (65). Taken all together, our results further corroborate the idea that the levels of F_oF_1–ATPase activity can affect the respiration rate, playing an unexplored role in controlling the glycolytic rate in the BSF stage of the parasite.

Experimental procedures

Plasmid construction and generation of cell lines

The generation of the PCF Tb1 RNAi cell line was described in an earlier study (8). To generate the BSF Tb1 5' and Tb1 3' RNAi cell lines, Tb1 (Tb927.10.520) ORF fragments of 460 bp (between nucleotides 30 and 489) and 636 bp (between nucleotides 424 and 1060), respectively, were amplified from the genome of the wild type (WT) BSF *T. brucei* strain Lister 427 using primers *1* and *2* for the 5' RNAi fragment, and primers *3* and *4* for the 3' RNAi fragment. The resulting 5' and 3' RNAi amplicons were cloned into p2T7-177 vector (66) *via* *Bam*HI and *Xho*I restrictions sites and transfected into the puromycin-resistant *T. brucei* SmOxB427 cell line (67) and the neomycin- and hygromycin-resistant *T. b. brucei* EATRO 1125 AnTat 1.1 90:13 cell line (68), respectively. For the inducible expression of Tb1 fused with a C-terminal 3x v5 tag, the Tb1 coding sequence was PCR-amplified from *T. brucei* strain Lister 427 genome using primers *5* and *6*. Using the *Hin*dIII and *Bam*HI restriction sites inherent in the primers, the fragment was cloned into the pT7_v5 vector (69). The construct was linearized with *Not*I and transfected into the neomycin-resistant transgenic BSF427 single-marker cell line as described previously (11).

To generate the BSF OSCP RNAi cell line, an OSCP (Tb927.10.8030) ORF fragment of 446 bp (between nucleotides 13 and 458) was amplified from the genome of the WT BSF *T. brucei* strain Lister 427 using primers *7* and *8*. The resulting amplicon was cloned into p2T7-177 vector (66) *via Bam*HI and *Xho*I restrictions sites, and the construct was linearized with *Not*I before transfection into the neomycin-resistant transgenic BSF427 single-marker cell line as described previously (11). For the generation of the BSF OSCP cDKO cell line, 5' and 3' intergenic region fragments from OSCP gene were amplified using primers *9* and *10* for the 5' intergenic region, and primers *11* and *12* for the 3' intergenic region. The resulting 5' intergenic region amplicon of 452 bp was cloned into *Not*I and *Mlu*I restriction sites within pLEW13 vector to generate pLEW13::5' IR_{452bp} vector. Subsequently, the 3' intergenic region amplicon of 414 bp was inserted into pLEW13::5' IR_{452bp} vector *via Xba*I and *Stu*I restriction sites to obtain the OSCP single KO construct. This construct was linearized using *Not*I and transfected into the WT BSF *T. brucei* strain Lister 427 to knock out the first OSCP allele. To generate the construct for the KO of the second OSCP allele, the T7 RNA polymerase and neomycin cassette from the OSCP single KO construct was replaced by a cassette containing a 10% activity T7 promoter, the tetracycline repressor, and the hygromycin resistance gene from pLEW90 vector. For the generation of the tetracycline-inducible OSCP ectopic copy construct, the OSCP ORF was amplified from the genome of the WT BSF *T. brucei* strain Lister 427 using primers *13* and *14*. The OSCP ORF was cloned into *Bam*HI and *Xho*I restriction sites within pLEW79 vector, replacing the luciferase ORF. It is important to mention that the pLEW79 vector was mutagenized for the purpose of this study to include an *Xho*I restriction site downstream its *Hin*dIII site due to the existence of a *Hin*dIII site within the sequence of the OSCP ORF. BSF *T. brucei* OSCP single KO cells were transfected with the OSCP ectopic copy construct before knocking out the second OSCP allele. The strategy used for the conditional KO of OSCP in BSF cells was adapted from the reference (70). The correct integration of the OSCP single KO construct was verified by PCR using the following primer pairs: primers *15* (annealing upstream the 5' intergenic region of the OSCP gene used as homologous recombination site) and *17* (binding the T7 RNA polymerase sequence); primers *18* (binding the neomycin resistance gene sequence) and *16* (annealing downstream the 3' intergenic region of the OSCP gene used as homologous recombination site). The correct integration of the OSCP double KO construct was verified by PCR using the following primer pairs: primers *15* and *19* (which binds the tetracycline repressor sequence); primers *20* (binding the hygromycin resistance gene sequence) and *16*. The presence of the OSCP inducible copy was verified by PCR using primers *21* (which anneals to the procyclic acidic repetitive protein promoter) and *22* (annealing downstream the aldolase 3' UTR that follows the OSCP ORF). A schematic representation of the PCR verification is depicted on Fig. S2. The sequences of all the primers used in this study are found in Table S1.

T. brucei *culture conditions*

The PCF Tb1 RNAi cell line was grown at 27 °C in the glucose-rich medium SDM-79 (27) (Invitrogen 07490916N) supplemented with 10% fetal bovine serum (BioSera FB-1090/500) and 7.5 mg/ml hemin (Sigma H9039) and containing 15 μg/ml G418 (Sigma G8168), 25 μg/ml hygromycin B Gold (InvivoGen ant-hg-1), and 2.5 μg/ml phleomycin (InvivoGen ant-ph-2p).

The BSF *T. b. brucei* Lister 427 strain, EATRO 1125 AnTat 1.1 (68), stable acriflavine-induced dyskinetoplastic *T. b. brucei* EATRO 164 (71), and dyskinetoplastic *T. b. evansi* AnTat 3/3 that lost mitochondrial DNA upon culturing (16) were all grown at 37 °C and 5% CO_2 in HMI-11 medium (Invitrogen 07490915N) supplemented with 10% fetal bovine serum. The BSF 5' Tb1 RNAi cell line was grown in the presence of puromycin and phleomycin. The BSF 3' Tb1 RNAi cell line was grown in the presence G418, hygromycin, puromycin, and phleomycin. The BSF OSCP RNAi cell line was grown in the presence of G418 and phleomycin. The BSF OSCP cDKO cell line was grown in G418, hygromycin, and phleomycin. The final concentrations of antibiotics in the culture medium were the following: 0.1 μg/ml puromycin, 2.5 μg/ml G418, 5 μg/ml hygromycin, and 2.5 μg/ml phleomycin.

The induction of RNAi and ectopically expressed tagged Tb1 was triggered by the addition of 1 μg/ml of tetracycline into the medium. BSF OSCP cDKO cells were constantly grown in the presence of 1 μg/ml of tetracycline to sustain OSCP expression. The expression of the OSCP ectopic copy was suppressed by cultivating BSF OSCP cDKO cells in the absence of tetracycline, preceded by a two-step washing of the cells with tetracycline-free medium. For all the experiments in this study, cells were maintained in a mid-late exponential growth phase, meaning 0.6×10^7 to 1.2×10^7 cells/ml in the case of PCF cells, and 0.6×10^6 to 1.2×10^6 cells/ml in the case of BSF cells.

SDS-PAGE and Western blotting

Appropriate volumes of PCF and BSF culture were spun down at 1400*g* for 10 min at 4 °C, and cell pellets were washed once with 1× PBS (10-mM phosphate buffer, 130-mM NaCl, pH 7.3). To prepare whole-cell lysates at a concentration of 1×10^7 cells in 30 μl, cell pellets were resuspended in 1× PBS before the addition of 3× Laemmli buffer (150-mM Tris-HCl, pH 6.8, 300-mM 1,4-dithiothreitol, 6% (w/v) SDS, 30% (w/v) glycerol, 0.02% (w/v) bromophenol blue). The mixture was boiled at 97 °C for 10 min and stored at −20 °C. For Western blot analysis, a volume of sample corresponding to 3×10^6 cells per well was separated by SDS-PAGE (Bio-Rad 4568094), blotted onto a polyvinylidene difluoride membrane (Pierce 88518), and probed with the appropriate monoclonal (mAb) or polyclonal (pAb) antibody. This was followed by incubation with a secondary HRP-conjugated anti-rabbit (Bio-Rad 1721019) or anti-mouse (Bio-Rad 1721011) antibody (1:2000), which immunoreacts, respectively, with the polyclonal or monoclonal primary antibodies. Proteins were visualized using the Clarity Western ECL substrate (Bio-Rad 1705060EM) on a ChemiDoc instrument (Bio-Rad). The PageRuler prestained protein ladder (Thermo Fisher Scientific 26617) was used to determine the size of the detected bands.

The primary antibodies used in this study were the following: mAb anti-v5 epitope tag (1:2000, Invitrogen), mAb anti-mitochondrial HSP70 (1:5000; 72 kDa) (72), mAb anti-AOX (PCF 1:300, BSF 1:1000, kindly provided by Minu Chaudhuri; 33 kDa), pAb anti-mitochondrial RNA-binding protein 1 (1:1000; 23 kDa), pAb anti-enolase (1:1000; 47 kDa) (73), pAb anti-AAC (1:1000; 34 kDa), and antibodies against F_oF_1–ATP synthase subunits β (1:2000; 54 kDa), p18 (1:1000; 18 kDa), Tb1 (1:1000; 47 kDa), Tb2 (1:1000; 43 kDa), and OSCP (1:1000; 27 kDa). The latter antibodies were produced in the Zíková lab and are available upon request. The densitometric analysis of the bands was carried out using the ImageLab software by relating the signal intensity from the lanes corresponding to RNAi-induced/tetracycline-depleted cells to that of the lane pertinent to control cells. The percentage of downregulation relative to the control sample was then normalized to the corresponding signal intensity of the bands from the blots probed with anti-enolase or anti-mitochondrial HSP70 (loading controls).

Isolation of crude mitochondrial vesicles

Crude mitochondrial vesicles were obtained by hypotonic lysis as described earlier (11, 72). In summary, cell pellets from 3×10^8 BSF cells were washed once with a buffer I (150-mM NaCl, 20-mM glucose, 20-mM phosphate buffer, pH 7.9), resuspended in a buffer II (1-mM Tris-HCl, pH 8.0, 1-mM EDTA), and homogenized in a Dounce homogenizer. Alternatively, cell pellets from 1×10^9 PCF cells were washed in a buffer III (150-mM NaCl, 100-mM EDTA, 10-mM Tris-HCl, pH 8.0), resuspended in the buffer II, and homogenized by passing through a 25G needle. To restore the physiological isotonic conditions, 60% sucrose was promptly added to the cell lysate to attain a final concentration of 250 mM. Samples were spun down at 16,000*g* for 10 min at 4 °C to clear the soluble cytoplasmic material from the lysates. The organelle-enriched pellets were resuspended in STM (250-mM sucrose, 2-mM $MgCl_2$, 20-mM Tris-HCl, pH 8.0) and supplemented with a final concentration of 3-mM $MgCl_2$ and 0.3-mM $CaCl_2$ before incubating with 5 μg/ml DNase I for 1 h on ice. Then, an equal volume of STE (250-mM sucrose, 2-mM EDTA, 20-mM Tris-HCl, pH 8.0) was added, and the material was centrifuged as before. Pellets enriched with the mitochondrial membrane vesicles were flash-frozen in liquid nitrogen and stored at −80 °C until their use.

Native electrophoresis and in-gel staining of F_oF_1–ATPase activity

The protocol for high-resolution clear native electrophoresis was adapted from published studies (74, 75). Briefly, crude mitochondrial vesicles from 5×10^8 cells were resuspended in a mitochondrial lysis buffer (2-mM ε-aminocaproic acid (ACA), 50-mM imidazole-HCl, 1-mM EDTA, 50-mM NaCl, pH 7.0) and lysed for 1 h on ice with 4 mg digitonin/1 mg protein. Samples were centrifuged at 16,000*g* for 30 min at 4 °C, and the protein concentrations of the cleared lysates were determined by bicinchoninic acid assay. Samples were mixed with 5× loading dye (0.1% (w/v) Ponceau-S, 50% (w/v) glycerol) and loaded onto a 3 to 12% native gradient gel. After electrophoresis (3 h, 100 V, 4 °C), the resolved mitochondrial proteins were transferred onto a nitrocellulose membrane (overnight, 20 V, 4 °C) and probed with selected antibodies (p18 1:1000 and Tb1 1:1000).

BNE was performed as described in an earlier study (9) with some modifications. Crude mitochondrial vesicles from 2×10^8 cells were resuspended in 1 M ACA and solubilized with either 2% (PCF) or 4% (BSF) dodecylmaltoside (DDM) for 1 h on ice. Samples were centrifuged at 16,000*g* for 30 min at 4 °C, and the protein concentrations of the cleared lysates were estimated using the bicinchoninic acid assay (Pierce 23225). Samples were mixed with 1.5 μl of the loading dye (500-mM ACA, 5% (w/v) Coomassie Brilliant Blue G-250) and loaded onto a 3 to 12% native gradient gel. After the electrophoresis (3 h, 140 V, 4 °C), proteins were blotted onto a polyvinylidene difluoride membrane (2 h, 100 V, 4 °C, stirring) and immunodetected using antibodies against different F_oF_1–ATP synthase subunits (subunit β 1:2000, p18 1:1000, Tb2 1:500, and OSCP 1:100). Alternatively, the gel was transferred into the ATPase reaction buffer (35-mM Tris-HCl, pH 8.0, 270-mM glycine, 19-mM $MgSO_4$, 0.3% (w/v) $Pb(NO_3)_2$, 11-mM ATP) for overnight incubation under slow agitation (in-gel staining of F_oF_1–ATPase activity). Subsequently, the gel was soaked in 30% methanol to stop the reaction. The ATPase activity appears as a white precipitate.

Sodium carbonate submitochondrial fractionation

Sodium carbonate extraction of mitochondrial membranes was adapted from an earlier study (76). Mitochondrial vesicles from 3×10^8 cells were isolated by hypotonic lysis as described previously. The resulting supernatant from a 25G needle homogenization step was kept as a cytosolic fraction. The mitochondrial pellet was further treated with digitonin (80 μg/ml) for 15 min on ice to disrupt the mitochondrial outer membrane. The material was then cleared by centrifugation at 12,000*g* for 20 min at 4 °C and the pelleted mitoplasts were resuspended in 0.1 M Na_2CO_3 buffer (pH 11.5) before incubation on ice for 30 min. A final ultracentrifugation step at 100,000*g* for 1 h at 4 °C carried out in an SW50Ti rotor of a Beckman Instrument yielded a supernatant comprised of proteins from the mitochondrial matrix, including stripped peripheral membrane proteins, and a pellet containing integral proteins isolated from the mitochondrial membrane fraction.

Glycerol gradient sedimentation

Hypotonically purified mitochondrial vesicles from ∼2.5×10^9 cells were resuspended in glycerol gradient lysis buffer (10-mM Tris-HCl, pH 7.2, 10-mM $MgCl_2$, 200-mM KCl, 1-mM 1,4-dithiothreitol) and solubilized with 1% Triton X-100 for 30 min on ice. The lysates were cleared by a centrifugation step (2× 16,000*g*, 30 min, 4 °C), and the protein concentration was determined by the Bradford assay. Cleared mitochondrial lysates were resolved by ultracentrifugation (Beckman Instrument, SW40 rotor) at 38,000*g* for 5 h on an 11- ml 10 to 30%

glycerol gradient, which was poured using the Gradient Station (Biocomp) according to the manufacturer's protocol. The glycerol gradients were then fractionated with the Gradient Station, and 500 μl fractions were stored at −80 °C.

ΔΨm measurement

The ΔΨm of live cells was estimated using the cell-permeant red-fluorescent dye TMRE (Thermo Fisher Scientific T669), whose fluorescence intensity is proportionally dependent on the ΔΨm values. Equal number of cells (3×10^6) were harvested for each time point and resuspended in the culture medium containing 60-nM TMRE. The staining of the cells was carried out for 30 min at the appropriate temperature for each life stage. Subsequently, cells were spun down at 1400*g* for 10 min at room temperature, resuspended in 1 ml of 1× PBS (see composition above) and immediately analyzed by flow cytometry using BD FACSCanto II instrument and its blue laser (488 nm) with the band pass PE filter (585/15). For each sample, 10,000 events were collected. Treatment with 20-μM carbonyl cyanide 4-(trifluoromethoxy) phenylhydrazone (Sigma C2920) was used as a control for mitochondrial membrane depolarization. Data were evaluated using BD FACS Diva (BD Company) software. The TMRE signal corresponding to RNAi-induced/tetracycline-depleted cells was normalized to that of control cells and expressed in percentage. The values were plotted and analyzed statistically using GraphPad Prism 8.0 software.

In situ ΔΨm of permeabilized cells was determined fluorometrically using safranin O dye (Sigma S2255) (77). For each sample, 2×10^7 cells were harvested and washed once with ANT buffer (8-mM KCl, 110-mM K-gluconate, 10-mM NaCl, 10-mM free-acid Hepes, 10-mM K_2HPO_4, 0.015-mM EGTA potassium salt, 10-mM mannitol, 0.5 mg/ml fatty acid–free bovine serum albumin, 1.5-mM $MgCl_2$, pH 7.25) (78). The cell pellet was resuspended in 2 ml of ANT buffer containing 5-μM safranin O and 4-μM digitonin. Fluorescence was recorded in a Hitachi F-7100 spectrofluorometer (Hitachi High-Technologies) at a 5-Hz acquisition rate, using 495 nm and 585 nm excitation and emission wavelengths, respectively. Substrates (1-mM ATP, PanReac AppliChem A13480025) and inhibitors (10 μg/ml oligomycin or 1-μM carboxyatractyloside, Sigma O4876 and Biorbyt orb259156-10, respectively) were added where indicated. Final addition of the uncoupler SF 6847 (250 nM; Enzo Life Sciences BML-EI215-0050) served as a control for maximal depolarization. All the experiments were performed at room temperature and constant stirring.

Mitochondrial $O_2^{\bullet-}$ and cellular ROS measurements

For the measurement of mitochondrial and cellular ROS molecules, the red mitochondrial $O_2^{\bullet-}$ indicator MitoSOX (Thermo Fisher Scientific M36008) and H_2DCFHDA dye (Thermo Fisher Scientific) were used, respectively. The staining procedure followed was essentially the same as for the determination of ΔΨm *in vivo* except that TMRE was replaced by 5-μM MitoSOX or 10-μM H_2DCFHDA in the corresponding assay. MitoSOX and H_2DCFHDA fluorescence signals were recorded using BD FACSCanto II instrument and its blue laser (488 nm) with the band pass phycoerythrin (585/15 nm) and fluorescein isothiocyanate (530/30 nm) filters, respectively. The fluorescence signal of RNAi-induced/tetracycline-depleted cells was normalized to that of control cells and expressed in percentage. The values were plotted and analyzed statistically using GraphPad Prism 8.0 software.

High-resolution respirometry

The oxygen consumption rate was determined using the Oroboros Oxygraph-2K (Oroboros Instruments Corp). For each sample, 2×10^7 cells were harvested and washed once with Mir05 mitochondrial respiration medium (0.5-mM EGTA, 3-mM $MgCl_2$, 60-mM lactobionic acid, 20-mM taurine, 10-mM KH_2PO_4, 20-mM Hepes, 110-mM sucrose, 1 mg/ml fatty acid–free bovine serum albumin, pH 7.1). The cell pellet was resuspended in 2.1 ml of Mir05 and transferred into the respiration chamber at the appropriate growth temperature for each life stage and under constant stirring. In the experiments carried out with intact PCF cells, 10-mM glycerol-3-phosphate (Sigma, 17766) was added, and complex IV- and AOX-mediated respirations were inhibited by injection of 1-mM KCN and 250-μM SHAM (Sigma S607), respectively. For the experiments performed with permeabilized BSF cells, the addition of 4-μM digitonin (Sigma D141) preceded the injection of 20-mM glycerol-3-phopshate into the chamber, and respiratory inhibition was achieved by addition of 250-μM SHAM. The most stable portion of either the oxygen consumption rate slope (PCF experiments) or the oxygen concentration in the chamber slope (BSF experiments) was determined for each biological replicate after the addition of substrates and inhibitors. The values were plotted and analyzed statistically using GraphPad Prism 8.0 software.

ADP/ATP ratio and total cellular ATP levels

Both the ADP/ATP ratio and the total cellular ATP were estimated using the bioluminescence-based ADP/ATP assay kit (Sigma MAK135) following the manufacturer's protocol. In brief, 1×10^6 cells per sample were harvested and washed once with PBS-G (1× PBS plus 6-mM glucose). Cells were resuspended in 10 μl of 1× PBS-G and transferred into a white flat-bottom 96-well microtiter plate. Luminescence was recorded in an Orion II microplate luminometer (Titertek-Berthold). The ATP levels and calculated ADP/ATP ratios of RNAi-induced/tetracycline-depleted cells were normalized to those of control cells and expressed in percentage. The values were plotted and analyzed statistically using GraphPad Prism 8.0 software.

Resazurin cell-viability assay

BSF cells were inoculated into a transparent flat-bottom 96-well microtiter plate at a density of 500 trypanosomes in a final volume of 200 μl of the culture medium per well. The cells were incubated in the presence of various drug concentrations (0.98- to 4000-μM carboxyatractyloside and 9.78–5000 ng/ml oligomycin) for 72 h at 37 °C. Wells without the drug served as

the control for cell viability. Subsequently, 20 µl of a 125 µg/ml resazurin (Sigma R7017) stock solution was added and fluorescence was measured 24 h later (total drug incubation time of 96 h) in a Tecan Spark plate reader using 544-nm and 590-nm excitation and emission wavelengths, respectively. Data were analyzed with GraphPad Prism 8.0 software using a nonlinear regression and a sigmoidal dose–response analysis. All the experiments were performed in triplicate.

Modeling of Tb1 structure

The structure of Tb1 was predicted with I-TASSER (34) using the structure of *E. gracilis* Tb1 as a template (PDB ID: 6TDU (6)).

Data availability

All data discussed are presented in the article.

Acknowledgments—The authors thank Martina Slapničková for excellent technical support of the Zíková lab.

Author contributions—A. Z., B. P., C. H. -Y., K. S., O. G., A. S., and C. C., conceived and designed research, C. H.-Y. performed majority of experiments and data analysis, K. S. generated strains and conducted the initial analysis, C. D. generated strains and conducted growth assays, and A. Z., C. H.-Y., O. G., A. S., and C. C. wrote the manuscript.

Funding and additional information—This work was supported by the Czech Science Foundation (18-17529S) and European Regional Development Fund and Ministry of Education, Youth and Sport (CZ.02.1.01/0.0/0.0/16_019/0000759) to A. Z., a Senior Fellowship from the UK Medical Research Council, United Kingdom (MR/L019701/1) to A. S., and by grants from NKFIH [KH129567] and [K135027] to C. C.

Conflict of interest—The authors declare that they have no conflicts of interest with the content of this article.

Abbreviations—The abbreviations used are: ΔΨm, mitochondrial membrane potential; AAC, ADP/ATP carrier; ACA, ε-aminocaproic acid; AOX, alternative oxidase; BNE, blue native electrophoresis; BSF, bloodstream form; cDKO, conditional double knock-out; DDM, dodecylmaltoside; H_2DCFHDA, dichlorodihydrofluorescein; KCN, potassium cyanide; Mdm38, mitochondrial distribution and morphology protein 38 (aka YOL027C); mAb, monoclonal antibody; $O_2^{\bullet-}$, superoxide; OSCP, oligomycin sensitivity-conferring protein; pAb, polyclonal antibody; PCF, procyclic form; ROS, reactive oxygen species; SHAM, salicylhydroxamic acid; Tb1, ATPaseTb1 (*T. brucei* F_oF_1–ATP synthase subunit 1); Tb2, ATPaseTb2 (*T. brucei* F_oF_1–ATP synthase subunit 2); TMRE, tetramethylrhodamine ethyl ester; WT, wild type.

References

1. Walker, J. E. (2013) The ATP synthase: The understood, the uncertain and the unknown. *Biochem. Soc. Trans.* **41**, 1–16
2. Kuhlbrandt, W. (2019) Structure and mechanisms of F-type ATP synthases. *Annu. Rev. Biochem.* **88**, 515–549
3. Miranda-Astudillo, H., Cano-Estrada, A., Vazquez-Acevedo, M., Colina-Tenorio, L., Downie-Velasco, A., Cardol, P., Remacle, C., Dominguez-Ramirez, L., and Gonzalez-Halphen, D. (2014) Interactions of subunits Asa2, Asa4 and Asa7 in the peripheral stalk of the mitochondrial ATP synthase of the chlorophycean alga Polytomella sp. *Biochim. Biophys. Acta* **1837**, 1–13
4. van Lis, R., Mendoza-Hernandez, G., Groth, G., and Atteia, A. (2007) New insights into the unique structure of the F0F1-ATP synthase from the chlamydomonad algae Polytomella sp. and Chlamydomonas reinhardtii. *Plant Physiol.* **144**, 1190–1199
5. Salunke, R., Mourier, T., Banerjee, M., Pain, A., and Shanmugam, D. (2018) Highly diverged novel subunit composition of apicomplexan F-type ATP synthase identified from Toxoplasma gondii. *PLoS Biol.* **16**, e2006128
6. Muhleip, A., McComas, S. E., and Amunts, A. (2019) Structure of a mitochondrial ATP synthase with bound native cardiolipin. *Elife* **8**, e51179
7. Balabaskaran Nina, P., Dudkina, N. V., Kane, L. A., van Eyk, J. E., Boekema, E. J., Mather, M. W., and Vaidya, A. B. (2010) Highly divergent mitochondrial ATP synthase complexes in Tetrahymena thermophila. *PLoS Biol.* **8**, e1000418
8. Zikova, A., Schnaufer, A., Dalley, R. A., Panigrahi, A. K., and Stuart, K. D. (2009) The F(0)F(1)-ATP synthase complex contains novel subunits and is essential for procyclic Trypanosoma brucei. *PLoS Pathog.* **5**, e1000436
9. Gahura, O., Subrtova, K., Vachova, H., Panicucci, B., Fearnley, I. M., Harbour, M. E., Walker, J. E., and Zikova, A. (2018) The F1 -ATPase from Trypanosoma brucei is elaborated by three copies of an additional p18-subunit. *FEBS J.* **285**, 614–628
10. Montgomery, M. G., Gahura, O., Leslie, A. G. W., Zikova, A., and Walker, J. E. (2018) ATP synthase from Trypanosoma brucei has an elaborated canonical F1-domain and conventional catalytic sites. *Proc. Natl. Acad. Sci. U. S. A.* **115**, 2102–2107
11. Subrtova, K., Panicucci, B., and Zikova, A. (2015) ATPaseTb2, a unique membrane-bound FoF1-ATPase component, is essential in bloodstream and dyskinetoplastic Trypanosomes. *PLoS Pathog.* **11**, e1004660
12. Bringaud, F., Riviere, L., and Coustou, V. (2006) Energy metabolism of trypanosomatids: Adaptation to available carbon sources. *Mol. Biochem. Parasitol.* **149**, 1–9
13. Hellemond, J. J., Bakker, B. M., and Tielens, A. G. (2005) Energy metabolism and its compartmentation in Trypanosoma brucei. *Adv. Microb. Physiol.* **50**, 199–226
14. Smith, T. K., Bringaud, F., Nolan, D. P., and Figueiredo, L. M. (2017) Metabolic reprogramming during the Trypanosoma brucei life cycle. *F1000Res.* **6**. F1000 Faculty Rev-683
15. Nolan, D. P., and Voorheis, H. P. (1992) The mitochondrion in bloodstream forms of Trypanosoma brucei is energized by the electrogenic pumping of protons catalysed by the F1F0-ATPase. *Eur. J. Biochem.* **209**, 207–216
16. Schnaufer, A., Clark-Walker, G. D., Steinberg, A. G., and Stuart, K. (2005) The F1-ATP synthase complex in bloodstream stage trypanosomes has an unusual and essential function. *EMBO J.* **24**, 4029–4040
17. Futai, M., and Kanazawa, H. (1983) Structure and function of proton-translocating adenosine triphosphatase (F0F1): Biochemical and molecular biological approaches. *Microbiol. Rev.* **47**, 285–312
18. Chinopoulos, C., and Adam-Vizi, V. (2010) Mitochondria as ATP consumers in cellular pathology. *Biochim. Biophys. Acta* **1802**, 221–227
19. Chinopoulos, C. (2011) Mitochondrial consumption of cytosolic ATP: Not so fast. *FEBS Lett.* **585**, 1255–1259
20. Chen, X. J., and Clark-Walker, G. D. (2000) The petite mutation in yeasts: 50 years on. *Int. Rev. Cytol.* **194**, 197–238
21. Appleby, R. D., Porteous, W. K., Hughes, G., James, A. M., Shannon, D., Wei, Y. H., and Murphy, M. P. (1999) Quantitation and origin of the mitochondrial membrane potential in human cells lacking mitochondrial DNA. *Eur. J. Biochem.* **262**, 108–116
22. Dean, S., Gould, M. K., Dewar, C. E., and Schnaufer, A. C. (2013) Single point mutations in ATP synthase compensate for mitochondrial genome loss in trypanosomes. *Proc. Natl. Acad. Sci. U. S. A.* **110**, 14741–14746
23. Campanella, M., Casswell, E., Chong, S., Farah, Z., Wieckowski, M. R., Abramov, A. Y., Tinker, A., and Duchen, M. R. (2008) Regulation of mitochondrial structure and function by the F1Fo-ATPase inhibitor protein, IF1. *Cell Metab.* **8**, 13–25

24. Panicucci, B., Gahura, O., and Zikova, A. (2017) Trypanosoma brucei TbIF1 inhibits the essential F1-ATPase in the infectious form of the parasite. *PLoS Negl. Trop. Dis.* **11**, e0005552
25. Gahura, O., Panicucci, B., Vachova, H., Walker, J. E., and Zikova, A. (2018) Inhibition of F1 -ATPase from Trypanosoma brucei by its regulatory protein inhibitor TbIF1. *FEBS J.* **285**, 4413–4423
26. Vertommen, D., Van Roy, J., Szikora, J. P., Rider, M. H., Michels, P. A., and Opperdoes, F. R. (2008) Differential expression of glycosomal and mitochondrial proteins in the two major life-cycle stages of Trypanosoma brucei. *Mol. Biochem. Parasitol.* **158**, 189–201
27. Frazier, A. E., Taylor, R. D., Mick, D. U., Warscheid, B., Stoepel, N., Meyer, H. E., Ryan, M. T., Guiard, B., and Rehling, P. (2006) Mdm38 interacts with ribosomes and is a component of the mitochondrial protein export machinery. *J. Cell Biol.* **172**, 553–564
28. Chaudhuri, M., Ott, R. D., and Hill, G. C. (2006) Trypanosome alternative oxidase: From molecule to function. *Trends Parasitol.* **22**, 484–491
29. Brand, M. D. (2010) The sites and topology of mitochondrial superoxide production. *Exp. Gerontol.* **45**, 466–472
30. Maxwell, D. P., Wang, Y., and McIntosh, L. (1999) The alternative oxidase lowers mitochondrial reactive oxygen production in plant cells. *Proc. Natl. Acad. Sci. U. S. A.* **96**, 8271–8276
31. Fernandez-Ayala, D. J., Sanz, A., Vartiainen, S., Kemppainen, K. K., Babusiak, M., Mustalahti, E., Costa, R., Tuomela, T., Zeviani, M., Chung, J., O'Dell, K. M., Rustin, P., and Jacobs, H. T. (2009) Expression of the Ciona intestinalis alternative oxidase (AOX) in Drosophila complements defects in mitochondrial oxidative phosphorylation. *Cell Metab.* **9**, 449–460
32. El-Khoury, R., Dufour, E., Rak, M., Ramanantsoa, N., Grandchamp, N., Csaba, Z., Duvillie, B., Benit, P., Gallego, J., Gressens, P., Sarkis, C., Jacobs, H. T., and Rustin, P. (2013) Alternative oxidase expression in the mouse enables bypassing cytochrome c oxidase blockade and limits mitochondrial ROS overproduction. *PLoS Genet.* **9**, e1003182
33. Chinopoulos, C. (2011) The "B space" of mitochondrial phosphorylation. *J. Neurosci. Res.* **89**, 1897–1904
34. Bakker, B. M., Michels, P. A., Opperdoes, F. R., and Westerhoff, H. V. (1999) What controls glycolysis in bloodstream form Trypanosoma brucei? *J. Biol. Chem.* **274**, 14551–14559
35. Alberto Luevano-Martinez, L., Girard, R., Alencar, M. B., and Silber, A. M. (2020) ATP regulates the activity of an alternative oxidase in Trypanosoma brucei. *FEBS Lett.* https://doi.org/10.1002/1873-3468.13790
36. Nowikovsky, K., Reipert, S., Devenish, R. J., and Schweyen, R. J. (2007) Mdm38 protein depletion causes loss of mitochondrial K+/H+ exchange activity, osmotic swelling and mitophagy. *Cell Death Differ.* **14**, 1647–1656
37. Bauerschmitt, H., Mick, D. U., Deckers, M., Vollmer, C., Funes, S., Kehrein, K., Ott, M., Rehling, P., and Herrmann, J. M. (2010) Ribosome-binding proteins Mdm38 and Mba1 display overlapping functions for regulation of mitochondrial translation. *Mol. Biol. Cell* **21**, 1937–1944
38. Perez, E., Lapaille, M., Degand, H., Cilibrasi, L., Villavicencio-Queijeiro, A., Morsomme, P., Gonzalez-Halphen, D., Field, M. C., Remacle, C., Baurain, D., and Cardol, P. (2014) The mitochondrial respiratory chain of the secondary green alga Euglena gracilis shares many additional subunits with parasitic Trypanosomatidae. *Mitochondrion* **19 Pt B**, 338–349
39. Horvath, A., Horakova, E., Dunajcikova, P., Verner, Z., Pravdova, E., Slapetova, I., Cuninkova, L., and Lukes, J. (2005) Downregulation of the nuclear-encoded subunits of the complexes III and IV disrupts their respective complexes but not complex I in procyclic Trypanosoma brucei. *Mol. Microbiol.* **58**, 116–130
40. Gnipova, A., Panicucci, B., Paris, Z., Verner, Z., Horvath, A., Lukes, J., and Zikova, A. (2012) Disparate phenotypic effects from the knockdown of various Trypanosoma brucei cytochrome c oxidase subunits. *Mol. Biochem. Parasitol.* **184**, 90–98
41. Coustou, V., Besteiro, S., Biran, M., Diolez, P., Bouchaud, V., Voisin, P., Michels, P. A., Canioni, P., Baltz, T., and Bringaud, F. (2003) ATP generation in the Trypanosoma brucei procyclic form: Cytosolic substrate level is essential, but not oxidative phosphorylation. *J. Biol. Chem.* **278**, 49625–49635
42. Lamour, N., Riviere, L., Coustou, V., Coombs, G. H., Barrett, M. P., and Bringaud, F. (2005) Proline metabolism in procyclic Trypanosoma brucei is down-regulated in the presence of glucose. *J. Biol. Chem.* **280**, 11902–11910
43. Krauth-Siegel, R. L., and Comini, M. A. (2008) Redox control in trypanosomatids, parasitic protozoa with trypanothione-based thiol metabolism. *Biochim. Biophys. Acta* **1780**, 1236–1248
44. Prochazkova, M., Panicucci, B., and Zikova, A. (2018) Cultured bloodstream Trypanosoma brucei adapt to life without mitochondrial translation release factor 1. *Sci. Rep.* **8**, 5135
45. Chowdhury, S. R., Djordjevic, J., Albensi, B. C., and Fernyhough, P. (2015) Simultaneous evaluation of substrate-dependent oxygen consumption rates and mitochondrial membrane potential by TMRM and safranin in cortical mitochondria. *Biosci. Rep.* **36**, e00286
46. Helfert, S., Estevez, A. M., Bakker, B., Michels, P., and Clayton, C. (2001) Roles of triosephosphate isomerase and aerobic metabolism in Trypanosoma brucei. *Biochem. J.* **357**, 117–125
47. Lai, D. H., Hashimi, H., Lun, Z. R., Ayala, F. J., and Lukes, J. (2008) Adaptations of Trypanosoma brucei to gradual loss of kinetoplast DNA: Trypanosoma equiperdum and Trypanosoma evansi are petite mutants of T. brucei. *Proc. Natl. Acad. Sci. U. S. A.* **105**, 1999–2004
48. Schnaufer, A. (2010) Evolution of dyskinetoplastic trypanosomes: How, and how often? *Trends Parasitol.* **26**, 557–558
49. Carnes, J., Anupama, A., Balmer, O., Jackson, A., Lewis, M., Brown, R., Cestari, I., Desquesnes, M., Gendrin, C., Hertz-Fowler, C., Imamura, H., Ivens, A., Koreny, L., Lai, D. H., MacLeod, A., *et al.* (2015) Genome and phylogenetic analyses of Trypanosoma evansi reveal extensive similarity to T. brucei and multiple independent origins for dyskinetoplasty. *PLoS Negl. Trop. Dis.* **9**, e3404
50. Brun, R., Hecker, H., and Lun, Z. R. (1998) Trypanosoma evansi and T. equiperdum: Distribution, biology, treatment and phylogenetic relationship (a review). *Vet. Parasitol.* **79**, 95–107
51. Motta, M. C. (2008) Kinetoplast as a potential chemotherapeutic target of trypanosomatids. *Curr. Pharm. Des.* **14**, 847–854
52. Shapiro, T. A., and Englund, P. T. (1990) Selective cleavage of kinetoplast DNA minicircles promoted by antitrypanosomal drugs. *Proc. Natl. Acad. Sci. U. S. A.* **87**, 950–954
53. Giordani, F., Morrison, L. J., Rowan, T. G., De Koning, H. P., and Barrett, M. P. (2016) The animal trypanosomiases and their chemotherapy: A review. *Parasitology* **143**, 1862–1889
54. Eze, A. A., Gould, M. K., Munday, J. C., Tagoe, D. N., Stelmanis, V., Schnaufer, A., and De Koning, H. P. (2016) Reduced mitochondrial membrane potential is a late adaptation of trypanosoma brucei brucei to Isometamidium preceded by mutations in the gamma subunit of the F1Fo-ATPase. *PLoS Negl. Trop. Dis.* **10**, e0004791
55. Gould, M. K., and Schnaufer, A. (2014) Independence from kinetoplast DNA maintenance and expression is associated with multidrug resistance in Trypanosoma brucei *in vitro*. *Antimicrob. Agents Chemother.* **58**, 2925–2928
56. Agbe, A., and Yielding, K. L. (1995) Kinetoplasts play an important role in the drug responses of Trypanosoma brucei. *J. Parasitol.* **81**, 968–973
57. Young, M. J., and Copeland, W. C. (2016) Human mitochondrial DNA replication machinery and disease. *Curr. Opin. Genet. Dev.* **38**, 52–62
58. Ghozlane, A., Bringaud, F., Soueidan, H., Dutour, I., Jourdan, F., and Thebault, P. (2012) Flux analysis of the Trypanosoma brucei glycolysis based on a multiobjective-criteria bioinformatic approach. *Adv. Bioinformatics* **2012**, 159423
59. Kiaira, J. K., and Njogu, M. R. (1994) Oligomycin-sensitivity of hexose-sugar catabolism in the bloodstream form of Trypanosoma brucei brucei. *Biotechnol. Appl. Biochem.* **20**, 347–356
60. Miller, P. G., and Klein, R. A. (1980) Effects of oligomycin on glucose utilization and calcium transport in African trypanosomes. *J. Gen. Microbiol.* **116**, 391–396
61. Heinrich, R., and Rapoport, T. A. (1974) A linear steady-state treatment of enzymatic chains. General properties, control and effector strength. *Eur. J. Biochem.* **42**, 89–95
62. Bakker, B. M., Walsh, M. C., ter Kuile, B. H., Mensonides, F. I., Michels, P. A., Opperdoes, F. R., and Westerhoff, H. V. (1999) Contribution of glucose transport to the control of the glycolytic flux in Trypanosoma brucei. *Proc. Natl. Acad. Sci. U. S. A.* **96**, 10098–10103

63. Schaaff, I., Heinisch, J., and Zimmermann, F. K. (1989) Overproduction of glycolytic enzymes in yeast. *Yeast* **5**, 285–290
64. Ruyter, G. J., Postma, P. W., and van Dam, K. (1991) Control of glucose metabolism by enzyme IIGlc of the phosphoenolpyruvate-dependent phosphotransferase system in Escherichia coli. *J. Bacteriol.* **173**, 6184–6191
65. Koebmann, B. J., Westerhoff, H. V., Snoep, J. L., Nilsson, D., and Jensen, P. R. (2002) The glycolytic flux in Escherichia coli is controlled by the demand for ATP. *J. Bacteriol.* **184**, 3909–3916
66. Wickstead, B., Ersfeld, K., and Gull, K. (2002) Targeting of a tetracycline-inducible expression system to the transcriptionally silent minichromosomes of Trypanosoma brucei. *Mol. Biochem. Parasitol.* **125**, 211–216
67. Poon, S. K., Peacock, L., Gibson, W., Gull, K., and Kelly, S. (2012) A modular and optimized single marker system for generating Trypanosoma brucei cell lines expressing T7 RNA polymerase and the tetracycline repressor. *Open Biol.* **2**, 110037
68. Engstler, M., and Boshart, M. (2004) Cold shock and regulation of surface protein trafficking convey sensitization to inducers of stage differentiation in Trypanosoma brucei. *Genes Dev.* **18**, 2798–2811
69. Flaspohler, J. A., Jensen, B. C., Saveria, T., Kifer, C. T., and Parsons, M. (2010) A novel protein kinase localized to lipid droplets is required for droplet biogenesis in trypanosomes. *Eukaryot. Cell* **9**, 1702–1710
70. Wirtz, E., Leal, S., Ochatt, C., and Cross, G. A. (1999) A tightly regulated inducible expression system for conditional gene knock-outs and dominant-negative genetics in Trypanosoma brucei. *Mol. Biochem. Parasitol.* **99**, 89–101
71. Stuart, K. D. (1971) Evidence for the retention of kinetoplast DNA in an acriflavine-induced dyskinetoplastic strain of Trypanosoma brucei which replicates the altered central element of the kinetoplast. *J. Cell Biol.* **49**, 189–195
72. Panigrahi, A. K., Zikova, A., Dalley, R. A., Acestor, N., Ogata, Y., Anupama, A., Myler, P. J., and Stuart, K. D. (2008) Mitochondrial complexes in Trypanosoma brucei: A novel complex and a unique oxidoreductase complex. *Mol. Cell. Proteomics* **7**, 534–545
73. Hannaert, V., Albert, M. A., Rigden, D. J., da Silva Giotto, M. T., Thiemann, O., Garratt, R. C., Van Roy, J., Opperdoes, F. R., and Michels, P. A. (2003) Kinetic characterization, structure modelling studies and crystallization of Trypanosoma brucei enolase. *Eur. J. Biochem.* **270**, 3205–3213
74. Wittig, I., Karas, M., and Schagger, H. (2007) High resolution clear native electrophoresis for in-gel functional assays and fluorescence studies of membrane protein complexes. *Mol. Cell. Proteomics* **6**, 1215–1225
75. Acestor, N., Zikova, A., Dalley, R. A., Anupama, A., Panigrahi, A. K., and Stuart, K. D. (2011) Trypanosoma brucei mitochondrial respiratome: Composition and organization in procyclic form. *Mol. Cell. Proteomics* **10**. M110 006908
76. Acestor, N., Panigrahi, A. K., Ogata, Y., Anupama, A., and Stuart, K. D. (2009) Protein composition of Trypanosoma brucei mitochondrial membranes. *Proteomics* **9**, 5497–5508
77. Akerman, K. E., and Wikstrom, M. K. (1976) Safranine as a probe of the mitochondrial membrane potential. *FEBS Lett.* **68**, 191–197
78. Chinopoulos, C., Vajda, S., Csanady, L., Mandi, M., Mathe, K., and Adam-Vizi, V. (2009) A novel kinetic assay of mitochondrial ATP-ADP exchange rate mediated by the ANT. *Biophys. J.* **96**, 2490–2504

ATP synthase from *Trypanosoma brucei* has an elaborated canonical F_1-domain and conventional catalytic sites

Martin G. Montgomery[a,1], Ondřej Gahura[a,b,1], Andrew G. W. Leslie[c], Alena Zíková[b], and John E. Walker[a,2]

[a]The Medical Research Council Mitochondrial Biology Unit, University of Cambridge, Cambridge CB2 0XY, United Kingdom; [b]Institute of Parasitology, Biology Centre, Czech Academy of Sciences, 37005 České Budějovice, Czech Republic; and [c]The Medical Research Council Laboratory of Molecular Biology, Cambridge CB2 0QH, United Kingdom

Contributed by John E. Walker, December 18, 2017 (sent for review December 1, 2017; reviewed by Thomas M. Duncan and Wayne D. Frasch)

The structures and functions of the components of ATP synthases, especially those subunits involved directly in the catalytic formation of ATP, are widely conserved in metazoans, fungi, eubacteria, and plant chloroplasts. On the basis of a map at 32.5-Å resolution determined in situ in the mitochondria of *Trypanosoma brucei* by electron cryotomography, it has been proposed that the ATP synthase in this species has a noncanonical structure and different catalytic sites in which the catalytically essential arginine finger is provided not by the α-subunit adjacent to the catalytic nucleotide-binding site as in all species investigated to date, but rather by a protein, p18, found only in the euglenozoa. A crystal structure at 3.2-Å resolution of the catalytic domain of the same enzyme demonstrates that this proposal is incorrect. In many respects, the structure is similar to the structures of F_1-ATPases determined previously. The $\alpha_3\beta_3$-spherical portion of the catalytic domain in which the three catalytic sites are found, plus the central stalk, are highly conserved, and the arginine finger is provided conventionally by the α-subunits adjacent to each of the three catalytic sites found in the β-subunits. Thus, the enzyme has a conventional catalytic mechanism. The structure differs from previous described structures by the presence of a p18 subunit, identified only in the euglenozoa, associated with the external surface of each of the three α-subunits, thereby elaborating the F_1-domain. Subunit p18 is a pentatricopeptide repeat (PPR) protein with three PPRs and appears to have no function in the catalytic mechanism of the enzyme.

ATP synthase | *Trypanosoma brucei* | p18 subunit | catalytic domain | structure

The ATP synthases, also known as F-ATPases or F_1F_o-ATPases, are multisubunit enzyme complexes found in energy-transducing membranes in eubacteria, chloroplasts, and mitochondria (1, 2). They make ATP from ADP and phosphate under aerobic conditions using a proton-motive force (pmf), generated by respiration or photosynthesis, as a source of energy. To date, studies of the subunit compositions, structures, and mechanism of the ATP synthases have been confined mainly to the vertebrates, especially humans and bovines, and to various fungi, eubacteria, and chloroplasts of green plants. These studies have established the conservation of the central features of these rotary machines. They are all membrane-bound assemblies of multiple subunits organized into membrane-intrinsic and membrane-extrinsic sectors.

The membrane-extrinsic sector, known as F_1-ATPase, is the catalytic part in which ATP is formed from ADP and inorganic phosphate. It can be detached experimentally from the membrane domain in an intact state, and retains the ability to hydrolyze, but not synthesize, ATP. The membrane intrinsic sector, sometimes called F_o, contains a rotary motor driven by pmf and is connected to the extrinsic domain by a central stalk and a peripheral stalk. The enzyme's rotor constitutes the central stalk and an associated ring of c-subunits in the membrane domain. The central stalk lies along an axis of sixfold pseudosymmetry and penetrates into the $\alpha_3\beta_3$-domain, where the catalytic sites of the enzyme are found at three of the interfaces of α- and β-subunits. The penetrant region of the central stalk is an asymmetric α-helical coiled coil, and its rotation inside the $\alpha_3\beta_3$-domain takes each catalytic site through a series of conformational changes that lead to the binding of substrates and the formation and release of ATP.

During ATP hydrolysis in the experimentally detached F_1-domain, the direction of rotation, now driven by energy released from the hydrolysis of ATP, is opposite to the synthetic sense. Extensive structural analyses, mostly by X-ray crystallography at atomic resolution, have shown that the F_1-domains of the enzymes from bovine (3–23) and yeast (24–30) mitochondria, chloroplasts (31, 32), and eubacteria (33–39) are highly conserved. Not only is there conservation of the subunit compositions of the $\alpha_3\beta_3$-domain and the central stalk ($\gamma_1\varepsilon_1$ in eubacteria and chloroplasts, and $\gamma_1\delta_1$ plus an additional unique subunit, confusingly called ε, attached to the δ-subunit in mitochondria orthologs), but also the sequences of subunits are either highly conserved or absolutely conserved in many key residues. This extensive conservation includes residues in catalytic interfaces and in the catalytic sites themselves. In the β-subunits, they

Significance

Mitochondria generate the cellular fuel ATP to sustain complex life. Production of ATP depends on the oxidation of energy-rich compounds to produce the proton motive force (pmf), a chemical potential difference for protons, across the inner membrane. The pmf drives the ATP synthase to synthesize ATP via a mechanical rotary mechanism. The structures and functions of the protein components of this molecular machine, especially those involved directly in the catalytic formation of ATP, are widely conserved in metazoans, fungi, and eubacteria. Here we show that the proposal that this conservation does not extend to the ATP synthase from *Trypanosoma brucei*, a member of the euglenozoa and the causative agent of sleeping sickness in humans, is incorrect.

Author contributions: A.Z. and J.E.W. designed research; M.G.M. and O.G. performed research; M.G.M., A.G.W.L., and J.E.W. analyzed data; J.E.W. wrote the paper; and J.E.W. supervised the project.

Reviewers: T.M.D., State University of New York Upstate Medical University; and W.D.F., Arizona State University.

The authors declare no conflict of interest.

Data deposition: The atomic coordinates and structure factors have been deposited in the Protein Data Bank, www.wwpdb.org (PDB ID code 6F5D).

[1]M.G.M. and O.G. contributed equally to this work.

[2]To whom correspondence should be addressed. Email: walker@mrc-mbu.cam.ac.uk.

This article contains supporting information online at www.pnas.org/lookup/suppl/doi:10.1073/pnas.1720940115/-/DCSupplemental.

Published online February 12, 2018.

include a hydrophobic pocket where the adenine ring of ADP (or ATP) is bound; a P-loop sequence that interacts with the α-, β-, and γ-phosphates of ATP and provides residues involved either directly or indirectly via water molecules in the binding of a hexacoordinate magnesium ion; and, in the adjacent α-subunit, an "arginine finger" residue, which senses whether ADP or ATP is bound to the catalytic site. Indeed, these catalytic features are common to a wide range of NTPases (40, 41), and together with conserved structural features are characteristic of the canonical ATP synthase.

Based on a structural model at 32.5-Å resolution derived by electron cryotomography (ECT), it has been suggested recently that the structure of the F_1-catalytic domain and its catalytic mechanism in the ATP synthase from *Trypanosoma brucei* have diverged extensively from the canonical complex in an unprecedented manner (42). It has been proposed that the structure of this F_1-domain is much more open than those described in other species, and that the "arginine finger" is provided not by the α-subunit, but rather by an additional p18-subunit found only in the euglenozoa (43–49). Here we examine this proposal in the context of a structure of the F_1-domain of the *T. brucei* ATP synthase determined by X-ray crystallography at 3.2-Å resolution.

Results and Discussion

Structure Determination. The crystals of the *T. brucei* F_1-ATPase have the unit cell parameters $a = 124.2$ Å, $b = 206.4$ Å, and $c = 130.2$ Å, with $\alpha = \gamma = 90.0°$ and $\beta = 104.9°$, and they belong to space group $P2_1$, with one F_1-ATPase in the asymmetric unit. Data processing and refinement statistics are presented in Table S1. The final model of the complex contains the following residues: α_E, 20–125, 137–416, and 423–560; α_{TP}, 22–127, 137–414, and 421–560; α_{DP}, 22–125, 137–416, and 424–560; β_E, 6–492; β_{TP}, 7–494; β_{DP}, 8–488; γ, 2–58 and 66–285; δ, 5–16 and 32–165; ε, 1–66; and three copies of p18, residues 6–169, 6–167, and 6–170, attached to the α_{TP}-, α_{DP}-, and α_E-subunits, respectively (see below). An ADP molecule and a magnesium ion are bound to each of the three α-subunits and to the β_{TP}- and β_{DP}-subunits, whereas the β_E-subunit has a bound ADP molecule without a magnesium ion. A similar nucleotide occupancy of catalytic and noncatalytic sites has been reported in the bovine F_1-ATPase crystallized in the presence of phosphonate (20) and in the F_1-ATPase from *Caldalkalibacillus thermarum* (38). These structures are interpreted as representing a posthydrolysis state in which the ADP molecule has not been released from the enzyme.

An unusual feature of the *T. brucei* F_1-ATPase is that the diphosphate catalytic interface is more open than the triphosphate catalytic interface, similar to the F_1-ATPase from *Saccharomyces cerevisiae* (24), whereas the converse is observed in all other structures (Table S2). As usual, the empty interface is the most open of the three catalytic interfaces (Table S2). The rotational position of the γ-subunit (determined by superposition of crown regions of structures) is +23.1° relative to the bovine phosphate release dwell, which is at or close to the catalytic dwell at +30° in the rotary catalytic cycle (6).

Structure of the F_1-ATPase from *T. brucei*. The structure consists of an $\alpha_3\beta_3$-complex with α- and β-subunits arranged in alternation around an antiparallel α-helical coiled coil in the γ-subunit (Fig. 1). The rest of the γ-subunit sits beneath the $\alpha_3\beta_3$-complex and is associated with the δ- and ε-subunits. Together, these three subunits form the central stalk. Thus, the overall structure of this catalytic domain of the ATP synthase complex is very close to structures of canonical F_1-ATPases determined in the mitochondria of other species, and in eubacteria and chloroplasts. For example, in a comparison of backbone atoms with the bovine F_1-ATPase crystallized in the presence of phosphonate (20), the rmsd is 3.24 Å. As in these other canonical structures, each of the α- and β-subunits in the *T. brucei* F_1-ATPase has three domains. The N-terminal domain (residues 1–103 and 1–88 in α- and β-subunits, respectively) consists of a six-stranded β-barrel in both α- and β-subunits, and these six β-domains are associated in a stable annulus known as the "crown". The central domain (residues 104–389 and 89–365 in α- and β-subunits, respectively) provides the nucleotide-binding sites (Fig. S1). The C-terminal domain consists of a bundle of seven and four α-helices in α- and β-subunits, respectively. The crown stabilizes the entire F_1-domain, and, during rotary catalysis, the rest of the α- and β-subunits swing from this crown in response to the rotation of the asymmetrical α-helical coiled-coil region of the γ-subunit.

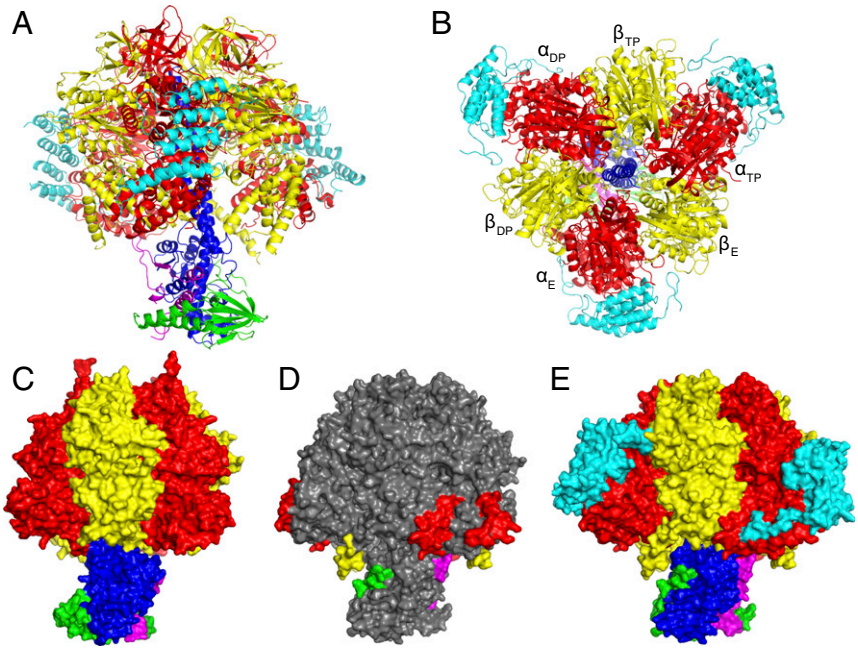

Fig. 1. Structure of the F_1-ATPase from *T. brucei*. The α-, β-, γ-, δ-, ε-, and p18-subunits are shown in red, yellow, blue, green, magenta, and cyan, respectively. (*A* and *B*) Side (*A*) and top (*B*) views in cartoon representation. (*C*–*E*) Side views in surface representation rotated 180° relative to *A*. (*C*) The bovine enzyme (12). (*D* and *E*) The *T. brucei* enzyme. In *D*, p18 has been omitted, and only additional regions not found in the bovine enzyme are colored; the rest of the structure is gray. The two additional sections in the α-subunit (red) interact with the p18-subunit. (*E*) p18 is present and is shown interacting with the α-subunit.

The six bound ADP molecules occupy nucleotide-binding sites that are very similar in structure to those in other ATP synthases. They retain the conventional features of a hydrophobic pocket to bind the adenine ring, and a characteristic P-loop sequence (GDRQTGKT in the α-subunit, residues 182–189; GGAGVGKT in the β-subunit, residues 162–169) interacting with the α- and β-phosphates of ADP or ATP (Fig. 2). The five magnesium ions are hexacoordinated by a threonine residue (residues 189 and 169 in α- and β-subunits, respectively) and four water molecules in each case. In the canonical enzymes, the nucleotides bound to the β-subunits participate in catalysis and exchange during a catalytic cycle, whereas those bound to the α-subunits are permanently bound to the enzyme and do not participate in catalysis. The close similarity of the structures of the *T. brucei* and bovine F_1-ATPases suggests strongly that the α- and β-subunits in the *T. brucei* enzyme have the same, or very similar, roles to those in the bovine enzyme. Thus, the nucleotide-binding sites in the β-subunits are part of the catalytic sites of the enzyme, the other important catalytic feature being αArg-386, the arginine finger residue, which is positioned in the catalytic site in the β_{DP}-subunit from *T. brucei*, for example, in exactly the same position occupied by the equivalent residue, αArg-373, in the bovine enzyme (Fig. 2).

Despite the general conservation of the structure and mechanism of the *T. brucei* F_1-ATPase, the euglenozoan enzyme is elaborated relative to the bovine enzyme, for example. First, the α-subunit in *T. brucei* is cleaved in vivo by proteolysis at two adjacent sites, removing residues 128–135 (Fig. S2) (50). The cleavage of α-subunits has been noted in other euglenozoan ATP synthases as well (48, 51–53), although the sites of cleavage have not been characterized precisely. In the bovine enzyme, the equivalent region (residues 117–123) forms an external loop (Fig. S2). These cleavages have no evident impact on the stability of either the α-subunit or the F_1-ATPase complex itself. Second, the α-, β-, δ-, and ε-subunits of the *T. brucei* enzyme have additional surface features that are not found in the known structures of other F_1-ATPases (Fig. 1). The most extensive are residues 483–498 and 536–560 in the C-terminal region of the α-subunit, and their significance is discussed below. The additional surface features in the β-, δ-, and ε-subunits are residues 485–499, 1–17, and 39–50, respectively. Those in the β- and ε-subunits have no obvious functions. The resolved residues of the additional sequence in the δ-subunit increases its area of interaction with the γ-subunit from 1,000 $Å^2$ to 1,700 $Å^2$. The C-terminal region of the γ-subunit from residues 286–304, although not resolved in the structure, is 19 residues longer than in the bovine enzyme, for example, and in the intact ATP synthase it could extend beyond the crown region, possibly making contacts, permanently or transiently, during rotary catalysis with the oligomycin sensitivity conferral protein (OSCP), a component of the peripheral stalk. In other species, the OSCP is bound to the F_1-domain by the N-terminal regions of the three α-subunits (19, 29, 37, 54).

Third, and most significantly from a structural standpoint, the *T. brucei* F_1-ATPase has an additional p18-subunit bound to each of its three α-subunits (50). The buried surface areas of interaction of the p18-subunits with their partner α_E-, α_{TP}-, and α_{DP}-subunits are 2,500, 2,600, and 2,500 $Å^2$, respectively. All three p18-subunits are folded into seven α-helices, H1–H7, with an unstructured C-terminal region from residues 151–170. The subunit is bound via H2 and H4 to the surface of the nucleotide-binding domain of an α-subunit and via H5 and H6 to the surface of its C-terminal domain. H7 is not in contact with the α-subunit (Fig. S2) but is bound to H6. The unstructured C-terminal tail interacts with the C-terminal domain of the α-subunit, traveling toward, but not entering, the noncatalytic interface with the adjacent β-subunit (Figs. 1 and 3 and Fig. S3). In this region, the extended C-terminal element of the p18-subunit interacts with the two additional segments of sequence (residues 483–498 and 536–560) found in the *T. brucei* α-subunit (Fig. S3). The first additional segment is largely extended, starting with one α-helical turn (residues 483–485). The second additional segment starts with one α-helical turn (residues 536–539), is followed by an extended region (residues 540–544), and terminates with an α-helix (residues 546–558) that doubles back into the noncatalytic interface and interacts with the extreme C-terminal end of the p18-subunit.

Role of the p18-Subunit. As noted previously, the sequence of the p18-subunit is related to the pentatricopeptide repeat (PPR) proteins (55), which are found in association with RNA molecules primarily in mitochondria and chloroplasts, as well as in some bacterial species. These proteins are characterized by a 35-aa degenerate sequence motif related to, but distinct from, the motif in the tetratricopeptide repeat (TPR) proteins (56). The PPR repeat is folded into a helix-turn-helix motif, and PPR proteins usually contain several tandem repeats associated into a superhelix, with a concave groove on one face that serves as a binding surface for RNA ligands. The p18-subunit of the F_1-ATPase from *T. brucei* is predicted to be a PPR protein with three PPRs, whereas it was previously thought to have two PPRs (50, 55). Although the probability score (49%) is rather low, as reflected in the weak correspondence of the sequences of the three predicted PPRs to the PPR consensus (Fig. S4), the

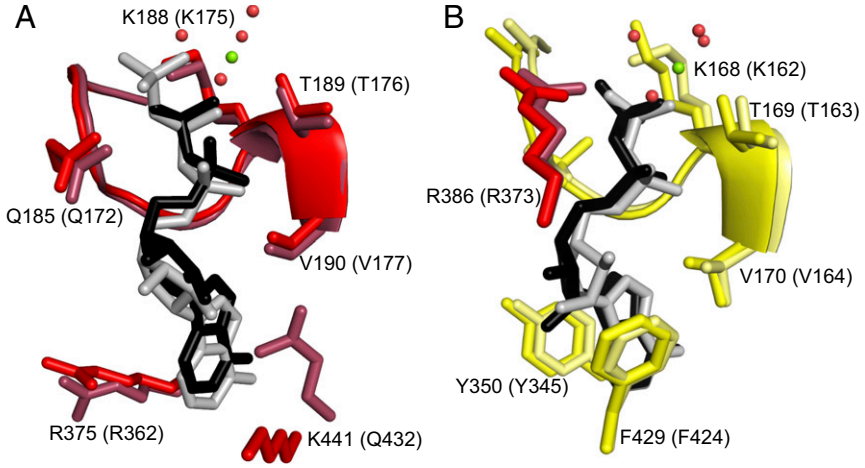

Fig. 2. Conservation of the noncatalytic and catalytic nucleotide-binding sites in the F_1-ATPase from *T. brucei*. (*A*) The noncatalytic site in the α_{DP}-subunit superposed onto the equivalent site in the bovine enzyme (12). (*B*) The catalytic site in the β_{DP}-subunit superposed onto the equivalent site in the bovine enzyme. Residue αR386 is the catalytically essential arginine finger (equivalent to αR373 in the bovine protein). Residues contributed by α- and β-subunits are shown in red and yellow, respectively (with the bovine residues in muted colors), and the bound ADP molecules are in black in the *T. brucei* enzymes and in gray in the bovine enzymes. The green and red spheres represent magnesium ions and water molecules, respectively (in *T. brucei* only). The residue numbers in parentheses denote the equivalent bovine residues.

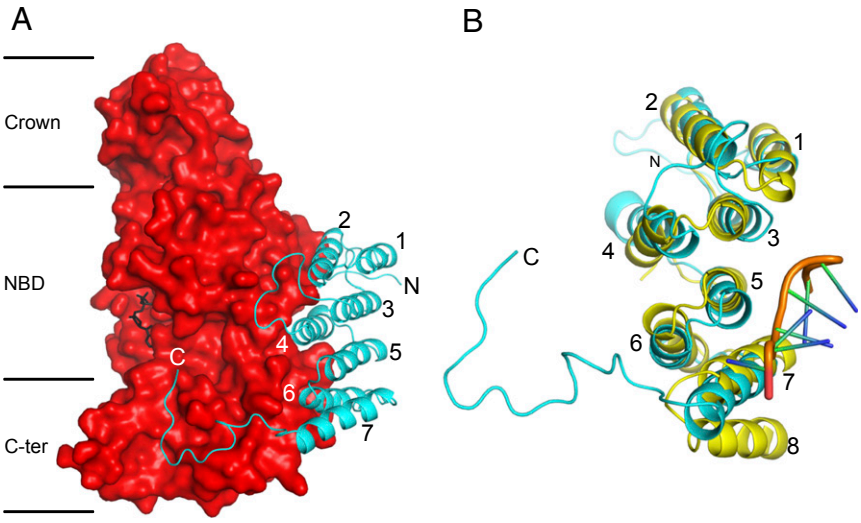

Fig. 3. Structure of the p18-subunit of the F_1-ATPase from *T. brucei*, and its relation to a PPR protein. (*A*) A p18 subunit (cyan) in cartoon representation, folded into α-helices H1–H7, with an extended C-terminal region from residues 151–170, bound to the α_{DP}-subunit in solid representation (red). The N-terminal, nucleotide-binding, and C-terminal domains of the α-subunit are indicated by Crown, NBD, and C-ter, respectively; the bound ADP molecule is in black. (*B*) Comparison of the p18-subunit with an example PPR protein, the PPR10 protein from *Z. mays* (yellow) (57). PPR10 has 18 PPRs; the structures of PPRs 11–14 are shown (Fig. S3). The orange region represents the backbone of an eight-residue ribonucleotide bound to PPR10. The three PPRs in the p18-subunit correspond to H1 plus H2 (residues 20–28 and 33–45), H3 plus H4 (residues 52–64 and 78–93), and H5 plus H6 (residues 99–112 and 115–126). PPR10 has an additional α-helix, labeled 8, which together with α-helix 7 constitutes a fourth PPR.

topography of p18 closely follows the topographies of other well-predicted and well-established PPR proteins, such as the RNA-binding PPR protein PPR10 from *Zea mays* (57) (Fig. S4).

This structural comparison (rmsd 2.3 Å) illustrates that, as predicted, the p18-subunit has three PPRs, consisting of H1 plus H2, H3 plus H4, and H5 plus H6. H7 could be a relic of the first element of a fourth PPR, in which H8 has evolved into the extended C-terminal tail region of the p18-subunit (Fig. 3*B*). However, p18 does not have a site equivalent to the RNA-binding site in PPR10, and other residues required for RNA binding in α-helix-7 of PPR10 have been substituted in H7 of p18. Therefore, there is no evidence suggesting that p18 has any role in binding an RNA molecule, and its role in the *T. brucei* F_1-ATPase remains obscure, although its presence is essential for assembly of the enzyme (50). The sequences of p18-subunits, including the PPR repeats, are highly conserved across the euglenozoa, suggesting that the structure and the mode of interaction of the various p18-proteins with their cognate F_1-ATPases are conserved as well (Fig. S5).

Structure of the *T. brucei* F_1-ATPase and the ECT Map. The structure of the F_1-ATPase from *T. brucei* described above at 3.2-Å resolution was docked into the map of the ATP synthase complex from the same organism at 32.5-Å resolution derived by ECT of mitochondrial membranes (Fig. 4). The structure of the catalytic domain described herein closely fits the region of the map with the mushroom shape, characteristic of the catalytic F_1-domain of other ATP synthases. Thus, this correspondence is also consistent with the *T. brucei* ATP synthase having a canonical catalytic domain elaborated by the attachment of the three p18-subunits. It does not support the proposal in Fig. 4 *C* and *D*)), where the map has been interpreted as having a catalytic domain in which the nucleotide-binding and C-terminal domains of the α-subunits are displaced outward away from the central stalk, and the role of the p18-subunit, bound in an unspecified position, is to provide the catalytically essential arginine finger residue (42).

Two other features in the ECT map can also be interpreted in terms of the characterized structures of canonical ATP synthases. First, the uninterpreted region of density above the F_1-domain in Fig. 4 corresponds to the upper part of the peripheral stalk in other ATP synthases. This region is occupied by the OSCP in the eukarya, and by the orthologous δ-subunit in eubacterial and chloroplast enzymes. As the ATP synthase in *T. brucei* and other euglenozoa that have been examined contain orthologs of the OSCP (49, 58, 59), it is highly probable that the *T. brucei* OSCP provides this feature in the ECT map and that, as in the well- characterized ATP synthases, it is attached to the F_1-domain via interactions with the N-terminal regions of the three α-subunits, which extend from the "top" of the crown domain. The role of the peripheral stalk in ATP synthases is to provide the stator of the enzyme with integrity by connecting the $\alpha_3\beta_3$-domain to the essential ATP6 (subunit a in eubacteria, subunit IV in chloroplasts) in the membrane domain. ATP6 and orthologs, together with the c-ring in the rotor, provide the transmembrane pathway for protons (2). To maintain the integrity of this pathway, and to keep ATP synthesis coupled to proton motive force, the static ATP6 and the rotating c-ring must be kept in contact by the action of the peripheral stalk.

The peripheral stalk is the most divergent of the essential features of ATP synthases (2). Apart from the OSCP and orthologous δ-subunits, the subunit compositions, sequences, and structures of the related and structurally simpler eubacterial and chloroplast peripheral stalks differ greatly from the more complex structurally characterized peripheral stalks in mitochondrial enzymes, although they are all dominated by approximately parallel, antiparallel, and apparently rigid long α-helical structures connecting the OSCP to the ATP6 subunit (and orthologs) running alongside the catalytic domains. The peripheral stalks of ATP synthases in the mitochondria of euglenozoa (59) and in the green alga, *Polytomella* (60), appear to be even more divergent than those in characterized mitochondrial enzymes. Their subunit compositions are more complex, and as is evident in the map feature to the left of the F_1-domain in Fig. 4 and in other published images, they are thicker and apparently more robust than structurally characterized peripheral stalks. More details are likely to emerge in the near future, most likely from the application of cryo-EM imaging of individual particles of these enzymes. These endeavors are driven by the imperative to use knowledge of the structure of the ATP synthase from *T. brucei* (61, 62) to aid the development of new drugs to treat patients with sleeping sickness by finding selective inhibitors of its activity.

Materials and Methods

Crystallization of F_1-ATPase from *T. brucei*. The F_1-ATPase purified from *T. brucei* (50) was crystallized at 4 °C by the microbatch method under paraffin oil. The enzyme was dissolved at a protein concentration of 9.0 mg/mL in buffer consisting of 20 mM Tris·HCl pH 7.5, 100 mM NaCl, 10 mM $MgSO_4$ and 1 mM ADP. This protein solution was mixed in wells in microbatch plates with an equal volume of 7.7% (wt/vol) PEG 10,000 dissolved in a buffer containing 100 mM 2-(*N*-morpholino)-ethanesulfonic acid pH 6.0 under a layer of paraffin oil. The plates were kept at 4 °C. Crystals appeared after 48 h, and were harvested 8 d later. They were cryoprotected by the addition of 15 μL of a solution containing 10 mM Tris·HCl pH 8.0, 10 mM NaCl, 5 mM

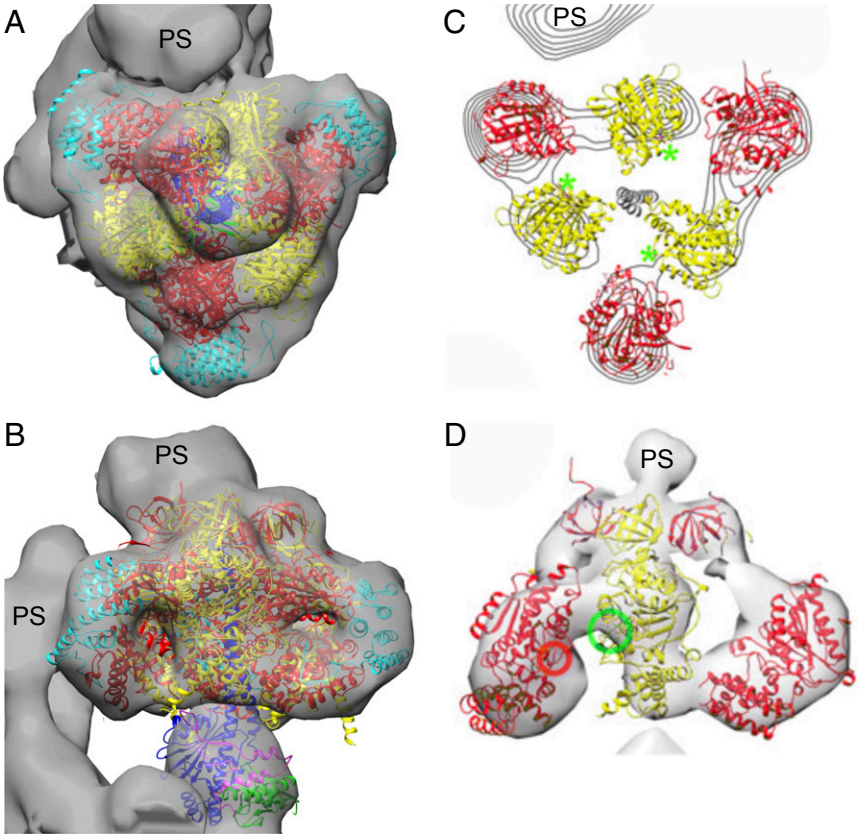

Fig. 4. Relationship of the crystallographic structure of the F_1-domain of the ATP synthase from *T. brucei* to an ECT map of the intact ATP synthase in situ in mitochondrial membranes from *T. brucei*. The subunits of the F_1-domain are colored as in Fig. 1. (*A* and *B*) Top (*A*) and side (*B*) views of the ECT map (gray), determined independently at 32.5-Å resolution with the crystallographic structure of the F_1-domain determined at 3.2-Å resolution docked manually inside the ECT map, with subunits α_{DP} and β_{TP} proximal to the peripheral stalk. (*C* and *D*) A published interpretation of the same ECT map proposing a structure of *T. brucei* F_1-ATPase in which the α-subunit is opened away from the central stalk, with the p18-subunit (not shown) contributing to the catalytic sites by providing the arginine finger residue (red circle) in *D* (42). The catalytic sites are indicated by green asterisks in *C* and by a green circle in *D*. PS, peripheral stalk of the enzyme. *C* and *D* modified from ref. 42.

$MgSO_4$, 0.5 mM ADP, 50 mM 2-(*N*-morpholino)-ethanesulfonic acid pH 6.0, 5% (wt/vol) PEG 12,000, and 30% (vol/vol) glycerol to each well. After 5 min, the crystals were harvested with a MicroLoop (MiTeGen), flash-frozen, and stored in liquid nitrogen.

Data Collection and Structure Determination. X-ray diffraction data were collected at 100 K from cryoprotected crystals with a PILATUS3 2M detector (Dectris) at a wavelength of 0.966 Å at the European Synchrotron Radiation Facility, Grenoble, France, using the MXPressE automated screening protocol (63, 64). Diffraction images were integrated with iMOSFLM (65), and the data were reduced with AIMLESS (66). Anisotropic correction was applied using STARANISO (staraniso.globalphasing.org). Molecular replacement using the $\alpha_3\beta_3$-domain from the structure of the ground state structure of bovine F_1-ATPase [Protein Data Bank (PDB) ID code 2JDI] was carried out with PHASER (67). Nucleotides, magnesium ions, and water molecules were removed from the model. Rigid body refinement and restrained refinement were performed with REFMAC5 (68). Manual rebuilding was performed with Coot (69), alternating with refinement performed with REFMAC5. For calculations of R_{free}, 5% of the diffraction data were excluded from the refinement. Additional electron density features, adjacent to the α-subunits, were attributed to p18. Initially, poly-Ala α-helices were fitted into this additional density with Coot (69), and the assignment of the direction of the α-helices was guided by secondary structure predictions performed with PSIPRED (70). This prediction also detected structural homology of p18 with PPR10 from *Z. mays* (PDB ID code 4M59). Stereochemistry was assessed with MolProbity (71), and images of structures and electron density maps were prepared with PyMOL (72). Structural comparisons of *T. brucei* F_1-ATPase with bovine F_1-ATPase inhibited with dicyclohexylcarbodiimide (PDB ID code 1E79) (12), bovine F_1-ATPase crystallized in the presence of phosphonate (PDB ID code 4ASU) (20), bovine F_1-ATPase inhibited with ADP-AlF_4 (PDB ID code 1H8E) (16), and the ground state structure of yeast F_1-ATPase (PDB ID code 2HLD) (24) and of the p18-subunit from *T. brucei* with PPR10 from *Z. mays* (PDB ID code 4M59) (57) were done with Coot (69) and PyMOL (72). The p18-subunit was assessed for the presence of PPR and TPR sequences with TPRpred (73), and α-helices were assigned according to PyMOL.

ACKNOWLEDGMENTS. We thank the staff at beamline ID30A-1 MASSIF-1 at the European Synchrotron Radiation Facility for their help. This work was supported by the Medical Research Council UK by Grants MC_U105663150 and MR/M009858/1 (to J.E.W.) and MC_U105184325 (to A.G.W.L.); the Czech Republic Ministry of Education, Youth, and Sports (European Research Council CZ Grant LL1205, to A.Z.); the Postdok_BIOGLOBE project, cofinanced by the European Social Fund and the Czech Republic (Grant CZ.1.07/2.3.00/30.0032, to A.Z. and O.G.); and European Molecular Biology Organization (Short-Term Fellowship ASTF 81-2016, to O.G.).

1. Walker JE (2013) The ATP synthase: The understood, the uncertain and the unknown. *Biochem Soc Trans* 41:1–16.
2. Walker JE (2017) Structure, mechanism, and regulation of ATP synthases. *Mechanisms of Primary Energy Transduction in Biology*, ed Wikström M (Royal Society of Chemistry, London), pp 338–373.
3. Abrahams JP, Leslie AGW, Lutter R, Walker JE (1994) Structure at 2.8-Å resolution of F_1-ATPase from bovine heart mitochondria. *Nature* 370:621–628.
4. Abrahams JP, et al. (1996) The structure of bovine F_1-ATPase complexed with the peptide antibiotic efrapeptin. *Proc Natl Acad Sci USA* 93:9420–9424.
5. Bason JV, Montgomery MG, Leslie AGW, Walker JE (2014) Pathway of binding of the intrinsically disordered mitochondrial inhibitor protein to F_1-ATPase. *Proc Natl Acad Sci USA* 111:11305–11310.
6. Bason JV, Montgomery MG, Leslie AGW, Walker JE (2015) How release of phosphate from mammalian F_1-ATPase generates a rotary substep. *Proc Natl Acad Sci USA* 112:6009–6014.
7. Bowler MW, Montgomery MG, Leslie AGW, Walker JE (2006) How azide inhibits ATP hydrolysis by the F-ATPases. *Proc Natl Acad Sci USA* 103:8646–8649.
8. Bowler MW, Montgomery MG, Leslie AGW, Walker JE (2007) Ground state structure of F_1-ATPase from bovine heart mitochondria at 1.9-Å resolution. *J Biol Chem* 282:14238–14242.
9. Braig K, Menz RI, Montgomery MG, Leslie AGW, Walker JE (2000) Structure of bovine mitochondrial F_1-ATPase inhibited by $Mg^{(2+)}$ ADP and aluminium fluoride. *Structure* 8:567–573.
10. Cabezón E, Montgomery MG, Leslie AGW, Walker JE (2003) The structure of bovine F_1-ATPase in complex with its regulatory protein IF_1. *Nat Struct Biol* 10:744–750.
11. Dickson VK, Silvester JA, Fearnley IM, Leslie AGW, Walker JE (2006) On the structure of the stator of the mitochondrial ATP synthase. *EMBO J* 25:2911–2918.
12. Gibbons C, Montgomery MG, Leslie AGW, Walker JE (2000) The structure of the central stalk in bovine F_1-ATPase at 2.4-Å resolution. *Nat Struct Biol* 7:1055–1061.

13. Gledhill JR, Montgomery MG, Leslie AGW, Walker JE (2007) How the regulatory protein, IF_1, inhibits F_1-ATPase from bovine mitochondria. *Proc Natl Acad Sci USA* 104: 15671–15676.
14. Gledhill JR, Montgomery MG, Leslie AGW, Walker JE (2007) Mechanism of inhibition of bovine F_1-ATPase by resveratrol and related polyphenols. *Proc Natl Acad Sci USA* 104:13632–13637.
15. Kagawa R, Montgomery MG, Braig K, Leslie AGW, Walker JE (2004) The structure of bovine F_1-ATPase inhibited by ADP and beryllium fluoride. *EMBO J* 23:2734–2744.
16. Menz RI, Walker JE, Leslie AGW (2001) Structure of bovine mitochondrial F_1-ATPase with nucleotide bound to all three catalytic sites: Implications for the mechanism of rotary catalysis. *Cell* 106:331–341.
17. Menz RI, Leslie AGW, Walker JE (2001) The structure and nucleotide occupancy of bovine mitochondrial F_1-ATPase are not influenced by crystallisation at high concentrations of nucleotide. *FEBS Lett* 494:11–14.
18. Orriss GL, Leslie AGW, Braig K, Walker JE (1998) Bovine F_1-ATPase covalently inhibited with 4-chloro-7-nitrobenzofurazan: The structure provides further support for a rotary catalytic mechanism. *Structure* 6:831–837.
19. Rees DM, Leslie AGW, Walker JE (2009) The structure of the membrane extrinsic region of bovine ATP synthase. *Proc Natl Acad Sci USA* 106:21597–21601.
20. Rees DM, Montgomery MG, Leslie AGW, Walker JE (2012) Structural evidence of a new catalytic intermediate in the pathway of ATP hydrolysis by F_1-ATPase from bovine heart mitochondria. *Proc Natl Acad Sci USA* 109:11139–11143.
21. van Raaij MJ, Abrahams JP, Leslie AGW, Walker JE (1996) The structure of bovine F_1-ATPase complexed with the antibiotic inhibitor aurovertin B. *Proc Natl Acad Sci USA* 93:6913–6917.
22. Watt IN, Montgomery MG, Runswick MJ, Leslie AGW, Walker JE (2010) Bioenergetic cost of making an adenosine triphosphate molecule in animal mitochondria. *Proc Natl Acad Sci USA* 107:16823–16827.
23. Zhou A, et al. (2015) Structure and conformational states of the bovine mitochondrial ATP synthase by cryo-EM. *Elife* 4:e10180.
24. Kabaleeswaran V, Puri N, Walker JE, Leslie AGW, Mueller DM (2006) Novel features of the rotary catalytic mechanism revealed in the structure of yeast F_1 ATPase. *EMBO J* 25:5433–5442.
25. Kabaleeswaran V, et al. (2009) Asymmetric structure of the yeast F_1 ATPase in the absence of bound nucleotides. *J Biol Chem* 284:10546–10551.
26. Stock D, Leslie AGW, Walker JE (1999) Molecular architecture of the rotary motor in ATP synthase. *Science* 286:1700–1705.
27. Robinson GC, et al. (2013) The structure of F_1-ATPase from *Saccharomyces cerevisiae* inhibited by its regulatory protein IF_1. *Open Biol* 3:120164.
28. Arsenieva D, Symersky J, Wang Y, Pagadala V, Mueller DM (2010) Crystal structures of mutant forms of the yeast F_1 ATPase reveal two modes of uncoupling. *J Biol Chem* 285:36561–36569.
29. Vinothkumar KR, Montgomery MG, Liu S, Walker JE (2016) Structure of the mitochondrial ATP synthase from *Pichia angusta* determined by electron cryo-microscopy. *Proc Natl Acad Sci USA* 113:12709–12714.
30. Hahn A, et al. (2016) Structure of a complete ATP synthase dimer reveals the molecular basis of inner mitochondrial membrane morphology. *Mol Cell* 63:445–456.
31. Groth G, Pohl E (2001) The structure of the chloroplast F_1-ATPase at 3.2-Å resolution. *J Biol Chem* 276:1345–1352.
32. Groth G (2002) Structure of spinach chloroplast F_1-ATPase complexed with the phytopathogenic inhibitor tentoxin. *Proc Natl Acad Sci USA* 99:3464–3468.
33. Shirakihara Y, et al. (1997) The crystal structure of the nucleotide-free $\alpha_3\beta_3$ subcomplex of F_1-ATPase from the thermophilic *Bacillus* PS3 is a symmetric trimer. *Structure* 5:825–836.
34. Cingolani G, Duncan TM (2011) Structure of the ATP synthase catalytic complex (F_1) from *Escherichia coli* in an autoinhibited conformation. *Nat Struct Mol Biol* 18: 701–707.
35. Roy A, Hutcheon ML, Duncan TM, Cingolani G (2012) Improved crystallization of *Escherichia coli* ATP synthase catalytic complex (F_1) by introducing a phosphomimetic mutation in subunit ε. *Acta Crystallogr Sect F Struct Biol Cryst Commun* 68:1229–1233.
36. Shirakihara Y, et al. (2015) Structure of a thermophilic F_1-ATPase inhibited by an ε-subunit: Deeper insight into the ε-inhibition mechanism. *FEBS J* 282:2895–2913.
37. Morales-Rios E, Montgomery MG, Leslie AGW, Walker JE (2015) Structure of ATP synthase from *Paracoccus denitrificans* determined by X-ray crystallography at 4.0-Å resolution. *Proc Natl Acad Sci USA* 112:13231–13236.
38. Ferguson SA, Cook GM, Montgomery MG, Leslie AGW, Walker JE (2016) Regulation of the thermoalkaliphilic F_1-ATPase from *Caldalkalibacillus thermarum*. *Proc Natl Acad Sci USA* 113:10860–10865.
39. Sobti M, et al. (2016) Cryo-EM structures of the autoinhibited *E. coli* ATP synthase in three rotational states. *Elife* 5:e21598.
40. Walker JE, Saraste M, Runswick MJ, Gay NJ (1982) Distantly related sequences in the alpha- and beta-subunits of ATP synthase, myosin, kinases and other ATP-requiring enzymes and a common nucleotide binding fold. *EMBO J* 1:945–951.
41. Ramakrishnan C, Dani VS, Ramasarma T (2002) A conformational analysis of Walker motif A [GXXXXGKT (S)] in nucleotide-binding and other proteins. *Protein Eng* 15: 783–798.
42. Mühleip AW, Dewar CE, Schnaufer A, Kühlbrandt W, Davies KM (2017) In situ structure of trypanosomal ATP synthase dimer reveals a unique arrangement of catalytic subunits. *Proc Natl Acad Sci USA* 114:992–997.
43. Balabaskaran Nina P, et al. (2010) Highly divergent mitochondrial ATP synthase complexes in *Tetrahymena thermophila*. *PLoS Biol* 8:e1000418.
44. Balabaskaran Nina P, et al. (2011) ATP synthase complex of *Plasmodium falciparum*: Dimeric assembly in mitochondrial membranes and resistance to genetic disruption. *J Biol Chem* 286:41312–41322.
45. Cardol P, et al. (2005) The mitochondrial oxidative phosphorylation proteome of *Chlamydomonas reinhardtii* deduced from the genome sequencing project. *Plant Physiol* 137:447–459.
46. van Lis R, Mendoza-Hernández G, Groth G, Atteia A (2007) New insights into the unique structure of the F_0F_1-ATP synthase from the chlamydomonad algae *Polytomella* sp. and *Chlamydomonas reinhardtii*. *Plant Physiol* 144:1190–1199.
47. Vaidya AB, Mather MW (2009) Mitochondrial evolution and functions in malaria parasites. *Annu Rev Microbiol* 63:249–267.
48. Perez E, et al. (2014) The mitochondrial respiratory chain of the secondary green alga *Euglena gracilis* shares many additional subunits with parasitic Trypanosomatidae. *Mitochondrion* 19 Pt B:338–349.
49. Zíková A, Schnaufer A, Dalley RA, Panigrahi AK, Stuart KD (2009) The F_0F_1-ATP synthase complex contains novel subunits and is essential for procyclic *Trypanosoma brucei*. *PLoS Pathog* 5:e1000436.
50. Gahura O, et al. (2017) The F_1-ATPase from *Trypanosoma brucei* is elaborated by three copies of an additional p18-subunit. *FEBS J*, 10.1111/febs.14364.
51. Speijer D, et al. (1997) Characterization of the respiratory chain from cultured *Crithidia fasciculata*. *Mol Biochem Parasitol* 85:171–186.
52. Nelson RE, Aphasizheva I, Falick AM, Nebohacova M, Simpson L (2004) The I-complex in *Leishmania tarentolae* is an uniquely-structured F_1-ATPase. *Mol Biochem Parasitol* 135:221–224.
53. Dean S, Gould MK, Dewar CE, Schnaufer AC (2013) Single point mutations in ATP synthase compensate for mitochondrial genome loss in trypanosomes. *Proc Natl Acad Sci USA* 110:14741–14746.
54. Carbajo RJ, et al. (2007) How the N-terminal domain of the OSCP subunit of bovine F_1F_0-ATP synthase interacts with the N-terminal region of an alpha subunit. *J Mol Biol* 368:310–318.
55. Pusnik M, Small I, Read LK, Fabbro T, Schneider A (2007) Pentatricopeptide repeat proteins in *Trypanosoma brucei* function in mitochondrial ribosomes. *Mol Cell Biol* 27: 6876–6888.
56. Small ID, Peeters N (2000) The PPR motif A TPR-related motif prevalent in plant organellar proteins. *Trends Biochem Sci* 25:46–47.
57. Yin P, et al. (2013) Structural basis for the modular recognition of single-stranded RNA by PPR proteins. *Nature* 504:168–171.
58. Cano-Estrada A, et al. (2010) Subunit–subunit interactions and overall topology of the dimeric mitochondrial ATP synthase of *Polytomella* sp. *Biochim Biophys Acta* 1797: 1439–1448.
59. Yadav KNS, et al. (2017) Atypical composition and structure of the mitochondrial dimeric ATP synthase from *Euglena gracilis*. *Biochim Biophys Acta* 1858:267–275.
60. Allegretti M, et al. (2015) Horizontal membrane-intrinsic α-helices in the stator a-subunit of an F-type ATP synthase. *Nature* 521:237–240.
61. Šubrtová K, Panicucci B, Zíková A (2015) ATPaseTb2, a unique membrane-bound F_0F_1-ATPase component, is essential in bloodstream and dyskinetoplastic trypanosomes. *PLoS Pathog* 11:e1004660.
62. Panicucci B, Gahura O, Zíková A (2017) *Trypanosoma brucei* $TbIF_1$ inhibits the essential F_1-ATPase in the infectious form of the parasite. *PLoS Negl Trop Dis* 11:e0005552.
63. Svensson O, Malbet-Monaco S, Popov A, Nurizzo D, Bowler MW (2015) Fully automatic characterization and data collection from crystals of biological macromolecules. *Acta Crystallogr D Biol Crystallogr* 71:1757–1767.
64. Bowler MW, et al. (2015) MASSIF-1: A beamline dedicated to the fully automatic characterization and data collection from crystals of biological macromolecules. *J Synchrotron Radiat* 22:1540–1547.
65. Battye TG, Kontogiannis L, Johnson O, Powell HR, Leslie AGW (2011) iMOSFLM: A new graphical interface for diffraction-image processing with MOSFLM. *Acta Crystallogr D Biol Crystallogr* 67:271–281.
66. Evans PR, Murshudov GN (2013) How good are my data and what is the resolution? *Acta Crystallogr D Biol Crystallogr* 69:1204–1214.
67. McCoy AJ, et al. (2007) Phaser crystallographic software. *J Appl Cryst* 40:658–674.
68. Murshudov GN, et al. (2011) REFMAC5 for the refinement of macromolecular crystal structures. *Acta Crystallogr D Biol Crystallogr* 67:355–367.
69. Emsley P, Lohkamp B, Scott WG, Cowtan K (2010) Features and development of Coot. *Acta Crystallogr D Biol Crystallogr* 66:486–501.
70. Buchan DW, Minneci F, Nugent TC, Bryson K, Jones DT (2013) Scalable web services for the PSIPRED protein analysis workbench. *Nucleic Acids Res* 41:W349–W357.
71. Chen VB, et al. (2010) MolProbity: All-atom structure validation for macromolecular crystallography. *Acta Crystallogr D Biol Crystallogr* 66:12–21.
72. Schrödinger LLC (2015) The PyMOL Molecular Graphics System, version 1.8. (Schrödinger, LLC, New York).
73. Alva V, Nam SZ, Söding J, Lupas AN (2016) The MPI bioinformatics Toolkit as an integrative platform for advanced protein sequence and structure analysis. *Nucleic Acids Res* 44:W410–W415.

PLOS | NEGLECTED TROPICAL DISEASES

RESEARCH ARTICLE

Trypanosoma brucei TbIF1 inhibits the essential F_1-ATPase in the infectious form of the parasite

Brian Panicucci[1], Ondřej Gahura[1], Alena Zíková[1,2]*

1 Biology Centre, Czech Academy of Sciences, Institute of Parasitology, Ceske Budejovice, Czech Republic,
2 Faculty of Science, University of South Bohemia, Ceske Budejovice, Czech Republic

* azikova@paru.cas.cz

OPEN ACCESS

Citation: Panicucci B, Gahura O, Zíková A (2017) *Trypanosoma brucei* TbIF1 inhibits the essential F_1-ATPase in the infectious form of the parasite. PLoS Negl Trop Dis 11(4): e0005552. https://doi.org/10.1371/journal.pntd.0005552

Editor: Jayne Raper, Hunter College, CUNY, UNITED STATES

Received: December 10, 2016

Accepted: April 4, 2017

Published: April 17, 2017

Data Availability Statement: All relevant data are within the paper.

Funding: This work was funded by Ministry of Education ERC CZ grant LL1205 and the Grant Agency of the Czech Republic 17-22248S (to AZ). This publication was also supported by project CZ.1.07/2.3.00/30.0032 (Promotion of post-doctoral positions in the Biology Centre of the Czech Academy of Sciences aimed to build the global competitiveness of the research teams in the Czech Republic) co-financed by the European Social Fund and the state budget of the Czech

Abstract

The mitochondrial (mt) F_oF_1-ATP synthase of the digenetic parasite, *Trypanosoma brucei*, generates ATP during the insect procyclic form (PF), but becomes a perpetual consumer of ATP in the mammalian bloodstream form (BF), which lacks a canonical respiratory chain. This unconventional dependence on F_oF_1-ATPase is required to maintain the essential mt membrane potential (Δψm). Normally, ATP hydrolysis by this rotary molecular motor is restricted to when eukaryotic cells experience sporadic hypoxic conditions, during which this compulsory function quickly depletes the cellular ATP pool. To protect against this cellular treason, the highly conserved inhibitory factor 1 (IF1) binds the enzyme in a manner that solely inhibits the hydrolytic activity. Intriguingly, we were able to identify the IF1 homolog in *T. brucei* (TbIF1), but determined that its expression in the mitochondrion is tightly regulated throughout the life cycle as it is only detected in PF cells. TbIF1 appears to primarily function as an emergency brake in PF cells, where it prevented the restoration of the Δψm by F_oF_1-ATPase when respiration was chemically inhibited. *In vitro*, TbIF1 overexpression specifically inhibits the hydrolytic activity but not the synthetic capability of the F_oF_1-ATP synthase in PF mitochondria. Furthermore, low μM amounts of recombinant TbIF1 achieve the same inhibition of total mt ATPase activity as the F_oF_1-ATPase specific inhibitors, azide and oligomycin. Therefore, even minimal ectopic expression of TbIF1 in BF cells proved lethal as the indispensable Δψm collapsed due to inhibited F_oF_1-ATPase. In summary, we provide evidence that *T. brucei* harbors a natural and potent unidirectional inhibitor of the vital F_oF_1-ATPase activity that can be exploited for future structure-based drug design.

Author summary

Enzymes are catalysts that drive both a forward and reverse chemical reaction depending on the thermodynamic properties. F_oF_1-ATP synthase is a multiprotein enzyme that under normal physiological conditions generates ATP. However, when respiration is impeded, this rotary molecular machine reverses and hydrolyzes ATP to pump protons and maintain the essential mitochondrial membrane potential. While this activity is

Republic. The funders had no role in study design, data collection and analysis, decision to publish, or preparation of the manuscript

Competing interests: The authors have declared that no competing interests exist.

exceptional in most eukaryotic cells, the unique composition of the *Trypanosoma brucei* mitochondrion dictates that the infectious stage of this human parasite is utterly dependent on the hydrolytic activity of F_oF_1-ATPase. While searching for better chemotherapeutics against Human African Trypanosomiasis, several trypanocidal compounds were determined to interact with this enzyme, but they indiscriminately inhibit both the ATP hydrolytic and synthetic activities. A more promising approach involves the conserved eukaryotic protein IF1, a unidirectional inhibitor that prevents just ATP hydrolysis. Auspiciously, we identified this protein homolog in *T. brucei* (TbIF1) and its expression is tightly regulated between life stages of the parasite. Importantly, the introduction of exogenous TbIF1 protein specifically inhibits F_oF_1-ATPase and is lethal for the infectious stage of *T. brucei*. Therefore, we have identified a natural inhibitor of an essential and druggable enzyme that can be exploited for future structure-based drug design.

Introduction

Trypanosoma brucei rhodesiense and *T. b. gambiense* are the flagellated protists responsible for Human African Trypanosomiasis in 36 sub-Saharan African countries where the tsetse fly insect vector resides. While vector control projects have greatly reduced the number of new cases (<3,000 annually) since the last epidemic subsided in the late 1990's, an alarming number of these extracellular parasites are demonstrating resistance to current drugs that already possess efficacy and toxicity problems, in addition to their complex treatment regimens. Furthermore, salivarian *Trypanosoma* species (e.g. *T. b. brucei*, *T. vivax*, *T. congolense*) cause disease in livestock, namely nagana in cattle, which inflict substantial economic burdens in rural areas where agricultural development is a necessity. For these reasons, there is a renewed urgency to develop a new generation of therapeutics based upon the unique *T. brucei* biological processes that have already been characterized [1].

A striking feature of *T. brucei* is the ability to rapidly adapt its metabolism while alternating between the glucose-rich blood of a mammalian host and the abundant proline found in the hemolymph and tissue fluids of the blood-feeding tsetse fly [2,3]. These different carbon sources dictate a shift in bioenergetics that manifests in the unique architecture and activities of the singular mitochondrion. The *T. brucei* insect stage or procyclic form (PF) utilizes a branched mitochondrion that is fully developed: composed of many cristae, eight Krebs cycle enzymes used for both anabolic and catabolic reactions in a partitioned cycle and respiratory chain complexes I, II, III and IV [4]. The enzymatic complexes III and IV pump protons into the mitochondrial (mt) intermembrane space, generating a membrane potential ($\Delta\psi m$) that is coupled to ATP production by the F_oF_1-ATP synthase [5,6]. This rotary molecular machine converts the potential energy of the proton gradient into the chemical energy of ATP when protons are allowed to flow down their energy gradient by passing through the proton pore located in the membrane-embedded F_o domain. This action drives the rotation of the asymmetrical central stalk within the matrix protruding F_1 catalytic domain, which undergoes three sequential conformational states that result in the synthesis of ATP.

In contrast, the streamlined mitochondrion of the mammalian bloodstream form (BF) lacks a functional cytochrome *c* mediated respiratory chain and the parasite must rely on glycolysis to provide sufficient energy for all of the cellular processes occurring during this life stage [7]. Although BF cells have a reduced mitochondrion, it still harbors vital processes like Fe-S cluster assembly, mt fatty acid synthesis, acetate production, Ca^{2+} homeostasis and RNA editing [8–11]. These functions are performed by proteins that are encoded in the nuclear

genome and imported into the mitochondrion, a process that absolutely requires a Δψm [12]. Since respiratory complexes III and IV are absent in BF trypanosomes, the Δψm is maintained by the reverse activity of F_oF_1-ATP synthase, which hydrolyzes ATP and translocates protons into the mt intermembrane space [13]. This ATPase activity is also essential for dyskinetoplastic (Dk) trypanosomes (i.e. *T. b. evansi*, *T. b. equiperdum*), which lack all or critical portions of their mt DNA [14]. Without a full complement of mt DNA, these parasites do not express the F_oF_1-ATPase subunit a, a critical component of the proton pore. Thus, dyskinetoplastic strains have acquired one of several different compensatory mutations that enables the catalytic F_1-ATPase to energize the inner mt membrane by coupling ATP hydrolysis with the electrogenic exchange of ADP^{3-} for ATP^{4-} by the ATP/ADP carrier (AAC) [15,16].

While this ATP hydrolase activity must be unrelenting in these infectious trypanosomes, it is only observed under specific conditions in other eukaryotes (i.e. during oxygen deprivation or in response to damaged mt respiratory chain complexes). On the rare occasion that mt respiration becomes compromised and the Δψm collapses, the rotation of F_oF_1-ATP synthase reverses and acts as an ATP-consuming proton pump. However, this unrestrained hydrolysis of ATP replenishes the Δψm so inefficiently, that it actually accelerates cell death due to the depletion of ATP [17]. Thus, specific F_oF_1-ATPase small molecule inhibitors are currently being developed to prevent human tissue damage during ischemia [18].

Intriguingly, eukaryotic cells already possess a specific inhibitor of the F_1-ATPase activity in the form of a nuclear encoded small protein, inhibitory factor 1 (IF1) [19]. The IF1 protein is highly conserved throughout evolution, with homologs found in plants, yeast, worms and vertebrates [19–22]. Since its discovery, many details have been gleaned about the molecular mechanism responsible for the interaction of IF1 with F_1-ATPase [23,24]. *In vitro*, this protein effectively inhibits the intact F_oF_1-ATPase from hydrolyzing ATP, but in the presence of a proton gradient, IF1 is not able to impede ATP synthesis [25]. Hence, unlike most other inhibitors, IF1 is a unidirectional inhibitor that only blocks the ATP hydrolytic activity of the F_oF_1-ATP synthase. *In vivo*, the activity of IF1 is dependent upon the acidification of the mt matrix, which occurs when mt respiration is compromised. Thus, it has been assumed that the physiological role of IF1 is to act as an emergency brake that prevents the futile hydrolysis of ATP by the F_oF_1-ATPase [26,27]. However, recent studies have suggested that IF1 can also play a role in the metabolic reprogramming observed during cellular differentiation and in some types of cancer [28,29].

Due to the ability of IF1 to inhibit the hydrolytic activity of F_oF_1-ATPase and its potential to selectively impact the viability of the infectious stage of *T. brucei*, we identified the IF1 homolog in this human pathogen and characterized its effect on the cellular growth and mt physiology in both parasitic life stages.

Methods

Plasmid preparation

The TbIF1 (Tb927.10.2970) RNAi construct, which targets all 345 bp of the mRNA coding sequence, was generated with a PCR product amplified from *T. brucei* strain 427 genomic DNA with the following oligonucleotides: Fw—CAC AAG CTT ATG CTG CCC CTC CGT GT, Rev—CAC CTC GAG TTG CTT CTC GTT CGT TAA C. Utilizing HindIII and XhoI restriction sites inherent in the primers (underlined), this fragment was cloned into the pZJM plasmid [30], which contains head-to-head, tetracycline (tet)-regulated T7 promoters. For the tet inducible expression of an ectopic TbIF1 fused with a C-terminal 3x V5 tag, the TbIF1 open reading frame was PCR amplified (Fw: ACA AAG CTT ATG C GC CGT GTA TC, Rev:

CAC GGA TCC TTG CTT CTC GTT CGT TAA C) and cloned into the pT7_V5 vector using HindIII and BamHI restriction enzymes [31].

Trypanosoma culture conditions and generation of cell lines

The wildtype PF *T. brucei* Lister 427 strain and tet-inducible PF 29–13 cells were grown *in vitro* at 27˚C in SDM-79 medium containing hemin (7.5 mg/ml) and 10% fetal bovine serum (FBS) [32]. Meanwhile, the following cultures were maintained at 37˚C with 5% CO_2 in HMI-9 media containing 10% FBS: wildtype BF *T. brucei* Lister 427, the derived BF single marker (SM) strain [32], laboratory induced dyskinetoplastic *T. brucei* Dk164 [33] and genetically modified Dk *T. b. evansi* cells [34]. The PF 29–13, BF SM and *T. b. evansi* cell lines constitutively express the ectopic bacteriophage T7 RNA polymerase and the prokaryotic tet repressor, which allows for the tet inducible expression of either ectopic V5-tagged proteins or dsRNA. As described previously [32], the appropriate cells were then transfected with NotI linearized pZJM or pT7_V5 plasmids containing the TbIF1 gene. Both plasmids were targeted to the rDNA intergenic spacer region. The addition of 1 μg/ml of tet into the media triggers either the induction of RNAi or the expression of tagged TbIF1. Throughout the analyses, a Z2 Cell Counter (Beckman Coulter Inc.) was used to measure cell densities in order to maintain the cultures within their exponential mid-log growth phase of $1x10^6$ to $1x10^7$ cells/ml for PF and between $1x10^5$ to $1x10^6$ cells/ml for BF cells.

SDS-PAGE and western blot

Protein samples were separated on SDS-PAGE, blotted onto a PVDF membrane (PALL) and probed with the appropriate monoclonal (mAb) or polyclonal (pAb) antibody. This was followed by incubation with a secondary HRP-conjugated anti-rabbit or anti-mouse antibody (1:2000, BioRad). Proteins were visualized using an ECL system (Biorad) on a ChemiDoc instrument (BioRad). The PageRuler prestained protein standard (Fermentas) was used to determine the size of detected bands. Primary antibodies used in this study were: mAb anti-V5 epitope tag (1:2000, Invitrogen), mAb anti-mtHsp70 (1:2000), pAb anti-APRT (1:1000). Native TbIF1 antigen was purified (see below) and was sent to Davids Biotechnologie (Regensburg, Germany) to produce a polyclonal antiserum (1:1000).

Digitonin subcellular fractionation

Whole cell lysates (WCL) were prepared from *T. brucei* PF 29–13 and PF 29–13 cells with an ectopic V5-tagged TbIF1 that were either induced for 48 hours or never induced. SoTe/digitonin fractionation was performed as follows: $1x10^8$ cells were harvested by centrifugation, washed in PBS-G, resuspended in 500μl SoTE (0.6 M Sorbitol, 2 mM EDTA, 20 mM Tris-HCl pH 7.5) and lysed with 500μl SoTE containing 0.03% digitonin. The cells were then incubated on ice for 5 minutes before centrifugation (4˚C, 7000 rpm, 3 min). This allowed us to separate the supernatant, consisting of the cytosolic subcellular fraction (CYTO), from the pellet, which represents the organellar fraction (ORG) of the parasite. These enriched fractions along with WCL were resolved by SDS-PAGE and analyzed by immunoblotting.

Immunofluorescence assay

T. brucei subcellular localization of the overexpressed TbIF1 V5-tagged protein was determined by an immunofluorescence assay that amplified the signal of a monoclonal anti-V5 antibody (Life Technologies) with a FITC-conjugated secondary anti-mouse antibody (Sigma). Co-localization was verified using Mitotracker RED (Invitrogen), a dye that stains

mitochondria in live cells and is well-retained after fixation. DAPI (4,6-diamidino-2-phenylindole; Sigma) treatment was used to visualize nuclear and mitochondrial DNA. The images of the stained cells and their fluorescence were captured with a Zeiss Axioplan 2 fluorescence microscope.

In situ Δψm measurement

Estimation of the Δψm *in situ* was done spectrofluorometrically using the indicating dye safranine O (Sigma). *T. brucei* PF cells ($2x10^7$ cells/ml) were resuspended in a reaction buffer containing: 200 mM sucrose, 10 mM HEPES-Na (pH 7.0), 2 mM succinate, 1 mM $MgCl_2$, 1 mM EGTA and 1 mM ATP. The reaction was activated with digitonin (50 μM), while NaCN (50 μM), oligomycin (2.5 μg/ml) and FCCP (5 μM) were injected at specific time points throughout the assay. Changes in the amount of fluorescence over time were detected on an Infinite M200 microplate reader (TECAN) (excitation = 496 nm; emission = 586 nm). Values were normalized according the following equation: normalized $(e_i) = \frac{e_i - E_{min}}{E_{max} - E_{min}}$

E_{min}—the minimum value for variable E

E_{max}—the maximum value for variable E

In vivo Δψm measurement

The Δψm was determined by utilizing the red-orange fluorescent stain tetramethylrhodamine ethyl ester (TMRE, Life Technologies). PF and BF cells maintained within their exponential growth phase were stained with 60 nM of the dye for 30 min at 27˚C or 37˚C, respectively. Cells were pelleted (1300 g, 10 min, RT), resuspended in 2 ml of PBS (pH 7.4) and immediately analyzed by flow cytometry (BD FACS Canto II Instrument). For each sample, 10000 events were collected. Treatment with the protonophore FCCP (20 μM) was used as a control for mt membrane depolarization. Data were evaluated using BD FACSDiva (BD Company) software.

ATPase assays

The ATPase activity was measured by two different methods. The first assay utilizes the Sumner reagent to detect the release of free phosphate when ATP is hydrolysed [35]. Briefly, crude mt lysates were obtained from $2x10^8$ cells by SoTe/digitonin extraction (0.015% digitonin, 0.6 M Sorbitol, 2 mM EDTA, 20 mM Tris-HCl pH 7.5). Mt pellets were resuspended in an assay buffer (200 mM KCl, 2 mM $MgCl_2$, Tris-HCl pH 8.0) and the addition of ATP to a final concentration of 5 mM initiated the 20 min reaction. Where indicated, samples were pre-treated with the F_1-ATPase specific inhibitor sodium azide (2 mM) for 10 min. The 100 μl enzymatic reactions were deproteinated by adding 1.9 μl of 70% perchloric acid. After a 30 min incubation on ice, the samples were spun down (16000g, 10 min, 4˚C) and 90 μl of the supernatant was incubated for 10 min with 0.5 ml of the Sumner reagent (8.8% $FeSO_4.7H_2O$, 375 mM H_2SO_4, 6.6% $(NH_4)Mo_7O_{24}.4H_2O$). 200 μl was then transferred to a 96 well plate and the absorbance was measured at 610 nm using a microplate reader (Infinite M200Pro, Tecan). To calibrate the assay, a standard curve was calculated from the absorbance values of linear inorganic phosphate samples (0–2 mM).

The ATPase activity was also measured spectrophotometrically by an ATP regenerating assay [36], wherein the hydrolysis of ATP is determined indirectly by coupling this activity to the oxidation of NADH by lactate dehydrogenase, resulting in a quantifiable decrease in the absorbance of NADH at 340 nm. The assay mixture contained 15 μg of purified mitochondria lysed with 1% dodecyl maltoside, 50 mM Tris-HCl (or 50 mM MOPS-NaOH for pH values under 7.0), 50 mM KCl, 2 mM $MgSO_4$, 0.2 mM NADH, 2 mM ATP, 1 mM phosphoenolpyruvate (PEP), 5 μl/ml

pyruvate kinase from rabbit muscle (PK; Sigma-Aldrich) and 5 μl/ml lactate dehydrogenase from bovine heart (LDH; Sigma-Aldrich). All measurements were performed in 1 ml spectroscopic cuvettes with the reaction mixture incubated at 37˚C.

ATP production assay

ATP production was measured as described previously [37,38]. Briefly, crude mt preparations from PF cells were obtained by digitonin extraction. ATP production was then activated by adding the oxidative phosphorylation substrates ADP (67 μM) and succinate (5 mM). The resulting concentrations of ATP were determined by using the ATP Bioluminescence Assay Kit HS II (Roche) and a microplate luminometer (Orion II). To determine how much of the synthesized ATP was due to oxidative phosphorylation, specific inhibitors against succinate dehydrogenase (6.7 mM malonate) and the ADP/ATP carrier (33 ug/ml atractyloside) were incubated with the enriched mitochondria samples for 10 min on ice prior to the start of the assay.

Cloning, expression, and purification of recombinant TbIF1

The gene fragment encoding TbIF1 without its predicted mt localization signal and stop codon was PCR amplified from PF *T. brucei* strain 427 genomic DNA with forward and reverse primers containing *Nde*I and *Hind*III restriction sites, respectively. The 3'-terminal primer included sequence encoding a hexahistidine tag. The digested PCR products were then ligated into the *Nde*I/*Hind*III linearized expression vector pRUN [39]. The verified plasmid was used to transform the *Escherichia coli* expression strain C41(DE3) [40], which was grown in LB medium. When the OD_{600} reached ~ 0.4, the expression of the recombinant protein (rTbIF1) was induced by the addition of 1 mM IPTG. After three hours, the cells were harvested, washed in PBS and resuspended in ice-cold buffer A (20 mM Tris-HCl pH 7.4, 10% (w/v) glycerol, 100 mM NaCl, 25 mM imidazole) supplemented with the complete EDTA-free protease inhibitor cocktail (Roche). The bacteria were then lysed with lysozyme (75 μg/ml) for 30 min at 4˚C in the presence of DNase I (15 U/ml). The lysate was sonicated (5 x 20 s with 1 min on ice between pulses), cleared by centrifugation (15000 g, 30 min, 4˚C), filtered through a syringe filter (0.45 μm) and loaded onto a HisTrap nickel affinity column using the Akta-Prime chromatography system (GE Healthcare). The column was thoroughly washed with buffer A before the rTbIF1 protein was eluted with a 50 ml linear gradient of buffer A containing imidazole ranging from 20 to 500 mM. SDS-PAGE analysis identified the fractions containing rTbIF1, which were pooled and dialyzed against 20 mM Tris-HCl pH 7.4 and 10% glycerol. Finally, the purified protein was concentrated to 10–20 mg/ml (PES, MWCO 3.5 kDa, Sartorius, Germany), flash-frozen in liquid N_2 and stored at -80˚C.

Results

T. brucei genome contains an IF1 homolog

IF1 is widespread throughout the eukaryotic kingdom, with homologs found in plants, yeast, worms and vertebrates. To search for a *T. brucei* IF1 homolog within the TriTrypDB database (www.tritrypdb.org), we employed a reciprocal blastp search using the yeast inhibitory protein Inh1 and bovine IF1. The putative candidates were further analyzed using HHpred toolkit (http://toolkit.tuebingen.mpg.de), a program based on the comparison of hidden Markov models that utilize structure prediction to identify homologous relationships. These analyses revealed that only the translated product of the candidate gene Tb927.10.2970 (TbIF1) truly resembled yeast Inh1 and bovine IF1. TbIF1 is annotated as a conserved hypothetical protein with a calculated molecular mass of 13.8 kDa, which includes the 23 N-terminal residues

predicted by Mitoprot II [41] to comprise the mt targeting sequence. A MAFFT alignment with IF1 proteins from different organisms depicts a conserved region within TbIF1 (residues 17–52) that corresponds to the minimal inhibitory domain of its bovine ortholog [42] (Fig 1). The identity and similarity of this entire bovine minimal inhibitory sequence with the putative TbIF1 is only 26% and 45%, respectively. These metrics are even less pronounced when comparing the C-terminal region, which has been characterized as a oligomerization domain in the bovine IF1 that regulates activity of the inhibitor [43].

TbIF1 localizes to the PF mitochondrion, but is not expressed in cells dependent on F_1-ATPase activity

To experimentally characterize this putative inhibitory peptide, we first determined its expression in cultured wildtype *T. brucei* Lister PF427 and BF427 strains and in the laboratory-induced dyskinetoplastic Dk164 *T. brucei* cells. Whole cell lysates harvested from an equivalent number of PF427, BF427 and Dk164 cells were resolved by SDS-PAGE and analyzed by western blot using a specific polyclonal antiserum raised against TbIF1 (Fig 2A). While there was robust TbIF1 expression in PF427 cells, this signal was not detected in the whole cell lysates from BF427 and Dk164 cells. Since we have previously observed that the expression of a purine salvage protein, adenine phosphoribosyl transferase (APRT), does not vary between the trypanosome life stages [46], it was used as a loading control (Fig 2A). These results suggest that one facet of regulating TbIF1 activity includes protein expression levels, since the inhibition of the F_1-ATPase would be lethal for BF and Dk cells.

To determine the localization of TbIF1, we used PF 29–13 and PF TbIF1 overexpressing (OE) cell line capable of regulating the expression of an ectopic TbIF1 gene product that contained a C-terminal V5-tag. The cytosolic and organellar fractions were isolated from these cells after they were permeabilized with 0.015% digitonin. The subsequent western analyses established the purity of the extracted fractions as the cytosolic APRT and mtHsp70 protein were confined within their respective subcellular fractions. Notably, the endogenous TbIF1 (12 kDa) and its V5-tagged version (17 kDa) were exclusively localized in the organellar fraction (Fig 2B). Furthermore, immunofluorescence assays with either polyclonal TbIF1 antiserum or a monoclonal V5 antibody demonstrated colocalization with the mitochondrion-specific dye, Mitotracker RED CMXRos, which illuminates the typical reticulated structure of a procyclic mitochondrion (Fig 2C).

Neither TbIF1 silencing nor overexpression produces a negative effect on PF *T. brucei* cell growth

Due to the expression pattern of TbIF1, we first evaluated its importance in the PF life stage of *T. brucei*. In addition to the PF TbIF1 OE cell line, we also created PF cells that silence TbIF1

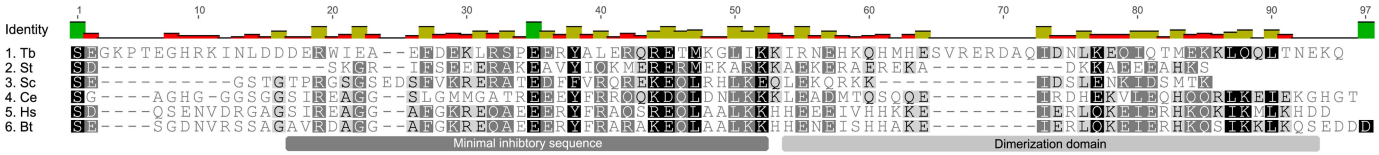

Fig 1. TbIF1 shares homology with IF1 proteins from various model organisms. Using the alignment program MAFFT, the amino acid sequence of IF1 from *T. brucei* (Tb) is compared to those of *Solanum tuberosum* (St, [20]), *Saccharomyces cerevisiase* (Sc, [22]), *Caenorhabditis elegans* (Ce, [21]), *Human sapiens* (Hs, [44]) and *Bos taurus* (Bs, [19]) IF1s. Identical and conservatively substituted resides are shaded in black and grey, respectively. Predicted mt import signal sequences were removed from each coding sequence prior to the analysis. The minimal inhibitory sequence [42] and dimerization domain of bovine IF1[45] are indicated. The green, yellow, and red bars above the alignment indicate when the nucleotides at each position have identities of 100%, between 100% and 30%, and <30%, respectively.

https://doi.org/10.1371/journal.pntd.0005552.g001

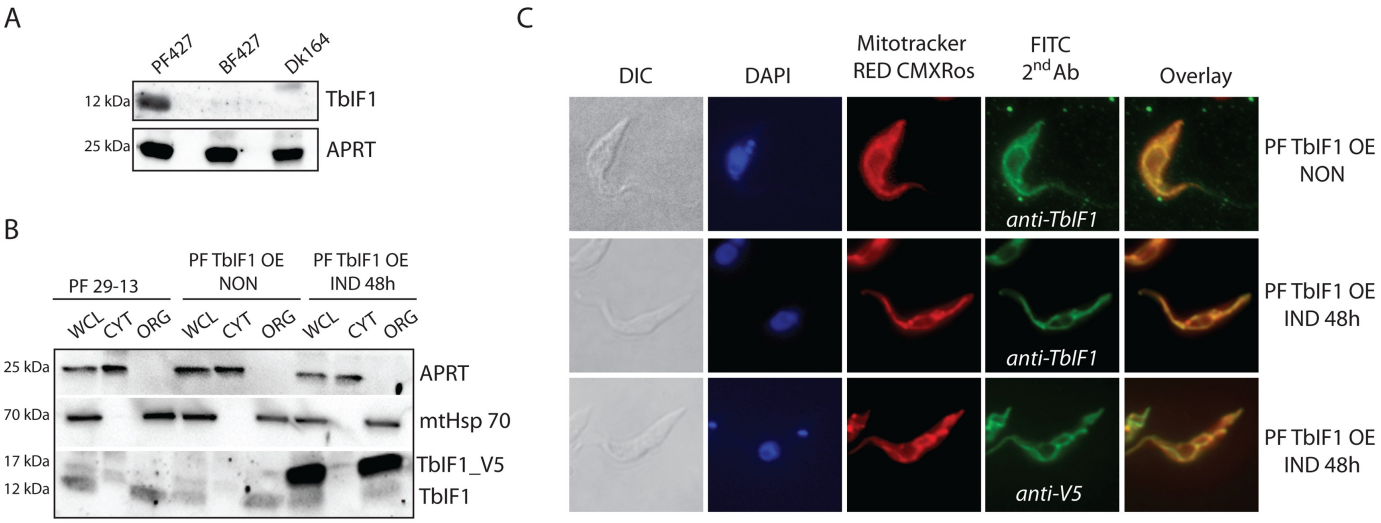

Fig 2. TbIF1 expression is only detected in PF *T. brucei*, where it is localized to the mitochondrion. (A) The steady state abundance of TbIF1 was determined in *T. brucei* PF427, BF427 and Dk164 whole cell lysates by western blot analysis using a specific polyclonal anti-TbIF1 antiserum. An anti-APRT1 antiserum was used to estimate equal protein loading on SDS-PAGE. The molecular weight of the detected proteins is indicated on the left. (B) TbIF1 subcellular localization was determined in PF 29–13 and PF TbIF1 OE cells either noninduced (NON) or expressing V5-tagged TbIF1 for 48 hours (IND 48h). Whole cell lysates (WCL) and digitonin extracted cytosolic (CYT) and organellar (ORG) fractions were analyzed by immunoblot with the following antibodies: anti-APRT (cytosol), anti-mtHsp70 (organellar fraction), anti-V5 and anti-TbIF1. (C) Immunofluorescence assays with a fluorescein isothiocyanate (FITC)-conjugated secondary antibody that recognizes primary antibodies detecting either all TbIF1 variants (anti-TbIF1) or just the ectopic V5-tagged TbIF1 (anti-V5) further verify that the protein is targeted to the mitochondrion in PF TbIF1 OE cells induced for 48 hours (IND 48h). Noninduced (NON) PF TbIF1 OE cells were included as a control, while the DNA contents and single reticulated mitochondrion were visualized using DAPI (4,6-diamidino-2-phenylindole) and MitoTracker Red CMXRos staining, respectively. The overall cell morphology is depicted in the differential interference contrast (DIC) microscopy images.

https://doi.org/10.1371/journal.pntd.0005552.g002

expression by RNA interference (TbIF1 RNAi). Neither the knockdown of endogenous TbIF1 nor the overexpression of its V5-tagged version resulted in a significant growth phenotype (Fig 3A and 3B). This indicates that TbIF1 is not essential under regular *in vitro* growth conditions and its overexpression doesn't have a negative effect on PF vitality. The knockdown of TbIF1 was confirmed by western blot analysis of whole cell lysates from TbIF1 RNAi cells that were induced throughout the RNAi time course or never induced (Fig 3C). The polyclonal TbIF1 antiserum revealed a 59% and 73% reduction of the targeted protein on day 1 and 2 of tet addition, respectively (Fig 3C). The partial recovery of the TbIF1 abundance levels on day 4 (35%) might be due to the emergence of RNAi revertants, which is a commonly observed phenomena in *T. brucei* cells [47]. Whole cell lysates from PF TbIF1 OE noninduced and induced cells were also analyzed by the same method to confirm the overexpression of the TbIF1-V5 protein (Fig 3D). A polyclonal TbIF1 antiserum detected endogenous TbIF1 in all protein samples, while the ectopic V5-tagged TbIF1 was detected only in tet induced WCL. Bio-Rad TGX stain-free precast gel technology demonstrated comparable loading between samples. Scanning densitometry was then employed to quantify the ratio between ectopic and endogenous TbIF1 in each sample, revealing that protein induction resulted in 1.8 times more V5-tagged TbIF1 on day 1 and up to 6.6 times more on day 4 (Fig 3D).

TbIF1 prevents the F_oF_1-ATPase from establishing a modified Δψm when respiration is chemically inhibited

Since TbIF1 expression levels don't affect the growth rate of PF *T. brucei* grown under normal culture conditions, we sought to characterize the function of TbIF1 when the cells were

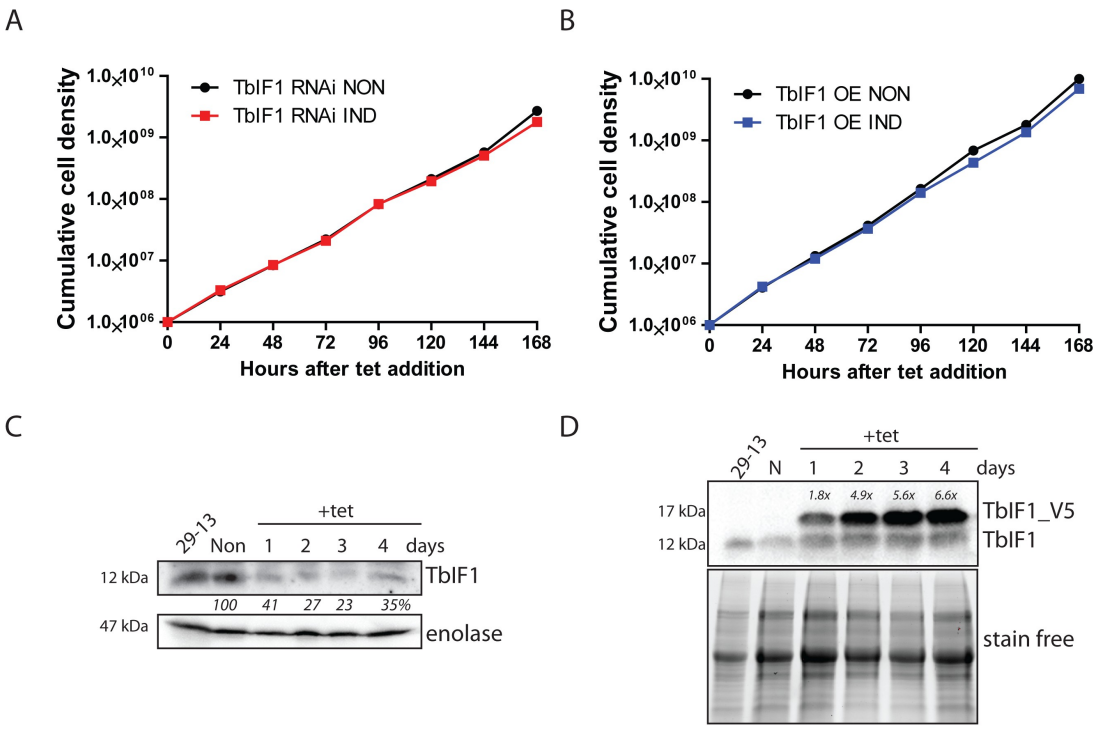

Fig 3. Neither TbIF1 silencing nor overexpression are harmful to PF *T. brucei* cells grown *in vitro*. (A) TbIF1 RNAi noninduced (NON) and induced (IND) cells were maintained in the exponential growth phase (between 10^6 and 10^7 cells/ml) and the cumulative cell number represents the normalization of cell densities by factoring in the daily dilution factor. The figure is representative of three independent RNAi inductions. B) The growth rate of cells either induced (IND) or noninduced (NON) for TbIF1 OE were determined in the same manner as in A. C) The steady-state abundance of TbIF1 in the parental cell line (29–13), TbIF1 RNAi noninduced (NON) and cells induced (IND) with tet for 1, 2, 3 and 4 days was determined by western blot analysis using a specific TbIF1 antiserum. Cytosolic enolase served as a loading control. The numbers depicted underneath the top panel represent the abundance of immunodetected protein as a percentage of the noninduced samples after normalizing to the loading control. D) Ectopic V5-tagged TbIF1 expression was confirmed by western blot analysis using whole cell lysates from PF 29–13, noninduced (NON) TbIF1 OE and cells induced (IND) for 1, 2, 3 and 4 days. The endogenous TbIF1 and the V5-tagged ectopic protein were visualized using a polyclonal TbIF1 antiserum. Comparable loading was confirmed by Bio-Rad TGX stain-free technology. Levels of V5-tagged TbIF1 overexpression as compared to the endogenous TbIF1 are indicated at the top of the immunoblot.

https://doi.org/10.1371/journal.pntd.0005552.g003

stressed by chemical hypoxia. While the Δψm in this life stage is normally maintained by the typical cytochrome-containing respiratory complexes III and IV, we wanted to determine if the rotation of the rotary F_oF_1 complex can be reversed to maintain the Δψm once the respiratory chain is inhibited. Therefore, we estimated the Δψm in digitonin permeabilized PF *T. brucei* cells by utilizing the dye safranin O, a lipophilic cationic dye whose fluorescence becomes quenched when it accumulates within energized mitochondria [48]. The addition of sodium cyanide (NaCN), a potent inhibitor of the respiratory chain, causes the Δψm to dissipate at a rate determined by the speed of a proton leak opposed to the reverse activity of F_oF_1-ATP synthase. Under these conditions, we could examine the impact of TbIF1 on this proton-pumping enzyme by observing the changes in these rates when TbIF1 is depleted.

The parental 29–13 PF trypanosomes served as a positive control to establish the rate of safranine O quenching by energized mitochondria. A baseline for the rapid Δψm depolarization was established when NaCN was injected into the same sample (Fig 4A, black line). Finally, the addition of FCCP, a proton uncoupler, caused the Δψm to completely collapse. A similar pattern depicting the depolarization of the Δψm was observed for TbIF1 RNAi noninduced

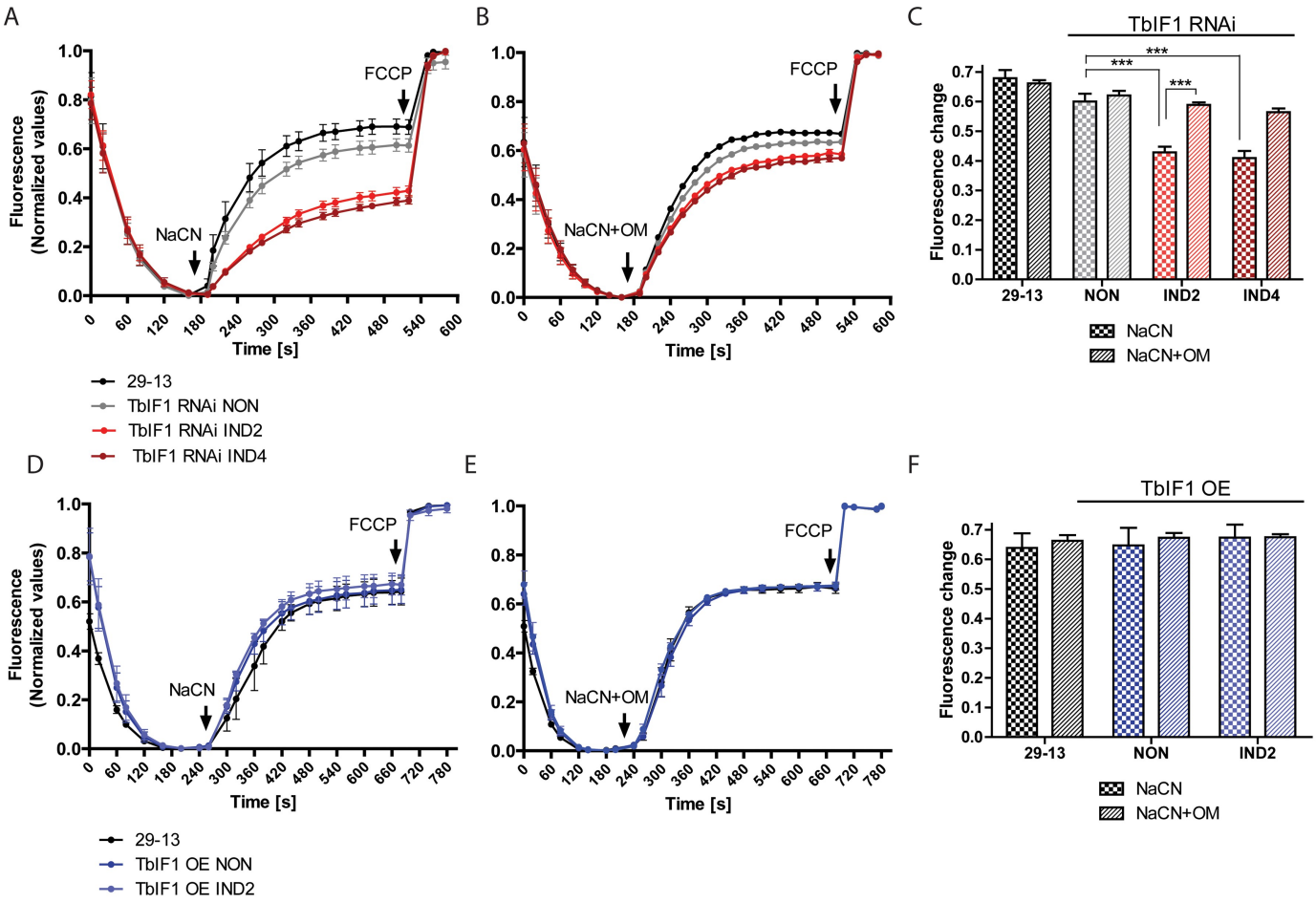

Fig 4. Upon chemical inhibition of respiration, TbIF1 prevents the establishment of a new F_oF_1-ATPase mediated Δψm. (A) and (D) The *in situ* dissipation of the Δψm in response to chemical treatment by NaCN was measured using the safranine O dye in the following cell lines: 29–13 (black line), TbIF1 RNAi noninduced (NON, grey line), TbIF1 RNAi induced for 2 and 4 days (IND2 and IND4, red lines), TbIF1 OE noninduced (NON, dark blue line) and TbIF1 OE induced for 2 days (IND2, light blue line). The reaction was initiated with digitonin (50 μM), whereas NaCN (50 μM) and FCCP (20 μM) were added when indicated. (means ± s.d.; n = 3). (B) and (E) The assay described for (A) and (D) was used to observe the dissipation of the Δψm when the same cells were simultaneously treated with 50 μM NaCN and 2.5 μg/ml oligomycin (NaCN+OM). (means ± s.d.; n = 3). (C) and (F) Changes in safranine O fluorescence after the addition of either NaCN or NaCN+OM to the cell lines outlined above. *** $p < 0.0002$, Student's *t* test.

https://doi.org/10.1371/journal.pntd.0005552.g004

cells. However, the extent of the Δψm depolarization was significantly smaller in TbIF1 RNAi cells induced for 2 and 4 days. The resulting Δψm was sustained at a new steady state, which is most likely attributable to the F_oF_1-ATPase activity (Fig 4A, red lines and Fig 4C). To confirm that the proton-pumping activity of this complex was indeed responsible for this phenotype, 29–13 cells and TbIF1 RNAi noninduced and tet induced cells were permeabilized, allowed to establish a Δψm and then treated with a mixture of NaCN and oligomycin, an inhibitor of F_oF_1-ATP synthase. Under these conditions, there were no significant differences observed between the Δψm depolarization rates of these samples (Fig 4B and 4C). These data validate that TbIF1 functions to prevent the reversal of F_oF_1-ATP synthase and limit ATP hydrolysis when respiration is disrupted in the parasite.

In a study involving mammalian cells [27], it was presented that the extent of the Δψm depolarization is even greater in cells overexpressing IF1. However, we did not observe this outcome as the rate of the Δψm dissipation remained similar upon NaCN treatment, with or

without oligomycin, when we compared either noninduced or induced PF TbIF1 OE cells with the parental line (Fig 4D–4F). This suggests that the abundance of endogenous TbIF1 is sufficient to inhibit the mitochondrial levels of F_oF_1-ATPase and thus avert the depletion of ATP under chemically induced hypoxic conditions.

Overexpression of TbIF1 in PF *T. brucei* cells affects the total ATPase activity but not ATP production

Numerous studies demonstrate that yeast and bovine IF1 is a unidirectional inhibitor that impedes the F_oF_1-ATPase direction of rotation without hindering the ATP synthesis activity of this complex [25]. Employing the PF TbIF1 OE cell line again, we were able to determine if this unique attribute also applies to *T. brucei* cells. The total ATPase activity in mt lysates was indirectly measured by spectrophotometrically detecting the inorganic phosphate that is released during the hydrolysis of ATP by ubiquitous ATPases. Azide (1 mM) and oligomycin (2.5 μg/ml) were used to discern the proportion of the detected ATPase activity that is attributed to F_oF_1-ATPase, which typically represents ~ 35–45% of total mt ATPase activity. Importantly, the overexpression of TbIF1 for 2 days resulted in decreased values of total ATPase activity that are comparable to the levels obtained when noninduced TbIF1 OE cells are treated with inhibitors of the rotary enzyme (Fig 5A). Furthermore, since the addition of either azide or oligomycin to samples containing overexpressed TbIF1 doesn't augment the phenotype, it indicates that TbIF1 specifically inhibits F_oF_1-ATPase (Fig 5A).

To assess the potential impact of TbIF1 on the traditional activity of F_oF_1-ATP synthase, we examined the ability of the same isolated mitochondria to produce ATP by oxidative phosphorylation. When incubated in a buffer containing ADP, free phosphate and the electron donor succinate, the mitochondria become energized and activate the oxidative phosphorylation pathway to produce ATP, which can be subsequently measured using a bioluminescent substrate. A comparison of the detected ATP levels between noninduced and induced TbIF1 OE cells revealed no major differences in the amount of ATP synthesized (Fig 5B). Additional controls containing malonate and atractyloside, the respective inhibitors of succinate dehydrogenase and the ADP/ATP translocator, were included to verify that the measured ATP truly resulted from oxidative phosphorylation. To define the baseline ATP levels produced from any of the remaining endogenous ADP molecules, a set of samples contained no additional ADP (Fig 5B). Altogether, it seems that under these conditions and elevated expression levels, TbIF1 is only a unidirectional inhibitor that prevents ATP hydrolysis, but does not interfere with ATP synthesis by F_oF_1-ATP synthase.

Overexpression of TbIF1 is lethal to BF and Dk cells

While TbIF1 overexpression does not impair PF growth rate, a quite different outcome was anticipated in BF and Dk cells, since their survival depends on ATP hydrolysis by F_oF_1-ATPase to generate the essential $\Delta\psi m$. Indeed, the induced expression of TbIF1 proved to be deleterious to BF and Dk cells, with a strong growth phenotype detected within the first 24 hours of adding tet (Fig 6A and 6B). Interestingly, the V5-tagged TbIF1 was at first not detectable when only whole cell lysates were analyzed by western blot. Thus, an anti-V5 mouse antibody was used to immunoprecipitate the tagged TbIF1, which was then immunodecorated with a TbIF1 rabbit antiserum. This enrichment allowed us to load approximately 40 times more antigen and confirm that very low levels of TbIF1-V5 were expressed upon tet induction (Fig 6C and 6D). Possibly, TbIF1 is so toxic that only cells harbouring a mutation for minimal ectopic expression were selected from the transfection population.

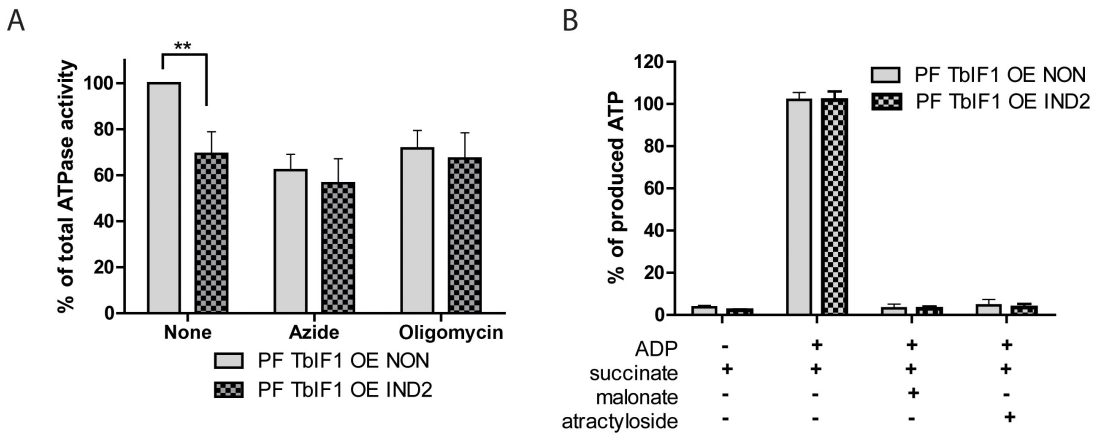

Fig 5. TbIF1 functions as a unidirectional inhibitor of *T. brucei* F_oF_1-ATP synthase. (A) Total ATPase activity was measured in TbIF1 OE cells that were noninduced (grey) or induced for 2 days with tet (grey cross-hatch). To define the contribution of F_oF_1-ATPase to the total ATPase activity measured, samples were also incubated with either azide (AZ, 1 mM) or oligomycin (OM, 2.5 μg/ml). The total amount of free-phosphate detected in the untreated noninduced sample was set at 100%. (means ± s.d.; n = 3; ** $p < 0.001$; Student's *t* test). (B) The amount of ATP synthesized by oxidative phosphorylation was measured in the digitonin-extracted mitochondria from both noninduced (NON) TbIF1 OE cells and cells induced for 2 days (IND2). The reaction was started by the addition of succinate and ADP. Malonate (mal.) and atractyloside (atract.) were added as specific inhibitors of succinate dehydrogenase and the ATP/ADP carrier, respectively.

https://doi.org/10.1371/journal.pntd.0005552.g005

TbIF1 diminishes the mt Δψm by inhibiting F_1-ATPase activity in BF and Dk cells

To determine if the overexpressed TbIF1 functioned as expected, the *in vivo* Δψm was measured in these verified cell lines. Flow cytometry analyses measured the changes observed in BF and Dk TbIF1 OE noninduced and induced cells stained with TMRE, whose fluorescence intensity is proportionally dependent on the magnitude of the membrane polarization. After only 4 hours of tet induction, there was already a substantial Δψm decrease (by 73%) in the BF TbIF1 OE cell population that remained low throughout the course of the experiment (Fig 6E). Intriguingly, while the Δψm of the Dk TbIF1 OE cells eventually diminished to similar levels (64% decrease) by 24 hours of TbIF1 expression, the observed decline was more gradual (Fig 6F). This phenotypic pattern might reflect the contrasting contributions of the F_oF_1-ATPase to the Δψm in BF and Dk mitochondria. Whereas this molecular machine in BF cells can translocate approximately three protons from the hydrolysis of one ATP molecule, its efficiency is significantly reduced in Dk parasites because it merely supplies the ADP substrate for the electrogenic exchange of ADP^{3-}/ATP^{4-} by AAC [34]. Finally, since it is not possible to quantify the absolute Δψm using this assay, it is possible that in Dk cells the Δψm is maintained at a lower level than in BF mitochondria and thus does not require as dramatic of a collapse to produce a detrimental effect.

Notably, we observe a sudden and robust decrease in the $\Delta\psi_m$ within the first 24 hours, but there is a lag before the induced BF TbIF1 OE cell culture transitions from an arrested cell division fate to a lethal phenotype. Therefore, the mitochondria of these cells were labelled with Mitotracker Red CMXRos dye, a marker for energized mitochondria, before and after TbIF1 induction. While fluorescence microscopy detected the resulting red dye in noninduced cells, there was no visible staining in cells expressing V5-tagged TbIF1 for 24 hours. However, when the mitochondria of these induced cells are immunostained with a monoclonal anti-mtHsp70 antibody, the overall mt morphology seems to be unaffected (Fig 6G). This suggests that while

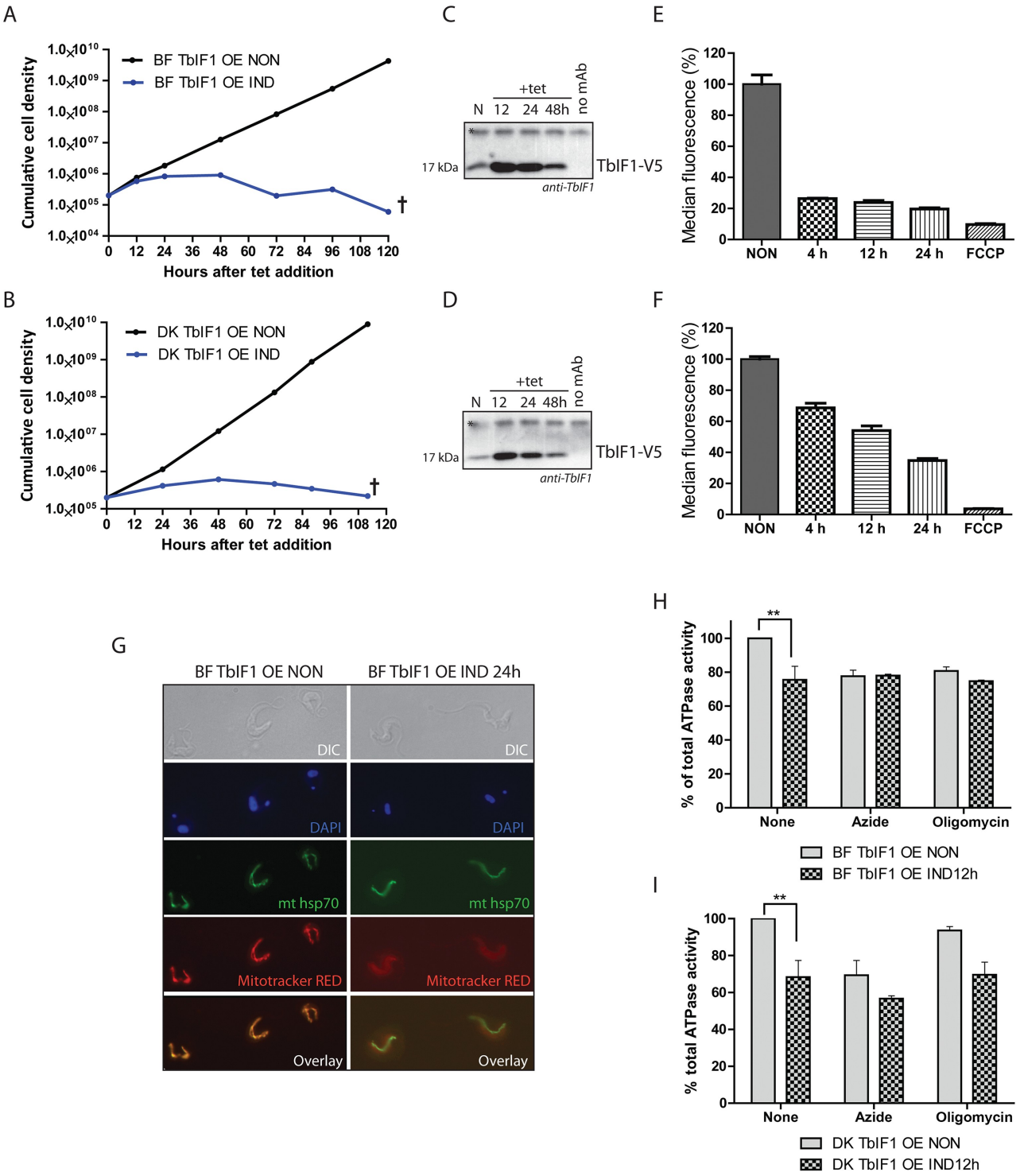

Fig 6. Overexpression of TbIF1 significantly affects the viability of BF and Dk cells due to the dramatic decrease of the $\Delta\psi_m$ when F_oF_1-ATPase is inhibited. (A, B) Growth curves of noninduced and tet induced BF (A) and Dk (B) TbIF1 OE cells. Cultures were maintained in the exponential growth phase (between 10^5 and 10^6 cells/ml) and the figure is representative of three independent tet inductions. (C, D) Western blot analysis of TbIF1_V5 immunoprecipitated with a V5 monoclonal antibody from BF (C) and Dk (D) TbIF1 OE cells that were noninduced (N) or induced for 12, 24 or 36 hours. The purified protein samples were probed with a polyclonal antiserum raised against TbIF1 and the asterisk identifies a nonspecific band that serves as a loading control. The no mAb lane represents nonspecific proteins isolated during an immunoprecipitation step that omitted the V5 antibody. (E, F) Using flow cytometry and the fluorescent dye TMRE, the *in vivo* $\Delta\psi_m$ was measured in BF (E) and Dk (F) TbIF1 OE cells that were either not induced or induced for 4, 12 or 24 hours. A

noninduced sample was also treated with FCCP to demonstrate that the assay was specifically measuring the Δψm. (means ± s.d.; n = 3). (G) Immunofluorescence of noninduced (NON) or induced (IND 24h) BF TbIF1 OE cells reveals an unchanged overall mt morphology upon TbIF1 induction. Mitochondria were visualized by immunostaining with an anti-mtHsp70 antibody (green) and by staining with MitoTracker Red CMXRos (red), a fluorescentdye that is $\Delta\psi_m$ dependent. DNA contents are stained with DAPI (blue) and the morphology of the cells was visualized using DIC imaging. (H, I) Total ATPase activity was quantified in crude mitochondrial preparations isolated from BF (H) and Dk (I) TbIF1 OE cells that were tet induced for 12 hours or not at all. Replicates of these samples were also treated either with oligomycin (OM, 2.5 μg/ml) or azide (AZ, 1 mM) to determine the proportion of this activity generated by F_oF_1-ATPase. (means ± s.d.; n = 3; ** $p < 0.01$; Student's *t* test)

https://doi.org/10.1371/journal.pntd.0005552.g006

the $\Delta\psi_m$ is required for cell replication, the lethality of TbIF1 overexpression is due to loss of mt protein import [49].

Similar to the results described for PF TbIF1 OE cells, inducing the inhibitory peptide in BF and Dk TbIF1 OE cells decreased the total ATPase activity by 25% and 32% in BF and Dk cells, respectively (Fig 6H and 6I). This correlates nicely with the decreased values obtained for non-induced BF (23%) and Dk (31%) cells treated with azide (Fig 6H and 6I). The potency of this natural inhibitor is further exemplified when compared to the 20% decrease in ATPase activity measured for BF TbIF1 OE noninduced cells treated with oligomycin (Fig 6H). The lack of oligomycin sensitivity observed in Dk TbIF1 OE noninduced cells (Fig 6I) is expected since they are without the mt encoded subunit a, which contains the binding site of this molecular inhibitor [34].

Recombinant TbIF1 inhibits the F_oF_1-ATPase activity in PF *T. brucei* mitochondria lysates

To directly demonstrate the ability of TbIF1 to inhibit F_oF_1-ATPase, rTbIF1 containing a C-terminal hexahistidine tag was expressed in bacteria, purified by nickel affinity chromatography and then incubated with isolated mitochondria (Fig 7). Titrating known amounts of rTbIF1 to a constant volume of a percoll purified mt extract decreased the total ATPase activity in a manner dependent on the concentration of the added inhibitor. The highest input of the recombinant protein (10 μM) caused a 64% drop in activity, which corresponds to the values acquired with azide and oligomycin. Importantly, treating mitochondria with a mixture of both rTbIF1 and azide did not result in an increased inhibition of the total ATPase activity, suggesting that rTbIF1 specifically targets only F_oF_1-ATPase.

In summation, these results validate that we have identified the endogenous TbIF1, which is a potent and specific inhibitor of the essential F_oF_1-ATPase activity in the BF and dyskinetoplastic trypanosomes.

Discussion

Under normal physiological conditions, the F-ATP synthase is a nanomotor that synthesizes ATP when the rotation of the machine is driven by protons moving down the electrochemical potential created across the biological membranes in bacteria, chloroplast and mitochondria. An inevitable consequence of the bioenergetic properties of this protein complex occurs when the Δψ collapses and the F-ATP synthase shifts to ATP hydrolysis, which provides the energy necessary to pump protons and create a new gradient. This attempt to maintain the essential Δψ exacts a high energetic toll on the cell and cannot be sustained for long. To prevent this wasteful ATP turnover, several different mechanisms have emerged throughout nature, with unique adaptations described in eubacteria, α-proteobacteria and chloroplasts [50–52]. In mitochondria, IF1 represents yet another distinct regulatory protein that interferes with the intrinsic rotational mechanism of the central stalk. Since its discovery in 1963, the function of this protein to mitigate cell injury upon a loss of respiration has been described in many

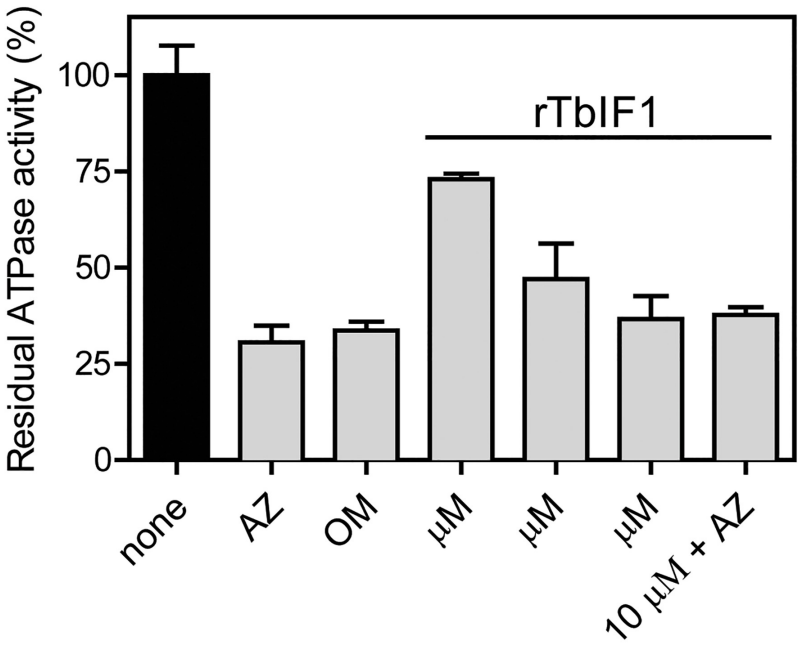

Fig 7. Recombinant TbIF1 inhibits the F_oF_1-ATPase activity *in vitro*. Mitochondria isolated from wildtype PF427 cells were lysed with dodecyl maltoside and the ATPase activity was measured by a Pullman assay. These samples were either treated with azide (AZ, 2 mM), oligomycin (OM, 50 μM) or the indicated rTbIF1 concentrations. (means ± s.d.; n > 3).

https://doi.org/10.1371/journal.pntd.0005552.g007

eukaryotic organisms [19–21,44,53]. The identification and characterization of this protein in the early diverging *T. brucei* suggests that IF1 inhibition of F_oF_1-ATPase has long been the preferred method to regulate this activity in mitochondria.

Typically, the bioenergetics of healthy cells promote ATP synthesis, thus the silencing of IF1 expression does not impact the fitness of mammalian and yeast cells grown *in vitro* [54,55]. Furthermore, this inhibitor is not required for the normal growth and breeding of mice [56]. To determine if TbIF1 functions in a manner similar to its eukaryotic homologs, we generated a cell line that suppresses the inhibitor by RNAi. In agreement, no growth abnormality was observed in PF *T. brucei* cells with significantly decreased TbIF1 expression. Nevertheless, the function of this protein became apparent when the $\Delta\psi_m$ was monitored in *Trypanosoma* cultures chemically treated to inhibit respiration. It was only after the depletion of TbIF1 that the F_oF_1-ATPase was able to hydrolyze ATP and stabilize a new, albeit lower, electrochemical potential.

Interestingly, relative to the expression levels of the F_1-ATPase β subunit, the amount of IF1 fluctuates in a variety of mammalian tissues [26]. Based on IF1 protein levels and the glycolytic capacity of the cell, there are two observed responses when cellular respiration is compromised: either the cell will attempt to endure depolarized mitochondria while sustaining ATP pools (high IF1 expression, low glycolytic capacity, e.g. neurons) or it will consume ATP in order to maintain an acceptable Δψm (low IF1 expression, high glycolytic capacity, e.g. astrocytes). Since the overexpression of TbIF1 in PF *T. brucei* treated with chemical hypoxia did not further destabilize the Δψm compared to the parental or noninduced cells, it suggests that wildtype PF parasites possess enough TbIF1 to inhibit a majority of the F_oF_1-ATPase activity. Therefore, it seems that PF trypanosome cells have chosen the route of high IF1 expression

because their energy metabolism is more dependent on proper mt function. The utility of employing this strategy to protect against hypoxic injury by preserving cellular ATP becomes relevant when these protists enter the tsetse midgut, an environment with extremely low oxygen tension [57,58].

Recently, another possible role for the inhibitory protein emerged from the observation that IF1 expression is strongly up-regulated in several types of cancer cells. It is proposed that in these cells, IF1 plays an important role in the metabolic shift from oxidative phosphorylation to aerobic glycolysis, a process known as the Warburg effect, which promotes cellular proliferation and survival [28]. Similar metabolic adaptations are also observed during the *T. brucei* life cycle as procyclic cells transition into a metacyclic stage before they fully convert to the long slender bloodstream form. It is possible that the infective metacyclic trypanosomes biding their time in the salivary glands before they are transmitted to the glucose-rich bloodstream of the mammalian host have already re-programed their metabolism and are primed for enhanced aerobic glycolysis. We are now exploring if TbIF1 contributes to this remarkable cellular transformation using an *in vitro* differentiation system [59].

Numerous genome-wide studies have previously shown that TbIF1 expression is strongly regulated between PF and BF parasites. Since TbIF1 mRNA is strongly down-regulated in bloodstream cells, its half-life was impossible to measure and was therefore assigned to the class of "procyclic form specific" mRNAs. This subset of molecules consists of only 29 transcripts, which notably includes GPEET2 and EP2 procyclins [60]. Furthermore, it has been reported that TbIF1 transcript levels are already upregulated after just 1 hour of inducing BF cells to transform into PF parasites with citrate/cis-aconitate at 27˚C. In fact, TbIF1 expression levels continue to rise throughout this differentiation process [61]. In agreement with the transcriptomic data [62–64], proteomic studies based on SILAC labeling of PF and BF cells confirmed TbIF1 is strongly up-regulated in the insect stage of the parasite [65,66]. The striking difference in TbIF1 expression between the PF and BF life stages illustrates the deleterious effects of TbIF1 when the $\Delta\psi_m$ is maintained by F_oF_1-ATPase. It also provides a nice model to study gene expression in an organism that predominantly regulates these processes at the post-transcriptional level.

While the activity of the mitochondrion is reduced during the infectious stage, several biological processes unique to *T. brucei* have previously been identified as potential drug targets within this organelle (alternative electron transport chain, kDNA and topoisomerases, tRNA import and fatty acid synthesis) [67]. The F_oF_1-ATPase in particular is an appealing target as it is required for maintaining the essential $\Delta\psi_m$ in BF trypanosomes, while the mammalian host cells almost exclusively rely on this nanomotor to synthesize ATP. In fact, it has been demonstrated that trypanocides belonging to two different classes of drugs, the aromatic diamidines (i.e., DB75) and bisphosphonate salts (i.e., AHI-9), can inhibit the F_oF_1-ATPase activity [68,69]. Unfortunately, it appears that these compounds are likely promiscuous inhibitors that not only interact with multiple cellular targets, but also indiscriminately inhibit both the ATP hydrolytic and synthetic activities of the enzyme. Furthermore, since the F_oF_1-ATPase binding sites and the exact mechanism of inhibition for these molecules would be challenging to ascertain, it would require significant effort to improve their efficacy. Since TbIF1 is a specific and unidirectional inhibitor of the *T. brucei* F_oF_1-ATPase, we can now exploit the intrinsic binding properties of this endogenous inhibitor to facilitate future structure-based drug design. Specifically, the development of peptidomimetics [70–73] that simulate the most important binding interactions of TbIF1 to *T. brucei* F_1-ATPase could potentially result in effective therapeutics that incapacitate these medically and economically important parasites.

Acknowledgments

We thank Ken Stuart (Seattle Biomed) for kindly providing antibodies. We would also like to express our gratitude to Adam Kocourek for his experimental contribution during the resubmission period.

Author Contributions

Conceptualization: AZ OG BP.

Data curation: AZ BP OG.

Formal analysis: AZ BP OG.

Funding acquisition: AZ.

Investigation: AZ OG BP.

Methodology: AZ OG BP.

Project administration: AZ.

Resources: AZ.

Writing – original draft: AZ OG BP.

Writing – review & editing: AZ BP.

References

1. Matthews KR (2015) 25 years of African trypanosome research: From description to molecular dissection and new drug discovery. Mol Biochem Parasitol 200: 30–40. https://doi.org/10.1016/j.molbiopara.2015.01.006 PMID: 25736427
2. Matthews KR (2005) The developmental cell biology of Trypanosoma brucei. J Cell Sci 118: 283–290. https://doi.org/10.1242/jcs.01649 PMID: 15654017
3. Tielens AG, Van Hellemond JJ (1998) Differences in energy metabolism between trypanosomatidae. Parasitol Today 14: 265–272. PMID: 17040781
4. van Hellemond JJ, Opperdoes FR, Tielens AG (2005) The extraordinary mitochondrion and unusual citric acid cycle in Trypanosoma brucei. Biochem Soc Trans 33: 967–971. https://doi.org/10.1042/BST20050967 PMID: 16246022
5. Bringaud F, Riviere L, Coustou V (2006) Energy metabolism of trypanosomatids: adaptation to available carbon sources. Mol Biochem Parasitol 149: 1–9. https://doi.org/10.1016/j.molbiopara.2006.03.017 PMID: 16682088
6. Zikova A, Schnaufer A, Dalley RA, Panigrahi AK, Stuart KD (2009) The F(0)F(1)-ATP synthase complex contains novel subunits and is essential for procyclic Trypanosoma brucei. PLoS Pathog 5: e1000436. https://doi.org/10.1371/journal.ppat.1000436 PMID: 19436713
7. Michels PA, Bringaud F, Herman M, Hannaert V (2006) Metabolic functions of glycosomes in trypanosomatids. Biochim Biophys Acta 1763: 1463–1477. https://doi.org/10.1016/j.bbamcr.2006.08.019 PMID: 17023066
8. Stephens JL, Lee SH, Paul KS, Englund PT (2007) Mitochondrial fatty acid synthesis in Trypanosoma brucei. J Biol Chem 282: 4427–4436. https://doi.org/10.1074/jbc.M609037200 PMID: 17166831
9. Schnaufer A, Panigrahi AK, Panicucci B, Igo RP Jr., Wirtz E, et al. (2001) An RNA ligase essential for RNA editing and survival of the bloodstream form of Trypanosoma brucei. Science 291: 2159–2162. PMID: 11251122
10. Huang G, Vercesi AE, Docampo R (2013) Essential regulation of cell bioenergetics in Trypanosoma brucei by the mitochondrial calcium uniporter. Nat Commun 4: 2865. https://doi.org/10.1038/ncomms3865 PMID: 24305511
11. Mazet M, Morand P, Biran M, Bouyssou G, Courtois P, et al. (2013) Revisiting the central metabolism of the bloodstream forms of Trypanosoma brucei: production of acetate in the mitochondrion is essential

for parasite viability. PLoS Negl Trop Dis 7: e2587. https://doi.org/10.1371/journal.pntd.0002587 PMID: 24367711

12. Neupert W (1997) Protein import into mitochondria. Annu Rev Biochem 66: 863–917. https://doi.org/10.1146/annurev.biochem.66.1.863 PMID: 9242927
13. Nolan DP, Voorheis HP (1992) The mitochondrion in bloodstream forms of Trypanosoma brucei is energized by the electrogenic pumping of protons catalysed by the F1F0-ATPase. Eur J Biochem 209: 207–216. PMID: 1327770
14. Lai DH, Hashimi H, Lun ZR, Ayala FJ, Lukes J (2008) Adaptations of Trypanosoma brucei to gradual loss of kinetoplast DNA: Trypanosoma equiperdum and Trypanosoma evansi are petite mutants of T. brucei. Proc Natl Acad Sci U S A 105: 1999–2004. https://doi.org/10.1073/pnas.0711799105 PMID: 18245376
15. Dean S, Gould MK, Dewar CE, Schnaufer AC (2013) Single point mutations in ATP synthase compensate for mitochondrial genome loss in trypanosomes. Proc Natl Acad Sci U S A 110: 14741–14746. https://doi.org/10.1073/pnas.1305404110 PMID: 23959897
16. Subrtova K, Panicucci B, Zikova A (2015) ATPaseTb2, a Unique Membrane-bound FoF1-ATPase Component, Is Essential in Bloodstream and Dyskinetoplastic Trypanosomes. PLoS Pathog 11: e1004660. https://doi.org/10.1371/journal.ppat.1004660 PMID: 25714685
17. St-Pierre J, Brand MD, Boutilier RG (2000) Mitochondria as ATP consumers: cellular treason in anoxia. Proc Natl Acad Sci U S A 97: 8670–8674. https://doi.org/10.1073/pnas.140093597 PMID: 10890886
18. Grover GJ, Atwal KS, Sleph PG, Wang FL, Monshizadegan H, et al. (2004) Excessive ATP hydrolysis in ischemic myocardium by mitochondrial F1F0-ATPase: effect of selective pharmacological inhibition of mitochondrial ATPase hydrolase activity. Am J Physiol Heart Circ Physiol 287: H1747–1755. https://doi.org/10.1152/ajpheart.01019.2003 PMID: 15371268
19. Pullman ME, Monroy GC (1963) A Naturally Occurring Inhibitor of Mitochondrial Adenosine Triphosphatase. J Biol Chem 238: 3762–3769. PMID: 14109217
20. Norling B, Tourikas C, Hamasur B, Glaser E (1990) Evidence for an endogenous ATPase inhibitor protein in plant mitochondria. Purification and characterization. Eur J Biochem 188: 247–252. PMID: 2138539
21. Ichikawa N, Ando C, Fumino M (2006) Caenorhabditis elegans MAI-1 protein, which is similar to mitochondrial ATPase inhibitor (IF1), can inhibit yeast F0F1-ATPase but cannot be transported to yeast mitochondria. J Bioenerg Biomembr 38: 93–99. https://doi.org/10.1007/s10863-006-9009-2 PMID: 16897438
22. Ichikawa N, Yoshida Y, Hashimoto T, Ogasawara N, Yoshikawa H, et al. (1990) Activation of ATP hydrolysis by an uncoupler in mutant mitochondria lacking an intrinsic ATPase inhibitor in yeast. J Biol Chem 265: 6274–6278. PMID: 2138617
23. Bason JV, Montgomery MG, Leslie AGW, Walker JE (2014) Pathway of binding of the intrinsically disordered mitochondrial inhibitor protein to F-1-ATPase. Proceedings of the National Academy of Sciences of the United States of America 111: 11305–11310. https://doi.org/10.1073/pnas.1411560111 PMID: 25049402
24. Gledhill JR, Montgomery MG, Leslie AG, Walker JE (2007) How the regulatory protein, IF(1), inhibits F(1)-ATPase from bovine mitochondria. Proc Natl Acad Sci U S A 104: 15671–15676. https://doi.org/10.1073/pnas.0707326104 PMID: 17895376
25. Runswick MJ, Bason JV, Montgomery MG, Robinson GC, Fearnley IM, et al. (2013) The affinity purification and characterization of ATP synthase complexes from mitochondria. Open Biol 3: 120160. https://doi.org/10.1098/rsob.120160 PMID: 23407638
26. Campanella M, Parker N, Tan CH, Hall AM, Duchen MR (2009) IF(1): setting the pace of the F(1)F(o)-ATP synthase. Trends Biochem Sci 34: 343–350. https://doi.org/10.1016/j.tibs.2009.03.006 PMID: 19559621
27. Campanella M, Casswell E, Chong S, Farah Z, Wieckowski MR, et al. (2008) Regulation of mitochondrial structure and function by the F1Fo-ATPase inhibitor protein, IF1. Cell Metab 8: 13–25. https://doi.org/10.1016/j.cmet.2008.06.001 PMID: 18590689
28. Garcia-Bermudez J, Cuezva JM (2016) The ATPase Inhibitory Factor 1 (IF1): A master regulator of energy metabolism and of cell survival. Biochimica Et Biophysica Acta-Bioenergetics 1857: 1167–1182.
29. Faccenda D, Nakamura J, Gorini G, Dhoot GK, Piacentini M, et al. (2017) Control of Mitochondrial Remodeling by the ATPase Inhibitory Factor 1 Unveils a Pro-survival Relay via OPA1. Cell Rep 18: 1869–1883. https://doi.org/10.1016/j.celrep.2017.01.070 PMID: 28228254

30. Wang Z, Morris JC, Drew ME, Englund PT (2000) Inhibition of Trypanosoma brucei gene expression by RNA interference using an integratable vector with opposing T7 promoters. J Biol Chem 275: 40174–40179. https://doi.org/10.1074/jbc.M008405200 PMID: 11013266

31. Flaspohler JA, Jensen BC, Saveria T, Kifer CT, Parsons M (2010) A novel protein kinase localized to lipid droplets is required for droplet biogenesis in trypanosomes. Eukaryot Cell 9: 1702–1710. https://doi.org/10.1128/EC.00106-10 PMID: 20833891

32. Wirtz E, Leal S, Ochatt C, Cross GA (1999) A tightly regulated inducible expression system for conditional gene knock-outs and dominant-negative genetics in Trypanosoma brucei. Mol Biochem Parasitol 99: 89–101. PMID: 10215027

33. Stuart KD (1971) Evidence for the retention of kinetoplast DNA in an acriflavine-induced dyskinetoplastic strain of Trypanosoma brucei which replicates the altered central element of the kinetoplast. J Cell Biol 49: 189–195. PMID: 4102002

34. Schnaufer A, Clark-Walker GD, Steinberg AG, Stuart K (2005) The F1-ATP synthase complex in bloodstream stage trypanosomes has an unusual and essential function. EMBO J 24: 4029–4040. https://doi.org/10.1038/sj.emboj.7600862 PMID: 16270030

35. Law RH, Manon S, Devenish RJ, Nagley P (1995) ATP synthase from Saccharomyces cerevisiae. Methods Enzymol 260: 133–163. PMID: 8592441

36. Pullman ME, Penefsky HS, Datta A, Racker E (1960) Partial resolution of the enzymes catalyzing oxidative phosphorylation. I. Purification and properties of soluble dinitrophenol-stimulated adenosine triphosphatase. J Biol Chem 235: 3322–3329. PMID: 13738472

37. Allemann N, Schneider A (2000) ATP production in isolated mitochondria of procyclic Trypanosoma brucei. Mol Biochem Parasitol 111: 87–94. PMID: 11087919

38. Gnipova A, Subrtova K, Panicucci B, Horvath A, Lukes J, et al. (2015) The ADP/ATP carrier and its relationship to OXPHOS in an ancestral protist, Trypanosoma brucei. Eukaryot Cell.

39. Silvester JA, Dickson VK, Runswick MJ, Leslie AG, Walker JE (2006) The expression, purification, crystallization and preliminary X-ray analysis of a subcomplex of the peripheral stalk of ATP synthase from bovine mitochondria. Acta Crystallogr Sect F Struct Biol Cryst Commun 62: 530–533. https://doi.org/10.1107/S1744309106015338 PMID: 16754973

40. Miroux B, Walker JE (1996) Over-production of proteins in Escherichia coli: mutant hosts that allow synthesis of some membrane proteins and globular proteins at high levels. J Mol Biol 260: 289–298. https://doi.org/10.1006/jmbi.1996.0399 PMID: 8757792

41. Claros MG, Vincens P (1996) Computational method to predict mitochondrially imported proteins and their targeting sequences. Eur J Biochem 241: 779–786. PMID: 8944766

42. van Raaij MJ, Orriss GL, Montgomery MG, Runswick MJ, Fearnley IM, et al. (1996) The ATPase inhibitor protein from bovine heart mitochondria: the minimal inhibitory sequence. Biochemistry 35: 15618–15625. https://doi.org/10.1021/bi960628f PMID: 8961923

43. Cabezon E, Runswick MJ, Leslie AG, Walker JE (2001) The structure of bovine IF(1), the regulatory subunit of mitochondrial F-ATPase. EMBO J 20: 6990–6996. https://doi.org/10.1093/emboj/20.24.6990 PMID: 11742976

44. Ichikawa N, Ushida S, Kawabata M, Masazumi Y (1999) Nucleotide sequence of cDNA coding the mitochondrial precursor protein of the ATPase inhibitor from humans. Biosci Biotechnol Biochem 63: 2225–2227. https://doi.org/10.1271/bbb.63.2225 PMID: 10664857

45. Cabezon E, Arechaga I, Jonathan P, Butler G, Walker JE (2000) Dimerization of bovine F1-ATPase by binding the inhibitor protein, IF1. J Biol Chem 275: 28353–28355. https://doi.org/10.1074/jbc.C000427200 PMID: 10918052

46. Luscher A, Lamprea-Burgunder E, Graf FE, de Koning HP, Maser P (2014) Trypanosoma brucei adenine-phosphoribosyltransferases mediate adenine salvage and aminopurinol susceptibility but not adenine toxicity. Int J Parasitol Drugs Drug Resist 4: 55–63. https://doi.org/10.1016/j.ijpddr.2013.12.001 PMID: 24596669

47. Chen Y, Hung CH, Burderer T, Lee GS (2003) Development of RNA interference revertants in Trypanosoma brucei cell lines generated with a double stranded RNA expression construct driven by two opposing promoters. Mol Biochem Parasitol 126: 275–279. PMID: 12615326

48. Figueira TR, Melo DR, Vercesi AE, Castilho RF (2012) Safranine as a fluorescent probe for the evaluation of mitochondrial membrane potential in isolated organelles and permeabilized cells. Methods Mol Biol 810: 103–117. https://doi.org/10.1007/978-1-61779-382-0_7 PMID: 22057563

49. Inoue M, Nakamura Y, Yasuda K, Yasaka N, Hara T, et al. (2005) The 14-3-3 proteins of Trypanosoma brucei function in motility, cytokinesis, and cell cycle. J Biol Chem 280: 14085–14096. https://doi.org/10.1074/jbc.M412336200 PMID: 15653691

50. Tsunoda SP, Rodgers AJ, Aggeler R, Wilce MC, Yoshida M, et al. (2001) Large conformational changes of the epsilon subunit in the bacterial F1F0 ATP synthase provide a ratchet action to regulate this rotary motor enzyme. Proc Natl Acad Sci U S A 98: 6560–6564. https://doi.org/10.1073/pnas.111128098 PMID: 11381110

51. Zarco-Zavala M, Morales-Rios E, Mendoza-Hernandez G, Ramirez-Silva L, Perez-Hernandez G, et al. (2014) The zeta subunit of the F1FO-ATP synthase of alpha-proteobacteria controls rotation of the nanomotor with a different structure. FASEB J 28: 2146–2157. https://doi.org/10.1096/fj.13-241430 PMID: 24522203

52. Ketcham SR, Davenport JW, Warncke K, McCarty RE (1984) Role of the gamma subunit of chloroplast coupling factor 1 in the light-dependent activation of photophosphorylation and ATPase activity by dithiothreitol. J Biol Chem 259: 7286–7293. PMID: 6233282

53. Cintron NM, Pedersen PL (1979) Purification of an ATPase inhibitor peptide fraction from rat liver mitochondria. Methods Enzymol 55: 408–414. PMID: 156850

54. Lu YM, Miyazawa K, Yamaguchi K, Nowaki K, Iwatsuki H, et al. (2001) Deletion of mitochondrial ATPase inhibitor in the yeast Saccharomyces cerevisiae decreased cellular and mitochondrial ATP levels under non-nutritional conditions and induced a respiration-deficient cell-type. J Biochem 130: 873–878. PMID: 11726289

55. Fujikawa M, Imamura H, Nakamura J, Yoshida M (2012) Assessing actual contribution of IF1, inhibitor of mitochondrial FoF1, to ATP homeostasis, cell growth, mitochondrial morphology, and cell viability. J Biol Chem 287: 18781–18787. https://doi.org/10.1074/jbc.M112.345793 PMID: 22493494

56. Nakamura J, Fujikawa M, Yoshida M (2013) IF1, a natural inhibitor of mitochondrial ATP synthase, is not essential for the normal growth and breeding of mice. Biosci Rep 33.

57. Hill GC, Degn H (1977) Steady-State Oxygen Kinetics of Cyanide-Insensitive Oxidase in Trypanosomes. Federation Proceedings 36: 905–905.

58. Hill GC, Degn H (1977) Steady-State Oxygen Kinetics of Terminal Oxidases in Trypanosoma-Mega. Journal of Protozoology 24: 563–565. PMID: 599502

59. Kolev NG, Ramey-Butler K, Cross GAM, Ullu E, Tschudi C (2012) Developmental Progression to Infectivity in Trypanosoma brucei Triggered by an RNA-Binding Protein. Science 338: 1352–1353. https://doi.org/10.1126/science.1229641 PMID: 23224556

60. Fadda A, Ryten M, Droll D, Rojas F, Farber V, et al. (2014) Transcriptome-wide analysis of trypanosome mRNA decay reveals complex degradation kinetics and suggests a role for co-transcriptional degradation in determining mRNA levels. Mol Microbiol 94: 307–326. https://doi.org/10.1111/mmi.12764 PMID: 25145465

61. Kabani S, Fenn K, Ross A, Ivens A, Smith TK, et al. (2009) Genome-wide expression profiling of in vivo-derived bloodstream parasite stages and dynamic analysis of mRNA alterations during synchronous differentiation in Trypanosoma brucei. BMC Genomics 10: 427. https://doi.org/10.1186/1471-2164-10-427 PMID: 19747379

62. Nilsson D, Gunasekera K, Mani J, Osteras M, Farinelli L, et al. (2010) Spliced leader trapping reveals widespread alternative splicing patterns in the highly dynamic transcriptome of Trypanosoma brucei. PLoS Pathog 6: e1001037. https://doi.org/10.1371/journal.ppat.1001037 PMID: 20700444

63. Siegel TN, Hekstra DR, Wang X, Dewell S, Cross GA (2010) Genome-wide analysis of mRNA abundance in two life-cycle stages of Trypanosoma brucei and identification of splicing and polyadenylation sites. Nucleic Acids Res 38: 4946–4957. https://doi.org/10.1093/nar/gkq237 PMID: 20385579

64. Jensen BC, Sivam D, Kifer CT, Myler PJ, Parsons M (2009) Widespread variation in transcript abundance within and across developmental stages of Trypanosoma brucei. BMC Genomics 10: 482. https://doi.org/10.1186/1471-2164-10-482 PMID: 19840382

65. Urbaniak MD, Guther ML, Ferguson MA (2012) Comparative SILAC proteomic analysis of Trypanosoma brucei bloodstream and procyclic lifecycle stages. PLoS One 7: e36619. https://doi.org/10.1371/journal.pone.0036619 PMID: 22574199

66. Butter F, Bucerius F, Michel M, Cicova Z, Mann M, et al. (2013) Comparative proteomics of two life cycle stages of stable isotope-labeled Trypanosoma brucei reveals novel components of the parasite's host adaptation machinery. Mol Cell Proteomics 12: 172–179. https://doi.org/10.1074/mcp.M112.019224 PMID: 23090971

67. Fidalgo LM, Gille L (2011) Mitochondria and trypanosomatids: targets and drugs. Pharm Res 28: 2758–2770. https://doi.org/10.1007/s11095-011-0586-3 PMID: 21935742

68. Lanteri CA, Tidwell RR, Meshnick SR (2008) The mitochondrion is a site of trypanocidal action of the aromatic diamidine DB75 in bloodstream forms of Trypanosoma brucei. Antimicrob Agents Chemother 52: 875–882. https://doi.org/10.1128/AAC.00642-07 PMID: 18086841

69. Alkhaldi AA, Martinek J, Panicucci B, Dardonville C, Zikova A, et al. (2016) Trypanocidal action of bisphosphonium salts through a mitochondrial target in bloodstream form Trypanosoma brucei. Int J Parasitol Drugs Drug Resist 6: 23–34. https://doi.org/10.1016/j.ijpddr.2015.12.002 PMID: 27054061

70. Caffrey CR, Steverding D (2008) Recent initiatives and strategies to developing new drugs for tropical parasitic diseases. Expert Opin Drug Discov 3: 173–186. https://doi.org/10.1517/17460441.3.2.173 PMID: 23480221

71. Dunny E, Doherty W, Evans P, Malthouse JP, Nolan D, et al. (2013) Vinyl sulfone-based peptidomimetics as anti-trypanosomal agents: design, synthesis, biological and computational evaluation. J Med Chem 56: 6638–6650. https://doi.org/10.1021/jm400294w PMID: 23952916

72. Lampa AK, Bergman SM, Gustafsson SS, Alogheli H, Akerblom EB, et al. (2014) Novel Peptidomimetic Hepatitis C Virus NS3/4A Protease Inhibitors Spanning the P2-P1' Region. ACS Med Chem Lett 5: 249–254. https://doi.org/10.1021/ml400217r PMID: 24900813

73. Qiu X, Liu ZP (2011) Recent developments of peptidomimetic HIV-1 protease inhibitors. Curr Med Chem 18: 4513–4537. PMID: 21864279

Received: 25 June 2020 | Accepted: 26 October 2020

DOI: 10.1096/fj.202001579RR

RESEARCH ARTICLE

THE FASEB JOURNAL

Depletion of cardiolipin induces major changes in energy metabolism in *Trypanosoma brucei* bloodstream forms

Mauro Serricchio[1] | **Carolina Hierro-Yap**[2,3] | **David Schädeli**[1,4] | **Hisham Ben Hamidane**[5] | **Andrew Hemphill**[6] | **Johannes Graumann**[5,7] | **Alena Zíková**[2,3] | **Peter Bütikofer**[1]

[1]Institute of Biochemistry and Molecular Medicine, University of Bern, Bern, Switzerland

[2]Faculty of Science, University of South Bohemia, Ceske Budejovice, Czech Republic

[3]Institute of Parasitology, Biology Centre, Czech Academy of Sciences, Ceske Budejovice, Czech Republic

[4]Graduate School for Cellular and Biomedical Sciences, University of Bern, Bern, Switzerland

[5]Weill Cornell Medicine - Qatar, Doha, State of Qatar

[6]Institute of Parasitology, Vetsuisse Faculty, University of Bern, Bern, Switzerland

[7]Biomolecular Mass Spectrometry, Max Planck Institute for Heart and Lung Research, Bad Nauheim, Germany

Correspondence
Alena Zíková, Institute of Parasitology, Biology Centre, Czech Academy of Sciences, Ceske Budejovice, Czech Republic.
Email: azikova@paru.cas.cz

Peter Bütikofer, Institute of Biochemistry and Molecular Medicine, University of Bern, Bühlstrasse 28, 3012 Bern, Switzerland.
Email: peter.buetikofer@ibmm.unibe.ch

Funding information
Schweizerischer Nationalfonds zur Förderung der Wissenschaftlichen Forschung (SNF), Grant/Award Number: 169355; Czech Science Foundation, Grant/Award Number: 18-17529S; ERD fund, Grant/Award Number: CZ.02.1.01/0.0/0.0/16_019/0000759

Abstract

The mitochondrial inner membrane glycerophospholipid cardiolipin (CL) associates with mitochondrial proteins to regulate their activities and facilitate protein complex and supercomplex formation. Loss of CL leads to destabilized respiratory complexes and mitochondrial dysfunction. The role of CL in an organism lacking a conventional electron transport chain (ETC) has not been elucidated. *Trypanosoma brucei* bloodstream forms use an unconventional ETC composed of glycerol-3-phosphate dehydrogenase and alternative oxidase (AOX), while the mitochondrial membrane potential ($\Delta\Psi m$) is generated by the hydrolytic action of the F_oF_1-ATP synthase (aka F_oF_1-ATPase). We now report that the inducible depletion of cardiolipin synthase (TbCls) is essential for survival of *T brucei* bloodstream forms. Loss of CL caused a rapid drop in ATP levels and a decline in the $\Delta\Psi m$. Unbiased proteomic analyses revealed a reduction in the levels of many mitochondrial proteins, most notably of F_oF_1-ATPase subunits and AOX, resulting in a strong decline of glycerol-3-phosphate-stimulated oxygen consumption. The changes in cellular respiration preceded the observed decrease in F_oF_1-ATPase stability, suggesting that the AOX-mediated ETC is the first pathway responding to the decline in CL. Select proteins and pathways involved in glucose and amino acid metabolism were upregulated to counteract the CL depletion-induced drop in cellular ATP.

KEYWORDS

ATP synthase, cardiolipin, electron transport chain, mitochondria, protein complexes, trypanosomes

Abbreviations: AOX, alternative oxidase; CL, cardiolipin; ETC, electron transport chain; TbCls, *Trypanosoma brucei* cardiolipin synthase; $\Delta\Psi m$, mitochondrial membrane potential.

1 | INTRODUCTION

Cardiolipin (CL) is a mitochondrial and bacterial glycerophospholipid consisting of four fatty acyl chains and two phosphate groups. Owing to its structure, CL has biophysical properties that set it apart from other glycerophospholipids (reviewed by 1). CL adopts a hexagonal phase and thus localizes preferentially to sites with high membrane curvature, such as bacterial septa and poles,[2,3] and it self-organizes in negatively curved membranes[4] found at cristae junctions[5] and cristae tips.[6] CL tightly associates with respiratory complexes[7-10] and is required for the assembly and stability of supercomplexes[11] and the oligomerization of ATP synthase.[6] In addition, several mitochondrial carriers have been shown to interact with CL.[12,13] Finally, CL promotes mitochondrial membrane fusion,[14] iron-sulfur cluster biogenesis[15] and induction of apoptosis.[16]

More recently, depletion of CL has been shown to affect a cell's energy metabolism. In a *Saccharomyces cerevisiae* mutant lacking CL, due to the deletion of the *crd1* gene encoding CL synthase, the production of acetyl-CoA was decreased as a result of a defect in the pyruvate dehydrogenase bypass pathway.[17] This, together with the observation that CL is required for the proper function of the iron-sulfur-containing enzymes aconitase and succinate dehydrogenase,[15] demonstrated that the tricarboxylic acid (TCA) cycle is impaired in CL-deficient yeast. As a result, in this *crd1*Δ mutant anaplerotic pathways are activated to restore acetyl-CoA and TCA cycle intermediates.[18]

Interestingly, aberrant intermediary metabolism is also a hallmark of Barth syndrome, a human disease caused by mutations in the CL-remodeling enzyme, tafazzin.[19] Analyses of plasma metabolites point to alterations in carbohydrate and amino acid metabolism in Barth syndrome patients compared to healthy controls.[20] Remarkably, perturbations in energy metabolism, in particular in the levels of TCA intermediates and amino acid metabolites, were recently also found in a tafazzin knock out mouse cell line,[21] linking CL to energy metabolism. Surprisingly, despite these important functions, CL is dispensable for viability in *Escherichia coli*, *S cerevisiae* and mammalian cell lines.[22-24] In contrast, CL is essential for the survival of *Trypanosoma brucei* procyclic forms in culture.[25]

The biosynthesis of CL occurs on the matrix side of the inner mitochondrial membrane in four steps via the intermediates phosphatidic acid, CDP-diacylglycerol, phosphatidylglycerophosphate and phosphatidylglycerol. In the final step, in most eukaryotes CL is formed from phosphatidylglycerol and CDP-diacylglycerol by eukaryotic-type CL synthases. In contrast, in certain parasitic protozoa and prokaryotes, CL is formed from two phosphatidylglycerol molecules (or from one phosphatidylglycerol and one phosphatidylethanolamine molecule) by prokaryotic-type CL synthases.[26] Most previous studies aiming to investigate the importance of CL for inner mitochondrial membrane protein complexes and mitochondrial function were carried out in cells after knocking out key enzymes in the CL biosynthetic pathway. While this approach has yielded a wealth of information on steady-state changes in mitochondrial protein levels and mitochondrial function, such systems are not suited to detect subtle changes and adaptations that occur *during* CL depletion. In *T brucei* procyclic form CL synthase (TbCls) conditional knock-out parasites, we have recently shown that gradual CL depletion not only affected the stability of mitochondrial respiratory complexes but also decreased the levels of several mitochondrial proteins that have not been previously linked to CL.[27] These proteins, named CL-dependent proteins, were identified by comparing the proteomes of procyclic form trypanosomes at different time-points after induction of CL depletion using an unbiased mass spectrometry-based approach.[27]

T brucei parasites cycle between the fly host, Glossina *spp*., and mammals, and are the causative agents of human African trypanosomiasis and nagana in domestic animals. To cope with the fundamentally different host environments during its life cycle, the parasite has adapted its energy metabolism to the availability of different nutrients. In the tsetse fly midgut, *T brucei* procyclic forms thrive mostly on amino acids, express functional TCA cycle enzymes and generate ATP by substrate-level and oxidative phosphorylation.[28] In contrast, bloodstream form parasites produce cellular ATP via cytosolic substrate-level phosphorylation by aerobic glycolysis. As a result of the constant availability of glucose in the blood, bloodstream form trypanosomes minimize mitochondrial energy metabolism and downregulate key enzymes of the TCA cycle as well as the cytochrome-containing respiratory chain protein complexes.[29] In the absence of the proton-pumping complexes III and IV, the electrochemical potential across the inner mitochondrial membrane in *T brucei* bloodstream forms is generated and maintained by the hydrolytic activity of the F_oF_1-ATP synthase (aka F_oF_1-ATPase).[30,31] As a result, the mitochondrion differs morphologically and metabolically between these life cycle stages.[32-36]

In the present study, we have exploited the unusual role of the *T brucei* bloodstream form mitochondrion to study the effects of CL depletion in a cell where a canonical respiratory chain is absent and the F_oF_1-ATP synthase works in reverse direction compared to most other eukaryotes. We generated bloodstream form TbCls conditional knock-out parasites and examined time-dependent changes in protein levels and metabolites during CL depletion using quantitative comparative mass spectrometry. Our results show that the ablation of TbCls expression causes a decreased respiration rate and a rapid drop in cellular ATP levels resulting in a reduction of the mitochondrial membrane potential ($\Delta\Psi m$). Proteomic and metabolomic analyses revealed a large number of proteins that were downregulated during CL depletion

and, unexpectedly, a set of mitochondrial proteins involved in energy metabolism that were upregulated, likely to counteract the loss of ATP and $\Delta\Psi m$.

2 | MATERIAL AND METHODS

Unless otherwise stated, reagents were purchased from Sigma (Buchs, Switzerland) or Merck (Darmstadt, Germany). Restriction enzymes were from Thermo Scientific (Reinach, Switzerland), DNA amplification and processing was performed with reagents from Promega (Dübendorf, Switzerland).

2.1 | Trypanosome cultures

Bloodstream form TbCls KO parasites were cultured at 37°C in HMI-9 containing 15% (v/v) heat-inactivated fetal bovine serum, 1 μg/mL of G418, 0.5 μg/mL of hygromycin, 0.1 μg/mL of puromycin, 1 μg/mL of blasticidin (InvivoGen, Muttenz, Schweiz), and in the presence or absence of 1 μg/mL of tetracycline to maintain or ablate, respectively, TbCls. TbCls KO parasites expressing in-situ-tagged proteins were cultured in the presence of an additional 1.5 μg/mL of phleomycin.

2.2 | Generation of TbCls conditional knock-out mutants

To generate plasmids to replace the endogenous TbCls genes, blasticidin, and hygromycin resistance cassettes consisting of a PARP promoter, the resistance gene and a tubulin 3′ UTR were amplified from pXS2 expression vectors (courtesy of James D. Bangs, University of Buffalo, NY) and inserted into a plasmid containing 400 bp long recombination sequences flanking the TbCls ORF.[25] Prior to transfections into NY single marker bloodstream forms,[37] plasmids were cut upstream and downstream of the recombination sequences using *Xho*I and *Not*I. The inducible hemagglutinin (HA)-tagged ectopic copy of TbCls was constructed by PCR amplification of the Tb927.4.2560 ORF as described.[25] Prior to transfection, the vector was linearized with *Not*I. Clones were obtained by limiting dilution and antibiotic selection using 1 μg/mL of blasticidin, 0.1 μg/mL of puromycin, 0.5 μg/mL of hygromycin, and 1 μg/mL of tetracycline. Clones were PCR-tested for correct integration using primer 5′UTR_control TCGTCCGCGCCTTTGTGTAGCTA, which binds 50 bp upstream of the 5′-recombination site, in combination with different reverse primers. Construction of c-Myc-tagged proteins was done as described.[27]

2.3 | Southern blot analysis

For Southern blot analysis, 1.5 μg *Nco*I or *Pst*I/*Sph*I-digested genomic DNA was separated on a 1% agarose gel and transferred to hybond-N + nylon transfer membrane (Amersham Pharmacia Biotech, Glattbrugg, Switzerland) using 10xSSC buffer (150 mM Na_3-citrate, pH 7.0, 1.5 M NaCl) as described.[25] The membrane was probed with a 400 bp ^{32}P-labeled PCR product of the TbCls 3′UTR generated with the prime-a-gene labeling system (Promega). Primers used for PCR were: 3′UTR_fwd CCCTCTAGACAGCTCACGAACCGTGCCCTA and 3′UTR_rev: CCCGCGGCCGCTATCCGTCGAGGGCCACCC. Hybridized probe was detected by autoradiography using BioMax MS films in combination with intensifying screens.

2.4 | Metabolic labeling

Approximately 10^7 parasites in mid-log phase were labeled with 10 μCi [^{3}H]-glycerol for 6 hours followed by washing, lipid extraction, thin-layer chromatography, and radioisotope scanning as described.[38]

2.5 | Preparation of crude membrane fractions and membrane proteins

Crude mitochondrial preparations were obtained by digitonin extraction as described elsewhere.[39] Briefly, 10^8 trypanosomes were washed in SBG buffer (150 mM Tris-HCl, pH 7.9, 20 mM glucose monohydrate, 20 mM NaH_2PO_4) and parasites collected by centrifugation (1500 *g*, 5 min). Cells were suspended in 0.5 mL of SoTE (20 mM Tris-HCl, pH 7.5, 0.6 M sorbitol, 0.2 mM EDTA) followed by the addition of SoTE containing 0.05% (w/v) digitonin. After 5 minutes incubation on ice, non-lysed cells were removed by centrifugation for 5 minutes at 800 *g* and crude membrane fraction was collected by another centrifugation step (6000 *g*, 5 minutes, 4°C). For complete membrane lysis and extraction of membrane proteins, the pellet was dissolved in 100 μL of extraction buffer (20 mM Tris-HCl, pH 7.2, 15 mM NaH_2PO_4, 0.6 M sorbitol) containing 1.5% (w/v) digitonin and incubated on ice for 15 minutes. Solubilized proteins were cleared from insoluble material by centrifugation (16 000 *g*, 30 minutes at 4°C) and used for further analysis. Carbonate extraction was done as described.[27]

2.6 | Immunoprecipitation of TbCls-HA

To immunoprecipitate TbCls-HA, crude membranes isolated from $5x10^8$ parasites were solubilized with 100 μL RIPA buffer (25 mM Tris-HCl, pH 7.4, 150 mM NaCl, 0.1% SDS,

0.5% sodium deoxycholate, 1% NP-40) and heated to 65°C for 5 minutes. After dilution with 900 µl of IP buffer (10 mM Tris-HCl, pH 7.4, 150 mM NaCl, 1 mM EDTA, 1% Triton X-100, 0.5% NP-40, protease inhibitors) and centrifugation (16 000 *g*, 30 minutes at 4°C), anti-HA (16B12, Enzo Life Sciences) antibody was added in combination with Protein G Dynabeads (Thermo Scientific) and incubated for 16 hours. After washing with IP buffer, proteins were eluted by SDS sample buffer and analyzed by immunoblotting as described below.

2.7 | Polyacrylamide gel electrophoresis and immunoblotting

Proteins were denatured by SDS and separated using 12% polyacrylamide gels under reducing conditions (SDS-PAGE). Alternatively, blue native polyacrylamide gel electrophoresis (BN-PAGE) was performed using digitonin extracts and separation by 4%-12% acrylamide gradient gels at 4°C.[40] Subsequently, proteins were transferred onto nitrocellulose membranes (Thermo Scientific) or Immobilon-P polyvinylidene difluoride membranes (Millipore, Billerica, MA) using a semi-dry protein blotting system (BioRad, Cressier, Switzerland). After blocking the membrane in TBS (10 mM Tris-HCl pH 7.5, 144 mM NaCl) containing 5% (w/v) milk powder, membranes were exposed to primary antibodies mouse anti-Hsp70 (provided by André Schneider, University of Bern, Switzerland or 41), mouse anti-HA (HA.11, 16B12, Enzo Life Sciences, Lausen, Switzerland), rabbit anti-ATP synthase subunits β, p18, ATPaseTb1, ATPaseTb2, and OSCP,[42] rabbit anti-AAC and anti-VDAC,[43] mouse anti-AOX (provided by Minu Chaudhuri, Chicago Medical School, Chicago, IL), diluted 1:1000-1:5000 in TBS containing 5% (w/v) milk powder. Horseradish peroxidase-conjugated secondary anti-mouse and anti-rabbit antibodies (Dako, Glostrup, Denmark) were used at concentrations of 1:5000 and 1:1000, respectively, and detected using an enhanced chemiluminescence detection kit (Thermo Scientific). Protein sizes were determined using PageRuler Plus Prestained Protein Ladder (Thermo Scientific) and NativeMark Unstained Protein Standard (Invitrogen). For protein quantitation, total cell lysates from 4×10^6 cells were loaded on TGX stain-free precast gels (BioRad) and subjected to SDS-PAGE before transfer to polyvinylidene difluoride membranes. Subsequently, proteins were immunodetected by specific antibodies and visualized using ChemiDoc Gel Imaging System. Signals from TbCls-depleted cells were compared to control samples and then normalized to Hsp70 loading control. The relative expression of the individual proteins was plotted using Graph Pad Prism 8.2.1.

2.8 | Transmission electron microscopy

TbCls KO parasites were cultured in the presence or absence of tetracycline to maintain or induce, respectively, ablation of TbCls expression. Trypanosomes were washed in PBS (pH 7.4, 137 mM NaCl, 2.7 mM KCl, 10 mM Na_2HPO_4, and 1.8 mM KH_2PO_4) and processed for TEM analysis as described elsewhere.[27,44]

2.9 | Stable isotope labeling with amino acids in cell culture

Stable isotope labeling with amino acids in cell culture (SILAC) and liquid chromatography-mass spectrometry/mass spectrometry was done as described before.[27]

2.10 | MitoTracker staining

Live trypanosomes (2×10^6 cells) were stained in culture medium with 100 nM MitoTracker Red CM-H_2XRos (Invitrogen) for 30 minutes. After washing, parasites were resuspended in PBS, allowed to adhere to a microscope slide (Thermo Scientific) for 15 minutes, fixed in PBS containing 4% (w/v) paraformaldehyde for 10 minutes, washed and air-dried before mounting with Vectashield (Vector Laboratories, Burlingame, CA) containing 1.5 µg/mL of 4′,6-diamidino-2-phenylindole (DAPI). The images were acquired using a Leica DMI6000 B microscope with 60x oil objective.

2.11 | Metabolomic analysis

Metabolites were extracted from 10^8 parasites by rapid cooling to 4°C by submersion of the tube in a dry ice/ethanol bath. After centrifugation for 10 minutes at 1000 *g*, the supernatant was removed completely and the pellet was suspended in 200 µL chloroform/methanol/water (1:3:1 ratio) at 4°C. After mixing with a pipette, samples were rocked for 1 hour at 4°C, cleared at 13 000 *g* for 3 minutes and 180 µL of the supernatant was transferred into a new tube and stored at −80°C until analysis.

Hydrophilic interaction liquid chromatography (HILIC) was carried out on a Dionex UltiMate 3000 RSLC system (Thermo Fisher Scientific, Hemel Hempstead, UK) using a ZIC-pHILIC column (150 mm × 4.6 mm, 5 µm column, Merck Sequant). The column was maintained at 30°C and samples were eluted with a linear gradient of solvent A (20 mM ammonium carbonate in water) in acetonitrile over 26 min at a flow rate of 0.3 mL/min. For mass spectrometry (MS) analyses, a Thermo Orbitrap Fusion (Thermo Fisher Scientific) was operated in polarity switching mode and the MS settings were as follows: resolution 120 000; AGC 2e5; m/z range 70-1000; sheath gas 40; Auxiliary gas 5; sweep gas 1; probe temperature 150°C; capillary temperature 325°C. For positive mode ionization: source voltage +4.3 kV. For negative mode ionization: source voltage −3.2 kV. S-Lens

RF level 30%. Fragmentation was performed with the following parameters: collision energy: 60%; stepped collision energy: 35%; isolation window: 2; dynamic exclusion after 1 time; exclusion duration: 6 seconds; exclude isotopes: true; minimum intensity: 50 000. Instrument raw files were converted to positive and negative ionization mode mzXML files. These files were then analyzed using PiMP[45] in combination with FrAnK (an in-house fragmentation tool).

2.12 | Mitochondrial membrane potential (ΔΨm)

In vivo ΔΨm was measured using the cell-permeant red-fluorescent dye TMRE (tetramethylrhodamine ethyl ester, Thermo Fisher Scientific). For each time point, an equal number of parasites (3×10^6) was harvested and resuspended in culture medium containing 60 nM TMRE. Mitochondrial staining was carried out for 30 minutes under standard culture conditions (37ºC and 5% CO_2). Subsequently, trypanosomes were spun down at 1400 *g* for 10 minutes at room temperature, resuspended in 1 mL of 1× PBS (10 mM phosphate buffer, 130 mM NaCl, pH 7.3), and immediately analyzed by flow cytometry (BD FACS Canto II Instrument) using the PE filter. For each sample, 10 000 events were collected. Treatment with 20 μM FCCP (carbonyl cyanide 4-(trifluoromethoxy) phenylhydrazone) was used as a control for mitochondrial membrane depolarization. Data were evaluated using BD FACS Diva (BD Company) software. The experiments were performed in triplicate.

In situ ΔΨm of permeabilized cells was determined fluorometrically employing safranin O. For each time point, 2×10^7 parasites were harvested and washed once with ANT buffer (8 mM KCl, 110 mM K-gluconate, 10 mM NaCl, 10 mM free-acid Hepes, 10 mM K_2HPO_4, 0.015 mM EGTA potassium salt, 10 mM mannitol, 0.5 mg/mL of fatty acid-free bovine serum albumin, 1.5 mM $MgCl_2$, pH 7.25).[46] The cell pellet was resuspended in 200 μL of ANT buffer containing 5 μM safranin O, 40 μM digitonin and 2 mM ATP (PanReac AppliChem), and subsequently transferred into a white flat-bottom 96-well microtiter plate. Fluorescence was recorded in a Tecan Infinite 200 PRO series plate reader using 496 and 586 nm excitation and emission wavelengths, respectively. The F_oF_1-ATP synthase inhibitor oligomycin (10 μg/mL) and the uncoupler SF6847 (250 nM) (Enzo Life Sciences) were added where indicated. The experiments were performed in triplicate.

2.13 | Oxygen flux analysis

The oxygen consumption rate was determined using the Oroboros Oxygraph-2K (Oroboros Instruments Corp., Innsbruck, Austria). For each time point, 2×10^7 parasites were harvested and washed once with Mir05 mitochondrial respiration medium (0.5 mM EGTA, 3 mM $MgCl_2$, 60 mM lactobionic acid, 20 mM taurine, 10 mM KH_2PO_4, 20 mM Hepes, 110 mM sucrose, 1 mg/mL of fatty acid-free bovine serum albumin, pH 7.1). The pellet was resuspended in 2.1 mL of Mir05 and transferred into the respiration chamber at 37ºC under constant stirring. To trigger AOX-mediated respiration, 20 mM DL-glycerol-3-phosphate was added. Once the maximal respiration rate was achieved, respiration was inhibited by addition of 250 μM SHAM (salicylhydroxamic acid). The most stable portion of either the oxygen consumption rate slope or the oxygen concentration in the chamber slope was determined for each biological replicate after the addition of the substrate and the inhibitor. The values were plotted and analyzed statistically using GraphPad Prism 8.0 software.

2.14 | ATP measurements

Both the ADP/ATP ratio and the total cellular ATP content were measured using a bioluminescence-based ADP/ATP assay kit (Sigma) following the manufacturer's protocol. In brief, 1×10^6 parasites per time point were harvested and washed once with PBS-G (1× PBS containing 6 mM glucose). Cells were resuspended in 10 μL of PBS-G and transferred into a white flat-bottom 96-well microtiter plate. Bioluminescence was recorded using an Orion II microplate luminometer (Titertek Berthold) and the ADP/ATP ratios were calculated according to the manufacturer's protocol. The ADP/ATP ratio and the ATP content (first fluorescence read of the assay) of TbCls-depleted trypanosomes were expressed relative to control parasites using GraphPad Prism 8.0 software.

3 | RESULTS

3.1 | Generation and characterization of bloodstream form conditional TbCls knock-out parasites

To study the importance of CL in an organism lacking a canonical cytochrome-containing electron transport chain (ETC), we generated *T brucei* bloodstream form TbCls conditional knock-out (TbCls KO) mutants by deleting both endogenous TbCls genes and expressing a tetracycline-dependent HA-tagged ectopic copy of TbCls (Figure 1A). Replacement of both TbCls alleles in the conditional TbCls knock-out mutant was confirmed by Southern blotting (Figure S1A) and the presence and correct genomic integration of the two antibiotic resistance genes was verified by

PCR using gene-specific primers (Figure S1B). Removal of tetracycline from the culture medium for 24 hours resulted in a reduction of TbCls mRNA (Figure 1B), disappearance of HA-tagged TbCls (Figure 1C) and growth arrest after 48 hours followed by parasite death (Figure 1D), demonstrating that expression of TbCls is essential in *T brucei* bloodstream forms and that growth of parasites can be maintained by expressing a tetracycline-dependent HA-tagged copy of TbCls. De novo production of CL was analyzed by in vivo [^{3}H]-glycerol labeling of TbCls KO parasites and revealed that after TbCls depletion for 24 hours no label was incorporated into CL (Figure 1E), showing that ablation of TbCls expression inhibits CL synthesis. To examine whether CL depletion leads to defects in mitochondrial structural and functional integrity, we first analyzed mitochondria ultrastructure by transmission electron microscopy. Electron micrographs of TbCls KO parasites after 0 and 48 hours of CL depletion showed no obvious morphological defects in mitochondria (Figure 2A). In contrast, examination of the ΔΨm using the potential-dependent dye MitoTracker Red and fluorescence microscopy revealed that parasites lacked the typical mitochondrial staining observed in control trypanosomes after depletion of TbCls for 24 hours (Figure 2B). In addition, we analyzed the ΔΨm during TbCls depletion using the fluorescent lipophilic dye, tetramethylrhodamine ethyl ester (TMRE), in non-quenching mode averaged over the entire

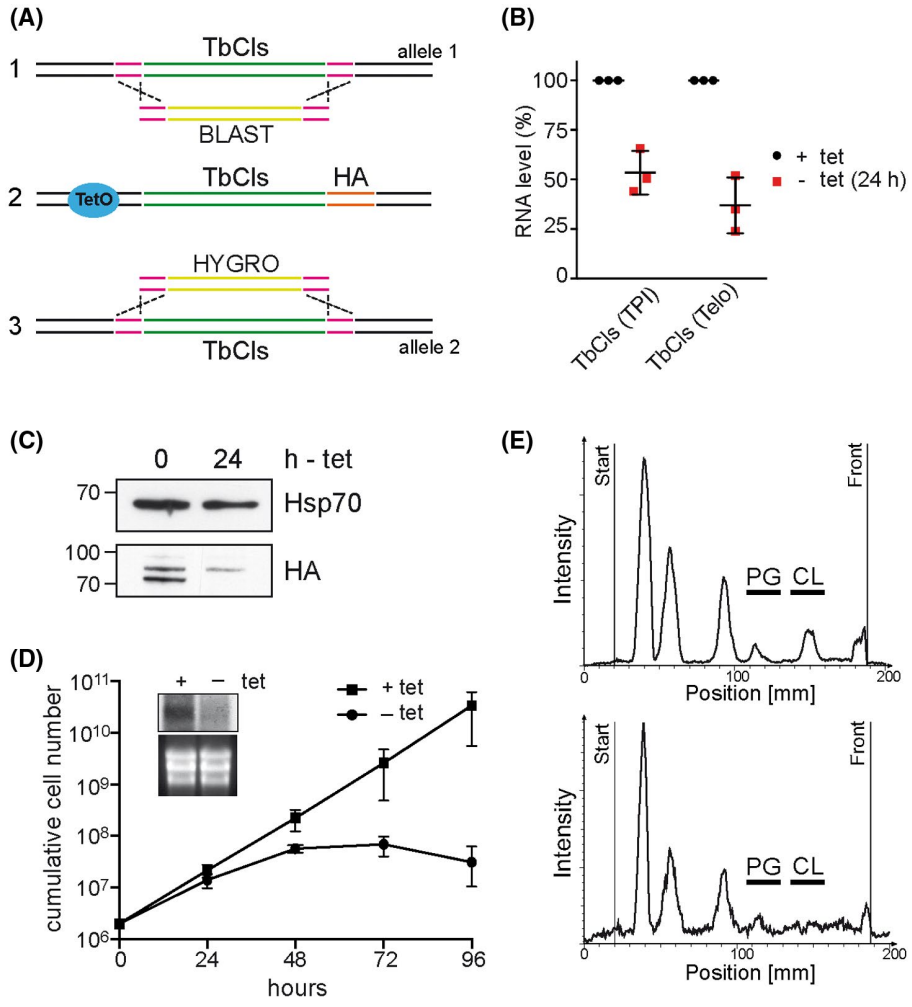

FIGURE 1 Characterization of conditional TbCls KO bloodstream form parasites. A, The strategy to generate an inducible TbCls KO involved replacement of one allele with a resistance gene conferring blasticidin resistance, introduction of an ectopic tetracycline-inducible C-terminally HA-tagged TbCls ORF followed by replacement of the second TbCls allele with a hygromycin resistance gene. B, Quantitative PCR assessment of TbCls mRNA after 24 hours of tetracycline removal relative to the two housekeeping genes triosephosphate isomerase (TPI) or telomerase (Telo). C, Immunoprecipitation and immunoblot analysis of HA-tagged TbCls before (0) or after 24 hours of tetracycline removal. Hsp70 was used as input control. D, Growth curve of conditional TbCls KO cells cultured in the presence (filled circles) or absence (filled squares) of tetracycline to induce TbCls depletion. The data points represent mean values ± SD from three independent experiments. The inset shows the TbCls mRNA abundance detected by Northern blot analysis after 0 and 48 hours of TbCls depletion (upper panel) and the rRNA loading control (lower panel). E, In vivo metabolic labeling of TbCls KO parasites before (top panel) or after TbCls depletion for 24 hours (bottom panel) with [^{3}H]-glycerol for 6 hours followed by phospholipid extraction and analysis using thin-layer chromatography and radioisotope scanning

cell population.[47] Our comparative measurements showed a marked reduction in ΔΨm by ~50% after 24 hours and ~75% after 48 hours of TbCls depletion compared to control parasites (Figure 2C).

3.2 | F_oF_1-ATPase complex organization and activity during CL depletion

In *T brucei* bloodstream forms, the ΔΨm is maintained by ATP-dependent proton-pumping activity of F_oF_1-ATPase complexes.[30,31] To test if the drop in ΔΨm was caused by a destabilization of F_oF_1-ATPase complexes as a result of decreased CL levels, light blue native gel electrophoresis was performed. Native complexes were detected after immunoblotting with specific antibodies against F_1 subunits β and p18 or F_o subunit Tb2.[42,48] The results show a mild reduction in the abundance of the monomeric/dimeric state of the F_oF_1-ATPase complex accompanied by an accumulation of the F_1 assembly intermediate after 24 hours of TbCls depletion, which becomes more pronounced after 48 hours of TbCls depletion (Figure 3A). To assess the ability of F_oF_1-ATPase complexes to pump protons, we measured uptake of safranin O into mitochondria of digitonin-permeabilized cells in the presence of exogenously added ATP. Safranin O is a lipophilic cationic dye that, upon membrane potential-dependent uptake into mitochondria, undergoes a spectral change and fluorescence quenching that can be used to estimate

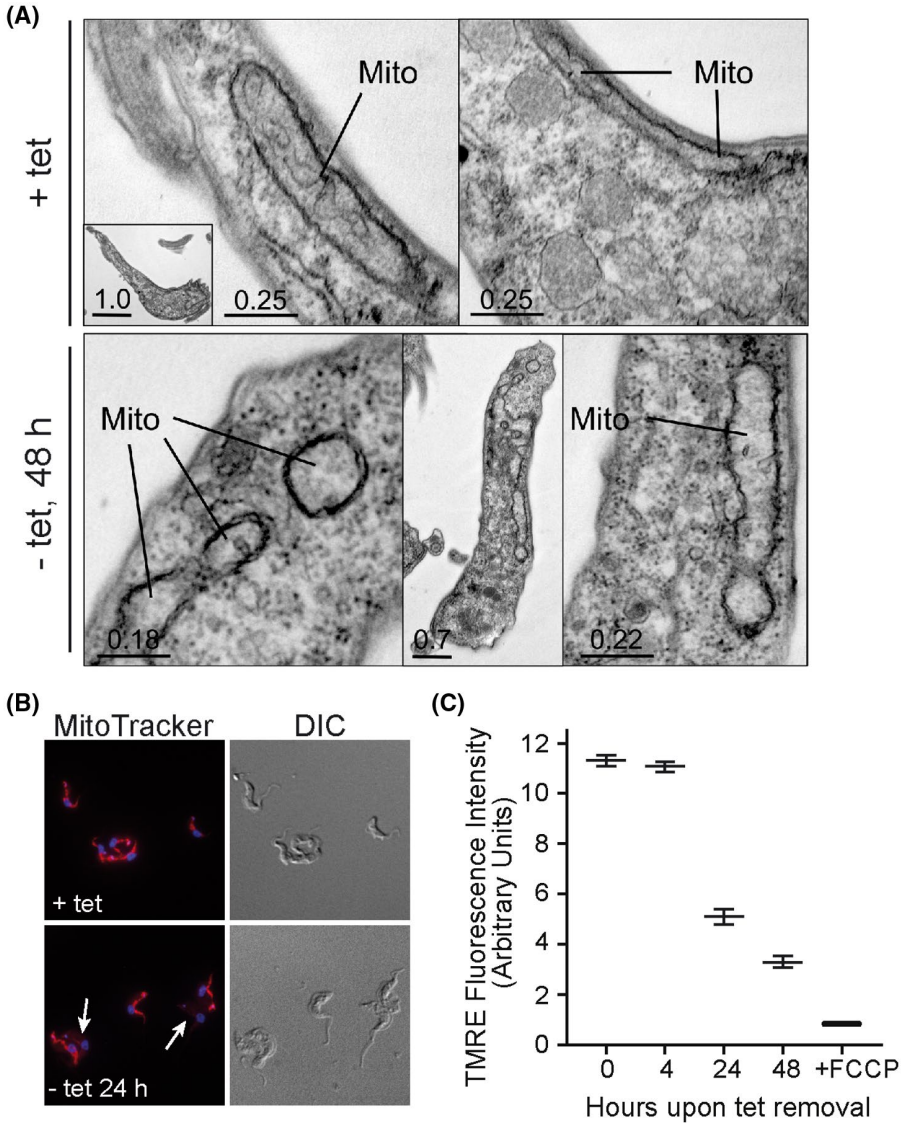

FIGURE 2 Mitochondrial characterization of TbCls KO parasites. A, Transmission electron microscopy of TbCls KO cells cultured in the presence (+tet) or the absence (−tet) of TbCls expression for 48 hours. B, MitoTracker staining of live parasites before (+tet) or after (−tet) TbCls depletion for 24 hours. Arrows point to cells lacking MitoTracker staining. C, The ΔΨm of TMRE-stained TbCls KO cells before (0) or after depletion of TbCls for 4, 24, or 48 hours was measured using flow cytometry. FCCP was used to dissipate ΔΨm. The median fluorescence ± SD from three biological replicates is depicted

ΔΨm.[49] Relative to control parasites expressing TbCls, we observed a ~20% reduction of safranin O uptake after depletion of TbCls for 24 hours, while a decrease of ~40% was detected after 48 hours of TbCls ablation (Figure 3B-D). The difference between the ΔΨm measured by TMRE in intact cells (see Figure 2C) and safranin O uptake measured in digitonin-permeabilized cells in the presence of excess ATP suggests that early during depletion of TbCls, ie, after 24 hours, lack of ATP rather than loss of F_oF_1-ATPase function is responsible for the drop in ΔΨm. Indeed, quantitation of the ADP/ATP ratio and total ATP levels after 24 hours of TbCls depletion revealed an increase in the ADP/ATP ratio

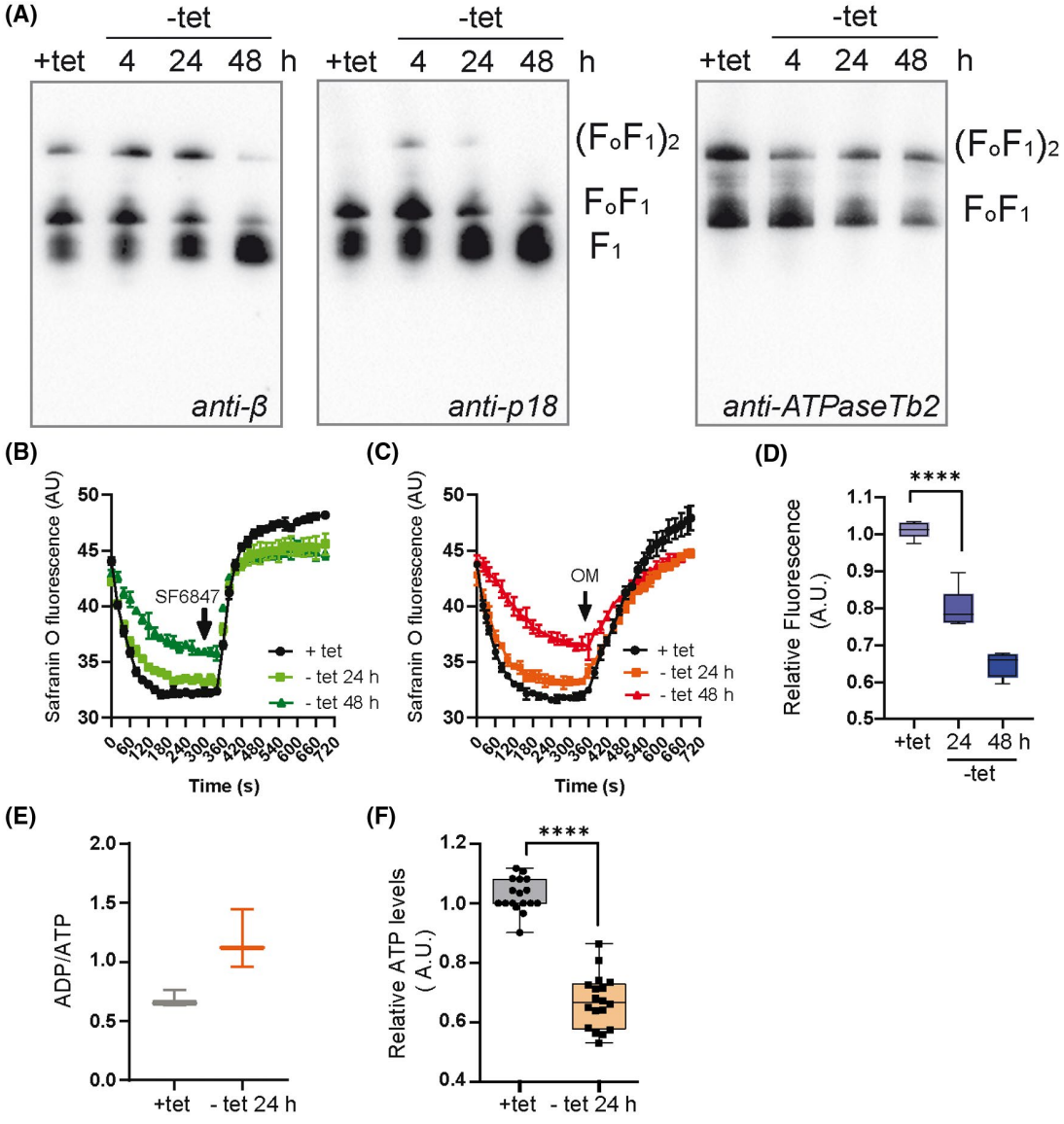

FIGURE 3 Functional assessment of the mitochondrial F_oF_1-ATP synthase complex. A, Native F_1- and F_oF_1-ATPase complexes were visualized using light blue native electrophoresis. Purified mitochondria from ±tet cultures were lysed with dodecyl maltoside, fractionated on 3%-12% Bis-Tris gels and blotted onto a PVDF membrane. The F_1-ATPase and F_oF_1-ATPase monomer and dimers were detected using polyclonal antibodies recognizing F_1-ATPase subunits β and p18, or F_oF_1-ATPase subunit Tb2. Representative images from two independent experiments are shown. B and C, The ability of TbCls KO parasites cultured in the presence (+tet) or absence of tetracycline (−tet) for 24 or 48 hours to establish ΔΨm in vitro was measured using a fluorescent indicator, safranin O, in the presence of excess ATP. The reaction was triggered by the addition of digitonin. The extent of the spectral change correlates linearly to ΔΨm. The ΔΨm was dissipated after the addition of the uncoupler SF6847 (B) or oligomycin (C). D, The fluorescence changes between the time points 0 and 340 seconds were normalized to the value of TbCls KO (+tet) and plotted using Graph Pad Prism 8.2.1 (n = 3); ****$P < .0001$, Student's t test). E and F, Comparison of ADP/ATP ratios (E) and cellular ATP content (F) in TbCls KO parasites cultured in the presence (+tet) or absence of tetracycline (−tet) for 24 hours (box and whisker plot, min to max, n > 3; ****$P < .0001$)

TABLE 1 Metabolomic changes triggered by depletion of TbCls

Log2 fold change (24 h)	Metabolite
−7.63	Tetracycline
−2.20	Torachrysone 8-glucoside
−2.14	10-formyldihydrofolate
−1.86	Nocardicin c
−1.57	kaempferol 3-(2″-acetylrhamnoside)
−1.53	Phosphoarginine
−1.29	(s)-dihydroorotate
−0.84	Galactonic acid
−0.84	D-Gluconic acid (or other oxidized hexose)
−0.69	L-Cystathionine
−0.51	Acetoacetate
−0.38	L-Threonine
0.49	Ethanolamine phosphate
0.73	sn-Glycerol-3-phosphate
0.78	Guanine
1.30	l-n2-(2-carboxyethyl) arginine
1.79	AMP

Note: List of mass spectrometry signals matched to known standards. The log2 fold change between metabolites found in parasites expressing TbCls and depleted of TbCls for 24 hours are listed. Metabolites shown had a significance at a *p*-value of <.05.

(Figure 3E) and a drop in cellular ATP (Figure 3F) compared to control cells. In summary, after 24 hours of TbCls depletion, F_oF_1-ATPase structure and activity appear to be only marginally affected, yet the $\Delta\Psi m$ is strongly reduced, likely due to the drop in cellular ATP.

3.3 | Metabolomic analyses of TbCls-depleted trypanosomes

To identify possible metabolic changes caused by TbCls depletion, we performed metabolomic analyses of parasites after 12 and 24 hours of TbCls depletion and compared metabolite levels to control cells. Interestingly, of a total of 5050 detected peaks, we observed significant changes (*P*-values < .05) in several key metabolites associated with energy deprivation. While the levels of phosphoarginine, acetoacetate, and oxidized hexoses were decreased, AMP levels were increased (Table 1). Phosphoarginine represents the equivalent to phosphocreatine in vertebrates by providing high-energy phosphate groups to replenish ATP levels on a short time-scale and is produced by multiple isoforms of phosphoarginine kinases.[50] Acetoacetate represents a ketone body produced under conditions of starvation and has been identified in *T brucei* before,[51] whereas oxidized hexoses, for example, D-gluconate, are substrates for the pentose-phosphate pathway for nucleotide biosynthesis and formation of NADPH, a key reducing agent for protection against oxidative stress in trypanosomes.[52]

Pathway analyses using Polyomics integrated Metabolomics Pipeline PiMP[45] revealed no consistent changes in metabolite levels in the glycolytic pathway, the TCA cycle or amino acid metabolism, while glycerolipid metabolism was the most significantly changed pathway between control and 24 hours TbCls-depleted parasites, highlighted by increased levels of glycerol and glycerol-3-phosphate (Figure S2). Together, the metabolomic analyses support the above observations that parasites after 24 hours of TbCls depletion are in an energy-deprived state.

3.4 | Proteomic changes during CL depletion

Using SILAC and mass spectrometry we subsequently compared the proteomes of mitochondria-enriched extracts from *T brucei* bloodstream forms after depletion of TbCls for 12 and 24 hours with parasites expressing TbCls. Previous experiments have shown that labeled amino acids are uniformly incorporated into the proteome in *T brucei* parasites[27,53] and that parasite growth was not affected by the different culture media used for SILAC (Figure S3).

Our analyses revealed >1100 proteins in each of the biological triplicate from all three time points (0, 12 and 24 hours of TbCls ablation). We identified a large number of proteins with altered expression levels after 12 and 24 hours of TbCls depletion compared to control trypanosomes (Figure 4A-C), with >110 proteins with fold-changes of downregulation of ≥1.6 (Figure 4D, Table S1) and >35 proteins with fold-changes of upregulation of ≥1.4 (Figure 4D, Table S2).

Among the downregulated proteins, (predicted) mitochondrial proteins comprised the largest group (Figure 4D, Table S1). Interestingly, we identified two known subunits of ATP synthase, Tb1 (Tb927.10.520) and Tb2 (Tb927.5.2930), and several proteins annotated as novel subunits of ATP synthase (Tb927.2.3610, Tb927.11.600, Tb927.3.1690, Tb927.11.1270) (Figure 4D, Table S1). In addition, among the downregulated proteins, we identified six (putative) proteins involved in amino acid metabolism, with two of them representing putative amino acid transporters of the AAT4 family with unknown specificities and localization (Tb927.4.4830/4850/4870; Tb927.4.4860), one being a putative mitochondrial amino acid transporter of the AAT17 family (Tb927.11.15950) and the other annotated as putative lysine transport protein (Tb927.11.15840/15860). Furthermore, downregulation was also observed for several mitochondrial and cytosolic proteins involved in energy metabolism,

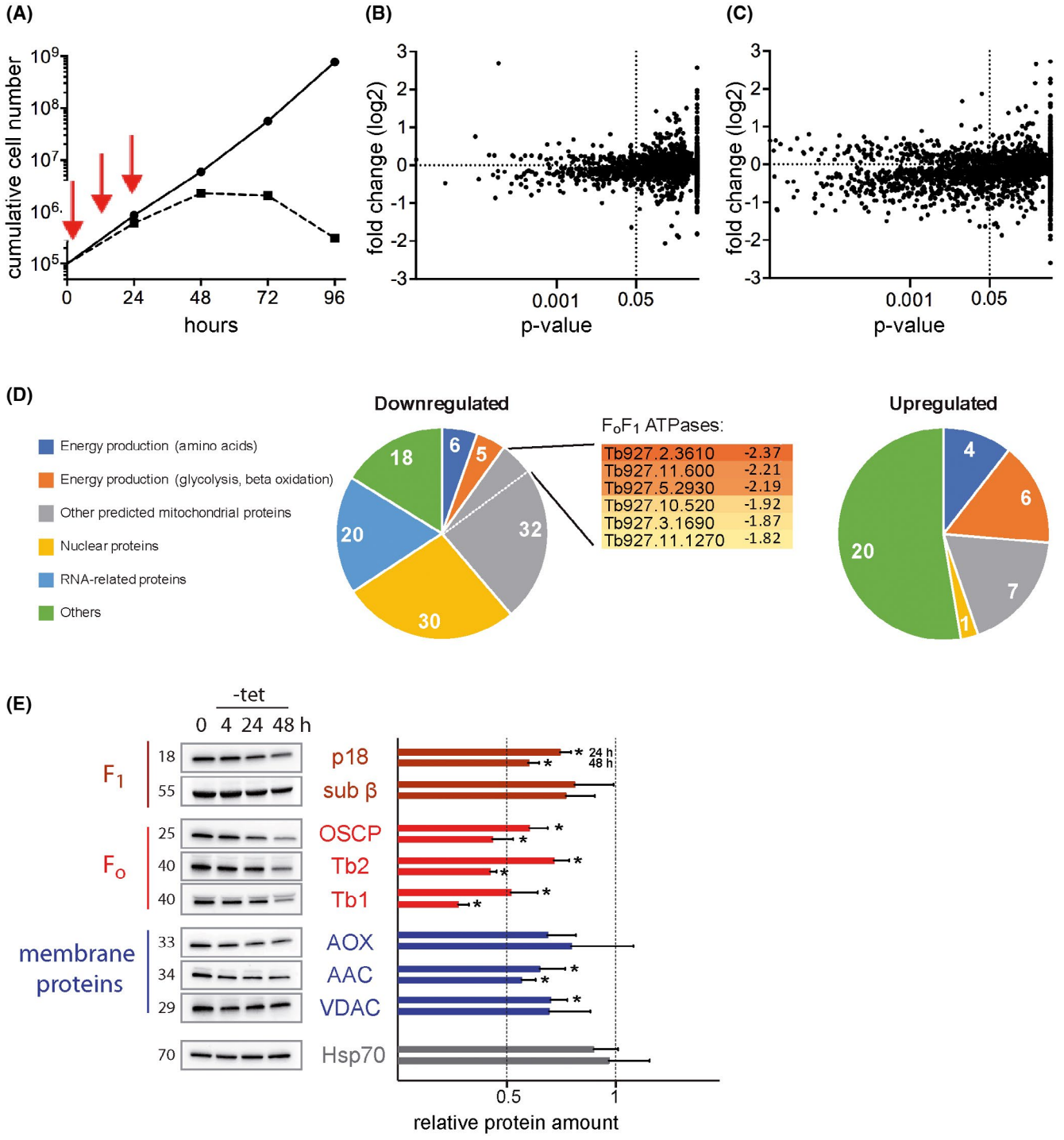

FIGURE 4 Cardiolipin-induced changes in protein levels. A-C, SILAC analysis of protein abundance during depletion of TbCls. Membrane-enriched fractions from TbClsKO parasites cultured for 0, 12, or 24 hours (indicated by red arrows in A) in the absence of tetracycline to induce ablation of TbCls expression were analyzed by mass spectrometry. The p-value of each data point was determined by a two-sample t test between time points 0 and 12 hours (B) and 0 and 24 hours (C) from three biological independent experiments and was plotted against the fold change in protein abundance after 12 and 24 hours, respectively, relative to the control sample taken at time 0 hours. D, Grouping of proteins that were down- or upregulated upon TbCls depletion for 24 hours. Gene IDs for downregulated ATP synthase subunits are shown. E, Immunoblot analyses of TbCls KO cells grown in the presence (0) or absence of tetracycline for 4, 24, and 48 hours (left panels). The bars (right panels) represent relative protein amounts in samples after 24 and 48 hours of TbCls depletion compared to controls and represent mean values ± SD from at least three independent experiments (quantitation of immunoblots). *$P < .01$

such as putative enoyl-CoA hydratase (Tb927.11.16480), malic enzyme (Tb927.11.5450), putative hydroxymethylglutaryl-CoA lyase (Tb927.4.2700), putative acyl-CoA synthetase (Tb927.6.2010), putative NADH-cytochrome b5 reductase (Tb927.5.1470), putative adenylate kinase (Tb927.10.2540) and pyruvate kinase 1 (Tb927.10.14140).

The list of downregulated proteins also comprised proteins involved in nucleotide metabolism (two adenosine transporters, ribonucleoside-diphosphate reductase) and *N*-glycosylation (putative dolichyl-P-Man:GDP-Man7GlcNAc2-PP-dolichyl alpha-1,6-mannosyltransferase, putative UDP-Gal/UDP-GlcNAc-dependent glycosyltransferase) and two large sets with nuclear/nucleolar proteins and proteins involved in RNA synthesis/processing (Table S1).

Among the upregulated proteins, we identified proteins involved in energy production via carbohydrate metabolism, including the bloodstream form-specific glucose transporter THT1 (Tb927.10.8440), hexokinase (Tb927.10.2010), fructose-bisphosphate aldolase (Tb927.10.5620) and glyceraldehyde 3-phosphate dehydrogenase (Tb927.10.6880) (Figure 4D, Table S2), and several mitochondrial enzymes connecting amino acid metabolism to the TCA cycle, such as glutamate dehydrogenase (Tb927.9.5900), putative hydroxyglutarate dehydrogenase (Tb927.10.9360), putative 2-oxoglutarate dehydrogenase, component E1 (Tb927.11.9980) and succinate dehydrogenase assembly factor 2 (Tb927.6.2510). Remarkably, several nutrient and ion transporters ranked among the most highly upregulated proteins, such as putative mitochondrial amino acid transporter AAT7 (Tb927.8.7610/8.7640; 2.3-fold upregulation), aquaglyceroporin 1 (Tb927.6.1520; 2.1-fold upregulation), mitochondrial folate transporter (Tb927.8.3650; 1.9-fold upregulation) and putative mitochondrial V-type ATPase (Tb927.4.1080; 1.5-fold upregulation).

To verify CL-dependent downregulation of selected mitochondrial proteins, protein extracts from *T brucei* bloodstream forms after downregulation of TbCls were analyzed by SDS-PAGE and immunoblotting using antibodies recognizing F_oF_1-ATPase subunits, mitochondrial membrane proteins or mitochondrial matrix proteins (Figure 4E). The results after TbCls depletion revealed decreased levels of several F_o subunits (>20 and >50% reduction after 24 and 48 hours, respectively) and F_1 subunits (>20% reduction after 24 and 48 hours) of the F_oF_1-ATPase complex (Figure 4E, top two panels) and the inner mitochondrial membrane proteins AOX (Tb927.10.7090; ~25% reduction after 24 hours) and ADP/ATP carrier (AAC; Tb927.10.14830; ~30% reduction after 24 hours) (Figure 4E, middle panel). These results are in line with the SILAC/mass spectrometry data showing reduced levels of several F_oF_1-ATPase complex subunits (see Table S1) and a reduction in AOX (~20% decrease after 24 hours; AAC was not detected in the SILAC experiments).

In bloodstream form trypanosomes, glycolysis and thus ATP production is directly coupled to mitochondrial respiration via an unconventional ETC composed of glycerol-3-phosphate dehydrogenase and AOX.[54] To assess if the CL-induced drop in ATP levels is linked to decreased cellular respiration, we measured oxygen consumption rates of live parasites during the depletion of TbCls. Our results show that O_2 consumption after 24 and 48 hours of CL depletion was significantly reduced relative to control cells (Figure 5A,B). Since AOX is a dimer bound to the inner mitochondrial membrane via a hydrophobic region in an interfacial fashion,[55] we tested if CL may be involved in membrane binding of AOX. We performed carbonate extraction experiments with isolated mitochondria from parasites before and after depletion of CL and found that AOX expression is indeed decreased (Figure 5C; see also Figure 4E), however, partitioning of AOX between pellet and supernatant fractions was unchanged between TbCls-depleted and control parasites (Figure 5C), demonstrating that depletion of CL affected AOX steady-state levels but not binding to the inner mitochondrial membrane.

4 | DISCUSSION

High-resolution structures have revealed specific binding of CL to mammalian and yeast respiratory complexes I,[7] III[8,9] and IV[10] of the inner mitochondrial membrane. In addition, CL stimulates the activities of these complexes and stabilizes supercomplex formation.[11] As a result, in CL-deficient mammalian, yeast and plant cells, mitochondrial ultrastructure and function, in particular respiration, is affected. In spite of these defects, the cells are viable.[24,56,57] In contrast, CL is essential for the survival of *T brucei* procyclic forms in culture.[25,38] Here, we investigated the effects of CL depletion in *T brucei* bloodstream forms, that is, in cells lacking a canonical ETC and ATP production via oxidative phosphorylation.[28]

To control de novo CL synthesis, we deleted both alleles of TbCls in *T brucei* bloodstream forms and introduced a tetracycline-dependent copy of HA-tagged TbCls. Upon removal of tetracycline from the culture medium, TbCls expression was downregulated and de novo synthesis of CL was inhibited. These conditions resulted in a growth arrest of parasites followed by cell death, demonstrating that the production of CL in *T brucei* bloodstreams forms is essential for parasite survival in culture.

Interestingly, after inhibition of CL synthesis, proteomic analyses revealed markedly reduced levels of many mitochondrial proteins. Most notably, several confirmed and predicted subunits of the inner mitochondrial membrane F_oF_1-ATPase complex were severely downregulated. CL is tightly associated with the F_oF_1-ATP synthase,[58,59] and crystal structures have revealed CL binding sites in the rotor-stator interface, the dimer interface, and in a peripheral F_o cavity.[59] Molecular modeling suggests that CL participates in proton translocation through the membrane domain.[60] Upon CL depletion in *Drosophila* flight-muscle mitochondria, F_oF_1-ATP synthase dimers are destabilized and their lateral membrane distribution is distorted.[6] In *T brucei* bloodstream forms, we observed a destabilization of F_oF_1-ATPase dimers and

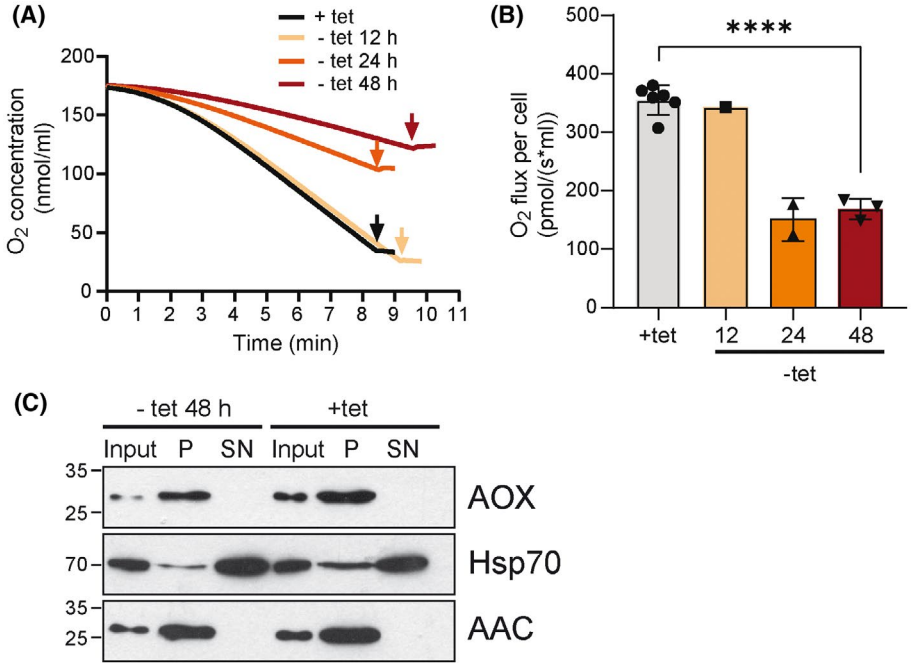

FIGURE 5 Oxygen consumption is affected by CL depletion. A, Representative respiratory traces of TbCls KO parasites cultured in the presence (+tet) or the absence of tetracycline (−tet) for 12, 24, or 48 h were determined using high-resolution respirometry. The graphs depict changes in oxygen concentration (nmol/ml) in the media over time (X-axis). Arrows indicate time of addition of the inhibitor SHAM. B, Oxygen flow in TbCls KO parasites cultured in the presence (+tet) or absence of tetracycline (-tet) for 12, 24, or 48 hours is expressed as respiration per million cells (pmol × s^{-1} × 10^{-6}cells) (mean values ± SD, ****$P < .0001$). C, Carbonate extraction from mitochondria-enriched fractions of TbCls KO parasites grown in presence or absence of TbCls expression for 48 hours. Fractionation of AOX was compared to the soluble protein Hsp70 and the integral membrane protein AAC. Representative images from two independent experiments are shown

monomers during CL depletion leading to accumulation of F_1-ATPase subcomplex. Functional uncoupling of the F_o and F_1 domains of the F_oF_1-ATPase has been observed before in naturally occurring and drug-induced dyskinetoplastic bloodstream form trypanosomes,[61] which maintain the ΔΨm in an F_o-independent fashion[30] by coupling F_1-ATPase activity with the electrogenic exchange of cytosolic ATP^{4-} for mitochondrial matrix ADP^{3-} by the AAC. However, this mechanism is conditioned by acquiring specific mutations in the F_1 subunits,[62,63] which presumably increase the enzyme's capacity to hydrolyze ATP. Without these mutations, bloodstream form parasites are not capable of maintaining ΔΨm in the F_o-independent mode.[30] These observations are consistent with our results of the ΔΨm measurements in vivo by TMRE and in vitro by safranin O at 48 hours of CL depletion. The decreased levels of the coupled F_oF_1-ATPase led to a substantial drop in ΔΨm. Interestingly, at 24 hours of TbCls depletion, the ΔΨm measured in vivo by TMRE was already decreased by 50%, while in vitro safranin O uptake measurements in presence of excess ATP revealed only a 20% reduction in ΔΨm, suggesting that at this early timepoint it is the lack of the substrate, that is, ATP, rather than the dysfunction of the F_oF_1-ATPase that leads to the observed ΔΨm phenotype.

In addition to a downregulation of F_oF_1-ATPase subunits, CL depletion resulted in a decrease of several (putative) transporters. It has been shown before that CL associates with and affects the activity of the mitochondrial AAC.[64,65] In addition, CL stimulates the activities of the carnitine/acylcarnitine transporter[66] and the phosphate carrier,[67] and it is possible that additional mitochondrial carriers also depend on CL for proper function.[13] Although the subcellular localization of several of the *T brucei* transporters downregulated after CL depletion has not been experimentally established, our data suggest that they may localize to the inner mitochondrial membrane, where they interact with CL and become depleted after inhibition of de novo CL synthesis. Two mitochondrial amino acid transporters, amino acid transporter AAT17 (Tb927.11.15950) and L-lysin transport protein (Tb927.11.15840), which have not yet been associated with CL, were downregulated as well. Whether or not they bind CL and are downregulated as a direct consequence of CL depletion is not clear, but deserves further attention. Similarly, although the association of AOX with the inner mitochondrial membrane was not disrupted during CL depletion, its expression was decreased. It is conceivable that the observed decrease in oxygen consumption by AOX is a direct consequence of reduced CL levels. The *T brucei* bloodstream form cellular respiration is coupled to the glycerol-3-phosphate/dihydroxyacetone phosphate shuttle in which the mitochondrial FAD-linked glycerol-3-phosphate dehydrogenase oxidizes

glycerol-3-phosphate to dihydroxyacetone phosphate and passes electrons to ubiquinone.[54] The reduced ubiquinone is then oxidized by AOX. Mitochondrial glycerol-3-phosphate dehydrogenase is tightly bound to the inner mitochondrial membrane and was proposed to function in a cardiolipin-dependent fashion.[68] It is possible that in the absence of CL, *T brucei* glycerol-3-phosphate dehydrogenase becomes dysfunctional, and glycerol-3-phosphate is instead converted to glycerol by glycerol kinase in glycosomes, thereby resembling anaerobic conditions during which only one molecule of ATP is produced per one molecule of glucose.[69] Indeed, the ablation of TbCls expression led to decreased ATP levels. Further, we also observed an accumulation of glycerol-3-phosphate and glycerol, indicating an improper function of glycerol-3-phosphate dehydrogenase. Interestingly, accumulation of glycerol is known to be toxic for *T brucei* parasites, which may explain the observed increased expression of aquaglyceroporins, the transporters mediating glycerol efflux,[70] during CL depletion.

In addition, ablation of TbCls expression resulted in downregulation of several mitochondrial and cytosolic enzymes. Since none of them is predicted to contain a transmembrane domain, we believe that their decrease was not a direct effect of CL depletion but a result of metabolic alterations (see below). The two sets of proteins comprising downregulated nuclear/nucleolar proteins and proteins involved in RNA synthesis/processing likely reflect the parasite's reduced metabolism and slowed growth after prolonged CL depletion. Together, these observations indicate that the primary effect of CL depletion in *T brucei* bloodstream forms is on cellular respiration and on the structural organization and activity of the F_oF_1-ATPase, leading to a progressive loss of the $\Delta\Psi m$ and a dramatic increase in the ADP/ATP ratio as well as steady-state levels of several (mitochondrial) transporters.

Unexpectedly, and in contrast to previous findings in procyclic forms,[27] depletion of CL in *T brucei* bloodstream forms led to an increase in the levels of a large number of proteins (Table S2). Many of these proteins are involved in metabolic reactions and pathways to increase ATP production. Increases in glutamate dehydrogenase (Tb927.9.5900), (putative) hydroxyglutarate dehydrogenase (Tb927.10.9360) and 2-oxoglutarate dehydrogenase (Tb927.11.9980), as well as in (putative) amino acid transporter AAT7 (Tb927.8.7610), are consistent with upregulation of amino acid metabolism, in particular glutamate catabolism. As reported before, *T brucei* bloodstream forms consume large quantities of glutamine, primarily as an amino group donor.[71,72] Recent intracellular metabolome analyses using ^{13}C-labeled tracking confirmed that glutamine is catabolized to glutamate and on to 2-oxoglutarate and succinate.[73] Among the different possible pathways leading to production of succinate from glutamate,[73] our proteomic data suggest that during CL depletion glutamate dehydrogenase (1.6-fold upregulated) converts glutamate to 2-oxoglutarate which is then metabolized to succinate by 2-oxoglutarate dehydrogenase (1.74-fold upregulated) and succinyl-CoA synthetase (Tb927.3.2230, 1.12-fold upregulated) to produce ATP. In addition, 2-oxoglutarate can be converted to hydroxyglutarate by promiscuous action of malate dehydrogenase[74] (Tb927.10.2560, 1.23-fold upregulated) and back to 2-oxoglutarate by hydroxyglutarate dehydrogenase (1.74-fold upregulated). Although the substrate specificity of (putative) amino acid transporter AAT7 (2.3-fold upregulated) is currently unknown, we propose that it may be responsible for the increased uptake of glutamine into the mitochondrion of bloodstream form trypanosomes. Alternatively, increased production of glutamate could also result from AAT7-mediated uptake of proline with subsequent degradation by proline dehydrogenase (Tb927.7.210; not detected in our study) and Δ1-pyrroline-5-carboxylate dehydrogenase (Tb927.10.3210; not detected in our study).

Furthermore, our data revealed increased levels of additional enzymes and transporters involved in energy production in *T brucei* (Table S2). Upregulation of the glycolytic enzymes hexokinase (Tb927.10.2010), glyceraldehyde-3-phosphate dehydrogenase (Tb927.10.6880) and fructose-bisphosphate aldolase (Tb927.10.5620), and of hexose transporter THT1 (Tb927.10.8440), are again consistent with the parasite's metabolic response to counteract CL-induced depletion of ATP. The severity of energy depletion is further reflected in a decrease in phosphoarginine levels and an increase in the arginine metabolite N2-(2-carboxyethyl) arginine. In a recent report, it was shown that in *T brucei* bloodstream forms phosphoarginine is exclusively generated by the action of arginine kinases.[73] Although arginine kinase knock-out parasites were viable in culture,[73] it is believed that phosphoarginine plays a central role in regenerating ATP from ADP in situations of high (short term) energy demand.[75]

Remarkably, while the analysis of the proteome during CL depletion revealed a pronounced decrease in the levels of several subunits of the inner mitochondrial membrane F_oF_1-ATPase (Table S1; see also above), one protein annotated as putative ATP synthase subunit (Tb927.11.9420, 1.4-fold upregulated) was found to be increased (Table S2). Interestingly, the protein has been described as a subunit of the peripheral stalk of the vacuolar H^+-ATPase.[76] *T brucei* bloodstream forms use V-type ATPases and mitochondrial ATPases to generate proton gradients,[30] and recently functional interdependency between both types of ATPases has been reported.[77] Knock-downs of V-type ATPase subunits were shown to induce kinetoplast independence and resistance of trypanosomes to isometamidium, a DNA intercalating drug that accumulates in the kinetoplast, indicating that loss of V-type ATPases affects F_oF_1-ATPase sector coupling.[77] The function of the upregulated V-type ATPase subunit during CL depletion is not known. The observation that depletion of V-type ATPase allows for kinetoplast-independent growth[77]

suggests, however, that its levels were increased in response to the observed CL-dependent F_oF_1-ATPase sector uncoupling.

ACKNOWLEDGMENTS

The work was supported by grant no. 169355 from the Swiss National Science Foundation to PB, and by Czech Science Foundation (18-17529S) and ERD fund (CZ.02.1.01/0.0 /0.0/16_019/0000759) to AZ We thank André Schneider (University of Bern) and Minu Chaudhuri (Chicago Medical School) for antibodies, Monika Rauch and Jennifer Jelk for technical assistance during parts of the study, and Anant K. Menon (Weill Cornell Medical College New York) for advice. PB thanks A. Niederer, M. Bütikofer and R. Plant for support.

CONFLICT OF INTEREST

The authors declare that they have no conflicts of interest with the contents of this article.

AUTHOR CONTRIBUTIONS

M. Serricchio, D. Schädeli, A. Zíková, and P. Bütikofer designed research; M. Serricchio, C. Hierro-Yap, D. Schädeli, H. Ben Hamidane, A. Hemphill, and J. Graumann performed research; M. Serricchio, C. Hierro-Yap, D. Schädeli, A. Hemphill, J. Graumann, A. Zíková, and P. Bütikofer analyzed data; M. Serricchio, A. Zíková, and P. Bütikofer wrote the manuscript. All authors reviewed the manuscript.

ORCID

Peter Bütikofer https://orcid.org/0000-0001-9360-1013

REFERENCES

1. Schlame M, Ren M. The role of cardiolipin in the structural organization of mitochondrial membranes. *Biochim Biophys Acta*. 2009;1788:2080-2083.
2. Renner LD, Weibel DB. Cardiolipin microdomains localize to negatively curved regions of *Escherichia coli* membranes. *Proc Natl Acad Sci USA*. 2011;108:6264-6269.
3. Mileykovskaya E, Dowhan W. Visualization of phospholipid domains in Escherichia coli by using the cardiolipin-specific fluorescent dye 10-N-nonyl acridine orange. *J Bacteriol*. 2000;182:1172-1175.
4. Beltran-Heredia E, Tsai FC, Salinas-Almaguer S, Cao FJ, Bassereau P, Monroy F. Membrane curvature induces cardiolipin sorting. *Commun Biol*. 2019;2:225.
5. Friedman JR, Mourier A, Yamada J, McCaffery JM, Nunnari J. MICOS coordinates with respiratory complexes and lipids to establish mitochondrial inner membrane architecture. *eLife*. 2015;4:e07739.
6. Acehan D, Malhotra A, Xu Y, Ren M, Stokes DL, Schlame M. Cardiolipin affects the supramolecular organization of ATP synthase in mitochondria. *Biophys J*. 2011;100:2184-2192.
7. Fiedorczuk K, Letts JA, Degliesposti G, Kaszuba K, Skehel M, Sazanov LA. Atomic structure of the entire mammalian mitochondrial complex I. *Nature*. 2016;538:406-410.
8. Solmaz SR, Hunte C. Structure of complex III with bound cytochrome c in reduced state and definition of a minimal core interface for electron transfer. *J Biol Chem*. 2008;283:17542-17549.
9. Lange C, Nett JH, Trumpower BL, Hunte C. Specific roles of protein-phospholipid interactions in the yeast cytochrome bc1 complex structure. *EMBO J*. 2001;20:6591-6600.
10. Shinzawa-Itoh K, Aoyama H, Muramoto K, et al. Structures and physiological roles of 13 integral lipids of bovine heart cytochrome c oxidase. *EMBO J*. 2007;26:1713-1725.
11. Mileykovskaya E, Dowhan W. Cardiolipin-dependent formation of mitochondrial respiratory supercomplexes. *Chem Phys Lipids*. 2014;179:42-48.
12. Klingenberg M. Cardiolipin and mitochondrial carriers. *Biochim Biophys Acta*. 2009;1788:2048-2058.
13. Claypool SM. Cardiolipin, a critical determinant of mitochondrial carrier protein assembly and function. *Biochem Biophys Acta*. 2009;1788:2059-2068.
14. Joshi AS, Thompson MN, Fei N, Huttemann M, Greenberg ML. Cardiolipin and mitochondrial phosphatidylethanolamine have overlapping functions in mitochondrial fusion in *Saccharomyces cerevisiae*. *J Biol Chem*. 2012;287:17589-17597.
15. Patil VA, Fox JL, Gohil VM, Winge DR, Greenberg ML. Loss of cardiolipin leads to perturbation of mitochondrial and cellular iron homeostasis. *J Biol Chem*. 2013;288:1696-1705.
16. Santucci R, Sinibaldi F, Cozza P, Polticelli F, Fiorucci L. Cytochrome c: an extreme multifunctional protein with a key role in cell fate. *Int J Biol Macromol*. 2019;136:1237-1246.
17. Li Y, Lou W, Raja V, et al. Cardiolipin-induced activation of pyruvate dehydrogenase links mitochondrial lipid biosynthesis to TCA cycle function. *J Biol Chem*. 2019;294:11568-11578.
18. Raja V, Salsaa M, Joshi AS, et al. Cardiolipin-deficient cells depend on anaplerotic pathways to ameliorate defective TCA cycle function. *Biochim Biophys Acta Mol Cell Biol Lipids*. 2019;1864:654-661.
19. Schlame M, Ren M. Barth syndrome, a human disorder of cardiolipin metabolism. *FEBS Lett*. 2006;580:5450-5455.
20. Cade WT, Spencer CT, Reeds DN, et al. Substrate metabolism during basal and hyperinsulinemic conditions in adolescents and young-adults with Barth syndrome. *J Inherit Metab Dis*. 2013;36:91-101.
21. Raja V, Greenberg ML. The functions of cardiolipin in cellular metabolism-potential modifiers of the Barth syndrome phenotype. *Chem Phys Lipids*. 2014;179:49-56.
22. Nishijima S, Asami Y, Uetake N, Yamagoe S, Ohta A, Shibuya I. Disruption of the *Escherichia coli* cls gene responsible for cardiolipin synthesis. *J Bacteriol*. 1988;170:775-780.
23. Jiang F, Gu Z, Granger JM, Greenberg ML. Cardiolipin synthase expression is essential for growth at elevated temperature and is regulated by factors affecting mitochondrial development. *Mol Microbiol*. 1999;31:373-379.
24. Raemy E, Montessuit S, Pierredon S, van Kampen AH, Vaz FM, Martinou JC. Cardiolipin or MTCH2 can serve as tBID receptors during apoptosis. *Cell Death Differ*. 2016;23:1165-1174.
25. Serricchio M, Bütikofer P. An essential bacterial-type cardiolipin synthase mediates cardiolipin formation in a eukaryote. *Proc Natl Acad Sci U S A*. 2012;109:E954-E961.
26. Schlame M. Cardiolipin synthesis for the assembly of bacterial and mitochondrial membranes. *J Lipid Res*. 2008;49:1607-1620.
27. Schädeli D, Serricchio M, Ben Hamidane H, et al. Cardiolipin depletion-induced changes in the *Trypanosoma brucei* proteome. *FASEB J*. 2019;33:13161-13175.

28. Hannaert V, Bringaud F, Opperdoes FR, Michels PA. Evolution of energy metabolism and its compartmentation in Kinetoplastida. *Kinetoplastid Biol Dis*. 2003;2:11.
29. Zíková A, Hampl V, Paris Z, Tyc J, Lukes J. Aerobic mitochondria of parasitic protists: diverse genomes and complex functions. *Mol Biochem Parasitol*. 2016;209:46-57.
30. Schnaufer A, Clark-Walker GD, Steinberg AG, Stuart K. The F1-ATP synthase complex in bloodstream stage trypanosomes has an unusual and essential function. *EMBO J*. 2005;24:4029-4040.
31. Nolan DP, Voorheis HP. The mitochondrion in bloodstream forms of *Trypanosoma brucei* is energized by the electrogenic pumping of protons catalysed by the F_1F_0-ATPase. *Eur J Biochem*. 1992;209:207-216.
32. Vickerman K. Developmental cycles and biology of pathogenic trypanosomes. *Br Med Bull*. 1985;41:105-114.
33. Priest JW, Hajduk SL. Developmental regulation of mitochondrial biogenesis in *Trypanosoma b*rucei. *J Bioenerg Biomembr*. 1994;26:179-191.
34. Tielens AG, van Hellemond JJ. Surprising variety in energy metabolism within Trypanosomatidae. *Trends Parasitol*. 2009;25:482-490.
35. Smith TK, Bringaud F, Nolan DP, Figueiredo LM. Metabolic reprogramming during the *Trypanosoma brucei* life cycle. *F1000Res*. 2017;6:683.
36. Zíková A, Verner Z, Nenarokova A, Michels PAM, Lukes J. A paradigm shift: the mitoproteomes of procyclic and bloodstream *Trypanosoma brucei* are comparably complex. *PLoS Pathog*. 2017;13:e1006679.
37. Wirtz E, Leal S, Ochatt C, Cross GA. A tightly regulated inducible expression system for conditional gene knock-outs and dominant-negative genetics in *Trypanosoma brucei*. *Mol Biochem Parasitol*. 1999;99:89-101.
38. Serricchio M, Bütikofer P. Phosphatidylglycerophosphate synthase associates with a mitochondrial inner membrane complex and is essential for growth of *Trypanosoma brucei*. *Mol Microbiol*. 2013;87:569-579.
39. Charriere F, Helgadottir S, Horn EK, Soll D, Schneider A. Dual targeting of a single tRNA(Trp) requires two different tryptophanyl-tRNA synthetases in Trypanosoma brucei. *Proc Natl Acad Sci USA*. 2006;103:6847-6852.
40. Wittig I, Braun HP, Schagger H. Blue native PAGE. *Nat Protoc*. 2006;1:418-428.
41. Panigrahi AK, Zikova A, Dalley RA, et al. Mitochondrial complexes in *Trypanosoma brucei*: a novel complex and a unique oxidoreductase complex. *Mol Cell Proteomics*. 2008;7:534-545.
42. Subrtova K, Panicucci B, Zíková A. ATPaseTb2, a unique membrane-bound FoF1-ATPase component, is essential in bloodstream and dyskinetoplastic trypanosomes. *PLoS Pathog*. 2015;11:e1004660.
43. Singha UK, Sharma S, Chaudhuri M. Downregulation of mitochondrial porin inhibits cell growth and alters respiratory phenotype in *Trypanosoma brucei*. *Eukaryot Cell*. 2009;8:1418-1428.
44. Dawoody Nejad L, Serricchio M, Jelk J, Hemphill A, Bütikofer P. TbLpn, a key enzyme in lipid droplet formation and phospholipid metabolism, is essential for mitochondrial integrity and growth of Trypanosoma brucei. *Mol Microbiol*. 2018;109:105-120.
45. Gloaguen Y, Morton F, Daly R, et al. PiMP my metabolome: an integrated, web-based tool for LC-MS metabolomics data. *Bioinformatics*. 2017;33:4007-4009.
46. Chinopoulos C, Vajda S, Csanady L, Mandi M, Mathe K, Adam-Vizi V. A novel kinetic assay of mitochondrial ATP-ADP exchange rate mediated by the ANT. *Biophys J*. 2009;96:2490-2504.
47. Perry SW, Norman JP, Barbieri J, Brown EB, Gelbard HA. Mitochondrial membrane potential probes and the proton gradient: a practical usage guide. *Biotechniques*. 2011;50:98-115.
48. Gahura O, Subrtova K, Vachova H, et al. The F1 -ATPase from *Trypanosoma brucei* is elaborated by three copies of an additional p18-subunit. *FEBS J*. 2018;285:614-628.
49. Figueira TR, Melo DR, Vercesi AE, Castilho RF. Safranine as a fluorescent probe for the evaluation of mitochondrial membrane potential in isolated organelles and permeabilized cells. *Methods Mol Biol*. 2012;810:103-117.
50. Voncken F, Gao F, Wadforth C, Harley M, Colasante C. The phosphoarginine energy-buffering system of trypanosoma brucei involves multiple arginine kinase isoforms with different subcellular locations. *PLoS ONE*. 2013;8:e65908.
51. Shah TD, Hickey MC, Capasso KE, Palenchar JB. The characterization of a unique *Trypanosoma brucei* beta-hydroxybutyrate dehydrogenase. *Mol Biochem Parasitol*. 2011;179:100-106.
52. Kovarova J, Barrett MP. The pentose phosphate pathway in parasitic trypanosomatids. *Trends Parasitol*. 2016;32:622-634.
53. Cirovic O, Ochsenreiter T. Whole proteome analysis of the protozoan parasite *Trypanosoma brucei* using stable isotope labeling by amino acids in cell culture and mass spectrometry. *Methods Mol Biol*. 2014;1188:47-55.
54. Opperdoes FR, Borst P, Bakker S, Leene W. Localization of glycerol-3-phosphate oxidase in the mitochondrion and particulate NAD+-linked glycerol-3-phosphate dehydrogenase in the microbodies of the bloodstream form to *Trypanosoma brucei*. *Eur J Biochem*. 1977;76:29-39.
55. Shiba T, Kido Y, Sakamoto K, et al. Structure of the trypanosome cyanide-insensitive alternative oxidase. *Proc Natl Acad Sci USA*. 2013;110:4580-4585.
56. Jiang F, Rizavi HS, Greenberg ML. Cardiolipin is not essential for the growth of *Saccharomyces cerevisiae* on fermentable or non-fermentable carbon sources. *Mol Microbiol*. 1997;26:481-491.
57. Pineau B, Bourge M, Marion J, et al. The importance of cardiolipin synthase for mitochondrial ultrastructure, respiratory function, plant development, and stress responses in Arabidopsis. *Plant Cell*. 2013;25:4195-4208.
58. Eble KS, Coleman WB, Hantgan RR, Cunningham CC. Tightly associated cardiolipin in the bovine heart mitochondrial ATP synthase as analyzed by 31P nuclear magnetic resonance spectroscopy. *J Biol Chem*. 1990;265:19434-19440.
59. Muhleip A, McComas SE, Amunts A. Structure of a mitochondrial ATP synthase with bound native cardiolipin. *eLife*. 2019;8:e51179.
60. Duncan AL, Robinson AJ, Walker JE. Cardiolipin binds selectively but transiently to conserved lysine residues in the rotor of metazoan ATP synthases. *Proc Natl Acad Sci USA*. 2016;113:8687-8692.
61. Schnaufer A, Domingo GJ, Stuart K. Natural and induced dyskinetoplastic trypanosomatids: how to live without mitochondrial DNA. *Int J Parasitol*. 2002;32:1071-1084.
62. Dean S, Gould MK, Dewar CE, Schnaufer AC. Single point mutations in ATP synthase compensate for mitochondrial genome loss in trypanosomes. *Proc Natl Acad Sci USA*. 2013;110:14741-14746.
63. Lai DH, Hashimi H, Lun ZR, Ayala FJ, Lukes J. Adaptations of *Trypanosoma brucei* to gradual loss of kinetoplast DNA: *Trypanosoma equiperdum* and *Trypanosoma evansi* are petite mutants of *T brucei*. *Proc Natl Acad Sci USA*. 2008;105:1999-2004.

64. Beyer K, Klingenberg M. ADP/ATP carrier protein from beef heart mitochondria has high amounts of tightly bound cardiolipin, as revealed by 31P nuclear magnetic resonance. *Biochemistry*. 1985;24:3821-3826.
65. Claypool SM, Oktay Y, Boontheung P, Loo JA, Koehler CM. Cardiolipin defines the interactome of the major ADP/ATP carrier protein of the mitochondrial inner membrane. *J Cell Biol*. 2008;182:937-950.
66. Paradies G, Ruggiero FM, Petrosillo G, Quagliariello E. Alterations in carnitine-acylcarnitine translocase activity and in phospholipid composition in heart mitochondria from hypothyroid rats. *Biochem Biophys Acta*. 1997;1362:193-200.
67. Kadenbach B, Mende P, Kolbe HV, Stipani I, Palmieri F. The mitochondrial phosphate carrier has an essential requirement for cardiolipin. *FEBS Lett*. 1982;139:109-112.
68. Beleznai Z, Jancsik V. Role of cardiolipin in the functioning of mitochondrial L-glycerol-3-phosphate dehydrogenase. *Biochem Biophys Res Comm*. 1989;159:132-139.
69. Bakker BM, Michels PA, Opperdoes FR, Westerhoff HV. Glycolysis in bloodstream form *Trypanosoma brucei* can be understood in terms of the kinetics of the glycolytic enzymes. *J Biol Chem*. 1997;272:3207-3215.
70. Uzcategui NL, Szallies A, Pavlovic-Djuranovic S, et al. Cloning, heterologous expression, and characterization of three aquaglyceroporins from *Trypanosoma brucei*. *J Biol Chem*. 2004;279:42669-42676.
71. Creek DJ, Nijagal B, Kim DH, Rojas F, Matthews KR, Barrett MP. Metabolomics guides rational development of a simplified cell culture medium for drug screening against *Trypanosoma brucei*. *Antimicrob Agents Chemother*. 2013;57:2768-2779.
72. Kim DH, Achcar F, Breitling R, Burgess KE, Barrett MP. LC-MS-based absolute metabolite quantification: application to metabolic flux measurement in trypanosomes. *Metabolomics*. 2015;11:1721-1732.
73. Johnston K, Kim DH, Kerkhoven EJ, Burchmore R, Barrett MP, Achcar F. Mapping the metabolism of five amino acids in bloodstream form *Trypanosoma brucei* using U-(13) C-labelled substrates and LC-MS. *Biosci Rep*. 2019;39(5): BSR20181601.
74. Intlekofer AM, Wang BO, Liu H, et al. L-2-Hydroxyglutarate production arises from noncanonical enzyme function at acidic pH. *Nat Chem Biol*. 2017;13:494-500.
75. Pereira CA, Alonso GD, Torres HN, Flawia MM. Arginine kinase: a common feature for management of energy reserves in African and American flagellated trypanosomatids. *J Eukaryot Microbiol*. 2002;49:82-85.
76. Huang G, Ulrich PN, Storey M, et al. Proteomic analysis of the acidocalcisome, an organelle conserved from bacteria to human cells. *PLoS Pathog*. 2014;10:e1004555.
77. Baker N, Hamilton G, Wilkes JM, Hutchinson S, Barrett MP, Horn D. Vacuolar ATPase depletion affects mitochondrial ATPase function, kinetoplast dependency, and drug sensitivity in trypanosomes. *Proc Natl Acad Sci USA*. 2015;112:9112-9117.

SUPPORTING INFORMATION

Additional Supporting Information may be found online in the Supporting Information section.

How to cite this article: Serricchio M, Hierro-Yap C, Schädeli D, et al. Depletion of cardiolipin induces major changes in energy metabolism in *Trypanosoma brucei* bloodstream forms. *The FASEB Journal*. 2021;35:e21176. https://doi.org/10.1096/fj.202001579RR

PLOS | PATHOGENS

RESEARCH ARTICLE

ATPaseTb2, a Unique Membrane-bound FoF1-ATPase Component, Is Essential in Bloodstream and Dyskinetoplastic Trypanosomes

Karolína Šubrtová[1,2], Brian Panicucci[1], Alena Zíková[1,2]*

1 Institute of Parasitology, Biology Centre, CAS, České Budějovice, Czech Republic, **2** Faculty of Science, University of South Bohemia, České Budějovice, Czech Republic

* azikova@paru.cas.cz

Citation: Šubrtová K, Panicucci B, Zíková A (2015) ATPaseTb2, a Unique Membrane-bound FoF1-ATPase Component, Is Essential in Bloodstream and Dyskinetoplastic Trypanosomes. PLoS Pathog 10(2): e1004660. doi:10.1371/journal.ppat.1004660

Editor: Achim Schnaufer, University of Edinburgh, UNITED KINGDOM

Received: June 13, 2014

Accepted: January 6, 2015

Published: February 25, 2015

Data Availability Statement: All relevant data are within the paper and its Supporting Information file.

Funding: This work was funded by Ministry of Education ERC CZ grant LL1205, the Czech Grant Agency grant P302/12/2513, the EMBO Installation grant 1965 (to AZ) and the Grant Agency of University of South Bohemia grants 140/2010/P and 04/092/2011/P (to KS). We acknowledge the use of research infrastructure that has received funding from the European Union Seventh Framework Programme (FP7/2007-2013) under grant agreement no.316304. The funders had no role in study design, data

Abstract

In the infectious stage of *Trypanosoma brucei*, an important parasite of humans and livestock, the mitochondrial (mt) membrane potential ($\Delta\psi_m$) is uniquely maintained by the ATP hydrolytic activity and subsequent proton pumping of the essential F_oF_1-ATPase. Intriguingly, this multiprotein complex contains several trypanosome-specific subunits of unknown function. Here, we demonstrate that one of the largest novel subunits, ATPaseTb2, is membrane-bound and localizes with monomeric and multimeric assemblies of the FoF1-ATPase. Moreover, RNAi silencing of ATPaseTb2 quickly leads to a significant decrease of the $\Delta\psi_m$ that manifests as a decreased growth phenotype, indicating that the F_oF_1-ATPase is impaired. To further explore the function of this protein, we employed a trypanosoma strain that lacks mtDNA (dyskinetoplastic, Dk) and thus subunit a, an essential component of the proton pore in the membrane F_o-moiety. These Dk cells generate the $\Delta\psi_m$ by combining the hydrolytic activity of the matrix-facing F_1-ATPase and the electrogenic exchange of ATP^{4-} for ADP^{3-} by the ATP/ADP carrier (AAC). Surprisingly, in addition to the expected presence of F1-ATPase, the monomeric and multimeric F_oF_1-ATPase complexes were identified. In fact, the immunoprecipitation of a F_1-ATPase subunit demonstrated that ATPaseTb2 was a component of these complexes. Furthermore, RNAi studies established that the membrane-bound ATPaseTb2 subunit is essential for maintaining normal growth and the $\Delta\psi_m$ of Dk cells. Thus, even in the absence of subunit a, a portion of the F_oF_1-ATPase is assembled in Dk cells.

Author Summary

The presence of the F_oF_1-ATP synthase in every aerobic organism suggests that evolution has settled on a basic blueprint for the complex rotary motor capable of synthesizing life's universal energy currency—ATP. However, compared to yeast and mammalian models of the F_oF_1-ATP synthase, several recent studies have reported unique structural and functional features of this complex from organisms representing the clades of Chromalveolata,

collection and analysis, decision to publish, or preparation of the manuscript.

Competing Interests: The authors have declared that no competing interests exist.

Archaeplastida and Excavata. One of the most striking cases is observed in trypanosomes, important parasites of humans and animals. Notably, the F_oF_1-ATP synthase/ATPase switches from synthesizing ATP in the insect vector life stage to hydrolyzing ATP in their mammalian hosts to generate the essential mitochondrial membrane potential ($\Delta\psi_m$). Moreover, this indispensable F_oF_1-ATPase contains up to 14 trypanosome-specific subunits. Here we characterize one such novel subunit, ATPaseTb2. We demonstrate that this subunit is crucial for the survival of the infectious stage of trypanosomes, part of the fully assembled F_oF_1-complex and it is essential for maintaining the $\Delta\psi_m$. Given the enzyme's irreplaceable function and extraordinary composition, we believe that the F_oF_1-ATPase is an attractive drug target.

Introduction

Trypanosomes are unicellular flagellates from the order Kinetoplastida, which is comprised of some of the most devastating human pathogens in the world. For example, in sub-Saharan Africa, infection from *Trypanosoma brucei gambiense* and *T. b. rhodesiense* causes Human African Trypanosomiasis, which is almost always fatal if left untreated [1]. The latest WHO reports estimate that there are 10,000 new cases annually in endemic regions. Meanwhile, a third subspecies, *T. b. brucei*, infects livestock and therefore negatively affects the human population through malnutrition and economic hardships [2,3].

T. brucei parasites have a complex life cycle, alternating between the mammalian host and the insect vector, a tse-tse fly. During this environmental switch, the protist undergoes rapid and dramatic changes in cell morphology and metabolism [4–6]. In particular, the single mitochondrion undergoes extensive remodelling, which reflects the adaptability of the parasite to consume different carbon sources based on their availability [4]. The procyclic (insect) form (PF) of trypanosomes catabolizes amino acids and maintains a well-developed mitochondrion with abundant cristae, Krebs cycle enzymes and a complete oxidative phosphorylation pathway. This pathway includes enzymatic complexes that generate a mitochondrial (mt) membrane potential ($\Delta\psi_m$) that is coupled to ATP synthesis by the F_oF_1-ATP synthase [5]. In contrast, the bloodstream form (BF) of this parasite populates the glucose-rich fluids (e.g. blood and spinal fluid) of its vertebrate host, allowing them to utilize just glycolysis for ATP production. This results in a drastically reduced mitochondrion that lacks significant cristae, key enzymes of the Krebs cycle and the cytochrome-containing respiratory complexes that pump protons into the inner mt membrane space [6,7]. Despite this reduction, the BF mitochondrion is still an active organelle, holding vital processes e.g. lipid metabolism [8], ion homeostasis [9], calcium signalling [10,11], FeS cluster assembly [12] and acetate production for *de novo* lipid biosynthesis [13]. Importantly, in the absence of proton-pumping respiratory complexes III and IV, the indispensable $\Delta\psi_m$ is sustained mainly by the hydrolytic activity of the F_oF_1-ATPase. Thus, this complex possesses an essential, unique and irreplaceable function in BF mitochondria [14].

In other eukaryotes, this reverse activity of the F_oF_1-ATP synthase is observed only rarely, for very brief moments of time and under very specific conditions (i.e. during oxygen deprivation or in response to damaged or mutated mt respiratory proteins). When the function of the respiratory complexes is compromised, the $\Delta\psi_m$ falls below a physiological threshold and is restored by the reverse proton pumping activity of the F_oF_1-ATPase, which is powered by ATP hydrolysis. The hydrolytic activity of the catalytic F_1-ATPase is also essential for exceptional cells that lack mtDNA (ρ° cells). These cells do not express several core subunits of the

membrane embedded F_o-moiety (subunits 6, 8 and 9 in yeast, subunits a and A6L in bovine) of the F_oF_1-ATPase, notably those that are components of the proton pore. Thus, the matrix protruding F_1-ATPase energizes the inner mt membrane by coupling ATP hydrolysis with the exchange of ADP^{3-} for ATP^{4-} by the ATP/ADP carrier (AAC) [15]. The same mechanism for producing the $\Delta\psi_m$ is utilized by trypanosomes that lack a mt genome, which is called a kinetoplast [16]. These naturally occuring dyskinetoplastic forms (Dk) of *T. brucei* (e.g. *T. b. evansi* or *T. b.equiperdum*) cause economically significant diseases in horses, camels, and water buffaloes. Remarkably, these parasites are not able to switch to the insect stage and are transmitted mechanically by bloodsucking insects or by coitus [17]. The mtDNA-lacking trypanosomes can also be chemically induced in the laboratory (e.g. Dk *T. brucei* EATRO164) [18]. Interestingly, each of the Dk cell lines characterized so far, bear one of several different compensatory mutations in the nuclear encoded subunit γ that enable the $\Delta\psi_m$ to be generated independently of the F_o-moiety [14,16,19].

In general, the F_oF_1-ATP synthase complex consists of two functionally distinct enzymatic segments: the hydrophilic F_1 catalytic moiety and the membrane-bound F_o pore. Both of these subcomplexes are linked together by the central and peripheral stalks. The central stalk rotates with the c-ring when protons are allowed to pass through the F_o pore, located between the c-ring and subunit a. In contrast to the rotation of the central stalk, the stationary peripheral stalk plays a crucial role in keeping the catalytic F_1 headpiece static, thus resisting the rotational torque. The eubacterial F_1-moiety consists of the catalytic domain and the central stalk, which are comprised of five subunits in a stoichiometry of α_3, β_3, γ_1, δ_1, ε_1. The F_o-moiety is composed of the oligomeric c_{10-15} ring and a single subunit a joined together with two copies of subunit b, which extend from the membrane and form the base of the peripheral stalk. The composition of the eukaryotic enzyme has been determined mainly from detailed studies of F_oF_1-ATP synthase purified from the mitochondria of *Bos taurus* and *Saccharomyces cerevisiae*, members of the clade Opisthokonta. These enzymes contain homologous prokaryotic-like core components, but also incorporate additional eukaryotic specific subunits involved in the structure, oligomerization and regulation of the complex [20]. These novel subunits have been assigned to various regions of the F_oF_1-ATP synthase: i) subunit ε and inhibitory factor 1 (IF_1) bind to the F_1-moiety; ii) the small hydrophobic subunit 8 (subunit A6L in bovine) is located in the membrane interacting with subunit a; iii) the soluble subunit h (subunit F_6 in bovine), oligomycin sensitivity-conferring protein (OSCP) and hydrophilic subunit d are assigned to the peripheral stalk; iv) subunits e, f, g, all containing one transmembrane helix, are regarded as accessory peripheral stalk proteins that predominantly reside in the inner membrane where they presumably stabilize the utmost hydrophobic subunit 6 (or subunit a in bovine), thereby assisting the peripheral stalk with its stator function [21–23].

Recently, however, several studies have reported unique structural and functional features of the F_oF_1-ATP synthase from medically relevant parasites and other organisms that represent the clades of Chromalveolata [24], Archaeplastida [25] and Excavata [26]. In *Plasmodium falciparum*, a member of the phylum Apicomplexa, the genomic data indicates the likely presence of all eukaryotic F_1 subunits and some of the F_o and stator subunits [27]. Conspicuously absent are the subunits a and b, which are crucial to the function of all known F_oF_1-ATP synthases. These subunits are also missing in the ATP synthase of *P. yoelii* and *Tetrahymena thermophila*, the latter a member of the sister phylum Ciliophora, both of which have been shown experimentally to possess ATP synthase activity [28–30]. This suggest that ciliates and apicomplexan species employ highly divergent or novel subunits to fulfil the functions of the classical subunits a and b. Another example of an unusual F_oF_1-ATP synthase complex comes from studies of the chlorophycean algea *Chlamydomonas reinhardtii* and *Polytomella* sp. that determined the

complex contains up to 9 unique subunits (Asa1-Asa9) that either form an innovative peripheral stator or are responsible for complex dimerization [31].

Trypanosoma F_oF_1-ATP synthase consists of the well conserved F_1-moiety comprised of subunits α, β, γ, δ, ε and the trypanosome-specific subunit p18 [26,32], and the less characterized F_o pore and peripheral stalk where only subunits c, a and OSCP were identified at the gene or protein level [26,33]. Additionally, the complex contains up to 14 Kinetoplastida-specific subunits that lack homology to any of the previously described subunits. Therefore, their position within the complex and their function is unknown. Interestingly, these recently identified F_oF_1-ATP synthase subunits specific for *T. brucei* (ATPaseTb) may represent early evolutionary attempts to create the functional and structural components of the eukaryotic accessory subunits for this early divergent species. Previously, two of these novel subunits, ATPaseTb1 (Tb10.70.7760) and ATPaseTb2 (Tb927.5.2930), were shown to be essential for the proper function and structural integrity of F_oF_1-ATP synthase in the procyclic form of this parasite [26].

Here, we have extended this study and functionally characterized ATPaseTb2 in the disease-relevant stage of *T. brucei* and Dk *T. b evansi*. Our results demonstrate that the membrane-bound ATPaseTb2 protein is indispensable for the survival of BF and Dk trypanosomes because it is crucial for maintaining the $\Delta\psi_m$ in these cells. Furthermore, the unexpected observation of assembled F_oF_1-ATPase complexes in two different strains of trypanosomes lacking mt DNA suggests that the composition of the Dk F_oF_1-ATPase complex is more similar to the BF F_oF_1-ATPase complex than previously thought.

Results

Bioinformatics reveals that ATPaseTb2 contains a putative transmembrane domain and a region homologous to the bovine subunit d

ATPaseTb2 is annotated as a hypothetical protein in the TriTrypDB database (www.tritrypdb.org) and its mt localization was predicted by the presence of an N-terminal mt targeting sequence assigned by Mitoprot II v1.101 [34] (probability 0.823). Strikingly, this subunit has no detectable homologs outside Kinetoplastida based on a similarity sequence search (e.g. BLAST). To uncover any homologous relationships for protein sequences that do not share high enough sequence identity, but might have similar secondary structure, we employed the HHpred toolkit (http://toolkit.tuebingen.mpg.de), which is based on an HMM-HMM comparison that reveals homologous relationships even if the sequences share less than 20% sequence identity [35]. All of the available Kinetoplastida ATPaseTb2 homologs obtained from the TriTrypDB (S1A Fig.) were analyzed using HHpred software. Among the first five structural homologs detected was the bovine F_oF_1-ATP synthase subunit d, with a probability of 44.7 and a P-value of 0.0021. Then a consensus sequence generated from an alignment of this 92 amino acids (aa) region from all identified kinetoplastida homologs was resubmitted for HHpred analysis. This search returned a significant hit to the bovine subunit d with a probability of 78.1 and a P-value of 0.0002 (S1B Fig.). This bovine F_oF_1-ATP synthase subunit is comprised of 160 aa and resides within the peripheral stalk where it interacts with all the other three components of the peripheral stalk (b, F_6 and OSCP). This subunit is predominantly hydrophilic, contains several long alpha-helices and is essential for the enzymatic function [23,36,37]. The region of similarity to subunit d falls in the middle of the ATPaseTb2 sequence and it is followed by a putative trans-membrane (TM) domain (aa 239–254) that was predicted by MEMSAT-SVM software (http://bioinf.cs.ucl.ac.uk/psipred/) [38] with a -0.738 prediction score (Fig. 1). This prediction is intriguing because a typical eukaryotic subunit d is not directly attached to the

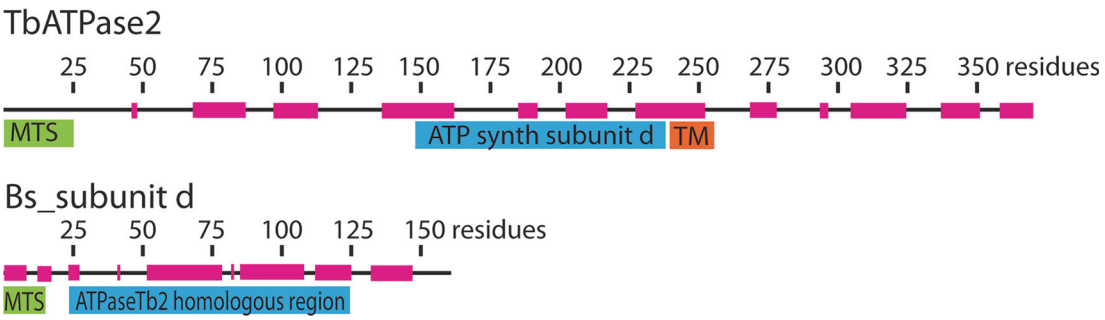

Fig 1. Bioinformatics reveal that ATPaseTb2 possesses a region of low homology to ATPase subunit d. A schematic representation depicting the ATPaseTb2 protein (370 aminoacids (AA)) and the *Bos taurus* subunit d (Bs_sub d, 161 AA) was created using Adobe Illustrator CS5.1. The mitochondrial targeting signals (MTS, green) were predicted by Mitoprot II v1.101. The transmembrane domain (TM, orange) within the ATPaseTb2 sequence was predicted by MEMSAT-SVM software. The homologous region (blue) to Bs_sub d was determined using HHpred toolkit. The regions of alpha-helices (magenta) depicted on the amino acid sequence line were predicted by software from EMBOSS garnier.

doi:10.1371/journal.ppat.1004660.g001

membrane, but rather it interacts with the soluble region of the membrane-bound subunit b via three coiled-coil interactions [23]. Thus, ATPaseTb2 may represent a novel subunit of the membrane-bound peripheral stalk that possibly depicts an early divergent functional alternative of the stator by creating a chimera of subunits b and d.

ATPaseTb2 is a mt membrane-bound protein expressed in various forms of *T. brucei*

The mitochondrial localization, as well as the structural and functional association of ATPaseTb2 with the F_oF_1-ATP synthase in PF *T. brucei* cells was previously described [26]. Because the activity of this complex significantly differs between the insect and mammalian stage of the parasite, we were interested if the ATPaseTb2 protein is also expressed in trypanosomes residing in the bloodstream of their host. Therefore, we cultured PF427 (insect stage), BF427 (bloodstream forms) and the laboratory-induced dyskinetoplastic Dk164 *T. brucei* cells, in addition to the naturally occurring Dk *T.b.evansi*. Whole cell lysates from PF427, BF427, Dk164 and *T. b.evansi* cells were fractionated by SDS-PAGE and analyzed by western blot using a specific polyclonal antibody against ATPaseTb2 (Fig. 2A). Interestingly, ATPaseTb2 is expressed in all four cell types; however, its expression is significantly decreased in BF427 and even more reduced in Dk164 and *T.b.evansi* cells. A similar expression pattern for F_1-ATPase subunit β and mt chaperone Hsp70 was also observed between PF, BF and Dk cells (Fig. 2A). These results are in agreement with the proposed reduction of the mitochondria size, function and activity in the various bloodstream forms of *T. brucei* [39].

To experimentally investigate the subcellular localization of ATPaseTb2 within the bloodstream *T. brucei* cell, the ATPaseTb2 gene product was C-terminally tagged with a v5-tag and inducibly expressed using tetracycline (tet). Cytosolic and mitochondrial fractions were isolated from a hypotonic lysate of cells over-expressing the ATPaseTb2_v5 protein. The mitochondrial fractions were then treated with digitonin to create mitoplasts that were further incubated with sodium carbonate (Na_2CO_3) to obtain mt membrane and mt matrix fractions. The subsequent western analyses established the purity of the extracted fractions as the cytosolic enolase, the mt inner membrane carrier protein (AAC) and the matrix-localized guide RNA binding protein (MRP1) were confined within their respective subcellular fractions. Notably, ATPaseTb2 was predominantly localized in the mt membrane fraction, while subunit β of the matrix-soluble F_1-ATPase was released into the matrix fraction (Fig. 2B), demonstrating that ATPaseTb2 is firmly embedded in the inner mt membrane.

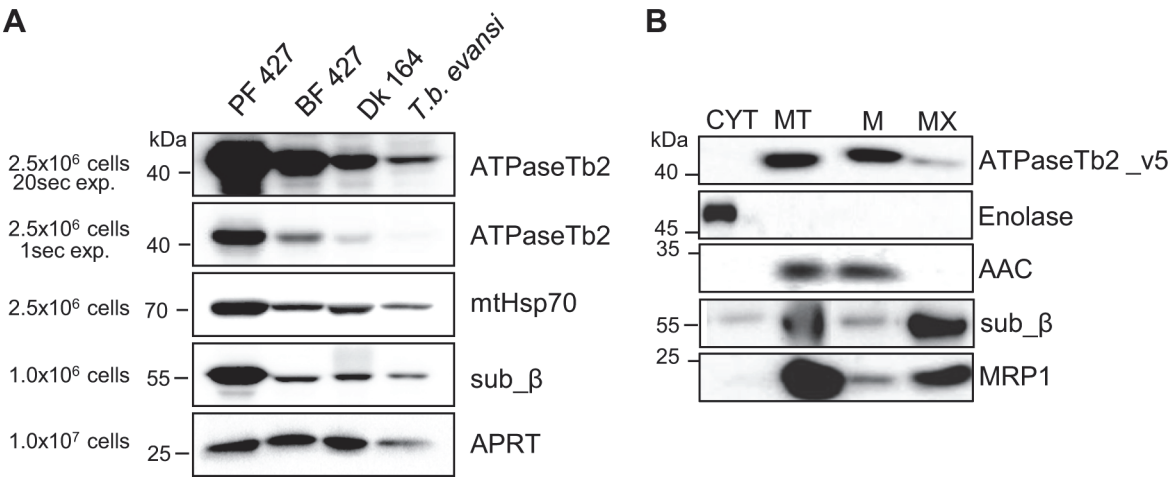

Fig 2. ATPaseTb2 is expressed in PF427, BF427, Dk164 *T. brucei* and *T. b. evansi* cells and it is a membrane-bound protein. A) The steady state abundance of ATPaseTb2 (two different exposure times), subunit β, mtHsp70 and cytosolic adenosine phosphoribosyl transferase (APRT) was determined in PF427, BF427, Dk164 and *T. b. evansi* cells by western blot analysis of whole cell lysates from $2.5x10^6$ cells or $1x10^6$ cells (for subunit β and APRT) resolved on SDS-PAGE gels. The pertinent sizes of the protein marker are indicated on the left. B) Subcellular localization of ATPaseTb2 was determined using BF cells expressing v5-tagged ATPaseTb2. Cytosolic (CYT) and mitochondrial (MT) fractions were obtained by hypotonic lysis. Mt pellets were further treated with Na_2CO_3 and spun at a high-speed to obtain mt membrane (M) and matrix (MX) fractions. Purified fractions were analyzed by western blot with the following antibodies: anti-v5 (ATPaseTb2_v5), anti-enolase (cytosol), anti-AAC (mt inner membrane), anti-β (F_1-ATPase subunit) and anti-MRP1 (mt matrix). The relevant sizes of the protein marker are indicated on the left.

doi:10.1371/journal.ppat.1004660.g002

ATPaseTb2 is a bona fide subunit of F_oF_1-ATPase monomers and higher oligomers

To confirm that ATPaseTb2 is a genuine subunit of both the BF and Dk F_oF_1-ATPase, we employed the same strategy applied previously for PF cells [26]. Therefore, we first created BF cell lines in which either the ATPaseTb2 or the F_1 subunit p18 were inducibly expressed with a C-terminal tag. Complexes assembled with a tagged protein were then purified using a one-step IgG affinity purification, followed by treatment with TEV protease to release bound complexes from the IgG beads. The TEV eluates were further analyzed by western blot for the presence of the tagged proteins, known F_oF_1-ATPase subunits, and AAC (Fig. 3A). Importantly, the presence of the tagged subunits ATPase Tb2 and p18 in the respective cell lines were confirmed using a specific antibody against the *c*-myc epitope that comprises part of the tag. In addition, the ATPaseTb2_TAP eluate contained F_oF_1-ATPase subunits β, p18 and ATPaseTb1. Vice versa, the p18_TAP eluate contained subunits ATPaseTb2, ATPaseTb1 and subunit β. While AAC has been described to associate with mammalian F_oF_1-ATPase under certain conditions [40], it is not a core component of the enzyme and the lack of its signal indicates the stringency of this technique. The TAP tag purification from non-induced cells was used as a negative control to verify that the detected proteins do not bind non-specifically to the charged beads. To analyze the composition of the Dk F_oF_1-ATPase, p18 tagged complexes were purified and subjected to the same set of antibodies described for the BF complexes (Fig. 3B). These results also depicted the same interactions seen in Fig. 3A. Therefore, the co-purification of ATPaseTb2 with known ATPase subunits p18 and β validates that it is an authentic constituent of the F_oF_1-ATPase complex in both BF and Dk cells.

The sedimentation profile of F_oF_1-ATP synthase in 10–30% glycerol gradients (GG) was previously published and revealed two distinct regions representing the F_1-moiety and the F_oF_1-monomer and multimeric complexes [26]. In order to specify if ATPaseTb2 is a component of the F_1-moiety or the F_oF_1-complex, the glycerol gradient sedimentation profile was

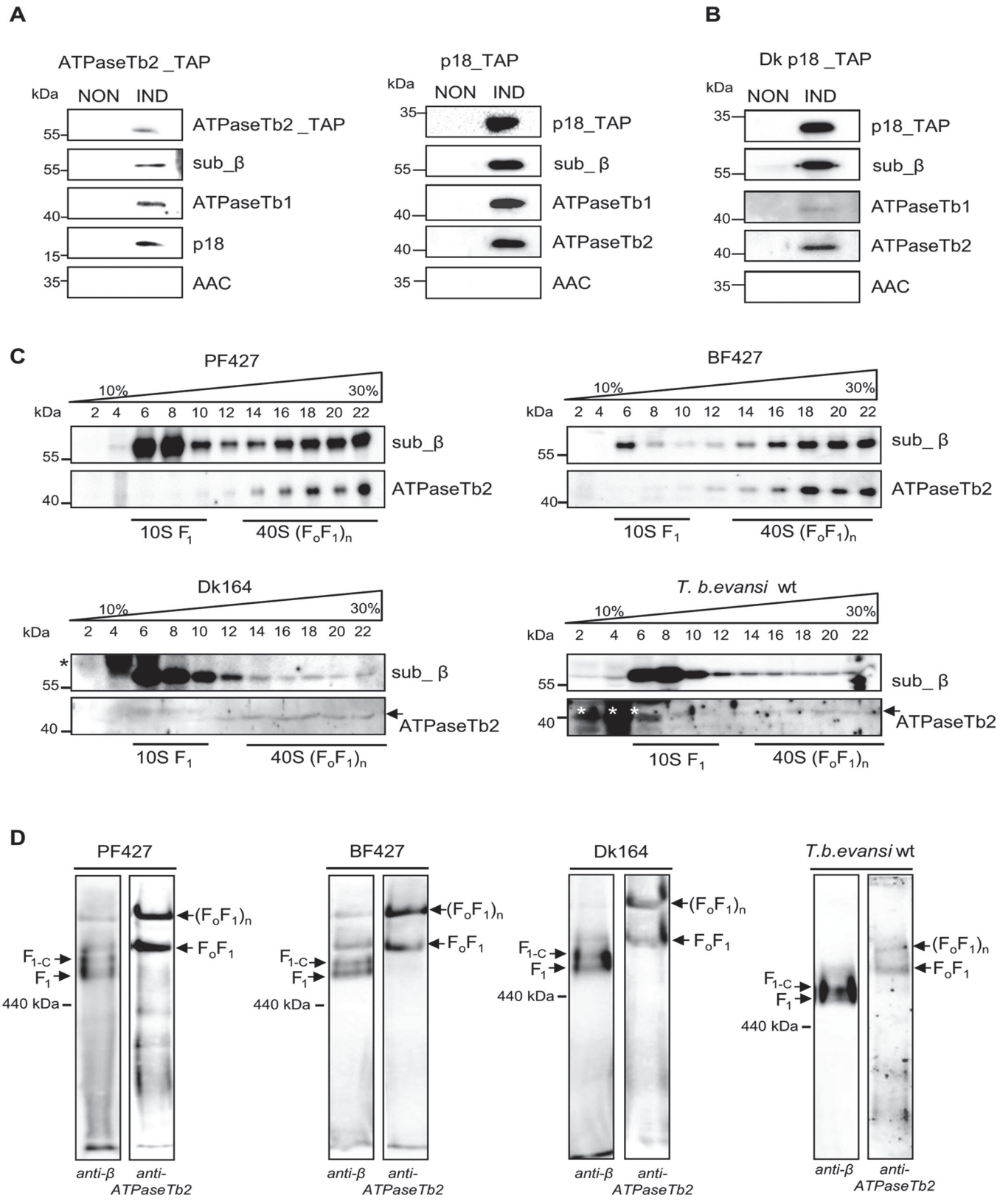

Fig 3. ATPaseTb2 is a bona fide subunit of the monomeric and multimeric F_oF_1-ATPases. A) ATPaseTb2_TAP and p18_TAP tagged complexes were purified from BF cells using one-step IgG affinity chromatography from non-induced (NON) and 2 days induced (IND) cells containing the regulatable ectopic

TAP tagged protein. The tagged protein complexes were eluated by TEV protease, fractionated on SDS-PAGE and examined by western blot analyzes. The presence of the tagged ATPaseTb2 and p18 subunits was verified using a *c*-myc antibody (top panels: ATPaseTb2_TAP and p18_TAP). The known F_oF_1-ATPase subunits (sub β, p18 and ATPase_Tb1) were detected using specific antibodies. The lack of signal for AAC serves as a control for specificity of the used method. The applicable sizes of the protein marker are indicated on the left. B) p18_TAP tagged complexes were purified from dyskinetoplastic *T. b. evansi* as described above for BF cells and subjected to the same set of antibodies. C) The sedimentation profile of F_1- and F_oF_1-ATPase complexes was determined using glycerol gradient sedimentation. Hypotonically purified mitochondria from PF427, BF427, Dk164 and *T. b. evansi* cells were lysed with 1% Triton X-100 and fractionated on a 10–30% glycerol gradient. The glycerol gradient fractions were collected, fractionated by SDS-PAGE and analyzed by western blots. Western analyzes with an anti-β antibody depicted the sedimentation profile of the F_1-ATPase and monomeric/multimeric F_oF_1-ATP synthase complexes, whereas the anti- ATPaseTb2 antibody only immunodecorates this protein within the monomeric/multimeric F_oF_1-ATPase complexes. The subdivision of the various structural forms of the F_oF_1-ATPase complexes are underlined as determined in [26]. The glycerol gradient fractions and the sizes of the protein marker are indicated. Nonspecific bands visible in Dk164 and *T. b. evansi* gradients are indicated by asterisks. D) The native F_1- and F_oF_1-ATPase complexes were visualized using hrCNE. Purified mitochondria from PF427, BF427, Dk164 and *T.b.evansi* cells were lysed with digitonin (4 mg/mg), fractionated on a 3%-12% hrCNE and blotted onto a nitrocellulose membrane. The F_1-ATPase (F_1), the F_1-ATPase bound with the c-ring (F_{1+C}) and the monomeric F_oF_1/multimeric $(F_oF_1)_n$ complexes were all visualized using specific polyclonal antibodies against either subunit β or ATPaseTb2. The size of ferritin from the equine spleen (440 kDa) is indicated on the left.

doi:10.1371/journal.ppat.1004660.g003

determined using mt lysates from all four cell types: PF427, BF427, Dk164 and *T.b.evansi*. In correlation with the literature, a new specific antibody raised against the F_1-subunit β depicted both regions, which are defined as ∼10S (fractions 6–10), and ∼40S (fractions 14–22) (Fig. 3C). A different sedimentation pattern was revealed when a specific antibody recognizing ATPaseTb2 detected only the 40S region (fractions 14–22), representing the F_oF_1-monomer and -multimers. These findings suggest that the novel subunit is not a component of the F_1-moiety, but rather a member of the fully assembled complex. Furthermore, compelling results hinting at the function of this hypothetical protein were also obtained when the mt lysates of Dk164 and *T. b. evansi* cells were fractionated on similar gradients. While the majority of the signal for subunit β was predictably detected in fractions 6–10, representing the F_1-ATPase complex, there was also a weak signal detected in higher S values. These same ∼40S complexes were identified using the ATPaseTb2 antibody (Fig. 3C). This indicates that in the absence of subunit a, the F_1-moiety is still attached to the mt membrane via a central stalk, a ring of subunit c and the peripheral stalk. Since the F_o subunit a is missing in these cells, the attachment of this complex to the membrane is presumably not as strong as in BF cells. Therefore, upon treatment with detergent to lyse the mitochondria, a majority of F_1-ATPase is released and detected in lower S values while a small portion of the F_oF_1-complexes is preserved and sediments at higher S value fractions. Consequently, our data suggests that previously undetected membrane-bound F_oF_1-complexes are present in the mitochondria of the Dk trypanosomes.

To verify our intriguing results, the F_oF_1-ATP synthase/ATPase complex was examined by an alternative method involving high resolution clear native electrophoresis (hrCNE) followed by western blot analysis. Results obtained using the antibody against subunit β revealed four predominant bands in both the PF427 and BF427 samples, representing various forms of the F_1-moiety and F_oF_1-complexes (Fig. 3D). The lowest band likely corresponds to the F_1-ATPase (subunits α, β, γ,δ,ε), while the one above it seemingly represents F_1-ATPase with a ring of subunit c, as it has been described for the mammalian complex [41]. Noticeably, in each sample the antibody against ATPaseTb2 immunodetected only two major bands corresponding to the F_oF_1-monomer and -multimers. When the mt lysates of Dk164 and *T. b. evansi* cells were fractionated on a hrCNE, subunit β was mainly detected in the lower bands representing the F_1-moiety and the F_oF_1-monomer, while only a weaker band was observed at the size depicting F_oF_1-multimers. But western blot analysis with the ATPaseTb2 antibody clearly demonstrated the existence of higher assemblies of the F_oF_1-ATPase complexes (Fig. 3D). Thus, ATPaseTb2 is a membrane-bound subunit of the monomeric and multimeric F_oF_1-ATP synthase/ATPase complex in all four *T. brucei* cell types examined. Furthermore, no significant differences in size were observed between the F_oF_1-monomeric and -multimeric complexes detected in

PF427, BF427 and Dk cells, indicating that subunit a might be the only missing component of the assembled F_oF_1-ATPase complex in dyskinetoplastic cells.

Silencing of ATPaseTb2 inhibits cell growth by decreasing the $\Delta\psi_m$ in BF *T. brucei*

To assess the importance of ATPaseTb2 in the infective stage of *T. brucei* and to evaluate its functional association with F_oF_1-ATPase, an ATPaseTb2 RNA interference (RNAi) cell line was created. The expression of dsRNA was triggered by the addition of tet to the culture medium and the *in vitro* growth of the ATPaseTb2 knock-down (KD) cells was inspected for seven days (Fig. 4A). Strikingly, a significant growth phenotype was already detected in RNAi induced cells on just the second day of tet addition. Presumably, the powerful selection forces acting on these cells missing a critical protein resulted in the emergence of a subpopulation that was no longer responsive to RNAi induction after only 120 hours, leading to the growth recovery of the culture (Fig. 4A). This phenomenon is often reported for RNAi experiments in BF *T. brucei* [42].

The targeted KD of ATPaseTb2 was confirmed by western blot analysis of whole cell lysates harvested from an equivalent number of cells for ATPaseTb2 RNAi non-induced and induced cells throughout the RNAi time course (Fig. 4B). Western blot analysis using the antibody against ATPaseTb2 exhibited a reduction of the targeted protein by 73% at day 2 of RNAi induction. A non-specific band detected on the same membrane was used to determine equal loading of the samples.

With the efficient knockdown of ATPaseTb2 verified, an *in vivo* assay was employed to measure the $\Delta\psi_m$ in the ATPaseTb2 KD cell population (Fig. 4C), since the $\Delta\psi_m$ is generated by the F_oF_1-ATPase in BF *T. brucei* [9]. Flow cytometry analysis was used to determine the changes observed in these cells stained with Mitotracker Red CMX-Ros, whose fluorescent intensity is proportionally dependent on the strength of the $\Delta\psi_m$. A substantial decrease of the $\Delta\psi_m$ in the KD cell population was observed two days (IND2) after RNAi induction, coinciding with the first time point to display a significant growth inhibition. Importantly, this result confirms the vital function of ATPaseTb2 within the F_oF_1-ATPase.

Depleting ATPaseTb2 does not significantly alter ATP hydrolysis capabilities

To assess if the decrease in the $\Delta\psi_m$ is the result of an impaired ATP hydrolytic activity of the enzyme, the total ATPase activity was measured in mt lysates with or without azide, an inhibitor of the catalytic F_1-ATPase [43]. Typically, the specific F_1-ATPase activity represents $\sim$ 35–45% of total mt ATPase activity. Our results indicate that neither the total ATPase nor azide-sensitive activities were significantly altered between the non-induced and ATPaseTb2 RNAi-induced cells (Fig. 5A). ATPase activity can also be visualized by in-gel activity staining when mitochondria from these cells are solubilized with dodecyl maltoside and separated on a 2–12% blue native PAGE (BNE) [41]. The specific ATPase staining revealed two major bands in non-induced cells, the predominant lower one representing the activity produced from the F_1-moiety and the less significant higher band representing the hydrolytic activity of the monomeric F_oF_1-ATPase (Fig. 5B). It is important to note that solubilizing mitochondria with any detergent can result in unintended structural consequences not found under normal physiological conditions, especially for a large complex comprised of a matrix moiety and a membrane embedded region. Although detergents tend to dissociate the F_1-moiety from F_oF_1-ATPase complexes, it is intriguing that there is still a portion of ATP hydrolysis being produced from

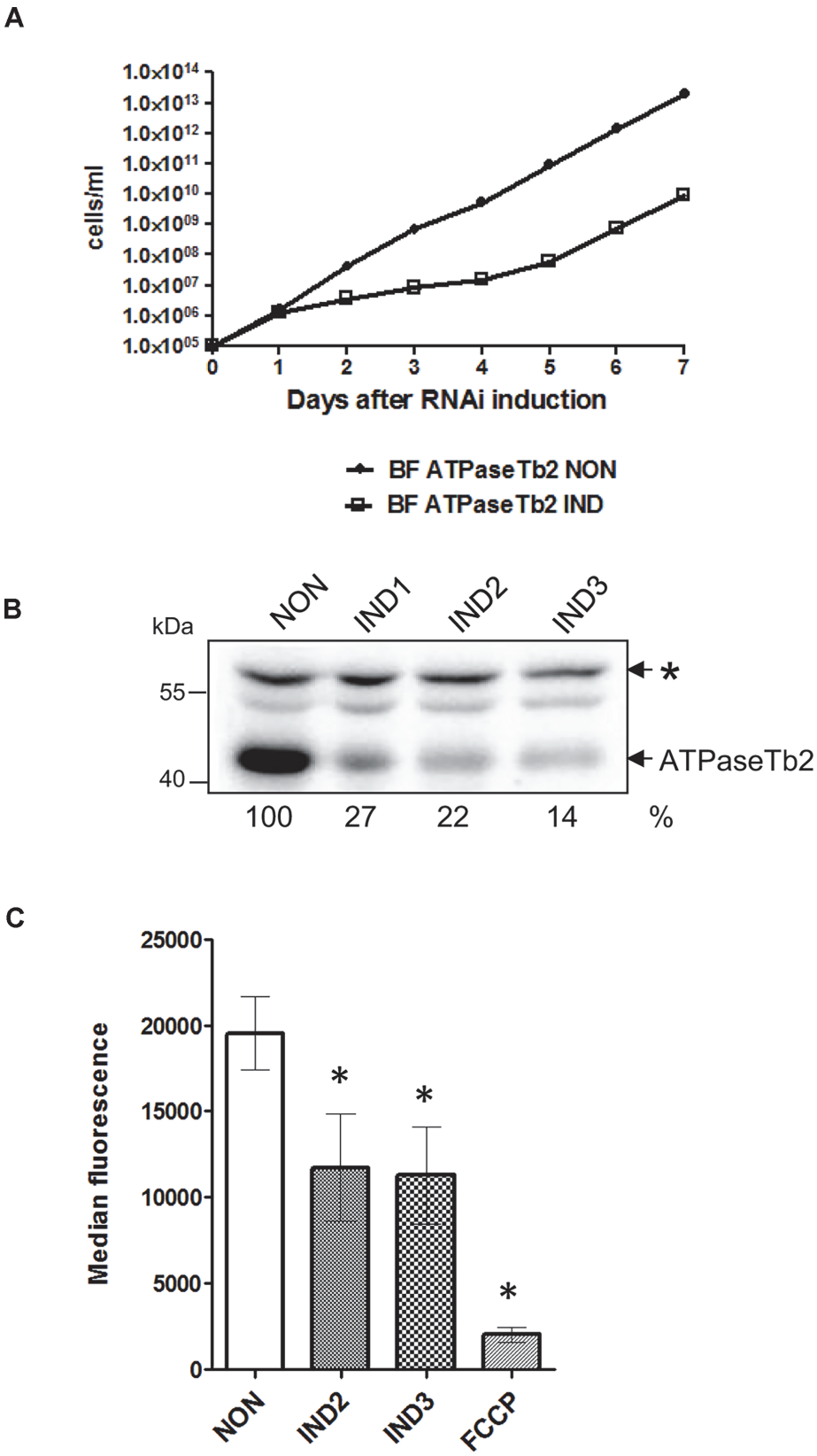
A
1.0x10^14
1.0x10^13
1.0x10^12
1.0x10^11
1.0x10^10
1.0x10^09
1.0x10^08
1.0x10^07
1.0x10^06
1.0x10^05
cells/ml
0 1 2 3 4 5 6 7
Days after RNAi induction
BF ATPaseTb2 NON
BF ATPaseTb2 IND
B
kDa
NON
IND1
IND2
IND3
55
40
*
ATPaseTb2
100 27 22 14 %
C
Median fluorescence
25000
20000
15000
10000
5000
0
*
*
*
NON
IND2
IND3
FCCP

Fig 4. RNAi silencing of ATPaseTb2 inhibits the growth and mt membrane potential of BF *T. brucei*. A) Growth curves of the noninduced (NON) and RNAi induced (IND) ATPaseTb2 RNAi bloodstream *T. brucei* cell lines were measured for 7 days. Cells were maintained in the exponential growth phase (between 10^5 and 10^6 cells/ml) and the cumulative cell number was calculated from cell densities adjusted by the dilution factor needed to seed the cultures at 10^5 cells/ml each day. The figure is representative of three independent RNAi-inductions. B) The steady-state abundance of ATPaseTb2 in non-induced (NON) RNAi cells and in cells induced with tet for 1, 2 and 3 days (IND1, IND2, IND3) was determined by western blot analysis using a specific ATPaseTb2 antibody. The non-specific band (marked with an asterisk) detected on the same membrane served as a loading control. The numbers beneath the blots represent the abundance of immunodetected ATPaseTb2 expressed as a percentage of the non-induced samples after normalizing to the loading control. The relevant sizes of the protein marker are indicated on the left. The figure is a representative western blot from three independent RNAi-inductions. C) Using Mitotracker Red CMX-Ros, the mt membrane potential was measured by flow cytometry in non-induced (NON) ATPaseTb2 RNAi cells and cells induced for 2 or 3 days (IND2 and IND3). The median fluorescence for each sample is depicted on the y-axis of the column graph. The results are means ± s.d. (n = 3). *$P < 0.05$, Student's *t*-test.

doi:10.1371/journal.ppat.1004660.g004

the complete F_oF_1-ATPase in the non-induced BF cells. Conspicuously, this activity is absent when ATPaseTb2 RNAi is induced (Fig. 5B).

Loss of ATPaseTb2 disrupts the F_oF_1-ATPase complexes in BF *T. brucei*

The absence of activity for the F_oF_1-monomeric complex might be explained by complex instability. Thus, the structural integrity of the coupled F_oF_1-complex was further analyzed using hrCNE, which were loaded with digitonin-lysed mitochondria from non-induced and ATPaseTb2 RNAi induced cells. After transferring the separated native protein complexes to a nitrocellulose membrane, a specific antibody against the p18 subunit detected the F_1-moiety as well as both monomeric and oligomeric F_oF_1-complexes (Fig. 5C). Interestingly, we repeatedly observed that the abundance of the monomeric and oligomeric complexes is decreased after RNAi induction and by day 3 these complexes are not detected at all. These results were complemented by the sedimentation profile of F_oF_1-ATPase complexes on glycerol gradients. Mitochondria were isolated from non-induced RNAi cells and cells induced for two days (IND2). These were then lysed by 1% Triton X-100 and an equal amount of mt protein from each sample was fractionated on a 10–30% GG. The resolved fractions were then analyzed by western blot and the anti-β and anti-p18 antibodies demonstrated the effect of the ATPaseTb2 KD on the F_oF_1-ATPase sedimentation profile. As indicated in Fig. 5D and the corresponding scanning densitometry results listed in S2 Fig., two days of RNAi induction resulted in a diminished amount of β and p18 signals from the higher S-values (IND2 panels), while the GG sedimentation pattern of RNAi non-induced cells was more similar to wild type BF427 (see Fig. 3C). These results are in agreement with the PF RNAi ATPaseTb2 cell lines, in which the stability of the monomeric and multimeric F_oF_1-ATP synthases was significantly affected upon RNAi [26].

Using a variety of methods employing various detergent types, we have established that the ATPaseTb2 subunit is an essential component of the F_oF_1-ATPase monomer and higher oligomers in the bloodstream stage of *T. brucei*. Furthermore, the depletion of ATPaseTb2 diminishes the abundance of membrane-bound F_oF_1-ATPase complexes, which directly initiates a substantial decrease in the $\Delta\psi_m$ that manifests as a strong growth phenotype.

ATPaseTb2 depletion affects cell growth, the $\Delta\psi_m$ and F_oF_1-ATPase integrity in Dk *T. b. evansi*

To further dissect the primary role of the membrane-bound ATPaseTb2 subunit, we investigated the effect of targeted gene silencing in transgenic Dk *T. b. evansi*, which facilitate the tet

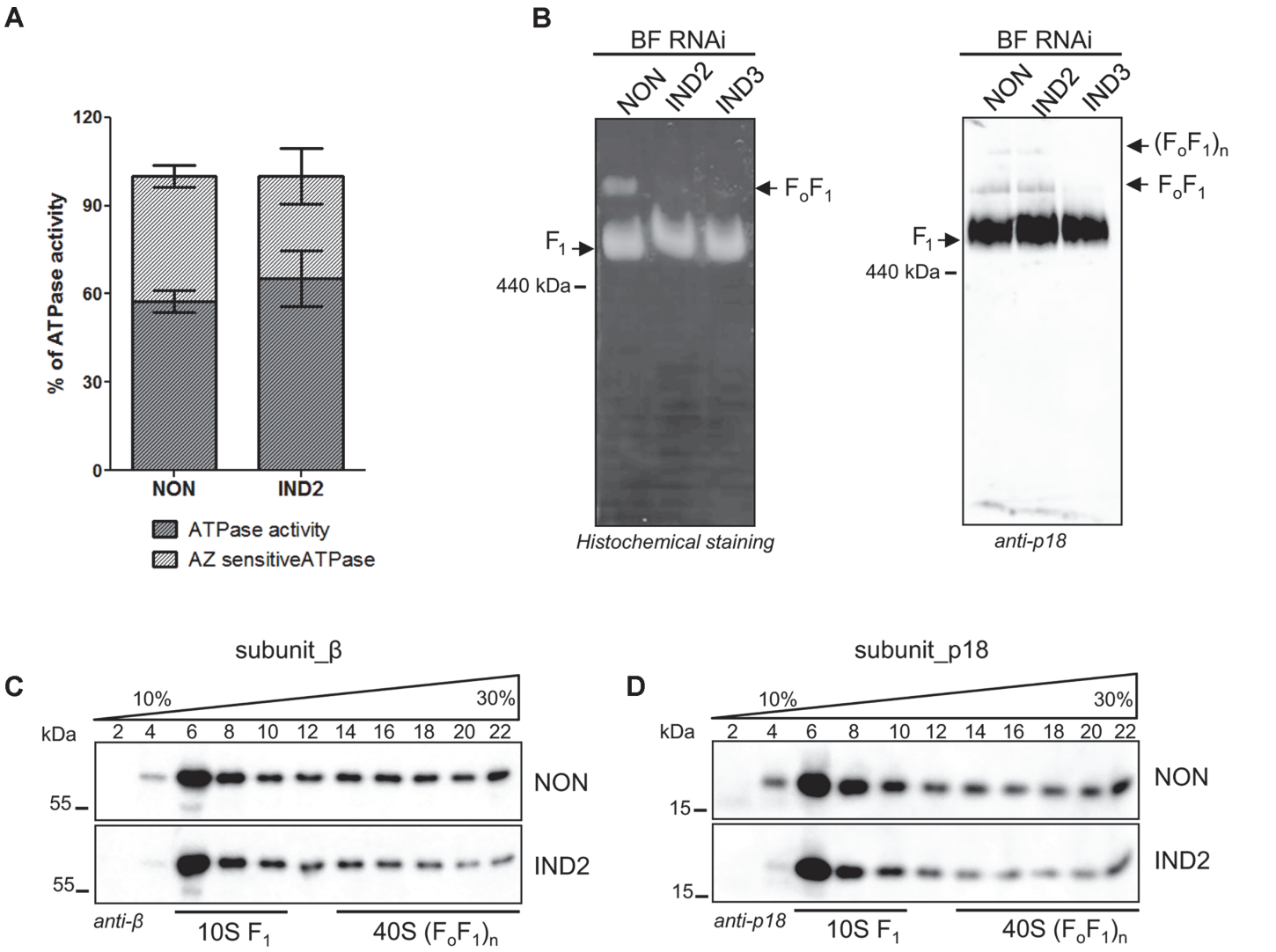

Fig 5. ATPaseTb2 depletion does not appreciably affect F_1-ATPase activity in BF *T. brucei* cells, but it does significantly diminish the stability of F_oF_1-ATPase complexes. A) Employing the Sumner ATPase assay, the F_1-ATPase hydrolytic activity was measured in ATPaseTb2 RNAi cells either not induced (NON) or induced for 2 days (IND2). Crude mt vesicles were obtained by digitonin extraction and the ATPase activity was assayed by measuring the release of free phosphates. The specific F_1-ATPase inhibitor, azide (AZ, 2 mM), was added as indicated. The total amount of free-phosphate created from all ATPase enzymes present in the sample was set at 100% (hatched column). The azide-sensitive activity representing the F_1-ATPase is depicted in dark grey. The results are means ± s.d. (n = 4). B) In-gel ATP hydrolysis activity of F_oF_1-ATPase was visualized after ATPaseTb2 reduction. Mitochondria from RNAi non-induced cells (NON) and cells induced for 2 (IND2) and 3 (IND3) days were lysed with 2% dodecyl maltoside. Equal amounts of lysed mitochondrial proteins (100 μg) were fractionated on a 2%-12% BNE and the F_oF_1-ATPase activity was visualized by in-gel histochemical staining resulting in a white lead phosphate precipitate. Positions of F_1-ATPase and monomeric F_oF_1-ATPase are depicted. The size of equine spleen ferritin (440 kDa) is indicated. C) The stability of F_oF_1-ATPase complexes upon ATPaseTb2 silencing was examined using hrCNE. Mitochondria from RNAi non-induced cells (NON) and cells induced for 2 (IND2) and 3 (IND3) days were lysed by digitonin (4 mg/mg). Equal amounts of lysed mitochondrial proteins (20 μg) were fractionated on a 3%-12% hrCNE, blotted onto a nitrocellulose membrane and probed with the anti-p18 antibody. Positions of F_1-ATPase and monomeric and dimeric F_oF_1-ATPases are depicted by arrows. The size of ferritin from equine spleen (440 kDa) is indicated. D) The sedimentation profile of F_oF_1-ATPase complexes was examined using western blot analysis of glycerol gradient fractions. Mitochondria from RNAi non-induced cells (NON) and cells induced for 2 days (IND2) were lysed with 1% Triton X-100. An equal amount of the cleared lysates (3,3 mg) were loaded on a manually poured 10–30% glycerol gradient. Western analyzes with anti-β and anti-p18 antibodies depicted the sedimentation profile of the F_oF_1-ATPase complexes. The manually fractionated glycerol gradient fractions are labelled and sizes of the protein marker are indicated.

doi:10.1371/journal.ppat.1004660.g005

inducible expression of dsRNA. These Dk cells were transfected with an ATPaseTb2 RNAi vector and several positive clones were screened for a growth phenotype. As shown in Fig. 6A, the surprising inhibition of cell growth in RNAi induced cells appeared two days after tet induction

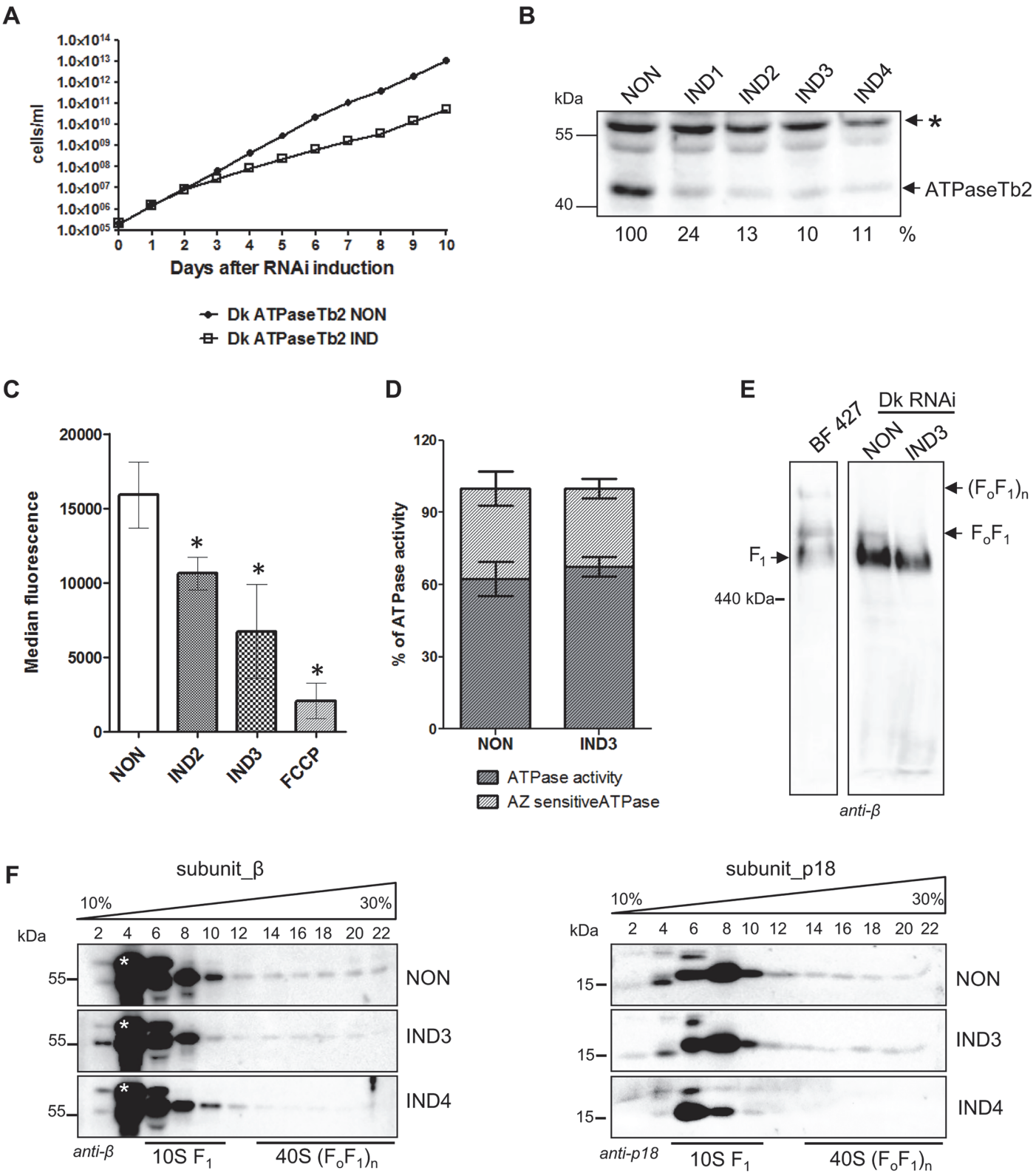

Fig 6. Cell growth, $\Delta\psi_m$ maintenance and the stability of FoF1-ATPase complexes are all affected by the loss of ATPaseTb2 in dyskinetoplastic *T.b. evansi*. A) Growth curves of the non-induced (NON) and induced (IND) ATPaseTb2 RNAi Dk *T. b. evansi* cell lines were measured for 10 days. Cells were maintained in the exponential growth phase (between 10^5 and 10^6 cells/ml) and the cumulative cell number represents the cell density adjusted by the daily dilution factor. The figure is representative of three independent RNAi-inductions. B) The steady-state abundance of ATPaseTb2 in non-induced (NON)

cells and cells harvested 1, 2, 3 and 4 days post RNAi induction (IND1, IND2, IND3, IND4) was determined by western blot analysis using a specific ATPaseTb2 antibody. Mt Hsp70 served as a loading control. The numbers underneath the ATPaseTb2 panel represent the abundance of immunodetected protein expressed as a percentage of the non-induced samples after normalizing to the loading control. The pertinent sizes of the protein marker are indicated on the left. The figure is a representative western blot from three independent RNAi-inductions. C) The $\Delta\psi_m$ was measured in non-induced (NON) ATPaseTb2 RNAi cells and cells induced for 2 and 3 days (IND2 and IND3) by flow cytometry using Mitotracker Red CMX-Ros. The results are means ± s.d. (n = 3). *$P < 0.05$, Student's *t*-test. D) The F_1-ATPase hydrolytic activity was measured for induced (IND3) or non-induced Dk ATPaseTb2 RNAi cells as described in Fig. 5A. The results are means ± s.d. (n = 4). E) The stability of F_oF_1-ATPase complexes upon ATPaseTb2 depletion was examined using hrCNE. Mitochondria from wild type BF427, ATPaseTb2 RNAi *T. b. evansi* non-induced cells (NON) and cells induced for 3 days (IND3) were lysed by digitonin (4 mg/mg). Equal amounts of lysed mitochondrial proteins (20 μg) were fractionated on a 3%-12% hrCNE, blotted onto a nitrocellulose membrane and probed with an anti-β antibody. Positions of F_1-ATPase and monomeric and multimeric F_oF_1-ATPases are depicted by arrows. The size of the equine spleen ferritin (440 kDa) is indicated on the left. F) The sedimentation profile of F_oF_1-ATPase complexes was examined using western blot analysis of glycerol gradient fractions. Mitochondria from RNAi non-induced cells (NON) and cells induced for 3 and 4 days (IND3 and IND4) were lysed by 1% Triton X-100 and an equal amount of the cleared samples (1.3 mg) were loaded on a 10–30% glycerol gradient. Western analyzes with anti-β and anti-p18 antibodies depicted the sedimentation profile of the F_oF_1-ATPase complexes. The glycerol gradient fractions are labelled and the relevant sizes of the protein marker are indicated. A nonspecific band only visible in Dk164 gradients is indicated by an asterisk.

doi:10.1371/journal.ppat.1004660.g006

and the doubling time remained reduced throughout the whole ten day experiment. Furthermore, western analysis of whole cell lysates harvested over the RNAi time course exhibited a significant reduction of ATPaseTb2 in the RNAi induced cells beginning on day 1 (Fig. 6B), while the analysis of a non-specific band served as the loading control. Interestingly, if the only role of the subunit was to stabilize the proton pore, it presumably would not be essential in cells that lack mtDNA and have adapted to the loss of a functioning proton pore. However, these results suggest that ATPaseTb2 is important for F_oF_1-ATPase complexes in these unique cells and thus this cell line was further exploited to characterize the function of ATPaseTb2.

Since the $\Delta\psi_m$ in Dk cells is generated using the hydrolytic activity of the F_1-moiety coupled with ATP/ADP translocation, the $\Delta\psi_m$ was examined in ATPaseTb2 non-induced and RNAi induced cell populations. As shown in Fig. 6C, a reduction of the $\Delta\psi_m$ was detected in the RNAi induced cell population after 2 (IND2) and 3 days (IND3). Since the reduction of the $\Delta\psi_m$ already appears at day 2 of tet induction and the growth phenotype does not truly manifest until day 3, we postulate that the observed decrease of the $\Delta\psi_m$ is a direct effect of ATPaseTb2 silencing and not a consequence of decreased cell viability. Furthermore, to assess if this decreased $\Delta\psi_m$ is caused by an impairment of the F_1-ATPase hydrolytic activity, the total ATPase activity was measured in mt lysates with or without azide. Similar to BF RNAi ATPaseTb2 cells (Fig. 5A), no changes in total or azide-sensitive activities were observed between the non-induced and ATPaseTb2 RNAi-induced cells (Fig. 6D).

The structural integrity of Dk F_oF_1-ATPase complexes was then investigated using mild non-denaturing hrCNE to fractionate mitochondrial proteins purified from BF427 cells and Dk cells either induced for ATPaseTb2 RNAi or not. A western blot containing BF427 mitochondria as a reference sample was probed with an anti-β antibody and used as marker to visualize each state of the F_1-moiety, either isolated by itself or being partnered with the monomeric and multimeric F_oF_1-complexes. Strikingly, while a majority of the β subunit signal in Dk RNAi non-induced cells was observed in the region of isolated F_1-ATPase, we also consistently detected an irrefutable signal corresponding to the F_oF_1-monomeric complex, presumably assembled intact with the exception of subunit a (Fig. 6E). While there is evidence of mammalian rho cells containing a similar complex [44–46], this is the first time it has been demonstrated in the comparable Dk trypanosomatids. Furthermore, the induction of ATPaseTb2 RNAi in the Dk cells led to the disappearance of the monomeric complex, leaving only the F_1-ATPase to be detected on the western blot (Fig. 6E). Once again, the evidence indicates that ATPaseTb2 is important for the structural integrity of the F_oF_1-ATPase and its depletion in Dk *T.b. evansi* cells leads to the disruption of the unique membrane-bound F_oF_1-ATPase complexes.

To corroborate this observation, we purified mitochondria from Dk *T. b. evansi* non-induced and ATPaseTb2 RNAi-induced cells and lysed them with Triton X-100. These gently disrupted lysates were then fractionated on glycerol gradients, which revealed that a majority of the signal from subunits β and p18 was located within fractions 6–10, representing the F_1-moiety (Fig. 6F). Nevertheless, weaker bands representing the F_oF_1-ATPase complexes (fractions 14–22) were again detected in the non-induced samples (Fig. 6F NON panels). Noticeably, these same protein markers in the mt fractionation of ATPaseTb2 RNAi induced cells displayed a significant reduction in fractions 14–22 (Fig. 6F IND4 panels), where the F_oF_1-monomer/oligomer sediments. This observation is quite surprising since the main role of this enzyme is to create the $\Delta\psi_m$, presumably using only the hydrolytic activity of the matrix facing F_1-moiety. In an attempt to determine if a portion of the F_1-ATPase is membrane associated and that the disruption of this attachment is the reason for the observed decrease in the $\Delta\psi_m$ and the detected growth phenotype, we decided to visualize these complexes *in situ* using immunogold labelling followed by electron microscopy.

Loss of ATPaseTb2 leads to the dissociation of F_1-ATPase from the mt membrane

Immunogold labeling with a primary anti-β antibody was performed on ultrasections of Dk *T. b. evansi* non-induced (NON) and ATPaseTb2 RNAi induced cells for 3 (IND3) and 5 (IND5) days. Electron micrographs illustrate that Dk trypanosomes have a simple and reduced mitochondrion (S3A Fig.), lacking both cristae and a typical kinetoplast structure, as previously reported for the dyskinetoplastic *T. b. evansi* [17]. Whenever these reduced double-membrane organelles could be unequivocally identified, we tallied the number of immunogold beads either in the close proximity of the mt membrane or in the matrix (S3A Fig.). Strikingly, 70% of the gold particles identified were found associated with the mt membrane in the NON images (S3B Fig.). From the 113 images captured from either NON, IND3 or IND5 samples, we performed a Chi-squared analysis on the immunogold beads associated with the mt membrane to determine if their distribution is random (S3C Fig.). With two degrees of freedom, the calculated $\chi^2 = 43.5$ ($p < 0.0001$), which signifies that the difference between the observed and expected particles was statistically significant. These values were then plotted to determine the relative labelling index ($RLI = N_{obs}/ N_{exp}$) for the mt membrane associated gold particles (S3D Fig.). This analysis reveals that the observed number of gold particles found in close proximity to the mt membrane for the NON electron micrographs is significantly greater than if the particles were randomly distributed (RLI = 1), while the opposite is true for the IND5 samples. Since we understand the general subjectivity of this method, we performed this experiment in a blinded study and only considered a gold bead to be associated with the mt membrane if it was in the immediate proximity of the membrane. For the very few scored beads that could potentially fall in a membrane-bound grey zone, it should be noted that the physical distance from the subunit β antigen to the gold particle can be up to 15–20 nm, not to mention that subunit β itself is projected from the membrane by subunit γ by as much as 13 nm [47,48]. Furthermore, very few immunogold beads were detected outside of defined mt structures and each mt image only contained 1–8 immunogold beads (average of 2.4 beads/mt image), suggesting that the labelling was very specific for our abundant mt antigen. It is important to note, that utilizing an assay that does not require the use of any detergents, we demonstrated that a majority of the F_1-ATPase is located within close proximity of the mt membrane and this association is disrupted when ATPaseTb2 is depleted.

Discussion

The *T. brucei* F_oF_1-ATPase has obtained unique properties in comparison to its eukaryotic counterparts. The occurrence of novel subunits combined with the lack of typical eukaryotic subunits that compose the F_o membrane-bound moiety and the peripheral stalk is intriguing from an evolutionary viewpoint. Because these atypical subunits lack significant homology to known proteins, questions arise concerning their authenticity as genuine subunits of the complex and what their function and localization within the complex might be. Here, we focused on the functional characterization of one of the trypanosomatid specific subunits, ATPaseTb2 in the bloodstream stages of *T. brucei*. Notably, we determined that its function is essential for maintaining the normal growth rate of the infectious stage of *T. brucei* and also for the important veterinary dyskinetoplastic parasite, *T. b. evansi*. Additional analyses demonstrated that the ATPaseTb2 is membrane embedded and a component of the F_oF_1-ATPase that is present in both BF and Dk cells. Furthermore, the depletion of this F_o-moiety subunit results in a decreased $\Delta\psi_m$ and a loss of F_oF_1-ATPase complexes. Combined with bioinformatic tools that predict a transmembrane domain and identify a low homology to subunit d, we suggest that ATPaseTb2 might be a component of the peripheral stalk of the F_oF_1-ATPase.

The peripheral stalk is indispensable for ATP synthesis as it serves to impede the movement of the catalytic $\alpha_3\beta_3$ headpiece while the proton motive force rotates the c-ring and the connected asymmetrical central stalk in a way that imposes conformational changes in the catalytic nucleotide binding sites of the β subunits. The peripheral stator is also essential when the complex harnesses the energy provided from ATP hydrolysis to drive the rotation of the enzyme in reverse, allowing protons to be pumped across the mt inner membrane to produce the $\Delta\psi_m$ when physiological conditions dictate.

The bovine and yeast peripheral stalk is composed of four subunits, OSCP, b, d, and F_6/h (bovine/yeast nomenclature). Subunit b ($\sim$20kDa protein) contains two trans-membrane segments at the N-terminus, while the rest of the protein is hydrophilic—protruding into the matrix and interacting with OSCP and subunit d [23,49–51]. The interaction between subunit b and OSCP is stabilized by subunit F_6 [22]. The predominantly hydrophilic subunit d interacts with all three mentioned subunits and it has been shown to be essential for the function of the F_oF_1-complex. The yeast knock-out of subunit d was characterized by the de-attachment of the catalytic F_1-ATPase from the protonophoric sector, the loss of detectable oligomycin sensitive ATPase activity and the absence of subunit a in the F_o-moiety [36]. Notably, of these four subunits, the only homolog identified in the *T. brucei* genome is OSCP and its protein product was identified as a bona fide subunit of the purified F_oF_1-ATP synthase [26]. Homologs for subunits b, d, and F_6 are missing and most likely have been replaced by the novel proteins that associate with the *T. brucei* F_oF_1-ATP synthase. Here we demonstrated that the ATPaseTb2 subunit is a membrane-bound protein, containing one predicted transmembrane domain, with a large hydrophilic region extending into the matrix that possesses a low homology to the bovine subunit d. In accordance with other yeast or bovine subunits of the peripheral stalk, the down-regulation of ATPaseTb2 affects the stability of the F_oF_1-complex and its oligomycin sensitivity (this study, [26]).

Considering the relatively large molecular mass of ATPaseTb2 (43 kDa), it is plausible to speculate that ATPaseTb2 functionally represents the membrane-bound subunit of the peripheral stalk fused with subunit d, offering an early attempt by eukaryotes to add layers of complexity that will allow for greater adaptability. It is noteworthy to mention that a species-specific architectural variant of the peripheral stalk was also proposed for colorless and green algae, where the novel subunits Asa2, Asa4 and Asa7 fulfil a structural role in forming the peripheral stalk [52,53]. Other discrepancies from the typical eukaryotic enzyme model can be

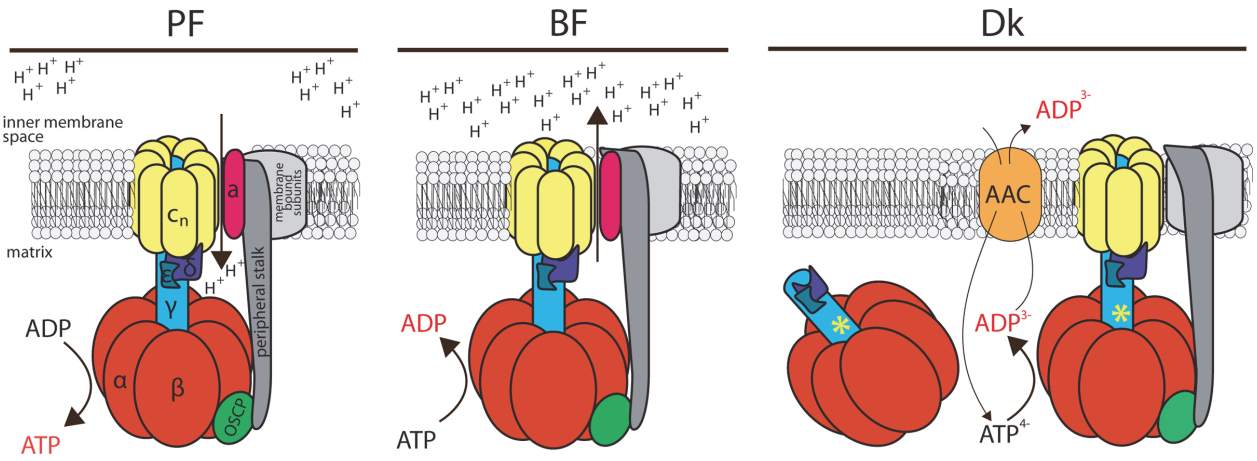

Fig 7. Schematic representation of the F_oF_1-ATP synthase/ATPase complex in trypanosome mitochondria. The F_oF_1-ATP synthase possesses the conventional function in the procyclic form (PF) of the parasite, coupling transmembrane proton transfer with ATP synthesis. In contrast, this enzymatic complex works in reverse in the bloodstream form (BF) of the parasite, hydrolyzing ATP to generate the $\Delta\psi_m$ in the absence of canonical cytochrome-containing respiratory complexes. This hydrolytic activity is also utilized in the dyskinetoplastid (Dk) form, which lacks mitochondrial DNA and thus a proton pore. Therefore, in Dk cells, enhanced ATP hydrolysis by a mutated F_1-moiety (a necessary mutation in the γ subunit is marked with the asterisk) provides substrate for the ATP/ADP carrier (AAC) and the $\Delta\psi_m$ is produced by the electrogenic exchange of ADP^{3-} for ATP^{4-}. Furthermore, we present that a minor fraction of F_1-ATPase still appears to be associated with F_o and that association may be functionally important for maintaining the $\Delta\psi_m$. Orthologues of the colored subunits (α, β, γ, δ, ε, OSCP, a and c) have been annotated in trypanosomes. In addition to OSCP, the peripheral stalk (dark grey) is usually composed of subunits b, F_6 and d, but these homologs have not been identified in the *T. brucei* genome. Also, conspicuously absent are subunits A6L, e, f and g, which are all membrane-bound (light grey).

doi:10.1371/journal.ppat.1004660.g007

found in the ciliate *Tetrahymena thermophila*, representing the superphylum of Alveolates, where the homolog of the conserved subunit b has so far not been identified in the genome. Instead, three novel proteins detected in this ATP synthase complex have been proposed to substitute for subunit b [28]. Thus, it seems that the composition and overall structural appearance of the F_oF_1-ATP synthase from organisms representing different lineages other than Opisthokonts, might be more diverse than previously thought and deserve more attention from basic researchers to elucidate alternate evolutionary solutions to a common thread of life.

T. brucei is a member of the Excavata clade and represents a desirable model to study the function and regulation of the F_oF_1-ATP synthase/ase complex since it utilizes the proton motive force to produce ATP in the PF life stage, while in the BF stage it hydrolyzes ATP to pump the protons necessary to create the $\Delta\psi_m$. Moreover, dyskinetoplastic *T. b. evansi* employs the hydrolytic activity of the F_1-ATPase and the electrogenic exchange of ADP^{3-} for ATP^{4-} by the AAC as yet another strategy to generate the $\Delta\psi_m$ (Fig. 7). Therefore, it was surprising that the ATPaseTb2 protein was detected in all four examined cell types (PF, BF, Dk 164 and *T. b. evansi*), albeit at a much lower abundance in BF and Dk cells, but that is in full agreement with the reduced mitochondria previously defined for these two forms [39]. Furthermore, when PF and BF mt lysates were resolved by GG and hrCNE, ATPaseTb2 was only detected when co-localized with the monomeric and oligomeric F_oF_1-ATP synthase/ase complexes. Interestingly, similar results were obtained from the mt lysates of cells lacking mtDNA. Considering that only the F_1-ATPase was previously assumed to be important for maintaining the $\Delta\psi_m$ in the Dk trypanosomes, the presence of these complexes is intriguing. Nevertheless, a proteomics study performed with osteosarcoma 143B ρ° cells revealed that in addition to the F_1-ATPase subunits, subunit d of the peripheral stalk was also identified [54]. In a similar project involving fibroblast MRC5 ρ° cells, the oligomycin insensitive complex was purified and determined to contain several F_o (b and c) subunits along with a couple of peripheral stalk subunits (OSCP, d). Notably, this complex was loosely associated with the mt membrane [45]. Furthermore,

several additional studies have shown that the F_1-ATPase in yeast or mammalian cells lacking a mt genome (i.e. mammalian subunits a/ATP6, A6L; yeast subunits 6, 8 and 9) is membrane associated, with the attachment most likely occurring via the central and/or peripheral stalk [44,46,55,56]. Our data also suggest that since ATPaseTb2 membrane-bound complexes (monomeric and multimeric) do not display significant differences in their native size or sedimentation values, then the mt encoded subunit a might be the only missing subunit from these complexes. Such a uniquely structured complex can be explained by the current model for the assembly of the F_oF_1-ATPase, in which the F_o subunit a is the last protein incorporated into the enzyme to ensure that it is able to function properly before introducing a complete proton pore. Furthermore, this integration is dependent on the presence of subunit b of the peripheral stalk [57].

RNAi silencing of ATPaseTb2 in BF cells caused a strong growth phenotype concurring with a decreased $\Delta\psi_m$. Importantly, ATPaseTb2 also proved to be essential for maintaining the normal growth rate and the $\Delta\psi_m$ of Dk cells. Combined with the hrCNE and glycerol gradient sedimentation assays that revealed a decrease of the high molecular weight complexes, but not the F_1-ATPase, our studies suggest that these membrane-bound enzymes might significantly contribute to the membrane potential in Dk cells. The biological significance of this localization of the F_1-ATPase might be to efficiently coordinate the activity of this enzyme with its substrate transporter, both of which are responsible for producing the $\Delta\psi_m$ in Dk. By restricting the F_1-ATPase to the mt membrane, it keeps it within the close vicinity of its biochemically functional partner, the AAC. In this way, it helps ensure that the hydrolysis of ATP results in a relatively concentrated region of substrate for the mt membrane embedded AAC, especially in a mitochondrion lacking defined cristae and the microenvironments they create. Indeed, there is precedence for such a close spatial collaboration to increase efficiency, as an actual physical interaction between these two enzymes has been reported as the ATP synthasome in mammals [40,58]. We are currently building a set of tools to perform additional functional assays and imaging techniques that we hope will further resolve the function of the F_oF_1-ATPase complexes in these pathogenic trypanosomes.

Materials and Methods

Plasmid construction

The ATPaseTb2 (Tb927.5.2930) RNAi constructs targeted an 825 bp fragment of the gene that was PCR amplified from *T. brucei* strain 427 genomic DNA with the following oligonucleotides: FW—CACGGATCCATGCGCCGTGTATC, REV-CACCTCGAGTTCGGCCCGATC. Utilizing the BamHI and XhoI restriction sites inherent in the primers (underlined), this fragment was cloned into the p2T7-TA blue plasmid [59] (used to create a BF RNAi cell line) and the p2T7–177 plasmid [60] (used to generate a Dk RNAi cell line). For the inducible expression of ATPaseTb2 fused with a C-terminal 3xv5 tag, the ATPaseTb2 coding sequence was PCR amplified (Fw: ACAAAGCTTATGC GCCGTGTATC, Rev: ATAGGATCCGTG ATGGGCCTTTTTC) and cloned into the pT7_v5 vector using HindIII and BamHI restriction enzymes [61]. The pLEW79MHTAP vectors for the tet inducible expression of ATPaseTb2 and Tb927.5.1710 (F_oF_1-ATPase subunit p18) TAP-tagged proteins were previously described in [26].

Trypanosoma culture conditions and generation of cell lines

Bloodstream form *T. brucei brucei* Lister 427 strain, stable acriflavin-induced dyskinetoplastic *T. b. brucei* EATRO 164 [18] and dyskinetoplastic *T. b. evansi* Antat 3/3 [62] were all grown *in vitro* at 37°C and 5% CO_2 in HMI-9 media containing 10% FBS. The BF427 single marker cell

line [63] and a *T. b. evansi* cell line [14], both constitutively expressing the ectopic T7 RNA polymerase and tet repressor (TetR were used for the tet inducible expression of dsRNA and the TAP- and v5-tagged proteins. Each plasmid was linearized with NotI enzyme and transfected into the appropriate cell line as described previously [63]. Linearized p2T7–177 was targeted to the minichromosome 177 basepair repeat region, while linear pTv5 and pLEW79MHTAP vectors were integrated into the rDNA intergenic spacer region [60,61,63]. The induction of RNAi and ectopically expressed tagged proteins was triggered by the addition of 1 μg/ml of tet into the media. Cell densities were measured using the Z2 Cell Counter (Beckman Coulter Inc.). Throughout the analyses, cells were maintained in the exponential mid-log growth phase (between $1x10^5$ to $1x10^6$ cells/ml).

Tandem affinity purification (TAP) of tagged complexes

The TAP protocol was generously provided by L. Jeacock and A. Schnaufer (personal communication) and optimized for BF cells. Briefly, $2x10^8$ cells were harvested and lysed for 20 min on ice with 1% Triton X-100 in an IPP150 buffer (150 mM NaCl, 0,1% NP40, 10mM Tris-HCl pH 8.0) containing Complete protease inhibitors (Roche). The lysates were then cleared by centrifugation (16,000 g, 15 min, 4°C). Meanwhile, IgG antibodies were covalently bound to Dynabeads M-270 Epoxy (Invitrogen) using a protocol previously described [64]. Charged beads were blocked with 1% BSA and then incubated with the cleared cell lysates (4°C for 2 hours, constantly rotating). The beads were then washed three times with IPP150 and once with a TEVCB buffer (150 mM NaCl, 0.1% NP40, 0.5 mM EDTA, 1 mM DTT, 10 mM Tris-HCl, pH 8.0). Finally, the bound protein complexes were released by AcTEV protease (Invitrogen) cleavage and the eluate was analyzed by SDS-PAGE.

Isolation of mt vesicles

Crude mt vesicles were obtained by hypotonic lysis as described in detail earlier [65]. Briefly, cell pellets from $\sim 2x10^9$ cells were washed with SBG (150 mM NaCl, 20 mM glucose, 20 mM $NaHPO_4$, pH 7.9), resuspended in DTE (1 mM Tris, 1 mM EDTA, pH 8.0) and homogenized in a Dounce homogenizer. Alternatively, for a smaller scale hypotonic isolation, cell pellets from $\sim 1x10^9$ cells were washed in NET buffer (150 mM NaCl, 100 mM EDTA, 10 mM Tris, pH 8.0), resuspended in DTE and homogenized by passing through a 25G needle. To re-create the physiological isotonic environment, 60% sucrose was immediately added to the lysed cells to reach a final concentration of 250 mM. Samples were spun down at 15,000 g, 10 min, 4°C to clear the soluble cytoplasmic material from the lysates. The resulting pellets were resuspended in STM (250 mM sucrose, 20 mM Tris pH 8.0, 2 mM $MgCl_2$), supplemented with a final concentration of 3 mM $MgCl_2$ and 0.3 mM $CaCl_2$ before incubating with 5 μg/ml DNase I for 1hr on ice. Then an equal volume of STE buffer (250 mM sucrose, 20 mM Tris pH 8.0, 2 mM EDTA pH 8.0) was added and the material was centrifuged at 15,000 g, 10 min, 4°C. Pellets enriched with the mt membrane vesicles were washed in STE and kept at -70°C.

SDS-PAGE and Western blot

Protein samples were separated on SDS-PAGE, blotted onto a PVDF membrane (PALL) and probed with the appropriate monoclonal (mAb) or polyclonal (pAb) antibody. This was followed by incubation with a secondary HRP-conjugated anti-rabbit or anti-mouse antibody (1:2000, BioRad). Proteins were visualized using the Pierce ECL system (Genetica/Biorad) on a ChemiDoc instrument (BioRad). When needed, membranes were stripped at 50°C for 30 min in a stripping buffer (62.5 mM Tris pH 6.8, 100 mM mercapthoethanol, 2% SDS) and re-probed. The PageRuler prestained protein standard (Fermentas) was used to determine the size

of detected bands. Primary antibodies used in this study were: mAb anti-v5 epitope tag (1:2000, Invitrogen), mAb anti-mtHsp70 (1:2000) [66], pAb anti-AAC (1:2000) [67], pAb anti-MRP1 (1:1000) [68], pAb anti-APRT (1:1000) and pAb anti-enolase (1:1000) [69]. Antibodies against ATPaseTb2 (1:1000), ATPaseTb1 (1:1000), subunit β (1:2000) and subunit p18 (1:1000) were prepared for the purpose of this study. The open reading frames of the respective genes without their predicted mt localization signal were cloned into the *E. coli* expression plasmid, pSKB3. The proteins were overexpressed in BL21 *E. coli* cells and purified under native conditions (subunit β) or denatured conditions (ATPaseTb2, ATPaseTb1 and p18) using a 6 M guanidinium lysis buffer and 8 M urea binding buffer. The denatured proteins were then refolded with a step-wise dialysis procedure that included 0.5 M arginine in the refolding buffer. Native and refolded antigens were sent to Pineda (Antikörper-Service, Germany) or Davids Biotechnologie (Regensburg, Germany) for polyclonal antibody production.

Mt membrane potential ($\Delta\psi_m$) measurement

The $\Delta\psi_m$ was determined utilizing the red-fluorescent stain Mitotracker Red CMX-Ros (Invitrogen). Cells in the exponential growth phase were stained with 100 nM of the dye for 30 min at 37°C. Cells were pelleted (1,300 g, 10 min, RT), resuspended in 2 ml of PBS (pH 7.4) and immediately analyzed by flow cytometry (BD FACS Canto II Instrument). For each sample, 10,000 events were collected. Treatment with the protonophore FCCP (20 μM) was used as a control for mt membrane depolarization. Data were evaluated using BD FACSDiva (BD Company) software.

F_1- ATPase assay

ATPase activity was measured with the Sumner assay, which is based on the release of free phosphate when ATP is hydrolyzed by the enzyme as described earlier [14,70]. Briefly, crude mt lysates were obtained from $2x10^8$cells by SoTe/digitonin extraction (0.015% digitonin, 0.6 M Sorbitol, 2 mM EDTA, 20 mM Tris-HCl pH 7.5). Mt pellets were resuspended in an assay buffer (200 mM KCl, 2 mM $MgCl_2$, Tris-HCl pH 8.0) and the 20 min reaction was initiated by the addition of ATP to a final concentration of 5 mM. Where indicated, samples were pre-treated with the F_1-ATPase specific inhibitor, sodium azide (2 mM) for 10 min at 37°C. The 100 μl enzymatic reactions were deproteinated by the addition of 1.9 μl of 70% perchloric acid. After a 30 min incubation on ice, the samples were spun down (16,000g, 10 min, 4°C) and 90 μl of the supernatant was incubated for 10 min with 0,5 ml of Sumner reagent (8.8% $FeSO_4.7H_2O$, 375 mM H_2SO_4, 6.6% $(NH_4)Mo_7O_{24}.4H_2O$)[62]. 200 μl was then transferred to a 96 well plate and the absorbance was measured at 610 nm using a Tecan Infinite plate reader (Infinite M200Pro, Tecan). To calibrate the assay, a standard curve was calculated from the absorbance values of linear inorganic phosphate samples (0–2 mM).

In-gel histochemical staining of F_1-ATPase activity

Blue native PAGE (BNE) of mt lysates, followed by in-gel activity staining was adapted from published protocols [26,32]. Briefly, mt vesicles from $\sim 2x10^9$ cells were resuspended in a mt lysis buffer (0,75 M amino-n-caproic acid—ACA, 50 mM Bis-Tris, 0,5 mM EDTA, pH 7.0), lysed with 2% dodecylmaltoside (DDM) for 1hr on ice and then cleared by centrifugation (16,000g for 30 min, 4°C). The protein concentration of each mt lysate was determined by a Bradford assay (BioRad), so that 100 μg of total mt protein could be mixed with 1 M ACA and 5% Coomassie brilliant blue G-250 before being loaded on a 2–12% Bis-Tris BNE gel. Immediately after the run (3 hr, 100 V, 4°C), the gel was incubated overnight in an ATPase reaction buffer (35 mM Tris pH 8.0, 270 mM glycine, 19mM MgSO4, 0.3% $Pb(NO_3)_2$, 11 mM ATP).

High resolution clear native PAGE (hrCNE)

The protocol for hrCNE was adapted from published studies [71,72]. In summary, crude mt vesicles from $\sim 5x10^8$ cells were resuspended in a mt lysis buffer (2 mM ACA, 50 mM Imidazole-HCl, 1 mM EDTA, 50 mM NaCl, pH 7) and lysed for one hour on ice with 4 mg digitonin/1 mg protein. The samples were spun down at 16,000 g for 30 min and the cleared lysate protein concentrations were determined by a Bradford assay. Samples were mixed with a 5x loading dye (0.1% Ponceau-S, 50% glycerol) and loaded onto a 3%-12% native gradient gel. After electrophoresis (3 hr, 100 V, 4°C), the resolved mt lysates were transferred onto a nitrocellulose membrane (overnight, 20 V, 4°C) and probed with selected antibodies.

Na_2CO_3 submitochondrial fractionation

Na_2CO_3 extraction of mt membranes was adapted from a previously published protocol [73]. Mt vesicles from $1x10^9$ cells were isolated by hypotonic lysis as described above. The resulting supernatant from the 25G needle homogenization step was kept as a cytosolic fraction (CYTO). The mt pellet was further treated with digitonin (80 μg/ml) for 15 min on ice to disrupt the mt outer membrane. The material was then cleared by centrifugation (12,000 g, 20 min, 4°C) and the pelleted mitoplasts were resuspended in 0.1 M Na_2CO_3 buffer (pH 11.5) and incubated for 30 min on ice. A final ultracentrifugation step (100,000 g, 4°C for 1 hr) performed in an SW50Ti rotor of a Beckman Instrument resulted in a supernatant comprised of proteins from the mt matrix (MX), including stripped peripheral membrane proteins, and a pellet containing integral proteins isolated from the mt membrane fraction (M).

Glycerol gradient (GG) sedimentation

Hypotonically purified mt vesicles from $\sim 2.5x10^9$ cells were resuspended in a GG lysis buffer (10 mM Tris, pH 7.2, 10 mM $MgCl_2$, 200 mM KCl, 1mM DTT) and lysed with 1% Triton X-100 (30 min, on ice). The lysates were cleared by a centrifugation step (2x 16,000 g, 30 min, 4°C) and the protein concentration was determined by a Bradford assay. Mt cleared lysates were resolved by ultracentrifugation (Beckman Instrument, SW40 rotor) at 38,000 g for 5 hr on 11ml 10–30% GG, which was poured manually or using the Gradient Station (Biocomp) according to the manufacturer's protocol. The glycerol gradients were then fractionated either manually or with the Gradient station and 500μl fractions were stored at -70°C.

Immunogold staining of ultrathin sections and transmission electron microscopy

Cells ($\sim 5x10^7$) were pelleted (1300 g, 10 min, RT), washed in PBS (pH 7.4) and immediately fixed in a 4% formaldehyde/ 0.1 M phosphate buffer. Samples were then dehydrated at -10°C through a series of seven steps that increased the concentration of ethanol from 30% to100%, pausing at each step for 1 hour. Next, the samples were embedded in LR White Resin (Electron Microscopy Sciences) and polymerized (UV light, 48 hours at -10°C). Ultrathin sections were prepared by the Ultracut UCT ultramicrotome (Leica) and mounted on nickel grids. Prepared sections were blocked in 5% BSA, labelled with primary anti-β antibody (1:10 dilution), washed three times with PBS and incubated with protein A conjugated to 10 nm gold particles (1:100 dilution, Aurion). The immunogold labelled grids were contrasted, carbon coated and examined by the TEM (JEM-1010, Jeol). Grids, which were immunolabeled with only the protein A conjugated to 10nM gold particles, were used as a negative control.

Quantification and statistical analysis of immunogold labelling

The number of gold particles was statistically evaluated as described earlier [12,74]. Using ImageJ software (NIH, USA), a grid consisting of squares (test points, P) with constant size (16,105 μm^2) was superimposed randomly on the electron micrographs of identified mitochondria. All test squares and immunogold particles within the immediate proximity to the mt membrane were counted separately for each micrograph. In order to statistically evaluate the labelling, all observed gold particles (N_{obs}) and all test points (P) from 113 images captured from NON, IND3 and IND5 samples were tallied. Expected numbers of gold particles (N_{exp}) for each sample were calculated as (total sum N_{obs} x P)/total sum P. To determine if the difference between the observed and expected particles was significant and not due to random fluctuations, a Chi-squared analysis $\chi^2 = (N_{obs}-N_{exp})^2/ N_{exp}$ was performed using GraphPad QuickCalcs calculator (www.graphpad.com/quickcalcs). In addition, the relative labeling index (RLI), where the predicted RLI = 1 for random labelling, was calculated as RLI = N_{obs}/ N_{exp}.

Gene IDs for the genes and proteins mentioned in this study

ATPaseTb2 (Tb927.5.2930), ATPaseTb1 (Tb927.10.520), TbAAC (Tb927.10.14820/30/40), p18 (Tb927.5.1710), mtHsp70 (Tb927.6.3740), MRP1 (Tb927.11.1710), APRT (Tb927.7.1780), enolase (Tb427.10.2890), subunit β (Tb927.3.1380).

Supporting Information

S1 Fig. Bioinformatics analysis of ATPaseTb2. A) The multiple sequence alignment of ATPaseTb2 homologs from the order Kinetoplastida was performed by ClustalW on the following species (accession number, name): *Trypanosoma vivax* Y486 (TvY486_0502300, ATPaseTv2), *T. cruzi* Sylvio X10/1 (TCSYLVIO_010784, ATPaseTc2), *T. congolense* IL3000 (TcIL3000_5_3200, ATPaseTco2), *T. cruzi* CL Brener Non-Esmeraldo-like (TcCLB.506321.280, ATPaseTcB2), *T. cruzi* marinkellei strain B7 (Tc_MARK_9008, ATPaseTcm2), *T. brucei* TREU927 (Tb927.5.2930, ATPaseTb2), *L. tarentolae* Parrot-TarII (LtaP08.0840, ATPaseLt2), *L. mexicana* MHOM/GT/2001/U1103 (LmxM.08.1100, ATPaseLmx2), *L.major* strain Friedlin (LmjF.08.1100, ATPaseLm2), *L. infantum* JPCM5 (LinJ.08.1010, ATPaseLin2), *L. donovani* BPK282A1 (LdBPK_081010.1, ATPaseLd2), *L. braziliensis* MHOM/BR/75/M2904 (LbrM.08.0870, ATPaseLbr2), *Bodo saltans* (ATPaseBs2), *Strigomonas culicis* (STCU_02070, ATPaseSc2). Sequences were obtained from GeneDB database or from Welcome Trust Sanger centrum (*B. saltans* sequence). Numbers at the top indicate the amino acid positions in *T. vivax* ATPaseTv2. The mitochondrial targeting signal for ATPaseTb2 (MTS, green) was predicted by Mitoprot II v1.101. The homologous region (red) to Bs_sub d was determined using HHpred toolkit. B) The homology of ATPaseTb2 to subunit d (*B. taurus*) was based on HHpred, which utilizes the homology detection & structure prediction by HMM-HMM comparison. (http://toolkit.tuebingen.mpg.de) The alignments consist of one or more blocks with the following lines: ss_pred: query secondary structure as predicted by PSIPRED (upper case letters: high probability, lower case letters: low probability). Q query_name: query sequence Q Consensus: query alignment consensus sequence Quality of colum-column match: very bad =; bad—; neutral.; good +; very good |T Consensus: template alignment consensus sequence T templ_name: template sequence T ss_dssp: template secondary structure as determined by DSSP T ss_pred: template secondary structure as predicted by PSIPRED (upper case letters: high probability, lower case letters: low probability) The consensus sequence uses capital letters for amino acids that occur with > = 60% probability and lower case letters for amino acids that have > = 40% probability. For unconserved columns a tilde is used. The line in the middle shows the column score between the query and template amino

acid distributions. It gives a valuable indication for the alignment quality. (A unit of column score corresponds approximately to 0.6 bits.)
=: very bad match column score below-1.5
-: bad match column score between-1.5 and-0.5
.: neutral match column score between -0.5 and +0.5
+: good match column score between +0.5 and +1.5
|: very good match column score above +1.5
(PDF)

S2 Fig. Densitometric analysis of anti-sub_β and anti-p18 immunoblots of the BF ATPaseTb2 RNAi glycerol gradients depicted in Fig. 5D. The glycerol gradient fractions analyzed by western blot using anti-β (A) and anti-p18 (B) antibodies (Fig. 5D) were also examined using densitometry analysis. The chemiluminescent blots were imaged with the LAS3000 Imaging System (FUJI). The specific bands for subunit β and p18 were selected using the band analysis tool from the ImageQuant TL software (Amersham Biosciences), which allowed their background-subtracted densities to be determined. The background-corrected volumes of the corresponding protein bands were normalized to the highest value of each blot, which was set to 100.
(PDF)

S3 Fig. ATPaseTb2 depletion alters the distribution of the F_1-ATPase subunit β in *T.b. evansi* mitochondria. A) Ultrathin sections of RNAi non-induced cells (NON) and cells induced for 3 (IND3) and 5 (IND5) days were immunostained with a primary anti-β antibody, followed by incubation with a 10 nM gold bead conjugated anti-protein A secondary antibody. Images of the electron micrographs were captured and the immunogold particles visualized within identified mitochondria. Particles located in the matrix are marked with dashed arrows, while gold beads located within the immediate proximity of the mt membrane are designated with a solid arrow. B) All immunogold beads identified from 113 images of NON, IND3 and IND5 electron micrographs were itemized according to their localization and plotted as either mt inner membrane associated (grey) or matrix (white). C) Counts of observed mt membrane associated gold particles (N_{obs}) and all test points (P) from NON, IND3 and IND5 images were recorded under their appropriate column. Expected numbers of gold particles (N_{exp}) were calculated as (total sum N_{obs} x P)/total sum P. D) The relative labeling index was calculated (RLI = N_{obs}/ N_{exp}) for the mt membrane associated gold particles tabulated in S3B Fig. and is depicted on the y-axis of the column graph.
(PDF)

Acknowledgments

We thank Ken Stuart (Seattle Biomed) and Minu Chaudhuri (Meharri Medical College) for kindly providing antibodies, Achim Schnaufer (University of Edinburgh) for providing the *T. b. evansi* strain used in this study. We would also like to express our gratitude to Marie Vancová from the Laboratory of Electron Microscopy (Biology Centre) for the sample preparation and an opportunity to use the JEM-1010 electron microscope.

Author Contributions

Conceived and designed the experiments: KS BP AZ. Performed the experiments: KS. Analyzed the data: KS BP AZ. Contributed reagents/materials/analysis tools: AZ KS BP. Wrote the paper: AZ BP KS.

References

1. Jamonneau V, Ilboudo H, Kabore J, Kaba D, Koffi M, et al. (2012) Untreated human infections by Trypanosoma brucei gambiense are not 100% fatal. PLoS Negl Trop Dis 6: e1691. doi: 10.1371/journal.pntd.0001691 PMID: 22720107
2. Stuart K, Brun R, Croft S, Fairlamb A, Gurtler RE, et al. (2008) Kinetoplastids: related protozoan pathogens, different diseases. J Clin Invest 118: 1301–1310. doi: 10.1172/JCI33945 PMID: 18382742
3. Steverding D (2008) The history of African trypanosomiasis. Parasit Vectors 1: 3. doi: 10.1186/1756-3305-1-3 PMID: 18275594
4. Bringaud F, Riviere L, Coustou V (2006) Energy metabolism of trypanosomatids: adaptation to available carbon sources. Mol Biochem Parasitol 149: 1–9. PMID: 16682088
5. Besteiro S, Barrett MP, Riviere L, Bringaud F (2005) Energy generation in insect stages of Trypanosoma brucei: metabolism in flux. Trends Parasitol 21: 185–191. PMID: 15780841
6. Hannaert V, Bringaud F, Opperdoes FR, Michels PA (2003) Evolution of energy metabolism and its compartmentation in Kinetoplastida. Kinetoplastid Biol Dis 2: 11. PMID: 14613499
7. Brown SV, Hosking P, Li J, Williams N (2006) ATP synthase is responsible for maintaining mitochondrial membrane potential in bloodstream form Trypanosoma brucei. Eukaryot Cell 5: 45–53. PMID: 16400167
8. Guler JL, Kriegova E, Smith TK, Lukes J, Englund PT (2008) Mitochondrial fatty acid synthesis is required for normal mitochondrial morphology and function in Trypanosoma brucei. Mol Microbiol 67: 1125–1142. doi: 10.1111/j.1365-2958.2008.06112.x PMID: 18221265
9. Nolan DP, Voorheis HP (1992) The mitochondrion in bloodstream forms of Trypanosoma brucei is energized by the electrogenic pumping of protons catalysed by the F1F0-ATPase. Eur J Biochem 209: 207–216. PMID: 1327770
10. Huang G, Vercesi AE, Docampo R (2013) Essential regulation of cell bioenergetics in Trypanosoma brucei by the mitochondrial calcium uniporter. Nat Commun 4: 2865. doi: 10.1038/ncomms3865 PMID: 24305511
11. Vercesi AE, Docampo R, Moreno SN (1992) Energization-dependent Ca2+ accumulation in Trypanosoma brucei bloodstream and procyclic trypomastigotes mitochondria. Mol Biochem Parasitol 56: 251–257. PMID: 1484549
12. Kovarova J, Horakova E, Changmai P, Vancova M, Lukes J (2014) Mitochondrial and nucleolar localization of cysteine desulfurase Nfs and the scaffold protein Isu in Trypanosoma brucei. Eukaryot Cell 13: 353–362. doi: 10.1128/EC.00235-13 PMID: 24243795
13. Mazet M, Morand P, Biran M, Bouyssou G, Courtois P, et al. (2013) Revisiting the central metabolism of the bloodstream forms of Trypanosoma brucei: production of acetate in the mitochondrion is essential for parasite viability. PLoS Negl Trop Dis 7: e2587. doi: 10.1371/journal.pntd.0002587 PMID: 24367711
14. Schnaufer A, Clark-Walker GD, Steinberg AG, Stuart K (2005) The F1-ATP synthase complex in bloodstream stage trypanosomes has an unusual and essential function. EMBO J 24: 4029–4040. PMID: 16270030
15. Buchet K, Godinot C (1998) Functional F1-ATPase essential in maintaining growth and membrane potential of human mitochondrial DNA-depleted rho degrees cells. J Biol Chem 273: 22983–22989. PMID: 9722521
16. Dean S, Gould MK, Dewar CE, Schnaufer AC (2013) Single point mutations in ATP synthase compensate for mitochondrial genome loss in trypanosomes. Proc Natl Acad Sci U S A 110: 14741–14746. doi: 10.1073/pnas.1305404110 PMID: 23959897
17. Brun R, Hecker H, Lun ZR (1998) Trypanosoma evansi and T. equiperdum: distribution, biology, treatment and phylogenetic relationship (a review). Vet Parasitol 79: 95–107. PMID: 9806490
18. Stuart KD (1971) Evidence for the retention of kinetoplast DNA in an acriflavine-induced dyskinetoplastic strain of Trypanosoma brucei which replicates the altered central element of the kinetoplast. J Cell Biol 49: 189–195. PMID: 4102002
19. Lai DH, Hashimi H, Lun ZR, Ayala FJ, Lukes J (2008) Adaptations of Trypanosoma brucei to gradual loss of kinetoplast DNA: Trypanosoma equiperdum and Trypanosoma evansi are petite mutants of T. brucei. Proc Natl Acad Sci U S A 105: 1999–2004. doi: 10.1073/pnas.0711799105 PMID: 18245376
20. Walker JE (2013) The ATP synthase: the understood, the uncertain and the unknown. Biochem Soc Trans 41: 1–16. doi: 10.1042/BST20110773 PMID: 23356252
21. Devenish RJ, Prescott M, Rodgers AJ (2008) The structure and function of mitochondrial F1F0-ATP synthases. Int Rev Cell Mol Biol 267: 1–58. doi: 10.1016/S1937-6448(08)00601-1 PMID: 18544496

22. Walker JE, Dickson VK (2006) The peripheral stalk of the mitochondrial ATP synthase. Biochim Biophys Acta 1757: 286–296. PMID: 16697972

23. Dickson VK, Silvester JA, Fearnley IM, Leslie AG, Walker JE (2006) On the structure of the stator of the mitochondrial ATP synthase. EMBO J 25: 2911–2918. PMID: 16791136

24. Vaidya AB, Mather MW (2009) Mitochondrial evolution and functions in malaria parasites. Annu Rev Microbiol 63: 249–267. doi: 10.1146/annurev.micro.091208.073424 PMID: 19575561

25. Lapaille M, Escobar-Ramirez A, Degand H, Baurain D, Rodriguez-Salinas E, et al. (2010) Atypical subunit composition of the chlorophycean mitochondrial F1FO-ATP synthase and role of Asa7 protein in stability and oligomycin resistance of the enzyme. Mol Biol Evol 27: 1630–1644. doi: 10.1093/molbev/msq049 PMID: 20156838

26. Zikova A, Schnaufer A, Dalley RA, Panigrahi AK, Stuart KD (2009) The F(0)F(1)-ATP synthase complex contains novel subunits and is essential for procyclic Trypanosoma brucei. PLoS Pathog 5: e1000436. doi: 10.1371/journal.ppat.1000436 PMID: 19436713

27. Mather MW, Henry KW, Vaidya AB (2007) Mitochondrial drug targets in apicomplexan parasites. Curr Drug Targets 8: 49–60. PMID: 17266530

28. Balabaskaran Nina P, Dudkina NV, Kane LA, van Eyk JE, Boekema EJ, et al. (2010) Highly divergent mitochondrial ATP synthase complexes in Tetrahymena thermophila. PLoS Biol 8: e1000418. doi: 10.1371/journal.pbio.1000418 PMID: 20644710

29. Nishi A, Scherbaum OH (1962) Oxidative phosphorylation in synchronized cultures of Tetrahymena pyriformis. Biochim Biophys Acta 65: 419–424. PMID: 13938753

30. Uyemura SA, Luo S, Vieira M, Moreno SN, Docampo R (2004) Oxidative phosphorylation and rotenone-insensitive malate- and NADH-quinone oxidoreductases in Plasmodium yoelii yoelii mitochondria in situ. J Biol Chem 279: 385–393. PMID: 14561763

31. Vazquez-Acevedo M, Cardol P, Cano-Estrada A, Lapaille M, Remacle C, et al. (2006) The mitochondrial ATP synthase of chlorophycean algae contains eight subunits of unknown origin involved in the formation of an atypical stator-stalk and in the dimerization of the complex. J Bioenerg Biomembr 38: 271–282. PMID: 17160464

32. Hashimi H, Benkovicova V, Cermakova P, Lai DH, Horvath A, et al. (2010) The assembly of F(1)F(O)-ATP synthase is disrupted upon interference of RNA editing in Trypanosoma brucei. Int J Parasitol 40: 45–54. doi: 10.1016/j.ijpara.2009.07.005 PMID: 19654010

33. Chi TB, Brown BS, Williams N (1998) Subunit 9 of the mitochondrial ATP synthase of Trypanosoma brucei is nuclearly encoded and developmentally regulated. Mol Biochem Parasitol 92: 29–38. PMID: 9574907

34. Claros MG, Vincens P (1996) Computational method to predict mitochondrially imported proteins and their targeting sequences. Eur J Biochem 241: 779–786. PMID: 8944766

35. Biegert A, Mayer C, Remmert M, Soding J, Lupas AN (2006) The MPI Bioinformatics Toolkit for protein sequence analysis. Nucleic Acids Res 34: W335–339. PMID: 16845021

36. Norais N, Prome D, Velours J (1991) ATP synthase of yeast mitochondria. Characterization of subunit d and sequence analysis of the structural gene ATP7. J Biol Chem 266: 16541–16549. PMID: 1832157

37. Walker JE, Runswick MJ, Poulter L (1987) ATP synthase from bovine mitochondria. The characterization and sequence analysis of two membrane-associated sub-units and of the corresponding cDNAs. J Mol Biol 197: 89–100. PMID: 2890767

38. Nugent T, Jones DT (2009) Transmembrane protein topology prediction using support vector machines. BMC Bioinformatics 10: 159. doi: 10.1186/1471-2105-10-159 PMID: 19470175

39. Vertommen D, Van Roy J, Szikora JP, Rider MH, Michels PA, et al. (2008) Differential expression of glycosomal and mitochondrial proteins in the two major life-cycle stages of Trypanosoma brucei. Mol Biochem Parasitol 158: 189–201. doi: 10.1016/j.molbiopara.2007.12.008 PMID: 18242729

40. Ko YH, Delannoy M, Hullihen J, Chiu W, Pedersen PL (2003) Mitochondrial ATP synthasome. Cristae-enriched membranes and a multiwell detergent screening assay yield dispersed single complexes containing the ATP synthase and carriers for Pi and ADP/ATP. J Biol Chem 278: 12305–12309. PMID: 12560333

41. Meyer B, Wittig I, Trifilieff E, Karas M, Schagger H (2007) Identification of two proteins associated with mammalian ATP synthase. Mol Cell Proteomics 6: 1690–1699. PMID: 17575325

42. Chen Y, Hung CH, Burderer T, Lee GS (2003) Development of RNA interference revertants in Trypanosoma brucei cell lines generated with a double stranded RNA expression construct driven by two opposing promoters. Mol Biochem Parasitol 126: 275–279. PMID: 12615326

43. Bowler MW, Montgomery MG, Leslie AG, Walker JE (2006) How azide inhibits ATP hydrolysis by the F-ATPases. Proc Natl Acad Sci U S A 103: 8646–8649. PMID: 16728506

44. Appleby RD, Porteous WK, Hughes G, James AM, Shannon D, et al. (1999) Quantitation and origin of the mitochondrial membrane potential in human cells lacking mitochondrial DNA. Eur J Biochem 262: 108–116. PMID: 10231371

45. Garcia JJ, Ogilvie I, Robinson BH, Capaldi RA (2000) Structure, functioning, and assembly of the ATP synthase in cells from patients with the T8993G mitochondrial DNA mutation—Comparison with the enzyme in Rho(0) cells completely lacking mtDNA. Journal of Biological Chemistry 275: 11075–11081. PMID: 10753912

46. Wittig I, Meyer B, Heide H, Steger M, Bleier L, et al. (2010) Assembly and oligomerization of human ATP synthase lacking mitochondrial subunits a and A6L. Biochim Biophys Acta 1797: 1004–1011. doi: 10.1016/j.bbabio.2010.02.021 PMID: 20188060

47. Stock D, Leslie AG, Walker JE (1999) Molecular architecture of the rotary motor in ATP synthase. Science 286: 1700–1705. PMID: 10576729

48. Strauss M, Hofhaus G, Schroder RR, Kuhlbrandt W (2008) Dimer ribbons of ATP synthase shape the inner mitochondrial membrane. EMBO J 27: 1154–1160. doi: 10.1038/emboj.2008.35 PMID: 18323778

49. Arnold I, Pfeiffer K, Neupert W, Stuart RA, Schagger H (1998) Yeast mitochondrial F1F0-ATP synthase exists as a dimer: identification of three dimer-specific subunits. EMBO J 17: 7170–7178. PMID: 9857174

50. Burger G, Lang BF, Braun HP, Marx S (2003) The enigmatic mitochondrial ORF ymf39 codes for ATP synthase chain b. Nucleic Acids Res 31: 2353–2360. PMID: 12711680

51. Heazlewood JL, Whelan J, Millar AH (2003) The products of the mitochondrial orf25 and orfB genes are FO components in the plant F1FO ATP synthase. FEBS Lett 540: 201–205. PMID: 12681508

52. Miranda-Astudillo H, Cano-Estrada A, Vazquez-Acevedo M, Colina-Tenorio L, Downie-Velasco A, et al. (2014) Interactions of subunits Asa2, Asa4 and Asa7 in the peripheral stalk of the mitochondrial ATP synthase of the chlorophycean alga Polytomella sp. Biochim Biophys Acta 1837: 1–13. doi: 10.1016/j.bbabio.2013.08.001 PMID: 23933283

53. van Lis R, Mendoza-Hernandez G, Groth G, Atteia A (2007) New insights into the unique structure of the F0F1-ATP synthase from the chlamydomonad algae Polytomella sp. and Chlamydomonas reinhardtii. Plant Physiol 144: 1190–1199. PMID: 17468226

54. Chevallet M, Lescuyer P, Diemer H, van Dorsselaer A, Leize-Wagner E, et al. (2006) Alterations of the mitochondrial proteome caused by the absence of mitochondrial DNA: A proteomic view. Electrophoresis 27: 1574–1583. PMID: 16548050

55. Orian JM, Hadikusumo RG, Marzuki S, Linnane AW (1984) Biogenesis of mitochondria: defective yeast H+-ATPase assembled in the absence of mitochondrial protein synthesis is membrane associated. J Bioenerg Biomembr 16: 561–581. PMID: 6242247

56. Paul MF, Velours J, Arselin de Chateaubodeau G, Aigle M, Guerin B (1989) The role of subunit 4, a nuclear-encoded protein of the F0 sector of yeast mitochondrial ATP synthase, in the assembly of the whole complex. Eur J Biochem 185: 163–171. PMID: 2553400

57. Rak M, Gokova S, Tzagoloff A (2011) Modular assembly of yeast mitochondrial ATP synthase. EMBO J 30: 920–930. doi: 10.1038/emboj.2010.364 PMID: 21266956

58. Chen C, Ko Y, Delannoy M, Ludtke SJ, Chiu W, et al. (2004) Mitochondrial ATP synthasome: three-dimensional structure by electron microscopy of the ATP synthase in complex formation with carriers for Pi and ADP/ATP. J Biol Chem 279: 31761–31768. PMID: 15166242

59. Alibu VP, Storm L, Haile S, Clayton C, Horn D (2005) A doubly inducible system for RNA interference and rapid RNAi plasmid construction in Trypanosoma brucei. Mol Biochem Parasitol 139: 75–82. PMID: 15610821

60. Wickstead B, Ersfeld K, Gull K (2002) Targeting of a tetracycline-inducible expression system to the transcriptionally silent minichromosomes of Trypanosoma brucei. Mol Biochem Parasitol 125: 211–216. PMID: 12467990

61. Surve S, Heestand M, Panicucci B, Schnaufer A, Parsons M (2012) Enigmatic presence of mitochondrial complex I in Trypanosoma brucei bloodstream forms. Eukaryot Cell 11: 183–193. doi: 10.1128/EC.05282-11 PMID: 22158713

62. Borst P, Fase-Fowler F, Gibson WC (1987) Kinetoplast DNA of Trypanosoma evansi. Mol Biochem Parasitol 23: 31–38. PMID: 3033499

63. Wirtz E, Leal S, Ochatt C, Cross GA (1999) A tightly regulated inducible expression system for conditional gene knock-outs and dominant-negative genetics in Trypanosoma brucei. Mol Biochem Parasitol 99: 89–101. PMID: 10215027

64. Oeffinger M, Wei KE, Rogers R, DeGrasse JA, Chait BT, et al. (2007) Comprehensive analysis of diverse ribonucleoprotein complexes. Nat Methods 4: 951–956. PMID: 17922018

65. Panigrahi AK, Ogata Y, Zikova A, Anupama A, Dalley RA, et al. (2009) A comprehensive analysis of Trypanosoma brucei mitochondrial proteome. Proteomics 9: 434–450. doi: 10.1002/pmic.200800477 PMID: 19105172

66. Panigrahi AK, Zikova A, Dalley RA, Acestor N, Ogata Y, et al. (2008) Mitochondrial complexes in Trypanosoma brucei: a novel complex and a unique oxidoreductase complex. Mol Cell Proteomics 7: 534–545. PMID: 18073385

67. Singha UK, Peprah E, Williams S, Walker R, Saha L, et al. (2008) Characterization of the mitochondrial inner membrane protein translocator Tim17 from Trypanosoma brucei. Mol Biochem Parasitol 159: 30–43. doi: 10.1016/j.molbiopara.2008.01.003 PMID: 18325611

68. Vondruskova E, van den Burg J, Zikova A, Ernst NL, Stuart K, et al. (2005) RNA interference analyses suggest a transcript-specific regulatory role for mitochondrial RNA-binding proteins MRP1 and MRP2 in RNA editing and other RNA processing in Trypanosoma brucei. J Biol Chem 280: 2429–2438. PMID: 15504736

69. Hannaert V, Albert MA, Rigden DJ, da Silva Giotto MT, Thiemann O, et al. (2003) Kinetic characterization, structure modelling studies and crystallization of Trypanosoma brucei enolase. Eur J Biochem 270: 3205–3213. PMID: 12869196

70. Law RH, Manon S, Devenish RJ, Nagley P (1995) ATP synthase from Saccharomyces cerevisiae. Methods Enzymol 260: 133–163. PMID: 8592441

71. Wittig I, Karas M, Schagger H (2007) High resolution clear native electrophoresis for in-gel functional assays and fluorescence studies of membrane protein complexes. Mol Cell Proteomics 6: 1215–1225. PMID: 17426019

72. Acestor N, Zikova A, Dalley RA, Anupama A, Panigrahi AP, et al. (2011) Trypanosoma brucei Mitochondrial Respiratome: Composition and organization in procyclic form. Molecular Cell Proteomics resubmitted.

73. Acestor N, Panigrahi AK, Ogata Y, Anupama A, Stuart KD (2009) Protein composition of Trypanosoma brucei mitochondrial membranes. Proteomics 9: 5497–5508. doi: 10.1002/pmic.200900354 PMID: 19834910

74. Mayhew TM, Lucocq JM (2008) Quantifying immunogold labelling patterns of cellular compartments when they comprise mixtures of membranes (surface-occupying) and organelles (volume-occupying). Histochem Cell Biol 129: 367–378. doi: 10.1007/s00418-007-0375-6 PMID: 18180944

PLOS | PATHOGENS

PEARLS

A paradigm shift: The mitoproteomes of procyclic and bloodstream *Trypanosoma brucei* are comparably complex

Alena Zíková[1,2]*, Zdeněk Verner[1,3], Anna Nenarokova[1,2], Paul A. M. Michels[4], Julius Lukeš[1,2]

1 Institute of Parasitology, Biology Centre, Czech Academy of Sciences, České Budějovice, Czech Republic, **2** Faculty of Science, University of South Bohemia, České Budějovice, Czech Republic, **3** Faculty of Sciences, Charles University, Prague, Czech Republic, **4** Centre for Immunity, Infection and Evolution, The University of Edinburgh, Edinburgh, United Kingdom

* azikova@paru.cas.cz

OPEN ACCESS

Citation: Zíková A, Verner Z, Nenarokova A, Michels PAM, Lukeš J (2017) A paradigm shift: The mitoproteomes of procyclic and bloodstream *Trypanosoma brucei* are comparably complex. PLoS Pathog 13(12): e1006679. https://doi.org/10.1371/journal.ppat.1006679

Editor: Laura J. Knoll, University of Wisconsin Medical School, UNITED STATES

Published: December 21, 2017

Funding: This work was supported by the ERC CZ awards LL1205 and LL1601 and by the Czech Grant Agency awards 17-22248S and 15-21974S to AZ and JL, respectively. ZV was supported by LQ1604 NPU II provided by MEYS. The funders had no role in study design, data collection and analysis, decision to publish, or preparation of the manuscript.

Competing interests: The authors have declared that no competing interests exist.

Metabolic adaptation during *Trypanosoma brucei*'s life cycle

Trypanosoma brucei is a parasitic protist that causes significant health burden in sub-Saharan countries endemic for the tsetse fly (*Glossina* spp.). During the bloodmeal of this insect vector, the flagellate is transmitted to a variety of mammals, including humans, in which *T. brucei* subs. *gambiense* and *T. brucei* subs. *rhodesiense* cause human African trypanosomiasis. During its life cycle, *T. brucei* encounters and adapts to very diverse environments that differ in available nutrients. In the mammalian host, it exists in two major forms: the replicating long-slender bloodstream form (LS-BSF) and the nondividing short-stumpy bloodstream form (SS-BSF), the latter being pre-adapted to infect the insect vector [1]. While the BSF flagellates primarily colonize the mammalian bloodstream and utilize the plentiful glucose for their energy needs, they can also be found in the cerebrospinal fluid and in extracellular spaces of several tissues, including the brain, adipose tissue, and skin [2,3]. In the insect vector, trypanosomes occur in three major forms occupying different locations within the fly: the procyclic form (PCF) resides in the midgut and proventriculus, while epimastigotes and metacyclic trypomastigotes are found in the salivary glands. During the fly's bloodmeal, the latter form infects the mammalian host. All three forms experience the glucose-poor and amino acid–rich environment within the insect host. These drastic environmental changes encountered by *T. brucei* during its development require significant morphological and metabolic changes and adaptations [4,5].

The seminal work of Keith Vickerman led to the widely accepted model of a highly reduced mitochondrial metabolism in the BSF [6,7]. Its single mitochondrion is incapable of oxidative phosphorylation, and the active electron transport chain (ETC) is minimized to an alternative pathway composed of glycerol-3-phosphate dehydrogenase (Gly-3-PDH) and the so-called trypanosome alternative oxidase (AOX), which are linked to each other via a ubiquinol/ubiquinone pool [8]. The cytochrome-containing ETC is absent, and the mitochondrial transmembrane proton gradient is generated by the reverse activity of the F_oF_1-ATP synthase complex at the expense of ATP [9–11]. The proton gradient across the mitochondrial inner membrane is essential for protein import and transport of metabolites and ions so that vital mitochondrial processes such as Fe-S cluster assembly [12], RNA editing and processing [13,14], and cellular Ca^{2+} homeostasis are maintained [15,16]. The seemingly simplified biochemical composition of the BSF organelle is underlined by its tube-shaped cristae-poor

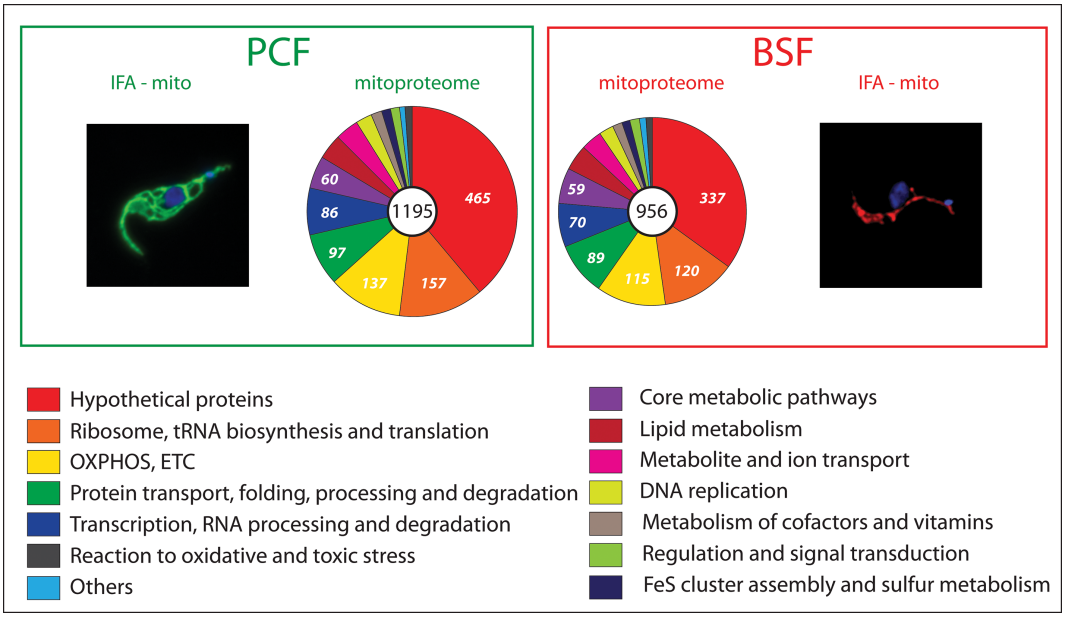

Fig 1. Pie charts showing distribution of mass spectrometry–identified mitochondrial proteins in PCF (left) and BSF (right) trypanosomes in terms of molecular functions. A total number of 1,195 and 956 proteins were assigned to PCF and BSF mitoproteome, respectively. Different colors show different metabolic pathways and categories. See also S1 Table. IFA-mito in PCF (left) and in BSF cell (right). BSF, bloodstream form; Hsp70, heat shock protein 70; IFA-mito, immunofluorescence analysis of a mitochondrial Hsp70; mitoproteome, mitochondrial proteome; PCF, procyclic form.

https://doi.org/10.1371/journal.ppat.1006679.g001

morphology, which is in striking contrast to the extensively reticulated cristae-rich mitochondrion of the PCF flagellates (Fig 1).

Because no indications have been obtained yet for the presence of a mitochondrial ATP-producing system in the BSF, the entire cellular ATP pool is considered to be generated solely by highly active glycolysis [17]. The glycolytic pathway in trypanosomes is unique in the sense of sequestration of most of its enzymes within peroxisome-like organelles called glycosomes [18]. Because the glycosomal membrane is impermeable to large solutes like NAD(H), the essential reoxidation of glycolytically produced intraglycosomal NADH occurs by a shuttle mechanism involving the oxidation of glycerol 3-phosphate to dihydroxyacetone phosphate by the mitochondrial Gly-3-PDH [8].

Classical metabolic studies performed with trypanosomes purified from the blood of infected rodents or with in vitro–cultured BSF supported the original hypothesis of a drastically simplified mitochondrial metabolism because under aerobic conditions, glucose is almost completely catabolized to pyruvate that is excreted from the cells, indicating no need for the mitochondrial enzymes of the tricarboxylic acid cycle. In the absence of oxygen or when AOX is chemically inhibited, glycerol 3-phosphate is converted into glycerol that is produced in a 1:1 ratio with pyruvate [19,20]. Occasionally, the production of small amounts of other compounds such as acetate, succinate, and alanine has been reported; however, these products were instead attributed to the presence of a minor fraction of SS-BSF, a life cycle stage possessing a more elaborated metabolism, with some traits characteristic of the metabolically complex PCF [21].

In preparation for differentiation into PCF, the SS-BSF up-regulates a subset of mitochondrial and other proteins [21]. Moreover, these cells are metabolically active, motile, regulate their internal pH [22], and excrete end products of glucose metabolism in ratios different than

the LS-BSF and PCF cells [21]. Differentiation of LS-BSF into SS-BSF is triggered by the stumpy-inducing factor, and only pleiomorphic strains (e.g., AnTat 1.1) are able to sense this/these yet-to-be-identified molecule(s) [23]. Extended passaging of pleiomorphic parasites in in vitro cultures or by syringe between laboratory animals leads to the loss of responsiveness to the stumpy-inducing factor and thus a failure to differentiate into SS-BSF. Consequently, such strains (e.g., Lister 427) are called monomorphic, i.e., they exist only as a single form [24].

Interestingly, recent analyses employing the monomorphic LS-BSF strain Lister 427 showed that, in addition to pyruvate, appreciable amounts of other carbon products (i.e., alanine, acetate, and succinate) are excreted into the cultivation medium [25], implying a need not only for cytosolic and glycosomal but also for mitochondrial enzymes thus far considered to be absent (Fig 2). An additional metabolomics study involving heavy-atom isotope-labeled glucose determined that a substantial fraction of succinate, as well as metabolic intermediates such as malate and fumarate, are glucose-derived and originate from phosphoenolpyruvate via oxaloacetate. Importantly, phosphoenolpyruvate carboxykinase, a glycosomal enzyme responsible for this conversion, is essential for the BSF parasites [26]. Moreover, the majority of excreted alanine and acetate is also derived from glucose. Alanine is most likely produced from pyruvate by the transamination reaction of alanine aminotransferase, a potentially essential enzyme [27], while glucose-derived acetate is produced from pyruvate by the mitochondrial pyruvate dehydrogenase (PDH) complex and additional subsequent enzymatic steps. A fraction of the acetate produced this way is exported to the cytosol for the de novo synthesis of fatty acids, which is an essential process (Fig 2) [25]. In addition to glucose, the BSF seems to uptake and metabolize amino acids such as cysteine, glutamine, phenylalanine, tryptophan, and threonine [28], implying the existence of an unexpectedly complex metabolic network in their mitochondrion.

The BSF mitoproteome

To map the BSF mitochondrial proteome (mitoproteome), we first used the available mass spectrometry data of purified PCF mitochondria [29–37] in order to assemble a comprehensive list of mitochondrial proteins. Next, we asked how many of these proteins were identified in any mass spectrometry data obtained from BSF cells [38–43]. To our surprise, out of 1,195 constituents of the PCF mitoproteome, 956 were also identified in at least one study of the BSF, suggesting that, when qualitatively measured, the corresponding mitoproteome is reduced by only approximately 20% (Fig 1; S1 Table). The surprisingly high, approximately 80% overlap with the PCF mitoproteome might also be a consequence of the heterogeneity of the examined BSF populations. The heterogeneity may be related to the experimental protocols, the environmental variations (cells grown in vivo versus in vitro), or variations within the cell cycle (e.g., ATP requirements vary between different cell cycle stages) as well as to the form type (monomorphic versus pleiomorphic). Indeed, some authors analyzed monomorphic strains grown in vitro [40,41], and others examined the pleiomorphic AnTat 1.1 strain grown either in immunosuppressed rats [43] or in vitro (S1 Table) [38]. Therefore, some LS-BSF cells may have a mitochondrion that is close to the "classical" version, while a subset of these flagellates may express an extended mitoproteome. However, no apparent differences were detected between the mitoproteomes from the pleiomorphic and monomorphic BSF cells, suggesting that, regardless of their status, a surprisingly large repertoire of mitochondrial proteins is expressed in the BSF stage.

All proteins were then organized into groups based on their Kyoto Encyclopedia of Genes and Genomes (KEGG) annotations. No striking qualitative differences were observed in the categories "oxidative phosphorylation" and "core metabolic pathways" comprising many

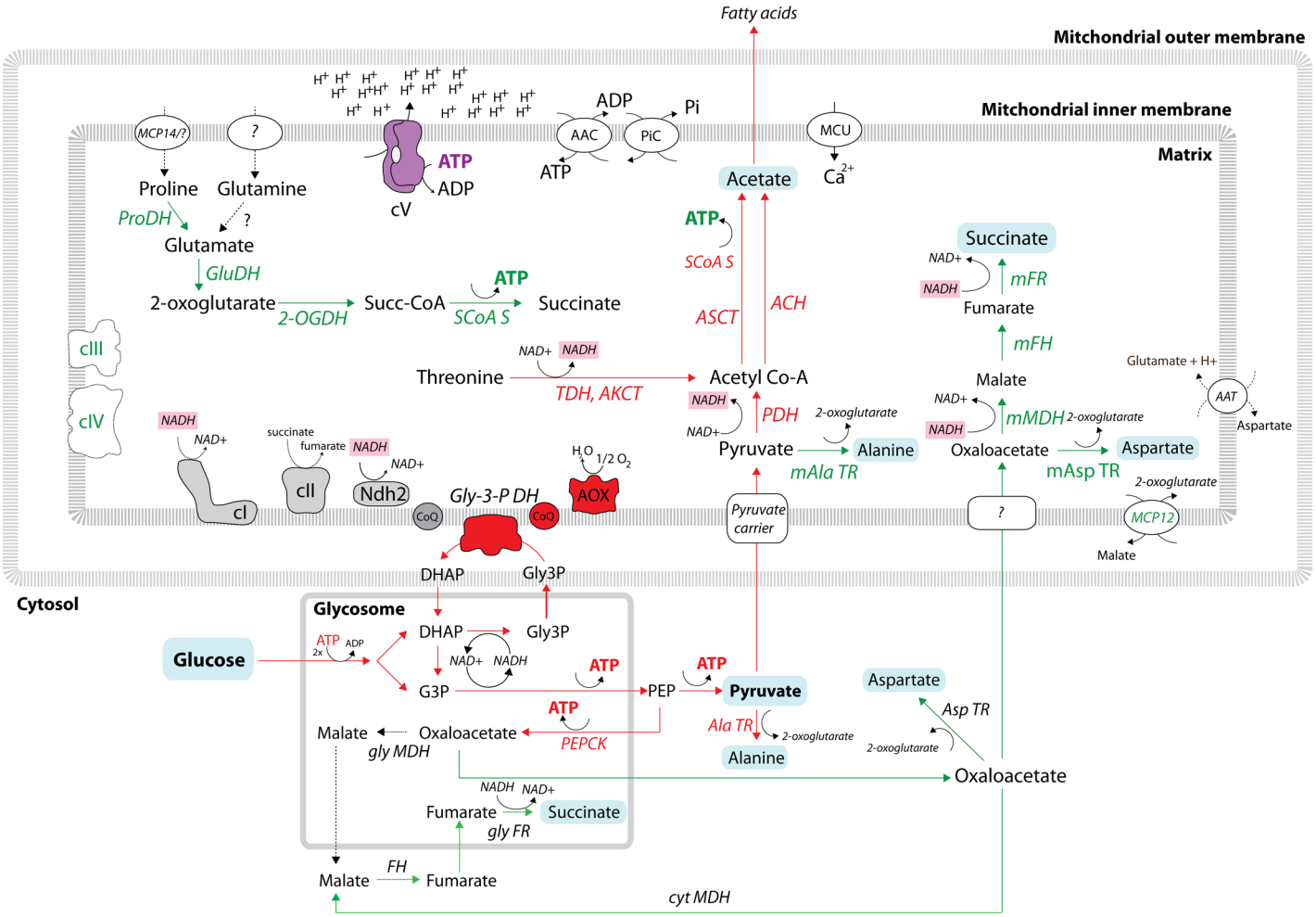

Fig 2. Schematic representation of carbon source metabolism in the bloodstream form of *T. brucei*. Red arrows represent enzymatic steps that were experimentally shown to be active in BSF. Green arrows represent enzymatic steps that might be active in BSF because the enzymes (in green) were identified in BSF proteomic data. Glucose-derived metabolites (acetate, pyruvate, succinate, alanine, aspartate) are on a blue background. NADH molecules are on a pink background. Dashed arrows indicate enzymatic steps for which no experimental proof exists. The glycosomal and mitochondrial compartments are indicated. 2-OGDH, 2-oxoglutarate dehydrogenase; AAC, ADP/ATP carrier; AAT, amino acid transporter; ACH, acetyl-CoA thioesterase; AKCT, 2-amino-3-ketobutyrate coenzyme A ligase; Ala TR, alanine transaminase; AOX, alternative oxidase; ASCT, acetate:succinate CoA-transferase; Asp TR, aspartate transaminase; BSF, bloodstream form; cI, complex I (NADH:ubiquinone oxidoreductase); cII, complex II (succinate dehydrogenase); cIII, complex III (cytochrome bc1 complex); cIV, complex IV (cytochrome c oxidase); cV, complex V (F_oF_1 ATPase); cyt, cytosolic; DHAP, dihydroxyacetone phosphate; FH, fumarate hydratase (i.e., fumarase); FR, fumarate reductase; G3P, glyceraldehyde 3-phosphate; GluDH, glutamate dehydrogenase; gly, glycosomal; Gly3P, glycerol 3-phosphate; Gly-3-PDH, glycerol-3-phosphate dehydrogenase; m, mitochondrial; MDH, malate dehydrogenase; PDH, pyruvate dehydrogenase; PEP, phosphoenolpyruvate; PEPCK, phosphoenolpyruvate carboxykinase; PiC, phosphate carrier; ProDH, proline dehydrogenase.

https://doi.org/10.1371/journal.ppat.1006679.g002

enzymes involved in the carbon, amino acid, and energy metabolism (Fig 1, S1 Table). Typical examples are components of the tricarboxylic acid cycle and subunits of the ETC complexes, most prominently of respiratory complexes III and IV (Fig 2, S1 Table). Nonetheless, when quantitative information was available, these proteins were often present in much lower amounts than in the PCF. While some of these proteins may not perform their expected function(s) under BSF steady state growth conditions, this finding strongly suggests that the parasite is capable of swift alterations or adjustments of its metabolism in response to various environments and differentiation cues. This ability can be exploited during environmental changes, for example when the LS-BSF migrates from the peripheral blood circulation to other

extravascular spaces (e.g., in adipose tissue, spinal and cerebral fluids) and during the differentiation to SS-BSF. Therefore, the BSF trypanosomes may uptake different substrates from the available nutrients according to their immediate needs and metabolize them via a variety of pathways.

Complex metabolic pathways in the BSF mitochondrion: Does presence equal activity?

The current metabolic model for BSF excludes a role of the mitochondrion in the ATP production by either oxidative or substrate-level phosphorylation [44]. In contrast to this premise, succinyl-CoA synthase (SCoAS), an enzyme responsible for substrate-level phosphorylation of ADP to ATP, has been detected in BSF cells, and more importantly, its RNA interference (RNAi)–mediated silencing produced a severe growth phenotype [45]. This enzyme can be involved in two ATP-producing pathways. The first one includes activity of 2-oxoglutarate dehydrogenase (2-OGDH) producing succinyl-CoA from 2-oxoglutarate that originates from amino acids such as proline and glutamine or can result from transamination reactions by mitochondrial alanine and aspartate transaminases (Fig 2). While all the enzymes involved in these reactions were detected in the LS-BSF mitoproteome (Fig 2 and S1 Table), the activity of 2-OGDH remains contradictory because some authors failed to detect it in the pleiomorphic cells [46], while others recorded its low activity in culture-adapted monomorphic LS-BSF cells [47]. Puzzlingly, the 2-OGDH subunits E1 and E2 were shown to be essential in BSF not because of their role in carbon metabolism but rather due to their moonlighting roles in glycosomes and mitochondrial DNA maintenance [46,48]. However, in an untargeted metabolomics study using isotope-labeled glucose, up to 30% of excreted succinate remained unlabeled, supporting its nonglucose origin [26] and making the occurrence of this substrate-level phosphorylation reaction even more plausible (Fig 2).

The second phosphorylation pathway includes the acetate:succinate CoA transferase/SCoAS cycle that contributes to acetate production in the BSF mitochondrion. A substrate for this reaction—acetyl-CoA—is produced by PDH, an enzymatic complex that is present and active in the BSF mitochondrion [15,25]. Moreover, PDH was shown to be indispensable for BSF cells but only in the absence of threonine because under these artificial conditions, PDH was the only system supplying acetyl-CoA for the essential acetate production [25]. Nonetheless, the mitochondrial pyruvate transporter was demonstrated to be essential for BSF in vivo, supporting PDH's vital role for the parasite [49]. These results imply that the BSF mitochondrion may become an ATP producer under certain conditions, perhaps just for intramitochondrial needs (Fig 2).

The presence and potential activity of the aforementioned dehydrogenases that produce NADH within the mitochondrion imply that the organelle would require reoxidation of this cofactor. Several possible scenarios for such a capacity can be deduced from the available data (S1 Table). Although complex I (NADH:ubiquinone oxidoreductase) was shown to be neither essential for BSF nor contributing to the observed NADH:ubiquinone oxidoreductase activity [50], it is still assembled in the BSF mitochondrion and may participate in NADH reoxidation under certain conditions. Reoxidation of reduced NADH molecules can also be achieved by the activity of the alternative dehydrogenase 2 (Ndh2), an enzyme shown to be important but not essential for maintaining the mitochondrial redox balance [51]. Last but not least, another scenario includes the activities of the mitochondrial malate dehydrogenase, fumarate hydratase (i.e., fumarase), and NADH-dependent fumarate reductase, with all three being present in the BSF mitoproteome (Fig 2, S1 Table). These enzymes reduce glucose-derived oxaloacetate via malate and fumarate to succinate. Indeed, 3-carbon–labeled succinate was identified in an

untargeted metabolomics study, implying that this pathway might be active [26]. Still, it should be noted that it is so far impossible to discriminate between the mitochondrial, glycosomal, and cytosolic derivations of this metabolite and that only a systematic deletion of the corresponding enzymatic isoforms followed by metabolomics would illuminate the cellular compartment in which this glucose-derived succinate is produced. To sum up, the collective activity of the aforementioned reoxidation enzymes is most likely responsible for the mitochondrial NADH regeneration. Possibly, RNAi silencing of the mitochondrial malate dehydrogenase and fumarate reductase in the background of complex I and Ndh2 null mutants would shed light on the quantitative role of each of these enzymes in mitochondrial NADH reoxidation.

The possible occurrence of the mitochondrial substrate-level phosphorylation reactions raises an interesting question regarding the mitochondrial bioenergetics of BSF and questions the origin of ATP that is needed by mitochondrial F_oF_1 ATPase in order to maintain the mitochondrial membrane potential. The classical model presumes that ATP is imported into the organelle via the activity of the ATP/ADP carrier [52,53]. However, the available data—such as low sensitivity of BSF to treatment with bongkreic acid, an inhibitor of this carrier—raise some doubts about this assertion. Interestingly, the BSF does not respire when the mitochondrial transmembrane proton gradient is dissipated upon treatment with the F_oF_1 ATPase inhibitor oligomycin or by addition of carbonyl cyanide-*4*-(trifluoromethoxy)phenylhydrazone (FCCP). However, when treated with bongkreic acid, which should halt the activity of F_oF_1 ATPase by restraining its substrate, the parasite consumes oxygen at the same rate as untreated cells [54,55]. On one hand, it is possible that the mitochondrial inner membrane harbors another ATP/ADP carrier; on the other hand, it is a plausible speculation that, when specific conditions emerge, the BSF mitochondrion has the capacity to employ its complex enzymatic network to produce ATP by substrate-level phosphorylation to power the F_oF_1 ATPase.

Concluding remarks

Combined, the available data reveal that the metabolic flexibility and adaptability of the BSF mitochondrion are much larger than appreciated so far. Mitochondrial metabolism appears to be controlled at various levels; a developmental program seems to be a major contributor, but recent advances in the field suggest that other cues may also play a role through fine-tuning mechanisms. However, the triggers and signaling pathways of these mechanisms remain to be identified. Furthermore, it should be realized that almost all metabolic studies have been performed with strains well adapted to laboratory conditions. While the proteomic data do not show any significant differences between the monomorphic and pleiomorphic strains, future work combining proteomics and metabolomics with functional genomics should be extended to the mitochondrion of trypanosomes isolated not only from blood but also from other tissues to determine whether their metabolism is tissue specific and, if so, what is/are the mechanism (s) that control(s) the changes. Therefore, the virtually unexplored array of pathways and enzymes begs for attention because it may have important implications for drug target identification and future novel chemotherapeutics. Moreover, a decreased morphological complexity, which is apparently not reflected in metabolic complexity, is an interesting and novel phenomenon that can now be efficiently addressed with emerging, increasingly sensitive methods.

Supporting information

S1 Table. List of mitochondrial proteins that were identified in proteomic analysis of PCF cells (columns F, G, and H) and of BSF cells (columns I, J, K, L, M, and N). The column

color coding is green for PCF, dark grey for monomorphic BSF, and light gray for pleiomorphic BSF cells.
1, identified; 0, not identified; BSF, bloodstream form; PCF, procyclic form.
(XLSX)

References

1. Rico E, Rojas F, Mony BM, Szoor B, Macgregor P, et al. (2013) Bloodstream form pre-adaptation to the tsetse fly in *Trypanosoma brucei*. Front Cell Infect Microbiol 3: 78. https://doi.org/10.3389/fcimb.2013.00078 PMID: 24294594
2. Trindade S, Rijo-Ferreira F, Carvalho T, Pinto-Neves D, Guegan F, et al. (2016) *Trypanosoma brucei* parasites occupy and functionally adapt to the adipose tissue in mice. Cell Host Microbe 19: 837–848. https://doi.org/10.1016/j.chom.2016.05.002 PMID: 27237364
3. Capewell P, Cren-Travaille C, Marchesi F, Johnston P, Clucas C, et al. (2016) The skin is a significant but overlooked anatomical reservoir for vector-borne African trypanosomes. Elife; 5:e17717.
4. Smith TK, Bringaud F, Nolan DP, Figueiredo LM (2017) Metabolic reprogramming during the *Trypanosoma brucei* life cycle. F1000Res 6.
5. Lukeš J, Hashimi H, Verner Z, Číčová Z (2010) The remarkable mitochondrion of trypanosomes and related flagellates. In: Structures and Organelles in Pathogenic Protists. de Souza W., editor. 1 ed: Springer-Verlag Berlin Heidelberg. pp. 227–252.
6. Vickerman K (1985) Developmental cycles and biology of pathogenic trypanosomes. Br Med Bull 41: 105–114. PMID: 3928017
7. Vickerman K (1965) Polymorphism and mitochondrial activity in sleeping sickness trypanosomes. Nature 208: 762–766. PMID: 5868887
8. Opperdoes FR, Borst P, Bakker S, Leene W (1977) Localization of glycerol-3-phosphate oxidase in the mitochondrion and particulate NAD+-linked glycerol-3-phosphate dehydrogenase in the microbodies of the bloodstream form to *Trypanosoma brucei*. Eur J Biochem 76: 29–39. PMID: 142010
9. Nolan DP, Voorheis HP (1992) The mitochondrion in bloodstream forms of *Trypanosoma brucei* is energized by the electrogenic pumping of protons catalysed by the F1F0-ATPase. Eur J Biochem 209: 207–216. PMID: 1327770
10. Schnaufer A, Clark-Walker GD, Steinberg AG, Stuart K (2005) The F1-ATP synthase complex in bloodstream stage trypanosomes has an unusual and essential function. EMBO J 24: 4029–4040. https://doi.org/10.1038/sj.emboj.7600862 PMID: 16270030
11. Vercesi AE, Docampo R, Moreno SN (1992) Energization-dependent Ca2+ accumulation in *Trypanosoma brucei* bloodstream and procyclic trypomastigotes mitochondria. Mol Biochem Parasitol 56: 251–257. PMID: 1484549
12. Lukeš J, Basu S (2015) Fe/S protein biogenesis in trypanosomes—A review. Biochim Biophys Acta 1853: 1481–1492. https://doi.org/10.1016/j.bbamcr.2014.08.015 PMID: 25196712
13. Schnaufer A, Panigrahi AK, Panicucci B, Igo RP Jr., Wirtz E, et al. (2001) An RNA ligase essential for RNA editing and survival of the bloodstream form of *Trypanosoma brucei*. Science 291: 2159–2162. https://doi.org/10.1126/science.1058955 PMID: 11251122
14. Read LK, Lukeš J, Hashimi H (2016) Trypanosome RNA editing: the complexity of getting U in and taking U out. Wiley Interdiscip Rev RNA 7: 33–51. https://doi.org/10.1002/wrna.1313 PMID: 26522170
15. Huang G, Vercesi AE, Docampo R (2013) Essential regulation of cell bioenergetics in *Trypanosoma brucei* by the mitochondrial calcium uniporter. Nat Commun 4: 2865. https://doi.org/10.1038/ncomms3865 PMID: 24305511
16. Docampo R, Lukeš J (2012) Trypanosomes and the solution to a 50-year mitochondrial calcium mystery. Trends Parasitol 28: 31–37. https://doi.org/10.1016/j.pt.2011.10.007 PMID: 22088944
17. Gualdron-Lopez M, Brennand A, Hannaert V, Quinones W, Caceres AJ, et al. (2012) When, how and why glycolysis became compartmentalised in the Kinetoplastea. A new look at an ancient organelle. Int J Parasitol 42: 1–20. https://doi.org/10.1016/j.ijpara.2011.10.007 PMID: 22142562
18. Gabaldon T, Ginger ML, Michels PA (2016) Peroxisomes in parasitic protists. Mol Biochem Parasitol 209: 35–45. https://doi.org/10.1016/j.molbiopara.2016.02.005 PMID: 26896770
19. Clarkson AB Jr., Grady RW, Grossman SA, McCallum RJ, Brohn FH (1981) *Trypanosoma brucei brucei*: a systematic screening for alternatives to the salicylhydroxamic acid-glycerol combination. Mol Biochem Parasitol 3: 271–291. PMID: 6795501

20. Grant PT, Fulton JD (1957) The catabolism of glucose by strains of *Trypanosoma rhodesiense*. Biochem J 66: 242–250. PMID: 13445679

21. van Grinsven KW, Van Den Abbeele J, Van den Bossche P, van Hellemond JJ, Tielens AG (2009) Adaptations in the glucose metabolism of procyclic *Trypanosoma brucei* isolates from tsetse flies and during differentiation of bloodstream forms. Eukaryot Cell 8: 1307–1311. https://doi.org/10.1128/EC.00091-09 PMID: 19542311

22. Nolan DP, Rolin S, Rodriguez JR, Van Den Abbeele J, Pays E (2000) Slender and stumpy bloodstream forms of *Trypanosoma brucei* display a differential response to extracellular acidic and proteolytic stress. Eur J Biochem 267: 18–27. PMID: 10601846

23. Mony BM, Matthews KR (2015) Assembling the components of the quorum sensing pathway in African trypanosomes. Mol Microbiol 96: 220–232. https://doi.org/10.1111/mmi.12949 PMID: 25630552

24. Turner CM (1990) The use of experimental artefacts in African trypanosome research. Parasitol Today 6: 14–17. PMID: 15463248

25. Mazet M, Morand P, Biran M, Bouyssou G, Courtois P, et al. (2013) Revisiting the central metabolism of the bloodstream forms of *Trypanosoma brucei*: production of acetate in the mitochondrion is essential for parasite viability. PLoS Negl Trop Dis 7: e2587. https://doi.org/10.1371/journal.pntd.0002587 PMID: 24367711

26. Creek DJ, Mazet M, Achcar F, Anderson J, Kim DH, et al. (2015) Probing the metabolic network in bloodstream-form *Trypanosoma brucei* using untargeted metabolomics with stable isotope labelled glucose. PLoS Pathog 11: e1004689. https://doi.org/10.1371/journal.ppat.1004689 PMID: 25775470

27. Spitznagel D, Ebikeme C, Biran M, Nic a' Bhaird N, Bringaud F, et al. (2009) Alanine aminotransferase of *Trypanosoma brucei*—a key role in proline metabolism in procyclic life forms. FEBS J 276: 7187–7199. https://doi.org/10.1111/j.1742-4658.2009.07432.x PMID: 19895576

28. Creek DJ, Nijagal B, Kim DH, Rojas F, Matthews KR, et al. (2013) Metabolomics guides rational development of a simplified cell culture medium for drug screening against *Trypanosoma brucei*. Antimicrob Agents Chemother 57: 2768–2779. https://doi.org/10.1128/AAC.00044-13 PMID: 23571546

29. Panigrahi AK, Ogata Y, Zíková A, Anupama A, Dalley RA, et al. (2009) A comprehensive analysis of *Trypanosoma brucei* mitochondrial proteome. Proteomics 9: 434–450. https://doi.org/10.1002/pmic.200800477 PMID: 19105172

30. Acestor N, Panigrahi AK, Ogata Y, Anupama A, Stuart KD (2009) Protein composition of Trypanosoma brucei mitochondrial membranes. Proteomics 9: 5497–5508. https://doi.org/10.1002/pmic.200900354 PMID: 19834910

31. Zíková A, Panigrahi AK, Dalley RA, Acestor N, Anupama A, et al. (2008) *Trypanosoma brucei* mitochondrial ribosomes: affinity purification and component identification by mass spectrometry. Mol Cell Proteomics 7: 1286–1296. https://doi.org/10.1074/mcp.M700490-MCP200 PMID: 18364347

32. Panigrahi AK, Zíková A, Dalley RA, Acestor N, Ogata Y, et al. (2008) Mitochondrial complexes in *Trypanosoma brucei*: a novel complex and a unique oxidoreductase complex. Mol Cell Proteomics 7: 534–545. https://doi.org/10.1074/mcp.M700430-MCP200 PMID: 18073385

33. Acestor N, Zíková A, Dalley RA, Anupama A, Panigrahi AK, et al. (2011) *Trypanosoma brucei* mitochondrial respiratome: composition and organization in procyclic form. Mol Cell Proteomics 10: M110 006908.

34. Niemann M, Wiese S, Mani J, Chanfon A, Jackson C, et al. (2013) Mitochondrial outer membrane proteome of *Trypanosoma brucei* reveals novel factors required to maintain mitochondrial morphology. Mol Cell Proteomics 12: 515–528. https://doi.org/10.1074/mcp.M112.023093 PMID: 23221899

35. Peikert CD, Mani J, Morgenstern M, Kaser S, Knapp B, et al. (2017) Charting organellar importomes by quantitative mass spectrometry. Nat Commun 8: 15272. https://doi.org/10.1038/ncomms15272 PMID: 28485388

36. Zíková A, Panigrahi AK, Uboldi AD, Dalley RA, Handman E, et al. (2008) Structural and functional association of *Trypanosoma brucei* MIX protein with cytochrome c oxidase complex. Eukaryot Cell 7: 1994–2003. https://doi.org/10.1128/EC.00204-08 PMID: 18776036

37. Zíková A, Schnaufer A, Dalley RA, Panigrahi AK, Stuart KD (2009) The F(0)F(1)-ATP synthase complex contains novel subunits and is essential for procyclic *Trypanosoma brucei*. PLoS Pathog 5: e1000436. https://doi.org/10.1371/journal.ppat.1000436 PMID: 19436713

38. Dejung M, Subota I, Bucerius F, Dindar G, Freiwald A, et al. (2016) Quantitative proteomics uncovers novel factors involved in developmental differentiation of *Trypanosoma brucei*. PLoS Pathog 12: e1005439. https://doi.org/10.1371/journal.ppat.1005439 PMID: 26910529

39. Butter F, Bucerius F, Michel M, Cicova Z, Mann M, et al. (2013) Comparative proteomics of two life cycle stages of stable isotope-labeled *Trypanosoma brucei* reveals novel components of the parasite's

host adaptation machinery. Mol Cell Proteomics 12: 172–179. https://doi.org/10.1074/mcp.M112.019224 PMID: 23090971

40. Urbaniak MD, Martin DM, Ferguson MA (2013) Global quantitative SILAC phosphoproteomics reveals differential phosphorylation is widespread between the procyclic and bloodstream form lifecycle stages of *Trypanosoma brucei*. J Proteome Res 12: 2233–2244. https://doi.org/10.1021/pr400086y PMID: 23485197

41. Urbaniak MD, Guther ML, Ferguson MA (2012) Comparative SILAC proteomic analysis of *Trypanosoma brucei* bloodstream and procyclic lifecycle stages. PLoS ONE 7: e36619. https://doi.org/10.1371/journal.pone.0036619 PMID: 22574199

42. Urbaniak MD, Mathieson T, Bantscheff M, Eberhard D, Grimaldi R, et al. (2012) Chemical proteomic analysis reveals the drugability of the kinome of *Trypanosoma brucei*. ACS Chem Biol 7: 1858–1865. https://doi.org/10.1021/cb300326z PMID: 22908928

43. Gunasekera K, Wuthrich D, Braga-Lagache S, Heller M, Ochsenreiter T (2012) Proteome remodelling during development from blood to insect-form *Trypanosoma brucei* quantified by SILAC and mass spectrometry. BMC Genomics 13: 556. https://doi.org/10.1186/1471-2164-13-556 PMID: 23067041

44. Verner Z, Basu S, Benz C, Dixit S, Dobáková E, et al. (2015) Malleable mitochondrion of *Trypanosoma brucei*. Int Rev Cell Mol Biol 315: 73–151. https://doi.org/10.1016/bs.ircmb.2014.11.001 PMID: 25708462

45. Zhang X, Cui J, Nilsson D, Gunasekera K, Chanfon A, et al. (2010) The *Trypanosoma brucei* MitoCarta and its regulation and splicing pattern during development. Nucleic Acids Res 38: 7378–7387. https://doi.org/10.1093/nar/gkq618 PMID: 20660476

46. Sykes SE, Hajduk SL (2013) Dual functions of alpha-ketoglutarate dehydrogenase E2 in the Krebs cycle and mitochondrial DNA inheritance in *Trypanosoma brucei*. Eukaryot Cell 12: 78–90. https://doi.org/10.1128/EC.00269-12 PMID: 23125353

47. Overath P, Czichos J, Haas C (1986) The effect of citrate/cis-aconitate on oxidative metabolism during transformation of *Trypanosoma brucei*. Eur J Biochem 160: 175–182. PMID: 3769918

48. Sykes S, Szempruch A, Hajduk S (2015) The krebs cycle enzyme alpha-ketoglutarate decarboxylase is an essential glycosomal protein in bloodstream African trypanosomes. Eukaryot Cell 14: 206–215. https://doi.org/10.1128/EC.00214-14 PMID: 25416237

49. Štafková J, Mach J, Biran M, Verner Z Bringaud F, et al. (2016) Mitochondrial pyruvate carrier in *Trypanosoma brucei*. Mol Microbiol 100: 442–456. https://doi.org/10.1111/mmi.13325 PMID: 26748989

50. Surve S, Heestand M, Panicucci B, Schnaufer A, Parsons M (2012) Enigmatic presence of mitochondrial complex I in *Trypanosoma brucei* bloodstream forms. Eukaryot Cell 11: 183–193. https://doi.org/10.1128/EC.05282-11 PMID: 22158713

51. Surve SV, Jensen BC, Heestand M, Mazet M, Smith TK, et al. (2016) NADH dehydrogenase of *Trypanosoma brucei* is important for efficient acetate production in bloodstream forms. Mol Biochem Parasitol 211:57–61. https://doi.org/10.1016/j.molbiopara.2016.10.001 PMID: 27717801

52. Pena-Diaz P, Pelosi L, Ebikeme C, Colasante C, Gao F, et al. (2012) Functional characterization of TbMCP5, a conserved and essential ADP/ATP carrier present in the mitochondrion of the human pathogen *Trypanosoma brucei*. J Biol Chem 287: 41861–41874. https://doi.org/10.1074/jbc.M112.404699 PMID: 23074217

53. Gnipová A, Šubrtová K, Panicucci B, Horváth A, Lukeš J, et al. (2015) The ADP/ATP carrier and its relationship to OXPHOS in an ancestral protist, *Trypanosoma brucei*. Eukaryot Cell 14:297–310. https://doi.org/10.1128/EC.00238-14 PMID: 25616281

54. Miller PG, Klein RA (1980) Effects of oligomycin on glucose utilization and calcium transport in African trypanosomes. J Gen Microbiol 116: 391–396. https://doi.org/10.1099/00221287-116-2-391 PMID: 6246194

55. Bienen EJ, Maturi RK, Pollakis G, Clarkson AB Jr. (1993) Non-cytochrome mediated mitochondrial ATP production in bloodstream form *Trypanosoma brucei brucei*. Eur J Biochem 216: 75–80. PMID: 8365419

OPEN ACCESS Freely available online

PLoS PATHOGENS

The F_0F_1-ATP Synthase Complex Contains Novel Subunits and Is Essential for Procyclic *Trypanosoma brucei*

Alena Zíková, Achim Schnaufer¤, Rachel A. Dalley, Aswini K. Panigrahi, Kenneth D. Stuart*

Seattle Biomedical Research Institute, Seattle, Washington, United States of America

Abstract

The mitochondrial F_0F_1 ATP synthase is an essential multi-subunit protein complex in the vast majority of eukaryotes but little is known about its composition and role in *Trypanosoma brucei*, an early diverged eukaryotic pathogen. We purified the F_0F_1 ATP synthase by a combination of affinity purification, immunoprecipitation and blue-native gel electrophoresis and characterized its composition and function. We identified 22 proteins of which five are related to F_1 subunits, three to F_0 subunits, and 14 which have no obvious homology to proteins outside the kinetoplastids. RNAi silencing of expression of the F_1 α subunit or either of the two novel proteins showed that they are each essential for the viability of procyclic (insect stage) cells and are important for the structural integrity of the F_0F_1-ATP synthase complex. We also observed a dramatic decrease in ATP production by oxidative phosphorylation after silencing expression of each of these proteins while substrate phosphorylation was not severely affected. Our procyclic *T. brucei* cells were sensitive to the ATP synthase inhibitor oligomycin even in the presence of glucose contrary to earlier reports. Hence, the two novel proteins appear essential for the structural organization of the functional complex and regulation of mitochondrial energy generation in these organisms is more complicated than previously thought.

Citation: Zíková A, Schnaufer A, Dalley RA, Panigrahi AK, Stuart KD (2009) The F_0F_1-ATP Synthase Complex Contains Novel Subunits and Is Essential for Procyclic *Trypanosoma brucei*. PLoS Pathog 5(5): e1000436. doi:10.1371/journal.ppat.1000436

Editor: John C. Boothroyd, Stanford University, United States of America

Received January 26, 2009; **Accepted** April 20, 2009; **Published** May 15, 2009

Funding: This work was supported by NIH grants AI065935 to KS and AI069057 to AS. Research was conducted using equipment made possible by Economic Development Administration - US Department of Commerce and the M.J. Murdock Charitable Trust. The funders had no role in study design, data collection and analysis, decision to publish, or preparation of the manuscript.

Competing Interests: The authors have declared that no competing interests exist.

* E-mail: ken.stuart@sbri.org

¤ Current address: Institute of Immunology & Infection Research, University of Edinburgh, Edinburgh, United Kingdom

Introduction

Trypanosomes and related kinetoplastids parasites are responsible for several serious infectious diseases of human and livestock worldwide. The few available drugs are difficult to administer, have severe side-effects, and suffer from increasing resistance [1]. For that reasons, improved drug therapy of kinetoplastid infections and the identification of new molecular targets are important goals.

Trypanosoma brucei has a complex life cycle alternating between a mammalian host and a blood-feeding insect vector, the tsetse fly. The procyclic insect stage (PF) lives in the insect midgut and feeds mainly on two amino acids, proline and threonine, which are converted into partially oxidized end products by so-called aerobic fermentation [2]. The single large branched mitochondrion of these PF cells is fully developed with many cristae, Krebs cycle enzymes, and abundant levels of mitochondrial (mt) F_0F_1-ATP synthase (respiratory complex V). It has a complete respiratory chain that oxidizes the reduced equivalents generated by amino acid metabolism and the glycolytic pathway and thus generates indispensable membrane potential [3].

The bloodstream form (BF) is well adapted to an environment with a constant level of blood glucose and energy requirements are met by an aerobic type of glycolysis where glucose is converted to pyruvate. The metabolic role of the single tubular BF mitochondrion is suppressed and the organelle lacks a functional respiratory chain and mt membrane potential involves the reverse function of the F_0F_1-ATP synthase: the complex hydrolyzes ATP produced by glycolysis to pump protons from the matrix to the inter-membrane space [4–7]. This reverse function of the F_0F_1-ATPase complex is indispensable for BF trypanosomes and an inhibitor specifically targeting the F_0F_1-ATPase activity would be expected to be lethal to trypanosomes, but not the host, which utilizes the conventional function of this complex to create ATP. Importantly, these inhibitors may be adapted from those already developed to prevent tissue damage caused by ischemic conditions in humans. Therefore, the trypanosomatid F_0F_1-ATPase is an attractive anti-trypanosomal drug target.

Generally, F_0F_1-ATPsynthase/ATPase is a ubiquitous enzyme comprised of two oligomeric components, F_0 and F_1, linked together by a central and a peripheral stalk [8,9]. The hydrophilic domain F_1 bears three catalytic sites and extends into the matrix. The hydrophobic domain F_0 is membrane embedded and contains a proton channel. The prokaryotic enzyme, which represents the simplest form of the complex, appears to consist of five different protein subunits of F_1 ($\alpha_3\beta_3\gamma\delta\varepsilon$) and three subunits of F_0 (ab_2c_{10-12}) (multiple stoichiometry indicated in subscript). These subunits form the core of the F_0F_1 motor structure. The eukaryotic enzyme

Author Summary

African trypanosomes (*Trypanosoma brucei* and related subspecies) are unicellular parasites that cause the devastating disease of African sleeping sickness in man and nagana in livestock. Both of these diseases are lethal, killing thousands of people each year and causing major economical complications in the developing world, thus affecting the lives of millions. Furthermore, available drugs are obsolete, difficult to administer and have many undesirable side-effects. Therefore, there is a reinvigorated effort to design new drugs against these parasites. From the pharmacological perspective, unique metabolic processes and protein complexes with singular structure, composition and essential function are of particular interest. One such remarkable protein complex is the mitochondrial F_0F_1-ATP synthase/ATPase. Here we show that F_0F_1-ATP synthase complex is essential for viability of procyclic *T. brucei* cells and it possesses unique and novel subunits. The three F_0F_1-ATP synthase subunits that were tested were shown to be crucial for the structural integrity of the F_0F_1-ATP synthase complex and its activities. The compositional and functional characterization of the F_0F_1-ATP synthase in *T. brucei* represents a major step towards deciphering the unique and essential properties of the respiratory chain of both an early diverged eukaryote and a lethal human parasite.

has homologous components, but also incorporates additional subunits involved in the structure and regulation of the complex (Table 1). With the exception of subunit ε and IF1, which bind to F_1, the additional subunits A6L (subunit 8 in yeast), F6 (subunit *h* in yeast), *d*, *e*, *f*, *g* and oligomycin sensitivity-conferring protein (OSCP) are associated with the F_0 proton channel or the peripheral stalk [10]. Additionally, the yeast enzyme contains supernumerary subunits *i* and *k* [11–13] and bovine complex contains additional subunits AGP and MLQ [14].

Comparison of bacterial, yeast and mammalian ATP synthase subunits to the *T. brucei* genome revealed *T. brucei* homologs of F_1 subunits α, β, γ, δ, ε and F_0 subunits *c* and OSCP. None of the other subunits found in other eukaryotic organisms have been identified. These are either absent from *Trypanosoma* mitochondrial ATP synthase, have been replaced by other proteins, or are so highly divergent that their relationship cannot be readily identified via sequence homology.

This observation prompted us to investigate the composition of the trypanosomal F_0F_1-ATP synthase. We identified 22 subunits in purified complexes of which 14 are unique to *T. brucei*. RNAi silencing of the subunit α and two novel components revealed these to be essential for PF cell viability and important for F_0F_1-ATP synthase structural integrity. We found a dramatic decrease in ATP production by oxidative phosphorylation in these silenced cell lines but no severe effect on substrate phosphorylation. The PF cells are sensitive to the ATP synthase inhibitor oligomycin

Table 1. F_0F_1-ATP synthase subunits nomenclature.

	Bacterial enzyme	Mitochondrial enzyme		
		Saccharomyces cerevisiae	*Bos taurus*	*Trypanosoma brucei* (*E*-value[a])
F_1	α	α	α	Tb927.7.7420/Tb927.7.7430 (5e-114)
	β	β	β	Tb927.3.1380 (5e-162)
	γ	γ	γ	Tb10.100.0070 (2e-13)
	ε	δ	δ	Tb927. 6.4990 (4e-13)
	-	ε	ε	Tb10.70.2155 (2e-4)
F_0	δ	OSCP	OSCP	Tb10.6k15.2510 (0.0021)
	a	6	*a*	NCBI: AAA97428 (mt encoded)[b]
	b	9	*b*	Tb927.5.1710[b]
	c	4	*c*	Tb10.70.6340 (5e-8)
				Tb11.02.2950 (8e-08)
				Tb927.7.1470 (6e-08)
	-	8	A6L	-[c]
	-	*d*	*d*	-
	-	*f*	*f*	-
	-	*h*	F6	-
Associated proteins	-	IF_1	IF_1	-
	-	*g*	*g*	-
	-	*e*	*e*	-
	-	*i*	-	-
	-	*k*	-	-
	-	-	AGP	-
	-	-	MLQ	-

[a]*E*-values were obtained by BLAST search analysis using bovine ATP synthase subunits as subject.
[b]*T. brucei* homologues of subunits *a* and *b* are not recognizable by BLAST search and their homology to eukaryotic and bacterial ATP synthase subunits *a* and *b*, respectively, was recognized previously by detailed sequence analysis and hydropathic profiles [36,37].
[c]dash indicates that no homologous proteins were identified in the *T. brucei* genome using BLAST search.
doi:10.1371/journal.ppat.1000436.t001

regardless of the presence or absence of glucose in the medium. This is consistent with the RNAi data but contrary to earlier reports [15,16]. Hence, regulation of mitochondrial energy generation in these parasitic organisms is more complex than previously thought.

Materials and Methods

Genes used in this study

Tb10.70.7760 (TAP_Tb7760, RNAi_Tb7760); Tb927.5.2930 (TAP_Tb2930, RNAi_Tb2930); Tb927.5.1710 (TAP_subunit *b*); Tb927.3.1380 (TAP_subunit β); Tb927.7.7430/Tb927.7.7420 (RNAi_subunit α).

Plasmid construction

To create the vectors for inducible expression of C-terminally TAP-tagged proteins the ORFs were PCR amplified from *T. brucei* strain 427 genomic DNA using the following oligonucleotides:

TAP_Tb7760	Fwd – ACAAAGCTTATGCAGGGCAGTTGG
	Rev – ACAGGATCCAGCTGTGTGTCGGCC
TAP_sub *b*	Fwd – CACAAGCTTATGATGCGCCGTG
	Rev – CACGGATCCCTCTACCTTTACATC
TAP_Tb2930	Fwd – ACAAAGCTTATGCGCCGTGTATC
	Rev – ACAGGATCCGTGATGGGCC
TAP_sub β	Fwd – ACAAAGCTTATGCTGACTCGTTTCC
	Rev – ACAGGATCCGCTACTGGCTTG

The PCR products were cloned into pGEM-T easy vector (Promega), digested with BamHI and HindIII enzymes and ligated into the pLew79-MHT vector which contains *c*-myc, His, calmodulin binding peptide and protein A tags in that order [17,18]. The last two tags are separated by a TEV protease cleavage site.

To create the construct for RNAi of Tb10.70.7760 and Tb927.5.2930 transcripts, fragments of 830 bp and 646 bp, respectively, were amplified by PCR using the oligonucleotides below and cloned into pZJM plasmid [19] via XhoI and HindIII restriction sites.

RNAi_Tb7760	Fw – CACAAGCTTGAAGCTCAGGACC
	Rev – CACCTCGAGGCAGAAACGCATC
RNAi_Tb2930	Fw – ACAAAGCTTATGCGCCGTGTATC
	Rev – CACCTCGAGTTCGGCCCGATC

The inducible RNAi plasmid for silencing ATP synthase subunit α was generated using the pQuadra system [20] as described in [4].

Cell culture and generation of cell lines

T. brucei PF cells strains 29.13, transgenic for T7 RNA polymerase and the tetracycline (tet) repressor, were grown *in vitro* at 27°C in SDM-79 media containing hemin (7.5 mg/ml) and 10% FBS. The TAP-plasmids and RNAi plasmids were linearized with NotI enzyme and transfected into the cell line as described previously [21]. Synthesis of dsRNAi was induced by the addition of tet at 1 μg/ml concentration. The cells were counted using the Z2 Cell Counter (Beckman Coulter Inc.) and growth curves were generated for clonal cell lines over a period of 13 days. In TAP-tagged cell lines the expression of tagged protein was induced by 100 ng/ml of tet.

SDS PAGE and Western blot analysis

The protein samples were fractionated by SDS-PAGE, blotted onto PVDF membrane and probed with monoclonal antibodies (mAb) anti-His_6 (1:2000, Invitrogen), anti-Rieske protein (1:1000) (kindly provided by L. Simpson) and anti-alternative oxidase TAO (1:25) (kindly provided by M. Chaudhuri), and polyclonal antibodies against trCOIV (1:1000) [22], the F_1 moiety of *Crithidia fasciculata* (kindly provided by R. Benne), which cross-reacts with the β subunit of the *T. brucei* complex (1:1000) and against subunit *b* of *Leishmania tarentolae* (1:2000) (kindly provided by L. Simpson), and developed using the ECL system (Roche).

Immunoprecipitation of F_0F_1-ATP synthase complex

The mitochondrial vesicles were isolated from PF 1.7a cells as described previously [23] by hypotonic lysis followed by density gradient floatation in a 20–35% linear Percoll gradient. The enriched vesicles were lysed with 1% Triton X-100 and the lysate was clarified by centrifugation. The cleared supernatant was fractionated on a 10–30% glycerol gradient at 38,000 rpm for 5 hours (SW40 rotor, Beckman Instrument). The fractions were collected from the top. Immunoprecipitation of F_0F_1-ATP synthase complex using mAb64 was performed on pooled gradient fractions from the 10S region (fraction 3–5) and from the 40S region (fractions 17–21) using anti-mouse IgG-coated magnetic beads (Dynabeads M-450) as described previously [23]. The pulled down proteins were identified by LC-MS/MS analysis.

Immunofluorescence assay (IFA)

Subcellular localization of the expressed tagged proteins within the cell was determined by IFA using polyclonal anti-*myc* (Invitrogen) as described [24]. Co-localization analysis was performed using mAb78 against mt heat shock protein 70 [23] coupled with Texas® Red-X conjugated secondary antibody (Invitrogen).

Tandem affinity purification (TAP) of tagged complexes

The TAP protocol was adapted from the published method [18,25,26]. We purified the tagged complexes from $1–4\times10^{10}$ cells by two complementary methods. Briefly, in method 1 the harvested cells were lysed by 1% Triton-X 100 and the tagged-complexes were isolated by IgG affinity chromatography. The bound complexes were eluted by TEV protease cleavage and fractionated on a 10–30% glycerol gradient by centrifugation for 5 h at 38,000 rpm at 4°C in an SW-40 Sorvall rotor [27]. The sedimentation profiles of the tagged complexes were monitored by Western blot analyses using anti-His_6 mAb. Peak reactive fractions were pooled and further purified by Calmodulin affinity chromatography. In method 2 the tagged complexes were purified from cells lysed with 0.25% NP-40, cleared by low speed centrifugation and the supernatant was further lysed with 1.25% NP-40 and cleared by high speed centrifugation (40,000 rpm at 4°C in a Sorvall SW-55 rotor for 40 min). The tagged complexes were isolated by sequential binding to IgG and calmodulin affinity columns. This method was adapted from the published protocol [28].

Mass spectrometry analysis

We prepared and analyzed the samples by gel-based and gel-free approaches as described previously [23,24]. Peptides were identified using a Thermo Electron LTQ Linear Ion Trap Mass Spectrometer. The CID spectra were compared to the *T. brucei* protein database downloaded from GeneDB using TurboSequest software, and protein matches determined using PeptideProphet and ProteinProphet software [29,30]. Proteins identified by at least two unique peptides with a minimum identification probability of 0.97 and in at least three TAP tag purified complexes are

considered as putative subunits of ATP synthase complex. All of the proteins reported in this study were identified by multiple peptide matches except for two ATP synthase subunits, subunit ε (predicted M_w 8.6 kDa) and subunit *c* (predicted M_w 12.3 kDa), which were identified by only 1 peptide match.

Digitonin fractionation, ATPase assay and ATP production assay

Crude mt preparations from the RNAi knock-down cell lines were obtained by digitonin extraction [31]. ATPase activity was measured based on release of free phosphate [32] as described [4]. Briefly, the reaction was started by addition of ATP to a final concentration of 5 mM; and where indicated, oligomycin and/or sodium azide was added to 2.5 μg/ml and 1 mM, respectively. After 20 min, 1.8 μl of 60% perchloric acid was added to 95 μl aliquots, the samples were kept on ice for 30 min, spun down and 90 μl of the supernatant was added to 0.5 ml of Sumner reagent [32], and absorbance was measured at 610 nm.

ATP production was measured as described [33]. Briefly, production of ATP was induced by 5 mM indicated substrates (succinate, pyruvate, α-ketoglutarate) and 67 μM ADP was added. Where indicated, 6.7 mM malonate or 33 μg/ml atractyloside were pre-incubated with mitochondria on ice for 10 min. The concentration of ATP was determined by a luminometer using the ATP Bioluminescence assay kit CLS II (Roche Applied Science).

Blue-native polyacrylamide gel electrophoresis (BN-PAGE) and histochemical staining

The mt vesicles from 5×10^8 cells were isolated by hypotonic cell lysis as described elsewhere [34] and lysed with 1% dodecyl maltoside; 50 μg and 100 μg of mitochondrial lysate and 75 μg of native high molecular weight marker (Amersham) was loaded per lane and analysed on a 3–12% gradient BN-PAGE gel. Immediately after the run, the gel was transferred into ATPase reaction buffer (35 mM Tris-HCl (pH 8.0); 270 mM glycine; 19 mM $MgSO_4$; 0.3% [w/v] $Pb(NO_3)_2$; 11 mM ATP) for overnight incubation by slow agitation. The ATPase activity appears as a white precipitate. The gel was subsequently fixed in 30% methanol.

Results

Genome analysis

Mitochondrial F_0F_1-ATP synthase consists of up to 19 different subunits in yeast, and mammals [10,35]. We searched the *T. brucei* genome database using these known subunits of the mitochondrial F_0F_1-ATP synthase and identified 7 homologs with varying degree of conservation as outlined in Table 1. The mitochondrial F_1 subcomplex with its central stalk contains five different subunits designated α, β, γ, δ, ε and they are conserved among eukaryotes. We found that all five are also conserved in *T. brucei*, three of which were already annotated and two were mis-designated in GeneDB database. They are ATP synthase subunits α (encoded by two identical open reading frames Tb927.7.7420/Tb927.7.7430), β (Tb927.3.1380), and γ (Tb10.100.0070). Subunit δ (Tb927.6.4990) is currently annotated as subunit ε in GeneDB (consistent with the bacterial nomenclature) (Table 1). Since the GeneDB annotation for ATP synthase subunits otherwise follows the mitochondrial nomenclature we propose re-annotating it accordingly. The hypothetical protein encoded by (Tb10.70.2155) has similarity to the mitochondrial ATP synthase subunit ε and thus we propose re-annotating it as such (Figure S1).

While genes for all five F_1 protein homologs were identified, only two of the 11 proteins that occur in the mitochondrial F_0 subcomplex with its peripheral stalk were identified in the *T. brucei* genome. These are subunit OSCP (Tb10.6k15.2510) and subunit *c*, which is encoded by three distinct open reading frames Tb10.70.6340, Tb11.02.2950, Tb927.7.1470 that differ only at the N-terminus of the protein sequence (Figure S1). The finding of three genes that specify proteins related to subunit c is intriguing given the respiratory changes that occur during the life cycle of *T. brucei*. Subunit *a* (which is mitochondrially encoded) and subunit *b* (Tb927.5.1710) are not recognizable by BLAST search and their homology to ATP synthase subunits was recognized previously by detailed sequence analysis and hydropathic profiles [36,37]. However, it should be noted that because the homology of Tb927.5.1710 to subunit *b* of other species is very low and limited to the N-terminal region of the protein, this identification should be treated as tentative. The homologs of the other conserved F_0 subunits or of species-specific ATP synthase complex proteins were not identified by these searches. Since this analysis provided little information with respect to the identity of any other ATP synthase complex proteins including diverged or species specific proteins, we decided to obtain a detailed picture of the protein composition of this complex in *T. brucei* after purification using a combination of immunoprecipitation, blue-native polyacrylamide gel electrophoresis (BN-PAGE) and tandem affinity purification (TAP).

ATP synthase complex immunoprecipitates

Analyses of Triton X-100 lysate of highly purified mitochondria that was fractionated in glycerol gradients using antibodies specific for ATPase subunits identified two predominant peaks at ~10S and ~40S (Figure 1). Polyclonal antibodies that are specific for subunits β and *b* and monoclonal antibody mAb64 which recognizes a conformational epitope of an unidentified subunit of the F_1 subcomplex (A. Panigrahi, unpublished) showed a similar sedimentation profile for two subunits in Western (upper panels) and native dot blot (lower panel) analyses. MAb64 was used to immunoprecipitate complexes from these two peaks and their protein compositions were analyzed by liquid-chromatography tandem mass spectrometry (LC-MS/MS). The immunoprecipitation of the pooled peak reactive fractions (10S and 40S) from the glycerol gradients was carried out in buffer containing 200 mM salt to increase the stringency. MS analysis of the immunoprecipitate from the 10S fraction revealed peptides from subunits α and β of the catalytic headpiece and subunits γ and δ of the central stalk. These subunits are part of the matrix-facing F_1-moiety, which is not directly membrane bound. MS analysis of the 40S complex identified, in addition to these F_1 subunits, OSCP protein and 9 hypothetical proteins of which homologs of three (Tb11.47.0022, Tb927.3.1690, Tb10.6k15.0480) had previously been identified as ATP synthase subunits in *C. fasciculata* [36] (Table 2). In agreement with MS data, a Sypro Ruby-stained gel of immunoprecipitated complexes revealed the presence of F_1 subunits α, β, γ, and δ in the 10S immunoprecipitate, which predicted positions are designated and additional protein bands in the 40S immunoprecipitate (Figure 1B). Peptides predicted from the genes for subunits ε, *a*, *b* and *c* that had been found in *T. brucei* genome were not identified in this analysis although three of these proteins were detected by other procedures as shown below. The failure to detect expected subunits in the immunoprecipitates may be due to purification of incomplete ATP synthase complexes or due to the high hydrophobicity of these subunits and the presence of few potential tryptic cleavage sites.

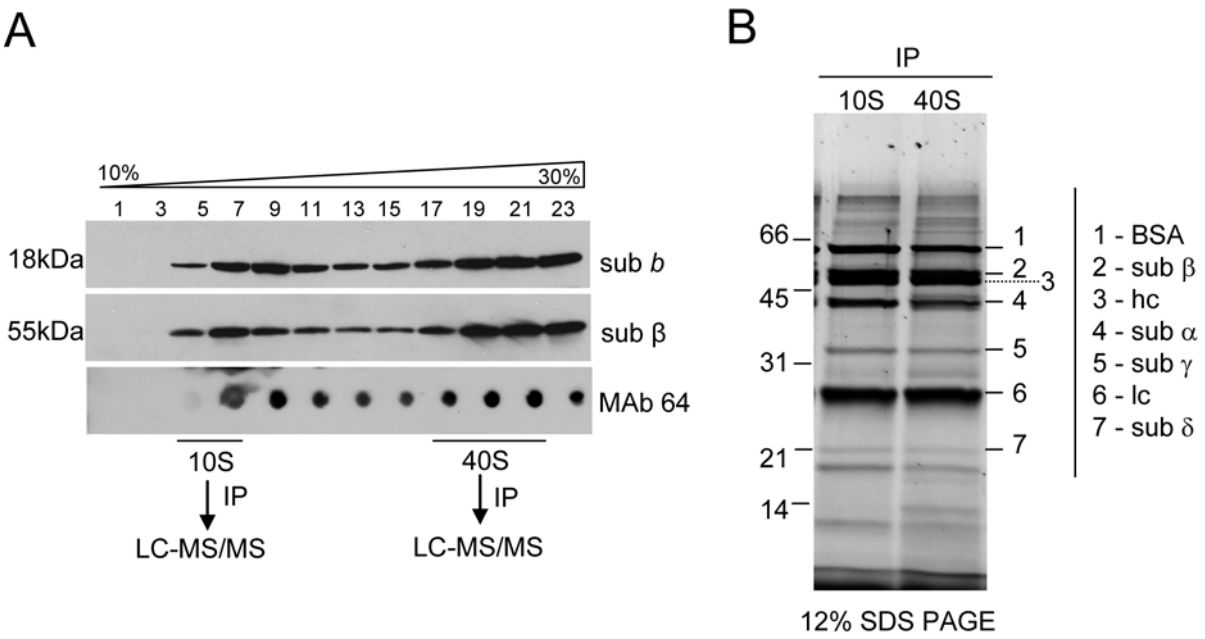

Figure 1. Glycerol gradient fractionation and immunoprecipitation of F_0F_1-ATP synthase complex from *T. brucei* mitochondria. (A) Western blot and native dot blot analyses of the 10–30% glycerol gradient-fractionated cleared mitochondrial lysate were performed using polyclonal antibodies against subunit *b* and β, and monoclonal antibody mAb64 to determine the sedimentation pattern of the F_0F_1-ATP synthase complex. MAb64 was further used to immunoprecipitate (IP) complexes from the 10S and 40S peaks and their protein compositions were analyzed by liquid-chromatography tandem mass spectrometry (LC-MS/MS). (B) Immunoprecipitated 10S and 40S complexes were fractionated on a 12% SDS PAGE gel and stained by Sypro Ruby. Protein bands corresponding to immunoglobulin heavy (hc) and light (lc) chains as well as predicted positions of F_1 subunits α, β, γ and δ and the size standards are indicated.
doi:10.1371/journal.ppat.1000436.g001

Tagged ATP synthase complexes and subunit composition

To obtain more detailed information about the composition of the ATP synthase complex and to assess the validity of the association of the novel proteins identified in the mAb64 immunoprecipitates we purified the F_0F_1-ATP synthase from *T. brucei* PF cells by tandem affinity purification (TAP) and analyzed the protein composition by LC-MS/MS analysis using published protocols [23,24]. F_1 subunit β (Tb927.3.1380) and F_0 subunit *b* (Tb927.5.1710) as well as two randomly selected hypothetical proteins identified in the 40S complex (Tb10.70.7760 and Tb927.5.2930) were tagged resulting in cell lines TAP_sub β, TAP_sub *b*, TAP_Tb7760 and TAP_Tb2930.

Immunofluoresence assays using anti-*myc* mAb (anti-tag) showed that TAP_sub β, TAP_sub *b*, TAP_Tb7760 and TAP_Tb2930 localized to the mitochondrion (Figure 2A). These results confirm the mitochondrial localization of these proteins and indicate that the TAP tags did not interfere with mitochondrial import and providing validity for purifying the F_0F_1-ATP complex.

Western analysis of the tagged complexes purified from cell lysate by IgG affinity chromatography, released by TEV cleavage, and fractionated on 10–30% glycerol gradients revealed sedimentation profiles that differed from those of untagged complexes from mitochondrial lysate (Figure 2B, compare to Figure 1). All tagged subunits were detected throughout the gradients, with the majority of tagged subunits β, *b* and 7760 sedimenting at around 10S. This may reflect the effect of over-expression of the tagged protein as well as potential effects of the tag on the assembly, stability, composition, and/or compactness of the complexes. The bands that are smaller than the predicted full length proteins and that are especially evident in glycerol gradient fractions of TAP_Tb7760 and TAP_Tb2930 are most likely degradation products of the tagged proteins reflecting the abundance of endogenous proteases in the whole cell lysates or results of a proteolytic degradation due to protein overproduction.

The tagged complexes were further purified from pooled gradient fractions corresponding to ~10S (fractions 3–5), ~20S (fractions 7–13) and ~40S (fractions 17–21), as indicated by the underlines in Figure 2B, using the second affinity purification step and analyzed by mass spectrometry. LC-MS/MS analyzes of the complexes from the 20S and 40S fractions from the four TAP-tag purifications identified 18 proteins that were all present in all 40S fractions and almost all of the 20S fractions (Table S1, Method 1). This very similar composition suggests that the 40S complex may be a dimer or oligomer of the 20S complex which may represent a F_0F_1-ATP synthase monomer. ATP synthase subunit α, β, γ, ε and *b* were identified in ~10S complexes from cells in which subunits β or *b* were tagged (i.e. TAP_sub β, TAP_sub *b*) perhaps representing the catalytic headpiece attached to the central stalk with bound subunit *b* (Figure 2B). However, only the OSCP protein (Tb10.6k15.2510) and hypothetical protein Tb11.02.4120 were identified in addition to the bait protein in ~10S complexes from TAP_Tb7760 and TAP_Tb2930 cells respectively (Figure 2B). Perhaps, these represent small sub-complexes of the tagged protein and binding partner(s) that are a consequence of partial assembly or TAP-tag induced disruption of the ATP synthase complex. Subunit ε, which is a small protein with a predicted mature size of 6.7 kDa was identified only in the ~10S complexes from TAP_sub β cells. This may indicate a weaker association with the central stalk of the ATP synthase (Table S1).

To investigate the sedimentation characteristics of the tagged complexes, glycerol gradient fractions of TAP_sub β and TAP_sub *b* were subjected to SDS PAGE followed by Sypro Ruby staining (Figure S2). The staining revealed that the majority of the tagged

Table 2. *Trypanosoma brucei* F_0F_1-ATP synthase subunits.

	Subunit	Protein ID[a]	Mw[b]	IP[c]		TAPtags[c]			BN gel[c]		
				10S	40S	Bands	M1	M2	F1	monomer	dimer
F_1	alpha	Tb927.7.7420/7430*	63.5	√	√	√	√	√	√	√	√
	beta	Tb927.3.1380*,TAP	55.7	√	√	√	√	√	√	√	√
	gamma	Tb10.100.0070*	34.3	√	√	√	√	√	√	√	√
	delta	Tb927.6.4990*	20.1	√	√	√	√	√	√	√	√
	epsilon	Tb10.70.2155	8.6	-	-	-	√	√	-	-	-
F_0	*a*	AAA97428	28	-	-	-	-	-	-	-	-
	b	Tb927.5.1710*,TAP	21.2	-	-	√	√	√	-	√	√
	c	Tb10.70.6340	12.3	-	-	-	-	√	-	-	-
	OSCP	Tb10.6k15.2510*	28.8	-	√	√	√	√	-	√	√
Associated proteins		Tb10.70.7760TAP	46.7	-	√	√	√	√	-	√	√
		Tb927.5.2930TAP	43.3	-	√	√	√	√	-	√	√
		Tb11.02.4120	27.5	-	√	√	√	√	-	√	√
		Tb10.6k15.0480*	17.1	-	√	√	√	√	-	√	√
		Tb927.3.1690*	17.1	-	√	√	√	√	-	√	√
		Tb11.47.0022*	20.2	-	√	√	√	√	-	√	√
		Tb927.7.840	14.5	-	√	√	√	√	-	√	√
		Tb11.03.0475	12	-	-	√	√	√	-	√	√
		Tb927.2.3610	16	-	√	√	√	√	-	-	√
		Tb927.3.2880	12.6	-	√	-	√	√	-	√	√
		Tb927.3.2180	17.9	-	-	-	√	√	-	√	√
		Tb927.5.3090	11.6	-	-	-	√	√	-	-	√
		Tb927.4.3450	13.7	-	-	-	-	√	-	√	√
		Tb927.8.3320	53.4	-	-	-	-	√	-	√	-

[a]GeneDB accession number except for subunit *a* (NCBI accession number).
[b]number indicates predicted molecular weight of the protein in kDa.
[c]√ indicates that the protein was identified by LC-MS/MS analyses, - not detected.
IP – immunoprecipitate of 10S and 40S complexes.
TAP – tandem affinity purification.
Bands – proteins were identified by gel band analysis of Sypro Ruby stained SDS PAGE gel.
M1, M2 – ATP synthase complex was purified by Method 1 or Method 2 (see Materials and Methods).
BN – proteins were identified in BN PAGE bands active for ATPase activity.
*proteins identified in *Crithidia fasciculata* F_0F_1-ATP synthase complex [36].
TAPproteins used as baits.
doi:10.1371/journal.ppat.1000436.t002

proteins migrated at S values <10. At greater S values there was a higher relative abundance of subunits α and β compared to approximately equal amounts of the other subunits, which is consistent if there are three copies of subunits α and β per complex as seen in other organisms.

We also purified the F_0F_1-ATP synthase complex by a complementary affinity purification method that entails two steps of NP-40 treatment and is designed to purify intact membrane complexes ([28], see method 2 in Methods section). SDS-PAGE analysis of all four tagged complexes showed very similar protein profiles, which differed mainly in the position of tagged bait (Figure 2C). Interestingly, in case of TAP_2930 and TAP_7760 the band corresponding to non-tagged endogenous protein was not apparent in the purified complexes, whereas in the case of subunits β and *b* such a band could be detected. This may imply that there is one copy of Tb7760 and Tb2930 protein per complex, while there are three copies of subunit β and potentially two or more copies of subunit *b* per complex. All visible gel bands were individually analyzed by mass spectrometry and the respective proteins were identified (Figure 2C, Table 2). The 15 proteins that correspond to F_1 subunits α, β, γ and δ, F_0 subunits *b* and OSCP, and nine hypothetical proteins (Tb10.70.7760, Tb927.5.2930, Tb11.02.4120, Tb11.47.0022, Tb927.3.1690, Tb10.6k15.0480, Tb927.2.3610, Tb927.7.840, Tb11.03.0475) were identified. In addition, one peptide for F_0 subunit *c* was identified only in complexes from TAP_Tb2930 cells (Table S1). Its small size (mature size of 8 kDa) and high hydrophobicity make the identification of its peptides by routine mass spectrometry analysis challenging. Subunit α was detected as separate ~14 kDa and ~44 kDa N- and C- terminal fragments, respectively (Figure S3). This implies a specific posttranslational cleavage that has been previously reported for *L. tarentolae* [38] and suggests that this cleavage occurs *in vivo* and it is not an artifact of purification. Six other proteins were identified in three samples when the SDS-PAGE step was omitted and samples were directly submitted to trypsin cleavage and LC-MS/MS analysis. These proteins are most likely associated with the F_0F_1-ATP synthase although their relative concentration (stoichiometry) may be lower compare to

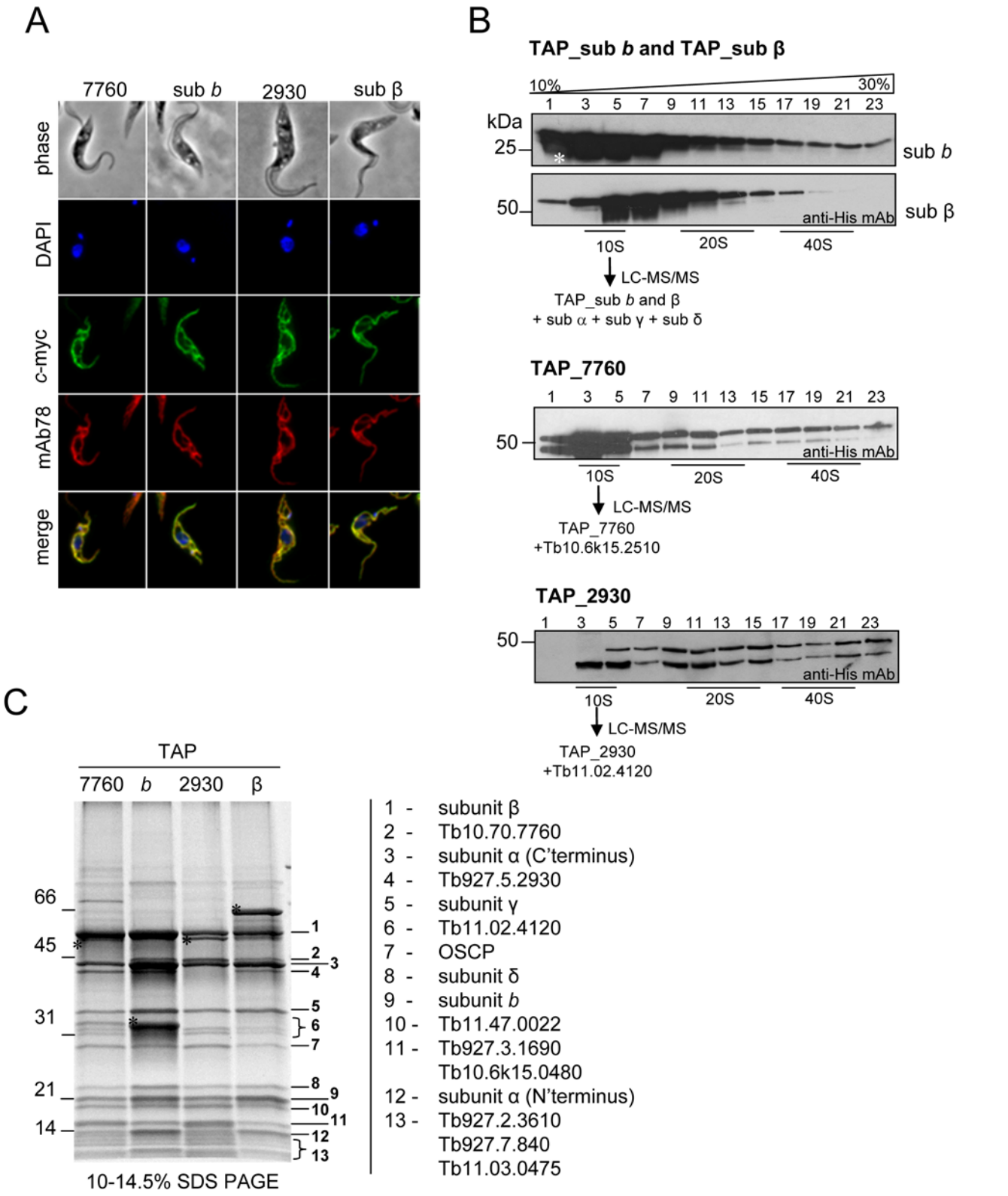

Figure 2. Subcellular localization of tagged subunits and tandem-affinity purification (TAP) of F_0F_1-ATP synthase complex from *T. brucei*. (A) Tagged subunits *b*, β, Tb7760 and Tb2930 of the F_0F_1-ATP synthase complex were visualized by fluorescence microscopy using polyclonal anti-*c* myc antiserum coupled with FITC-conjugated secondary antibody. Co-localization immunofluorescence was performed with monoclonal antibody mAb78 against the mt heat shock protein 70 [23]. Top row, phase-contrast light microscopy of *T. brucei* cells; second row, 4,6-diamidino-2-phenylindole (*DAPI*)-staining of nuclear and kinetoplast DNA; third row, localization of tagged proteins; fourth row, staining of mitochondrial hsp70; bottom row, merged fluorescence images. (B) Fractionation of TAP_sub *b*, TAP_sub β, TAP_Tb2930 and TAP_Tb7760 TEV eluates on 10–30% glycerol gradients. Fractions were collected from the top of the gradients. Aliquots of odd-numbered fractions were analyzed by SDS-PAGE and probed with

anti-His_6 mAb. Positive fractions designated by a black line were further subjected to the second affinity purification step. Proteins identified in 10S complexes by LC-MS/MS are shown. The asterisk in the TAP_sub *b* panel indicates the position of the 25-kDa His-tagged TEV protease. The sizes of the protein marker are indicated on the left. (C) TAP_Tb7760, TAP_sub *b*, TAP_Tb2930 and TAP_sub β complexes were purified by Method 2, separated on a 10–14.5% polyacrylamide Tris-glycine gel and stained with Sypro Ruby. Numbers on the right indicate the results of MS analysis of individual bands. The asterisks indicate the tagged proteins. The sizes of the protein marker are indicated.
doi:10.1371/journal.ppat.1000436.g002

the 15 proteins identified by gel-band analysis (Table 2, Table S1). The mitochondrial encoded subunit *a* was not identified, perhaps due to transient association with subunit *c* and/or its high hydrophobicity, membrane association, non-migration into SDS-PAGE gels and few potential trypsin cleavage sites.

Fourteen novel proteins found associated with the ATP synthase complex are currently annotated as hypothetical proteins in the GeneDB database. Direct comparison to the known subunits of yeast and mammalian ATP synthases did not reveal any similiarity. To explore the homology of these proteins to any other proteins we performed PSI-BLAST searches against the "nr" NCBI database and CDD, PFAM, PROSITE, and InterPro domain searches. We found that these proteins appear to be unique to the order *Kinetoplastida* and that they share no apparent motifs and similarities with any proteins outside of these organisms.

In summary, we find the trypanosomal F_0F_1-ATP synthase complex is composed of up to 22 subunits. This complexity is similar to that seen in higher eukaryotes, although the degree of subunit sequence similarity to those in higher eukaroytes is very low or none.

Native *T. brucei* F_0F_1-ATP synthase

The *T. brucei* ATP synthase complex was examined using blue-native (BN) PAGE in which the charge shift induced by the binding of Coomassie Blue to proteins is used to separate and visualize membrane complexes under native conditions [39]. BN PAGE of dodecyl maltoside-solubilized mitochondria followed by ATPase activity staining revealed three predominant stained bands of which the lower band appears as a doublet, with apparent molecular weights of ~450 kDa, ~700 kDa, and >1 MDa, respectively, relative to the 440 kDa and 669 kDa marker proteins (Figure 3). The three bands active for ATPase activity were excised from the BN gels, destained, digested with trypsin and analysed by LC-MS/MS. We identified only the known subunits of the F_1 moiety in the lower doublet, suggesting that it corresponds to the dissociated F_1 moiety of ATP synthase. The upper two bands contained in addition to the the F_1 moiety proteins the 16 other proteins which were identified in TAP-tagged purified complexes (Table 2, Table S1). This reinforces the likelihood that these proteins are novel subunits of F_0F_1-ATP synthase complex or are at least tightly associated with this complex. Two proteins (Tb927.2.3610 and Tb927.5.3090) were identified only in the >1 MDa gel band, implying specific association with F_0F_1dimers but additional studies are neccessary to assess this.

The molecular mass observed for the smallest band corresponds well to that estimated for the F_1 moiety. This smaller band of the doublet might represents the F_1 headpiece (subunit α and β) and the larger this headpiece together with central stalk (subunit αβγδε) with or without a ring of subunit *c* as has been shown for mammalian F_1 [14]. The observed size of the middle BN gel band corresponds roughly to the ~820 kDa sum of 22 proteins identified in purified complexes that may be stable constituents of this complex (Table 2) and thus may correspond to the F_0F_1 monomer. The upper band thus may represent a dimer or oligomer of the ATP synthase complex. This is with agreement with BN PAGE analysis of other trypanosomatid species, *L. tarentolae* and *Phytomonas serpens*, which also revealed dissociated F_1 ATP synthase particles and monomeric and dimeric/oligomeric F_0F_1-ATP synthase complexes [22,40].

Depletion of subunit α, Tb2930, or Tb7760 inhibits growth of PF *T. brucei*

To assess the requirement of the ATP synthase complex in PF stage of *T. brucei* and to evaluate the functional association of the newly identified subunits of the F_0F_1-ATP synthase complex we constructed cell lines in which the expression of subunits α, Tb927.5.2930 and Tb10.70.7760 can be silenced using RNA interference (RNAi). RNAi of the ATP synthase subunit α was mediated by a stem-loop construct containing a 530 bp fragment of the gene's coding region. RNAi of the Tb2930 and Tb7760 was mediated by pZJM construct. Both vectors allow tetracycline (tet)-dependent and thus regulatable expression of dsRNA which results in RNAi-mediated degradation of the target mRNA. The efficiency of RNAi was confirmed by Northern blot analysis showing that mRNA for Tb2930 and Tb7760 is almost eliminated

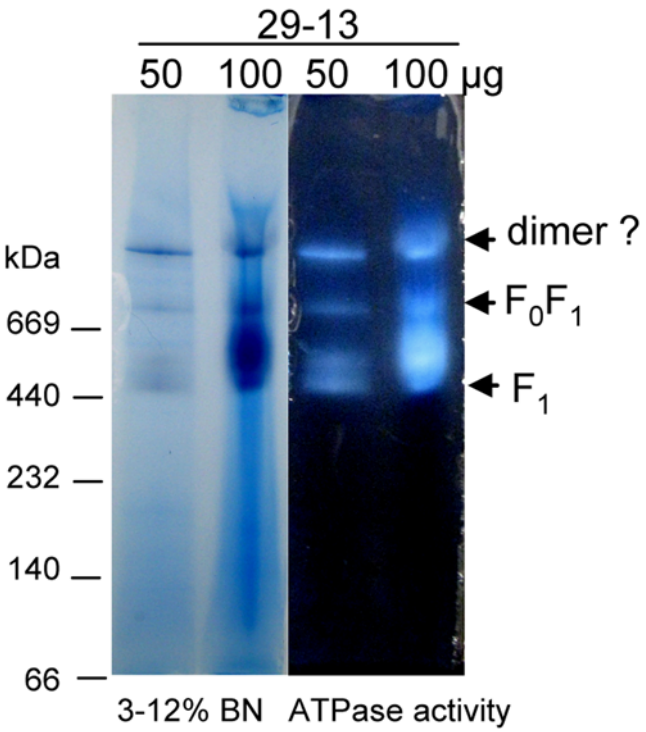

Figure 3. Analysis of the supramolecular organization of F_0F_1-ATP synthase complex from PF *T. brucei*. Mt membranes from parental 29-13 cell line were solubilized by dodecyl maltoside and the mt complexes were separated on 3–12% BN PAGE. ATP synthase F_1 particles, F_0F_1 monomer and putative dimer were identified by lead phosphate precipitates formed during the in-gel ATP hydrolysis assay followed by LC-MS/MS analysis of the corresponding gel bands. The sizes of the native high molecular weight marker (Amersham) are indicated.
doi:10.1371/journal.ppat.1000436.g003

by day 2 after RNAi induction (Figure 4A). Tb7760 and Tb2930 protein levels could not be directly assessed in the RNAi cells due to the lack of antibodies against these proteins. Since a specific antibody against F_1 subunit β is available and the stability of subunit α and β is mutually dependent [4,5] we confirmed the RNAi efficiency of RNAi_subα cell line by Western blot analysis (Figure 5A). After the addition of tet into the culture medium the growth of RNAi_subα, RNAi_Tb2930 and RNAi_Tb7760 cells lines was strongly inhibited and almost complete cessation of growth was evident by day 4 (Figure 4B).

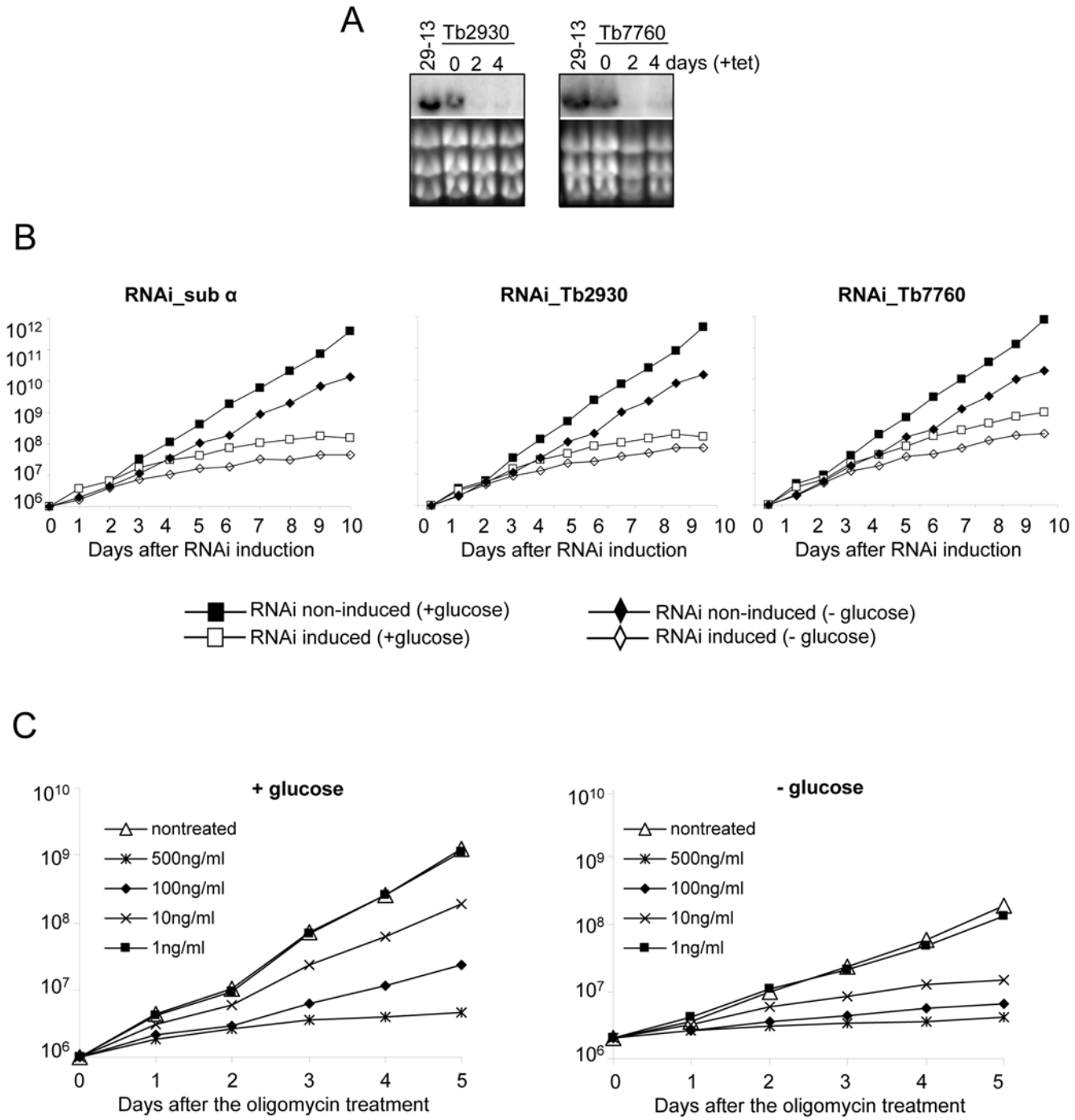

Figure 4. Subunits α, Tb7760 and Tb2930 are important for the *in vitro* growth of procyclic parasites. (A) Northern analyses of the corresponding mRNAs for Tb7760 and Tb2930 RNAi cell lines with the days sampled indicated; and stained gels of rRNAs in the lower panel serving as loading controls. (B) Growth curves of uninduced and induced RNAi-sub α (left), RNAi_Tb2930 (middle panel) and RNAi_Tb7760 (right) cell lines in the presence or absence of glucose. Cells were maintained in the exponential growth phase (between 10^6 and 10^7 cells/ml) and cumulative cell number represents the normalization of cell density by multiplication with the dilution factor. (C) Growth of the 29-13 procyclic cell line in the presence or absence of glucose and in response to treatment with the indicated concentrations of oligomycin. Cells were cultured and their growth measured as described for (B).

doi:10.1371/journal.ppat.1000436.g004

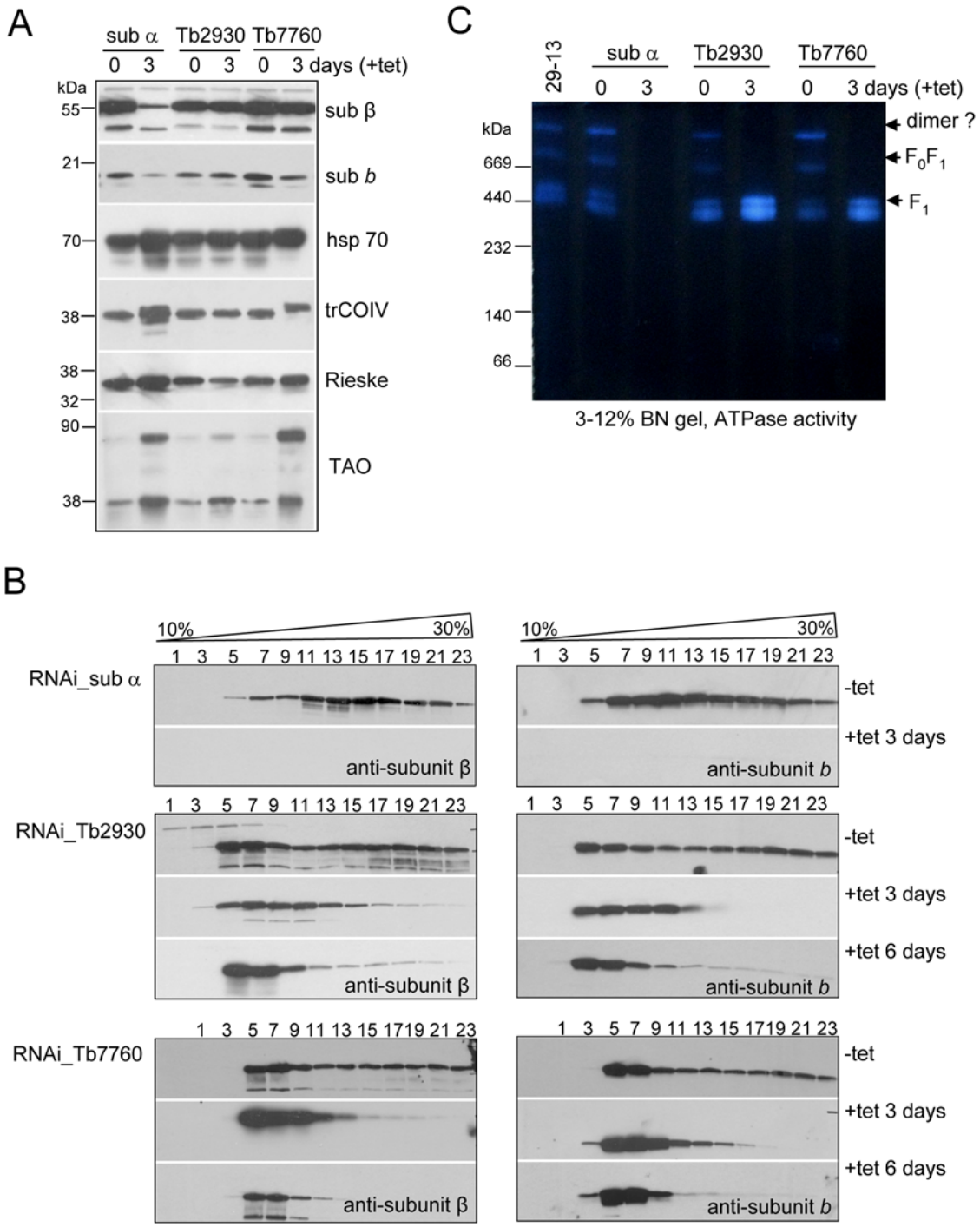

Figure 5. Effect of RNAi silencing of subunits α, Tb7760 or Tb2930 on steady-state abundance and integrity of F_0F_1-ATP synthase complex. (A) The steady state abundance of examined proteins was analyzed by Western analysis of lysed crude mitochondria (7.5 μg of proteins per well) prepared from RNAi-induced cells after 3 days and from uninduced control cells. The blots were probed with antibodies against subunits β, *b*, trCOIV, Rieske protein, mt alternative oxidase (TAO) and mt hsp 70 as a loading control. (B) Western analyses of glycerol gradient fractions (numbered from top to bottom) from crude mitochondrial lysate of RNAi cell lines grown in the absence (−tet) or presence (+tet) of tetracycline for 3 and 6 days are shown. (C) In-gel ATP hydrolysis activity of *T. brucei* F_0F_1-ATP synthase complexes after ablation of subunit α, Tb7760 or Tb2930. Mitochondrial preparations were solubilized using dodecyl maltoside and separated by 3–12% BN PAGE. In-gel ATP hydrolysis/lead phosphate precipitation assay revealed bands representing putative monomeric and dimeric ATP synthase complexes and free F_1 particles. The sizes of the native high molecular weight marker (Amersham) are indicated.
doi:10.1371/journal.ppat.1000436.g005

These observed results are intriguing because it has been proposed that, under the growth conditions used in our RNAi studies (i.e. 6 mM glucose), the function of ATP synthase is not crucial for procyclic cell survival. This was concluded from the observations that in the presence of glucose these cells are 1000-times less sensitive to the ATP synthase inhibitor oligomycin than

in the absence of glucose and that depletion of subunit β by RNAi led to cell death in glucose-depleted, but not in glucose-rich medium [15,16]. This discrepancy between our observations and published data led us to examine the growth rate of RNAi induced cells and the oligomycin sensitivity of our cell lines in the absence of glucose in the media. The parental 29–13 cells (derived from strain 427) and RNAi non-induced cells were grown in the absence of glucose for three weeks. Interestingly, the doubling time for the cells grown in the presence of glucose was between 13.9–15.5 hours, whereas the cells grown in the absence of glucose grew much slower with the doubling time reaching the values of 19.7–21.4 hours (Table 3). RNAi induction of RNAi_subα, RNAi_Tb2930 and RNAi_Tb7760 cell lines increased the doubling time significantly to 34.5, 34.5 and 28.2 hours, respectively (Figure 4B, Table 3). Addition of 1 ng/ml oligomycin to the 29–13 cell grown in the presence or absence of glucose had no effect (Figure 4C, Table 3). Higher concentrations of oligomycin slowed growth significantly for both cell lines in a similar manner. At the highest concentration of oligomycin (1 μg/ml) both cell lines died. At intermediate concentration of oligomycin (500 ng/ml and 100 ng/ml), the cells cultivated in presence of glucose survived, although they were radically elongated, thin, and did not proliferate, whereas cells cultivated in the absence of glucose died. These results suggests that the 29–13 procyclic cells are more sensitive to oligomycin treatment than EATRO1125 cells used in the published studies [15,16] and ATP synthase plays an important role in the growth and proliferation of these cells even in the presence of glucose.

Silencing of subunits α, Tb2930 or Tb7760 disrupts the ATP synthase complex

Western analysis of crude mitochondrial fractions prepared three days after RNAi induction of subunit α revealed a substantial loss of subunits β and *b* compared to non-induced cells (Figure 5A). The same Western analysis using the crude mitochondrial fraction from Tb2930 and Tb7760 RNAi-induced cells showed almost no changes in steady-state abundance of subunits β and *b*, suggesting that the F_1 moiety together with subunit b was still assembled and stable in these cells (Figure 5A). To investigate potentially secondary effects on mt membrane biogenesis, we probed the same samples with antibodies against two subunits of the respiratory complexes III and IV. The abundance of the subunit trCOIV and Rieske protein remained unaltered in the analyzed cells. However, the level of the alternative oxidase protein was increased by day 3 in all examined RNAi cell lines suggesting that cells may have undergone some compensation for the perturbation of the classical respiratory pathway. Mt heat-shock protein (hsp) 70 was used as a loading control (Figure 5A).

Table 3. Effect of RNAi and oligomycin on the doubling time of procyclic *T. brucei* cell lines growing in the presence (+) or absence (−) of glucose in the media.

Cell line	Doubling time	
	+glucose	−glucose
RNAi subunit α – NON	15.5	21.4
RNAi subunit α – IND	34.5	38.0
RNAi Tb2930 – NON	15.3	21.3
RNAi Tb2930 – IND	34.5	36.0
RNAi Tb7760 – NON	14.5	20.8
RNAi Tb7760 – IND	28.2	32.6
29-13	13.9	19.7
29-13+1 ug/ml oligomycin	34.4	41.7
29-13+500 ng/ml oligomycin	34.9	41.4
29-13+100 ng/ml oligomycin	26.7	37.4
29-13+10 ng/ml oligomycin	17.6	30.4
29-13+1 ng/ml oligomycin	14.3	18.4

doi:10.1371/journal.ppat.1000436.t003

To further characterize the consequences of a lack of subunit α, Tb2930 or Tb7760, all of which resulted in slower growth, we investigated the structural integrity of the ATP synthase complex. Crude mitochondrial lysates of RNAi cells, in which subunits α, Tb2930, or Tb7760 were expressed or repressed for 3 and 6 days, were fractionated on glycerol gradients and examined by Western analysis using the polyclonal antibodies against subunits β and *b*. In RNAi-sub α non-induced cells these two subunits co-sedimented in glycerol gradient fractions 5–23 (10–50S). However, no signal was observed with glycerol gradient fractions of crude mt lysate from 3 days RNAi-sub α induced cells (Figure 5B). This is in agreement with the reduced level of the steady state abundance of the subunit β and *b* (Figure 5A). These findings are similar to those observed in yeast [41], where the absence of the α subunit led to reduced levels of subunits β and b, presumably because the F_0F_1-ATP synthase does not assemble properly and its unincorporated subunits are degraded and/or mislocalized. In contrast, silencing of the Tb2930 and Tb7760 genes had a strong qualitative effect on integrity of the complex, resulting in a shift of complexes from higher to lower S values. This effect was even more pronounced at day 6 after RNAi induction when most of the signal for subunit β and *b* was found in fractions 5–7 (Figure 5B). Based on our data from immunoprecipitation experiments we may conclude that the F_0F_1 ATP synthase is disrupted in the absence of Tb2930 and Tb7760 and only the free F_1 particles with bound subunit *b* are observed by Western blot. To assess whether sedimentation of other mt complexes does not change we used monoclonal antibody mAb52, which recognizes a native epitope of the NADH-ubiquinone oxidoreductase complex [23]. No significant changes were observed (Figure S4).

The influence of lack of subunit α, Tb7760, or Tb2930 on the ATP synthase assembly was further examined by BN PAGE analysis of dodecyl-maltoside-solubilized mitochondria in combination with activity-based staining, as described above (Figure 5C). For the parental 29.13 cells as well as for uninduced controls, the ATP synthase was found as monomer, putative dimer, and also as free F_1 particles, as observed in Figure 3. For the subunit α-silenced cells, no ATPase activity was detected. This is in agreement with the experiments described above showing that F_1 and F_0F_1 complexes are absent from the mitochondria of RNAi-sub α silenced cells. For subunit Tb2930- and Tb7760-silenced mitochondria, activity based bands representing the putative F_1F_0 monomer and dimer disappeared. In contrast, abundance and activity of the free F_1 moiety both increased. Altogether, these analyses indicated that subunit Tb2930 and Tb7760 are required for a correct assembly of the other ATP synthase subunits and/or for the stability of the supramolecular structure of the complex.

Subunits α, Tb2930, and Tb7760 are essential for ATP synthesis but only subunit α is also essential for ATP hydrolysis

Mitochondrial ATP is produced in PFs via three different pathways that can be assayed in isolated intact mitochondria [33]. (i) Succinate appears to be the main substrate for oxidative

phosphorylation with succinate dehydrogenase loading the respiratory chain with electrons, which generates a proton gradient that drives mitochondrial F_0F_1 ATP synthase. (ii) α-ketoglutarate induces ATP production by substrate level phosphorylation occurring in a partial citric acid cycle and (iii) pyruvate induces ATP production by substrate level phosphorylation occurring in the acetate-succinate CoA transferase/succinyl-CoA synthetase cycle. In all three knockdown cell lines the succinate dehydrogenase-dependent ATP production was reduced 80–90% at day three after RNAi induction (Figure 6A, B, C). Both pyruvate and α-ketoglutarate-induced ATP synthesis appear somewhat decreased upon down-regulation of Tb2930 and Tb7760 proteins (Figure 6B, C); suggesting that other mitochondrial processes may be secondarily affected by the silencing of these two subunits. Taken together, these results showed that subunits α, Tb2930 and Tb7760 are critical for ATP synthesis by oxidative phoshorylation in PF stage *T. brucei*.

In addition to ATP synthetic activity the ATP synthase complex possesses also ATP hydrolytic activity, but this reverse function is not dependent on the F_0 moiety. ATPase activity was measured via release of free phosphate in digitonin-extracted mitochondria prepared from non-induced and from RNAi-induced cells. In non-induced cells the concentration of free phosphate was 80 ± 3.7, 96 ± 3.1 and 95 ± 8.4 nmol in RNAi_α, RNAi_2930 and RNAi_7760 samples, respectively. This minor increase of ATPase activity observed in non-induced RNAi-Tb7760 and Tb2930 compared to non-induced RNAi-sub α cell line may be caused by leaky transcription of dsRNAi even in the absence of tet, thus inducing a partial RNAi phenotype. This effect was also noticeable in Western analysis of glycerol gradient fractions, where an

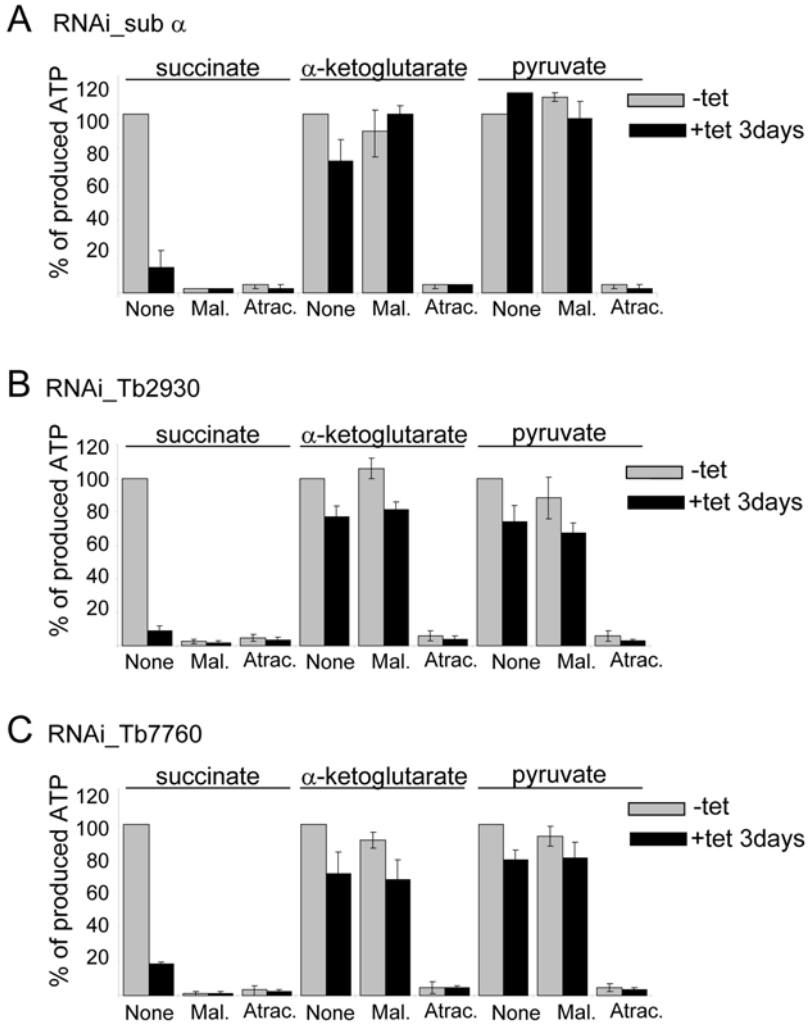

Figure 6. Effect of RNAi-mediated ablation of subunits α, Tb7760 or Tb2930 on mitochondrial ATP production. Crude mitochondrial preparations from uninduced and 3-day RNAi-silenced RNA_sub α (A), RNAi_Tb2930 (B) and RNAi_Tb7760 (C) cells were obtained by digitonin extraction and ATP production in the three mitochondrial pathways was measured individually. ATP-production was triggered by the addition of ADP plus one of the following substrates, succinate, α-ketoglutarate and pyruvate/succinate. Uninduced cells (−tet) are shown in grey, induced (+tet) are shown in black. The tested substrate is indicated at the top. Malonate (Mal.), a specific inhibitor of succinate dehydrogenase, was used to inhibit ATP production by oxidative phosphorylation and atractyloside (Atrac.) was used to inhibit import of ADP into mitochondria. Addition of these compounds to the sample is indicated at the bottom of each panel. ATP production in mitochondria isolated from uninduced cells and tested without additions of malonate or atractyloside (None) was set to 100%. The bars represent means expressed as percentages from three independent RNAi inductions. Standard deviations are indicated.
doi:10.1371/journal.ppat.1000436.g006

accumulation of 10S complexes is obvious in non-induced RNAi-Tb7760 and Tb2930 cells (Figure 5B, middle and lower panels). Leaky RNAi is not unusual in this system [19,42].

Oligomycin is a specific inhibitor of the F_0F_1 ATP synthase complex, putatively binding on the interface of subunit *a* and *c*-ring oligomer and blocking the rotary proton translocation in F_0. If the enzyme is well-coupled, the activity of F_1 is also blocked.

After the oligomycin treatment the concentration of free phosphate decreased down to 54±0.7 nmol, 59±8 and 61±0.7 in non-induced RNAi_α, RNAi_2930 and RNAi_7760 samples, respectively, which corresponds to reduction of ATPase activity by 33%, 37% and 36%.

Azide, an inhibitor of both F_0F_1 and the F_1 moiety alone decreased the ATPase activity slightly more by 38%, 50% and 42% (Figure 7). This is comparable to oligomycin- and azide-induced inhibition observed in other experiments with crude mt fractions from *T. brucei*, indicating the presence of other ATP hydrolytic activities in these crude mt preparations [43,44]. Silencing of sub α for three days led to a reduction of the concentration of free phosphate down to 48±3.8, which is comparable to the reduction obtained with oligomycin and/or azide. Addition of oligomycin and/or azide to these extracts resulted in minor further decreases of ATPase activity (Figure 7). These results demonstrate that the azide- and oligomycin- sensitive ATPase activities in these extracts were almost completely abolished, consistent with the results from the Western and BN PAGE analyses (Figure 5B, C). Thus, silencing of ATP synthase subunit α resulted in extensive and specific reduction of both azide- and oligomycin- sensitive activities of F_0F_1-ATP synthase complex.

Different results were observed for subunits Tb2930 and Tb7760. When the Tb2930 and Tb7760 subunits were silenced for three days, the total amount of the free phosphate increased to 112±5.2 and 104±7.6 nmol, respectively (Figure 7). This ATPase activity was still slightly oligomycin sensitive, suggesting that some of the 20S and 40S intact complexes remained in the mitochondria after three days of RNAi induction, consistent with the results from the Western analyses (Figure 5B). It should be noted that oligomycin in high concentrations also affects the activity of mitochondrial F_1 and $Na^{+/}K^+$ ATPases [45,46]. Treatment with azide decreased the amount of the free phosphate down to 45±6.3 and 46±6.8 nmol, respectively, which is comparable to the levels seen in non-induced oligomycin- or azide-treated cells (Figure 7). These results show that after the RNAi induction the azide-sensitive and oligomycin-insensitive ATPase activity increased significantly compared to non-induced cells. Thus, the loss of Tb2930 and Tb7760 subunits disrupts the F_0F_1 complex, resulting in release of functional F_1 sector.

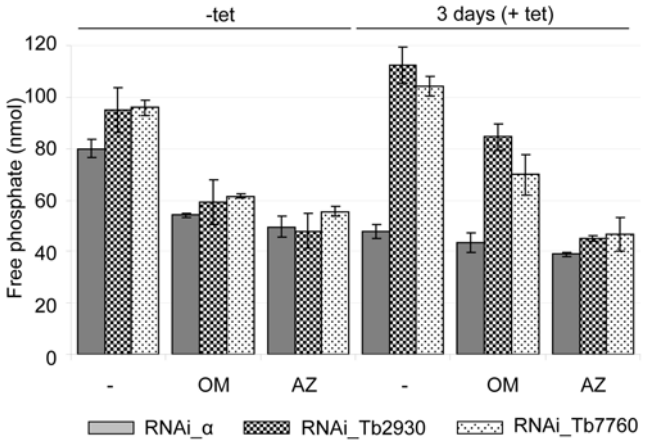

Figure 7. Effect of RNAi-mediated ablation of subunits α, Tb7760 or Tb2930 on mitochondrial ATPase activity. Crude mitochondrial preparations from uninduced and 3 days RNAi-silenced cells were obtained by digitonin extraction and ATPase activity was assayed by measuring release of free phosphate. Shown are data for RNAi_sub α (grey columns), RNAi_Tb2930 (small checker board columns) and RNAi_7760 (dotted diamonds columns) cell lines uninduced and induced for three days. ATP synthase inhibitors oligomycin (OM, 2.5 µg/ml) and azide (AZ, 1 mM) were added as indicated. Average numbers for three assays are shown, using extract preparation from three independent RNAi experiments.
doi:10.1371/journal.ppat.1000436.g007

Discussion

We report here the composition of the *T. brucei* F_0F_1-ATP synthase complex and its importance for the survival of the procyclic stage of the parasite. ATP synthase complexes and subcomplexes were purified by a combination of tandem-affinity chromatography, glycerol gradient sedimentation, immunoprecipitation, and blue native gel electrophoresis. The complexes were found by mass spectrometry to be composed of up to 22 subunits with molecular masses ranging from 8.6 to 55.7 kDa. Eight of these proteins are related to F_1 subunits α, β, γ, δ, and ε and F_0 subunits *b*, *c* and OSCP. The other 14 proteins have no recognizable eukaryotic counterparts and thus appear to be specific to *Trypanosoma*. The association of two of the novel proteins with the F_0F_1-ATP synthase complex was verified using reciprocal TAP tag analyzes, which also confirmed the association of other novel components. Some of these F_0F_1 associated novel proteins may have functionally and structurally replaced the accessory subunits *d*, *e*, *g*, *h*, IF1 that are conserved among the eukaryotic mitochondrial F_0F_1-ATP synthases. Gene silencing studies show that F_0F_1-ATP synthase subunit α and two of the novel proteins are essential for structural integrity of the F_0F_1-ATP synthase complex and for survival of PF *T. brucei*.

The 22 proteins identified in the F_0F_1-ATP synthase complex have an approximate total mass of ≤820 kDa. This size was calculated using the predicted protein mass without the predicted mt signal peptides, which are cleaved after the import into mitochondria and assuming that the monomer contains three subunits each of α and β and 10 subunits *c* (Table S1). This predicted molecular weight of the F_0F_1-ATP synthase complex roughly corresponds to that of an ATP hydrolytic complex that was resolved by BN PAGE, consistent with it being the F_0F_1-ATP synthase monomer. The BN PAGE also revealed bands consistent with dissociated F_1-ATPase particles and a putative dimer of the complex. The *Trypanosoma* F_0F_1-ATP may exist as a dimer *in vivo*, which might be essential for biogenesis of cristae as has recently been shown for yeast and mammalian mitochondria [47,48]. This profile is similar to those observed for mammalian and yeast F_0F_1-ATP synthase complexes on BN PAGE, although their molecular masses are only between 550–580 kDa [12,49–51].

The mitochondrially encoded subunit *a* was not identified in our purified F_0F_1-ATP synthase complex preparations. This may due to its possible transient association with the oligomeric *c*-ring as has been seen in other systems [52] and indeed this subunit was identified in *Escherichia coli* only using cross-linkers [53]. Subunit ε and the small and hydrophobic subunit *c* were each identified in only one TAP-tag experiment. This probably reflects technical difficulties with routine mass spectrometric identification of the proteins which are smaller than 10 kDa, have few tryptic fragments, are strongly hydrophobic, and are membrane associated.

The RNAi knockdown studies showed that F_0F_1-ATP synthase is essential for growth of the PF *T. brucei* cells. Knockdown of subunit α expression resulted in dramatic loss of the complex while knockdowns of Tb2930 or Tb7760 protein expression resulted in dissociation of the complex and release of the F_1 subcomplex, showing that these subunits are essential for complex integrity. ATP synthase monomer and dimer and their ATPase activities were not detected by BN PAGE analyses of mitochondria from induced RNAi-Tb7760 and -Tb2930 cells. However, dissociated F_1 particles were present and had increased ATPase activity in the BN PAGE gel assay and in our metabolic assays. This resembles the result of deletion of yeast subunit *d* (ATP7), *f* (ATP17) or *h* (ATP14), which result in correct assembly of the F_1 moiety, its dissociation from the F_0 moiety, and increased turnover of unassembled F_0 subunits [54–56]. Whether the novel subunits Tb7760 and Tb2930 have functional homologs in other systems remain to be determined. In contrast to subunit Tb7760- and Tb2930-depleted cells, purified mitochondria from RNAi_sub α induced cells lacked all three complexes active for ATPase activity, and oligomycin- and azide-sensitive ATPase activities were almost completely abolished. These results resemble those observed in yeast where the absence of the α subunit resulted in absence of the F_1 moiety, impaired assembly of the F_0 moiety, and degradation and/or mislocalization of its unincorporated subunits [41]. While we did not assess the status of the F_0 moiety directly we conclude that the novel subunits Tb2930 and Tb7760 are required for structural integrity of the F_0F_1-ATP synthase while subunit α is essential for proper assembly of the F_1 sector and the integrity of the F_0F_1-ATP synthase complex.

The requirement for F_0F_1-ATP synthase complex function in PF cells is intriguing since importance of mt ATP generation by oxidative phosphorylation in PF cells has been questioned [15,33]. *T. brucei* EATRO1125 PF cells were reported to be 1000 times less sensitive to the F_0F_1-ATP synthase inhibitor oligomycin in the presence of glucose than in its absence [57]. In addition, silencing of subunit β of the F_0F_1-ATPsynthase led to cell death in glucose-depleted, but not in glucose-rich medium [16]. In contrast, we found that glucose could not rescue the lethal effects of knocking down expression of any of the three subunits tested in our 29–13 PF cells (Figure 4B). Furthermore, the presence of glucose in the medium had little effect on sensitivity of the parental 29–13 cell line to oligomycin (Figure 4C). Finally, while the EATRO1125 PF strain was able to adapt to glucose-depleted medium without a decrease of the doubling time, our PF 29–13 cells grew more slowly after removal of glucose from the medium (doubling time 19.7 h vs. 13.8 h). Thus, the 29–13 PF strain that was used in this study, which is derived from strain 427 [21], appears to differ in its relative glycolytic and oxidative phosphorylation capacity from the EATRO1125 strain that was used in other studies [15,16]. Moreover, while the bloodstream 1125 cell line is a pleomorphic line and may be more dependent on substrate phosphorylation, the 427 cells are laboratory adapted and unable to establish metacyclic infections in tsetse fly [58,59]. Thus, they may have lost some of the original metabolic flexibility of procyclic trypanosomes. It would be interesting to test in future studies the dependency on substrate vs. oxidative phosphorylation in recent field isolates of procyclic trypanosomes. Our results, including the fact that mitochondria isolated from RNAi-induced cells had lost the ability to produce ATP via the oxidative phosphorylation pathway suggest that the observed severe growth phenotype after silencing of ATP synthase subunits is caused by inhibition of oxidative phosphorylation and the consequent lack of ATP.

Overall, this study characterized the composition of the F_0F_1-ATP synthase complex, identified several protein components that are unique to the *Trypanosoma*, and showed that the conserved α subunit protein and two newly identified subunits, Tb2930 and Tb7760, are important for the structural integrity and proper function of the complex as well as for viability of *T. brucei* PF stage cells. The structural organization of the F_0F_1-ATP synthase complex and the specific functions of its protein components remain to be elucidated as does its physiological integration within this organism that regulates oxidative phosphorylation and glycolysis during its life cycle. In conclusion, the identification and characterization of ATP synthase in *T. brucei* represents a major step towards deciphering the unique and essential properties of the respiratory chain of both an early diverged eukaryote and a lethal human parasite.

Supporting Information

Figure S1 Alignments of ATP synthase subunits delta (A), epsilon (B) and c (C).
Found at: doi:10.1371/journal.ppat.1000436.s001 (0.02 MB PDF)

Figure S2 Fractionation of TAP_sub b (A) and TAP_sub β (B) TEV eluates on 10–30% glycerol gradients.
Found at: doi:10.1371/journal.ppat.1000436.s002 (0.92 MB PDF)

Figure S3 MS analysis of *T. brucei* ATP synthase subunit α.
Found at: doi:10.1371/journal.ppat.1000436.s003 (0.02 MB PDF)

Figure S4 Dot blot analysis of the glycerol gradient-fractionated cleared mitochondrial lysates showing the sedimentation profile of the oxidoreductase complex.
Found at: doi:10.1371/journal.ppat.1000436.s004 (0.31 MB PDF)

Table S1 LC-MS/MS analysis of *T. brucei* ATP synthase complex.
Found at: doi:10.1371/journal.ppat.1000436.s005 (0.03 MB XLS)

Acknowledgments

We thank Yuko Ogata and Atashi Anupama for help with mass spectrometry and data analysis. We also thank Rob Benne, Dave Speijer, Larry Simpson and Minu Chaudhuri for kindly providing antibodies. We are grateful to other members of the Stuart lab for helpful discussions.

Author Contributions

Conceived and designed the experiments: AZ AS AKP KDS. Performed the experiments: AZ AS RAD. Analyzed the data: AZ AS RAD. Wrote the paper: AZ AS KDS.

References

1. Simarro PP, Jannin J, Cattand P (2008) Eliminating human African trypanosomiasis: where do we stand and what comes next? PLoS Med 5: e55. doi:10.1371/journal.pmed.0050055.
2. Bringaud F, Riviere L, Coustou V (2006) Energy metabolism of trypanosomatids: adaptation to available carbon sources. Mol Biochem Parasitol 149: 1–9.
3. Besteiro S, Barrett MP, Riviere L, Bringaud F (2005) Energy generation in insect stages of Trypanosoma brucei: metabolism in flux. Trends Parasitol 21: 185–191.
4. Schnaufer A, Clark-Walker GD, Steinberg AG, Stuart K (2005) The F(1)-ATP synthase complex in bloodstream stage trypanosomes has an unusual and essential function. EMBO J 24: 4029–4040.
5. Brown SV, Hosking P, Li J, Williams N (2006) ATP synthase is responsible for maintaining mitochondrial membrane potential in bloodstream form *Trypanosoma brucei*. Eukaryot Cell 5: 45–53.
6. Nolan DP, Voorheis HP (1992) The mitochondrion in bloodstream forms of *Trypanosoma brucei* is energized by the electrogenic pumping of protons catalysed by the F_1F_0-ATPase. Eur J Biochem 209: 207–216.
7. Opperdoes FR, Borst P, De Rijke D (1976) Oligomycin Sensitivity of the Mitochondrial Atpase as a Marker for Fly Transmissability and the Presence of Functional Kinetoplast DNA in African Trypanosomes. Comp Biochem Physiol (B) 55B: 25–30.

8. Walker JE, Dickson VK (2006) The peripheral stalk of the mitochondrial ATP synthase. Biochim Biophys Acta 1757: 286–296.
9. von BC, Cook GM, Dimroth P (2008) Unique rotary ATP synthase and its biological diversity. Annu Rev Biophys 37: 43–64.: 43–64.
10. Velours J, Arselin G (2000) The *Saccharomyces cerevisiae* ATP synthase. J Bioenerg Biomembr 32: 383–390.
11. Arnold I, Pfeiffer K, Neupert W, Stuart RA, Schagger H (1999) ATP synthase of yeast mitochondria. Isolation of subunit j and disruption of the ATP18 gene. J Biol Chem 274: 36–40.
12. Arnold I, Pfeiffer K, Neupert W, Stuart RA, Schagger H (1998) Yeast mitochondrial F1F0-ATP synthase exists as a dimer: identification of three dimer-specific subunits. EMBO J 17: 7170–7178.
13. Vaillier J, Arselin G, Graves PV, Camougrand N, Velours J (1999) Isolation of supernumerary yeast ATP synthase subunits e and i. Characterization of subunit i and disruption of its structural gene ATP18. J Biol Chem 274: 543–548.
14. Meyer B, Wittig I, Trifilieff E, Karas M, Schagger H (2007) Identification of two proteins associated with mammalian ATP synthase. Mol Cell Proteomics 6: 1690–1699.
15. Coustou V, Besteiro S, Biran M, Diolez P, Bouchaud V, et al. (2003) ATP generation in the *Trypanosoma brucei* procyclic form: cytosolic substrate level is essential, but not oxidative phosphorylation. J Biol Chem 278: 49625–49635.
16. Coustou V, Biran M, Breton M, Guegan F, Riviere L, et al. (2008) Glucose-induced remodeling of intermediary and energy metabolism in procyclic *Trypanosoma brucei*. J Biol Chem 283: 16342–16354.
17. Jensen BC, Kifer CT, Brekken DL, Randall AC, Wang Q, et al. (2006) Characterization of protein kinase CK2 from *Trypanosoma brucei*. Mol Biochem Parasitol 151: 28–40.
18. Panigrahi AK, Schnaufer A, Ernst NL, Wang B, Carmean N, et al. (2003) Identification of novel components of *Trypanosoma brucei* editosomes. RNA 9: 484–492.
19. Wang Z, Morris JC, Drew ME, Englund PT (2000) Inhibition of *Trypanosoma brucei* gene expression by RNA interference using an integratable vector with opposing T7 promoters. J Biol Chem 275: 40174–40179.
20. Inoue M, Nakamura Y, Yasuda K, Yasaka N, Hara T, et al. (2005) The 14-3-3 proteins of *Trypanosoma brucei* function in motility, cytokinesis and cell cycle. J Biol Chem 280: 14085–14096.
21. Wirtz E, Leal S, Ochatt C, Cross GAM (1999) A tightly regulated inducible expression system for conditional gene knock-outs and dominant-negative genetics in *Trypanosoma brucei*. Mol Biochem Parasitol 99: 89–101.
22. Maslov DA, Zikova A, Kyselova I, Lukes J (2002) A putative novel nuclear-encoded subunit of the cytochrome c oxidase complex in trypanosomatids. Mol Biochem Parasitol 125: 113–125.
23. Panigrahi AK, Zikova A, Dalley RA, Acestor N, Ogata Y, et al. (2008) Mitochondrial complexes in *Trypanosoma brucei*: a novel complex and a unique oxidoreductase complex. Mol Cell Proteomics 7: 534–545.
24. Zikova A, Panigrahi AK, Dalley RA, Acestor N, Anupama A, et al. (2008) *Trypanosoma brucei* mitochondrial ribosomes: affinity purification and component identification by mass spectrometry. Mol Cell Proteomics 7: 1286–1296.
25. Puig O, Caspary F, Rigaut G, Rutz B, Bouveret E, et al. (2001) The tandem affinity purification (TAP) method: a general procedure of protein complex purification. Methods 24: 218–229.
26. Rigaut G, Shevchenko A, Rutz B, Wilm M, Mann M, Seraphin B (1999) A generic protein purification method for protein complex characterization and proteome exploration. Nat Biotechnol 17: 1030–1032.
27. Schnaufer A, Ernst N, O'Rear J, Salavati R, Stuart K (2003) Separate Insertion and Deletion Sub-complexes of the *Trypanosoma brucei* RNA Editing Complex. Mol Cell 12: 307–319.
28. Gavin AC, Bosche M, Krause R, Grandi P, Marzioch M, et al. (2002) Functional organization of the yeast proteome by systematic analysis of protein complexes. Nature 415: 141–147.
29. Keller A, Purvine S, Nesvizhskii AI, Stolyar S, Goodlett DR, Kolker E (2002) Experimental protein mixture for validating tandem mass spectral analysis. OMICS 6: 207–212.
30. Nesvizhskii AI, Keller A, Kolker E, Aebersold R (2003) A statistical model for identifying proteins by tandem mass spectrometry. Anal Chem 75: 4646–4658.
31. Tan TH, Bochud-Allemann N, Horn EK, Schneider A (2002) Eukaryotic-type elongator tRNAMet of *Trypanosoma brucei* becomes formylated after import into mitochondria. Proc Natl Acad Sci U S A 99: 1152–1157.
32. Law RH, Manon S, Devenish RJ, Nagley P (1995) ATP synthase from *Saccharomyces cerevisiae*. Methods Enzymol 260: 133–163.
33. Bochud-Allemann N, Schneider A (2002) Mitochondrial substrate level phosphorylation is essential for growth of procyclic *Trypanosoma brucei*. J Biol Chem 277: 32849–32854.
34. Horvath A, Horakova E, Dunajcikova P, Verner Z, Pravdova E, et al. (2005) Downregulation of the nuclear-encoded subunits of the complexes III and IV disrupts their respective complexes but not complex I in procyclic *Trypanosoma brucei*. Mol Microbiol 58: 116–130.
35. Collinson IR, Runswick MJ, Buchanan SK, Fearnley IM, Skehel JM, et al. (1994) Fo membrane domain of ATP synthase from bovine heart mitochondria: purification, subunit composition, and reconstitution with F1-ATPase. Biochemistry 33: 7971–7978.
36. Speijer D, Breek CK, Muijsers AO, Hartog AF, Berden JA, et al. (1997) Characterization of the respiratory chain from cultured *Crithidia fasciculata*. Mol Biochem Parasitol 85: 171–186.
37. Bhat GJ, Koslowsky DJ, Feagin JE, Smiley BL, Stuart K (1990) An extensively edited mitochondrial transcript in kinetoplastids encodes a protein homologous to ATPase subunit 6. Cell 61: 885–894.
38. Nelson RE, Aphasizheva I, Falick AM, Nebohacova M, Simpson L (2004) The I-complex in *Leishmania tarentolae* is an uniquely-structured F(1)-ATPase. Mol Biochem Parasitol 135: 221–224.
39. Schagger H, von Jagow G (1991) Blue native electrophoresis for isolation of membrane protein complexes in enzymatically active form. Anal Biochem 199: 223–231.
40. Maslov DA, Nawathean P, Scheel J (1999) Partial kinetoplast-mitochondrial gene organization and expression in the respiratory deficient plant trypanosomatid Phytomonas serpens. Mol Biochem Parasitol 99: 207–221.
41. Lai-Zhang J, Xiao Y, Mueller DM (1999) Epistatic interactions of deletion mutants in the genes encoding the F1-ATPase in yeast *Saccharomyces cerevisiae*. EMBO J 18: 58–64.
42. Durand-Dubief M, Kohl L, Bastin P (2003) Efficiency and specificity of RNA interference generated by intra- and intermolecular double stranded RNA in *Trypanosoma brucei*. Mol Biochem Parasitol 129: 11–21.
43. Bienen EJ, Shaw MK (1991) Differential expression of the oligomycin-sensitive ATPase in bloodstream forms of *Trypanosoma brucei brucei*. Mol Biochem Parasitol 48: 59–66.
44. Williams N (1994) The mitochondrial ATP synthase of *Trypanosoma brucei*: Structure and regulation. J Bioenerg Biomembr 26: 173–178.
45. Homareda H, Ishii T, Takeyasu K (2000) Binding domain of oligomycin on Na(+),K(+)-ATPase. Eur J Pharmacol 400: 177–183.
46. rato-Oshima T, Matsui H, Wakizaka A, Homareda H (1996) Mechanism responsible for oligomycin-induced occlusion of Na+ within Na/K-ATPase. J Biol Chem 271: 25604–25610.
47. Arselin G, Vaillier J, Salin B, Schaeffer J, Giraud MF, et al. (2004) The modulation in subunits e and g amounts of yeast ATP synthase modifies mitochondrial cristae morphology. J Biol Chem 279: 40392–40399.
48. Minauro-Sanmiguel F, Wilkens S, Garcia JJ (2005) Structure of dimeric mitochondrial ATP synthase: novel F0 bridging features and the structural basis of mitochondrial cristae biogenesis. Proc Natl Acad Sci U S A 102: 12356–12358.
49. Schagger H (1995) Native electrophoresis for isolation of mitochondrial oxidative phosphorylation protein complexes. Methods Enzymol 260: 190–202.: 190–202.
50. Jansch L, Kruft V, Schmitz UK, Braun HP (1996) New insights into the composition, molecular mass and stoichiometry of the protein complexes of plant mitochondria. Plant J 9: 357–368.
51. Kruft V, Eubel H, Jansch L, Werhahn W, Braun HP (2001) Proteomic approach to identify novel mitochondrial proteins in Arabidopsis. Plant Physiol 127: 1694–1710.
52. Wittig I, Velours J, Stuart R, Schagger H (2008) Characterization of domain-interfaces in monomeric and dimeric ATP synthase. Mol Cell Proteomics 7: 995–1004.
53. Jiang W, Fillingame RH (1998) Interacting helical faces of subunits a and c in the F1Fo ATP synthase of Escherichia coli defined by disulfide cross-linking. Proc Natl Acad Sci U S A 95: 6607–6612.
54. Norais N, Prome D, Velours J (1991) ATP synthase of yeast mitochondria. Characterization of subunit d and sequence analysis of the structural gene ATP7. J Biol Chem 266: 16541–16549.
55. Spannagel C, Vaillier J, Arselin G, Graves PV, Velours J (1997) The subunit f of mitochondrial yeast ATP synthase–characterization of the protein and disruption of the structural gene ATP17. Eur J Biochem 247: 1111–1117.
56. Goyon V, Fronzes R, Salin B, di-Rago JP, Velours J, Brethes D (2008) Yeast cells depleted in Atp14p fail to assemble Atp6p within the ATP synthase and exhibit altered mitochondrial cristae morphology. J Biol Chem 283: 9749–9758.
57. Lamour N, Riviere L, Coustou V, Coombs GH, Barrett MP, Bringaud F (2005) Proline metabolism in procyclic *Trypanosoma brucei* is down-regulated in the presence of glucose. J Biol Chem 280: 11902–11910.
58. Szoor B, Wilson J, McElhinney H, Tabernero L, Matthews KR (2006) Protein tyrosine phosphatase TbPTP1: A molecular switch controlling life cycle differentiation in trypanosomes. J Cell Biol 175: 293–303.
59. Herder S, Votypka J, Jirku M, Radrova J, Janzen CJ, Lukes J (2007) *Trypanosoma brucei* 29-13 strain is inducible in but not permissive for the tsetse fly vector. Exp Parasitol 117: 111–114.